Irregular Breaking Wave Transformation on a Beach and Runup on a Revetment

by

Peter G. Kearney

and

Nobuhisa Kobayashi

RESEARCH REPORT NO. CACR-01-01

May, 2001

Center for Applied Coastal Research
Ocean Engineering Laboratory
University of Delaware
Newark, DE 19716

ABSTRACT

An experiment was conducted to examine the probability distributions of the waterline elevation on a stone revetment with a 1:2 slope located in the surf zone on a gently sloping beach. The experiment consisted of 27 tests for three spectral peak periods and nine water depths at the toe of the revetment. For each test, 10 wave gauges were utilized to measure the irregular wave transformation from outside the surf zone to the revetment. A runup wire was placed parallel to the revetment to measure the waterline oscillations. An acoustic Doppler velocimeter was also utilized to measure the fluid velocities at the toe of the revetment. The wave reflection coefficients, estimated using a three-gauge array, placed just seaward of the surf zone, were estimated to be less than 0.4. The measured time series and spectra indicate the dissipation of incident waves and the generation of low-frequency waves as the water depth was decreased at the toe of the revetment. The exponential gamma distribution, with measured mean, standard deviation, and skewness, can describe all of the measure probability distributions adequately for all of the tests. The time-averaged model CSHORE predicts the measured cross-shore variations of the mean, standard deviation, and skewness fairly well. CSHORE tends to poorly predict the measured variations of kurtosis. In addition, CSHORE underpredicts the standard deviation of the waterline elevation noticeably as the depth is increased.

ACKNOWLEDGEMENTS

This study was supported by the U.S. Army Corps of Engineers' Coastal and Hydraulics Laboratory under Contract No. DACW-39-99-P-0330.

TABLE OF CONTENTS

LIST OF TABLES

LIST OF FIGURES

Chapter 1

INTRODUCTION

1.1 Coastal Structures

Various types of coastal structures can be seen protecting shorelines, ports, and harbors throughout the world and the prediction of irregular wave runup on those structures is necessary in determining the crest height of the structure. The crest height of the structure must be of significant magnitude so that overtopping of design waves does not occur. Common types of coastal structure constructed in the United States are jetties and revetments that are most often constructed as rubble mound structures (Kobayashi 1999). Rubble mound structures are typically inclined structures constructed of stone, referred to as armor units, of uniform or variable mass depending upon the design and application. Wave uprush and downrush on the seaward slope of the structure affect the wave forces acting on armor units and the stability and movement of the armor units. Currently, numerical models developed to predict the free surface elevations and velocity on permeable and impermeable slopes are available and accurate within errors of approximately 20 % (Kobayashi 1999). A simple, predictive model, as proposed in this study, is required to accurately represent irregular wave runup on coastal structures (Kearney and Kobayashi 2000).

1.2 Previous Experiments and Models

Empirical formulas for irregular wave and armor stability were developed using laboratory experiments for coastal structures in relatively deep water to reduce the number of dimensionless parameters in the formulas. Experiments were conducted to examine the effects of toe depth on irregular wave runup (Rathbun, *et al.* 1998) and armor stability (Melby and Kobayashi, 1998). However, it is difficult to develop empirical formulas that can deal with various irregular wave transformations and breaking on the beach seaward of the toe of the structure.

Time-dependent numerical models based on the finite-amplitude shallow-water equations including bottom friction have been shown to be capable of predicting the irregular wave transformation on the fronting beach and wave runup on the structure as reviewed by Kobayashi (1999). However, the time-dependent numerical models require significant computation time to resolve the breaking wave profiles varying rapidly in time and space. The present use of such models is essentially limited to research applications.

1.3 Objectives and Overview

The following study is, in part, an attempt to propose and verify a time-averaged probabilistic model, CSHORE, for practical applications as a compromise between purely empirical formulas and highly computational models. The time-averaged cross-shore momentum and energy equations derived from the finite-amplitude shallow-water equations including bottom friction are solved numerically to predict the cross-shore variation of the wave setup, $\overline{\eta}$, and root-mean-square wave height, H_{rms}, from outside the

breaking wave zone to the swash zone (Kobayashi and Johnson 1998). This model has been shown to predict the wave setup and height in the surf and swash zones on beaches. This model is extended in this study to predict the mean and standard deviation of the waterline elevation on the seaward slope of a rubble mound structure.

The probabilistic distribution of the waterline elevation with the known mean and standard deviation was expressed by the exponential gamma distribution. For shoreline elevations on natural beaches, the Gaussian distribution was shown to be a good approximation of measured distributions (Huntley *et al.* 1977) but systematic discrepancies related to time series skewness were observed (Holland and Holman 1993). On the other hand, irregular wave runup on coastal structures has not been analyzed in this manner probably because empirical formulas developed originally for regular waves deal with only the maxima of the oscillating waterline.

To verify the time-averaged model and the appropriateness of the exponential gamma distribution for irregular wave runup, experiments were conducted in a wave tank that is 30 m long, 2.44 m wide and 1.5 m high. A plywood beach with an approximate 1:32 slope and a stone revetment with a 1:2 slope were installed in the wave tank. Irregular waves based on the TMA spectrum were generated with a piston-type wave paddle. Three wave gages placed outside the surf zone were used to separate incident and reflected waves. Three movable wave gages were used to measure the irregular wave transformation on the 1:32 slope. A swash gage was placed at the toe of the 1:2 slope to measure the free surface oscillations in very shallow water. A runup wire placed parallel to the stone revetment was used to measure the waterline oscillations. An

acoustic Doppler velocimeter (ADV) was placed at the toe of the stone revetment to measure fluid velocities. The velocity data was analyzed to predict the statistics and probabilities of fluid velocities, which will be required for the future probabilistic analysis of stone movement and dislodgment.

Twenty-seven tests were conducted for three spectral peak periods; T_p = 1.5, 2.4, and 4.7 s and nine different toe depths; d_t = 4, 6, 8, 10, 12, 14, 16, 18, and 20 cm. The incident root-mean-square wave heights were taken as large as possible to avoid wave breaking at the paddle and were approximately 12 cm. The 27 data sets were analyzed to calibrate and verify the time-averaged probabilistic model for irregular wave transformation on the beach and the runup on the structure.

The following chapter provides an overview of the experimental procedures including experimental setup and armor and filter stone characteristics, as well as the equipment calibration. Free surface, wave runup, and velocity measurements are also discussed. In Chapter 3 the time series and frequency spectra are presented for the free surface and runup elevations. Statistical parameters for each test such as wave setup or setdown, $\overline{\eta}$, root-mean-square wave height, H_{rms}, skewness, s, and kurtosis, K, are also presented. Chapter 4 presents the results from the separation of incident and reflected waves. Chapter 5 presents the time series and spectra for the measured cross-shore velocities. Comparisons of the measured cross-shore time series parameters to those parameters predicted by linear long wave theory are also presented. The exponential gamma probability distribution is presented in Chapter 6 along with figures comparing the distribution with probability distribution functions for normalized free surface

elevation and runup, η^*, and normalized cross-shore component of the horizontal velocity, u_*. In Chapter 7, the numerical model CSHORE is presented along with a comparison of the results from CSHORE to the free surface and runup statistical parameters $\overline{\eta}$, H_{rms}, s, and K presented in Chapter 3. Conclusions based on the results of this study are presented in Chapter 8.

Chapter 2

EXPERIMENTAL PROCEDURES

Twenty-seven tests were conducted as a part of the experiment for this project in order to collect sufficient irregular wave, runup, and velocity data to validate the model. Because this experiment was performed to gather a broad range of data, over a relatively large range of water depths, special considerations had to be made for the revetment construction, experimental setup, and performance of the tests, to ensure the collection of reliable data. This chapter will review the experimental setup, procedures for calibration and collection of free surface and runup data, collection of velocity data, as well as a summary of the tests performed.

2.1 Experimental Setup

Tests for the experiment were conducted in a wave tank that was 30 m long, 2.44 m wide, and 1.5 m high. A plywood beach with an approximate 1:32 slope and a stone revetment with a 1:2 slope were installed in the tank as shown in Figure 2.1. The 1:2 slope consisted of an impermeable plywood layer, an approximate 4 cm filter layer of two stone thicknesses, and an approximate 14 cm armor layer of two stone thickenesses.

Irregular waves based on the TMA spectrum (Bouws, *et al.* 1985) were generated with a piston-type wave paddle. Three paddle time series were created for each of the three spectral peak periods; T_p =1.5, 2.4, and 4.7 s based on a toe water depth of 12 cm. The incident root-mean-square wave height was taken as large as possible to avoid wave breaking at the paddle and was approximately equal to 12 cm for all tests.

2.2 Stone Characteristics

The purpose of the experiment was to collect information regarding irregular wave transformation and runup on a stone revetment that was stable. Because the revetment would be subject to a large variety of water depths and wave periods, stones of sufficiently large mass were chosen to resist movement or being dislodged under the most extreme wave conditions that could be experienced during the performance of the tests. The median armor layer stone mass was calculated to be approximately equal to 100 g for a series of irregular waves with the peak period, T_p = 4.7 s, and water depth of d_t = 20 cm at the toe of the revetment (Shore Protection Manual 1984). The target median mass of the filter layer was selected as roughly half of the armor layer stone mass, but the stones for both layers were selected based on availability at the time of the experiment. To determine the basic characteristics of the armor and filter stone, tests were conducted to determine the average specific gravity of each according to the ASTM testing standard for large aggregate (ASTM C:127 2000). Mass, volume, density, and percent finer by mass were determined for each stone chosen for the

sample set of 50 stones for each layer. The results from the stone characteristic analysis were tabulated and are presented in Table 2.1 for the armor stone and Table 2.2 for the filter stone. From these results the median mass, M_{50}, was interpolated for the armor stone and the filter stone. Once the median mass was determined, the nominal diameter was calculated as defined in equation (2.1)

$$D_{n50} = \left({}^{M_{50}}\!/_{\rho_s} \right)^{1/3} \tag{2.1}$$

where ρ_s = stone density. The median mass of the armor layer was approximately equal to 89 grams, while the median mass of the filter stone was approximately equal to 16 grams. The approximate nominal diameter of the armor stone and filter stone was 7 cm and 2 cm respectively.

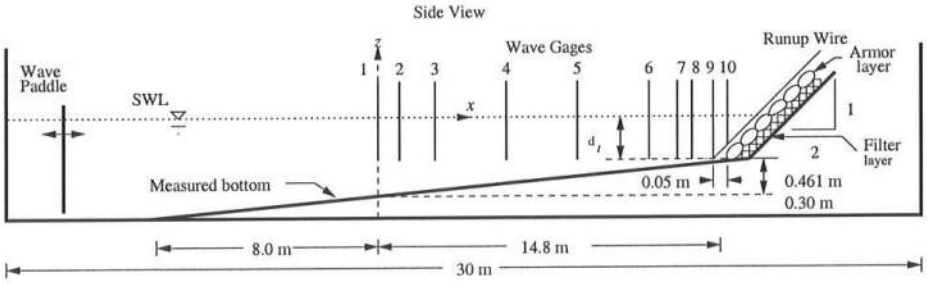

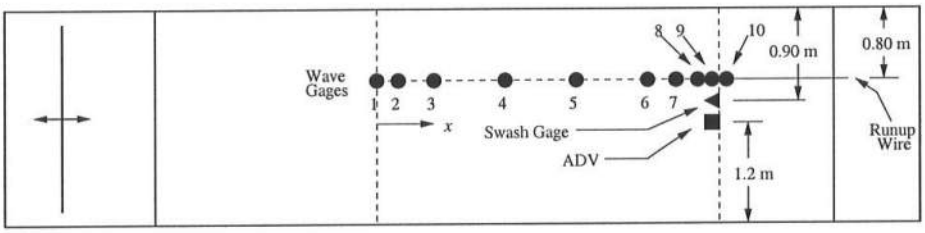

Gage Location Information

Gage Number	1	2	3	4	5	6	7	8	9 [1]	10	Runup Wire
Gage Location x = (m)	0.0	0.23	2.0	6.0	9.0	12.0	14.0	14.5	14.8	14.9	$14.75 + 2d_t$

NOTE: 1) Swash gage utilized in place of gage # 9 when d_t = 4, 6, 8, and 10 cm.
2) ADV not utilized when d_t = 4 and 6 cm.

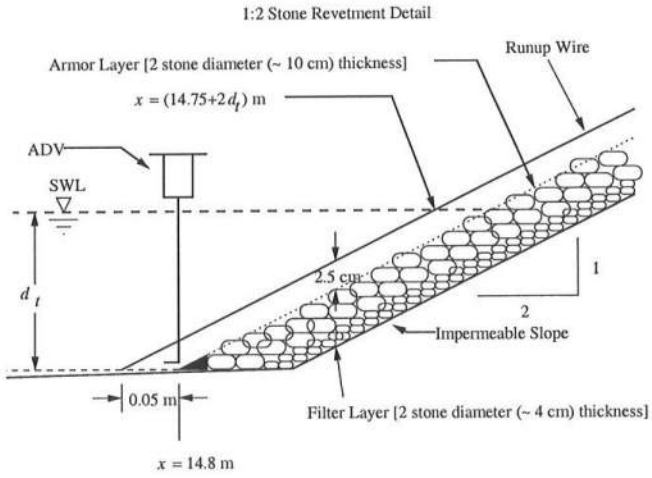

Figure 2.1: Wave Tank Configuration for 1:2 Rock Slope Experiment.

Table 2.1: Armor Stone Characteristics

Stone number	Mass (g)	Volume (cm^3)	Density (g/cm^3)	Cumulative Mass	% Finer By Mass
46	49.3	19.5	2.52	49.2	1.1
10	50.7	19.6	2.56	100.0	2.2
37	55.6	22.1	2.51	155.7	3.4
45	55.8	28.1	2.94	211.4	4.6
8	57.3	21.6	2.63	268.8	5.8
21	58.5	23.3	2.50	327.3	7.1
33	59.3	21.5	2.74	386.6	8.4
48	60.4	22.0	2.74	447.0	9.7
30	65.9	24.3	2.69	512.9	11.1
17	66.0	24.9	2.63	578.9	12.5
49	69.2	26.0	2.64	648.1	14.0
12	69.9	25.7	2.72	718.0	15.5
44	70.4	25.6	2.73	788.4	17.0
27	75.2	26.1	2.87	863.6	18.7
32	77.3	32.0	2.40	940.9	20.3
13	78.0	28.4	2.73	1018.9	22.0
43	79.5	35.7	2.21	1098.4	23.7
4	79.8	30.7	2.59	1178.1	25.5
3	79.9	30.3	2.62	1258.1	27.2
18	80.4	30.7	2.53	1338.4	28.9
40	81.0	31.3	2.57	1419.4	30.7
31	81.5	32.4	2.51	1500.9	32.4
23	82.9	36.0	2.24	1583.9	34.2
26	84.9	32.1	2.62	1668.7	36.0
50	85.22	30.8	2.75	1754.0	37.9

Table 2.1 continued: Armor Stone Characteristics

Stone number	Mass (g)	Volume (cm^3)	Density (g/cm^3)	Cumulative Mass	% Finer By Mass
19	85.4	32.0	2.65	1839.4	39.7
2	85.7	35.0	2.43	1925.1	41.6
41	86.4	32.0	2.66	2011.5	43.5
15	88.5	34.6	2.53	2100.0	45.4
9	88.6	31.5	2.75	2188.6	47.3
29	89.8	35.4	2.51	2278.4	49.2
42	93.3	35.6	2.61	2371.7	51.2
24	93.9	36.8	2.52	2465.6	53.3
47	95.5	35.7	2.66	2561.1	55.3
7	98.8	36.9	2.65	2659.8	57.5
36	103.3	38.7	2.66	2763.1	59.7
14	106.0	39.2	2.67	2869.1	62.0
25	107.7	39.3	2.73	2976.8	64.3
16	110.9	43.1	2.51	3087.7	66.7
34	112.9	41.8	2.69	3200.6	69.1
11	113.7	40.5	2.79	3314.2	71.6
5	113.9	42.3	2.68	3428.2	74.1
20	115.4	40.0	2.86	3543.5	76.5
28	118.6	44.9	2.63	3662.2	79.1
1	121.0	43.0	2.80	3783.2	81.7
35	136.2	49.1	2.76	3919.4	84.7
38	136.5	47.8	2.84	4055.9	87.6
6	177.7	64.4	2.75	4233.6	91.5
39	191.0	76.0	2.50	4424.6	95.6
22	204.6	72.3	2.80	4629.2	100.0
Total	4929.2	1748.4	131.8		
Average	92.6	35.0	2.64		

Table 2.2: Filter Stone Characteristics

Stone number	Mass (g)	Volume (cm^3)	Density (g/cm^3)	Cumulative Mass	% Finer By Mass
38	8.4	3.4	2.48	8.4	1.0
14	8.9	2.3	3.94	17.4	2.1
6	9.1	2.7	3.39	26.5	3.3
7	9.2	2.5	3.71	35.7	4.4
19	9.8	4.1	2.38	45.5	5.6
22	10.0	4.1	2.41	55.4	6.8
31	10.4	5.8	1.79	65.8	8.0
53	10.4	4.9	2.12	76.2	9.3
26	10.8	3.9	2.75	87.1	10.6
34	11.4	5.0	2.30	98.5	12.0
37	11.9	5.0	2.38	110.3	13.5
9	12.0	4.4	2.72	122.3	14.9
27	12.2	5.4	2.27	134.5	16.4
32	12.3	5.2	2.39	146.8	17.9
12	12.6	5.2	2.41	159.4	19.5
44	12.9	5.3	2.41	172.3	21.0
66	13.0	8.0	1.63	185.3	22.6
41	13.4	6.6	2.04	198.7	24.3
13	13.7	4.5	3.03	212.4	26.0
30	13.7	6.4	2.13	226.2	27.6
21	13.9	4.8	2.89	240.1	29.3
63	14.2	7.7	1.83	254.3	31.1
45	14.5	4.6	3.16	268.8	32.8
36	14.9	6.7	2.22	283.7	34.7
48	14.9	7.6	1.97	298.6	36.5

Table 2.2 continued: Filter Stone Characteristics

Stone number	Mass (g)	Volume (cm^3)	Density (g/cm^3)	Cumulative Mass	% Finer By Mass
25	15.1	7.4	2.03	313.9	38.3
55	15.3	6.1	2.51	329.0	40.2
40	15.5	6.3	2.47	344.5	42.1
65	15.6	7.2	2.17	360.1	44.0
3	15.7	6.2	2.51	375.7	45.9
39	15.8	5.9	2.66	391.5	47.8
64	15.9	7.1	2.23	407.4	49.8
11	17.4	7.6	2.29	424.8	51.9
62	17.5	7.3	2.38	442.2	54.0
16	17.8	7.7	2.31	460.0	56.2
43	17.8	7.7	2.31	477.8	58.4
47	17.9	7.1	2.52	495.7	60.6
15	18.1	6.1	2.95	513.9	62.8
28	19.1	7.1	2.67	532.9	65.1
4	20.0	8.0	2.50	552.9	67.5
61	20.5	7.6	2.69	573.4	70.0
1	22.0	9.4	2.35	595.4	72.7
23	23.6	10.7	2.20	619.0	75.6
33	25.1	10.4	2.41	644.1	78.7
5	27.3	12.5	2.19	671.4	82.0
17	27.7	13.0	2.13	699.1	85.4
18	27.9	11.8	2.36	727.0	88.8
29	28.4	14.1	2.02	755.4	92.3
10	29.3	13.7	2.13	784.7	95.9
2	33.9	17.8	1.90	819.6	100.0
Total	819.6	352.1	121.71		
Average	16.4	7.0	2.43		

2.3 Free Surface Measurements

During each test, 10 capacitance-type wave gauges and a capacitance-type runup wire were utilized to take free surface and runup measurements. The only exception was that a swash gauge was utilized in place of gauge number 9 when the toe depth d_t = 4, 6, 8, and 10 cm. An additional swash gauge was placed approximately half way up the 1:2 slope. Data gathered from this gauge proved to be difficult to interpret and unreliable. Therefore, data from this gauge was not utilized during the analysis for the experiment. The gauge locations are indicated using the cross-shore coordinate x, which is taken to be positive onshore, with $x = 0$ at gauge 1. The still water depth at each gauge location was also measured when the water depth at the toe of the revetment was $d_t = 0$ cm. These values, along with their cross-shore coordinate, are displayed in Table 2.3. The waterline elevation measured by the runup wire is assumed to be located at the intersection of the runup wire and the still water level (SWL).

Table 2.3: Still Water Depth at Gauge Locations

Wave Gauge Number	1	2	3	4	5	6	7	8	9	10
Cross-Shore Location x = (m)	0.0	0.23	2.0	6.0	9.0	12.0	14.0	14.5	14.8	14.9
Still Water Depth (m)	0.461 + d_t	0.459 + d_t	0.373 + d_t	0.268 + d_t	0.156 + d_t	0.082 + d_t	0.26 + d_t	0.01 + d_t	d_t	d_t - 0.05

Wave gauges 1, 2, and 3 were placed just seaward of the surf zone and utilized to separate incident and reflected waves. The remaining gauges were placed in stationary positions to measure the irregular wave transformation on the 1:32 slope at approximately constant spatial intervals. Because of the limited number of gauges available during the running of the tests, two runs had to be performed for each test. During the second run for each test, three gauges were moved to the region near the toe for better spatial resolution.

2.3.1 Wave Gauge Calibration

Each wave gauge was calibrated prior to the beginning of the tests over a period of 4 to 5 hours. Calibrations were conducted by raising and lowering the water level in the tank by 2 cm over the range of water elevations anticipated during all of the tests. Once the calibration water level was achieved, the gauge voltage readings were recorded. Nineteen or twenty points were used for the calibration of all gauges, except for the swash gauge, which had 12 points of calibration. The calibration data for all of the gauges generally followed a straight line, as illustrated in Figure 2.2 for gauge 1. The conversion factor for the wave gauges and the swash gauge was obtained by performing a linear fit to the data. This calibration process was time consuming, but necessary for accurate measurements of the free surface elevations.

2.4 Wave Runup Measurement

To measure the free surface oscillation at the revetment, a runup wire was utilized and placed parallel to the 1:2 stone revetment, approximately 2.5 cm vertically

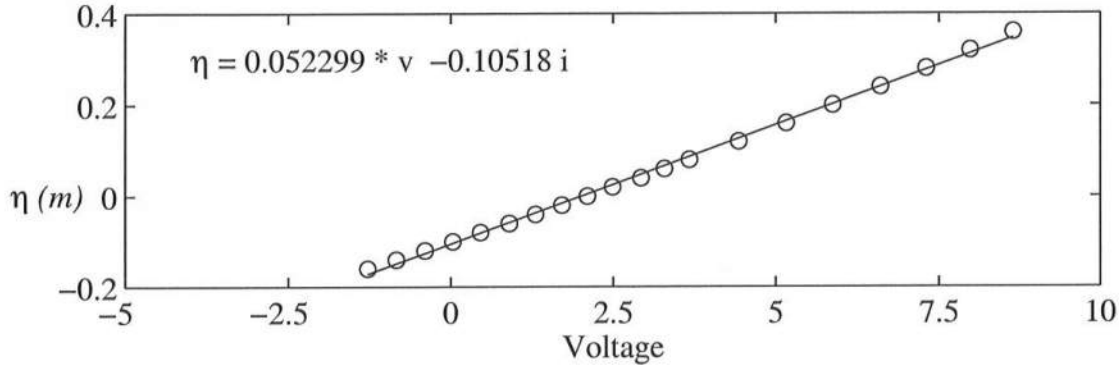

Figure 2.2: Calibration Points and Linear Fit for Gauge 1.

from the approximate mean surface of the stone. It was difficult to place the wire close to the slope because of the large size and irregular shape of the stones, which were stationary for this experiment.

2.4.1 Runup Wire Calibration

The runup wire was calibrated simultaneously and in the same manner as the wave gauges. Nineteen points of calibration were used for the runup wire. Because the runup wire was significantly longer than the wire used for the wave gauges, the data collection system had to be modified to accommodate this length. An extra capacitor was added in series with the standard wave gauge, and adjusted so that values could be recorded over the entire length of the wire. Due to this modification, a first order approximation through the calibration points was no longer valid, so a third order fit had to be utilized. The calibration curve for the runup wire is shown in Figure 2.3

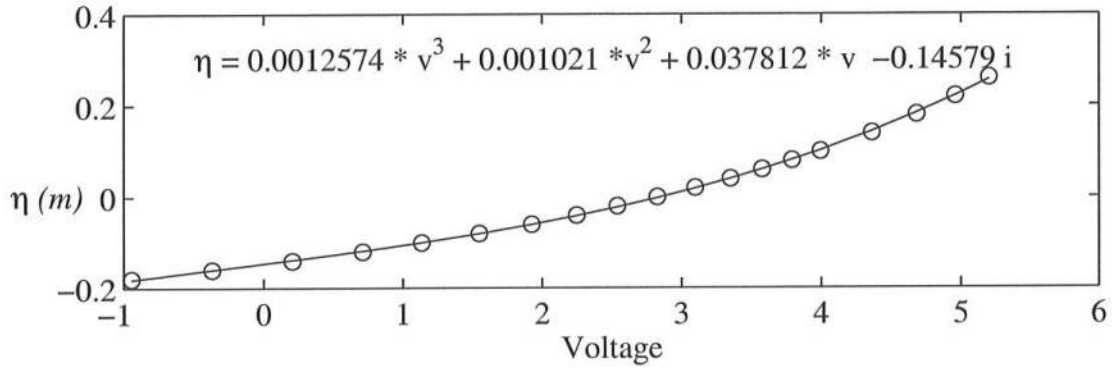

Figure 2.3: Runup Wire Calibration Points and Third Order Fit.

2.5 Velocity Measurement

To measure fluid velocities, a 2-dimensional, side-looking acoustic Doppler velocimeter (ADV) was utilized. When compared with the cross-shore velocities, which were dominated by waves and wave-induced currents, cross-tank velocities associated with three-dimensional turbulence were small and therefore not presented herein.

The ADV was placed immediately seaward of the slope (x = 14.8 m) to measure the cross-shore velocities at the toe of the 1:2 stone revetment. It was the intent of this experiment to gather cross-shore velocity data at the mid-still water depth for all of the tests. During preliminary tests, it became apparent that it would be difficult to mount the ADV in an adequate position to measure the fluid velocities at those depths, because of the wave tank configuration and large range of water depths. Subsequently, the ADV was mounted so that the probe was approximately 1.5 cm vertically above the plywood beach, so that consistent data could be recorded. During

test performance for the shallowest water depths (d_t = 4 and 6 cm) fluid velocities could not be reasonably recorded, because of the relatively long downrush durations during which the ADV probe would emerge from the water.

Although the ADV cannot be calibrated prior to testing in the same way as wave gauges are calibrated, the ADV software contains a self-diagnostic program, which was run prior to the performance of the tests.

2.6 Summary of Tests

Twenty-seven tests were conducted for each of the three spectral peak periods; T_p = 1.5, 2.4, and 4.7 s and nine different toe depths; d_t = 4, 6, 8, 10, 12, 14, 16, 18, and 20 cm. Each test was conducted for a duration of 400 s and sampled at a rate of 20 Hz, with the exception of the tests for the 4.7 s peak period, which were conducted for 800 s and sampled at a rate of 10 Hz. Initial transient waves of 60 s or 120 s (1200 data points) were removed from each test. The data acquisition parameters are summarized in Table 2.4 where A, B, and C indicated the test with T_p = 1.5, 2.4, and 4.7 s, respectively. The toe depth d_t is used to designate each of the nine tests for each T_p as listed in Table 2.5.

Table 2.4: Data Acquisition Parameters

Test	$T_{p\,(s)}$	Sampling Rate (Hz)	Test Duration (s)	Effective Data Interval (s)
A	4.7	10	800	120 – 800
B	2.4	20	400	60 – 400
C	1.5	20	400	60 – 400

Table 2.5: Test Designation Table

Test	Toe depths – d_t (cm)								
	20	18	16	14	12	10	8	6	4
A	A20	A18	A16	A14	A12	A10	A8	A6	A4
B	B20	B18	B16	B14	B12	B10	B8	B6	B4
C	C20	C18	C16	C14	C12	C10	C8	C6	C4

Chapter 3

MEASURED FREE SURFACE AND RUNUP ELEVATIONS

In this chapter, cross-shore surface elevation time series and frequency spectra are presented. Time series plots and frequency spectra plots were generated at each gauge location and for the runup wire for each test run. These time series and spectral plots are based on the recorded data and therefore include the effects of reflected waves. Representative plots for time series and frequency spectra will be displayed in the chapter as examples, the data as a whole is presented in Appendix A.

In addition, cross-shore surface elevation statistics are also presented. The wave setup or setdown, $\overline{\eta}$, the root-mean-square-wave height, H_{rms}, the skewness, s, and kurtosis, K, for each of the measured time series of the free surface elevation, η, are computed under the assumption of equivalency of probabilistic and time averaging, as was done by Kobayashi *et al.*(1998).

3.1 Free Surface Time Series

Time series were plotted for each test, including the effects of reflected waves. Figure 3.3 is an example of the recorded time series for test B12. Data from five wave

gauges and the runup wire are presented to show the shoreward wave transformation. For test B12 some wave breaking occurred in the region of gauge 6 and waves are almost completely broken at gauge 9 and the runup wire. Similar conditions were observed for tests A12 and C12 of the same d_t, shown in Figure 3.2 and Figure 3.4 respectively. As d_t was decreased, the zone of wave breaking moved offshore. On the other hand, as d_t was increased, the region of wave breaking moved closer to the stone revetment.

3.2 Frequency Spectra

Frequency spectra were plotted for each test, including the effects of reflected waves. Figure 3.6 is an example of the shoreward transformation of the frequency spectra for test B12. The spectral peak period at $f = 0.42$ Hz, corresponding to a peak period of 2.4 s at gauge 1, was reduced shoreward due to wave breaking, while low frequency components increased landward. As d_t was decreased, the peak of the frequency spectra began to disappear farther offshore and the shallow water waves and waterline oscillations on the revetment were dominated by low frequency wave components. Similar results were observed as d_t was varied for T_p =4.7 s and 1.5 s as shown in Figure 3.5 and Figure 3.7 respectively. As d_t was increased, the spectral peak observed at gauge 1 remains discernible at gauges 2 through 10 and the runup wire.

3.3 Time Series Parameters

Complete free surface statistical data were calculated for each test and are presented in Table 3.1, Table 3.2, and Table 3.3 for $T_p = 4.7$ s, 2.4 s, and 1.5 s. Wave setup or setdown, $\overline{\eta}$, root-mean-square wave height, H_{rms}, skewness, s, and kurtosis, K,

are tabulated for each gauge location and the runup. The values for gauge 1, at $x = 0$, are utilized as the primary input for the numerical model CSHORE. The free surface statistical data is compared to the output of CHSORE and these comparisons are discussed further in Chapter 7.

3.4 Bottom Elevation Uncertainty on the Revetment

Gauge 10 was mounted immediately landward of the toe of the revetment at $x = 14.9$ m. The gauge never emerged from the water during the test even though part of the gauge was "buried" within the armor stones of the slope. Considering the 1:2 slope, the theoretical slope surface at the gauge location should be approximately 5 cm above the plywood beach. The times series in shallow water were adjusted or truncated to this elevation, which had a significant effect on the free surface statistics for this gauge location as well as the shape of the probability distribution. Figure 3.1 shows an example of an uncorrected time series and the subsequent time series after truncation. Time series were truncated for $T_p = 4.7$ s when d_t was less than or equal to 16 cm, for $T_p = 2.4$ s when d_t was less than or equal to 10 cm, and for $T_p = 1.5$ s when d_t was less than or equal to 6 cm. For consistency throughout the experiment, the truncated time series were utilized for all analyses performed.

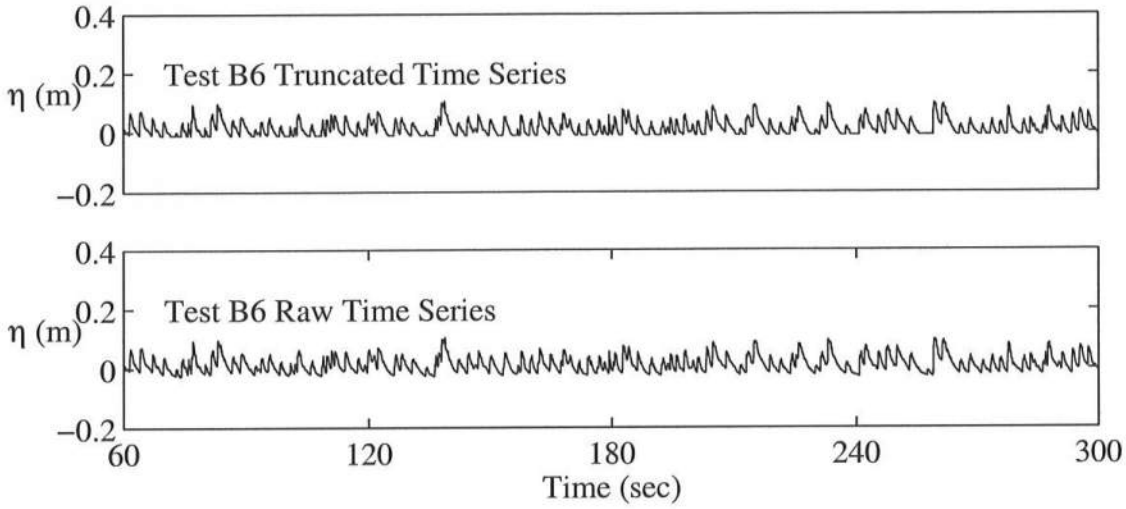

Figure 3.1: Corrected and Uncorrected Time Series of Free Surface at Gauge Location 1.

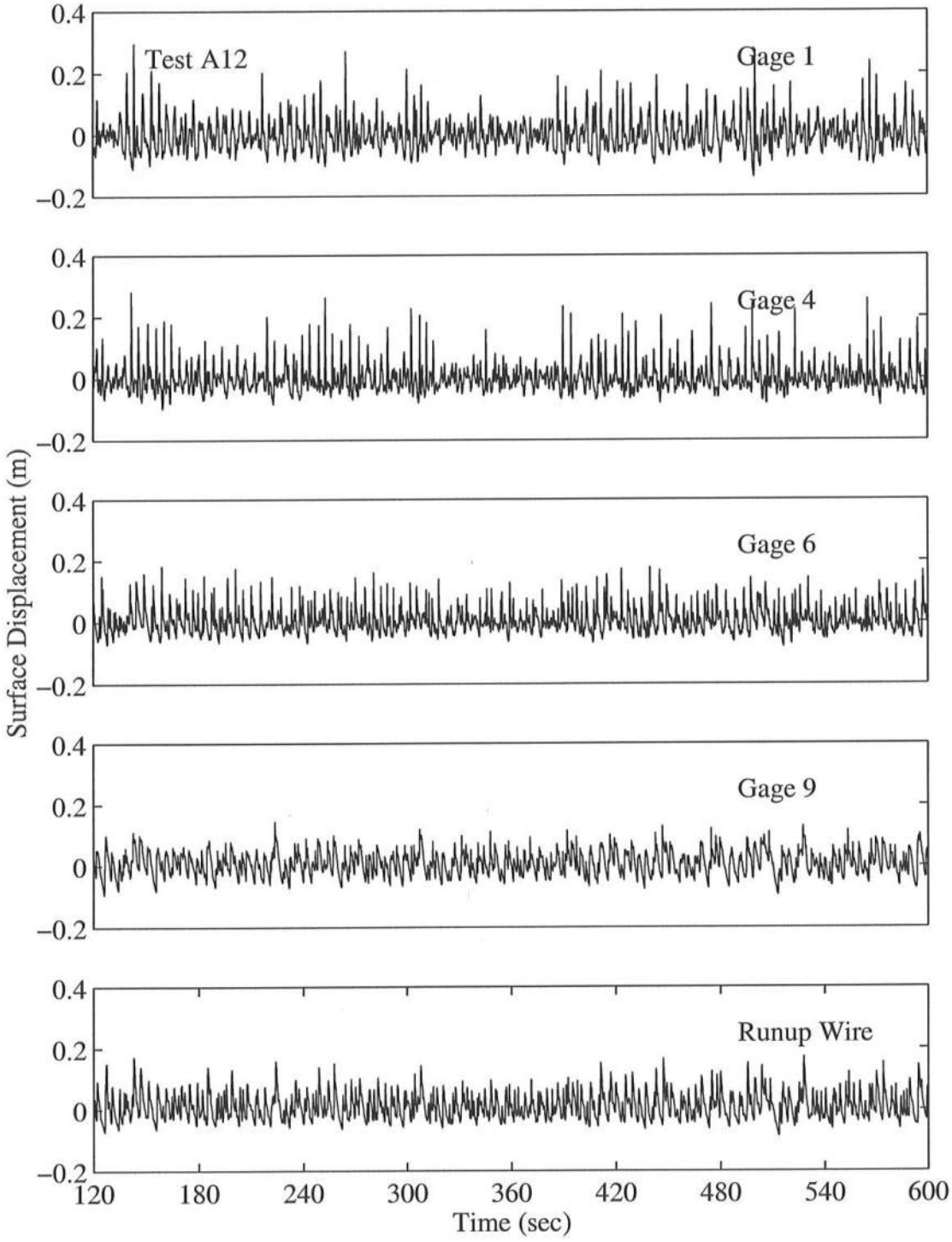

Figure 3.2: Recorded Time Series for Test A12 ($T_p = 4.7$ s and $d_t = 12$ cm) at Gauge Locations $x = 0$, 6, 12, 14.8 m, and Runup Wire.

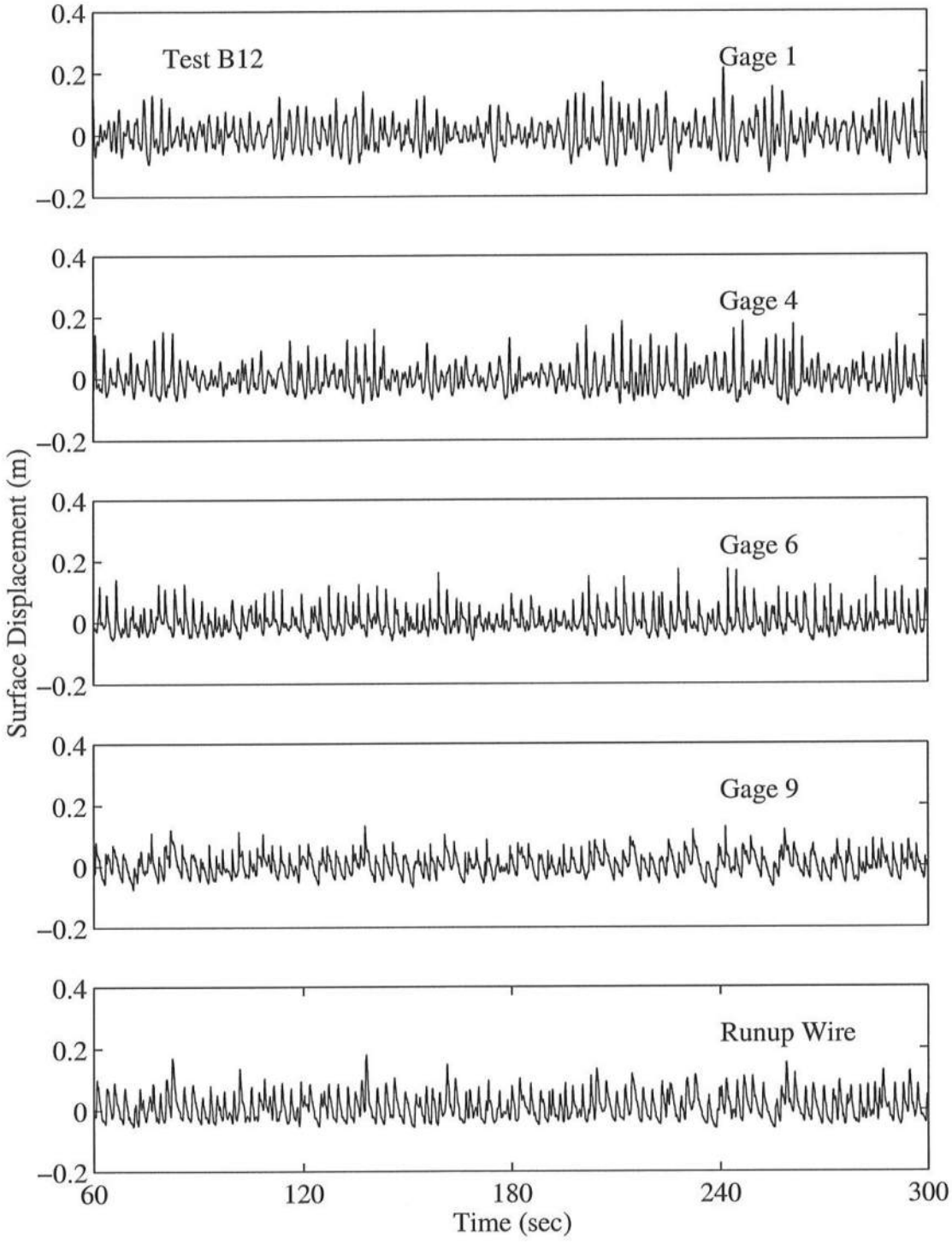

Figure 3.3: Recorded Time Series for Test B12 ($T_p = 2.4$ s and $d_t = 12$ cm) at Gauge Locations $x = 0$, 6, 12, 14.8 m, and Runup Wire.

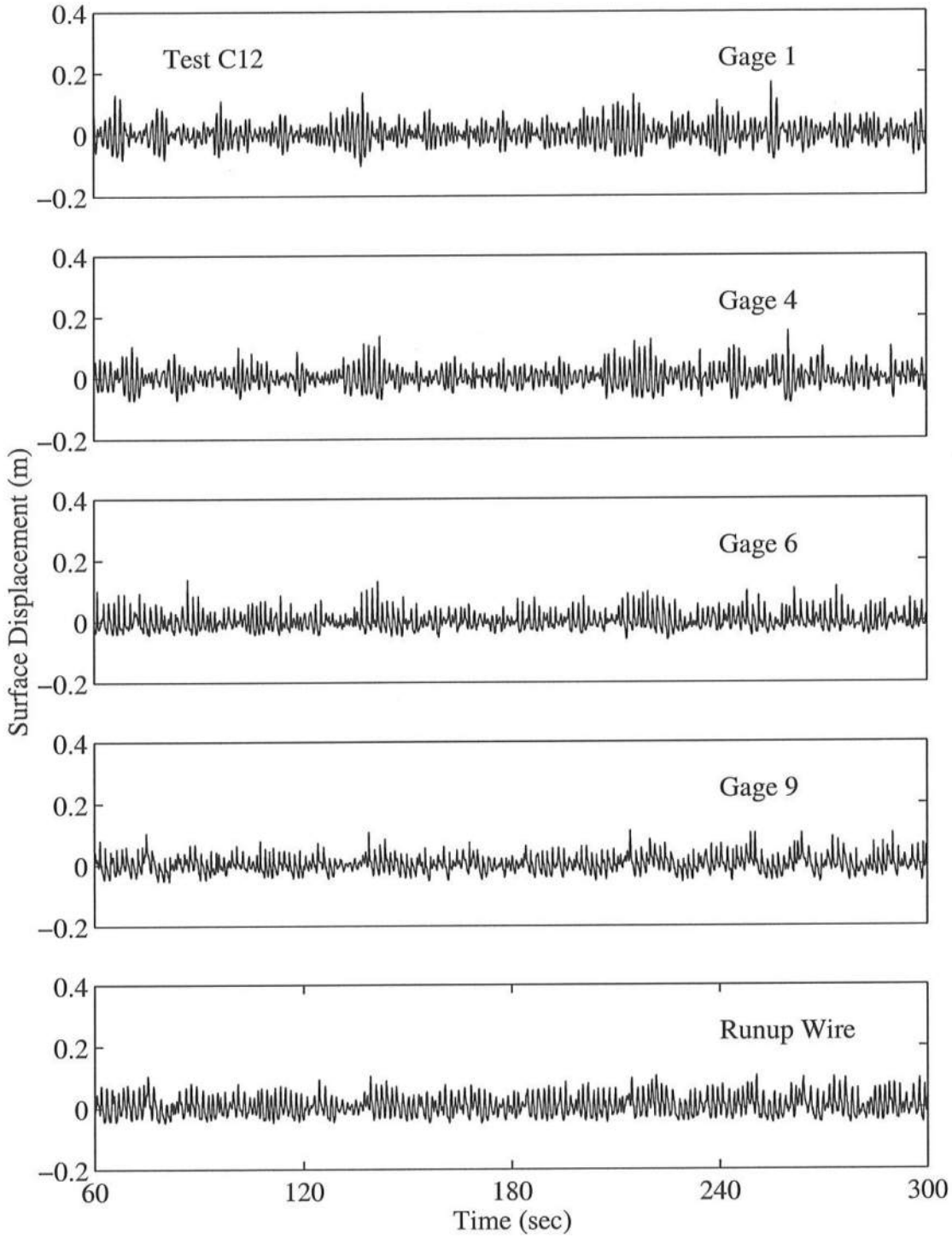

Figure 3.4: Recorded Time Series for Test C12 ($T_p = 1.5$ s and $d_t = 12$ cm) at Gauge Locations $x = 0$, 6, 12, 14.8 m, and Runup Wire

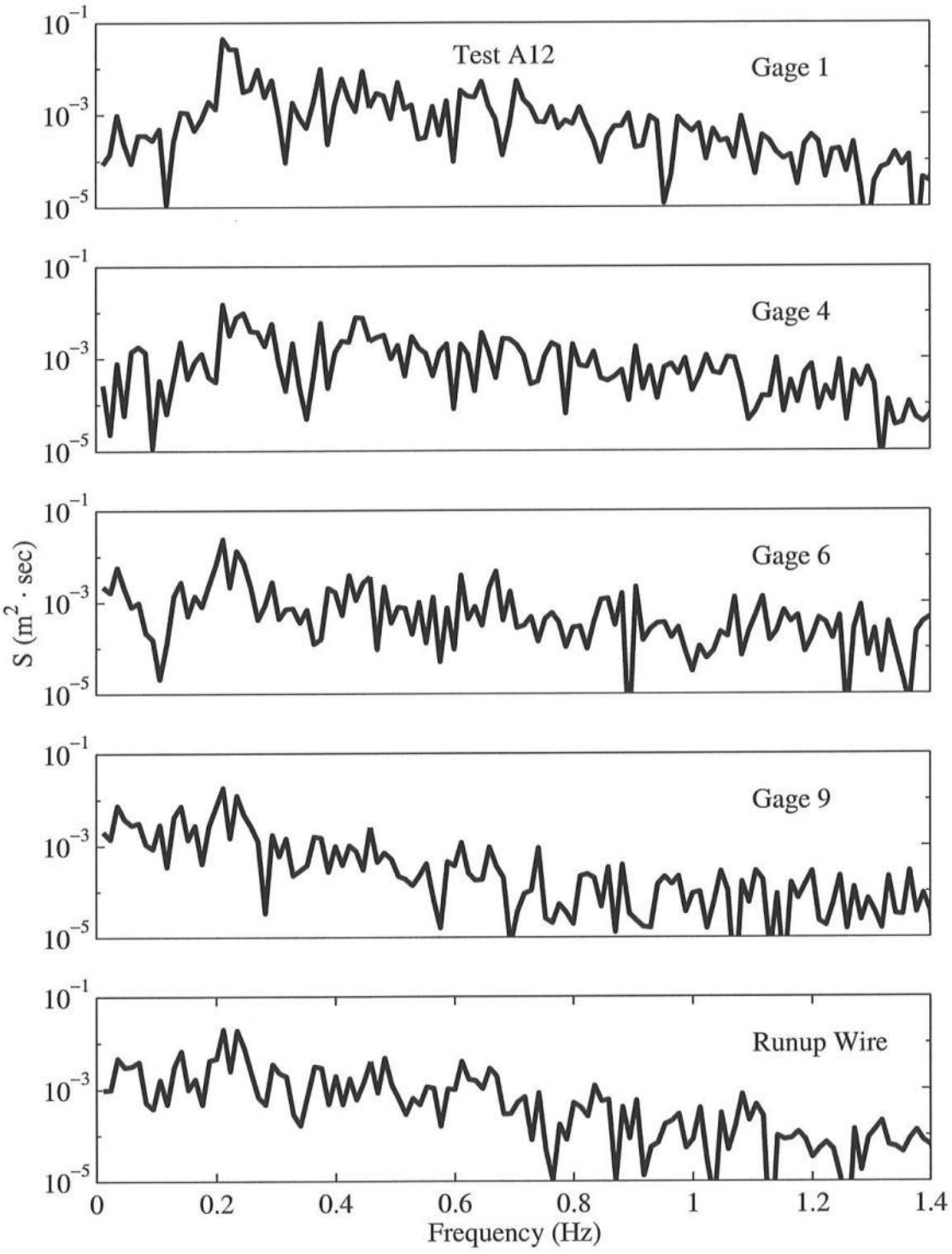

Figure 3.5: Frequency Spectra for Test A12 ($T_p = 4.7$ s and $d_t = 12$ cm) at Gauge Locations $x = 0$, 6, 12, 14.8 m, and Runup Wire.

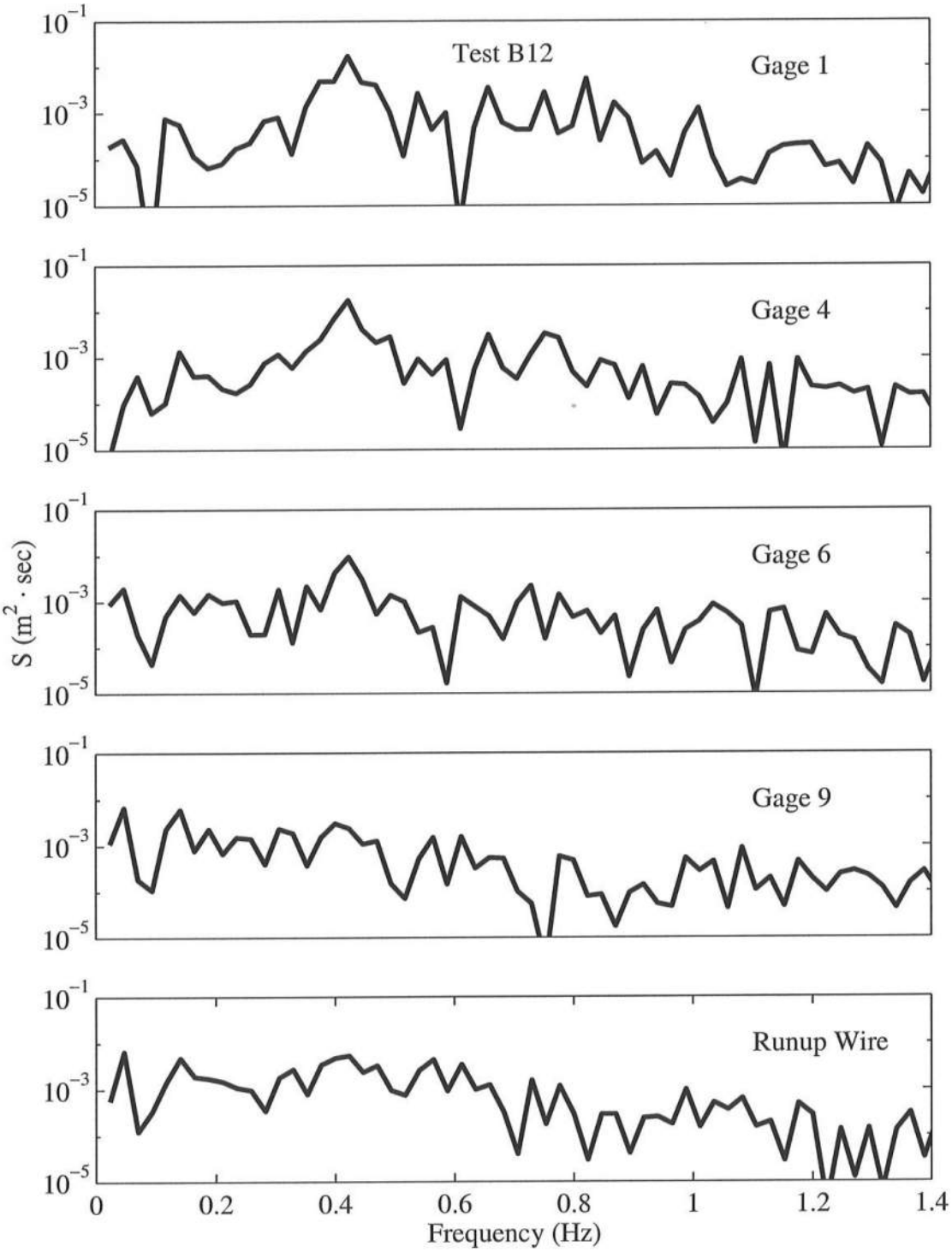

Figure 3.6: Frequency Spectra for Test B12 ($T_p = 2.4$ s and $d_t = 12$ cm) at Gauge Locations $x = 0$, 6, 12, 14.8 m, and Runup Wire.

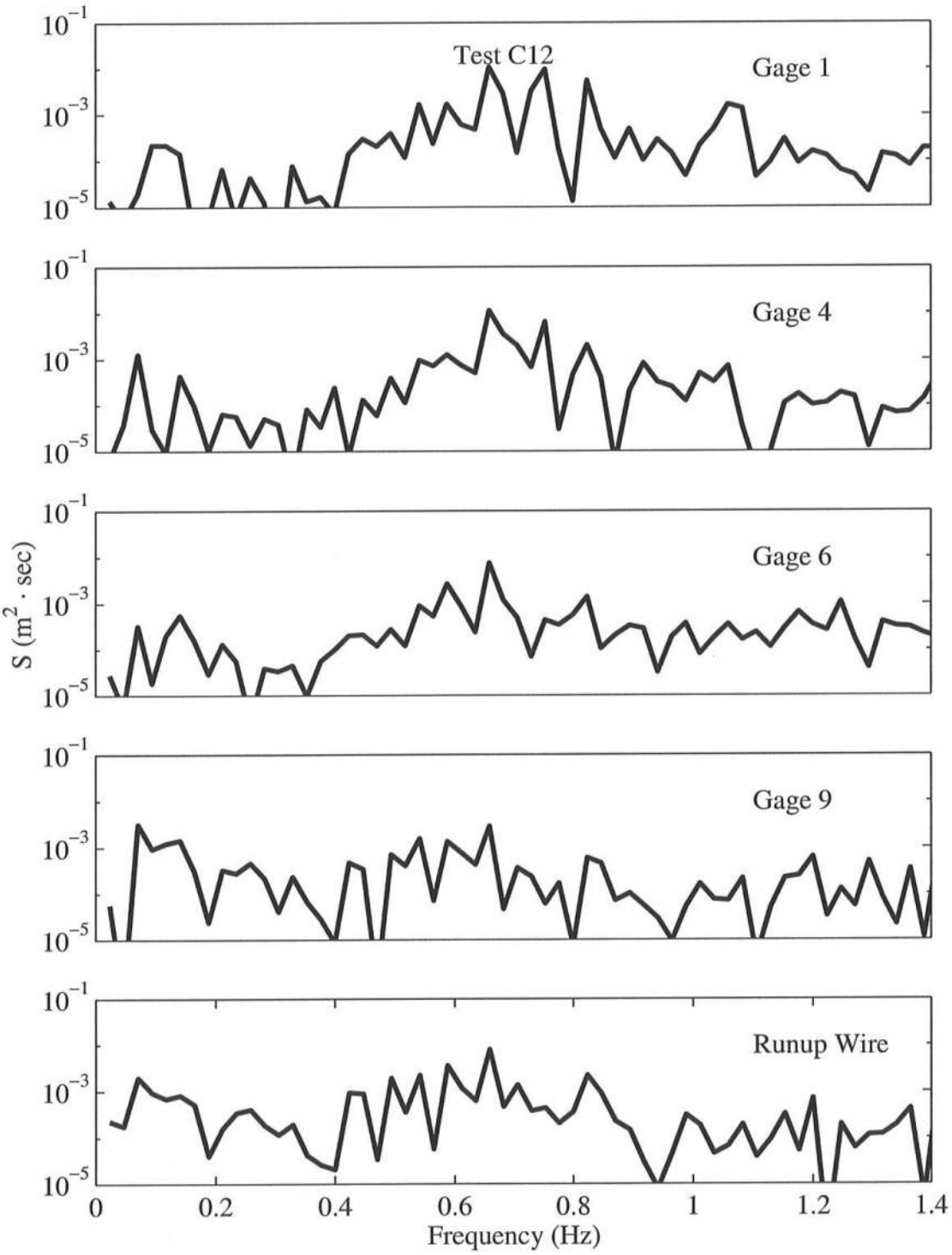

Figure 3.7: Frequency Spectra for Test C12 (T_p = 1.5 s and d_t = 12 cm) at Gauge Locations x = 0, 6, 12, 14.8 m, and Runup Wire.

Table 3.1: Time Series Parameters for $T_p = 4.7$ s.

Test	Parameter	Gage 1	Gage 2	Gage 3	Gage 4	Gage 5	Gage 6	Gage7	Gage 8	Gage 9	Gage 10	Runup Wire
A20	$\overline{\eta}$ (cm)	-0.08	-0.12	-0.14	-0.11	-0.04	0.11	0.18	0.23	0.18	0.12	1.18
	H_{rms} (cm)	15.8	16.1	16.2	14.3	13.2	13.1	10.6	11.0	12.7	12.4	17.2
	s	0.80	0.79	1.04	1.46	1.43	1.39	0.81	0.55	0.29	0.36	1.00
	K	4.52	4.65	5.21	6.26	6.46	5.63	4.51	3.94	3.20	3.16	3.72
A18	$\overline{\eta}$ (cm)	-0.12	-0.14	-0.11	-0.02	-0.08	0.14	0.22	0.27	0.28	0.27	1.14
	H_{rms} (cm)	15.1	15.4	15.5	13.4	12.7	12.3	10.1	10.5	12.1	12.0	15.5
	s	0.88	0.85	1.05	1.43	1.43	1.26	0.74	0.42	0.23	0.31	0.94
	K	4.89	4.85	5.37	6.48	6.64	5.21	4.42	3.67	3.03	2.99	3.68
A16	$\overline{\eta}$ (cm)	-0.13	-0.15	-0.12	-0.03	0.03	0.19	0.23	0.35	0.37	0.39	1.08
	H_{rms} (cm)	14.7	15.0	14.8	12.9	12.3	11.6	9.6	10.2	11.7	11.7	14.3
	s	0.87	0.88	1.11	1.53	1.50	1.24	0.64	0.36	0.23	0.25	0.89
	K	4.77	4.77	5.65	7.16	6.78	5.11	4.05	3.47	2.97	2.80	3.61
A14	$\overline{\eta}$ (cm)	-0.12	-0.16	-0.12	-0.02	0.06	0.22	0.32	0.41	0.49	0.56	1.13
	H_{rms} (cm)	14.3	14.6	14.4	12.3	11.8	11.3	9.2	9.7	11.2	13.0	13.0
	s	0.99	0.95	1.14	1.56	1.47	1.16	0.59	0.30	0.19	0.81	0.81
	K	5.23	5.16	5.73	7.00	6.51	4.86	4.07	3.32	2.83	3.61	3.61
A12	$\overline{\eta}$ (cm)	-0.14	-0.17	-0.11	-0.03	0.09	0.27	0.40	0.54	0.64	0.64	1.01
	H_{rms} (cm)	13.9	14.2	14.2	12.1	11.5	10.7	8.6	9.3	10.7	10.7	11.7
	s	0.97	0.96	1.25	1.72	1.46	1.13	0.61	0.29	0.16	0.29	0.70
	K	4.98	5.05	6.30	7.94	6.51	4.76	4.00	3.22	2.72	2.62	3.41
A10	$\overline{\eta}$ (cm)	-0.16	-0.19	-0.13	-0.03	0.13	0.33	0.41	0.65	1.49	0.89	1.04
	H_{rms} (cm)	13.7	13.9	13.7	11.7	11.1	10.1	8.1	8.7	9.94	10.0	10.4
	s	1.00	0.99	1.23	1.75	1.47	1.04	0.58	0.24	0.14	0.38	0.64
	K	5.06	5.06	5.83	7.81	6.46	4.40	3.82	3.82	2.67	2.99	3.24

Table 3.1 continued: Time Series Parameters for $T_p = 4.7$ s.

Test	Parameter	Gage 1	Gage 2	Gage 3	Gage 4	Gage 5	Gage 6	Gage7	Gage 8	Gage 9	Gage 10	Runup Wire
A8	$\overline{\eta}$ (cm)	-0.14	-0.19	-0.13	-0.03	0.10	0.32	0.53	0.77	0.93	1.14	1.08
	H_{rms} (cm)	13.2	13.4	13.3	11.2	10.6	9.37	7.55	8.20	9.35	9.0	9.3
	s	1.04	0.98	1.32	1.76	1.43	0.98	0.50	0.24	0.15	0.49	0.49
	K	5.12	4.97	6.42	7.63	6.37	4.30	3.63	2.91	2.67	2.65	3.09
A6	$\overline{\eta}$ (cm)	-0.18	-0.21	-0.15	-0.03	0.09	0.45	0.68	0.91	1.16	1.48	1.12
	H_{rms} (cm)	12.9	13.2	13.0	11.0	9.9	8.7	7.2	7.7	8.9	8.1	8.6
	s	1.14	1.10	1.33	1.83	1.34	0.84	2.53	2.74	0.23	2.86	3.06
	K	5.56	5.56	6.27	8.11	5.95	3.80	3.37	2.99	2.70	2.96	2.96
A4	$\overline{\eta}$ (cm)	-0.22	-0.25	-0.17	-0.04	0.15	0.55	0.80	1.08	1.32	1.98	1.18
	H_{rms} (cm)	12.5	12.7	12.7	10.6	9.7	8.1	6.7	7.4	8.3	6.9	7.9
	s	1.17	1.12	1.35	1.74	1.27	0.86	0.47	0.43	0.41	1.07	0.44
	K	5.67	5.55	6.35	7.46	5.50	3.83	3.15	2.92	2.70	3.66	2.85

Table 3.2: Time Series Parameters for T_p = 2.4 s.

Test	Parameter	Gage 1	Gage 2	Gage 3	Gage 4	Gage 5	Gage 6	Gage7	Gage 8	Gage 9	Gage 10	Runup Wire
B20	$\overline{\eta}$ (cm)	-0.01	-0.06	-0.10	-0.14	-0.13	-0.11	-0.02	-0.01	-0.08	-0.11	1.20
	H_{rms} (cm)	13.8	13.6	12.9	12.7	13.7	11.5	10.5	9.3	10.8	11.1	16.2
	s	0.53	0.53	0.56	0.85	0.95	1.35	1.37	0.95	0.39	0.26	0.79
	K	3.72	3.69	3.28	4.14	4.65	5.39	5.53	5.30	3.78	3.04	3.10
B18	$\overline{\eta}$ (cm)	-0.06	-0.07	-0.07	-0.04	-0.07	-0.06	0.03	0.04	0.03	-0.01	1.12
	H_{rms} (cm)	13.4	13.1	12.6	12.3	13.3	11.1	9.5	8.9	10.2	10.8	14.8
	s	0.49	0.50	0.56	0.79	1.01	1.38	1.28	0.87	0.35	0.25	0.79
	K	3.67	3.72	3.53	4.04	4.74	5.54	5.16	4.88	3.43	2.83	3.04
B16	$\overline{\eta}$ (cm)	-0.05	-0.09	-0.08	-0.06	-0.08	-0.03	0.06	0.11	0.12	0.15	1.03
	H_{rms} (cm)	13.2	12.8	12.1	12.0	12.8	10.8	9.5	8.5	9.9	10.5	13.4
	s	0.45	0.44	0.55	0.79	1.10	1.34	1.19	0.71	0.28	0.25	0.76
	K	3.47	3.41	3.54	3.90	4.77	5.17	4.82	4.46	3.10	2.67	3.14
B14	$\overline{\eta}$ (cm)	-0.04	-0.06	-0.06	-0.06	-0.09	-0.01	0.16	0.22	0.26	0.35	1.09
	H_{rms} (cm)	12.9	12.7	11.8	11.6	12.1	10.5	9.2	8.32	9.6	10.3	12.4
	s	0.46	0.46	0.64	0.82	1.10	1.24	1.18	0.70	0.32	0.31	0.73
	K	3.39	3.30	3.84	3.97	4.68	4.71	4.80	4.22	2.94	2.54	3.17
B12	$\overline{\eta}$ (cm)	-0.07	-0.08	-0.08	-0.09	0.08	0.05	0.29	0.36	0.48	0.48	0.99
	H_{rms} (cm)	12.6	12.5	11.3	11.6	11.9	9.8	8.66	7.94	9.2	9.7	11.1
	s	0.47	0.47	0.67	0.95	1.13	1.16	1.15	0.71	0.33	0.34	0.79
	K	3.48	3.55	3.88	4.20	4.79	4.54	4.83	4.05	2.83	2.49	3.14
B10	$\overline{\eta}$ (cm)	-0.08	-0.10	-0.09	-0.09	-0.06	0.12	0.34	0.55	0.94	0.79	1.06
	H_{rms} (cm)	12.3	12.1	10.9	11.5	11.5	9.3	8.00	7.4	8.3	9.0	9.7
	s	0.49	0.49	0.68	0.96	1.20	1.11	1.02	0.61	0.36	0.45	0.73
	K	3.40	3.32	3.88	4.10	5.09	4.28	4.36	3.84	2.85	2.53	3.04

Table 3.2 continued: Time Series Parameters for $T_p = 2.4$ s.

Test	Parameter	Gage 1	Gage 2	Gage 3	Gage 4	Gage 5	Gage 6	Gage7	Gage 8	Gage 9	Gage 10	Runup Wire
B8	$\overline{\eta}$ (cm)	-0.07	-0.10	-0.10	-0.10	-0.10	0.15	0.52	0.71	0.86	1.03	1.09
	H_{rms} (cm)	11.9	11.8	10.5	11.1	11.0	8.8	7.2	6.8	7.8	8.1	8.5
	s	0.49	0.50	0.70	1.04	1.29	1.10	0.94	0.53	0.34	0.64	0.75
	K	3.42	3.45	3.82	4.43	5.44	4.37	4.39	3.40	2.79	2.83	3.35
B6	$\overline{\eta}$ (cm)	-0.11	-0.12	-0.12	-0.12	-0.11	0.30	0.67	0.89	1.13	1.36	1.14
	H_{rms} (cm)	11.6	11.5	10.3	11.2	10.6	8.2	6.4	6.4	7.4	7.2	7.6
	s	0.54	0.56	0.78	1.18	1.40	1.00	0.77	0.52	0.43	0.81	0.64
	K	3.48	3.53	4.28	4.95	5.69	3.94	3.90	3.99	2.95	3.96	4.64
B4	$\overline{\eta}$ (cm)	-0.14	-0.17	-0.17	-0.14	-0.06	0.46	0.84	1.06	1.21	1.81	1.21
	H_{rms} (cm)	11.3	11.3	10.1	11.1	10.2	7.4	5.7	5.2	6.79	5.9	6.7
	s	0.53	0.52	0.82	1.16	1.31	0.87	0.66	0.54	0.44	1.12	0.58
	K	3.42	3.41	4.36	4.82	5.30	3.52	3.55	3.29	2.96	4.01	3.21

Table 3.3: Time Series Parameters for T_p = 1.5 s.

Test	Parameter	Gage 1	Gage 2	Gage 3	Gage 4	Gage 5	Gage 6	Gage7	Gage 8	Gage 9	Gage 10	Runup Wire
C20	$\overline{\eta}$ (cm)	0.00	-0.05	-0.1	-0.15	-0.12	-0.06	0.02	0.00	-0.18	-0.21	0.71
	H_{rms} (cm)	10.0	10.1	9.9	9.6	9.7	8.8	8.2	8.0	7.3	7.7	11.0
	s	0.24	0.24	0.22	0.35	0.61	0.75	0.81	0.94	0.63	0.09	0.39
	K	3.84	3.84	3.69	3.74	4.16	3.74	4.10	4.20	4.02	3.57	2.87
C18	$\overline{\eta}$ (cm)	-0.06	-0.04	-0.10	-0.04	-0.06	-0.05	-0.01	-0.04	-0.13	-0.15	0.67
	H_{rms} (cm)	9.7	9.8	9.6	9.3	9.7	8.4	7.9	7.6	7.2	7.8	10.1
	s	0.25	0.20	0.25	0.33	0.63	0.76	0.83	0.97	0.55	0.10	0.54
	K	3.95	3.86	3.77	3.88	4.26	3.66	4.07	4.27	3.99	3.47	3.04
C16	$\overline{\eta}$ (cm)	-0.06	-0.05	-0.09	-0.05	-0.07	-0.04	-0.02	0.02	-0.06	-0.61	0.59
	H_{rms} (cm)	9.4	9.5	9.3	9.0	9.5	9.1	7.9	7.3	7.0	7.7	9.1
	s	0.27	0.24	0.27	0.37	0.69	0.87	0.86	1.02	0.53	0.17	0.59
	K	4.07	3.95	4.03	3.77	4.19	3.95	4.06	4.33	4.01	3.31	3.29
C14	$\overline{\eta}$ (cm)	-0.05	-0.04	-0.08	-0.04	-0.05	-0.05	0.05	0.06	-0.02	0.08	0.66
	H_{rms} (cm)	9.2	9.4	9.2	9.0	9.24	7.8	7.7	6.9	6.9	7.7	8.8
	s	0.25	0.24	0.28	0.43	0.74	0.92	0.94	1.15	0.53	0.22	0.46
	K	3.88	3.85	3.96	3.72	4.06	3.99	4.38	4.95	3.97	3.21	3.07
C12	$\overline{\eta}$ (cm)	-0.05	-0.05	-0.07	-0.06	-0.07	-0.05	0.08	0.10	0.07	0.13	0.59
	H_{rms} (cm)	9.0	9.1	9.0	8.7	8.8	7.4	7.5	6.7	7.0	7.6	8.7
	s	0.28	0.22	0.28	0.45	0.76	0.99	0.98	1.23	0.55	0.32	0.54
	K	3.98	3.84	3.92	3.87	4.26	4.20	4.35	5.26	3.95	3.03	2.86
C10	$\overline{\eta}$ (cm)	-0.05	-0.05	-0.07	-0.06	-0.05	-0.02	0.09	0.21	0.21	0.13	0.67
	H_{rms} (cm)	8.9	9.1	8.8	8.7	8.7	7.2	6.9	6.2	6.2	7.6	7.6
	s	0.27	0.24	0.33	0.45	0.83	1.04	0.97	1.19	1.19	0.32	0.67
	K	4.00	3.90	3.82	3.81	4.17	4.27	4.14	5.15	5.14	3.03	3.11

Table 3.3 continued: Time Series Parameters for T_p = 1.5 s.

Test	Parameter	Gage 1	Gage 2	Gage 3	Gage 4	Gage 5	Gage 6	Gage7	Gage 8	Gage 9	Gage 10	Runup Wire
C8	$\overline{\eta}$ (cm)	-0.03	-0.05	-0.08	-0.05	-0.07	-0.02	0.08	0.10	0.41	0.13	0.59
	H_{rms} (cm)	8.8	9.0	8.8	8.4	8.5	6.6	7.5	6.7	5.9	7.6	8.7
	s	0.30	0.23	0.33	0.51	0.92	1.01	0.98	1.23	0.46	0.32	0.54
	K	4.08	4.04	3.89	3.82	4.52	4.15	4.35	5.26	3.33	3.03	2.860.
C6	$\overline{\eta}$ (cm)	-0.05	-0.06	-0.07	-0.07	-0.10	-0.08	0.29	0.45	0.99	0.86	0.76
	H_{rms} (cm)	8.6	8.7	8.6	8.3	8.30	6.2	5.5	5.25	5.4	5.38	5.8
	s	0.27	0.22	0.38	0.51	0.91	1.05	0.93	0.98	0.58	0.79	0.59
	K	4.06	3.91	4.02	3.86	4.32	4.18	4.22	4.38	3.54	3.23	3.05
C4	$\overline{\eta}$ (cm)	-0.07	-0.09	-0.11	-0.08	-0.06	0.17	0.42	0.60	0.71	1.22	0.77
	H_{rms} (cm)	8.5	8.6	8.5	8.2	8.0	5.8	4.7	4.6	4.9	4.29	4.9
	s	0.33	0.26	0.36	0.50	0.86	1.00	0.82	0.76	0.55	1.23	0.66
	K	4.11	4.08	3.82	3.77	4.05	3.99	3.86	3.92	3.70	4.64	3.74

Chapter 4

INCIDENT AND REFLECTED WAVES

For the purposes of this experiment, separating the incident and reflected waves was an important step in the process in determining the feasibility of using the numerical model CSHORE for irregular wave runup prediction on a revetment. CSHORE does not account for reflected waves explicitly, but was calibrated using the experimental and field data, which included both incident and reflected waves. The model has already been shown to reasonably predict cross-shore transformations of irregular waves, but such comparisons were made on relatively gentle slopes compared to the 1:2 revetment utilized for this experiment. Separation of the incident and reflected waves and subsequent determination of average reflection coefficient showed that even though the revetment was steeply sloped, reflection was relatively small and therefore did not have an adverse affect on the predictive accuracy of the model.

4.1 Separated Time Series and Spectra

The incident and reflected wave time series were estimated at the seaward gauge location, $x = 0$, using the three gauge method used by Kobayashi *et al.* (1998).

The three gauge method is an extension of the original separation method developed by Goda and Suzuki (1976). The original model was limited in its ability to separate incident and reflected waves at frequencies where the wavelength was an integer multiple of the gauge spacing. The three gauge method reduces this limitation by utilizing and combing the results from three pairs of gauges to cover a wider range of frequencies. Gauge spacing for the separation of incident and reflected waves was chosen such that adequate frequency resolution was achieved for all three peak periods. The spacing is shown in Table 4.1 where there still water depth at wave gauges 1, 2, and 3 has been listed in Table 2.3.

Table 4.1: Three-gauge Array Separation.

Gauge Pair	Spacing (m)
1,2	0.23
1,3	2.0
2,3	1.77

The three gauges used for the separation of the incident and reflected waves were mounted in a section of the tank where the bottom was gently sloping. The gauges were mounted in this location to be located outside the surf zone, but also sufficiently far away from the paddle where wave breaking occasionally occurred due to large wave generation. Although the method to separate incident and reflected waves was developed for constant depth, it has been shown that the effects of a gently sloping beach on the separation of incident and reflected waves is negligible (Kobayashi and Raichle 1994).

Once the waves were separated, the incident and reflected wave spectra were calculated and smoothed using a Bartlett Window to band-average the data with 16 degrees of freedom for each run. The incident and reflected spectra are shown in Figure 4.1 and Figure 4.2 for $T_p = 4.7$ s, Figure 4.3 and Figure 4.4 for $T_p = 2.4$ s, and Figure 4.5 and Figure 4.6 for $T_p = 1.5$ s. Although the energy or zero spectral moment for each peak period is different, the trend of the data is the same. The spectra indicate that a majority of the wave energy near the peak frequency was being dissipated with little wave reflection, while the low frequency waves were almost completely reflected.

4.2 Spectral Parameters and Average Reflection Coefficient

To evaluate the incident spectral root-mean-square wave height and average reflection coefficients, the zero-moment or m_o, for the incident spectrum S_i, and reflected spectrum S_r, are defined in equation (4.1) and (4.2) respectively.

$$(m_o)_i = \int_{f_{min}}^{f_{max}} S_i(f)df \tag{4.1}$$

$$(m_o)_r = \int_{f_{min}}^{f_{max}} S_r(f)df \tag{4.2}$$

where f_{min} and f_{max} are the minimum and maximum frequencies resolved by the separation method. Once the incident wave zero-moment is determined, the spectral estimate of the incident root-mean-square wave height H_i can be determined using equation (4.3).

$$H_i = \sqrt{8(m_o)_i} \tag{4.3}$$

The measured root-mean-square wave height H_{rms} and H_i are compared in Table 4.2. The percentage difference between the two wave heights fell between –0.1 and 0.1 with the exception of those calculated for tests with $T_p = 2.4$ s.

The average reflection coefficient R, defined as $R = \sqrt{(m_o)_r/(m_o)_i}$ was estimated for all the tests. The reflection coefficients R were very similar for $T_p = 4.7$s and 2.4 s, with values ranging from $R = 0.33$ - 0.36 for $d_t = 20$ cm to $R = 0.26$ when $d_t = 4$ cm. The reflection coefficient R decreases as d_t is decreased because of the increased wave breaking. The reflection coefficients for $T_p = 1.5$ s were in a narrow range for all water depths, ranging from $R = 0.23$ for $d_t = 20$ cm to $R = 0.20$ for $d_t = 4$ cm.

Table 4.2: Incident and Reflected Waves at Gauge 1.

Test	Still Water Depth (cm)	Reflection Coefficient, R	Incident RMS Height H_i (cm)	Measured H_{rms} (cm)	$\frac{H_{rms} - H_i}{H_{rms}}$
A20	66.1	0.33	15.8	16.4	0.04
A18	64.1	0.32	15.1	16.0	0.06
A16	62.1	0.34	15.3	14.7	-0.04
A14	60.1	0.28	14.5	14.3	-0.01
A12	58.1	0.27	14.4	13.9	-0.04
A10	56.1	0.28	14.0	13.7	-0.02
A8	54.1	0.27	13.2	13.7	0.04
A6	52.1	0.26	12.9	12.4	-0.04
A4	50.1	0.26	12.5	12.7	0.02
B20	66.1	0.36	13.8	11.4	-0.21
B18	64.1	0.36	13.4	10.9	-0.23
B16	62.1	0.36	13.2	10.3	-0.28
B14	60.1	0.35	12.9	9.9	-0.30

Table 4.2 continued: Incident and Reflected Waves at Gauge 1.

Test	Still Water Depth (cm)	Reflection Coefficient, R	Incident RMS Height H_i (cm)	Measured H_{rms} (cm)	$\frac{H_{rms} - H_i}{H_{rms}}$
B12	58.1	0.34	12.6	9.9	-0.27
B10	56.1	0.30	12.3	10.0	-0.23
B8	54.1	0.32	11.9	9.1	-0.31
B6	52.1	0.29	11.6	9.2	-0.26
B4	50.1	0.26	11.3	9.1	-0.24
C20	66.1	0.23	10.0	9.7	-0.03
C18	64.1	0.22	9.7	9.4	-0.03
C16	62.1	0.23	9.4	9.4	0.00
C14	60.1	0.24	9.2	9.1	-0.01
C12	58.1	0.24	9.0	8.9	-0.01
C10	56.1	0.22	8.9	8.8	-0.01
C8	54.1	0.20	8.8	8.6	-0.02
C6	52.1	0.20	8.6	8.4	-0.02
C4	50.1	0.20	8.5	8.4	-0.01

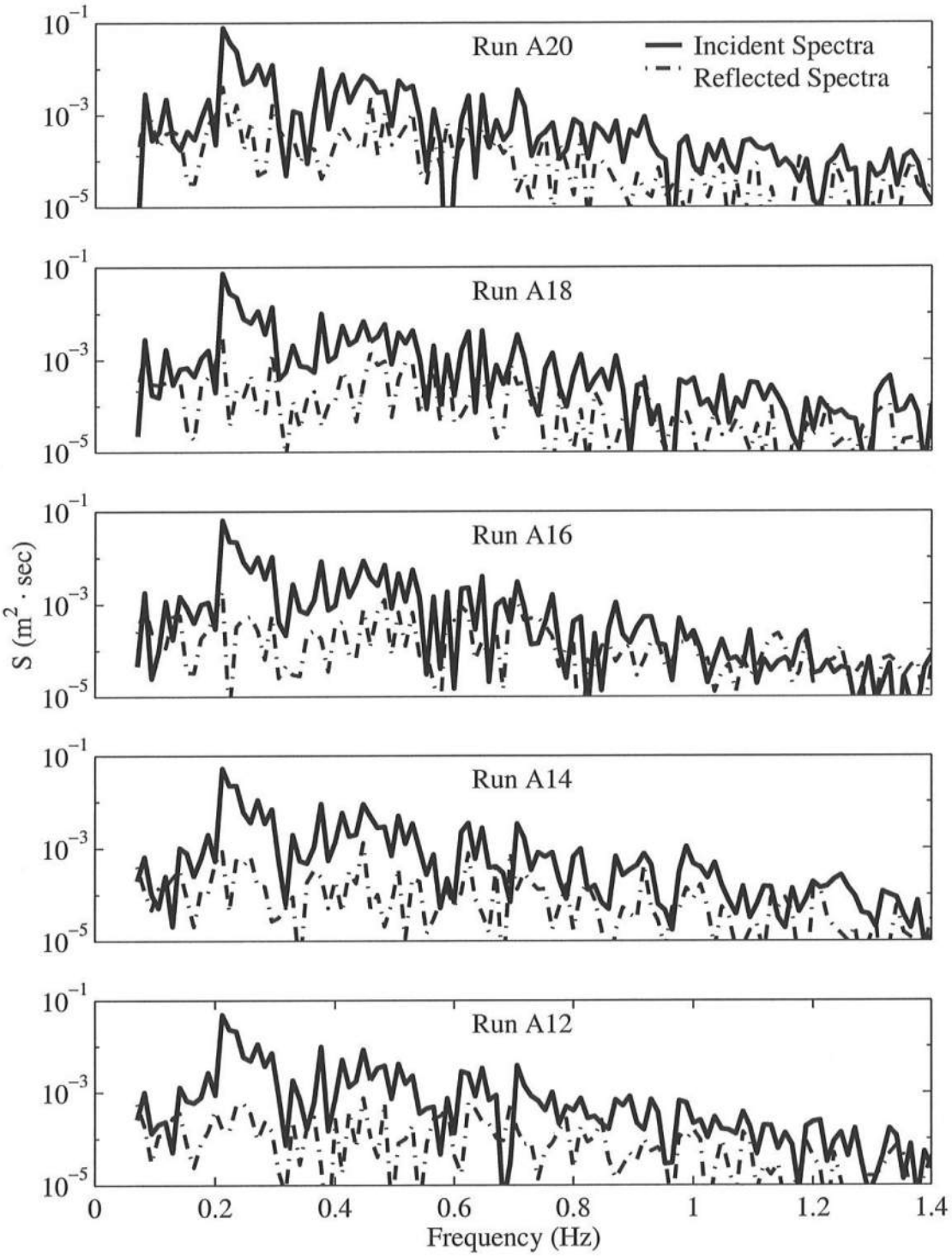

Figure 4.1: Incident and Reflected Spectra for $T_p = 4.7$ s; $d_t = 20$, 18, 16, 14, and 12 cm.

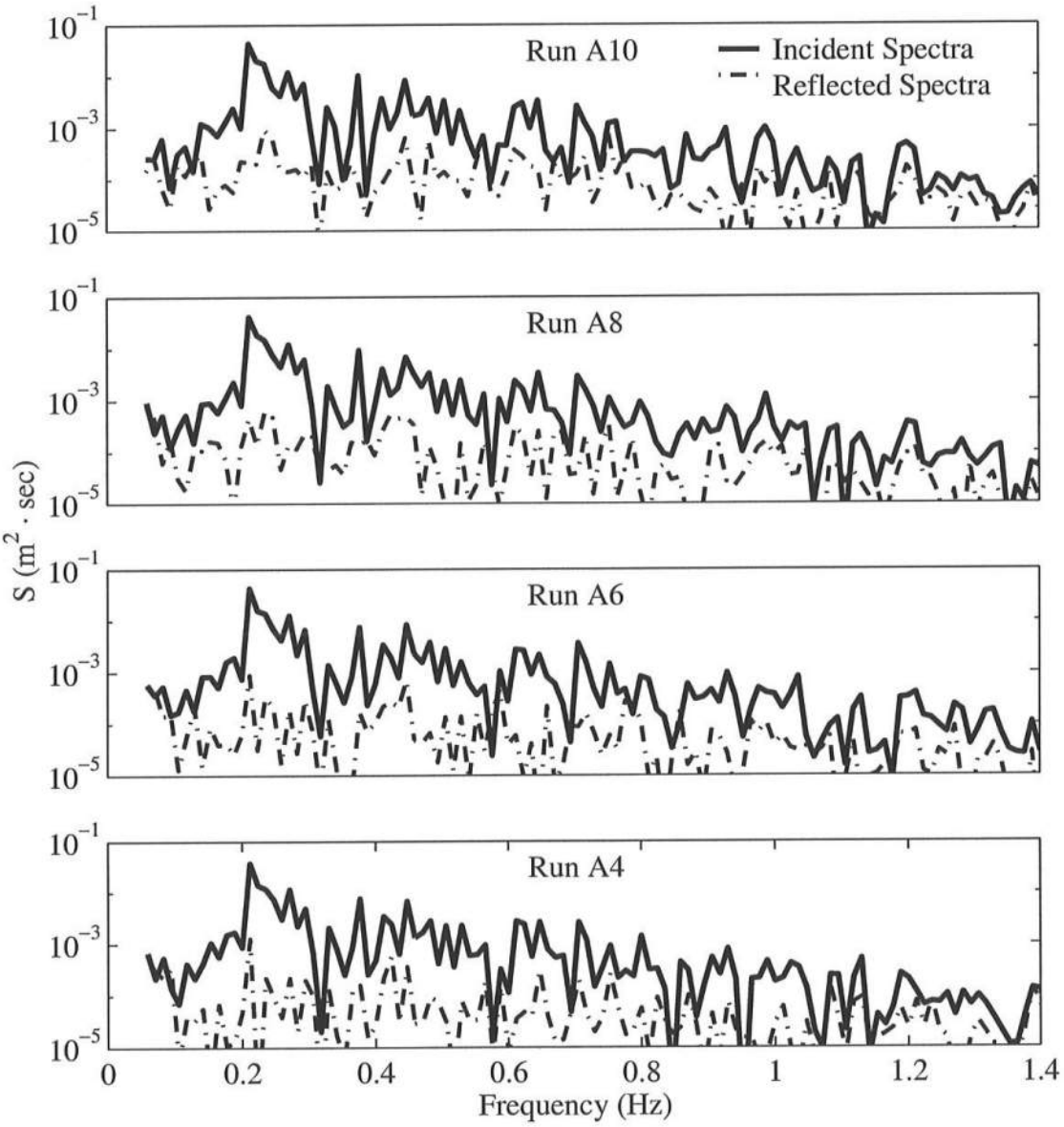

Figure 4.2: Incident and Reflected Spectra for $T_p = 4.7$ s; $d_t = 10$, 8, 6, and 4 cm.

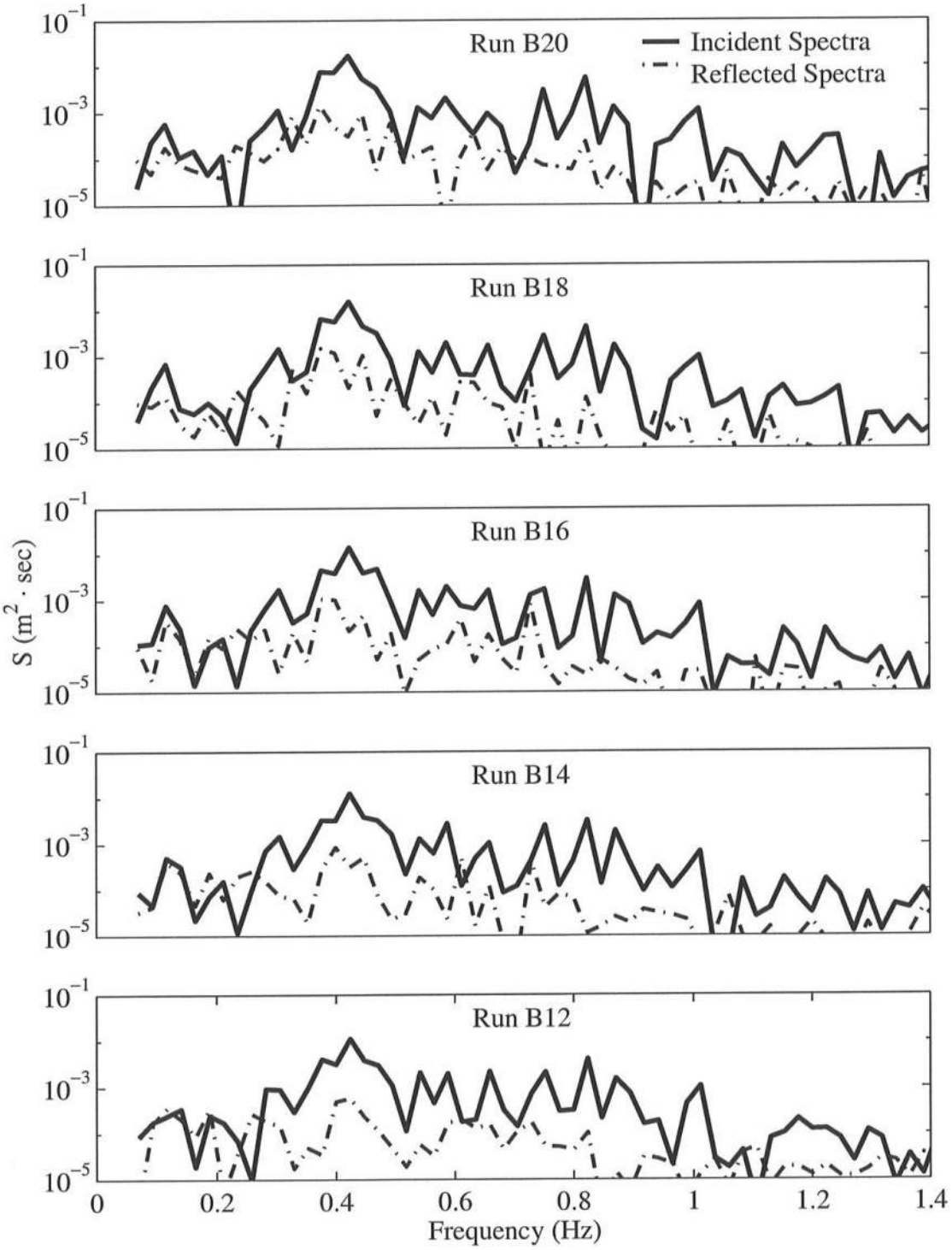

Figure 4.3: Incident and Reflected Spectra for $T_p = 2.4$ s; $d_t = 20$, 18, 16, 14, and 12 cm.

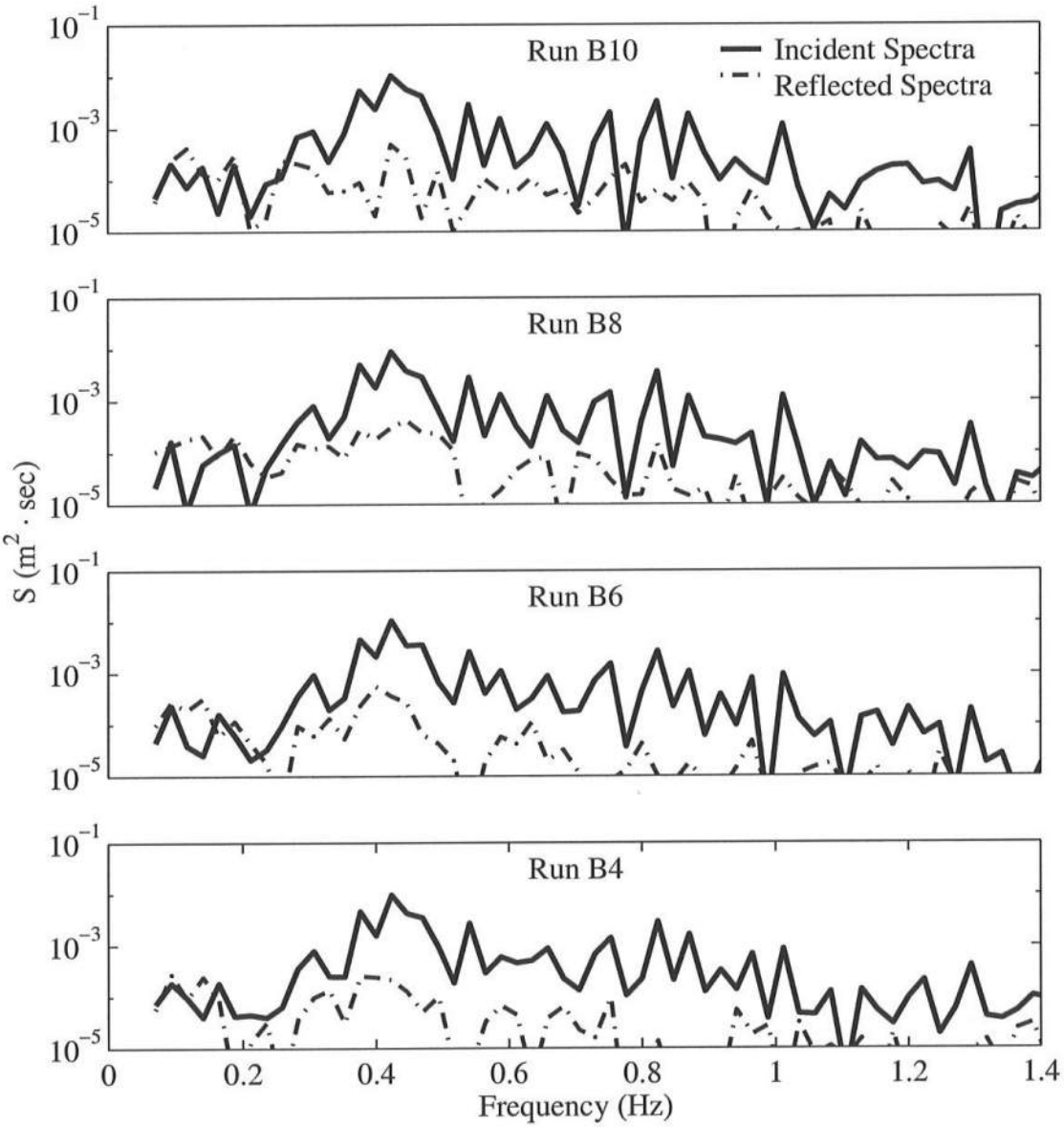

Figure 4.4: Incident and Reflected Spectra for $T_p = 2.4$ s; $d_t = 10$, 8, 6, and 4 cm.

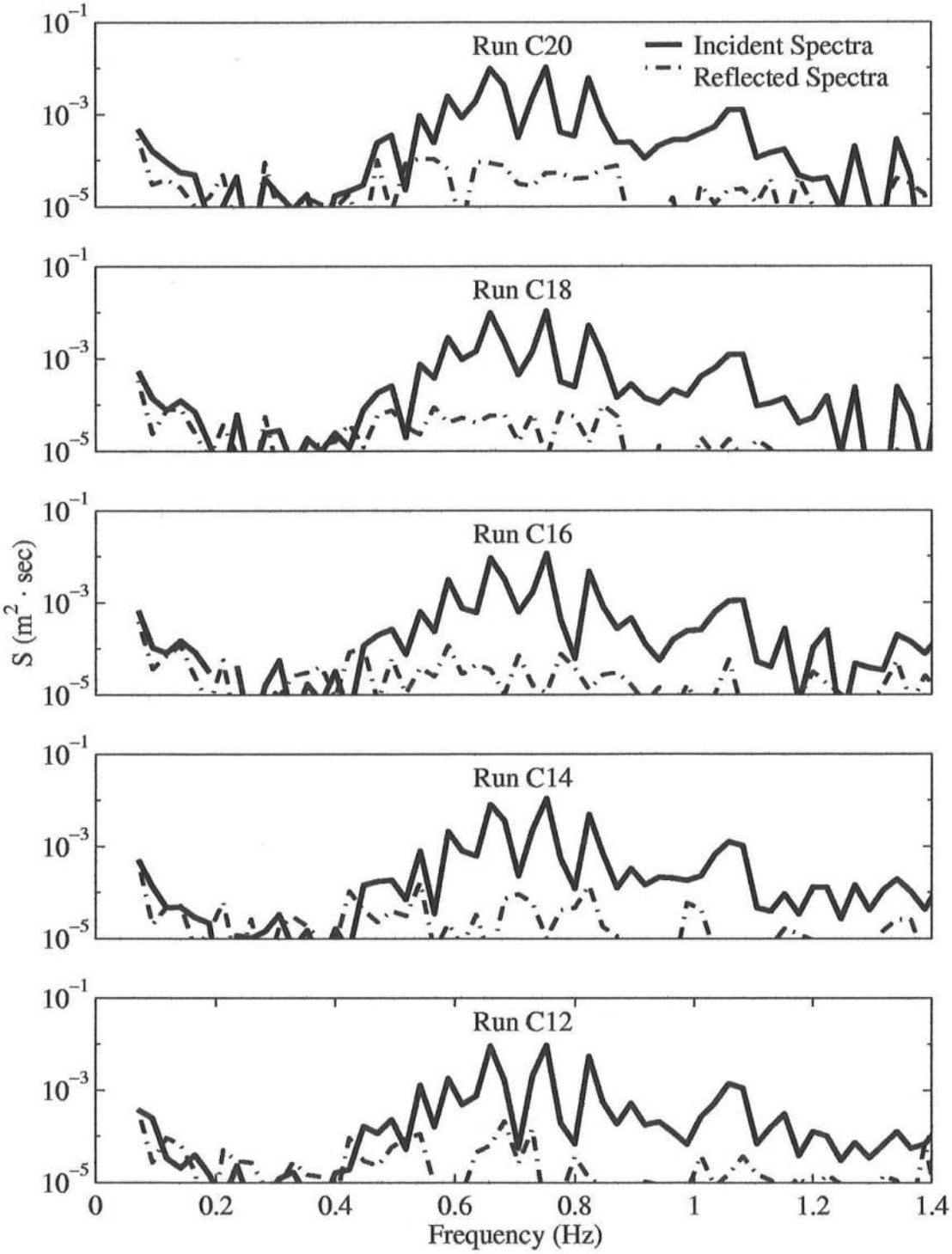

Figure 4.5: Incident and Reflected Spectra for $T_p = 1.5$ s; $d_t = 20$, 18, 16, 14, and 12 cm.

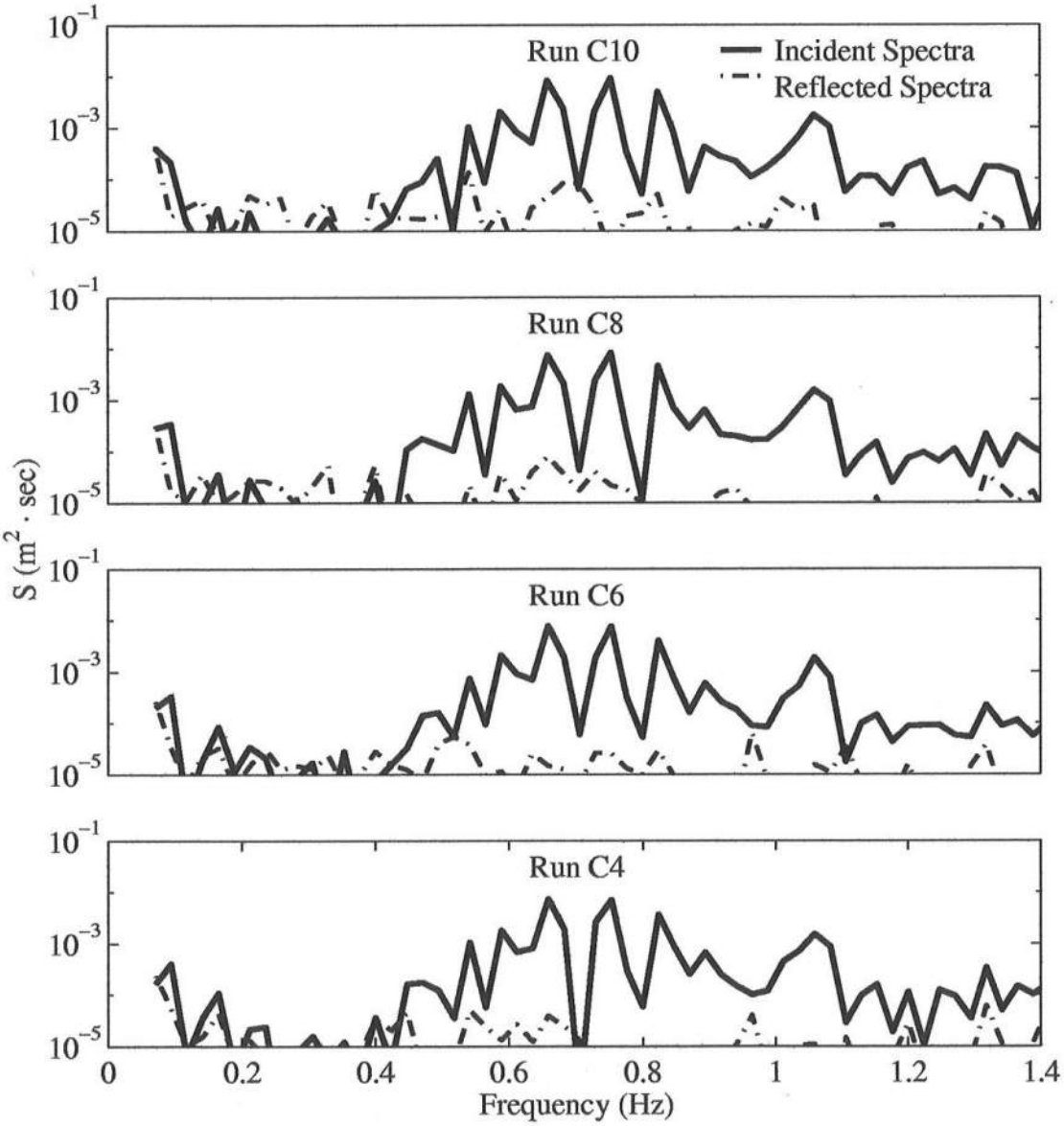

Figure 4.6: Incident and Reflected Spectra for T_p = 1.5 s; d_t = 10, 8, 6, and 4 cm.

Chapter 5

MEASURED CROSS-SHORE VELOCITIES

Horizontal velocities were measured at the toe of the revetment for test runs with d_t greater than or equal to 8 cm. Measurements could not be made for d_t less than 8 cm due to the extended emergence of the ADV probe from the water. The long-shore velocities were measured and found to be negligible, consisting mostly of three-dimensional turbulence and signal noise.

In this chapter, cross-shore velocity time series, spectra, and parameters will be presented as well as the approximate relationships between the free surface statistics and cross-shore velocity statistics. The mean velocity $\overline{u}$, standard deviation σ_u, skewness s_u, and kurtosis K_u for each time series are computed under the assumption of equivalency of the probabilistic and time averaging as stated in Chapter 3 for the free surface parameters. The cross-shore velocity u, is taken to be positive landward.

5.1 Cross-shore Velocity Time Series

The cross-shore velocity time series were recorded for each test if the water depth at the toe was equal to or greater than 8 cm. Time series plots for each water depth and respective incident peak period are displayed in Figure 5.1, Figure 5.2, and

Figure 5.3. The velocity time series appear jagged due to turbulence caused by wave breaking, similar to the free surface time series for gauge 9 at the toe of the slope. Cross-shore velocity is taken to be positive onshore. Peak velocities from the time series are observed onshore while offshore velocity appears to occur for longer durations especially for the longer peak period T_p = 4.7 s. This occurs partly because of wave nonlinearity and partly because a certain volume of water stored in the stone is released from the revetment stone during subsequent wave downrush.

5.2 Cross-shore Velocity Frequency Spectra

Frequency spectra were plotted for each test, including the effects of reflected waves. The cross-shore velocity data was analyzed in the same manner as the free surface data, utilizing a Bartlett window to band-average the data with 16 degrees of freedom.

The frequency spectra were plotted for each peak period with all tests for the water depths over which data could be recorded. The plots are included on Figure 5.4 displaying the results for T_p = 4.7 s, Figure 5.5 displaying the results for T_p = 2.4 s, and Figure 5.6 displaying the results for T_p = 1.5 s. Similar to the spectral analysis results from gauge 9 of the free surface data, an increase of low frequency velocity components were observed with the decrease of d_t. The results are similar for all peak periods.

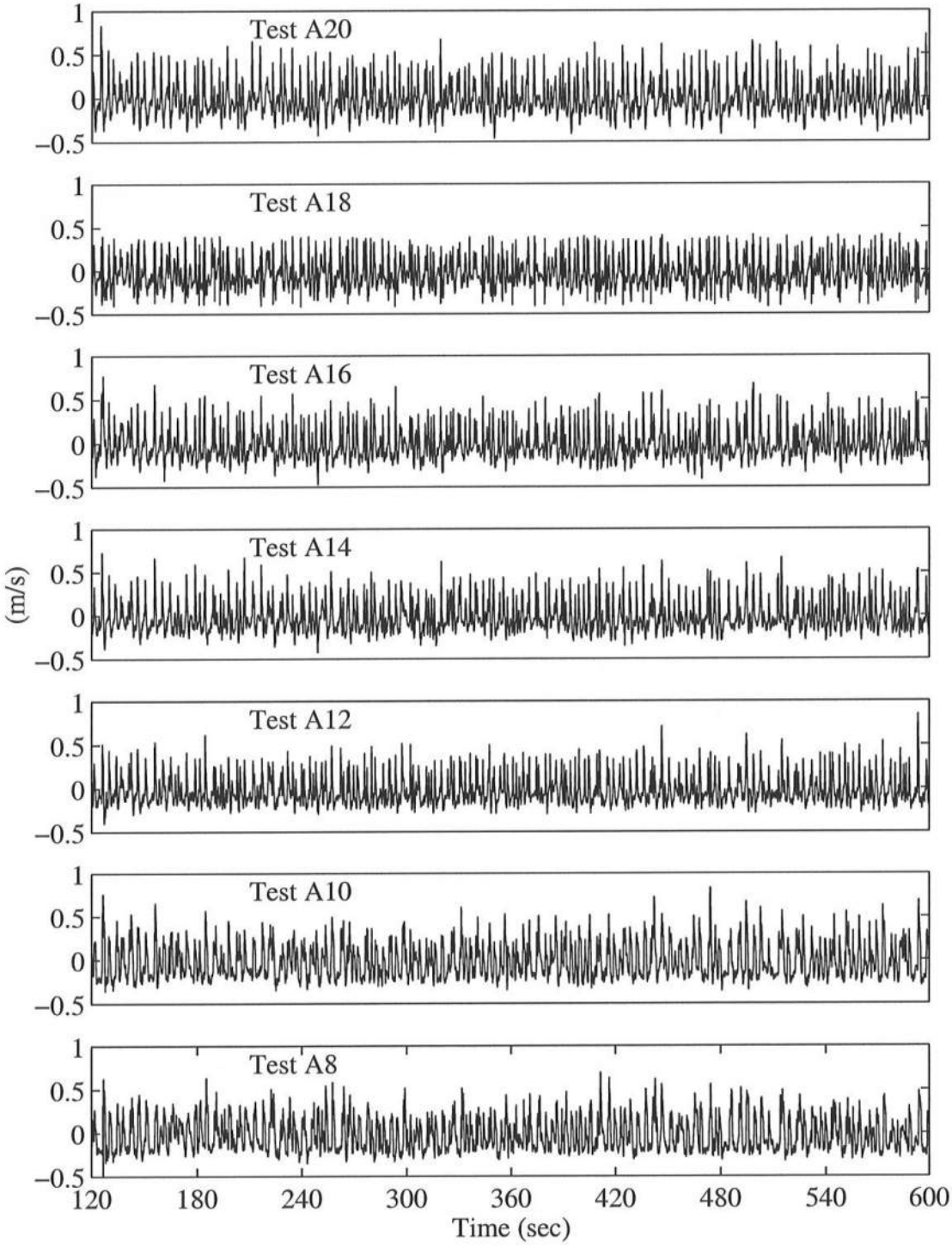

Figure 5.1: Cross-shore Velocities for $T_p = 4.7$ s; $d_t = 20$, 18, 16, 14, 12, 10 and 8 cm.

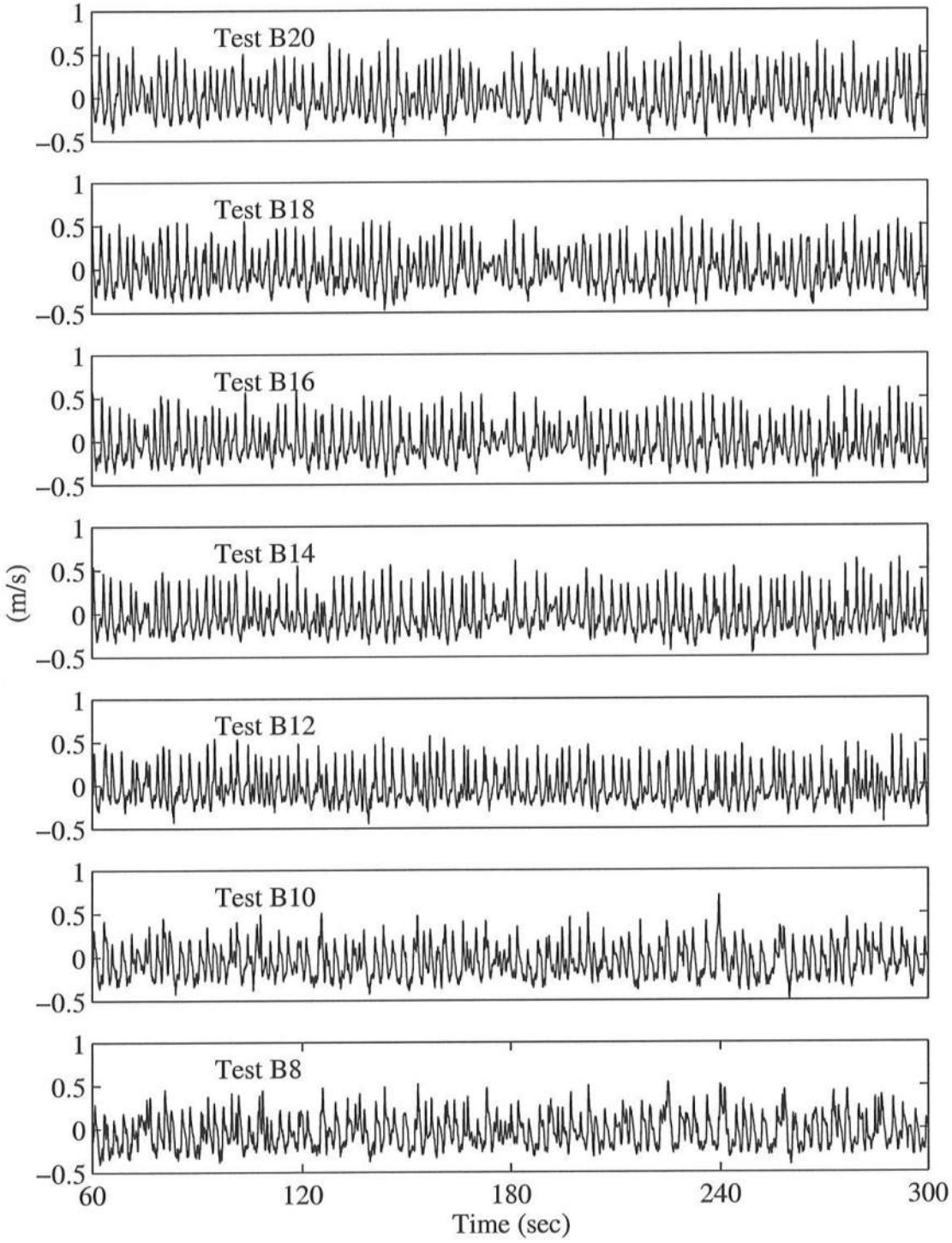

Figure 5.2: Cross-shore Velocities for $T_p = 2.4$ s; $d_t = 20$, 18, 16, 14, 12, 10 and 8 cm.

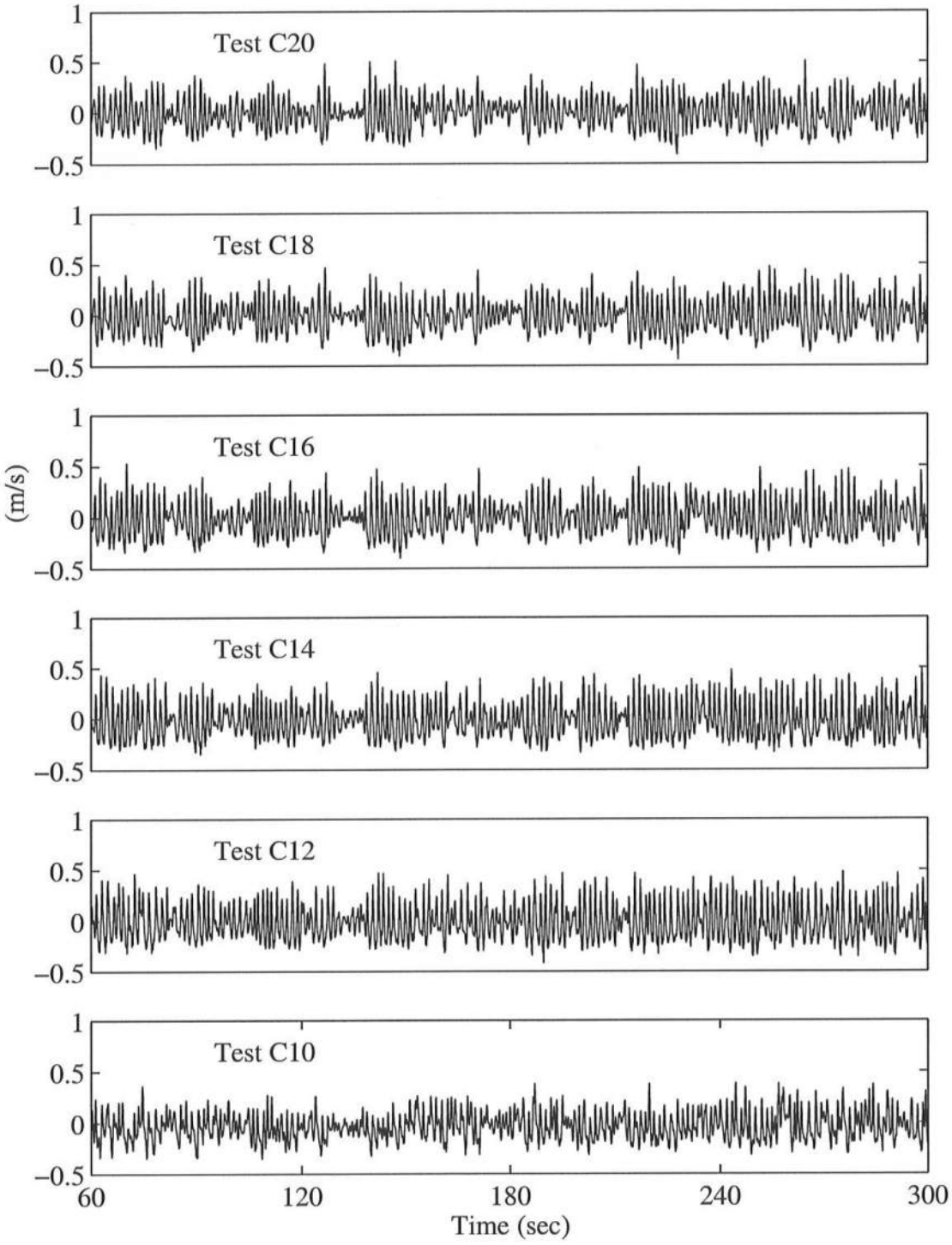

Figure 5.3: Cross-shore Velocities for $T_p = 1.5$ s; $d_t = 20$, 18, 16, 14, 12, and 10 cm.

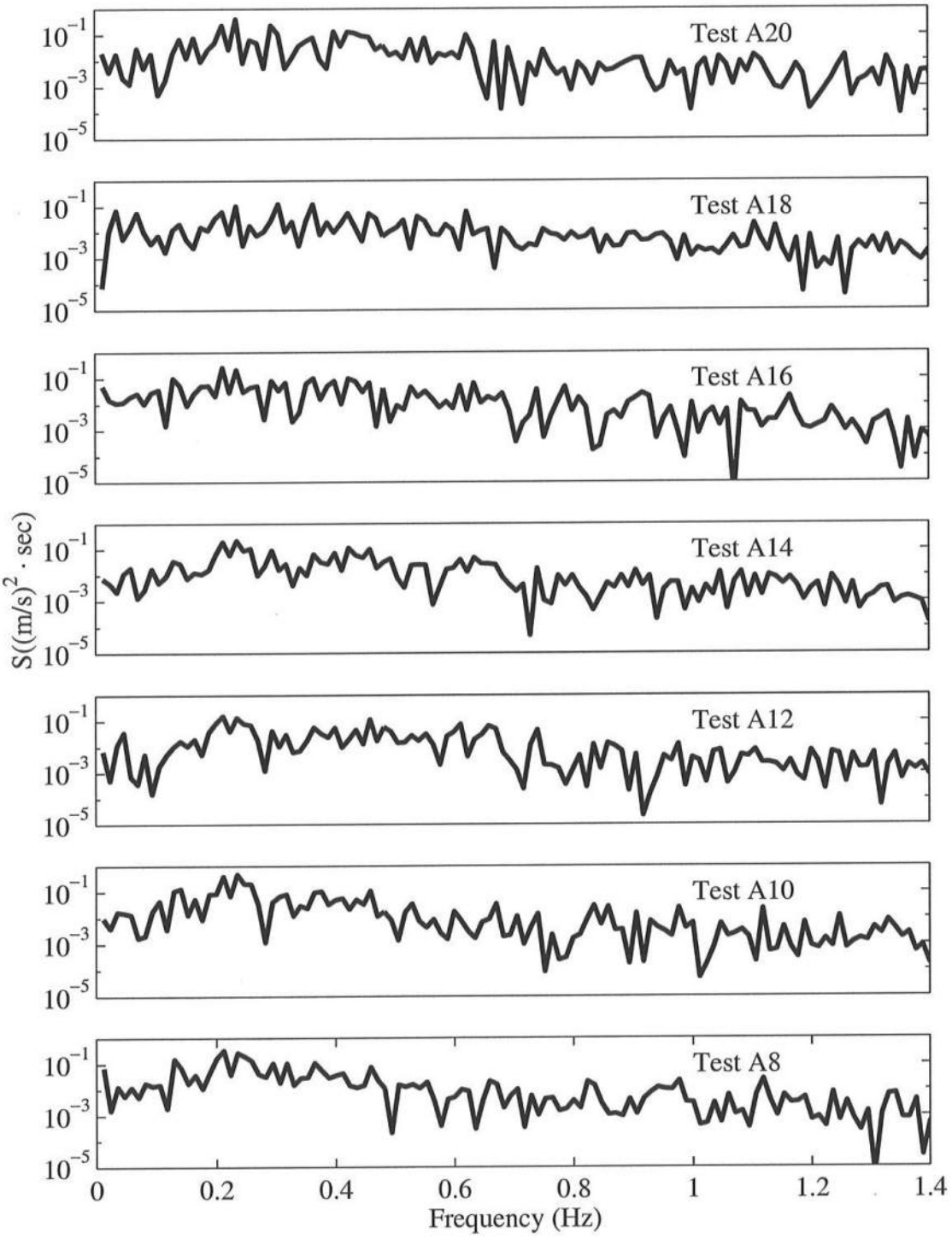

Figure 5.4: Frequency spectra for $T_p = 4.7$ s and $d_t = 20$, 18, 16, 14, 12, 10 and 8 cm.

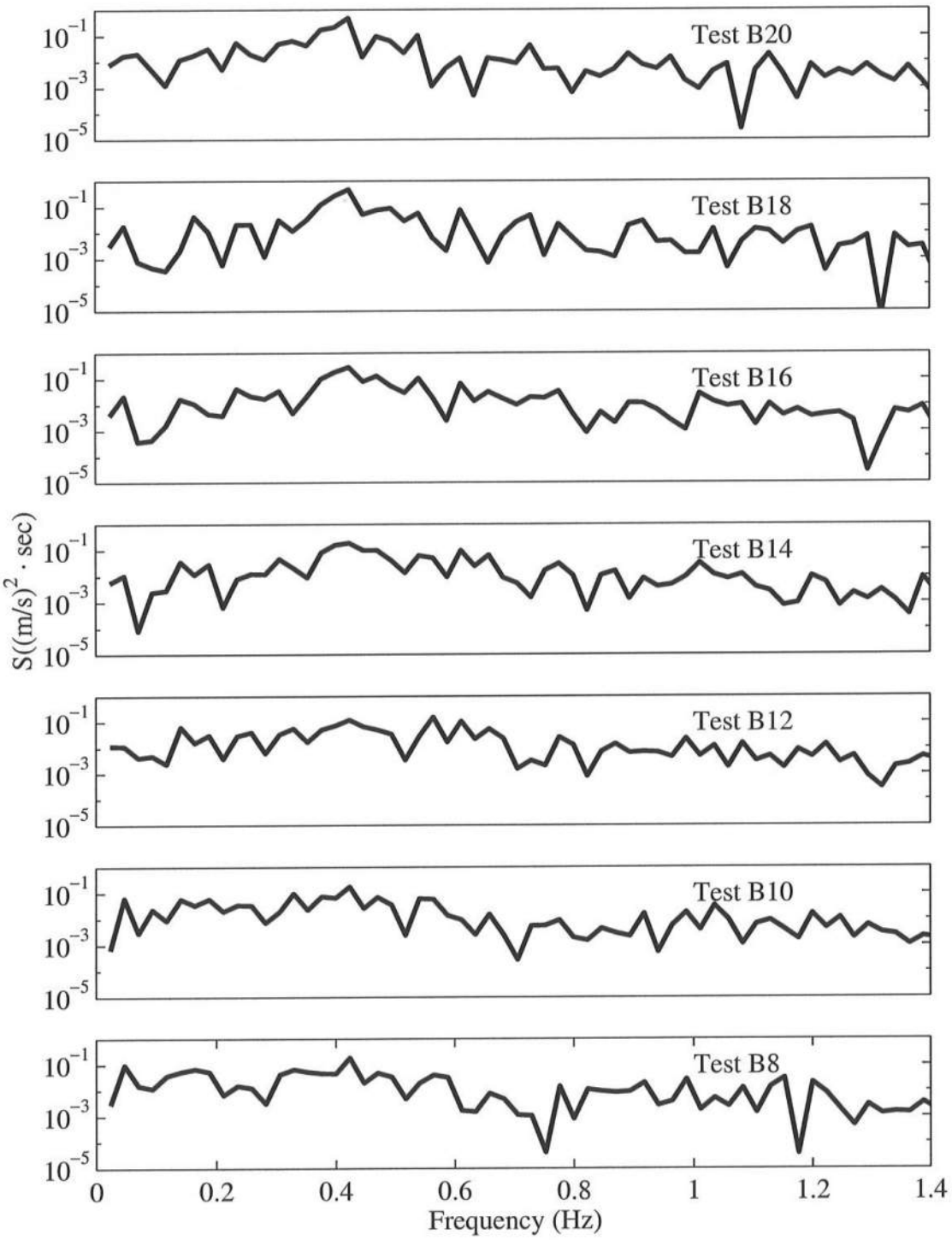

Figure 5.5: Frequency spectra for $T_p = 2.4$ s and $d_t = 20$, 18, 16, 14, 12, 10 and 8 cm.

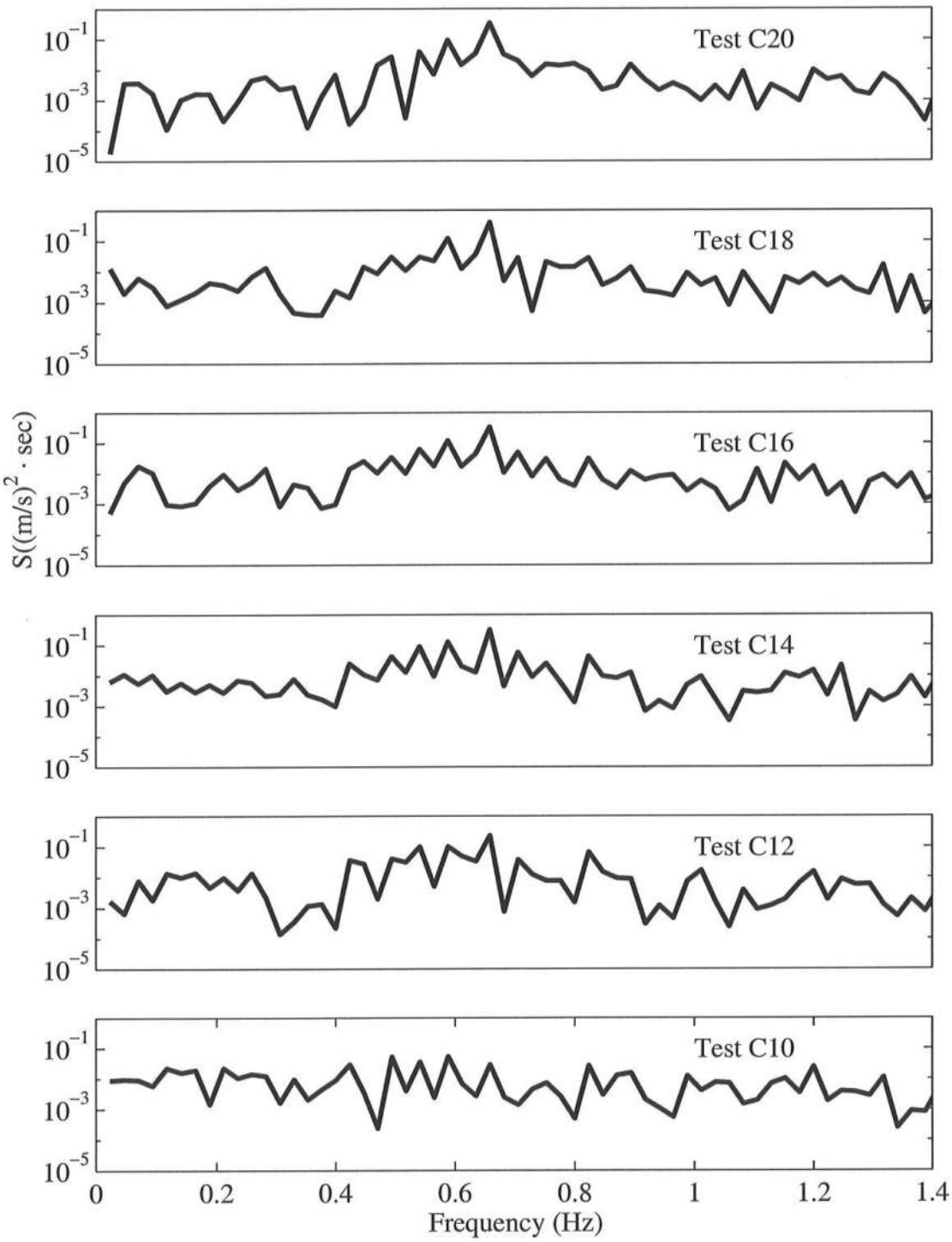

Figure 5.6: Frequency spectra for T_p = 1.5 s and d_t = 20, 18, 16, 14, 12, and 10 cm.

5.3 Horizontal Velocity and Linear Theory

To obtain the approximate relationships between the free surface and cross-shore velocity statistics, local nonlinearity may be neglected and linear progressive long-wave theory may be assumed to be approximately valid locally, even inside the surf zone (Guza and Thornton 1980). The relationship of the oscillatory components of the cross-shore velocity and free surface elevation is expressed as

(5.1)

where g = gravitational acceleration and = mean water depth, defined as

where d = still water depth. If equation (5.1) holds, the following statistical relationships can be derived

; ; (5.2)

in which , s, and, K are the standard deviation, skewness, and kurtosis of the free surface elevation .

To estimate the mean velocity or undertow , it has been assumed that the cross-shore velocity measured near the bottom, but well outside the boundary layer, is approximately equal to the depth-averaged velocity U. The time-averaged continuity equation, , for an impermeable beach yields (Kobayashi *et al.* 1998).

(5.3)

Substituting and equation (5.1) into (5.3) yields the following equation for undertow velocity:

(5.4)

5.4 Cross-shore Velocity Statistics

Cross-shore velocity statistical data were calculated for each test, given the limitations on water depth, and are presented in Table 5.1, Table 5.2, and Table 5.3 for T_p = 4.7 s, 2.4 s, and 1.5 s, respectively. Undertow velocity, , standard deviation of the cross-shore velocity , skewness, s_u, and kurtosis, K_u, are tabulated and compared to predicted values from the equations previously presented. The theoretical values are calculated utilizing free surface data gathered from gauge 9, which was co-located with the ADV at the toe of the revetment.

Comparison of the theoretical results to the measured results from the cross-shore velocity yield poor to fair results. This poor correlation appears to be related to a variety of factors. As stated earlier, the ADV was placed at the toe of the revetment with the probe approximately 1.5 cm from the bottom. The gauge was placed at this location in order to gather as much comparable data as possible. The assumption of linear long wave theory, with no reflected waves, appears to be crude at the toe of the 1:2 slope. In the tests performed, moderate wave reflection was generally observed outside the surf zone, but the wave reflection coefficient may have increased landward (Baquerizo *et al.* 1999).

Table 5.1: Comparison of Measured Cross-shore Velocity Statistics to those Predicted by Linear Long Wave Theory for $T_p = 4.7$ s.

Test	(cm/s)		(cm/s)		S_u		K_u	
	Meas.	Theory	Meas.	Theory	Meas.	Theory	Meas.	Theory
A20	-1.3	-7.0	18.6	31.3	0.87	0.29	3.73	3.20
A18	-1.8	-7.3	19.4	31.3	1.08	0.23	3.99	3.03
A16	-2.1	-8.1	17.1	32.0	0.93	0.23	3.76	2.97
A14	-2.8	-8.9	16.5	32.6	1.04	0.19	3.98	2.83
A12	-3.1	-10.0	15.6	33.3	1.12	0.16	4.18	2.72
A10	-2.5	-9.9	19.2	32.5	0.81	0.14	3.13	2.67
A8	-2.4	-12.8	19.0	34.6	0.79	0.15	3.04	2.67

Table 5.2: Comparison of Measured Cross-shore Velocity Statistics to those Predicted by Linear Long Wave Theory for T_p = 2.4 s.

Test	$\bar{u}$ (cm/s)		u_{rms} (cm/s)		S_u		K_u	
	Meas.	Theory	Meas.	Theory	Meas.	Theory	Meas.	Theory
B20	-1.6	-5.1	20.1	26.8	0.65	0.39	2.94	3.78
B18	-2.7	-5.3	19.3	26.6	0.69	0.35	3.00	3.43
B16	-3.0	-5.9	18.9	27.3	0.80	0.28	3.19	3.10
B14	-4.0	-7.5	18.1	28.1	0.89	0.32	3.34	2.94
B12	-3.9	-7.5	17.3	28.8	0.91	0.33	3.34	2.83
B10	-5.7	-7.5	17.5	27.8	0.48	0.36	2.64	2.85
B8	-4.3	-9.0	17.1	29.0	0.49	0.34	2.60	2.79

Table 5.3: Comparison of Measured Cross-shore Velocity Statistics to those Predicted by Linear Long Wave Theory for T_p = 1.5 s.

Test	$\bar{u}$ (cm/s)		u_{rms} (cm/s)		S_u		K_u	
	Meas.	Theory	Meas.	Theory	Meas.	Theory	Meas.	Theory.
C20	-1.1	-2.4	14.1	18.1	0.27	0.63	2.84	4.02
C18	-1.6	-2.7	14.9	18.9	0.26	0.55	2.71	3.99
C16	-1.6	-3.0	15.4	19.4	0.36	0.53	2.66	4.01
C14	-2.5	-3.6	15.8	20.4	0.53	0.53	2.69	3.97
C12	-1.9	-4.6	16.3	22.3	0.52	0.55	2.59	3.95
C10	-2.5	-4.6	12.5	21.5	0.18	1.19	2.66	5.14

Chapter 6

PROBABILITY DISTRIBUTIONS

Wave statistics were calculated from every measured free surface time series, including the runup time series and cross-shore velocity time series. The mean, the standard deviation, and the skewness, were calculated from the time series. The waterline elevation above the still water level (SWL) measured by the runup wire was analyzed in the same way as the free surface elevation η above the SWL. The normalized free surface elevation $\eta*$ is defined as

$$\eta* = \frac{\eta - \overline{\eta}}{\sigma} \tag{6.1}$$

where $\overline{\eta}$ = mean of η. The mean and standard deviation of $\eta*$ are zero and unity, respectively. The measured probability density function for $\eta*$ was compared with the exponential gamma distribution (Kobayashi *et al.* 1998) together with the measured value of skewness *s*. Similarly the mean, standard deviation, and skewness were also calculated from the cross-shore velocity times series, *u*. The normalized cross-shore velocity $u*$ is defined in the same manner as the normalized free surface elevation in equation (6.1) with $\overline{u}$ defined as the mean cross-shore velocity and σ_u defined as the standard deviation of the cross-shore velocity.

6.1 Exponential Gamma Distribution

Given the definition of the normalized free surface elevation $\eta*$, the mean and standard deviation are equal to zero and unity, respectively. The skewness s of $\eta*$ is the same as the skewness of η. The exponential gamma distribution for $\eta*$ can be expressed as

$$f(\eta*) = [\Gamma(a)]^{-1} \sqrt{\psi'(a)} e^{-ay} \exp\left(-e^{-y}\right) \tag{6.2}$$

with

$$y = \sqrt{\psi'(a)}\eta* - \psi(a) \tag{6.3}$$

in which a = shape parameter; Γ = gamma function; ψ = digamma function; and ψ' = trigamma function. The relationship between s and a is given by

$$s = -\psi''(a)[\psi'(a)]^{-1.5} \tag{6.4}$$

in which ψ'' = tetragamma function. The kurtosis K of $\eta*$ is given by

$$K = \psi'''(a)[\psi'(a)]^{-2} + 3 \tag{6.5}$$

in which ψ''' = pentagamma function.

The gamma and related function are explained in Abramowitz and Stegun (1972) and tabulated by Gran (1992). The values of $\Gamma(a)$, $\psi(a)$, $\psi'(a)$, $\psi''(a)$, and $\psi'''(a)$ for given a can be found using *Mathematica* (Wolfran 1991). The value of a for given s can be obtained by solving (6.4) using an iteration method as shown in Gran (1992) (Orzech and Kobayashi 1997).

The exponential gamma distribution can be limited, because we assume a range of $0 \leq s \leq 2$ for the skewness. This range is consistent with available field and laboratory data [Bitner (1980); Huang and Long (1980); Goda (1985); Mase and Kobayashi (1991); Raubenheimer *et al.* (1995)]. Farther offshore, where water is relatively deep, s approached zero and equation (6.2) reduces to a Gaussian distribution:

$$f(\eta*) = \frac{1}{\sqrt{2\pi}} \exp\left(-\eta_*^2/2\right) \qquad \text{for } s = 0 \tag{6.6}$$

Closer to the shoreline, where the swash zone is always wet, s approaches zero and equation (6.2) becomes the exponential distribution:

$$f(\eta*) = e^{-(\eta_* + 1)} \qquad \text{for } s = 2 \tag{6.7}$$

This exponential distribution is limited to the range $\eta* = [(\eta - \overline{\eta})/\sigma] \geq -1$. This lower limit may be interpreted in terms of the instantaneous water depth, $h = (\eta - z_b)$ as expressed by Kobayashi *et al.* (1998), where z_b = the bottom elevation which is taken to be positive above the still water level.

6.2 Free Surface and Runup Elevations

For each test, the measured probability density function $f(\eta*)$, was plotted along with the predicted exponential gamma distribution for each gauge location and the runup wire. In these comparisons, the measured $\overline{\eta}$, σ, and s are used in the exponential gamma distribution. Examples of the distributions are shown in Figure 6.1, Figure 6.2, and Figure 6.3 for T_p = 4.7 s, 2.4 s, and 1.5 s, respectively. Figures for all of the data collected are presented in Appendix C. Only gauge locations 1, 4, 6, and 9 are plotted in

this section along with the runup wire. This is to give a general understanding of how the distribution changes as the waves propagate towards the revetment and the impact the revetment has on the runup distribution. In general the exponential gamma distribution compared well with the measured probability distributions. Deviations are apparent in the regions where intense wave breaking is occurring or frequent spilling breakers are observed.

The exponential gamma distribution does not always represent the runup distribution as well as the free surface comparisons, as can be seen in Figure 6.1, Figure 6.2, and Figure 6.3. This is most likely due to prolonged wave run-down on the revetment. In addition, the agreement is poor when compared to measured distributions for wave gauge 10 when d_t is small. This occurs, because gauge 10 was mounted on the slope of the 1:2 revetment as explained in section 3.4. For example, when $d_t = 4$ cm, the still water elevation was 1 cm below the surface elevation of the 1:2 slope at gauge 10, therefore the time series upon which the analysis was based, was truncated so that $\eta \geq 1$ cm. In these cases of shallow water above the porous stone the distribution agreement is not favorable. However, for the engineering applications for which this model is intended, the exponential gamma distribution performs well because in all cases it compares well with very large values of η^* related to the small probability of the waterline elevation upper limit corresponding to large wave runup elevations.

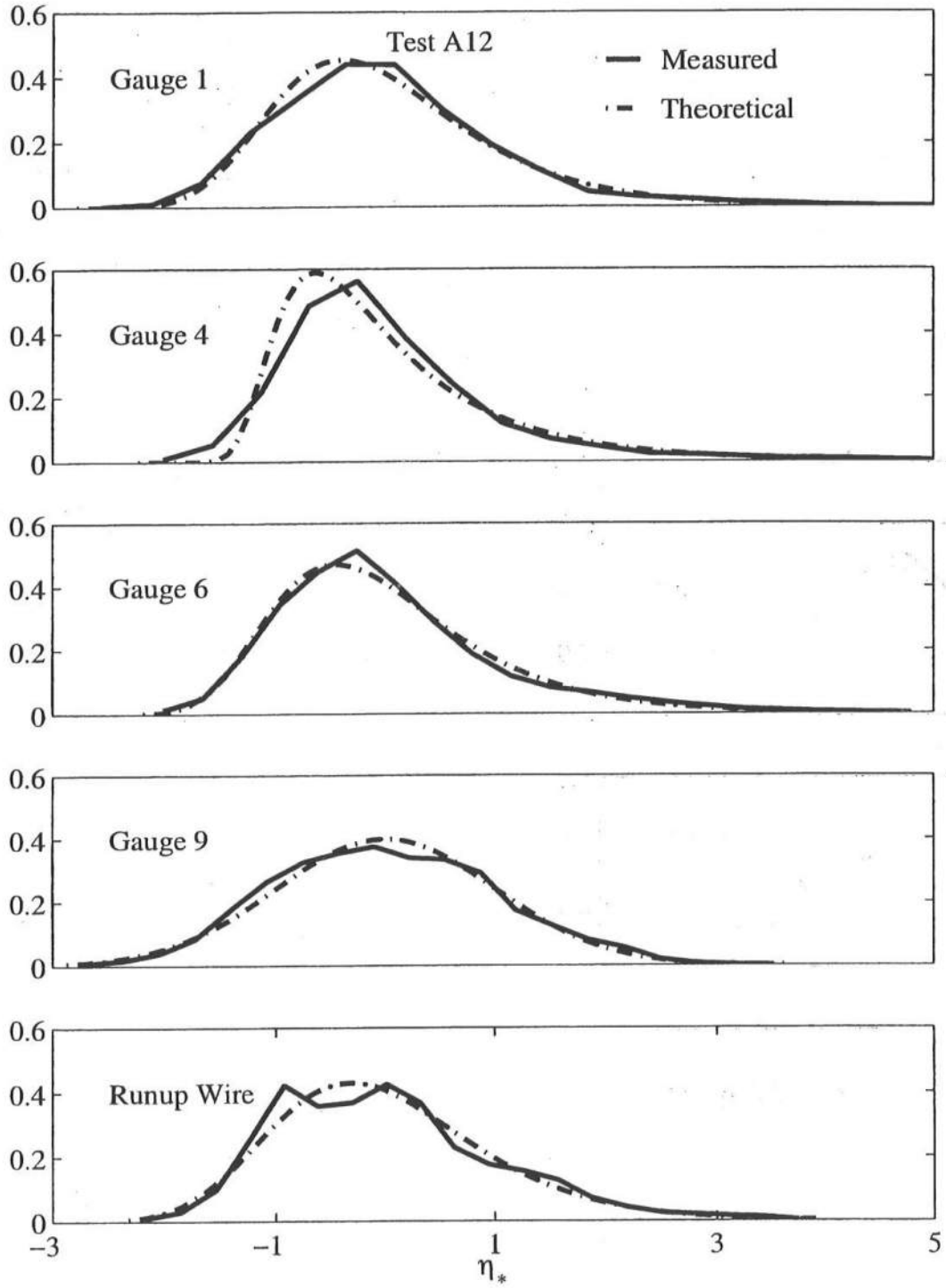

Figure 6.1: Free Surface Comparison of Measured Probability Distributions to the Exponential Gamma Distribution for $T_p = 4.7$ s.

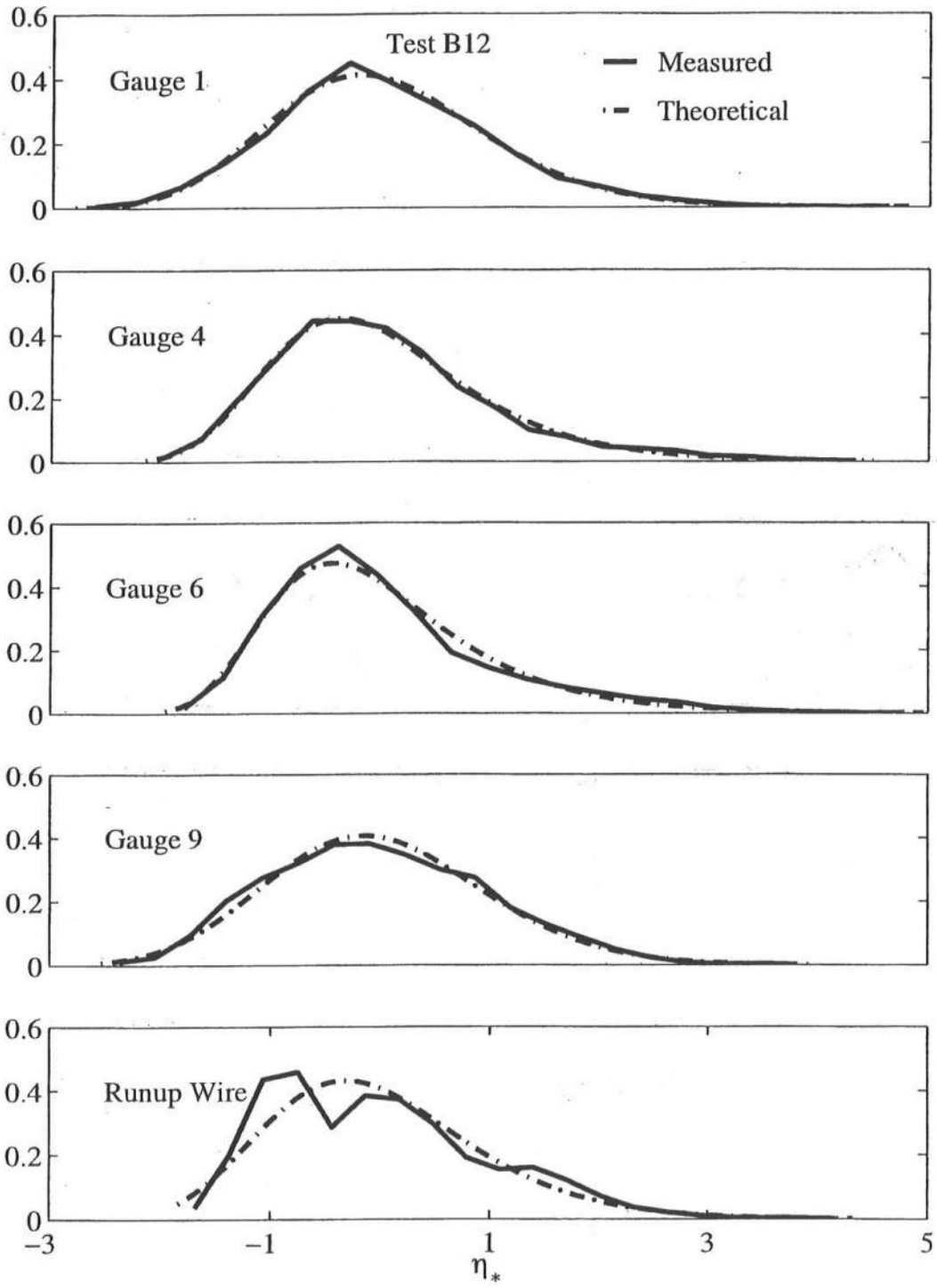

Figure 6.2: Free Surface Comparison of Measured Probability Distributions to the Exponential Gamma Distribution for $T_p = 2.4$ s.

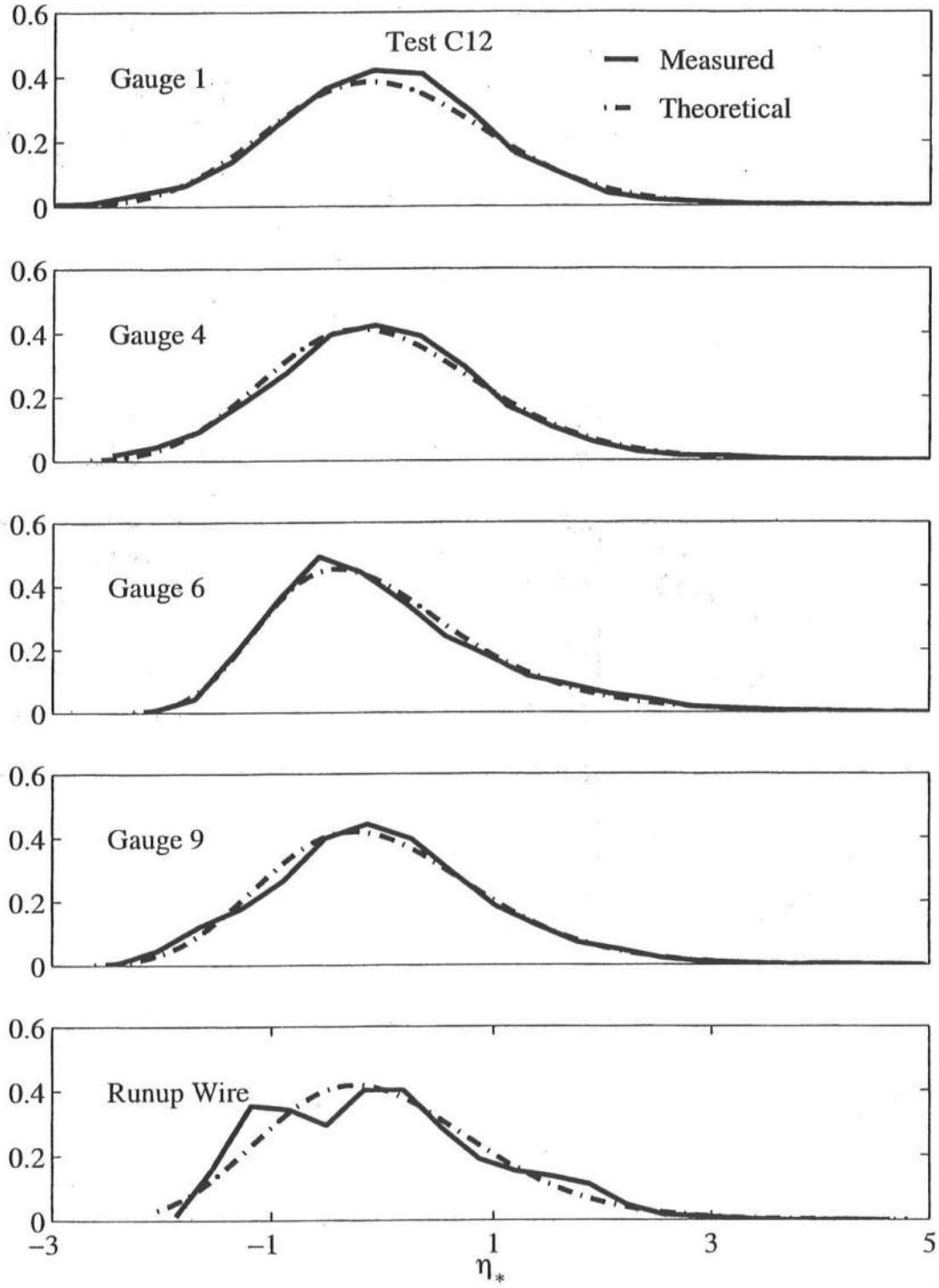

Figure 6.3: Free Surface Comparison of Measured Probability Distributions to the Exponential Gamma Distribution for $T_p = 1.5$ s.

6.3 Cross-shore Velocity

Cross-shore velocities u were analyzed where the normalized cross-shore velocity $u*$ is defined in the same manner as the free surface elevation from equation (6.1). Probability distributions for the cross-shore velocity $f(u*)$, were compared to the exponential gamma distribution when $d_t \geq 8$ cm for tests conducted with $T_p = 4.7$ s and 2.4 s, and when $d_t \geq 10$ cm for tests conducted with $T_p = 1.5$ s due to the emergence of the ADV probe from the water. Comparisons are displayed in Figure 6.4 for $T_p = 4.7$ s, Figure 6.5 for $T_p = 2.4$ s ,and Figure 6.6 for $T_p = 1.5$ s. In general the agreement between the exponential gamma distribution and the measured distribution was good, as can be seen in the figures. The agreement is similar to the free surface comparisons, but became worse as d_t was decreased. This is due to the prolonged offshore velocities at the toe that occur in shallow water depths.

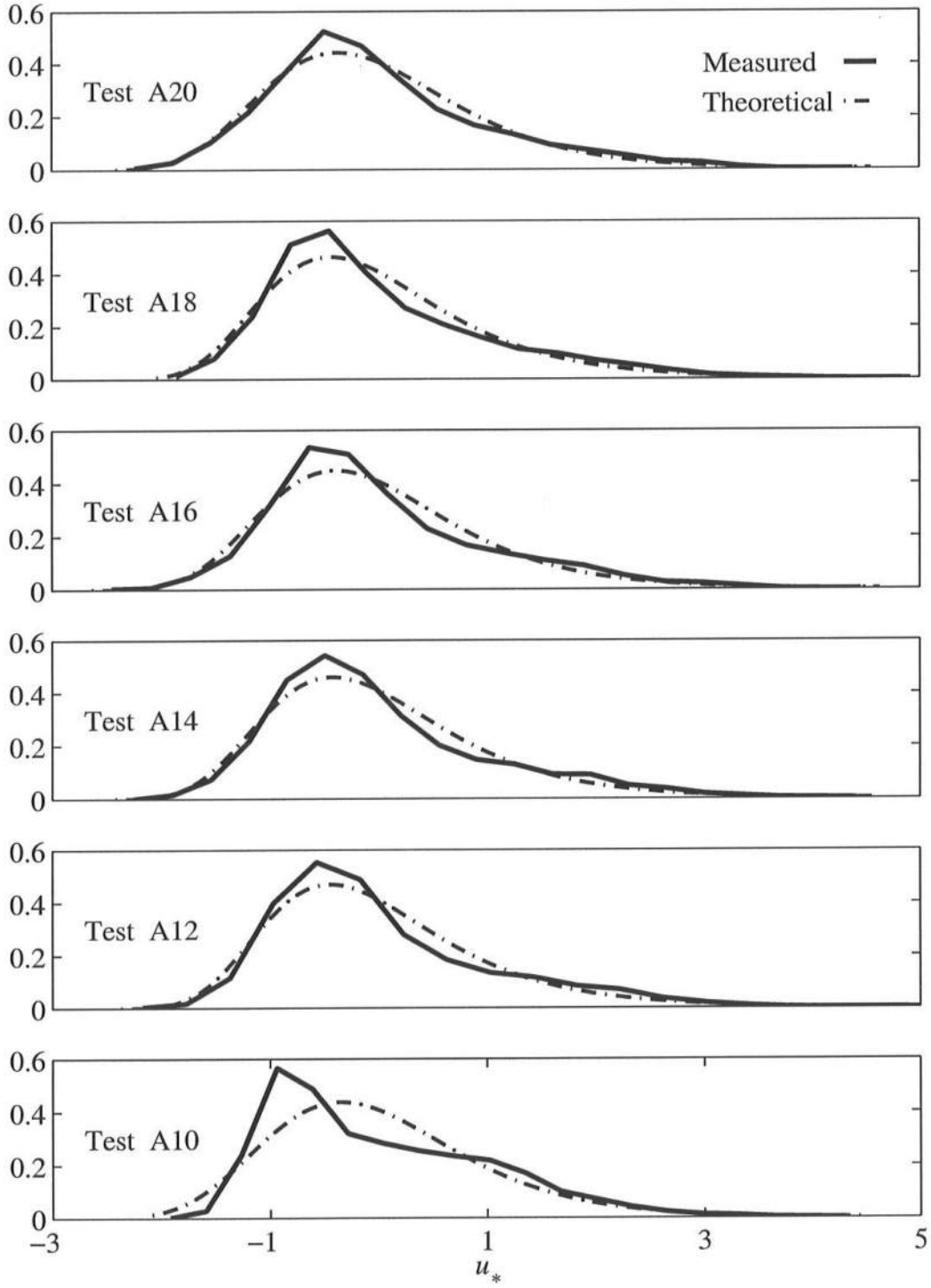

Figure 6.4: Cross-shore Velocity Comparison of Measured Probability Distributions to the Exponential Gamma Distribution for $T_p = 4.7$ s.

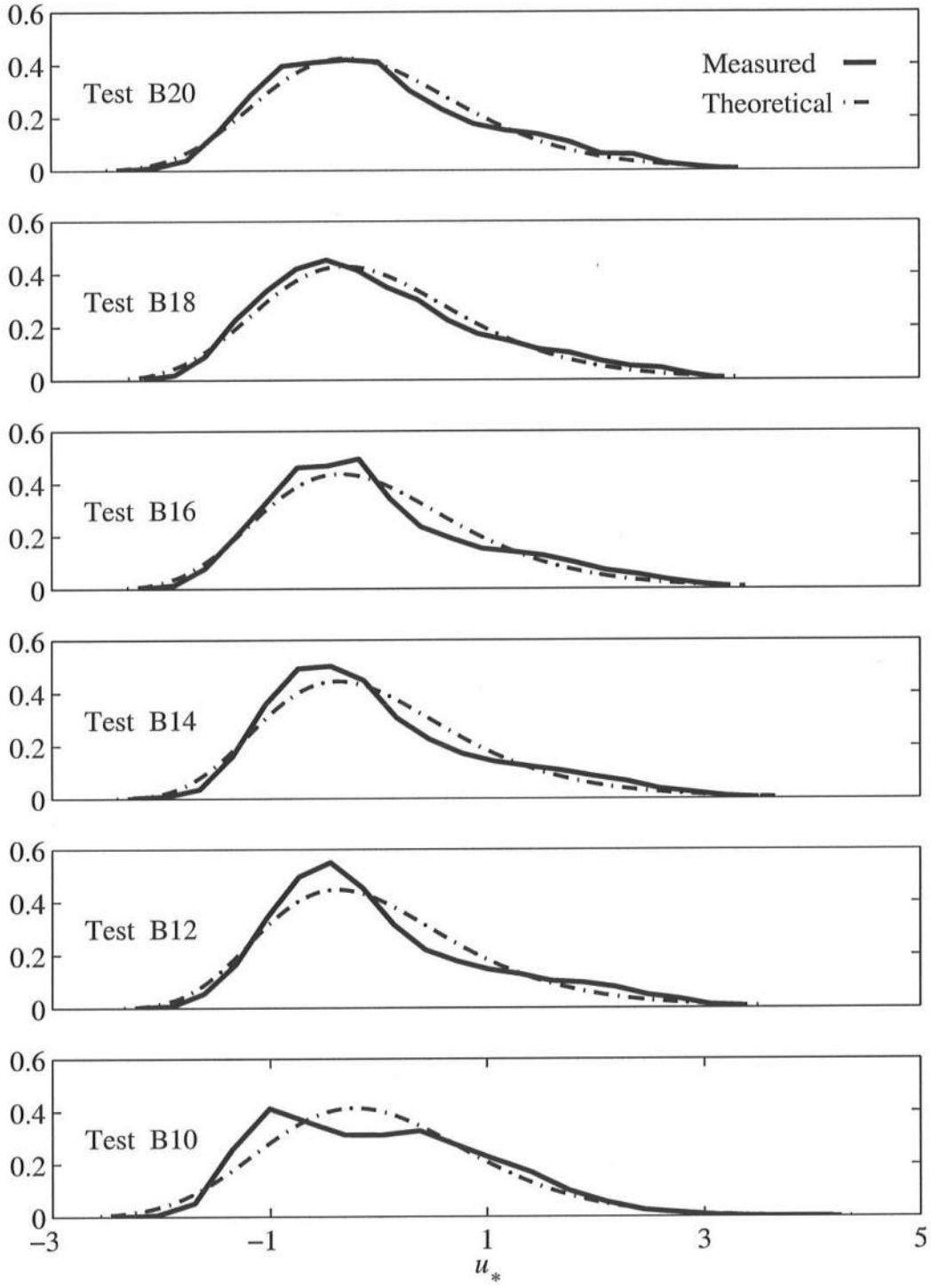

Figure 6.5: Cross-shore Velocity Comparison of Measured Probability Distributions to the Exponential Gamma Distribution for $T_p = 2.4$ s.

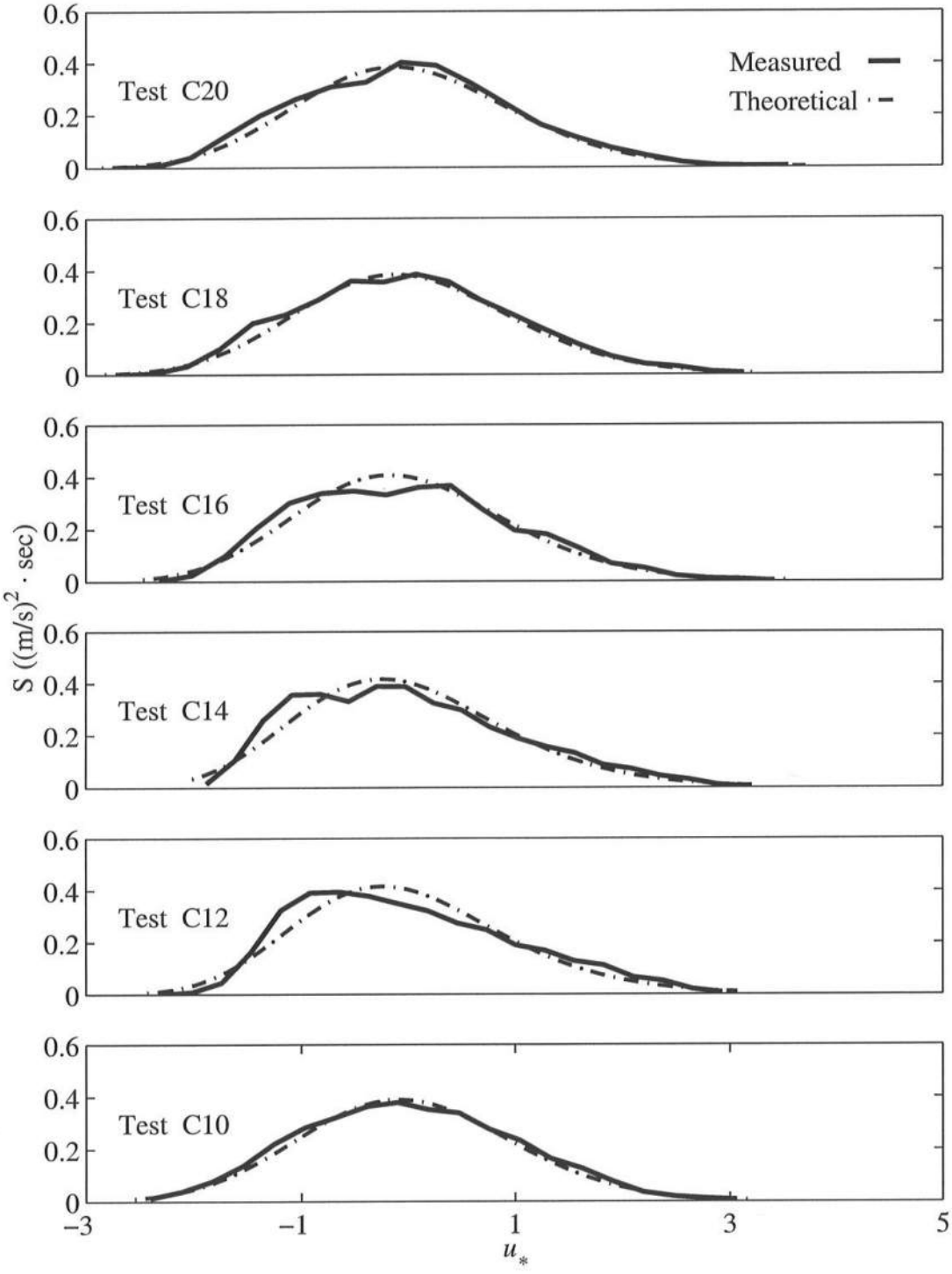

Figure 6.6: Cross-shore Velocity Comparison of Measured Probability Distributions to the Exponential Gamma Distribution for T_p = 1.5 s.

Chapter 7

CROSS-SHORE VARIATION OF TIME SERIES PARAMETERS

In Chapter 5, it was shown that the measured probability distribution can be fitted by the exponential gamma distribution. In this chapter, the numerical model CSHORE is presented, as well as the comparison of the measured cross-shore variations of $\overline{\eta}$, $H_{rms} = \sqrt{8}\sigma$, s and K.

7.1 Numerical Model CSHORE

CSHORE is a nonlinear time-averaged model developed to predict cross-shore variations in wave setup, $\overline{\eta}$, and the root-mean-square wave height, H_{rms}, from outside the surf zone to the swash zone where H_{rms} is defined as $H_{rms} = \sqrt{8}\sigma$ with σ = standard deviation of the free surface elevation (Kobayashi and Johnson 1998). This model is based on the time-averaged continuity, momentum, and energy equations derived by time-averaging the nonlinear equations used in a time-dependent model by Kobayashi and Wurjanto (1992). Alongshore uniformity and normally incident irregular waves were assumed in the model formulation. To account for nonlinear affects in very shallow water, the finite-amplitude shallow-water equations including bottom friction were time-averaged.

7.1.1 Governing Equations for CSHORE

The governing equations for CSHORE are presented here, the detailed model formulation is not discussed as it has been previously presented by Kobayashi and Johnson (1998). Assuming an impermeable bottom, the time-averaged continuity equation can be expressed as

$$\overline{hU} = 0 \tag{7.1}$$

where h = instantaneous water depth; and U = instantaneous depth-averaged horizontal velocity. The time-averaged cross-shore momentum equation is written as (Kobayashi *et al.* 1989)

$$\frac{dS_{xx}}{dx} = -\rho g\bar{h}\ \frac{d\bar{\eta}}{dx} - \bar{\tau}_b \tag{7.2}$$

with

$$S_{xx} = \rho\left[\overline{hU^2} + \frac{1}{2}g\overline{(\eta-\bar{\eta})^2}\right] \tag{7.3}$$

$$\tau_b = \frac{1}{2}\rho\ f_b\overline{|U|U} \tag{7.4}$$

in which x = cross-shore coordinate taken to be positive landward; S_{xx} = cross-shore radiation stress; ρ = fluid density; g = gravitational acceleration; η = instantaneous free surface elevation above the still water level; $\bar{\tau}_b$ = time-averaged bottom shear stress; f_b = bottom friction factor. The bottom elevation z_b is defined as $z_b = (\eta - h)$. It is assumed that z_b depends only on x. The time-averaged energy equation

corresponding to the time-averaged continuity and momentum equations is expressed as (Kobayashi and Wurjanto 1992)

$$\frac{d}{dx}\left(\overline{E_F}\right) = -\overline{D_f} - \overline{D}_B \tag{7.5}$$

with

$$\overline{E_F} = \frac{1}{2}\rho h\overline{U^3} + \rho g\overline{\eta h U} \tag{7.6}$$

$$\overline{D_f} = \frac{1}{2}\rho\, f_b\overline{|U|U^2} \tag{7.7}$$

in which $\overline{E_F}$ =energy flux per unit width; $\overline{D_f}$ = energy dissipation rate due to bottom friction; and $\overline{D_B}$ = energy dissipation rate due to wave breaking. The value for $\overline{D_B}$ is estimated empirically for the model.

7.1.2 Empirical Relationships for Prediction of *s* and *K*

To develop a method for predicting s and K, CSHORE was calibrated against five random wave tests. Three tests were performed on a plywood beach with a 1:16 slope, with the remaining tests performed on an equilibrium fine sand beach. The following empirical relationships for s and K were developed based on $H_* = H_{rms}/\overline{h}$.

$$s = 2H_* \qquad \text{for} \quad 0.1 \le H_* \le 0.5 \tag{7.8}$$

$$s = 1.5 - H_* \qquad \text{for} \quad 0.5 \le H_* \le 1.0 \tag{7.9}$$

$$s = 0.7H_* - 0.2 \qquad \text{for} \quad 1.0 \le H_* \lesssim 5 \tag{7.10}$$

with kurtosis estimated as

$$K = 3 + s^{2.2} \qquad \text{for } 0.2 < s \lesssim 3 \tag{7.11}$$

7.2 Required Input for CSHORE

CHSORE requires wave data and certain parameters to predict the shoreward progression of irregular waves. The required wave input data is the spectral peak period T_p, the root-mean-square wave height, and wave setup or setdown at an offshore location. The offshore location for all tests performed was at the cross-shore coordinate x = 0 m, which is the location of gauge 1. The input root-mean-square wave height H_{rms} and setup $\overline{\eta}$ values were entered from measured values at gauge 1, presented earlier in Table 3.1 for T_p = 4.7 s, Table 3.2 for T_p = 2.4 s, and Table 3.3 for T_p = 1.5 s. In addition to the wave statistical parameters, the bottom friction factor and bathymetry has to be specified at cross-shore locations landward of x = 0 m. The bottom friction factor f_b was chosen to range between 0.1 and 0.5 for the revetment (Kobayashi *et al.* 1990) and set to zero for the plywood beach seaward of the revetment. Results for bottom friction factor of 0.1 on the 1:2 slope are the only results presented. The measured bathymetry was input as depicted in Figure 2.1. The number of spatial nodes (defined as JSWL by the CSHORE) also has to be input as well. The number of spatial nodes must be chosen large enough so that the computed cross-shore variations of the time-averaged quantities do not depend on Δx. The constant nodal spacing Δx is defined as x_s/JSWL where x_s = the cross-shore distance between the seaward boundary and the still water line defined as z_b = 0 at $x = x_s$

(Kobayashi and Johnson 1998). The values for JSWL and the corresponding water depth d_t are shown in Table 7.1.

Table 7.1: Toe Water Depth and Nodal Spacing Used for CSHORE.

Toe depths – d_t (cm)	20	18	16	14	12	10	8	6	4
JSWL	760	758	756	754	752	750	748	746	744

7.3 Measured Free Surface Statistics Compared to CSHORE

Output data from CSHORE was plotted along with the discrete wave and runup statistical values to show the comparison of the measured data to that predicted by CSHORE. Figures 7.1 – 7.27 include comparisons of $\overline{\eta}$, H_{rms}, s, and K from the offshore gauge location 1 to the revetment. Measured wave data values are displayed as open circles on the plots, while the runup wire data is shown as an open diamond, and the computed variation is a solid line.

In general, agreement between the measured and predicted values is good for $\overline{\eta}$ and H_{rms} for most of the tests performed, particularly for those tests performed when the water depth at the toe of the slope was shallow. As the water depth was increased, the ability of CSHORE to predict runup decreased. This is because the runup wire cannot be assumed to be equivalent to the hypothetical vertical wave gauge at the intersection between the wire and the still water level as depicted in Figure 2.1 for larger values of d_t. In short, a direct comparison of wave runup measured by a

runup wire cannot be made to a wave gauge at the same location. Free surface elevations measured by a runup wire can vary greatly over the length of the wire, resulting in a large standard deviation of the runup signal, while the lower limit of a vertical gauge near the still waterline is limited by the slope surface as was the case with gauge, therefore yielding a significantly lower standard deviation. The difference between the gauge data and the runup wire data becomes evident when $d_t \geq 14$ cm as can be seen in Figure 7.6 for $T_p = 4.7$ s, Figure 7.15 for $T_p = 2.4$ s, and Figure 7.24 for $T_p = 1.5$ s. As wave propagate shoreward, the wave height or standard deviation of the vertical gauge will approach zero onshore, but a runup wire will show a significant standard deviation, because of the large oscillation along the wire placed parallel on the slope.

The bottom friction factor f_b for the revetment was varied from 0.1 to 0.5. The model results indicated that, at least for the variety of tests performed during the experiment, CSHORE was relatively insensitive to large changes in the friction factor. The computed results presented here are based on $f_b = 0.1$ on the revetment. In addition, some difficulties may arise from the fact that CSHORE is a calibrated model. While CSHORE does not include wave reflection explicitly, there is some inclusion of wave reflection in its calibration. Although this may seem like a possible source of error, comparison of predicted and measured data at shallow depths shows that the model agrees well with the measured data as can be seen in Figures 7.1, 7.10, and 7.20.

The agreement between the measured and predicted values for the skewness and kurtosis range from fair to poor. When the value for s or K at $x = 0$ does not agree well with the measured values, the agreement for skewness tends to be marginal, while the agreement for kurtosis tends to be poor. This may be attributed to the fact that skewness and kurtosis are not included as input at $x = 0$ for CSHORE.

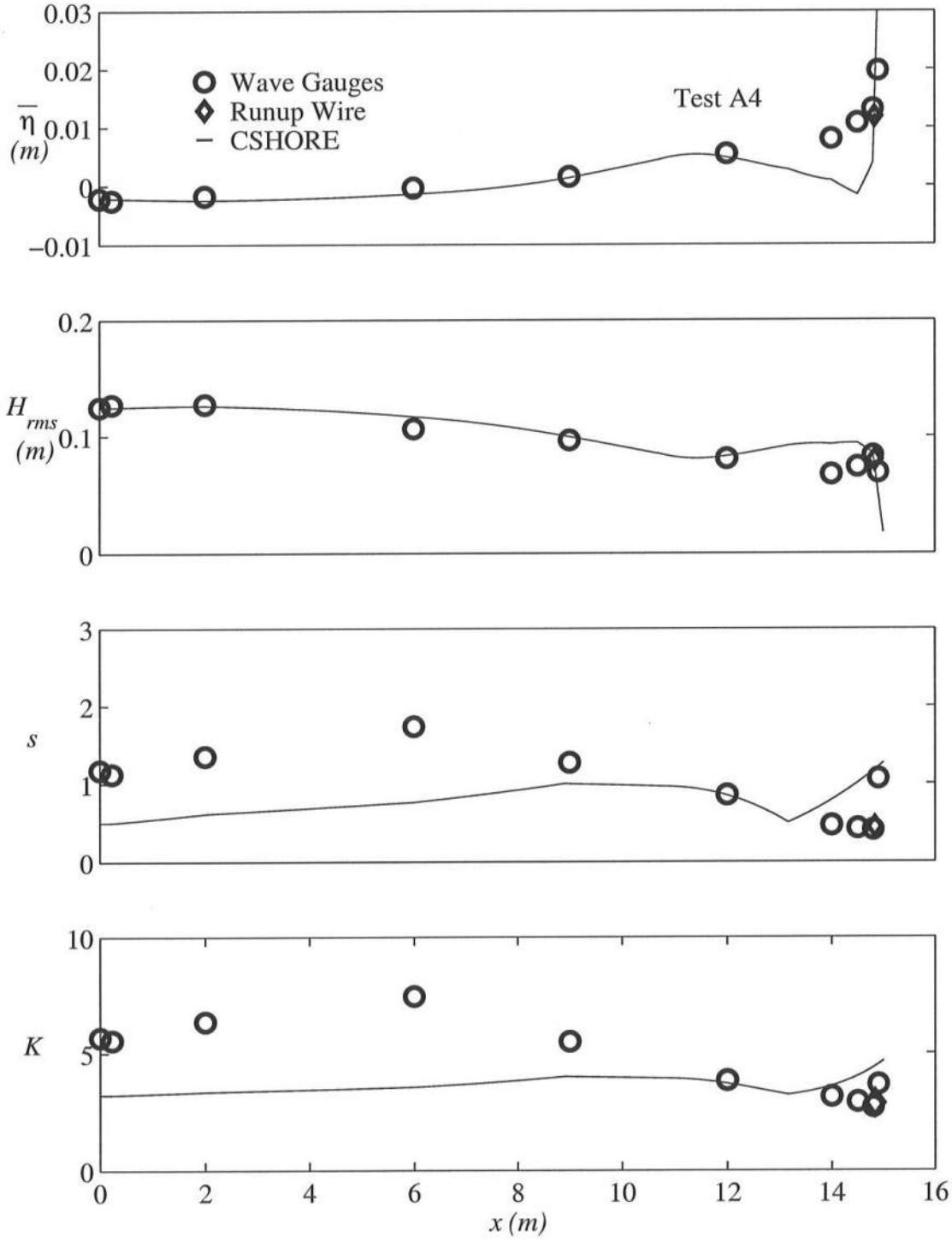

Figure 7.1: Measured and Predicted Values of $\overline{\eta}$, H_{rms}, s, and K Vs. x for $T_p = 4.7$ s and $d_t = 4$ cm.

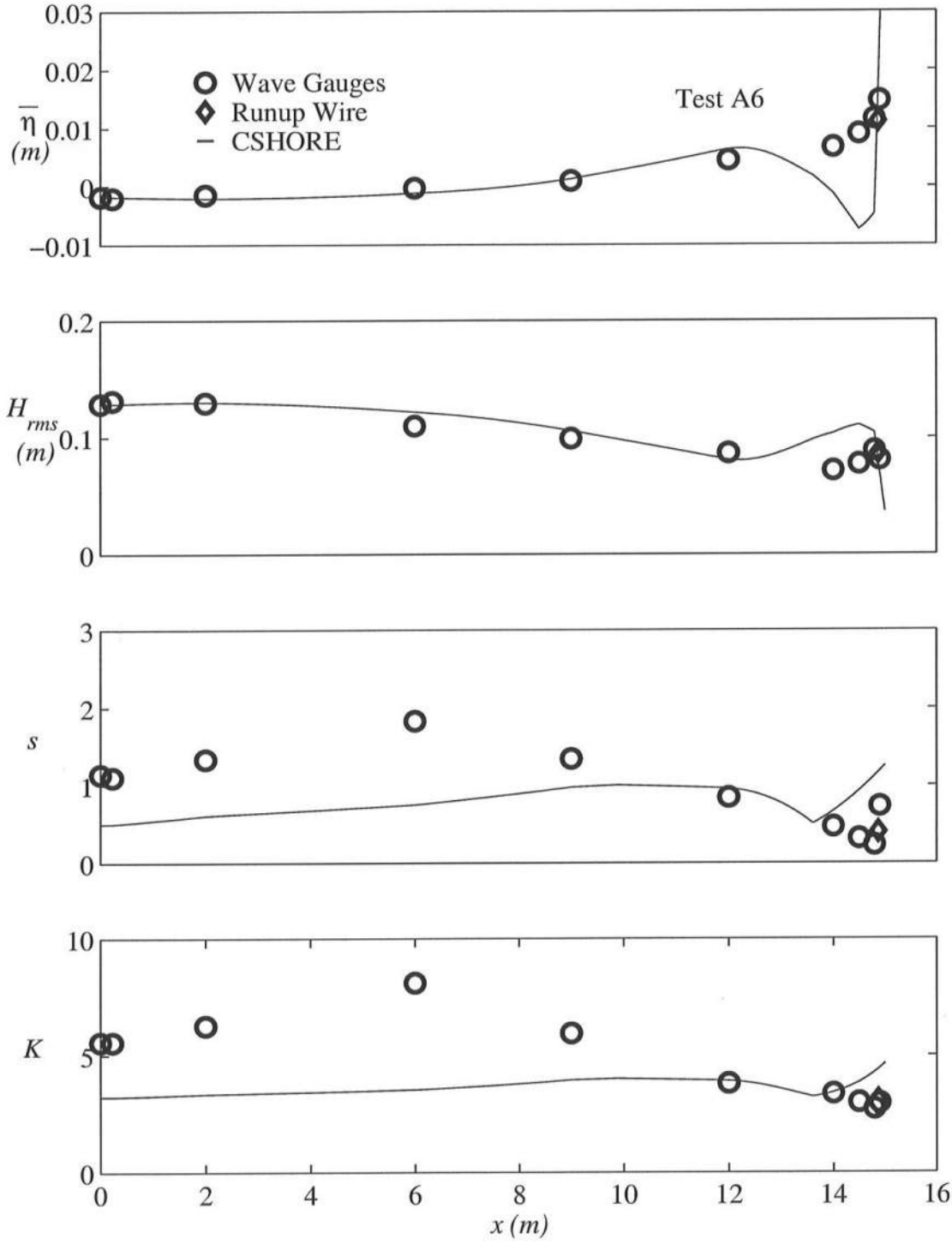

Figure 7.2: Measured and Predicted Values of $\overline{\eta}$, H_{rms}, s, and K Vs. x for $T_p = 4.7$ s and $d_t = 6$ cm.

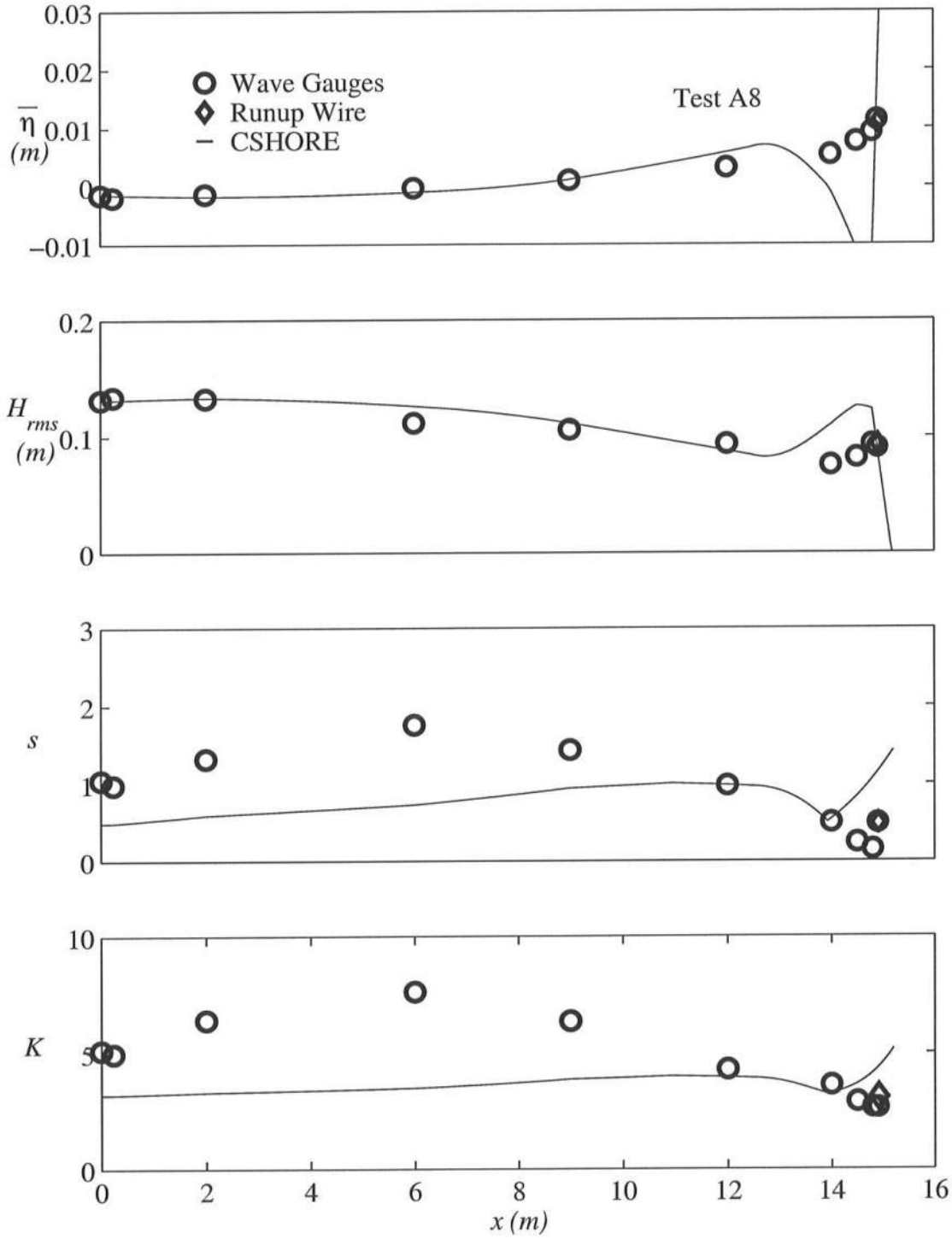

Figure 7.3: Measured and Predicted Values of $\overline{\eta}$, H_{rms}, s, and K Vs. x for $T_p = 4.7$ s and $d_t = 8$ cm.

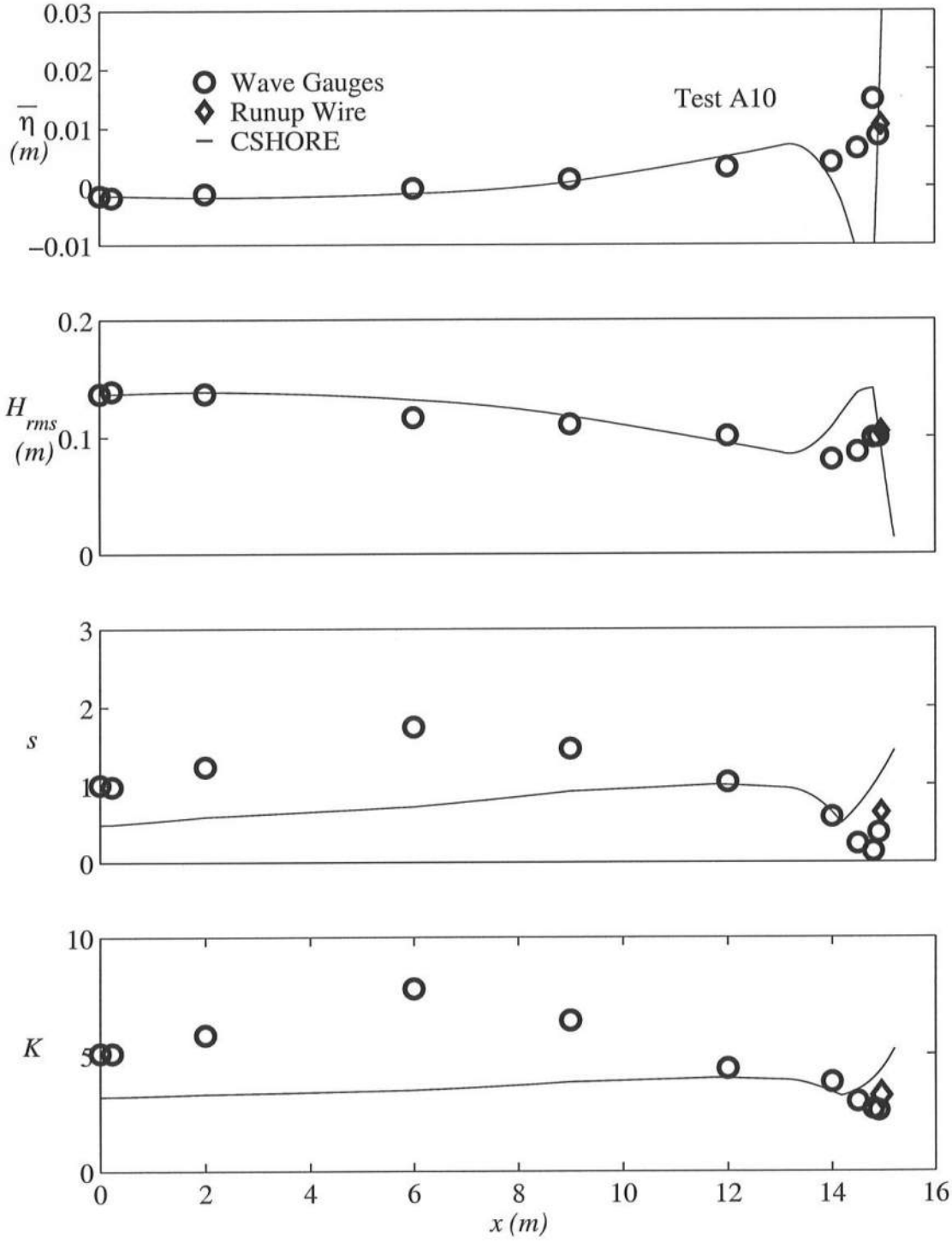

Figure 7.4: Measured and Predicted Values of $\overline{\eta}$, H_{rms}, s, and K Vs. x for $T_p = 4.7$ s and $d_t = 10$ cm.

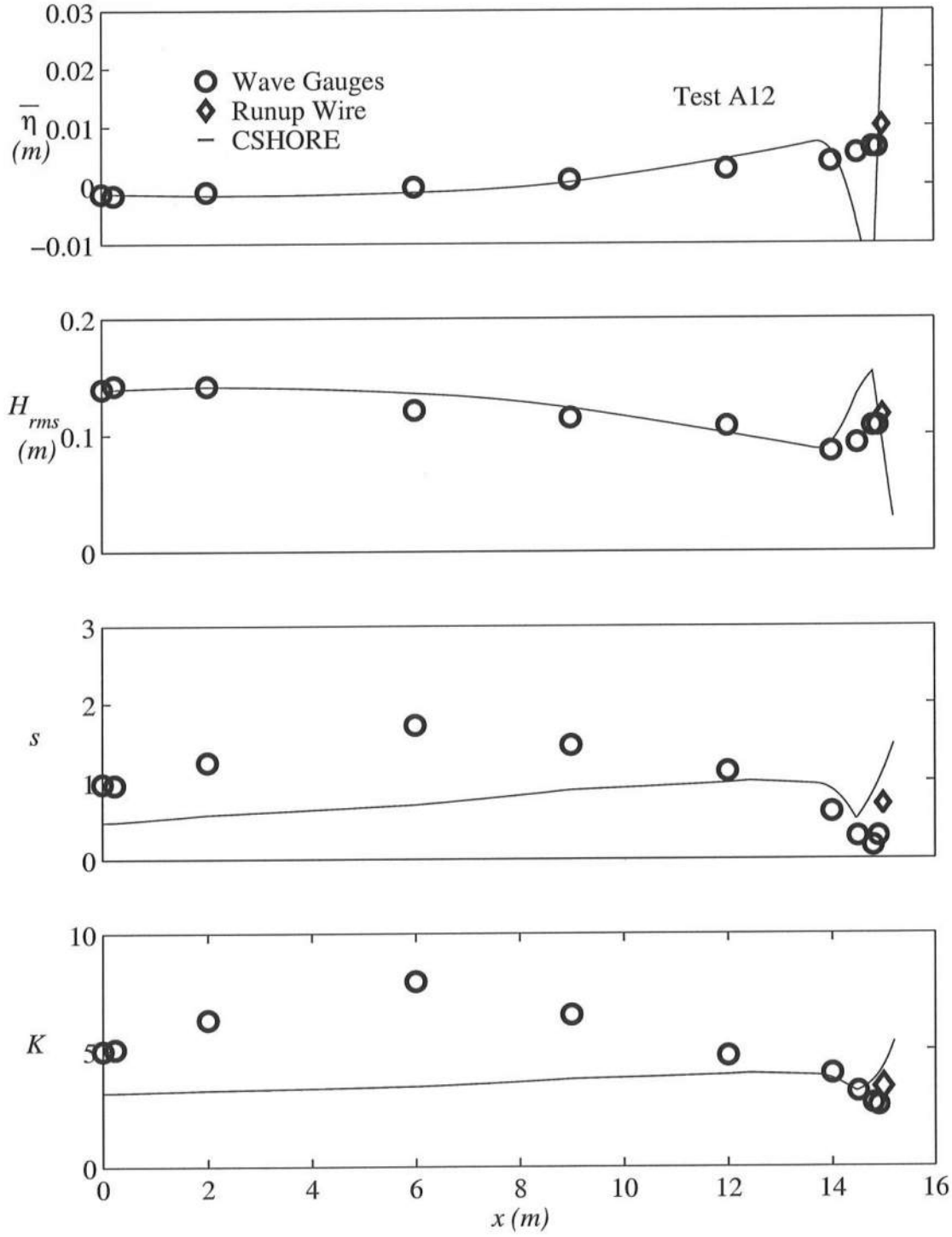

Figure 7.5: Measured and Predicted Values of $\overline{\eta}$, H_{rms}, s, and K Vs. x for $T_p = 4.7$ s and $d_t = 12$ cm.

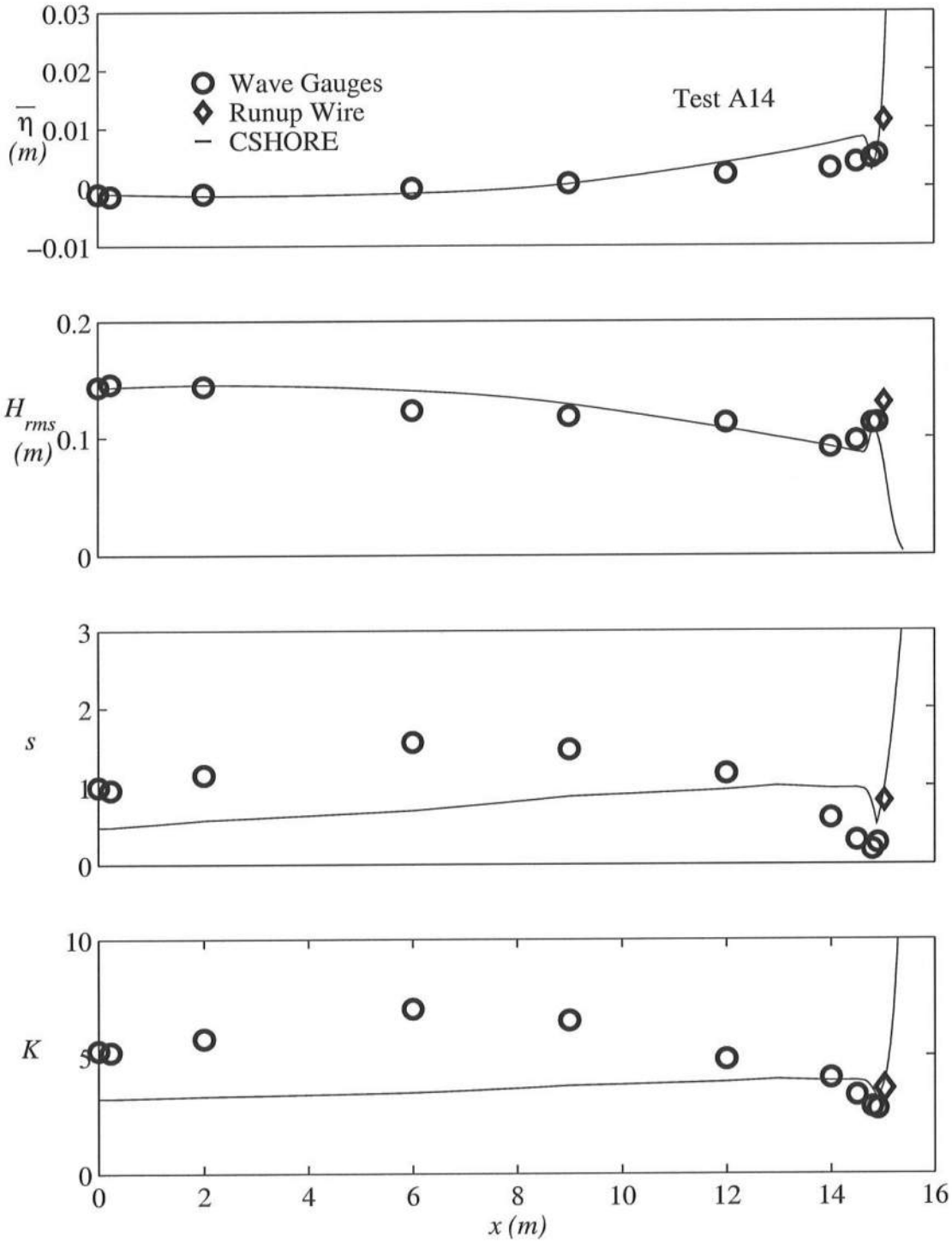

Figure 7.6: Measured and Predicted Values of $\overline{\eta}$, H_{rms}, s, and K Vs. x for $T_p = 4.7$ s and $d_t = 14$ cm.

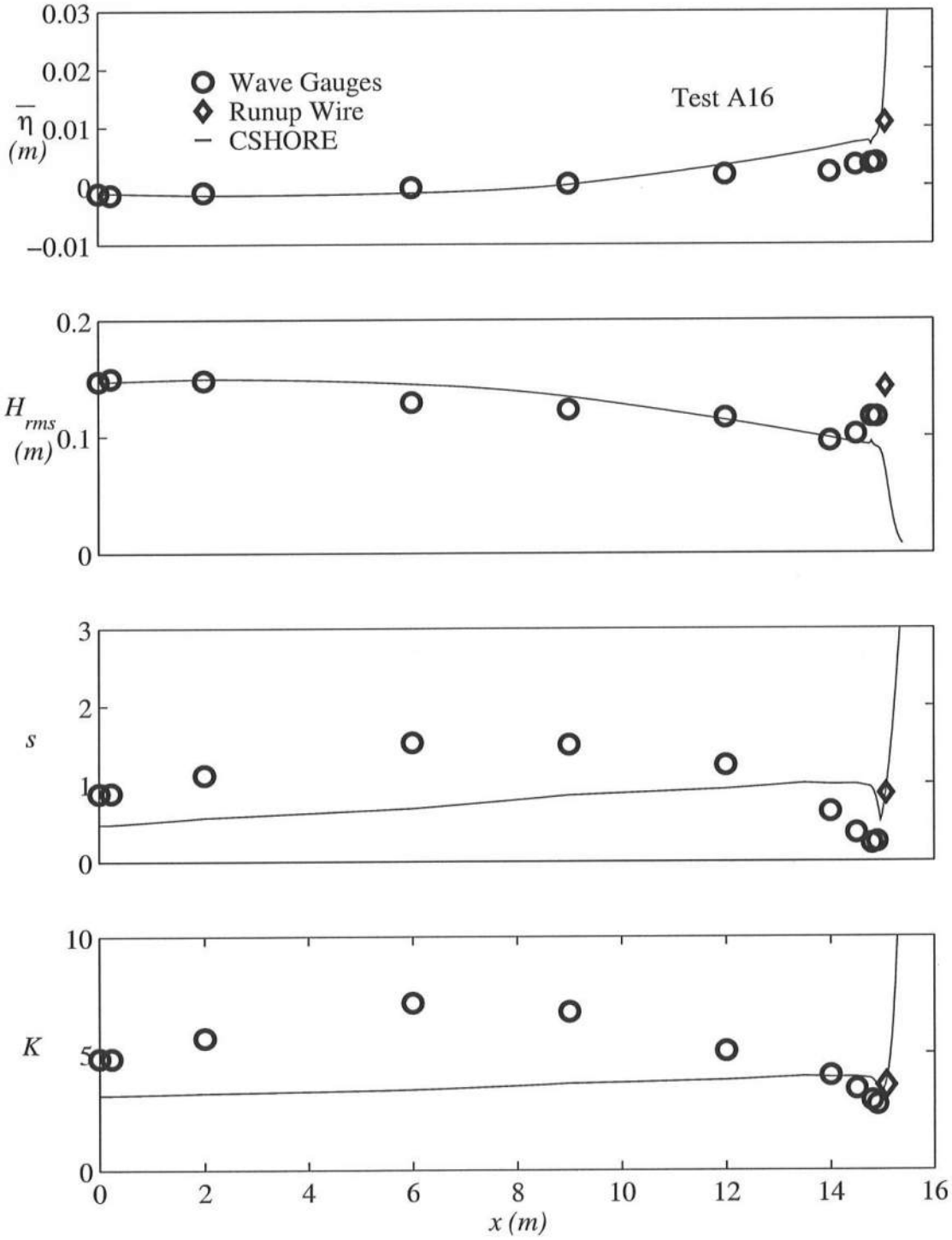

Figure 7.7: Measured and Predicted Values of $\overline{\eta}$, H_{rms}, s, and K Vs. x for $T_p = 4.7$ s and $d_t = 16$ cm.

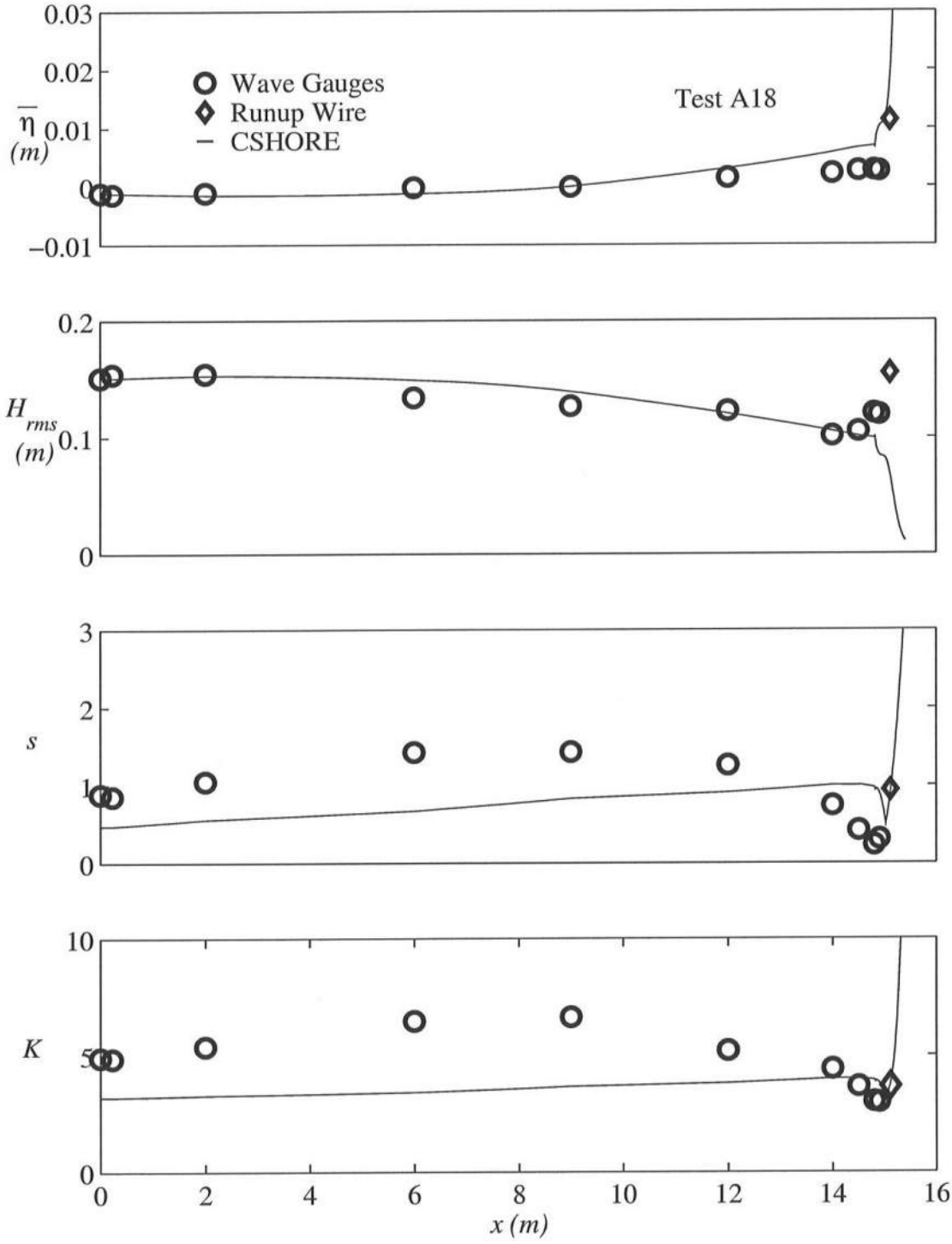

Figure 7.8: Measured and Predicted Values of $\overline{\eta}$, H_{rms}, s, and K Vs. x for $T_p = 4.7$ s and $d_t = 18$ cm.

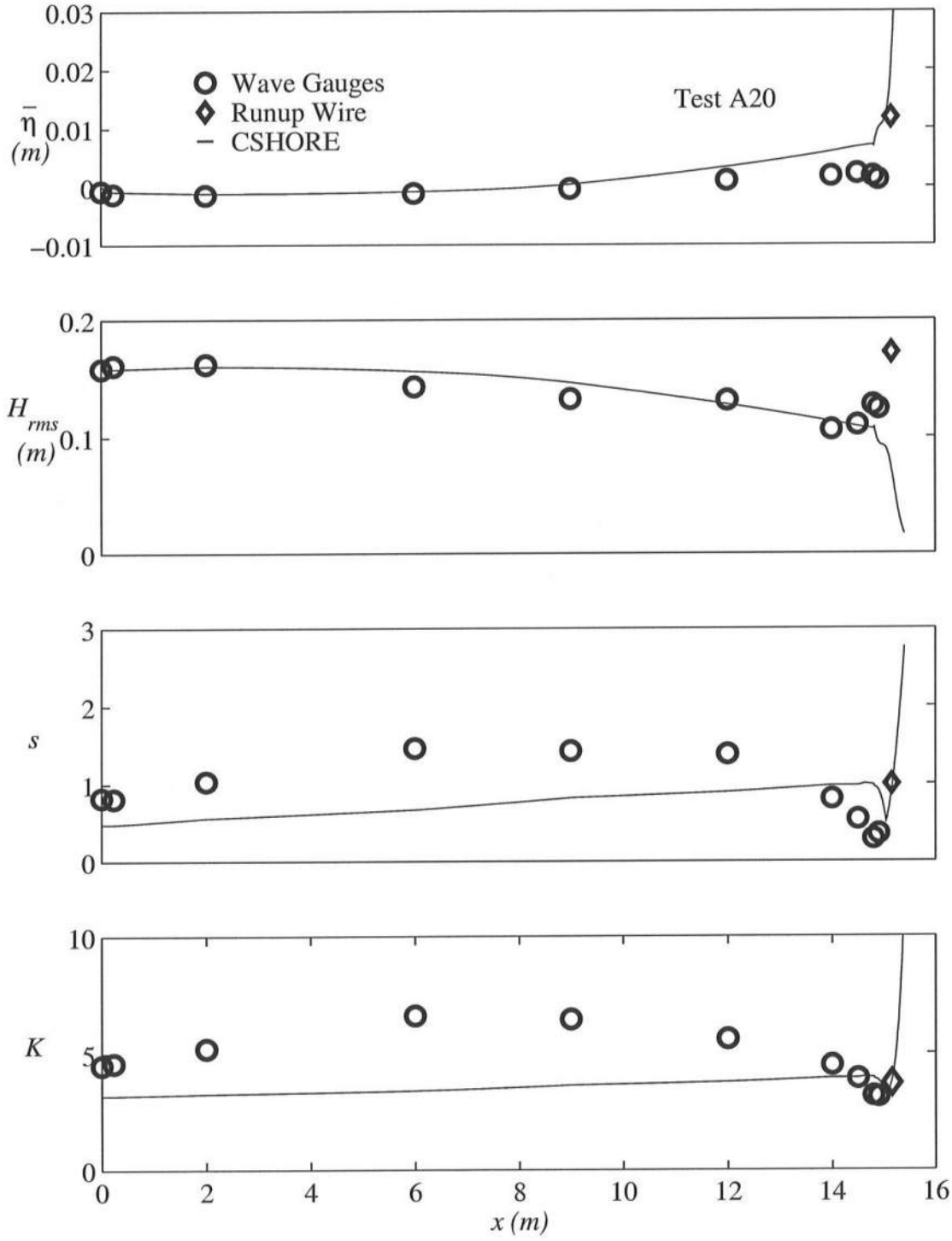

Figure 7.9: Measured and Predicted Values of $\overline{\eta}$, H_{rms}, s, and K Vs. x for $T_p = 4.7$ s and $d_t = 20$ cm.

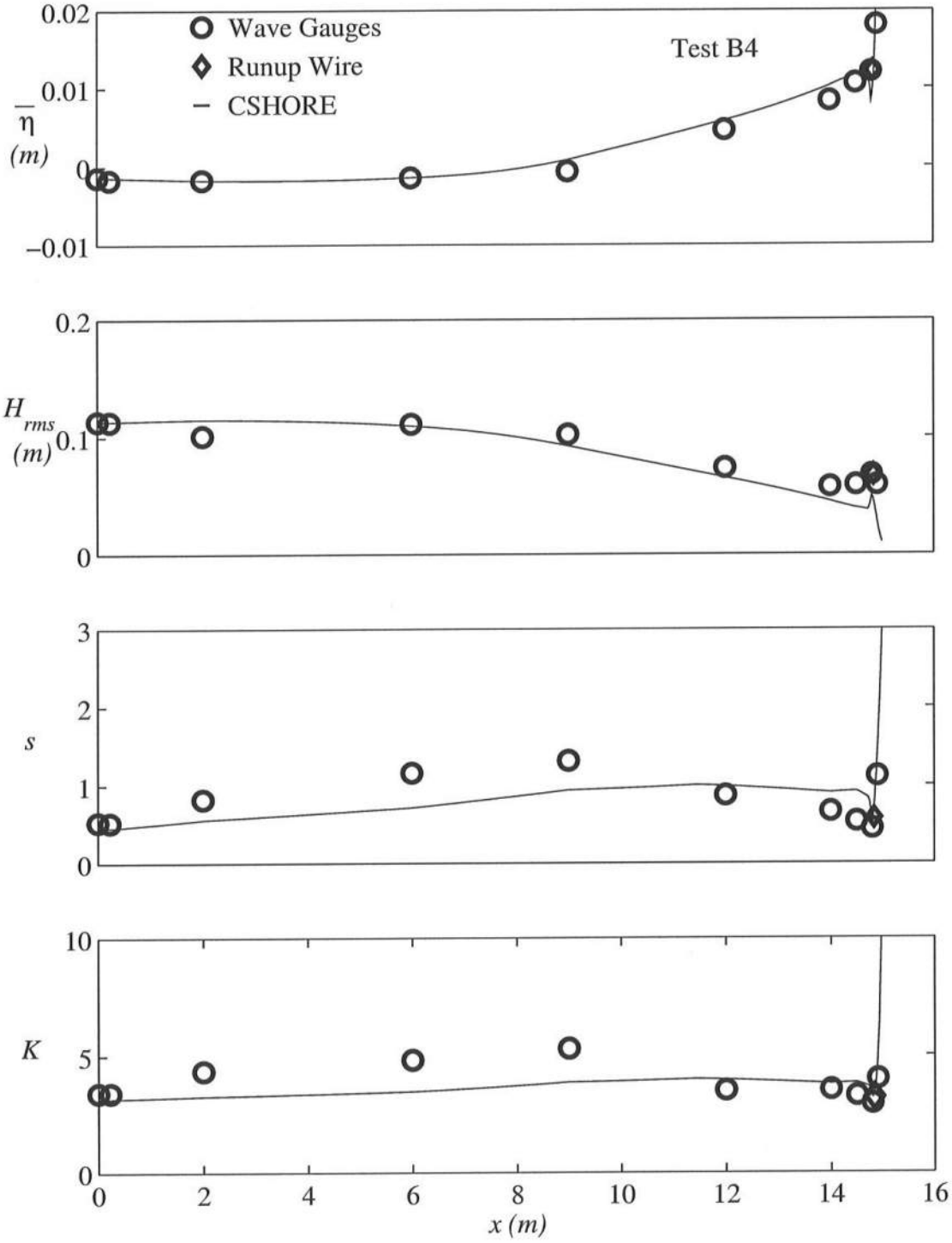

Figure 7.10: Measured and Predicted Values of $\overline{\eta}$, H_{rms}, s, and K Vs. x for $T_p = 2.4$ s and $d_t = 4$ cm.

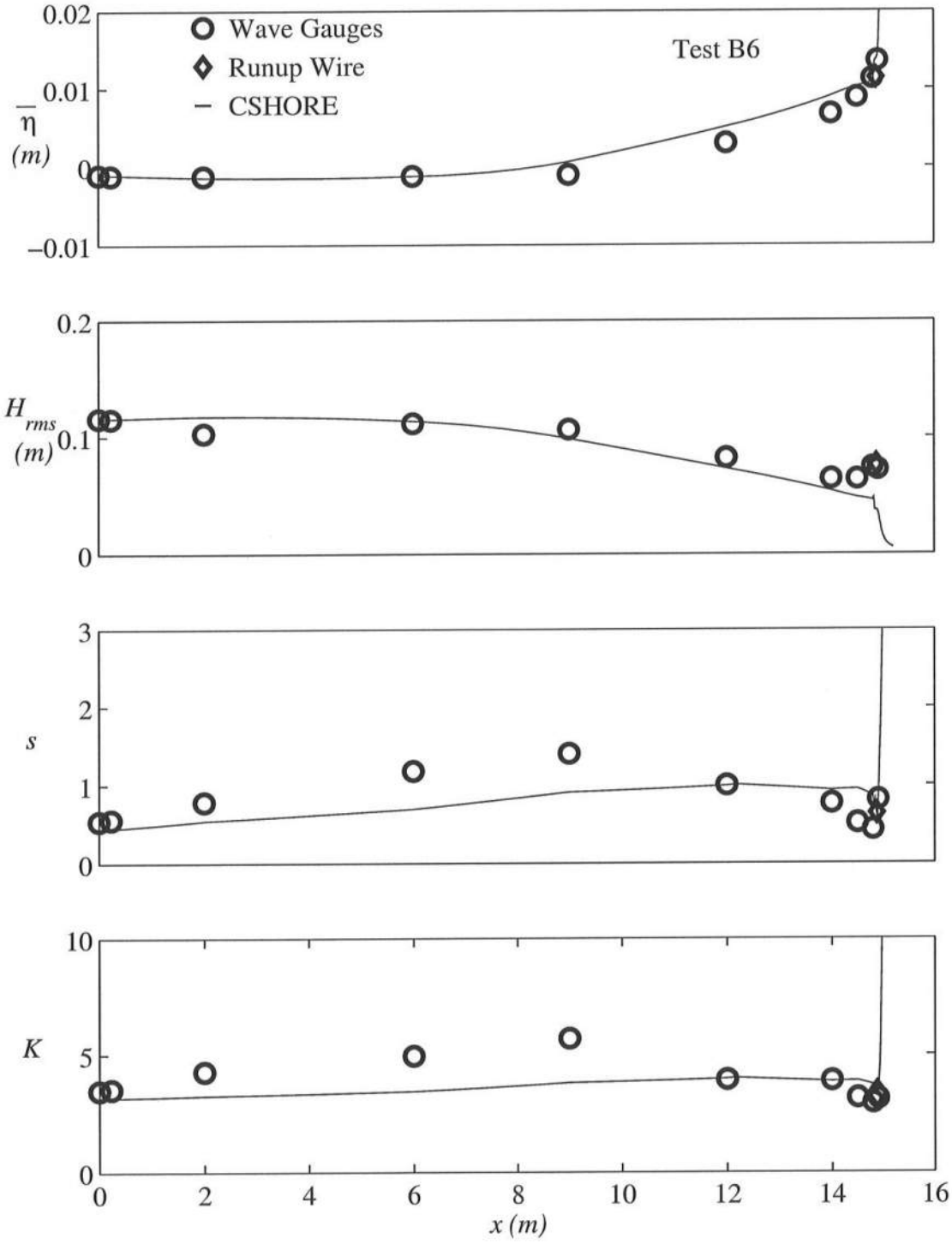

Figure 7.11: Measured and Predicted Values of $\overline{\eta}$, H_{rms}, s, and K Vs. x for $T_p = 2.4$ s and $d_t = 6$ cm.

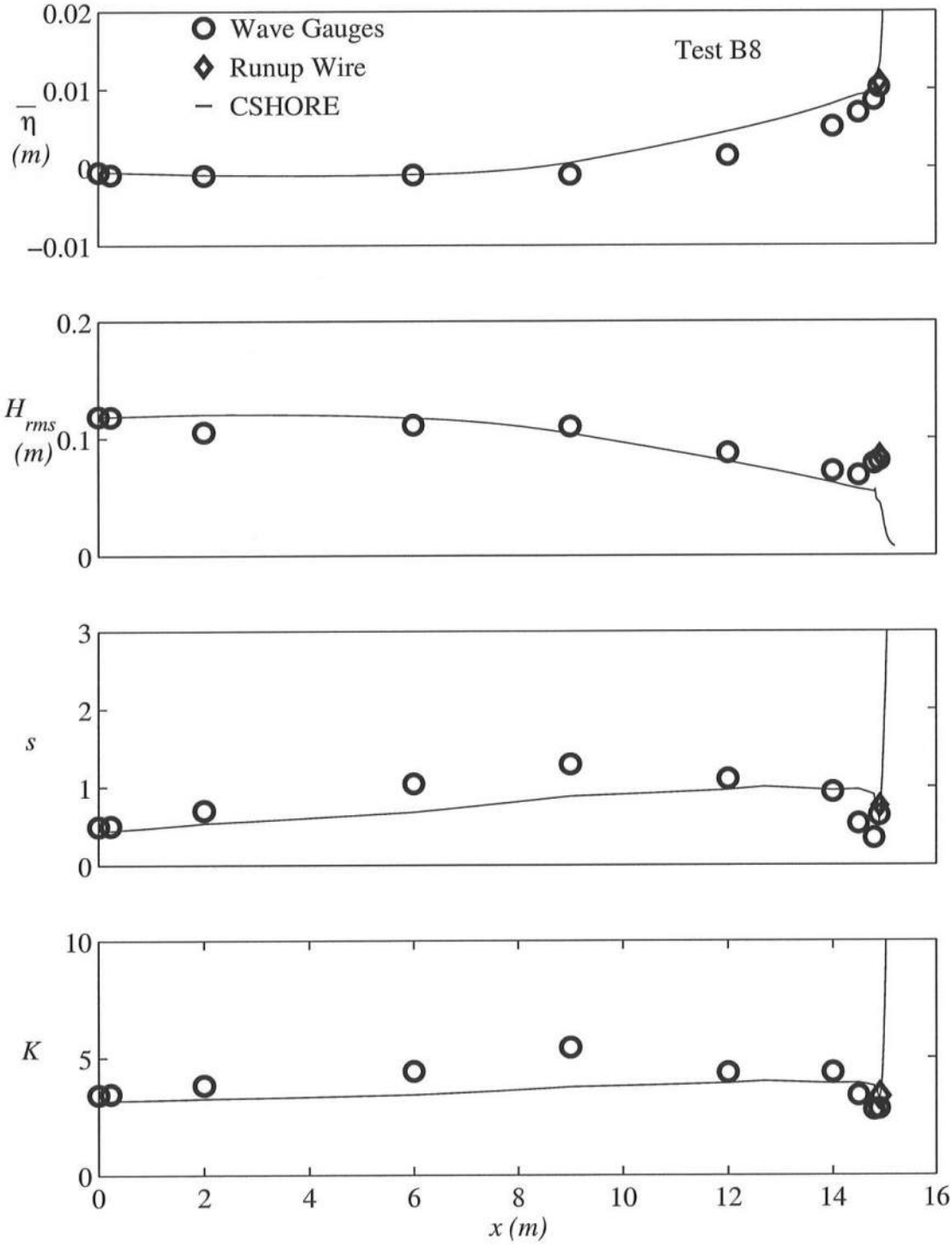

Figure 7.12: Measured and Predicted Values of $\overline{\eta}$, H_{rms}, s, and K Vs. x for $T_p = 2.4$ s and $d_t = 8$ cm.

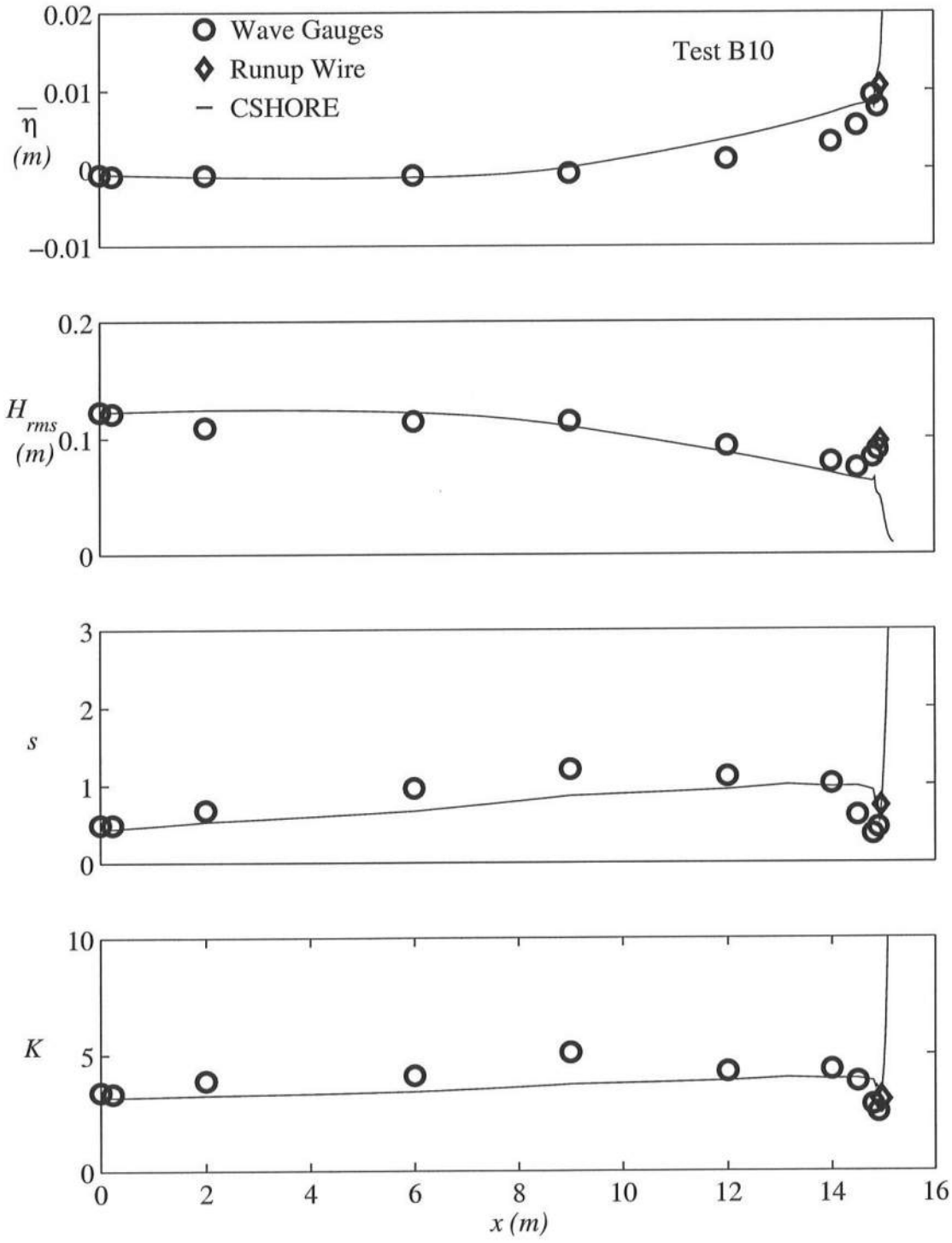

Figure 7.13: Measured and Predicted Values of $\overline{\eta}$, H_{rms}, s, and K Vs. x for $T_p = 2.4$ s and $d_t = 10$ cm.

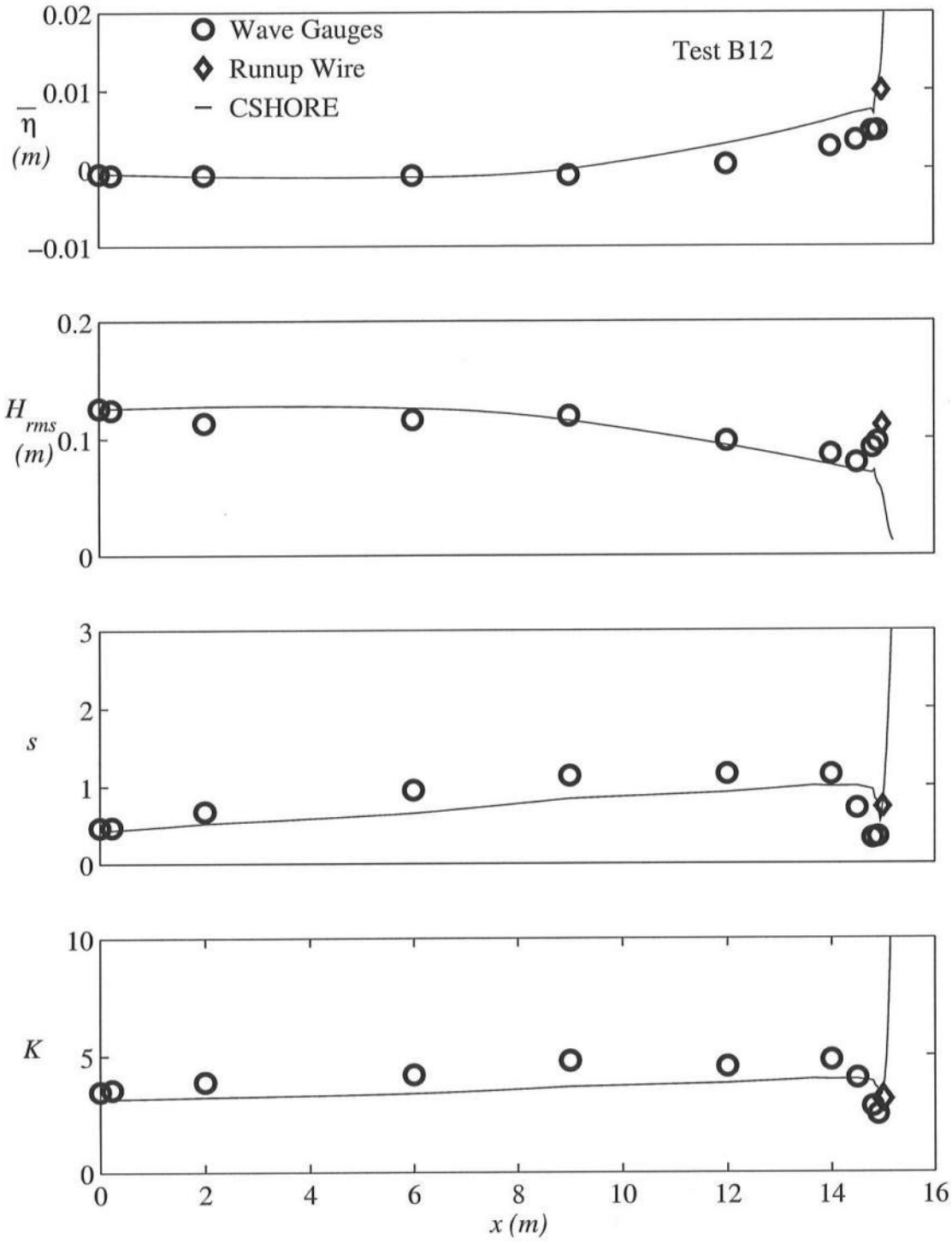

Figure 7.14: Measured and Predicted Values of $\overline{\eta}$, H_{rms}, s, and K Vs. x for $T_p = 2.4$ s and $d_t = 12$ cm.

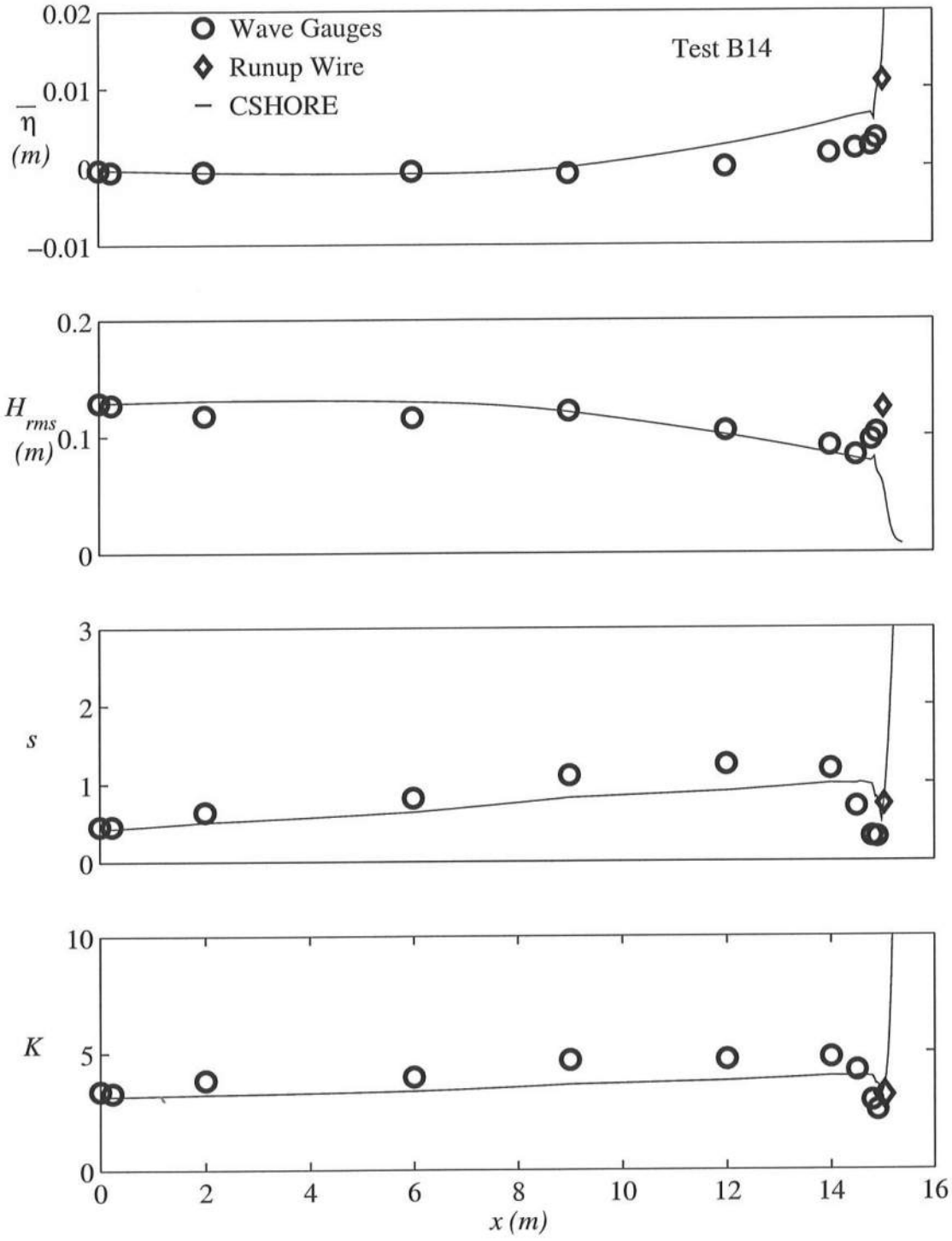

Figure 7.15: Measured and Predicted Values of $\overline{\eta}$, H_{rms}, s, and K Vs. x for $T_p = 2.4$ s and $d_t = 14$ cm.

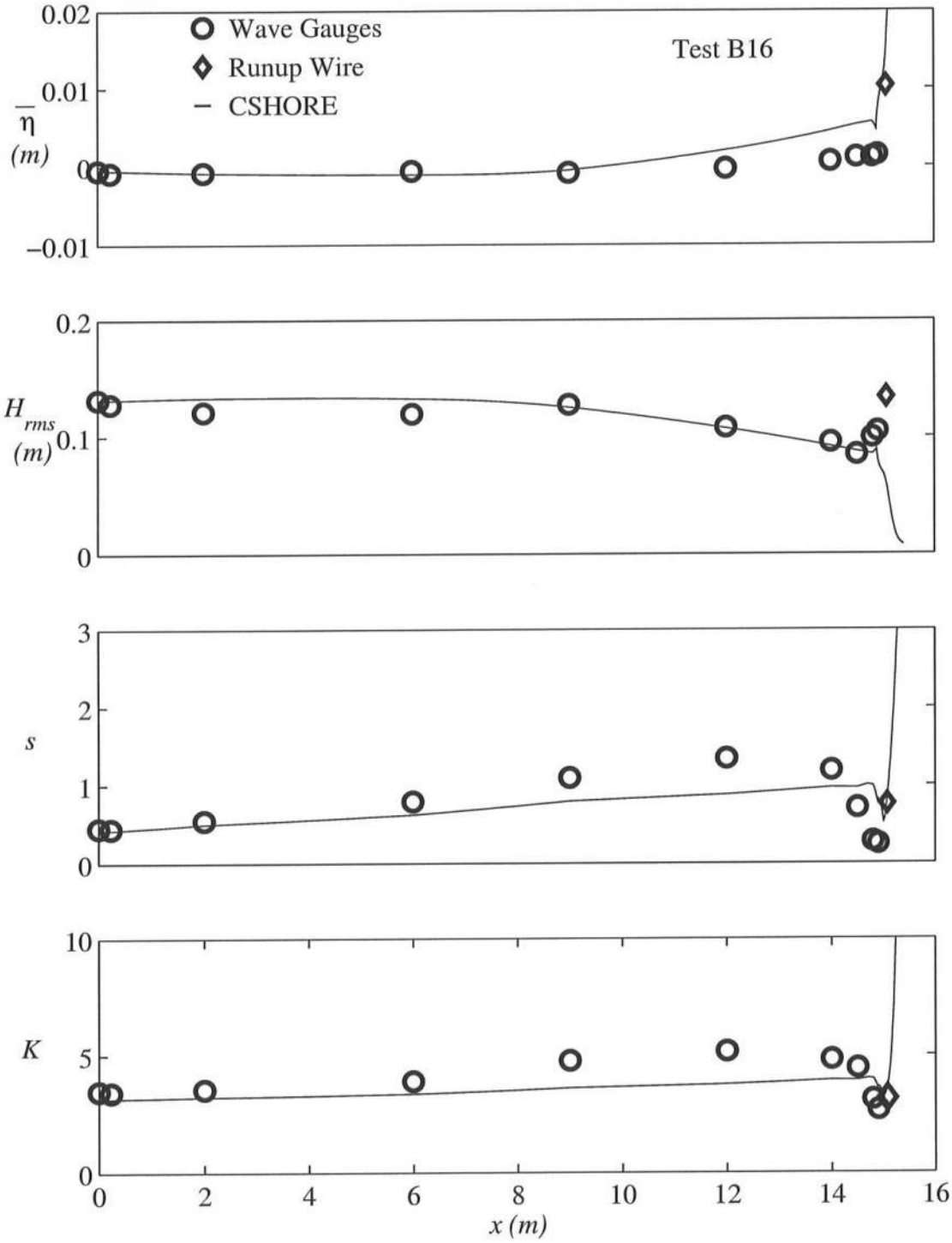

Figure 7.16: Measured and Predicted Values of $\overline{\eta}$, H_{rms}, s, and K Vs. x for $T_p = 2.4$ s and $d_t = 16$ cm.

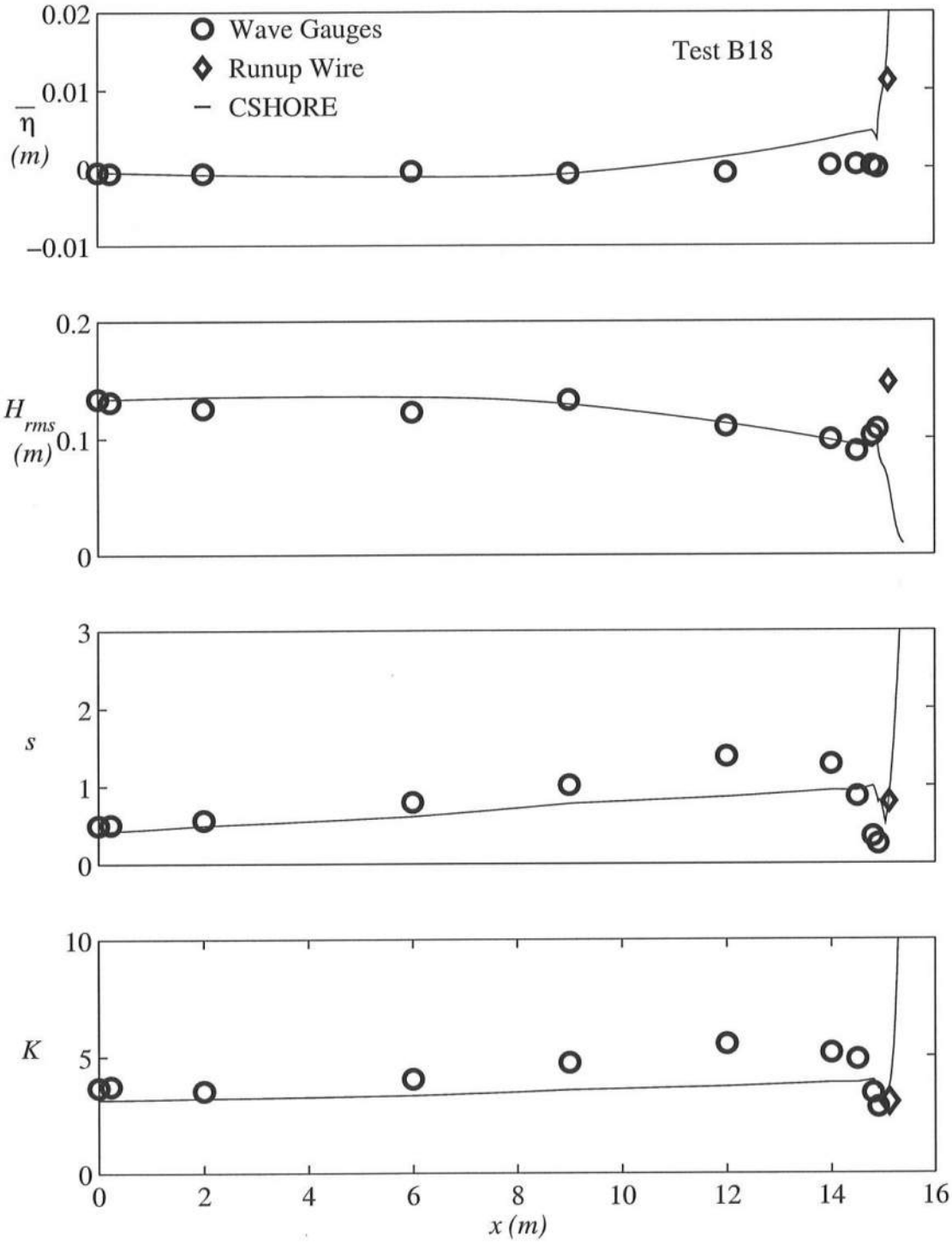

Figure 7.17: Measured and Predicted Values of $\overline{\eta}$, H_{rms}, s, and K Vs. x for $T_p = 2.4$ s and $d_t = 18$ cm.

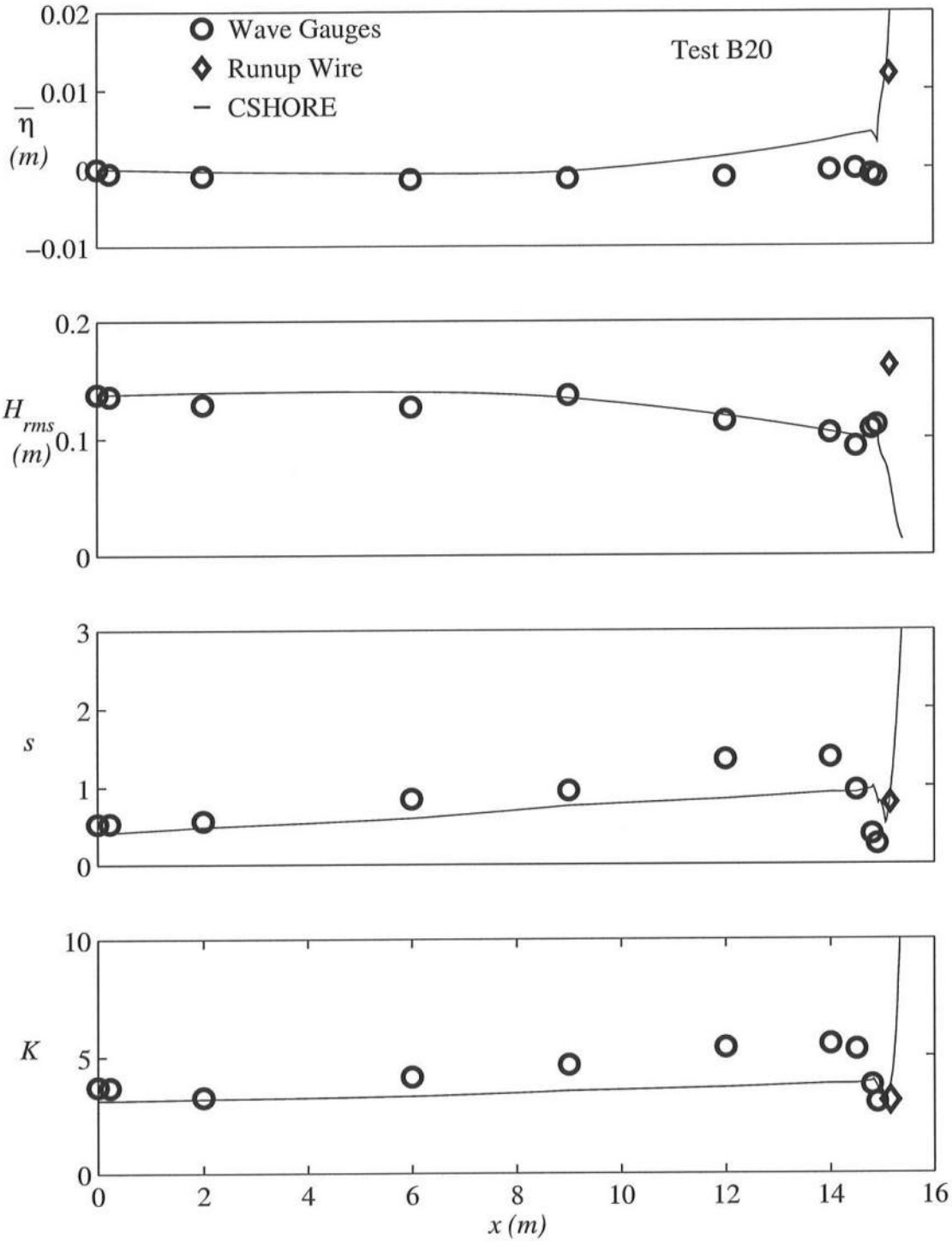

Figure 7.18: Measured and Predicted Values of $\overline{\eta}$, H_{rms}, s, and K Vs. x for $T_p = 2.4$ s and $d_t = 20$ cm.

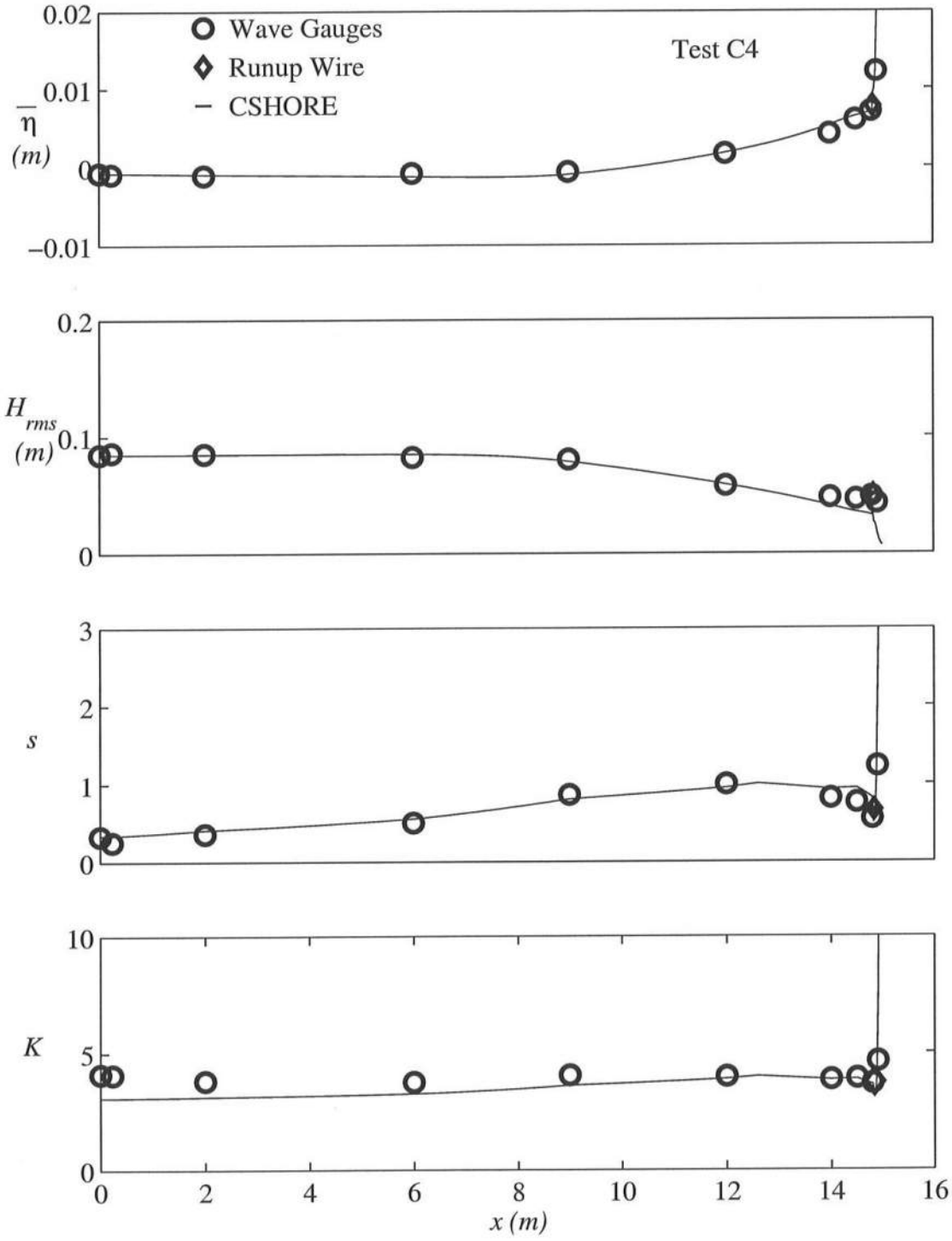

Figure 7.19: Measured and Predicted Values of $\overline{\eta}$, H_{rms}, s, and K Vs. x for $T_p = 1.5$ s and $d_t = 4$ cm.

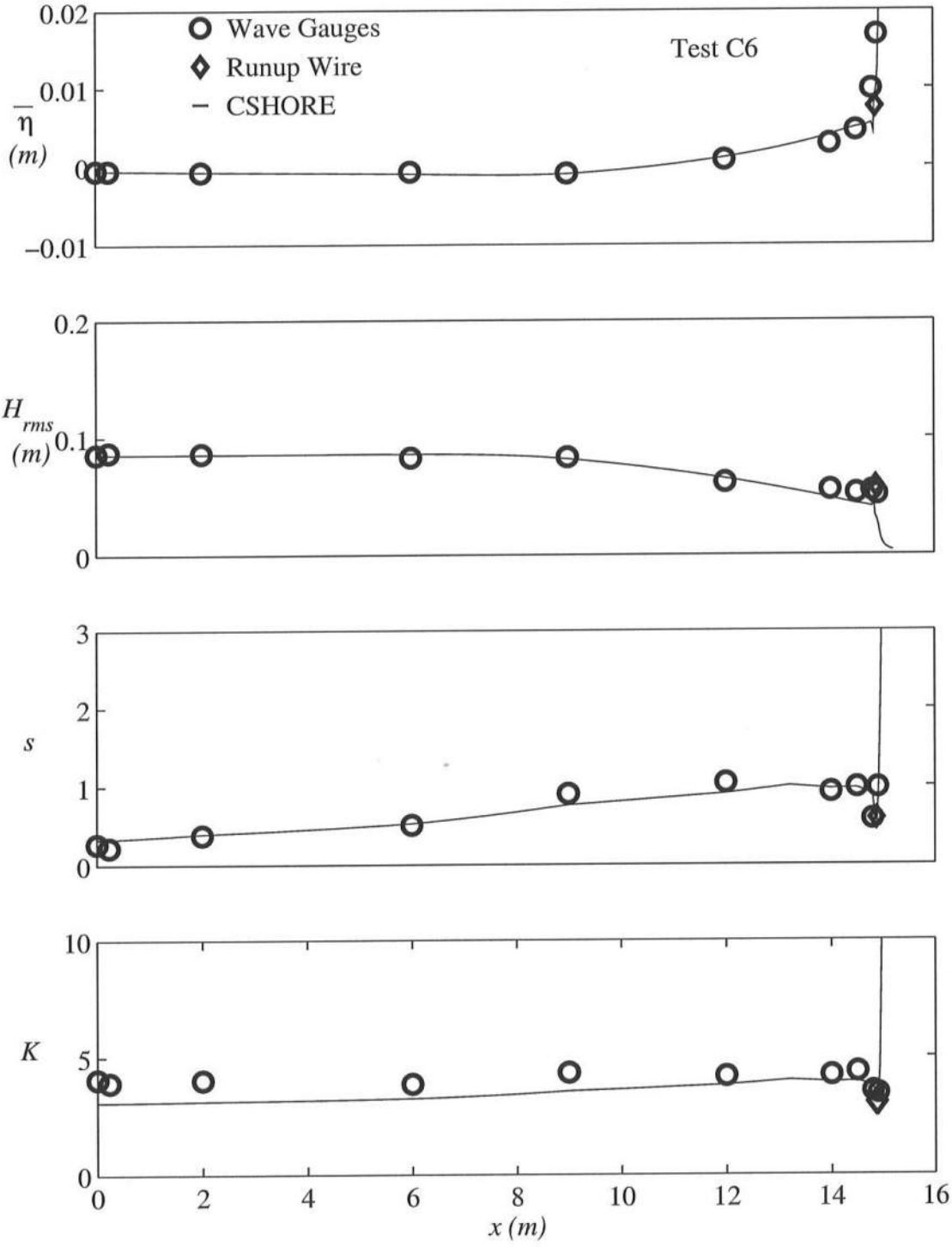

Figure 7.20: Measured and Predicted Values of $\overline{\eta}$, H_{rms}, s, and K Vs. x for $T_p = 1.5$ s and $d_t = 6$ cm.

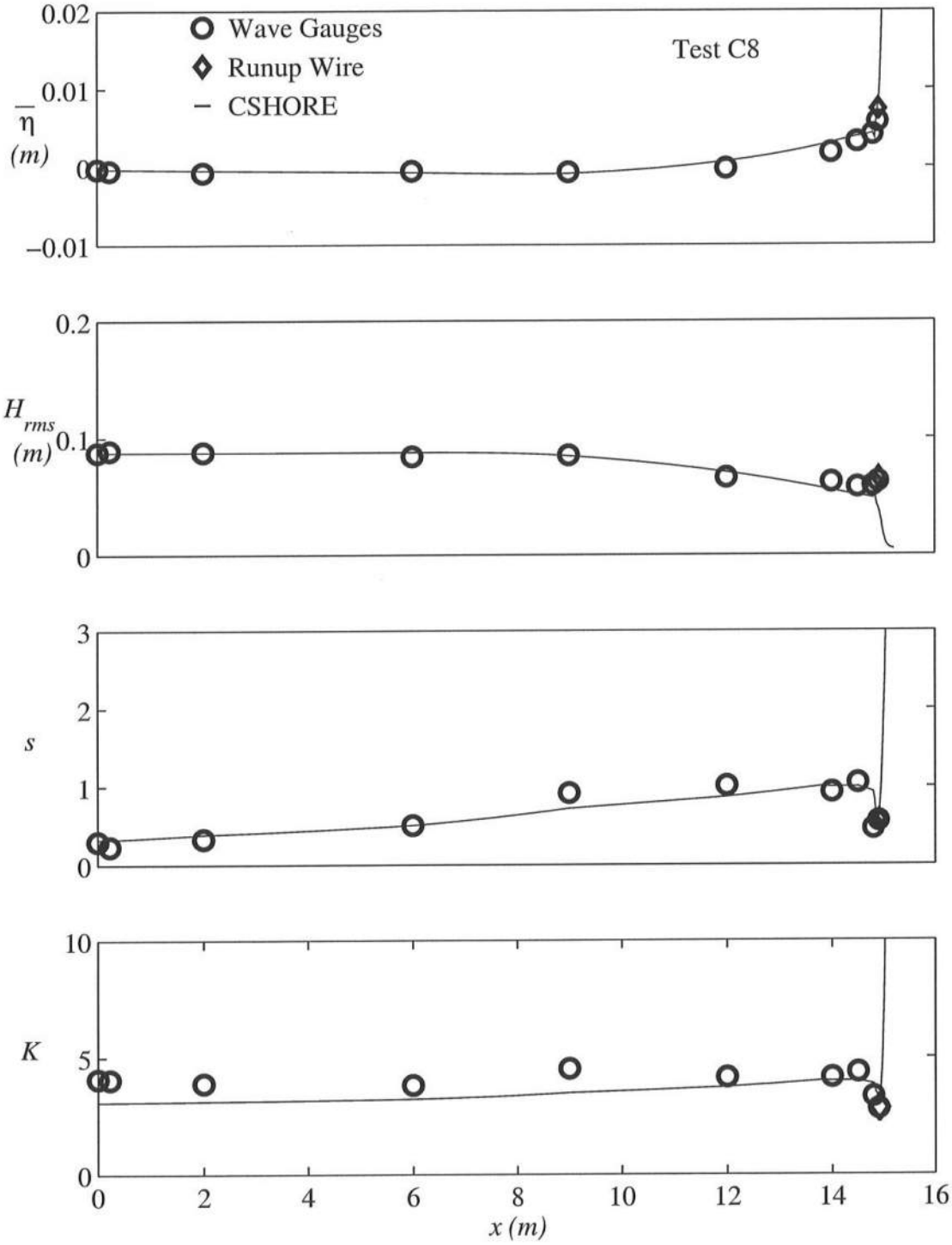

Figure 7.21: Measured and Predicted Values of $\overline{\eta}$, H_{rms}, s, and K Vs. x for T_p = 1.5 s and d_t = 8 cm.

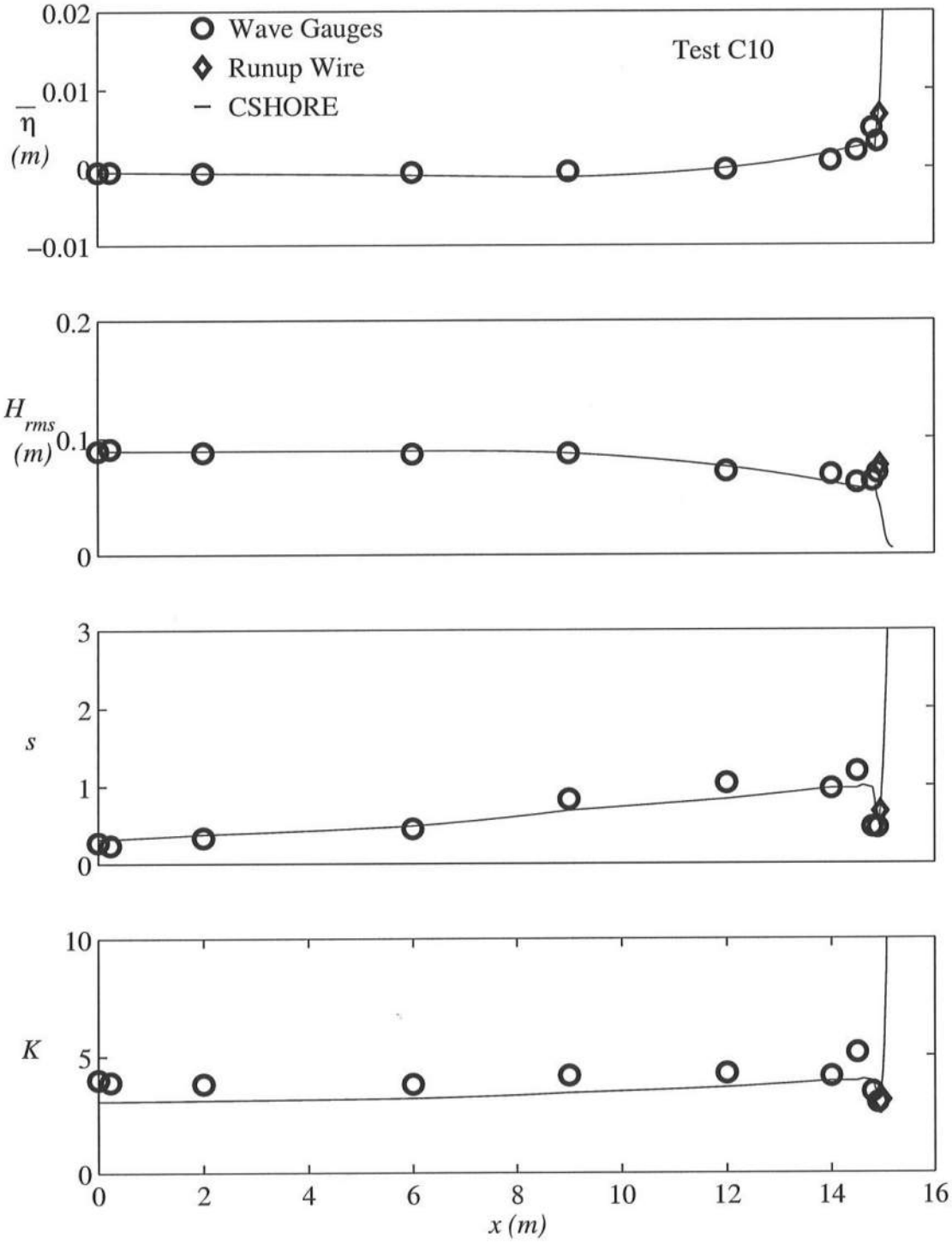

Figure 7.22: Measured and Predicted Values of $\overline{\eta}$, H_{rms}, s, and K Vs. x for $T_p = 1.5$ s and $d_t = 10$ cm.

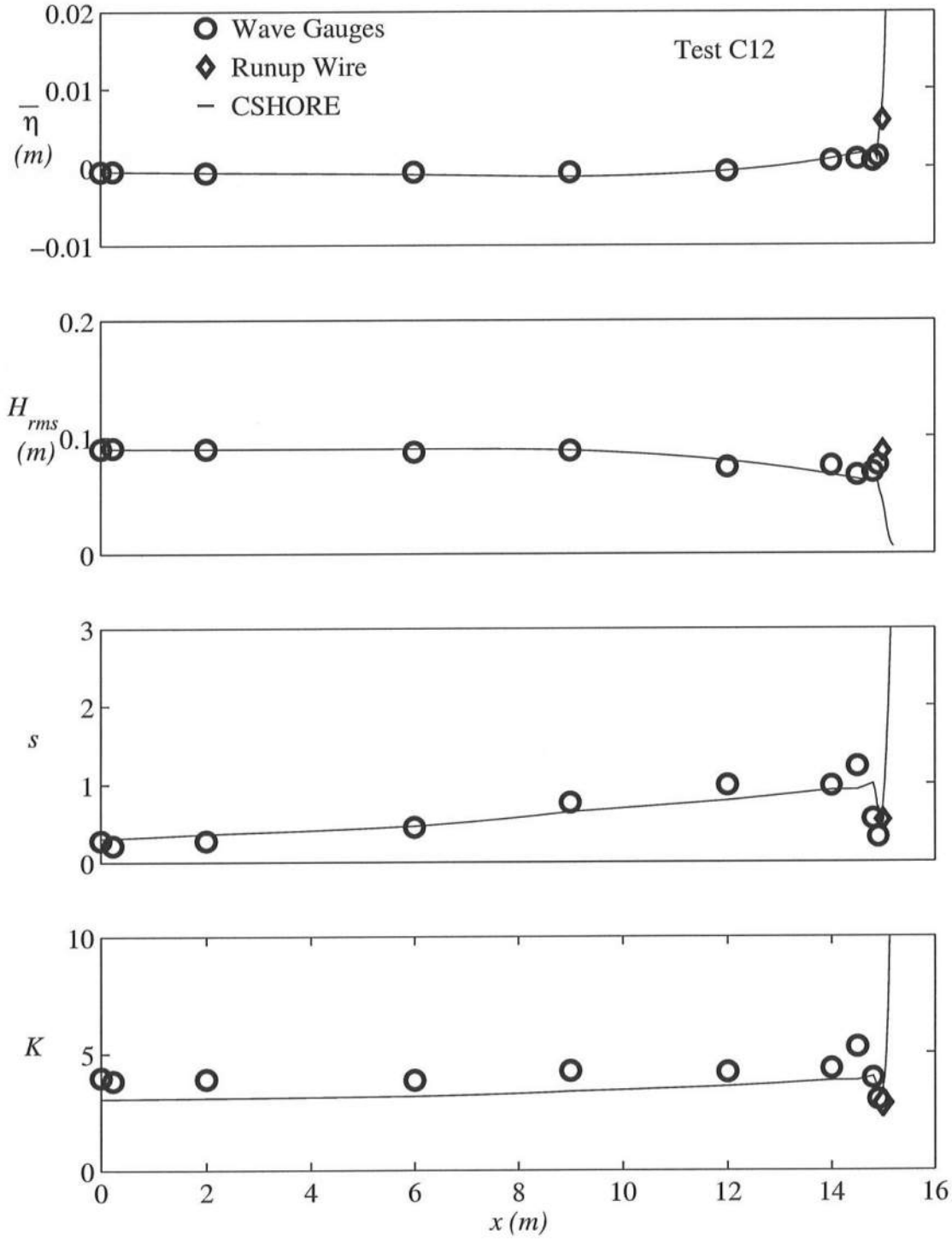

Figure 7.23: Measured and Predicted Values of $\overline{\eta}$, H_{rms}, s, and K Vs. x for $T_p = 1.5$ s and $d_t = 12$ cm.

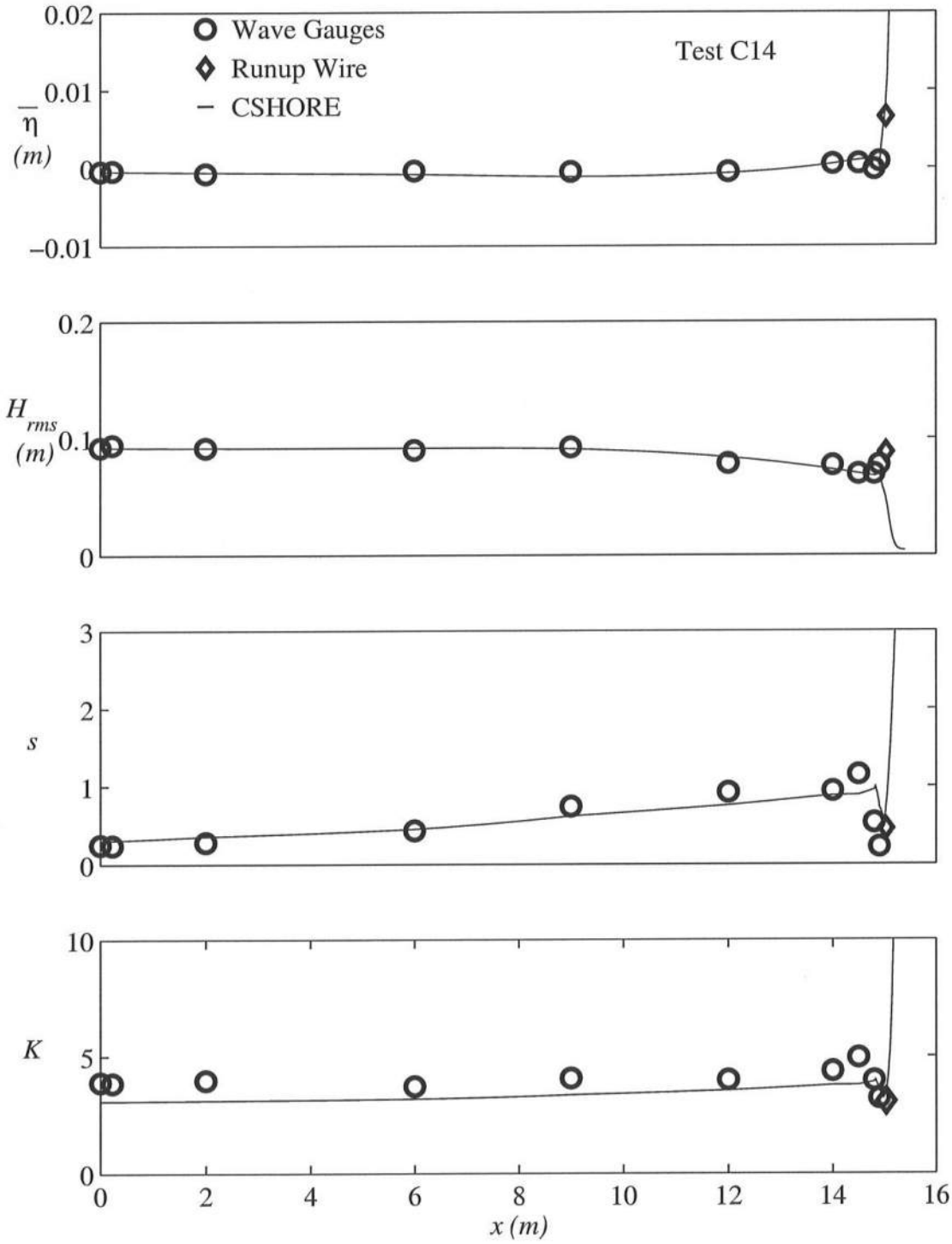

Figure 7.24: Measured and Predicted Values of $\overline{\eta}$, H_{rms}, s, and K Vs. x for $T_p = 1.5$ s and $d_t = 14$ cm.

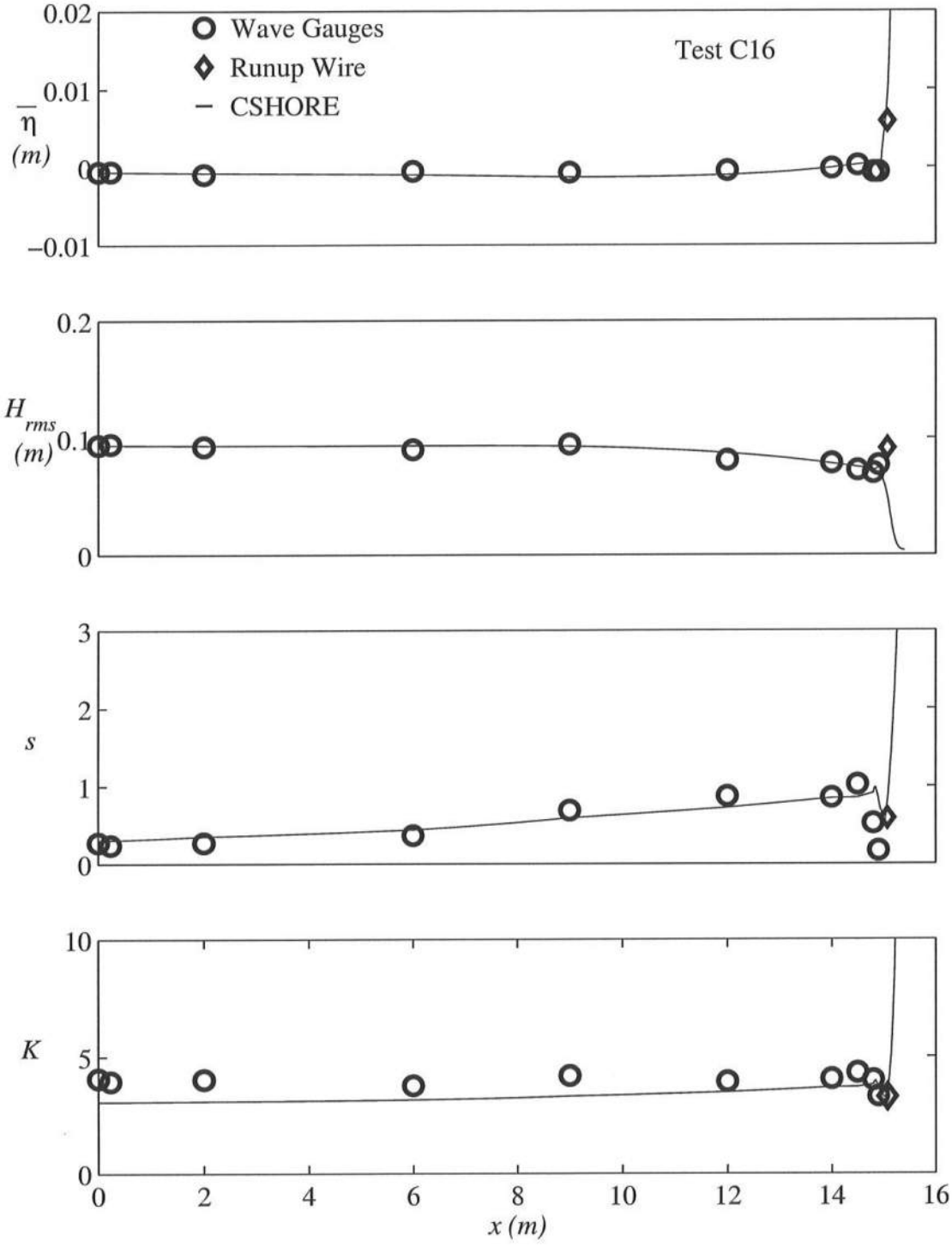

Figure 7.25: Measured and Predicted Values of $\overline{\eta}$, H_{rms}, s, and K Vs. x for $T_p = 1.5$ s and $d_t = 16$ cm.

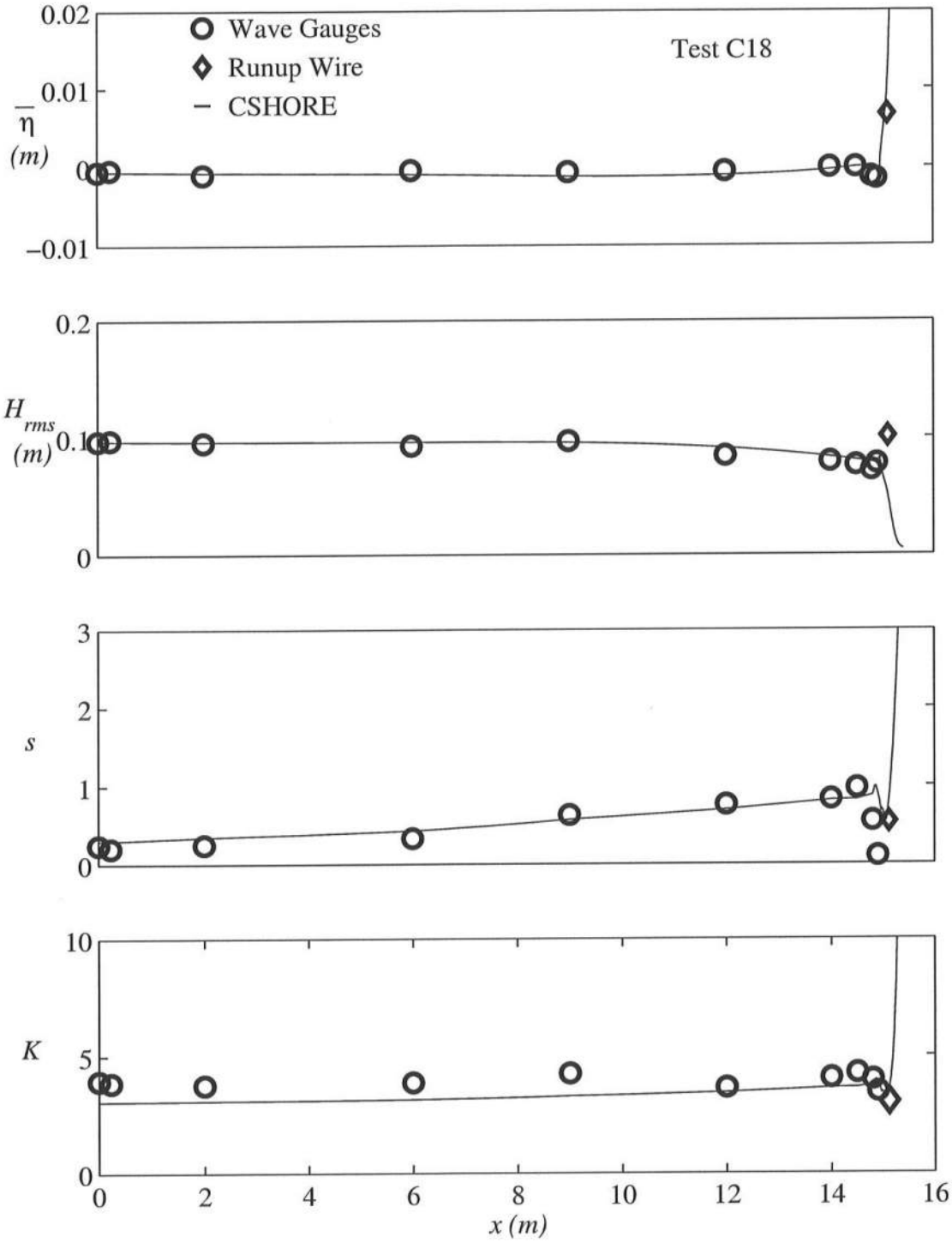

Figure 7.26: Measured and Predicted Values of $\overline{\eta}$, H_{rms}, s, and K Vs. x for $T_p = 1.5$ s and $d_t = 18$ cm.

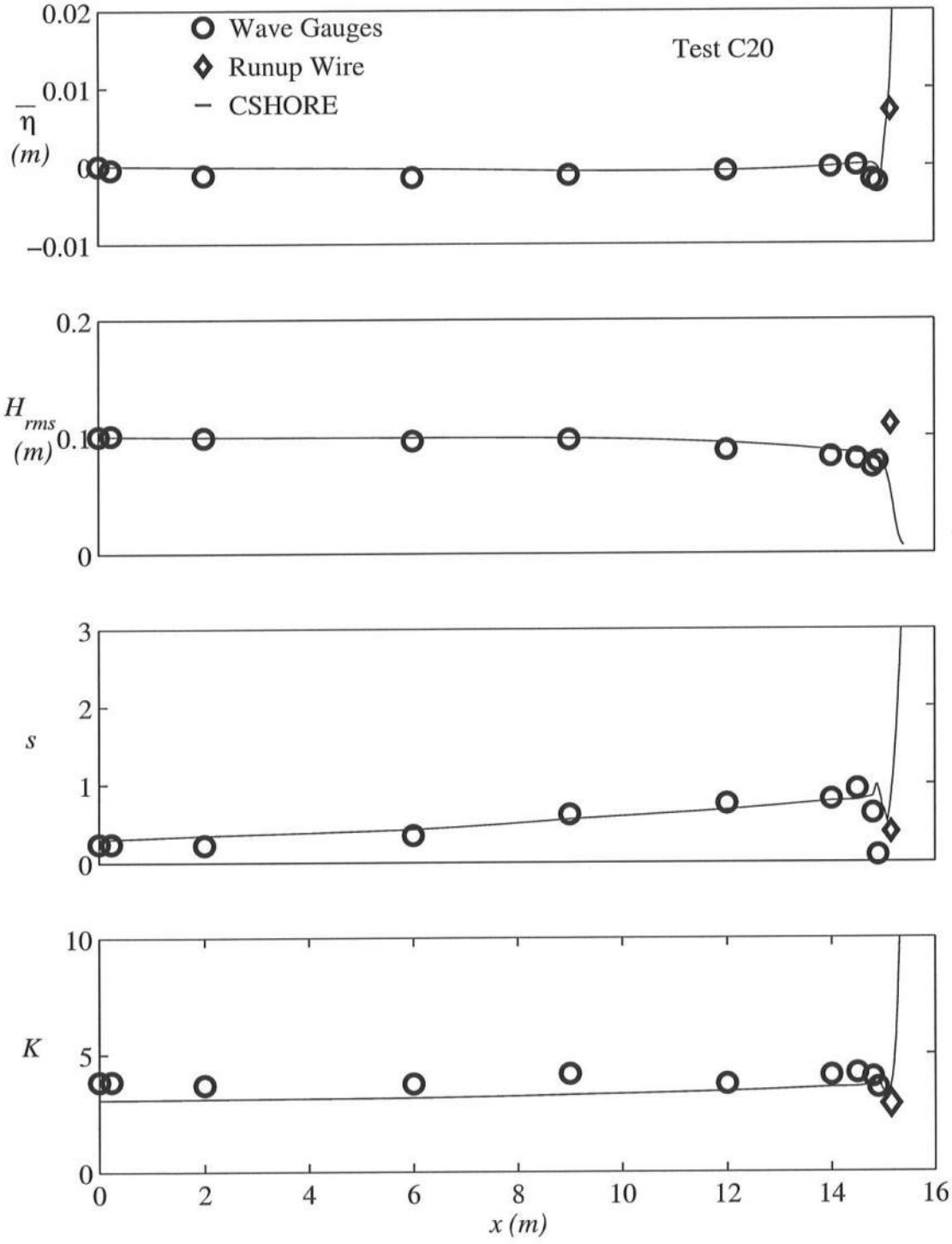

Figure 7.27: Measured and Predicted Values of $\overline{\eta}$, H_{rms}, s, and K Vs. x for $T_p = 1.5$ s and $d_t = 20$ cm.

Chapter 8

CONCLUSIONS

Twenty-seven irregular wave tests were performed for three spectral peak periods and nine toe depths, with incident wave heights generated as large as possible. For each test 10 wave gauges, an ADV (if not limited by toe depth), and runup wire were utilized to measure the free surface, horizontal velocity and waterline oscillations at the toe of the rock revetment. The exponential gamma distribution with measured mean, standard deviation, and skewness can describe the measured probability distributions of the free surface elevations from outside the surf zone to the waterline elevation on the 1:2 revetment. CSHORE is shown to predict the cross-shore variations of the mean, standard deviation, skewness, and kurtosis of the free surface from outside the surf zone to the revetment. CSHORE does not account for wave reflection, but the average reflection coefficients for these tests were less than 0.4. In the future, improvement is needed to relate the waterline elevation measured by a wire placed parallel to the slope with the free surface elevation measured by a vertical gauge, because CSHORE predicts the wave statistics measured by the vertical gauge.

REFERENCES

Abramowitz, M. and Stegun, I.A. (1972). *Handbook of mathematical functions*. Dover, New York, N.Y.

American Society for Testing and Materials. (2000). "ASTM C:127, Standard test method for specific gravity and absorption of coarse aggregates." *Annual Book of ASTM Standards.*, Vol. 4. Construction, ASTM, Conshohoken, PA, 64 – 68.

Baquerizo, A., Losada, M.A., Smith, J.M., and Kobayashi, N. (1997). "Cross-shore variation of wave reflection from beaches." *J. Wtrwy., Port, Coast. and Oc. Eng.*, ASCE, 123(5), 274-279.

Bitner, E.M. (1980). "Non linear effects of the statistical model of shallow-water wid waves." *J. Applied Ocean Res.*, 2(2), 63-73.

Bouws, E., Gunter, H., Rosenthal, W., and Vincent, C.L. (1985). "Similarity of the wind wave spectrum in finite depth water. 1. Spectral form." *J. Geophy. Res.*, 90(C1), 975-986.

CETN-III-9, Revetments – Their applications and limitations. (1981). U.S. Army Corps of Engineers, Coast Engrg. Res. Ctr., Fort Belvoir, VA.

CETN-III-2, Riprap revetment design. (1985). Coast Engrg. Res. Ctr., U.S. Army Engr. Wtrwy. Experiment Station, Vicksburg, MS.

Goda, Y. 2000. *Random seas and design of maritime structures*. World Scientific Publishing Co. Pte. Ltd., River Edge, N.J.

Goda, Y. and Suzuki, Y. (1976). "Estimation of incident and reflected waves in random wave experiments." *Proc. 15th Coast. Eng. Conf.*, ASCE, 842-845.

Gran, S. (1992). *A course in ocean engineering*. Elsevier, New York, N.Y.

Guza, R.T. and Thornton, E.B. (1980). "Local and shoaled comparisons of sea surface elevations, pressures, and velocities." *J. Geophys. Res.*, 85(C3), 1524-1530.

Holland, K.T. and Holman, R.A. (1993). "The statistical distribution of swash maxima on natural beaches." *J. Geophys. Res.*, 98(C6), 10271-10278.

Huang, N.E. and Long, S.R. (1980). "An experimental study of the surface elevation probability distribution and statistics of wind-generated waves." *J. Fluid Mech.,* 101(1), 179-200.

Huntley, D.A., Guza, R.T., and Bowen, A.J. (1977). "A universal form for shoreline runup spectra?" *J. Geophy. Res.*, 82(18), 2577-2581.

Johnson, B.D. and Kobayashi, N. (1998). "Nonlinear time-averaged model in surf and swash zones." *Proc. 26th Coast. Eng. Conf.*, ASCE, 3, 2785-2798.

Kearney, P.G. and Kobayashi, N. (2000). "Irregular breaking wave transformation on a beach and runup on a revetment." *Res. Rept. No. CACR-00-06*, Ctr. for Applied Coast. Res., Univ. of Delaware, Newark, Del.

Kobayashi, N. (1999). "Wave runup and overtopping on beaches and coastal structures." *Advances in Coastal and Ocean Engineering*, Vol. 5, World Scientific, Singapore, 95-154.

Kobayashi, N., Cox, D.T., and Wurjanto, A. (1990). "Irregular wave reflection and runup on rough impermeable slopes." *J. Wtrwy., Port, Coast. and Oc. Eng.*, ASCE, 116(6), 708-726.

Kobayashi, N., DeSilva, G.S., and Watson, K.D. (1989). "Wave transformation and swash oscillations on gentle and steep slopes." *J. Geophys. Res.*, 94(C1), 951-966.

Kobayashi, N., Herrman, M.N., Johnson, B.D. and Orzech, M.D. (1998)."Probability distributions of surface elevation in surf and swash zones." *J. Wtrwy., Port, Coast. and Oc. Eng.*, ASCE, 124(3), 99-107.

Kobayashi, N. and Johnson, B.D. (1998). "Computer program CSHORE for predicting cross-shore transformation of irregular breaking waves." *Res. Rept. No. CACR-98-04*, Ctr. for Applied Coast. Res., Univ. of Delaware, Newark, Del.

Kobayashi, N. and Raichle, A.W. (1994). "Irregular wave overtopping of revetments in surf zones." *J. Wtrwy., Port, Coast. and Oc. Eng.*, ASCE, 120(1), 56-73.

Kobayashi, N. and Wurjanto, A. (1992). "Irregular wave setup and runup on beaches." *J. Wtrwy., Port, Coast. and Oc. Eng.*, ASCE, 118(4), 368-386.

Mase H. and Kobayashi, N. (1991). "Transformation of random breaking waves and its empirical numerical model considering surf beat." *Proc. Coast. Sediments '91*, ASCE, 1.668-702.

Melby, J.A. and Kobayashi, N. (1998) "Progression and variability of damage on rubble mound breakwaters." *J. Wtrwy., Port, Coast. and Oc. Eng.*, ASCE, 124(6), 286-294.

Rathbun, J.R., Cox, D.T. and Edge, B.L. (1998). "Wave runup and reflection on coastal structures in depth-limited conditions." *Proc. 26th Coast. Eng. Conf.*, ASCE, 1, 1053-1067.

Raubenheimer, B., Guza, R.T., Elgar, S., and Kobayashi, N. (1995). "*Swash on a gently sloping beach.*" *J. Geophys. Res.*, 100(C5), 8751-8760.

Shore Protection Manual. (1984). Coast Engrg. Res. Ctr., U.S. Army Engr. Wtrwy. Experiment Station, U.S. Government Printing Office, Washington, D.C.

Wolfran, S. (1991). *Mathematica*, 2nd ed., Addison-Wesley, Redwood City, CA.

APPENDIX A

TIME SERIES PLOTS

This appendix contains representative time series plots for all tests performed.

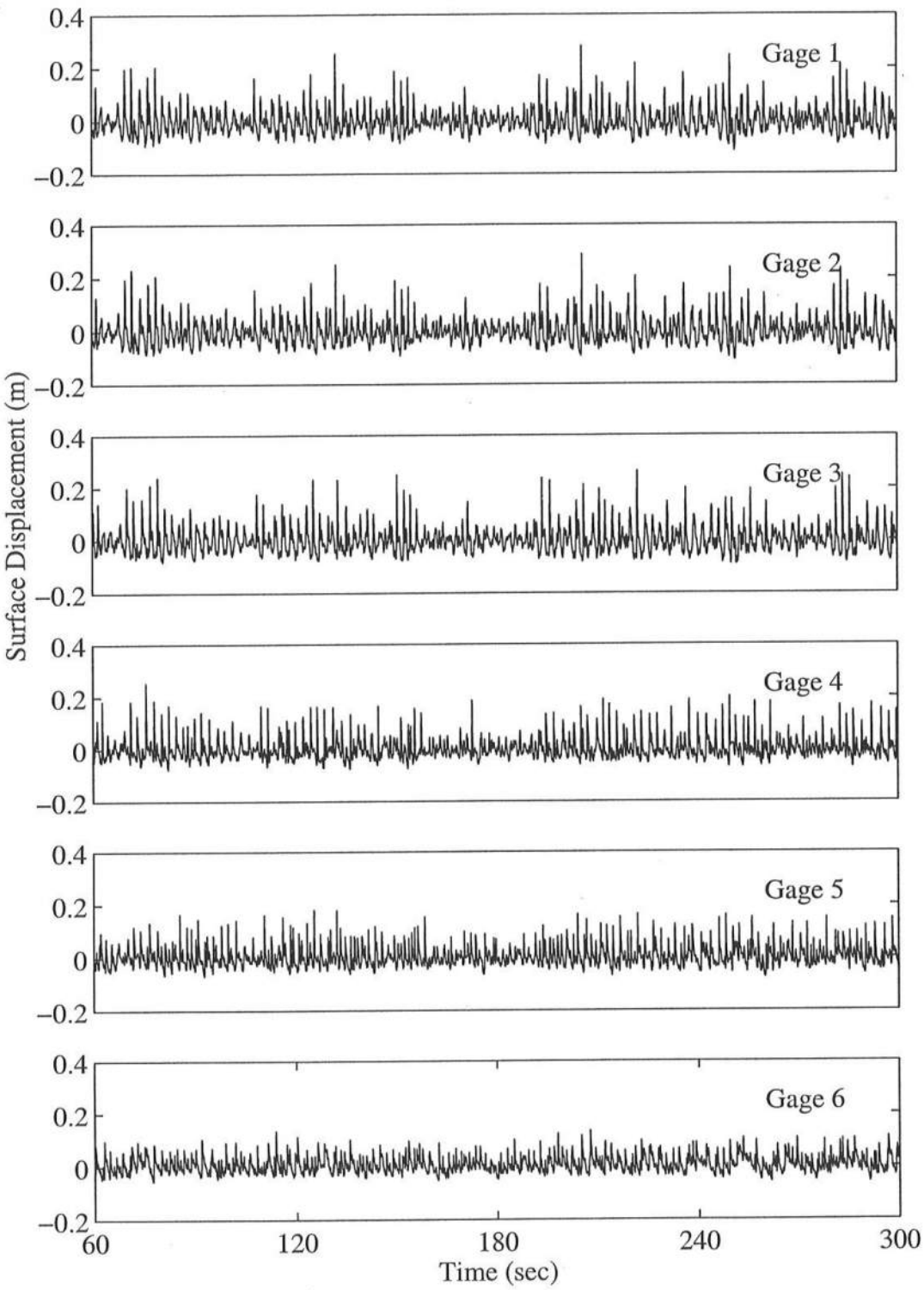

Figure A.1: Time Series for T_p = 4.7 s, d_t =4 cm, for Gauge 1 – Gauge 6.

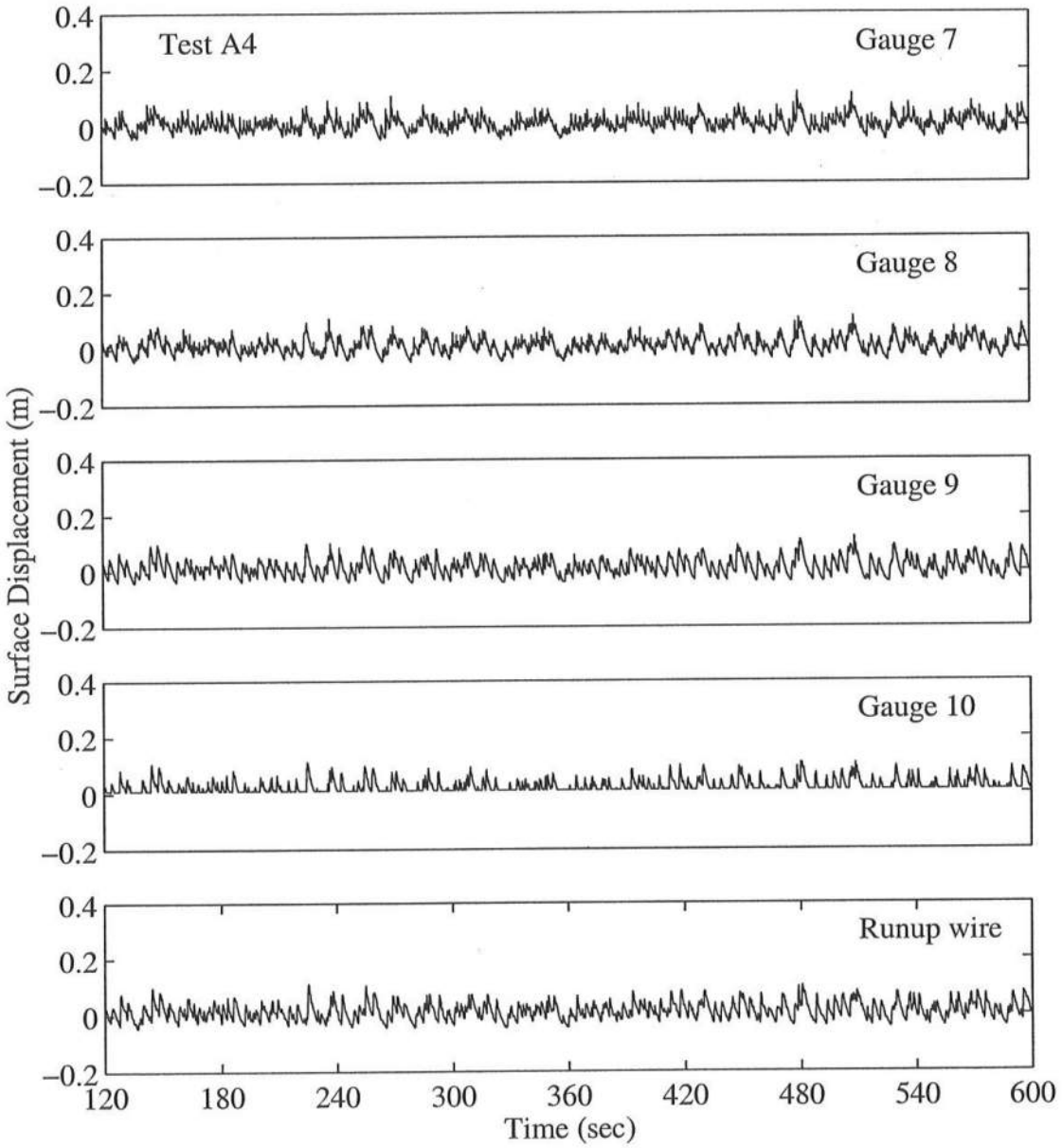

Figure A.2: Time Series for $T_p = 4.7$ s, $d_t = 4$ cm, for Gauge 7 – Runup Wire.

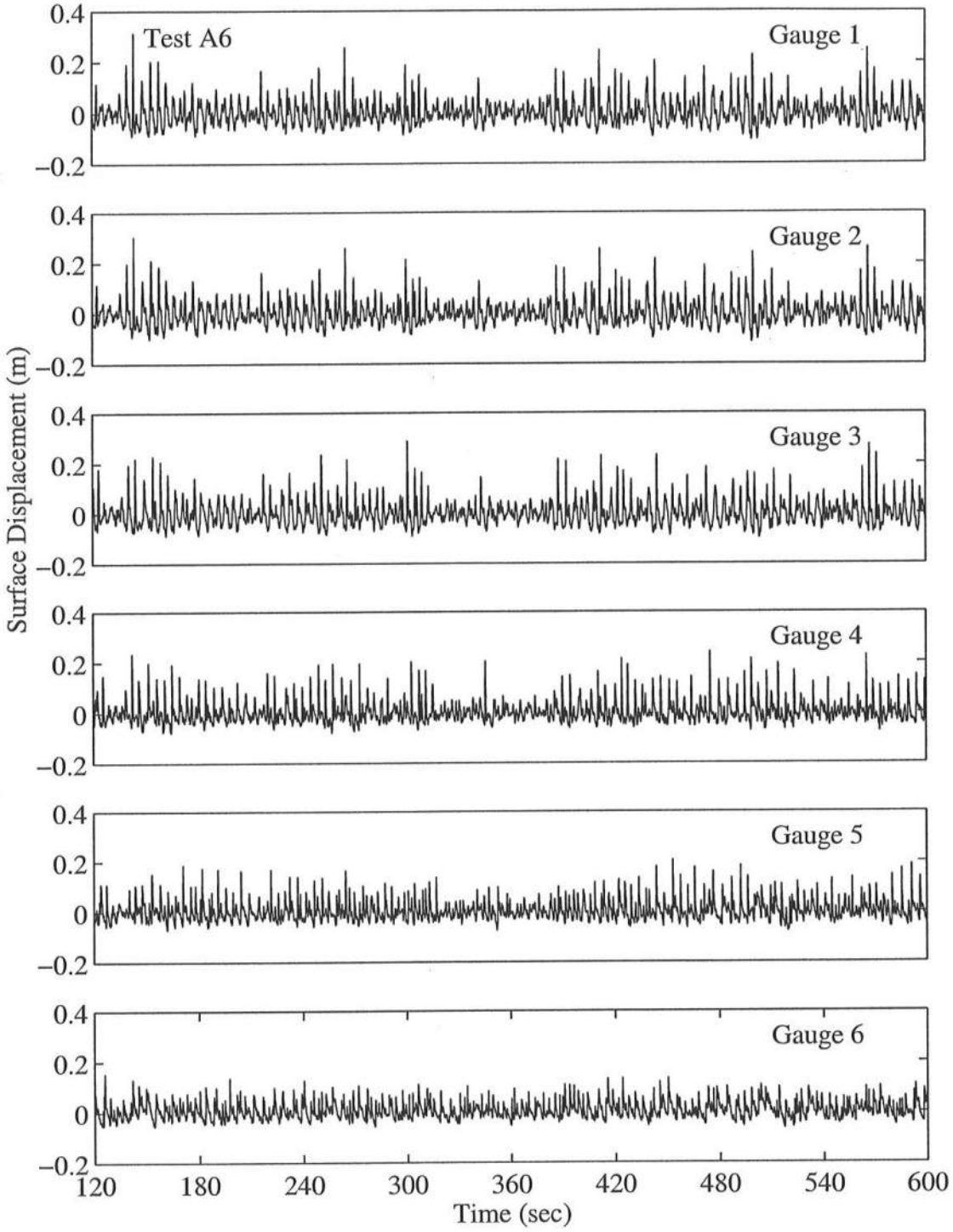

Figure A.3: Time Series for $T_p = 4.7$ s, $d_t = 6$ cm, for Gauge 1 – Gauge 6.

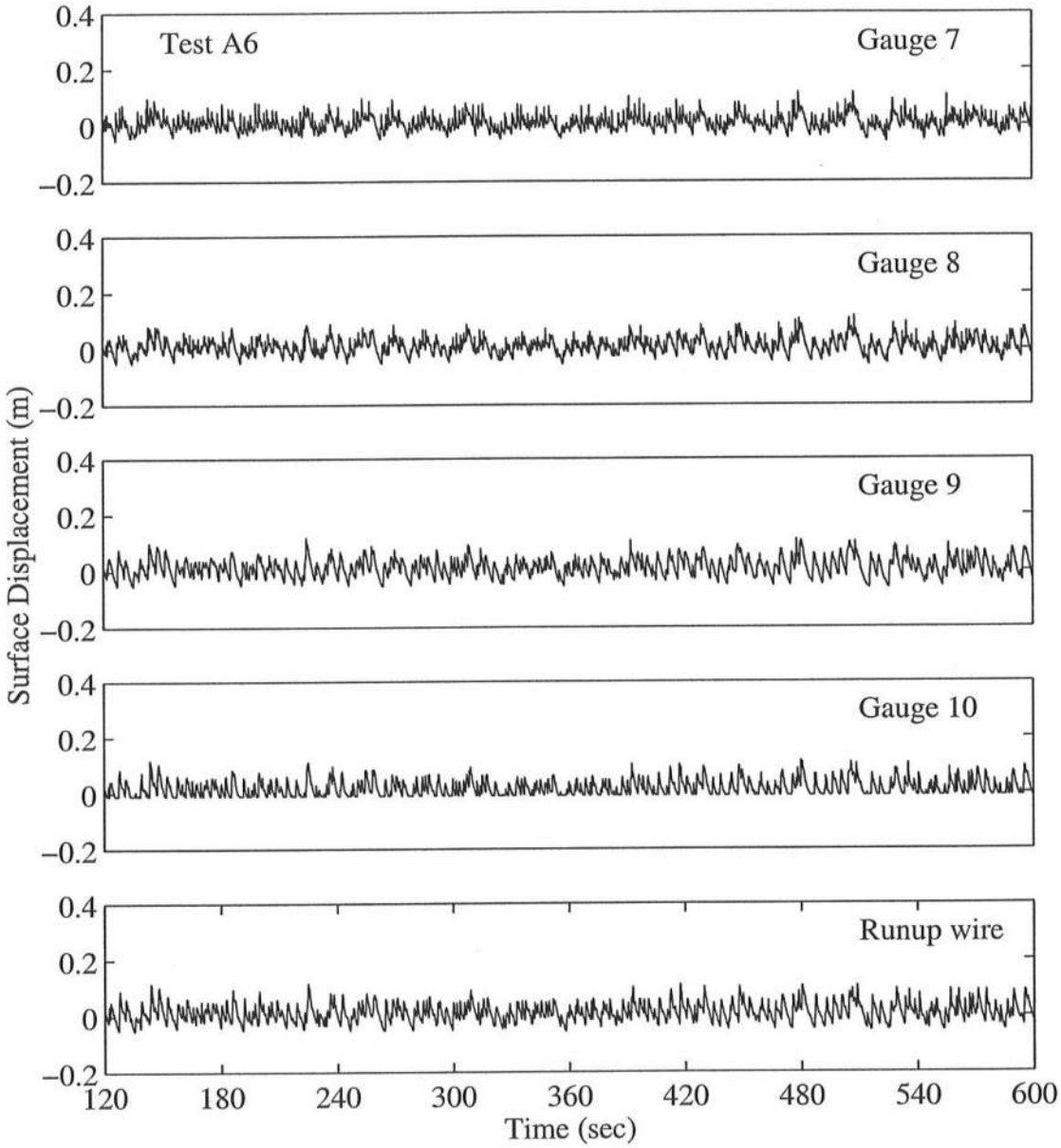

Figure A.4: Time Series for $T_p = 4.7$ s, $d_t = 6$ cm, for Gauge 7 – Runup Wire.

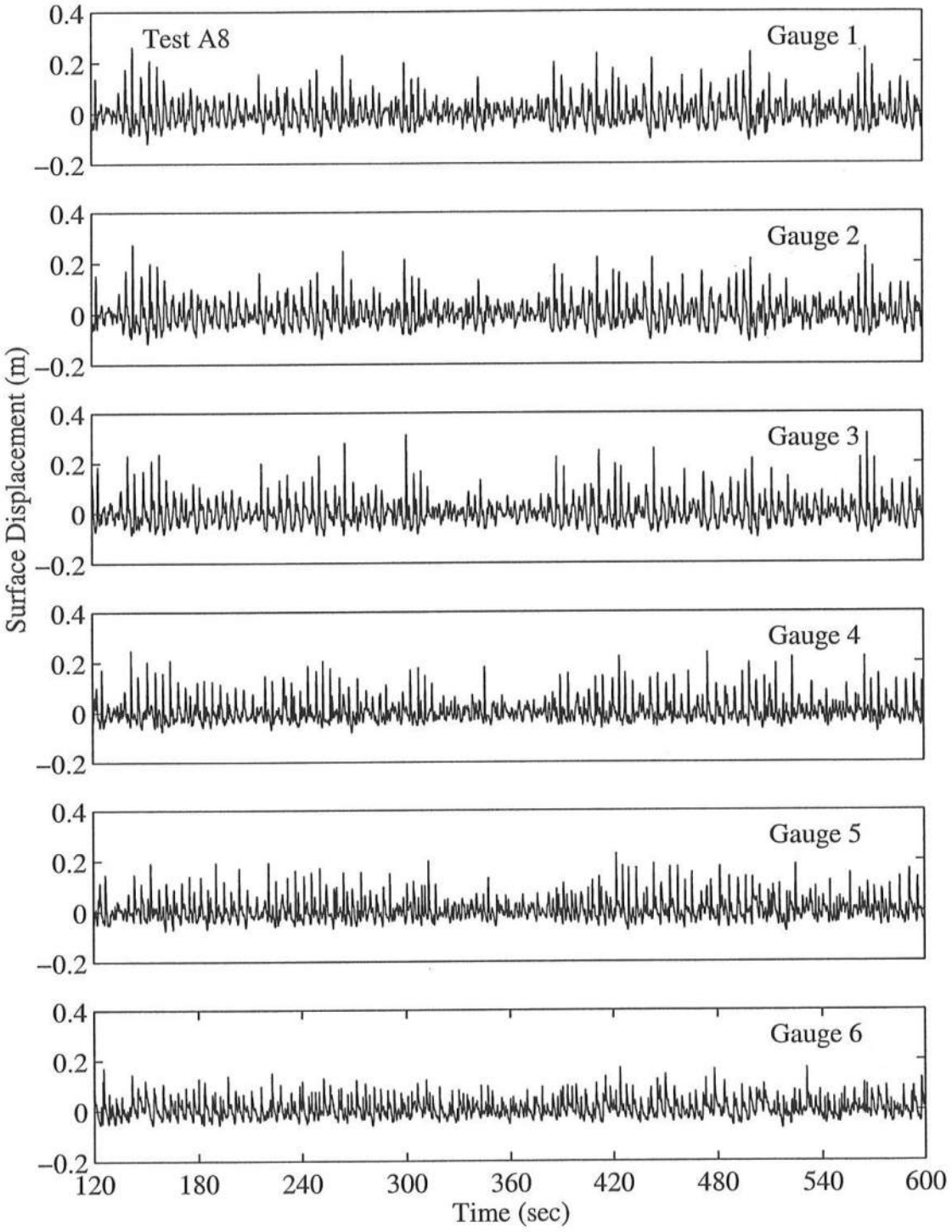

Figure A.5: Time Series for $T_p = 4.7$ s, $d_t = 8$ cm, for Gauge 1 – Gauge 6.

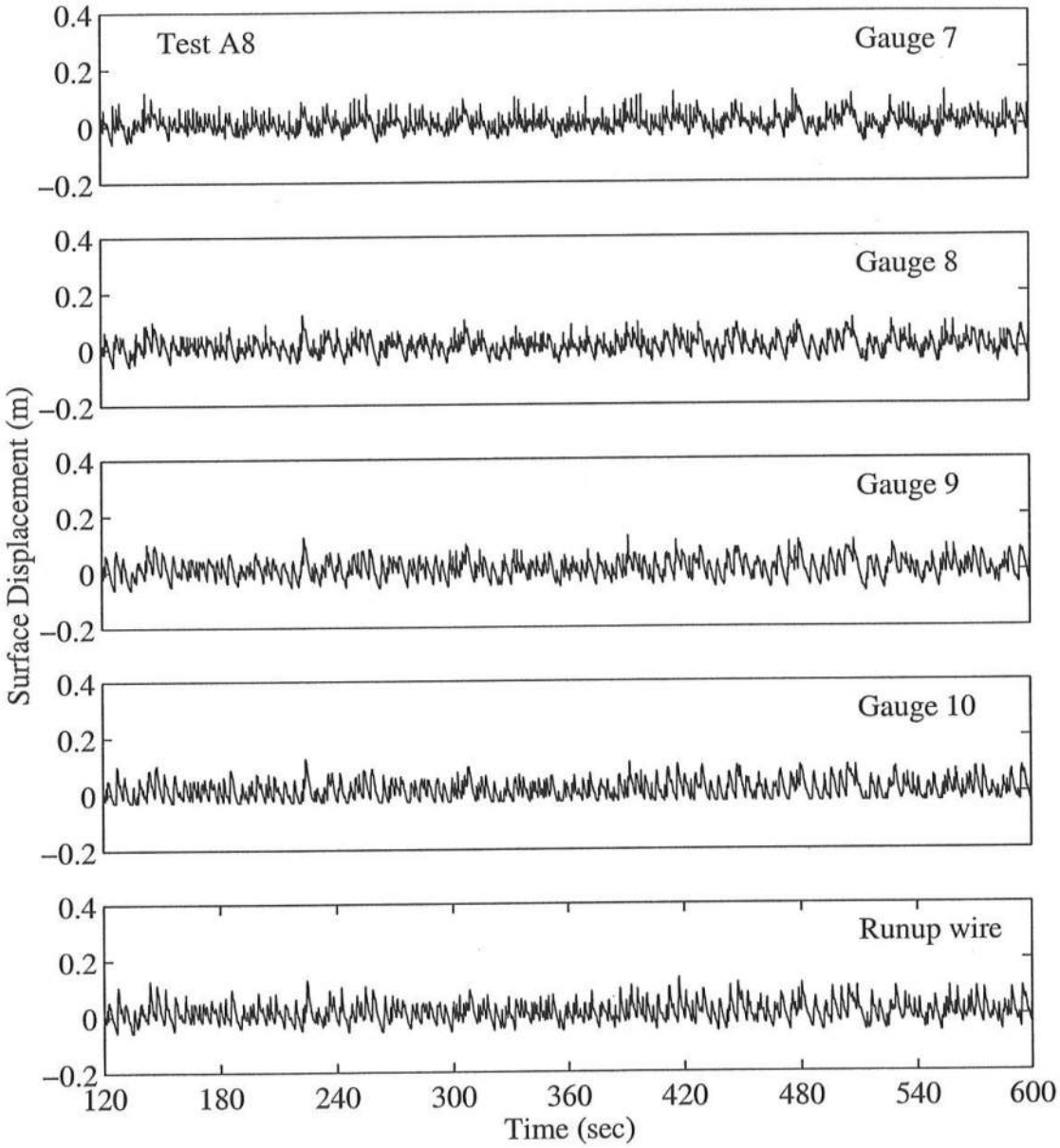

Figure A.6: Time Series for $T_p = 4.7$ s, $d_t = 8$ cm, for Gauge 7 – Runup Wire.

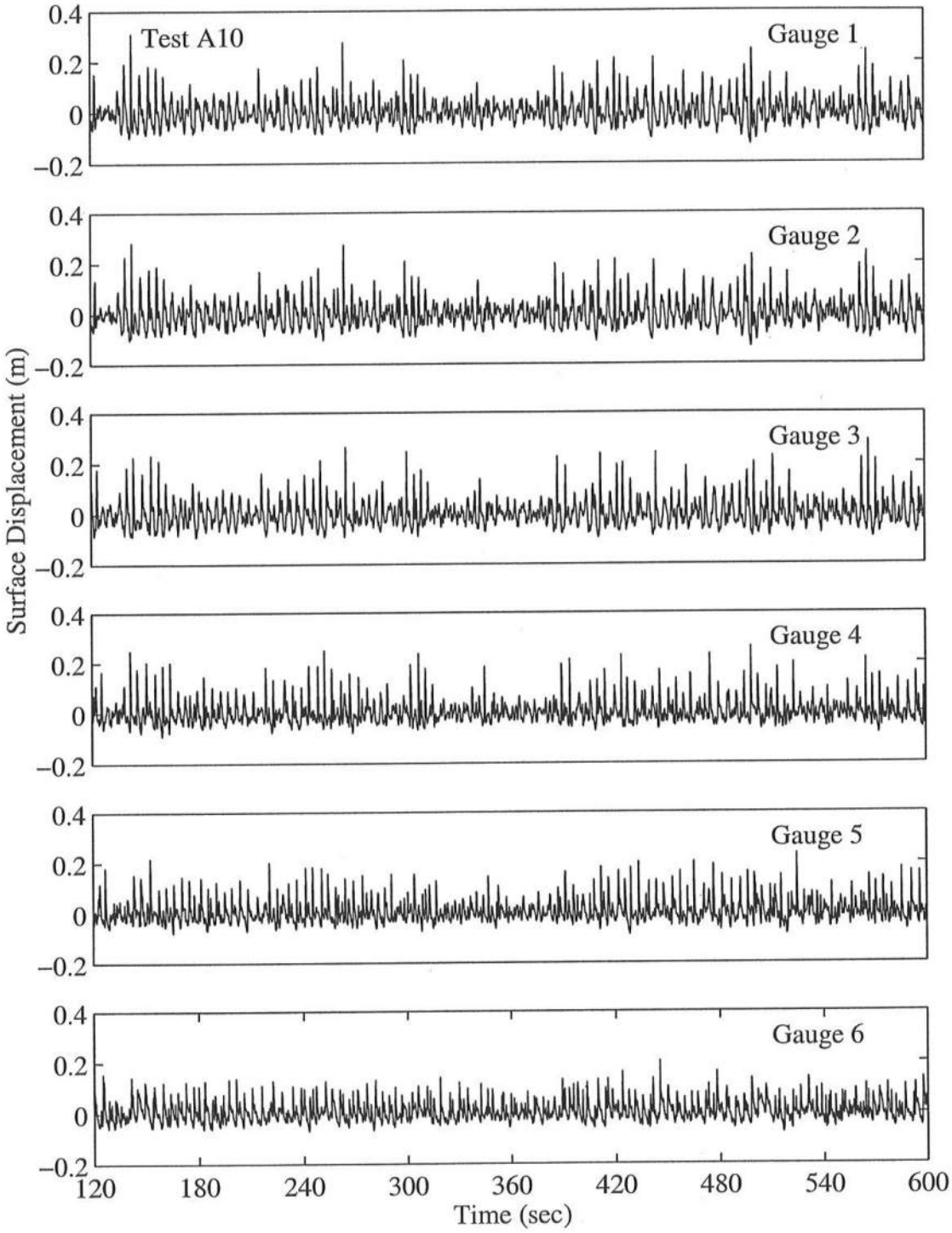

Figure A.7: Time Series for $T_p = 4.7$ s, $d_t = 10$ cm, for Gauge 1 – Gauge 6.

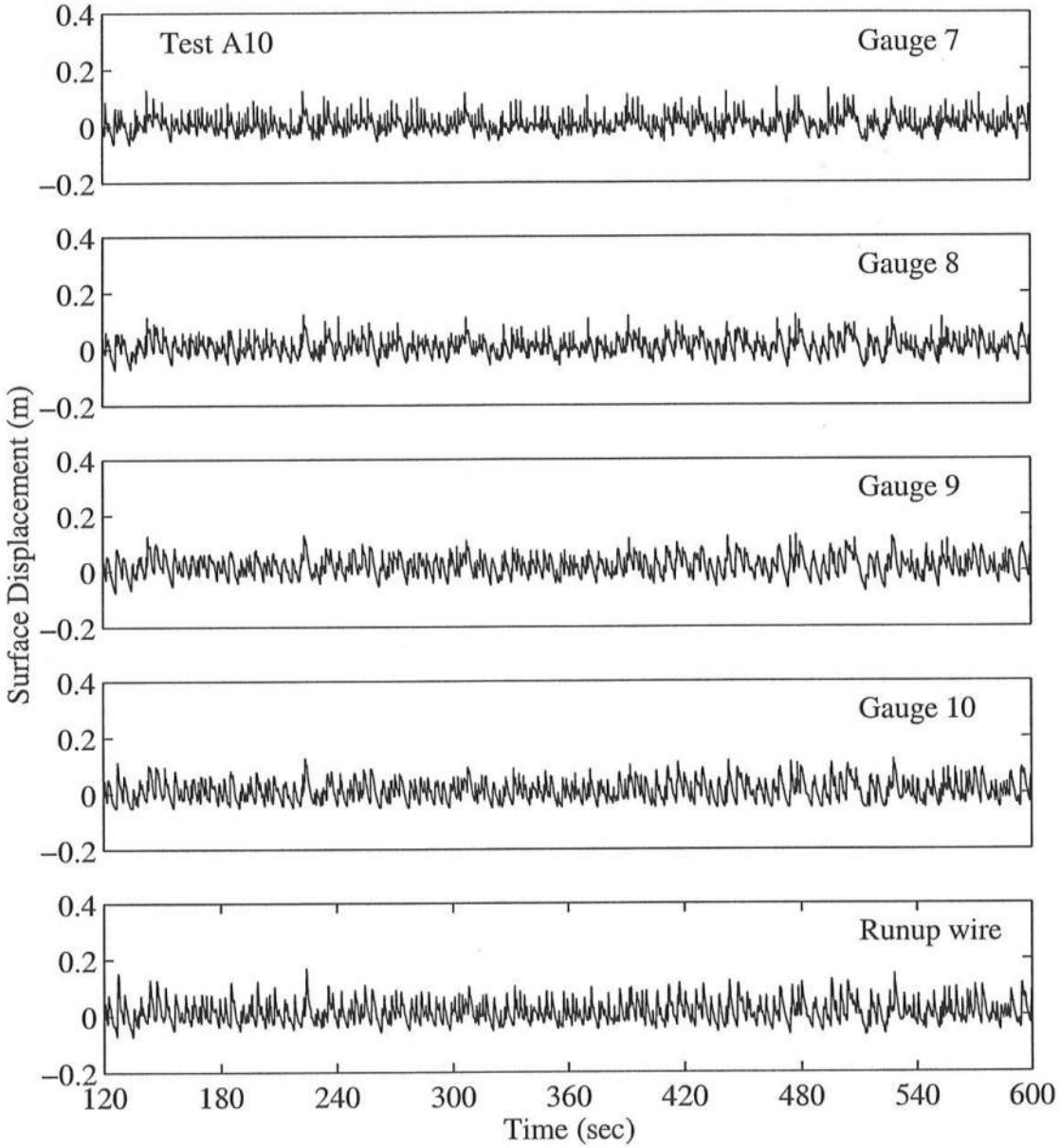

Figure A.8: Time Series for $T_p = 4.7$ s, $d_t = 10$ cm, for Gauge 7 – Runup Wire.

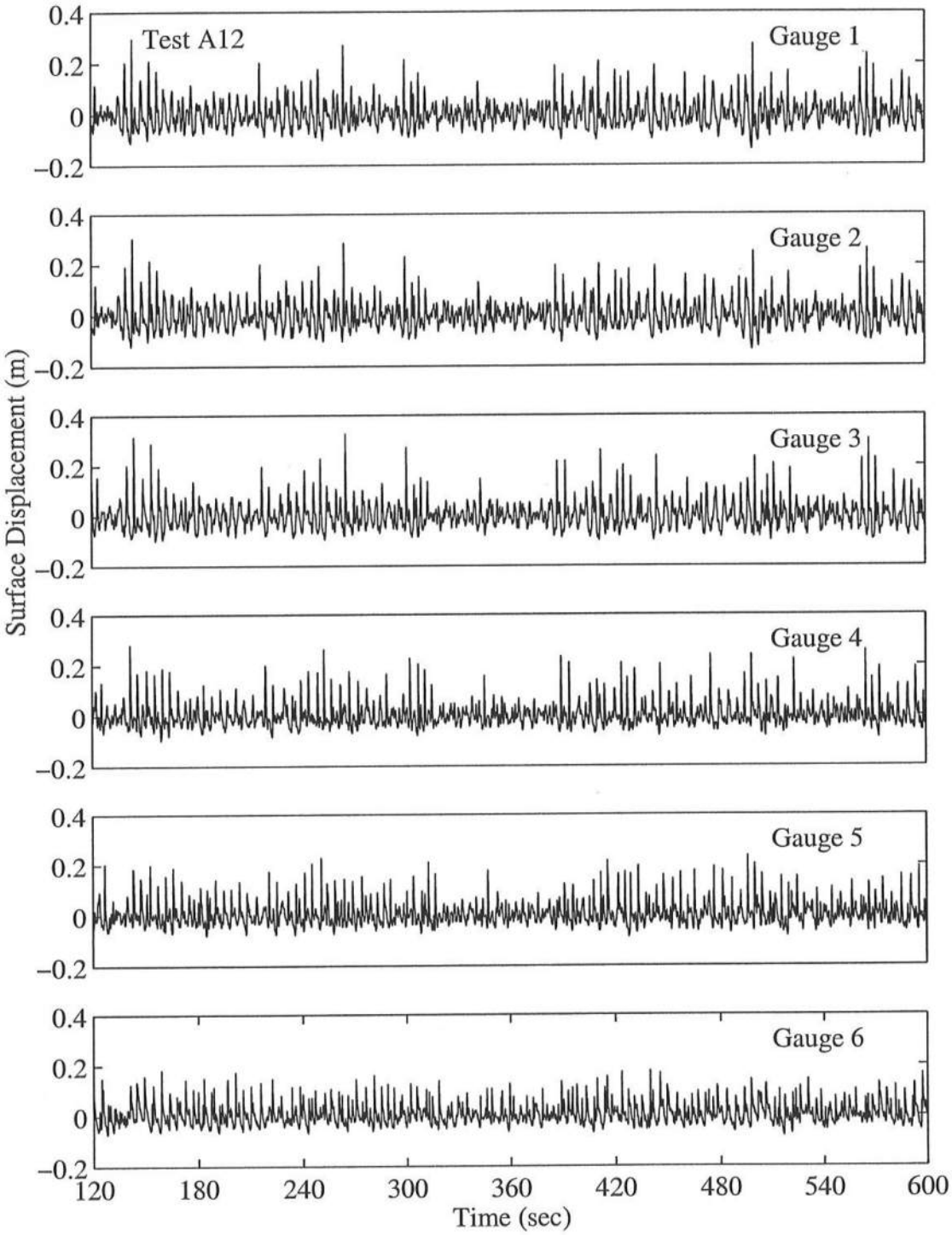

Figure A.9: Time Series for $T_p = 4.7$ s, $d_t = 12$ cm, for Gauge 1 – Gauge 6.

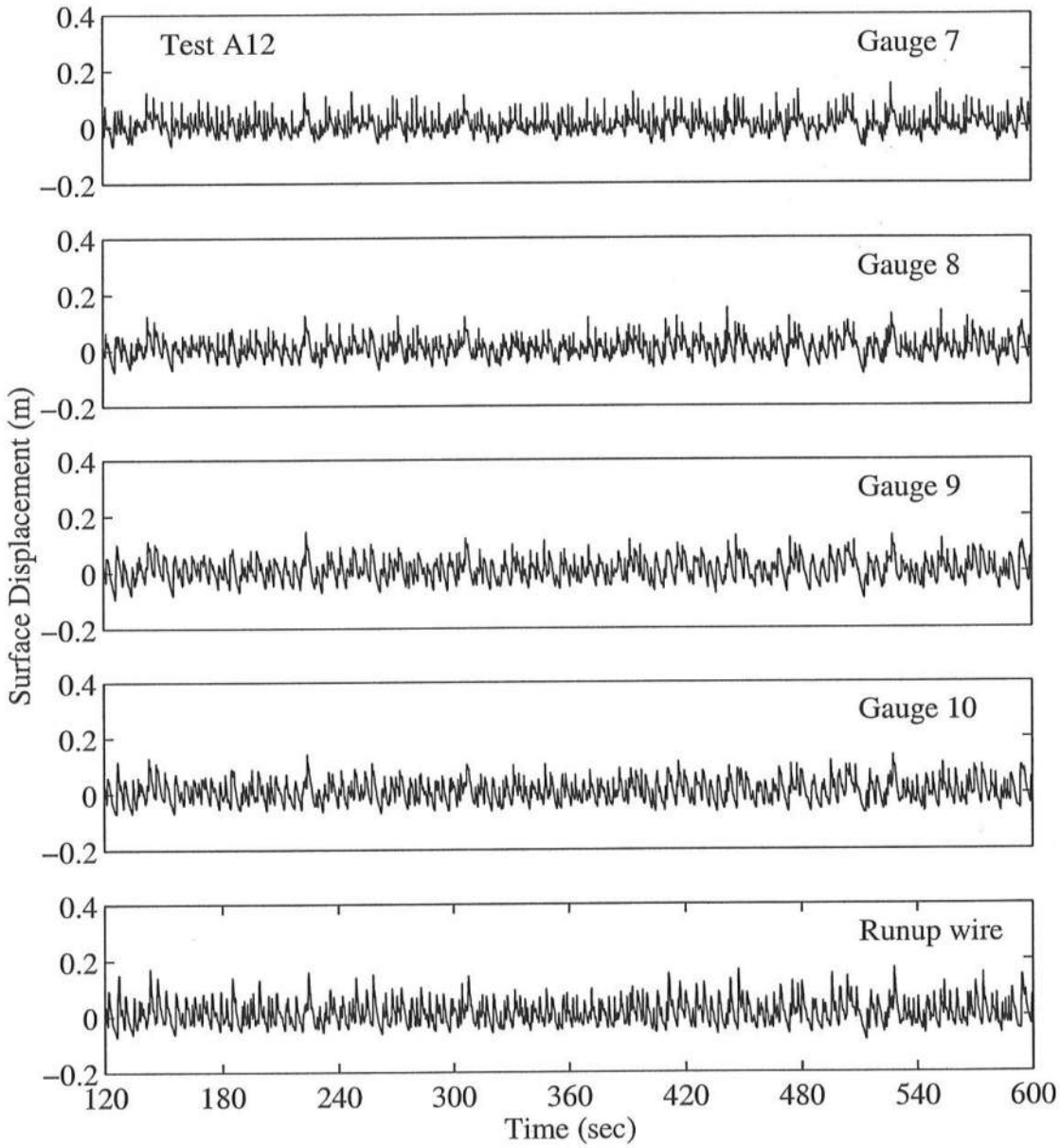

Figure A.10: Time Series for $T_p = 4.7$ s, $d_t = 12$ cm, for Gauge 7 – Runup Wire.

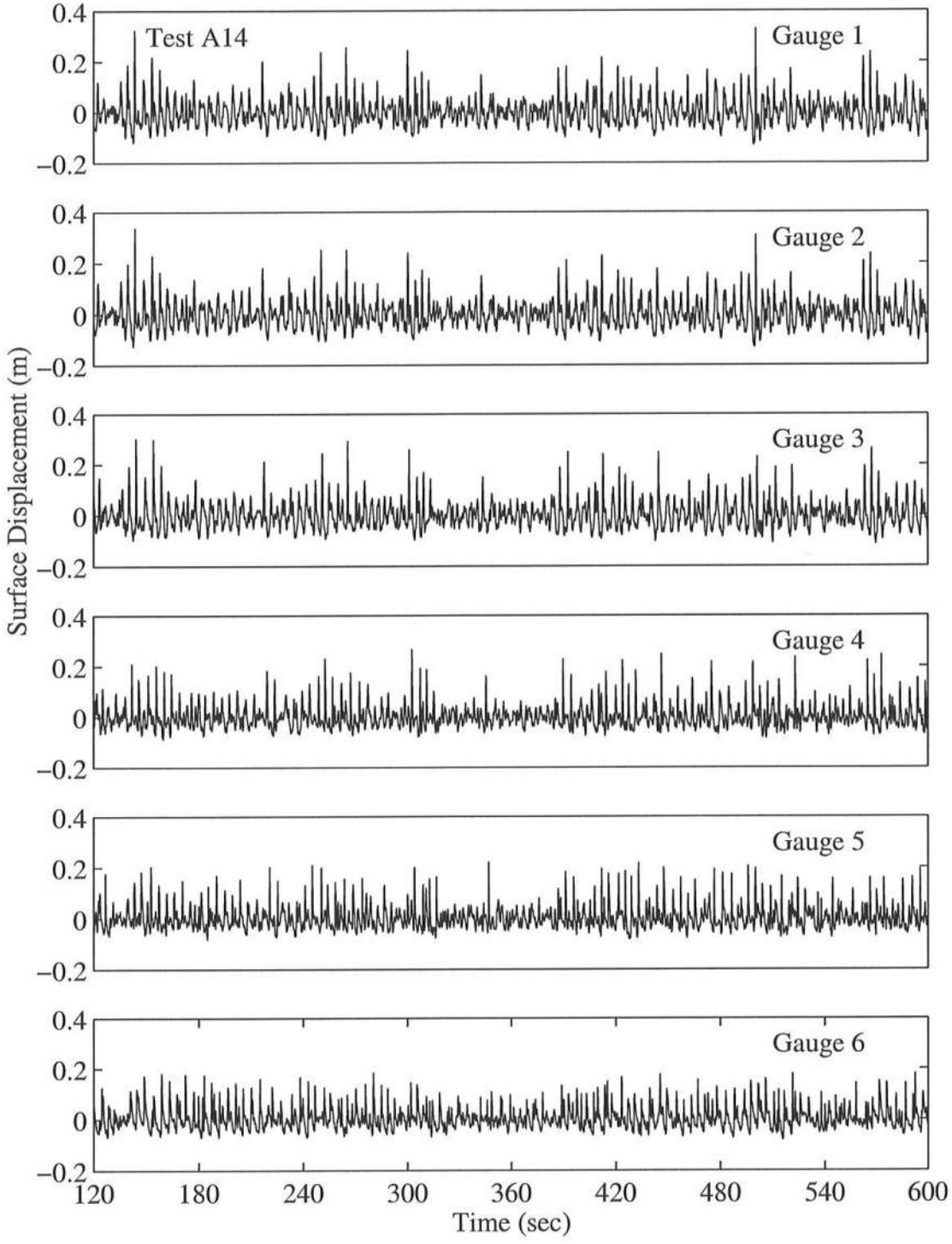

Figure A.11: Time Series for $T_p = 4.7$ s, $d_t = 14$ cm, for Gauge 1 – Gauge 6.

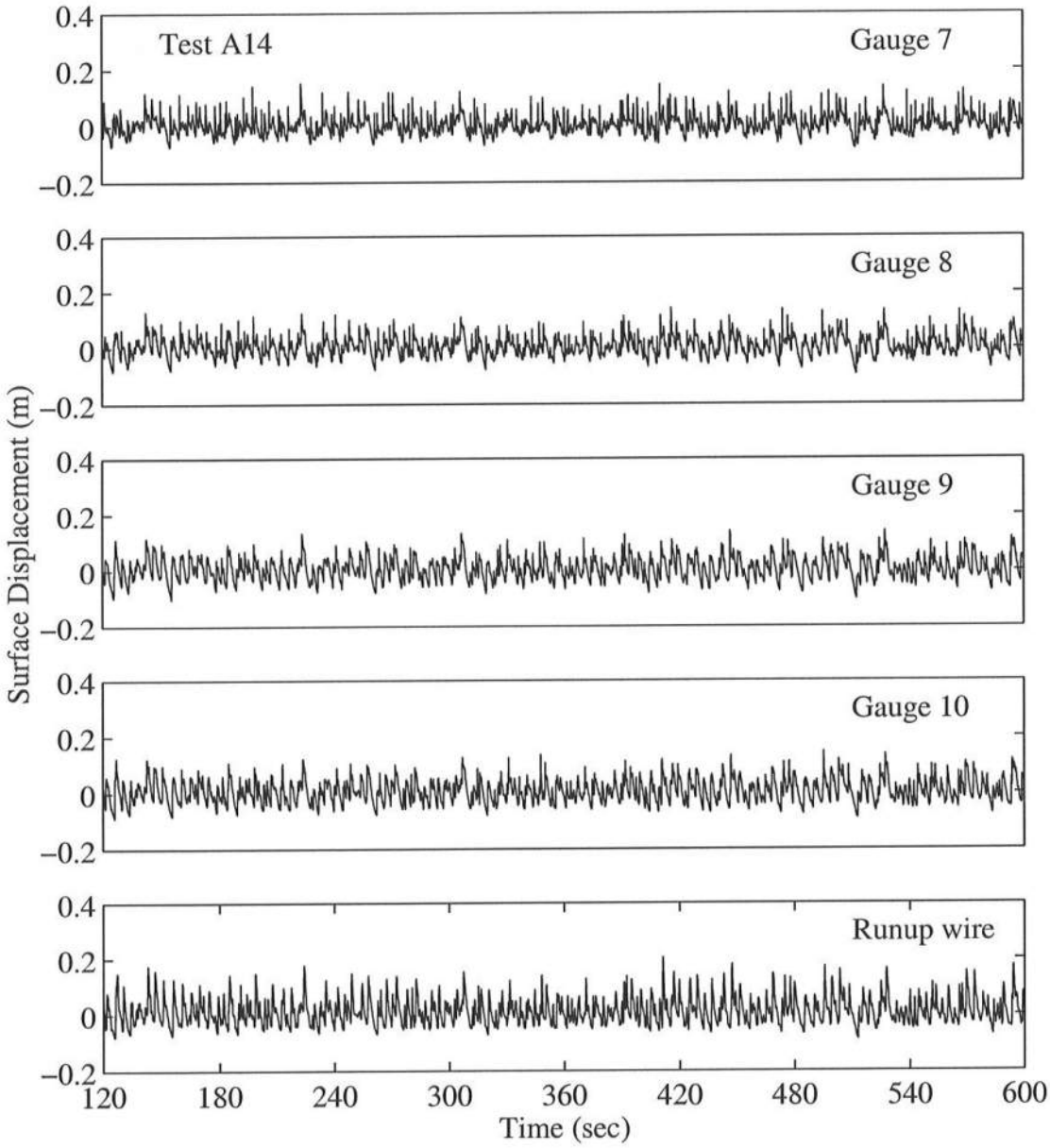

Figure A.12: Time Series for $T_p = 4.7$ s, $d_t = 14$ cm, for Gauge 7 – Runup Wire.

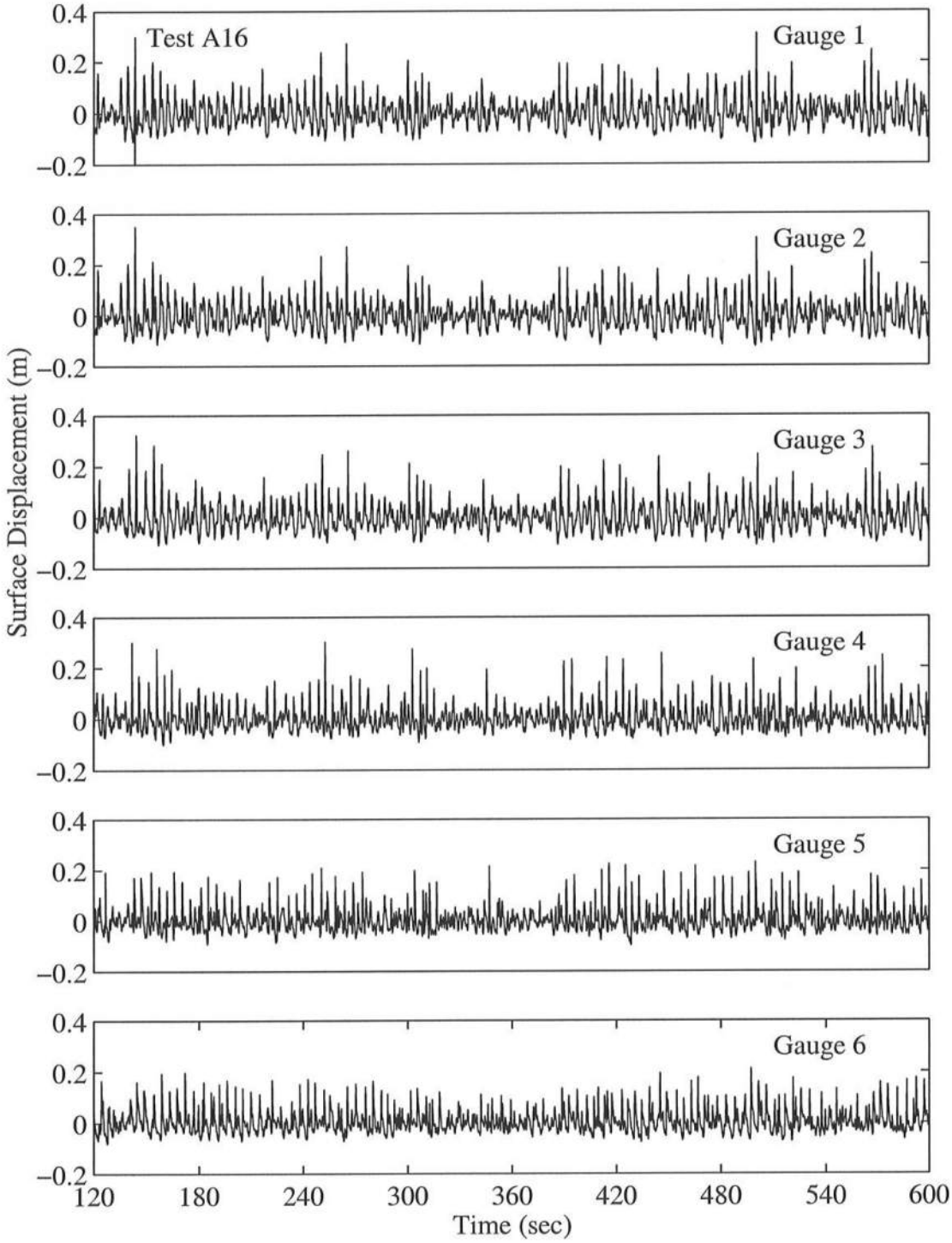

Figure A.13: Time Series for $T_p = 4.7$ s, $d_t = 16$ cm, for Gauge 1 – Gauge 6.

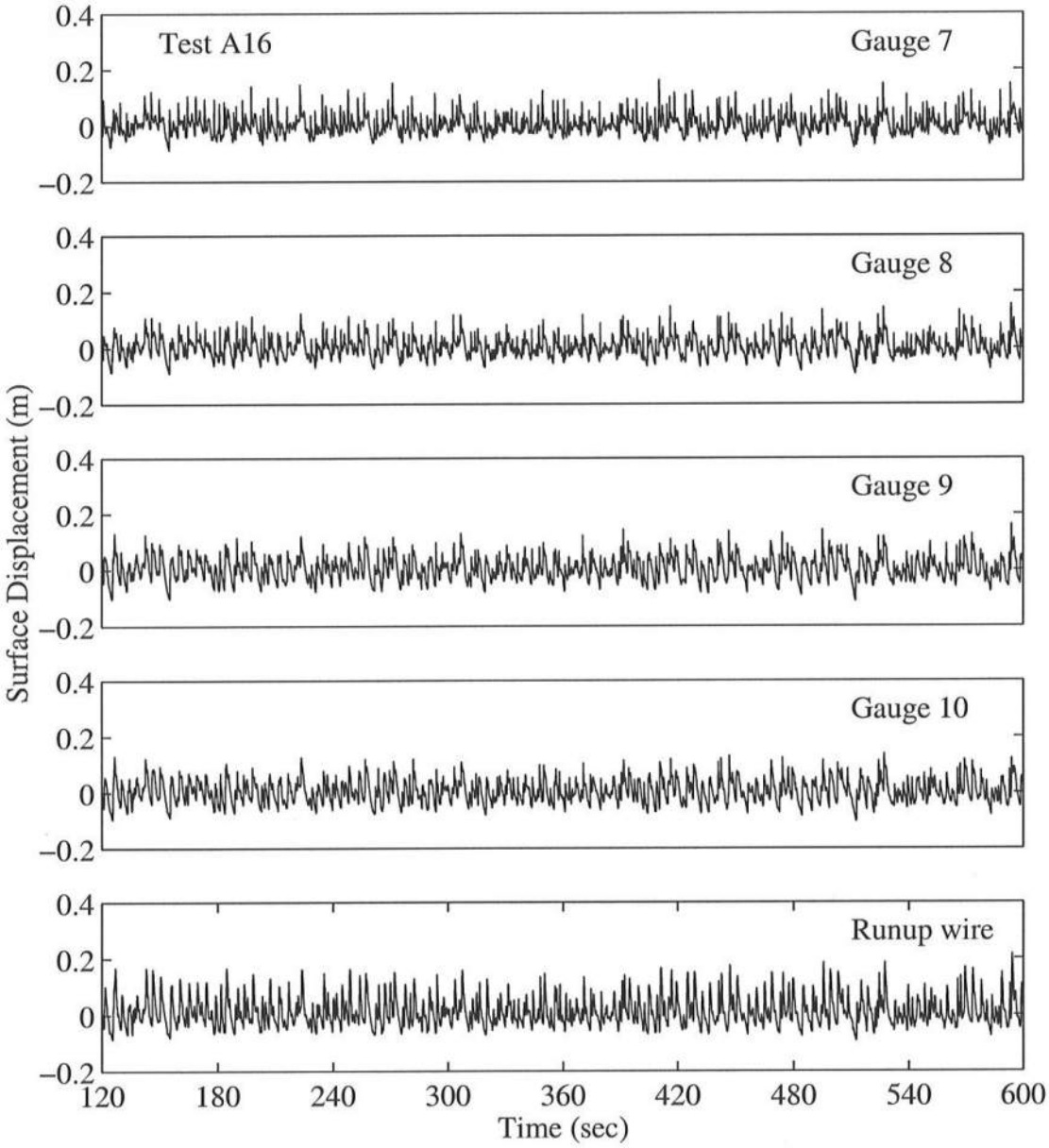

Figure A.14: Time Series for $T_p = 4.7$ s, $d_t = 16$ cm, for Gauge 7 – Runup Wire.

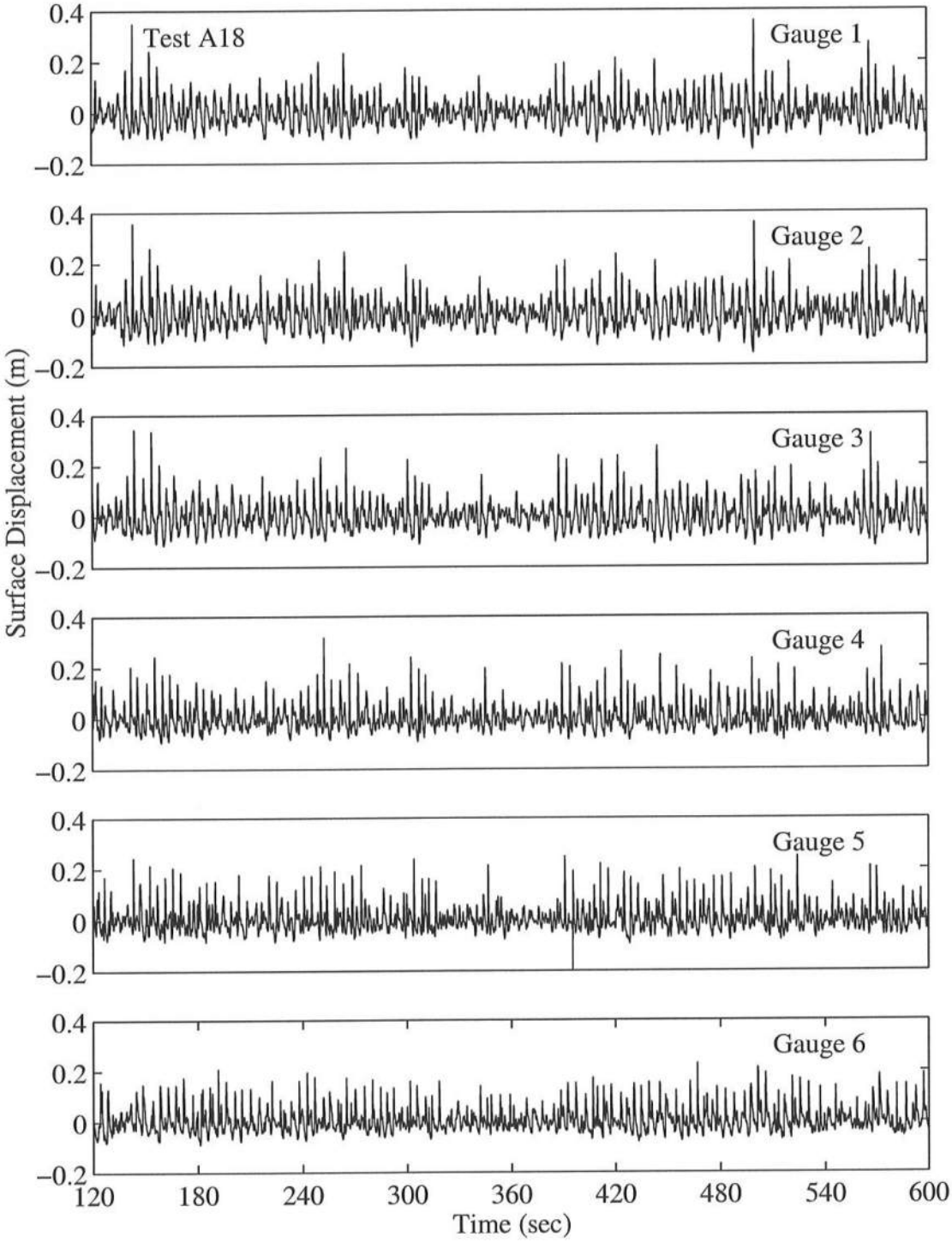

Figure A.15: Time Series for $T_p = 4.7$ s, $d_t = 18$ cm, for Gauge 1 – Gauge 6.

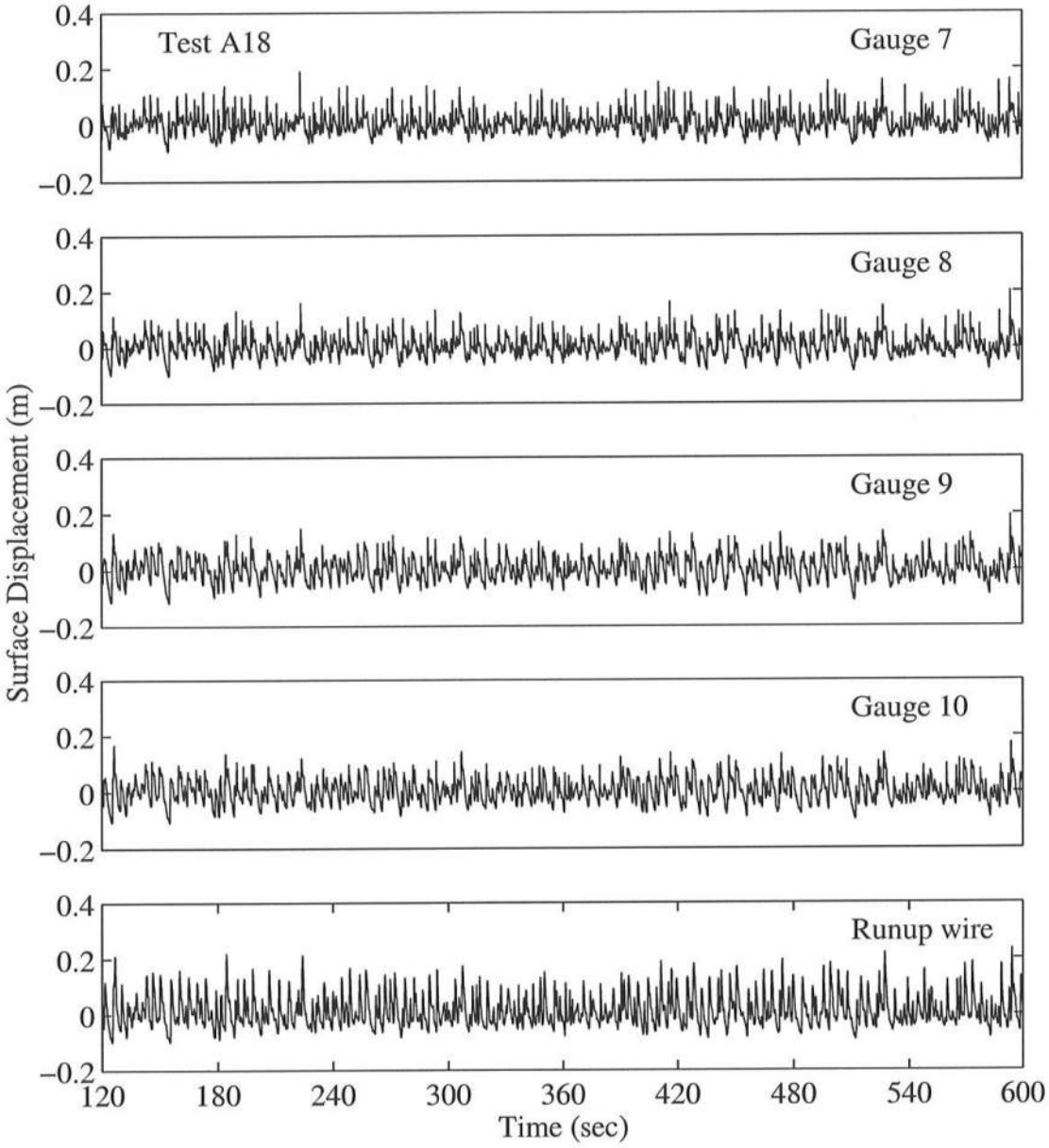

Figure A.16: Time Series for $T_p = 4.7$ s, $d_t = 18$ cm, for Gauge 7 – Runup Wire.

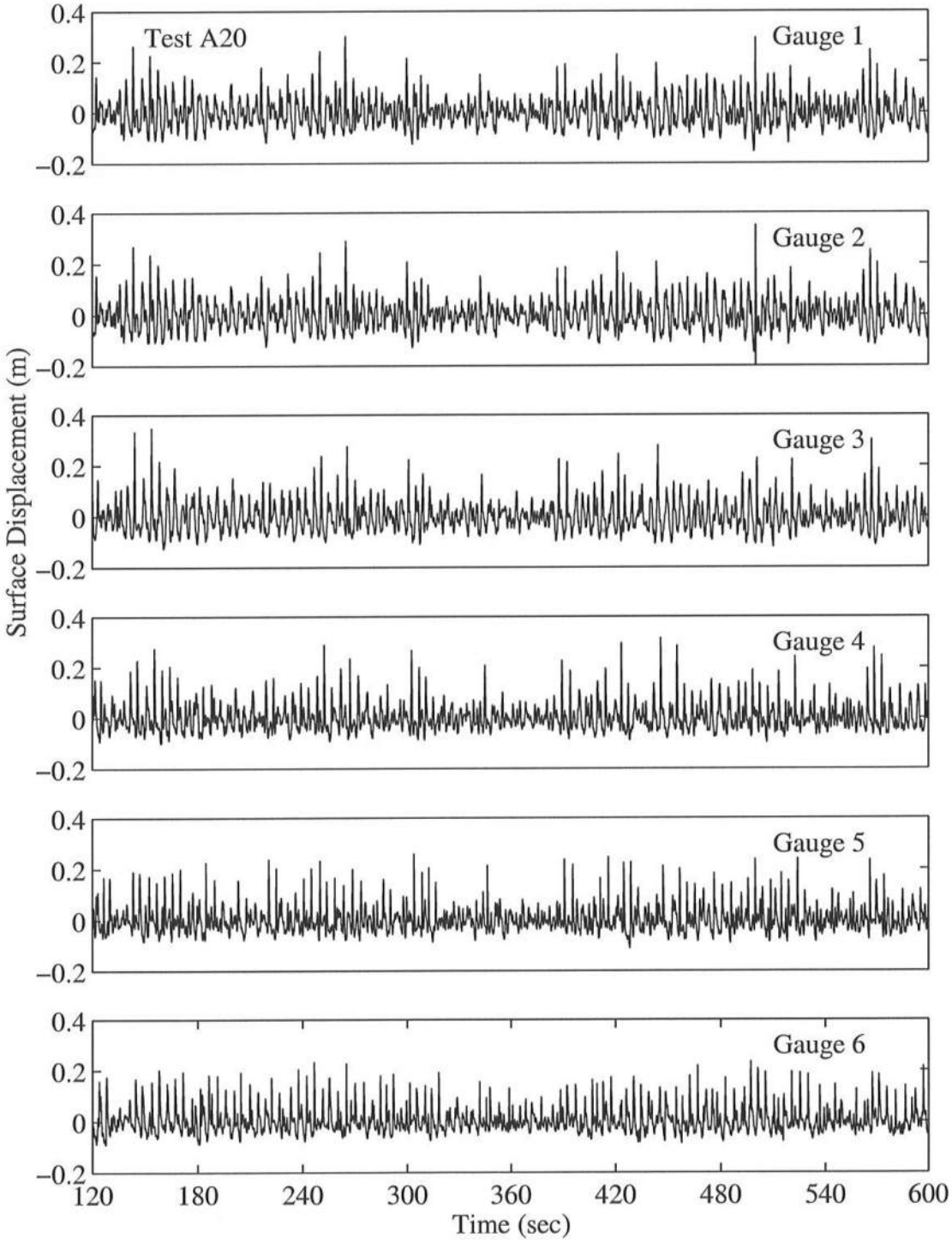

Figure A.17: Time Series for $T_p = 4.7$ s, $d_t = 20$ cm, for Gauge 1 – Gauge 6.

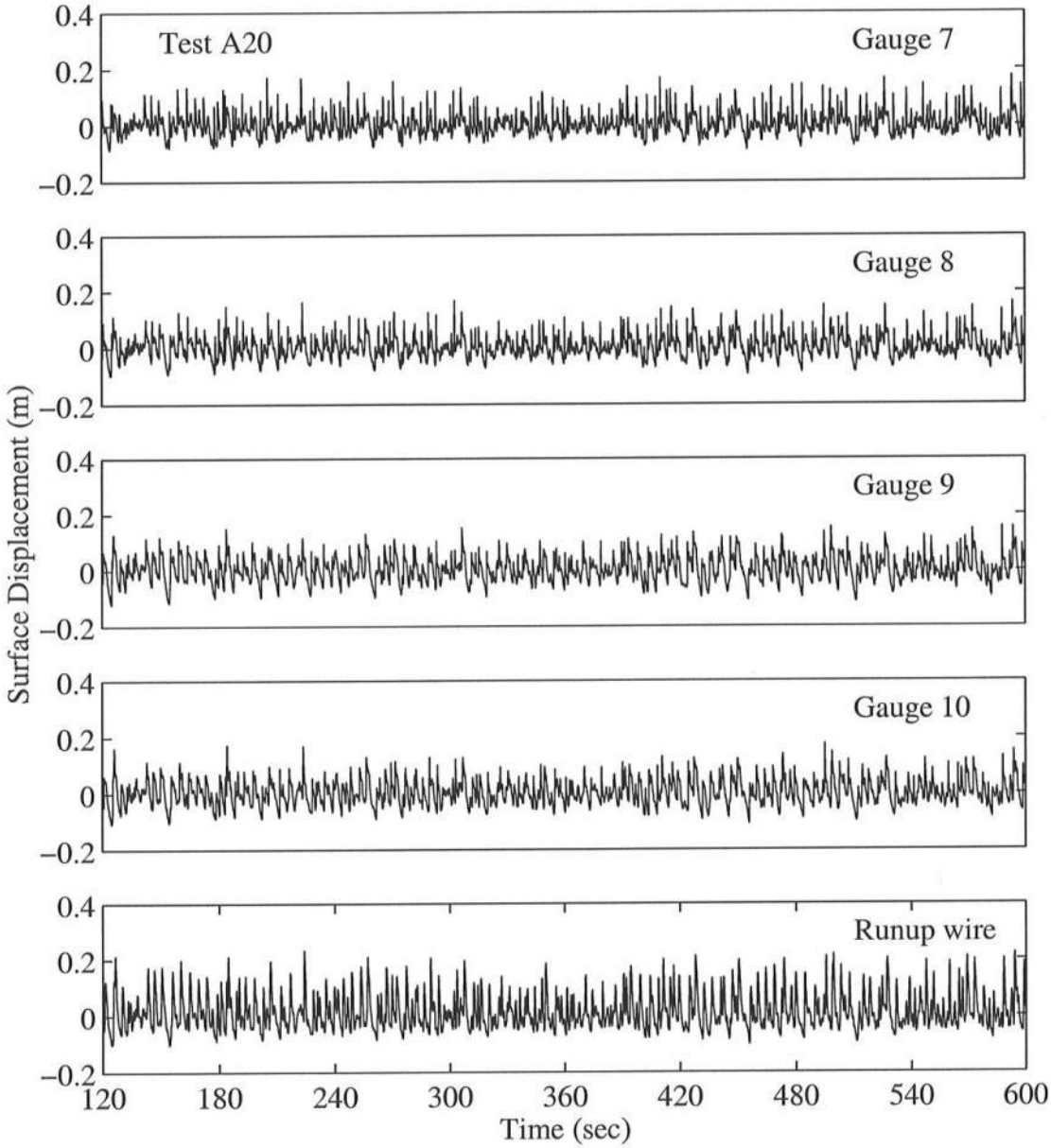

Figure A.18: Time Series for $T_p = 4.7$ s, $d_t = 20$ cm, for Gauge 7 – Runup Wire.

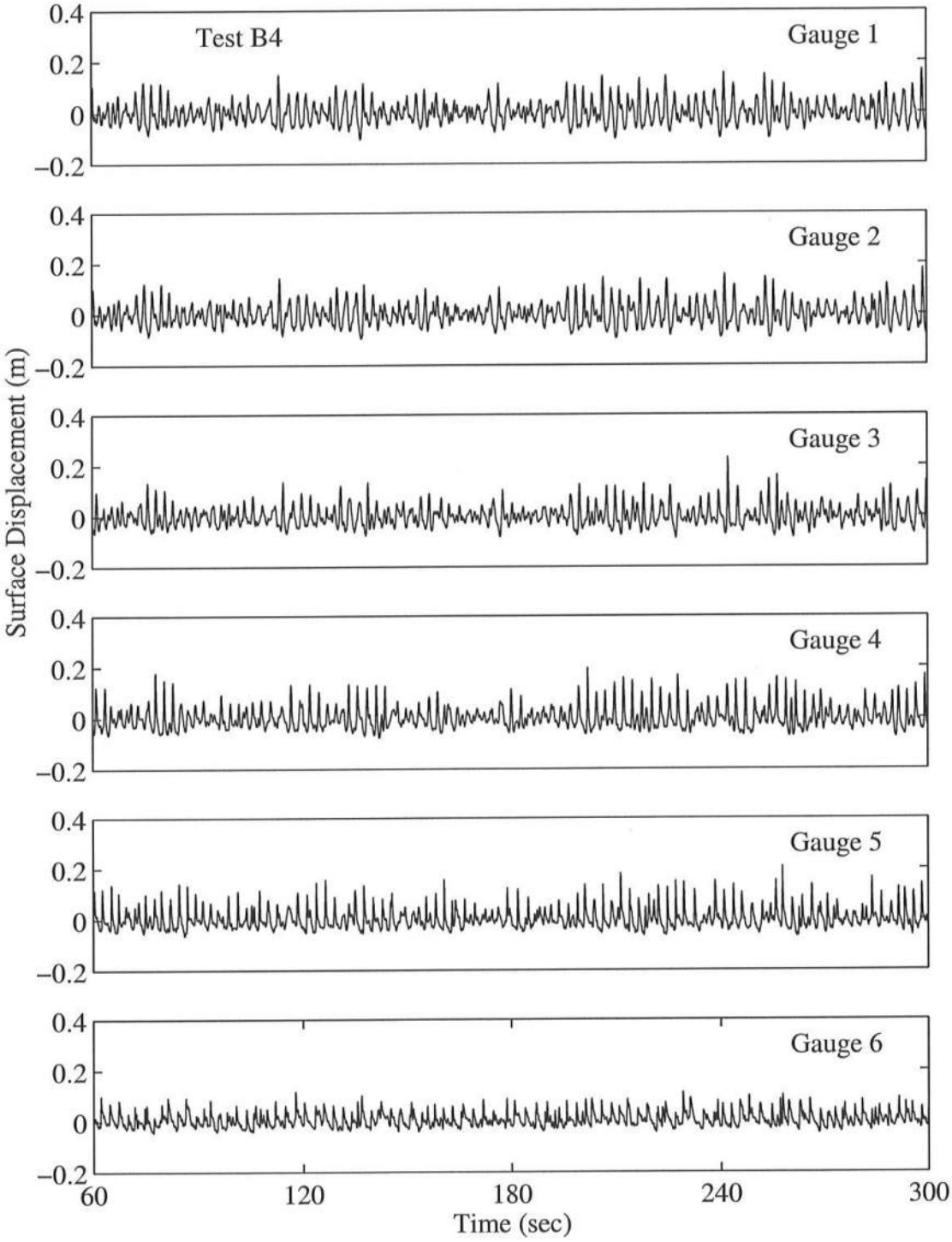

Figure A.19: Time Series for $T_p = 2.4$ s, $d_t = 4$ cm, for Gauge 1 – Gauge 6.

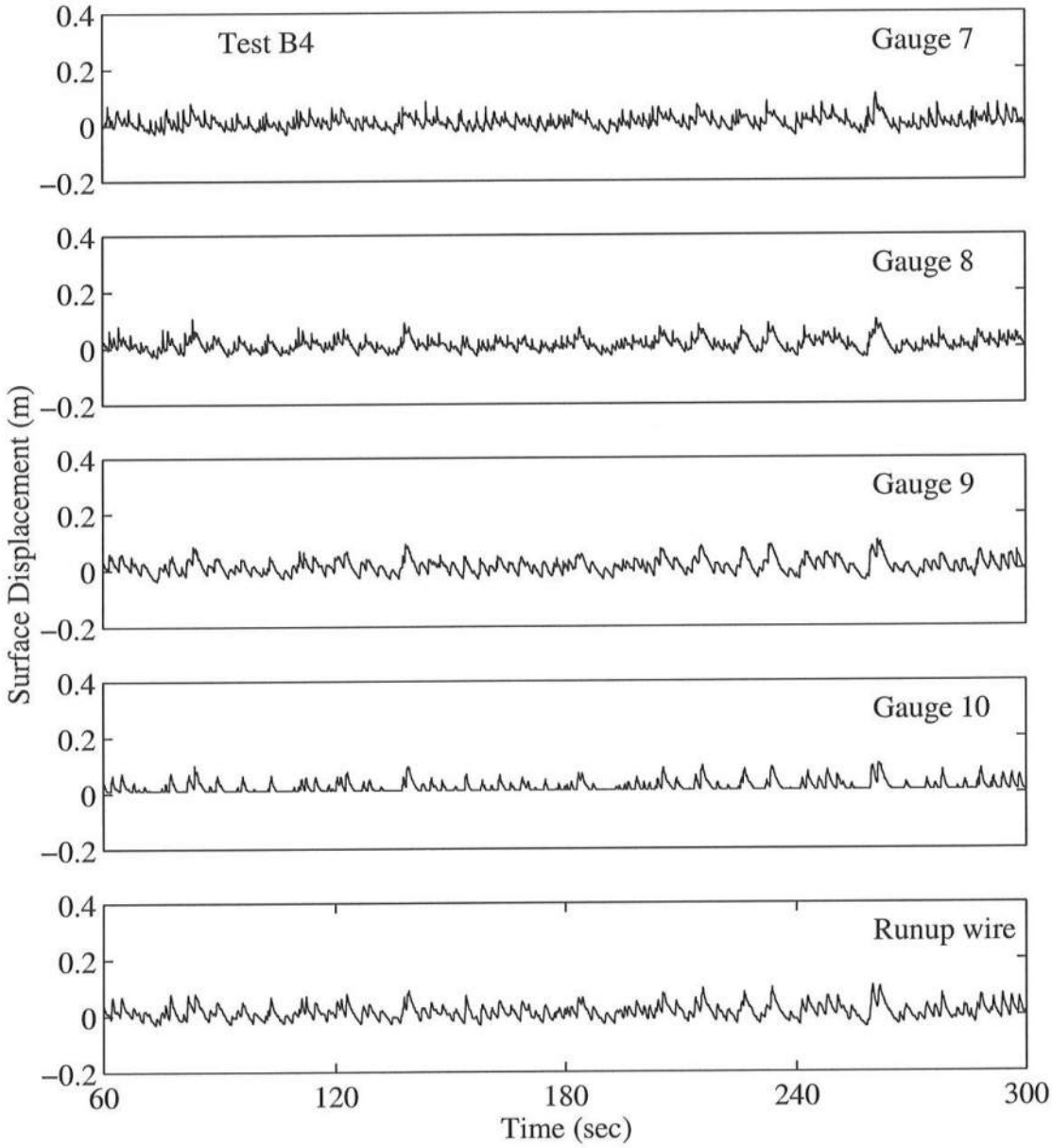

Figure A.20: Time Series for $T_p = 2.4$ s, $d_t = 4$ cm, for Gauge 7 – Runup Wire.

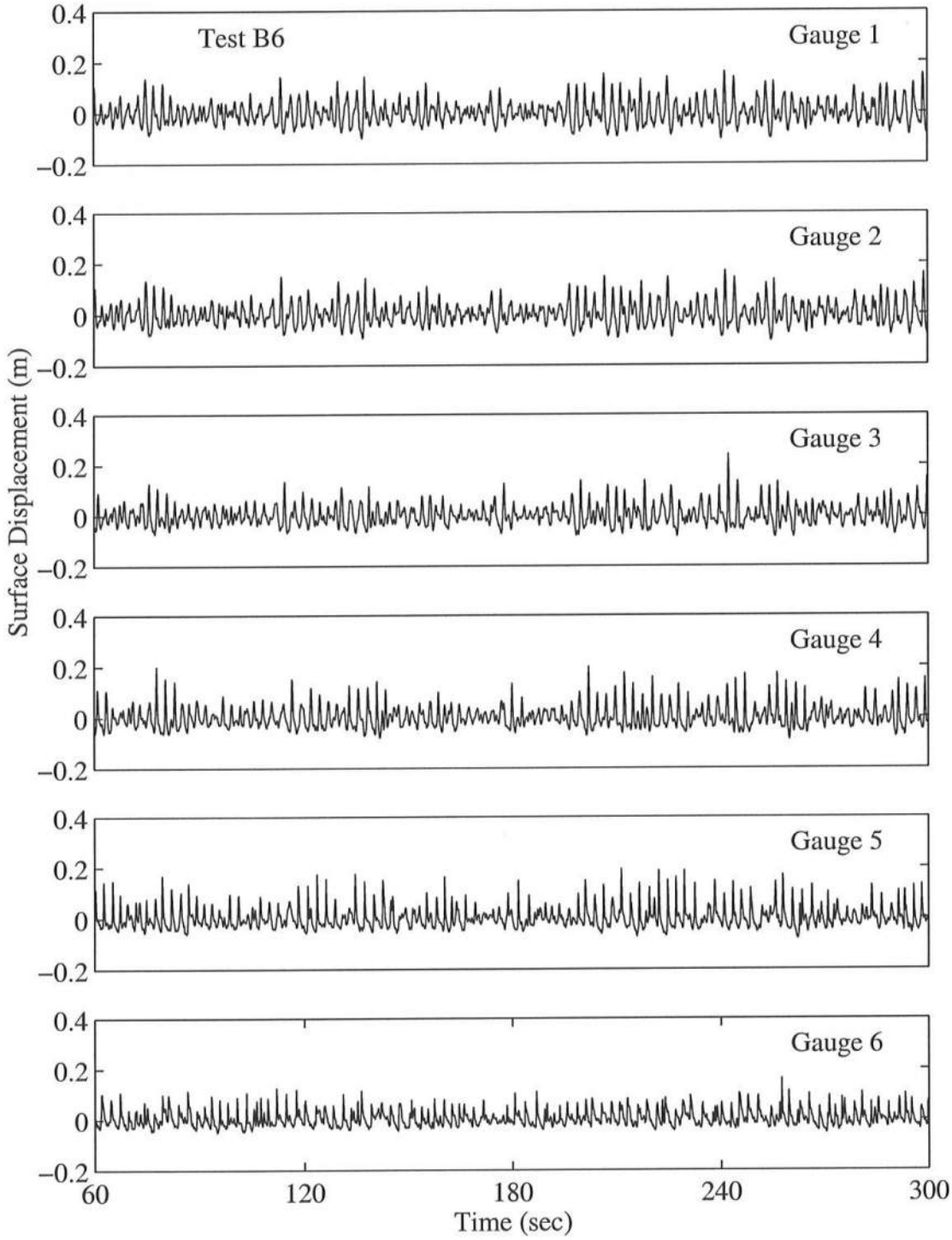

Figure A.21: Time Series for $T_p = 2.4$ s, $d_t = 6$ cm, for Gauge 1 – Gauge 6.

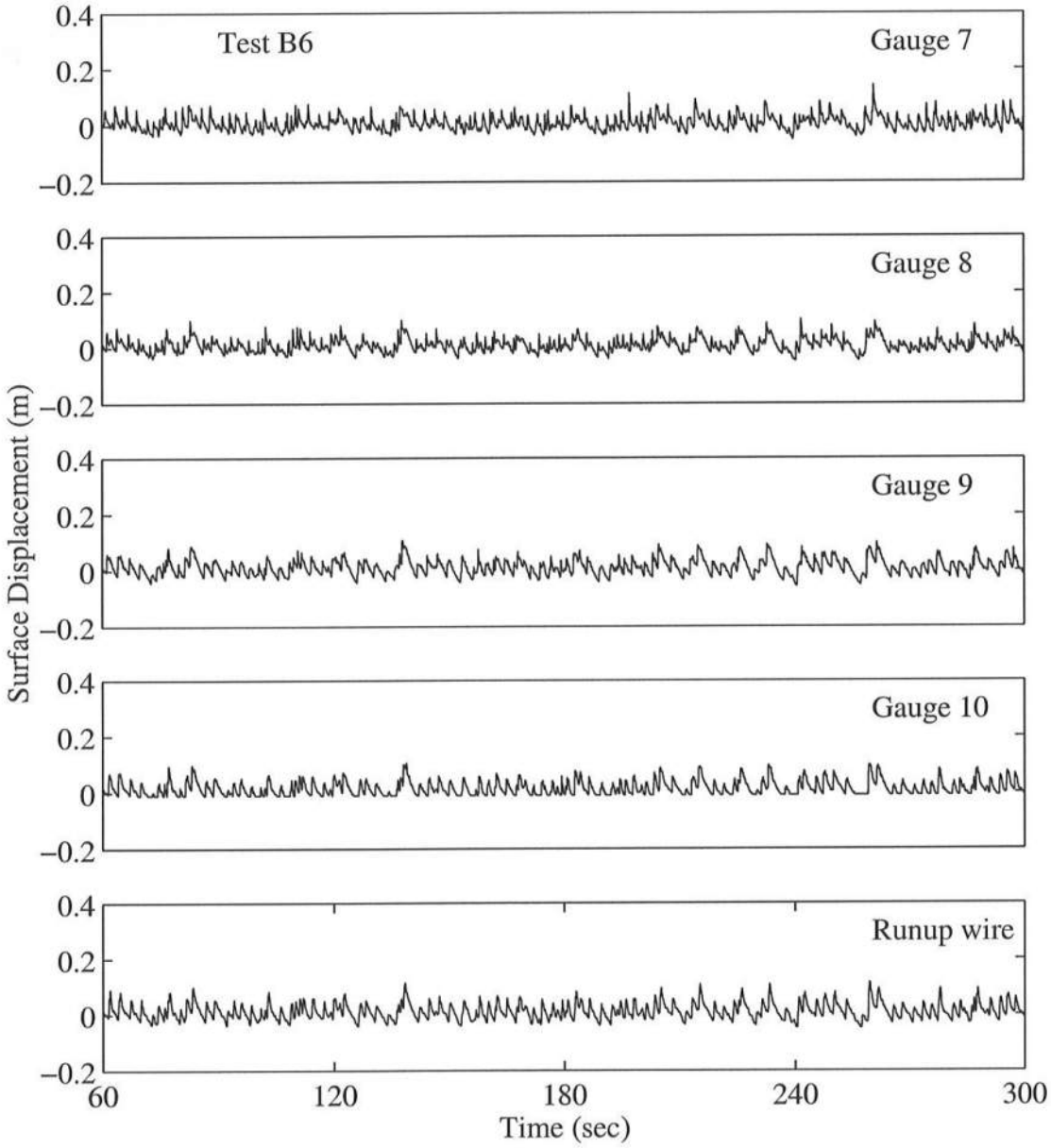

Figure A.22: Time Series for $T_p = 2.4$ s, $d_t = 6$ cm, for Gauge 7 – Runup Wire.

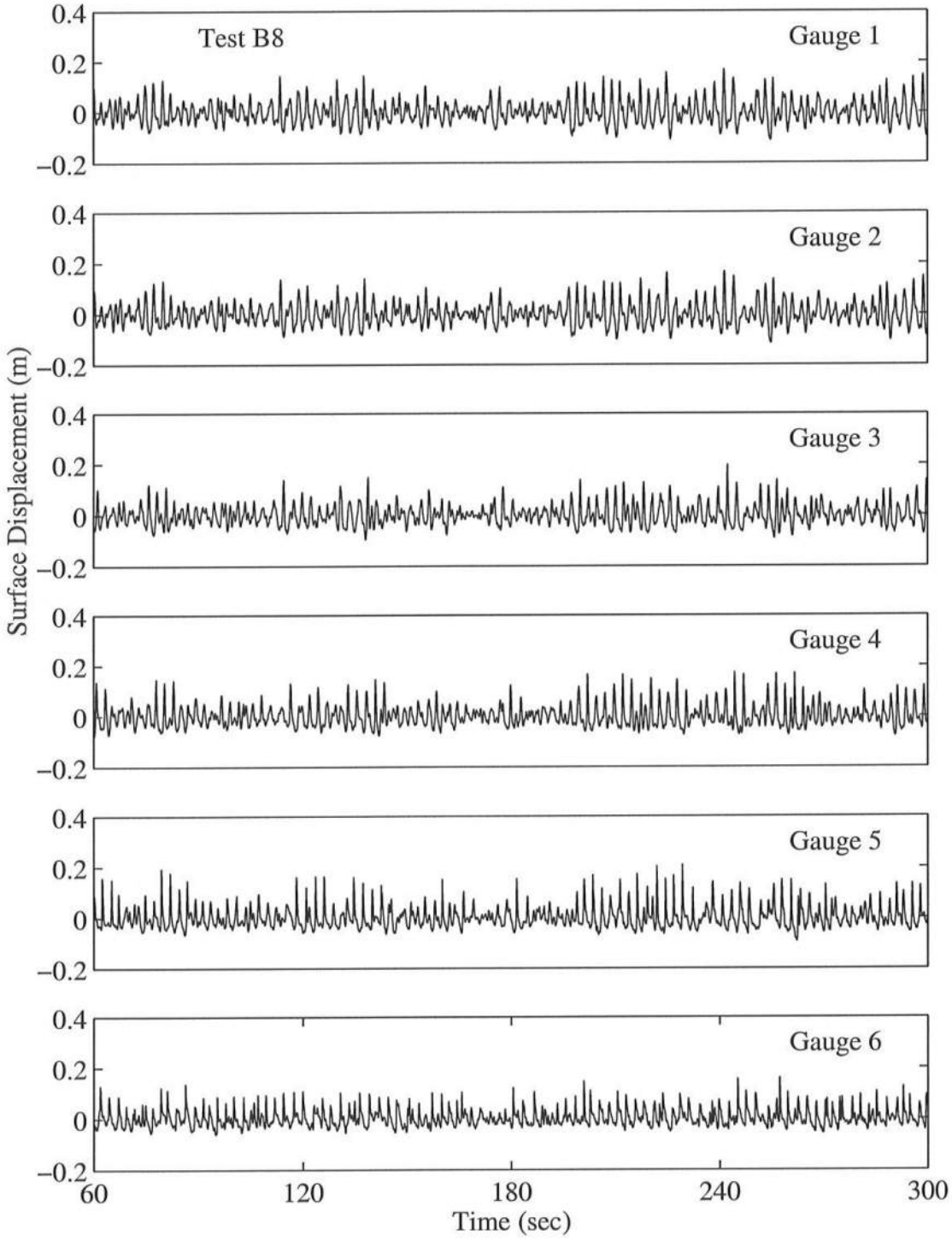

Figure A.23: Time Series for $T_p = 2.4$ s, $d_t = 8$ cm, for Gauge 1 – Gauge 6.

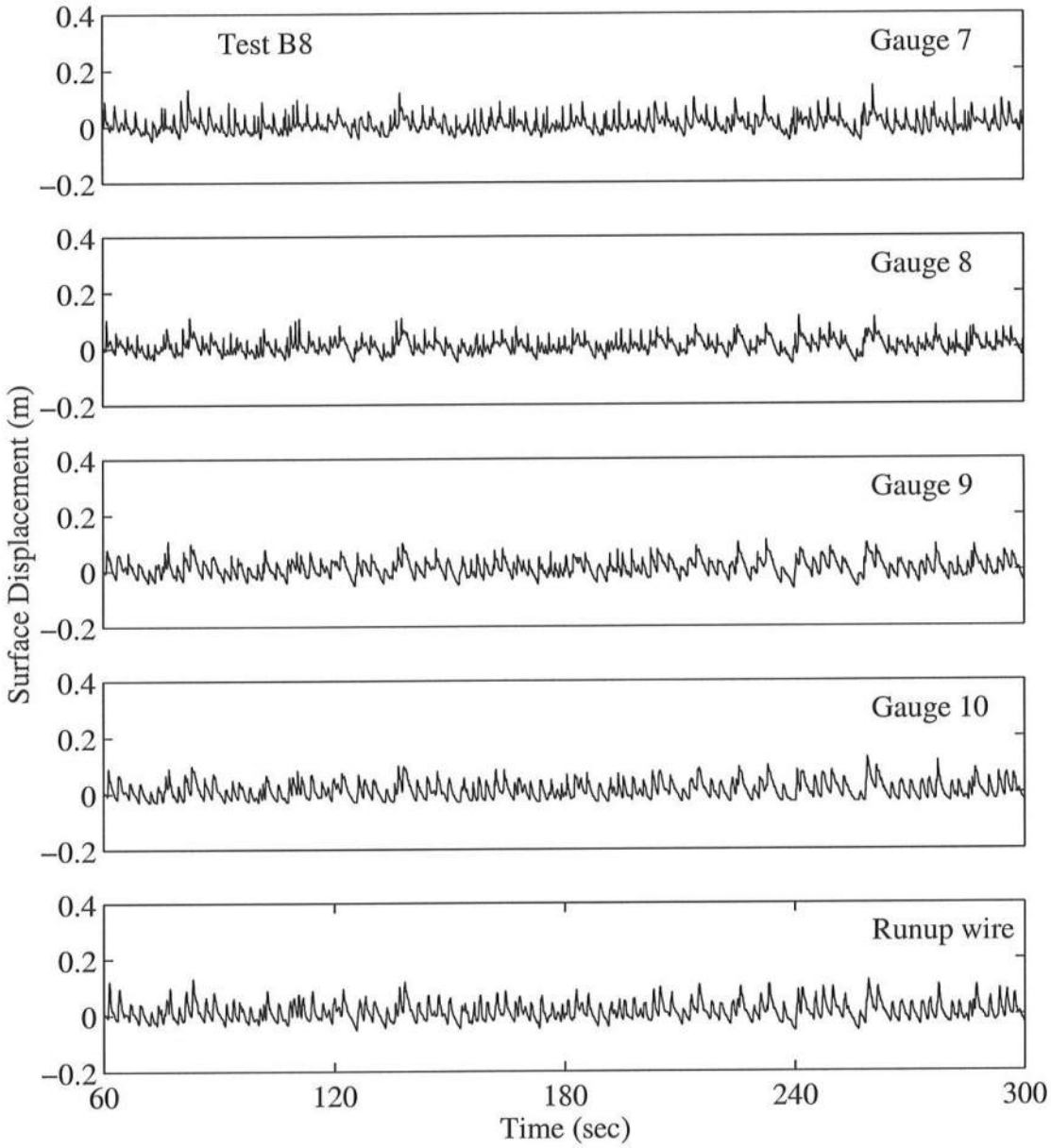

Figure A.24: Time Series for $T_p = 2.4$ s, $d_t = 8$ cm, for Gauge 7 – Runup Wire.

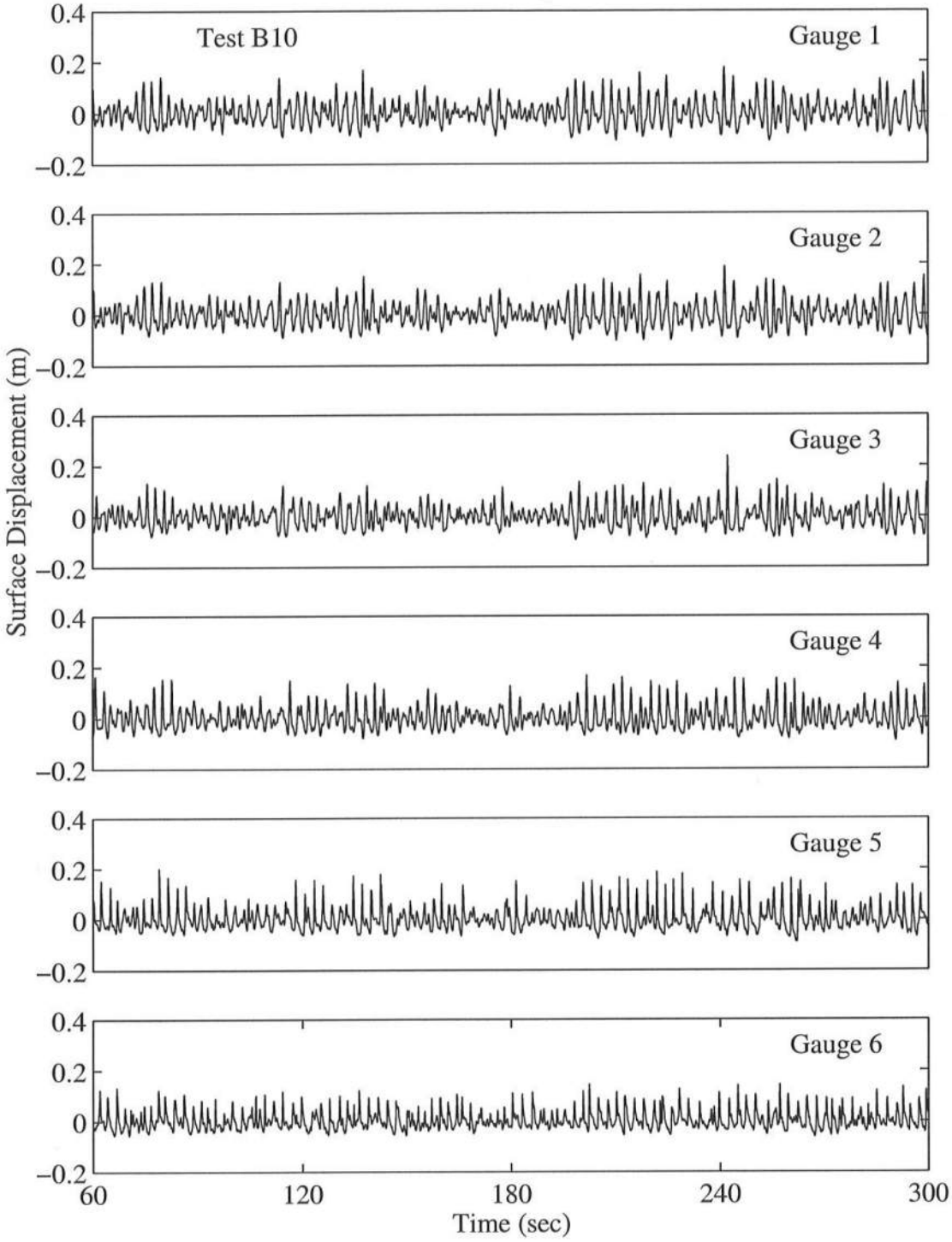

Figure A.25: Time Series for $T_p = 2.4$ s, $d_t = 10$ cm, for Gauge 1 – Gauge 6.

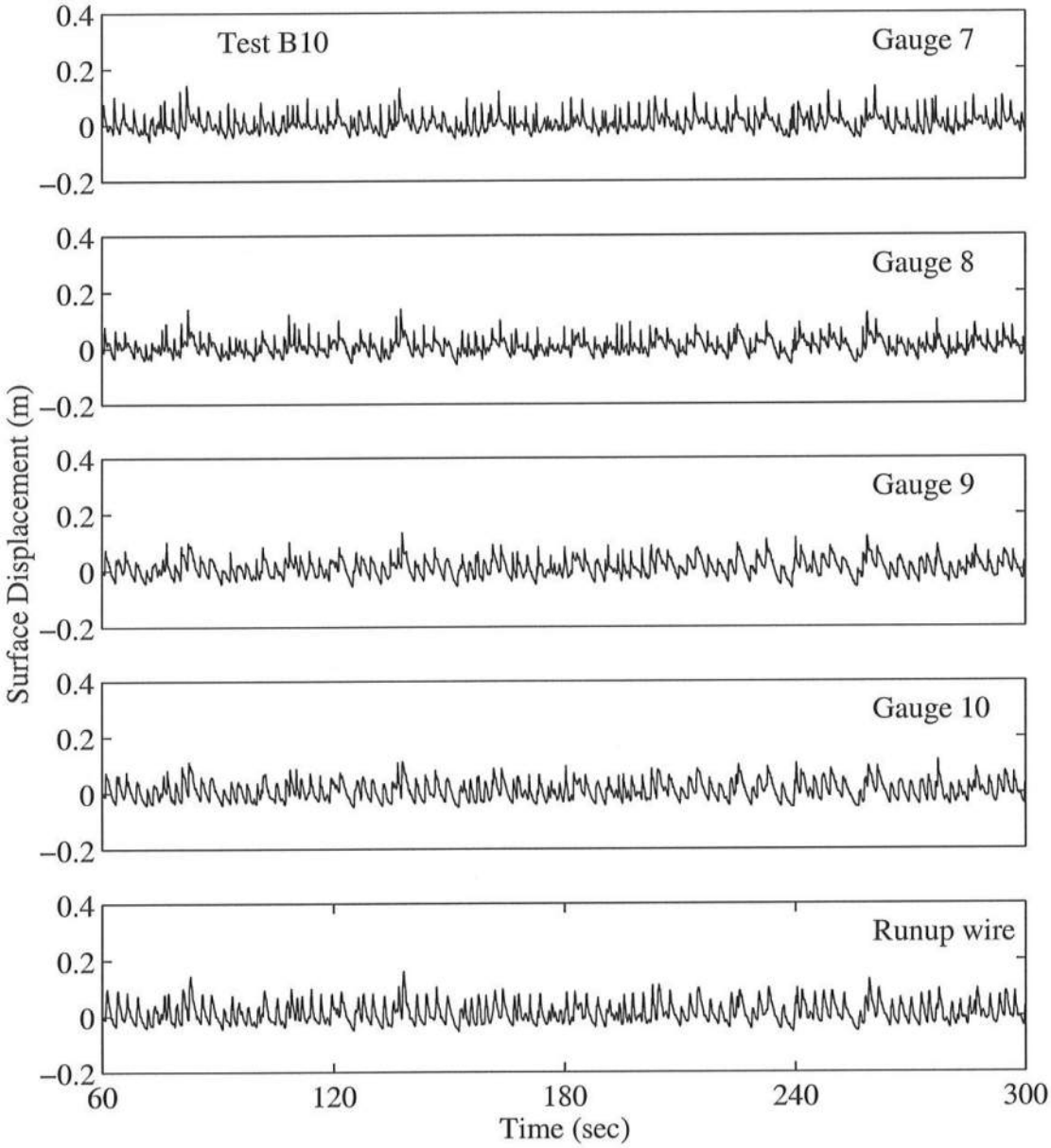

Figure A.26: Time Series for T_p = 2.4 s, d_t = 10 cm, for Gauge 7 – Runup Wire.

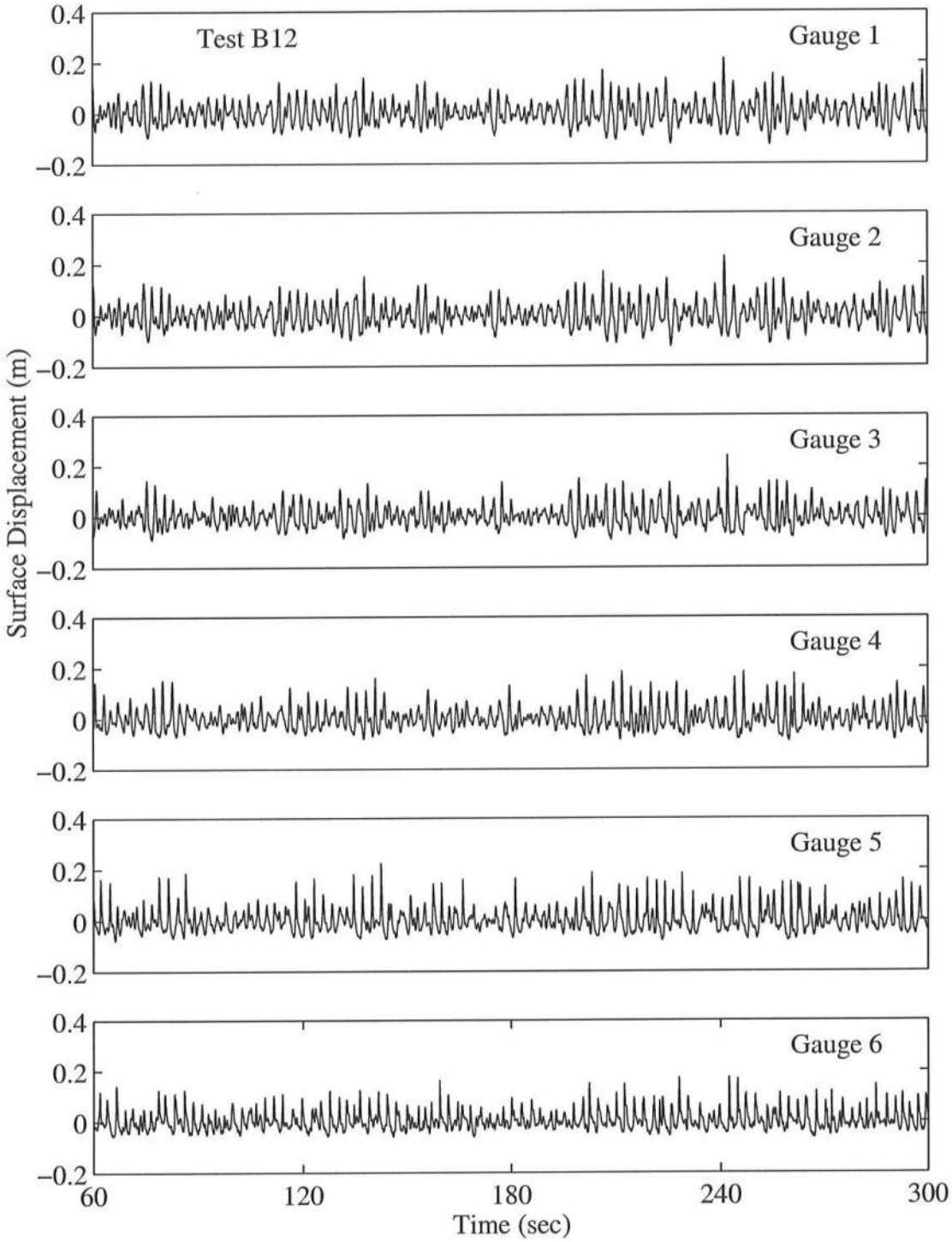

Figure A.27: Time Series for $T_p = 2.4$ s, $d_t = 12$ cm, for Gauge 1 – Gauge 6.

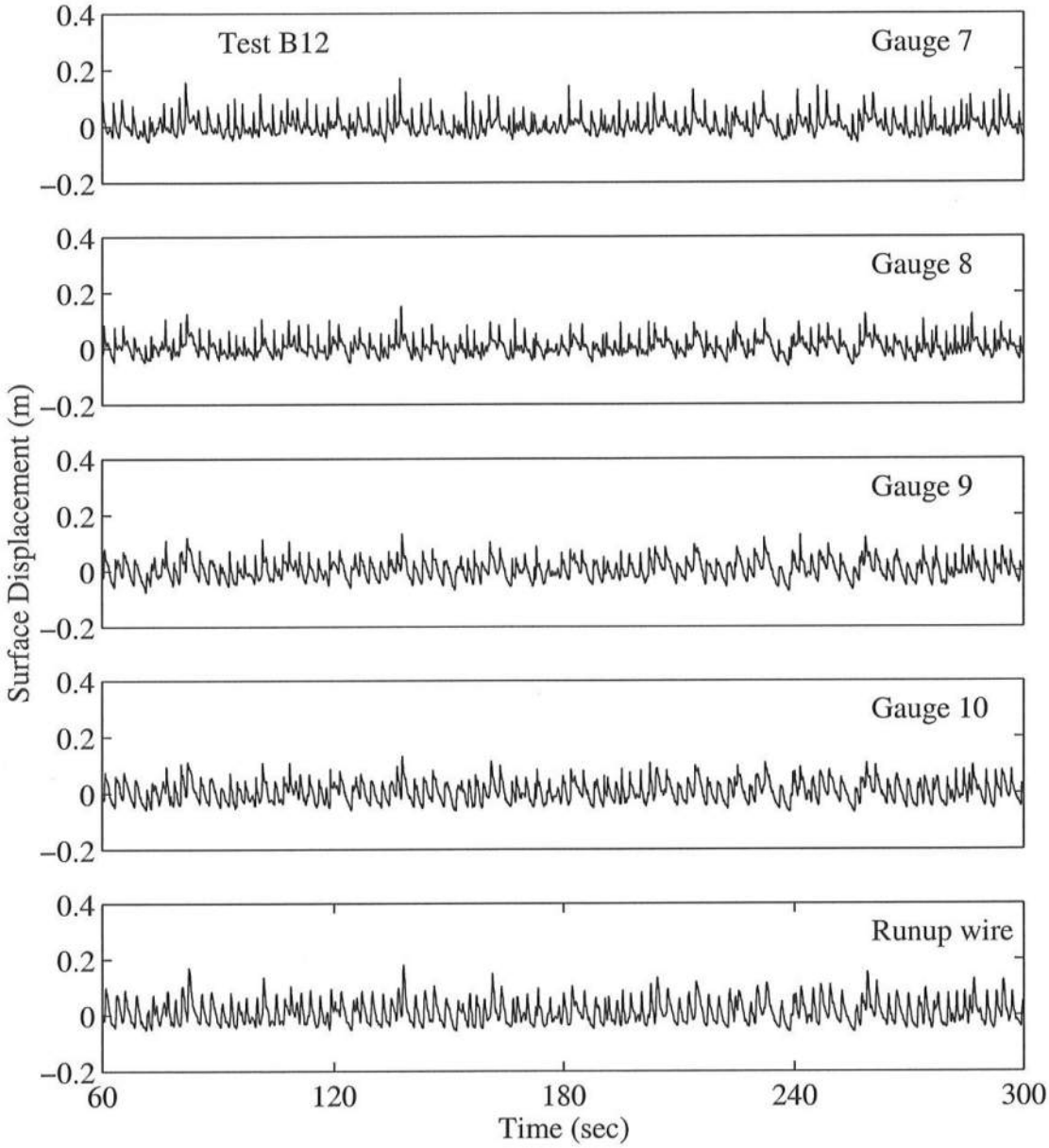

Figure A.28: Time Series for $T_p = 2.4$ s, $d_t = 12$ cm, for Gauge 7 – Runup Wire.

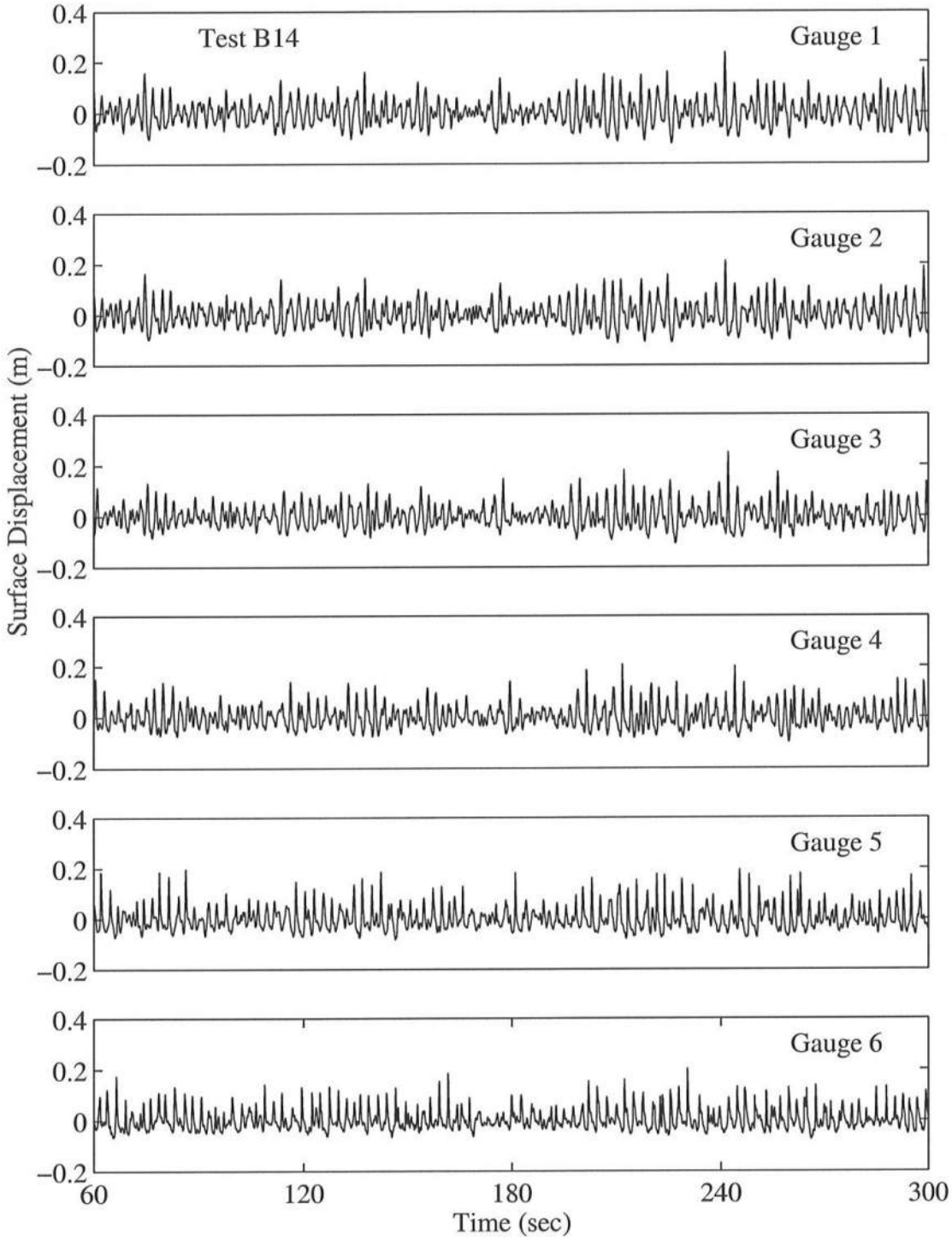

Figure A.29: Time Series for $T_p = 2.4$ s, $d_t = 14$ cm, for Gauge 1 – Gauge 6.

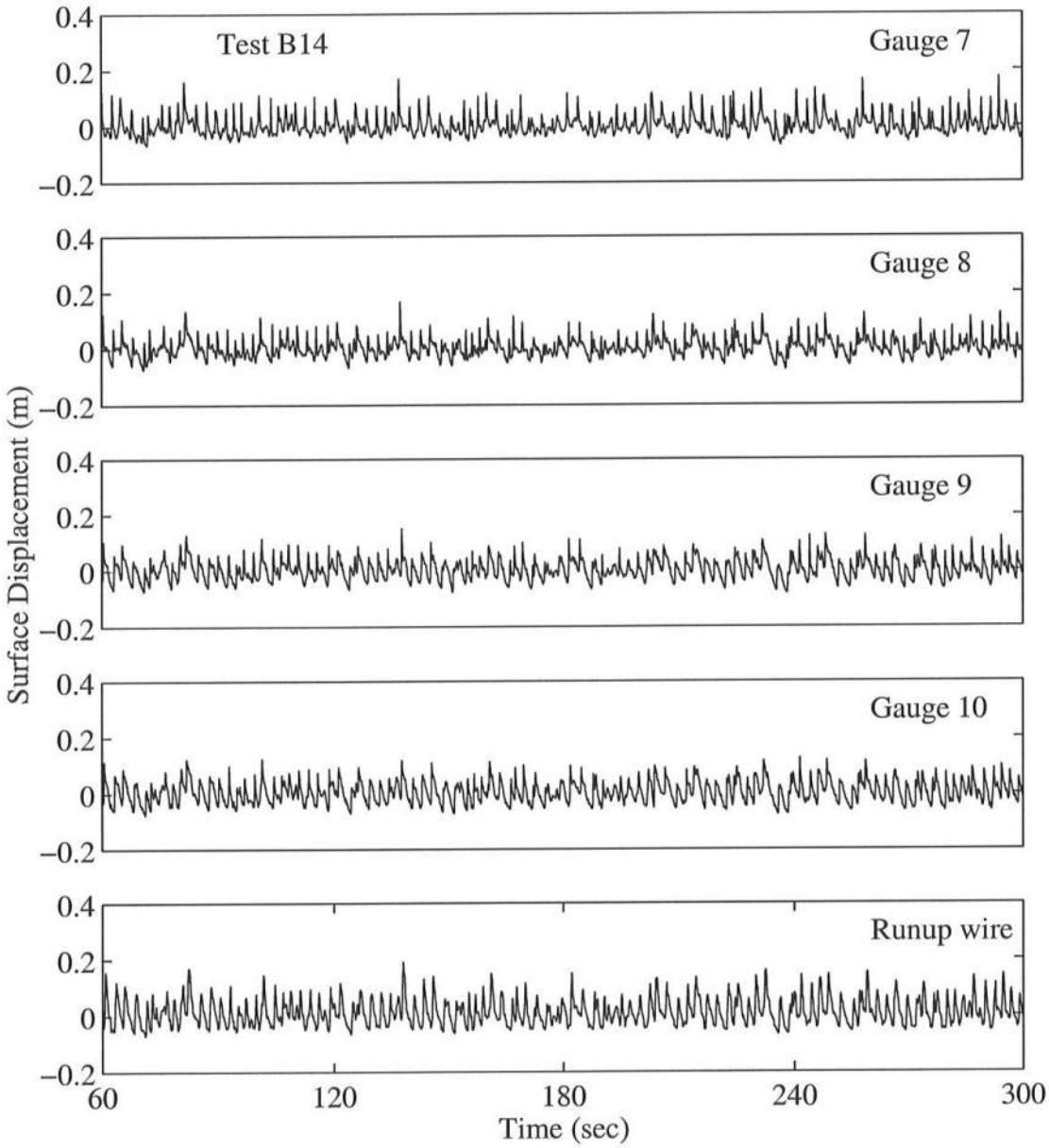

Figure A.30: Time Series for $T_p = 2.4$ s, $d_t = 14$ cm, for Gauge 7 – Runup Wire.

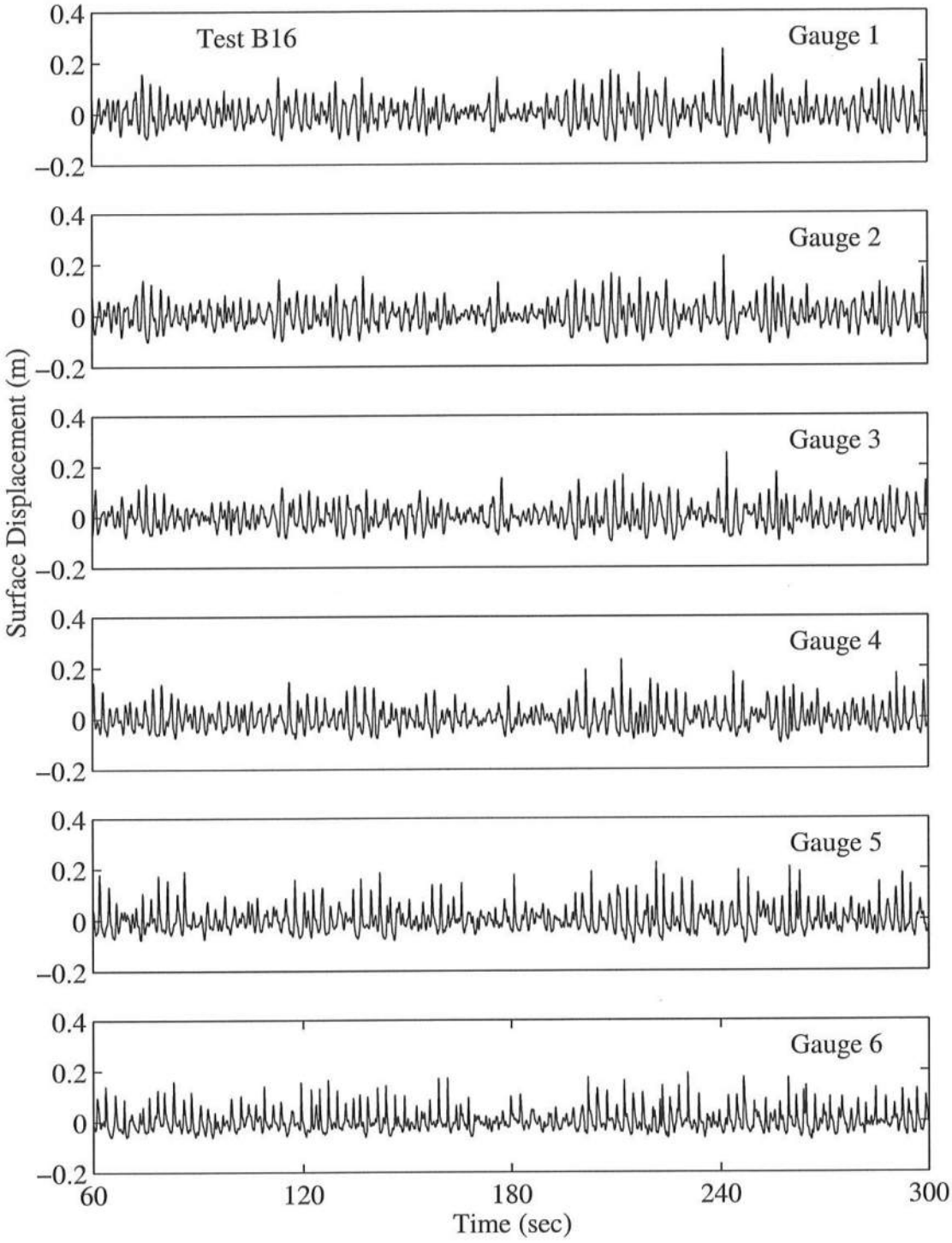

Figure A.31: Time Series for T_p = 2.4 s, d_t =16 cm, for Gauge 1 – Gauge 6.

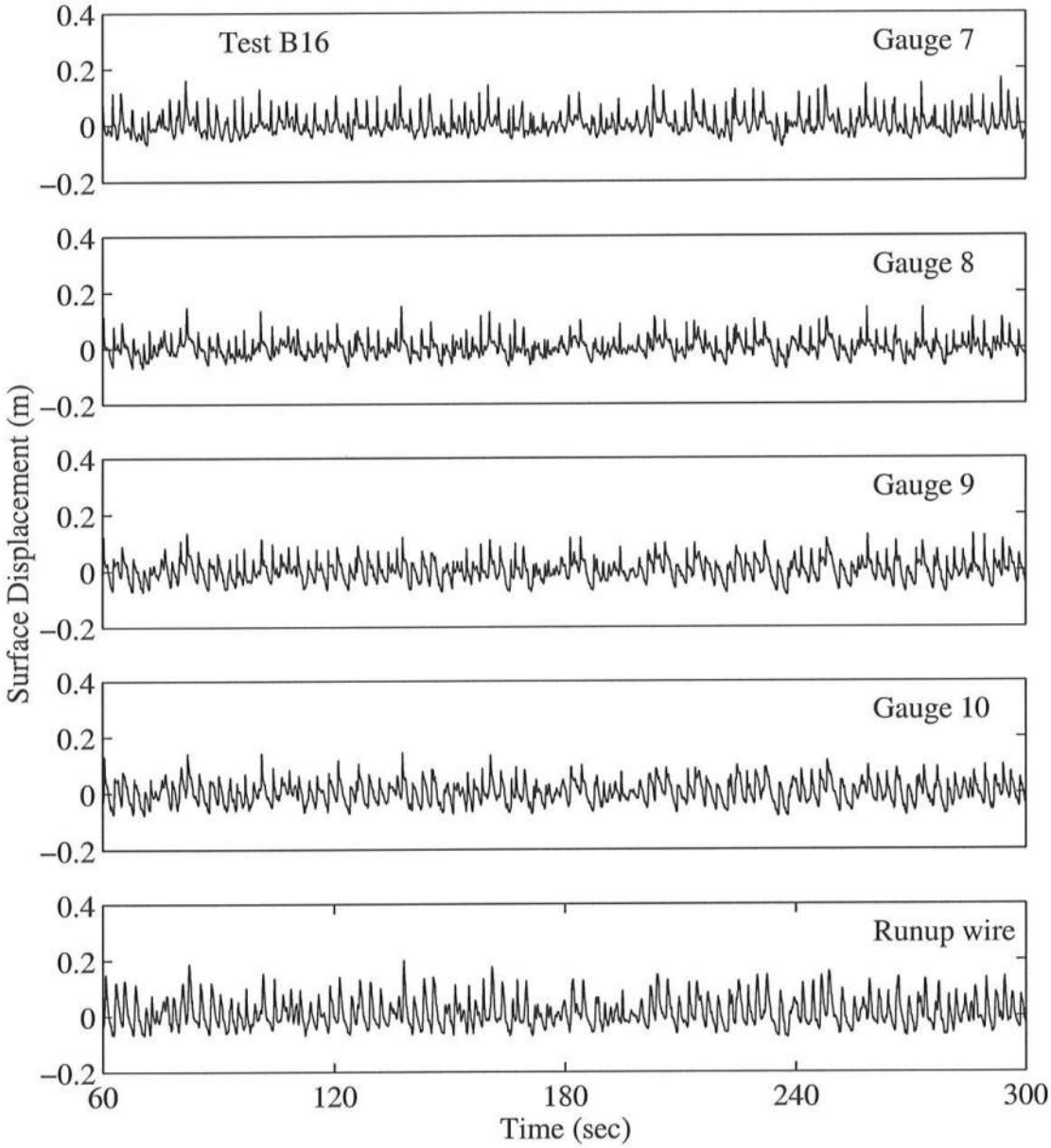

Figure A.32: Time Series for T_p = 2.4 s, d_t =16 cm, for Gauge 7 – Runup Wire.

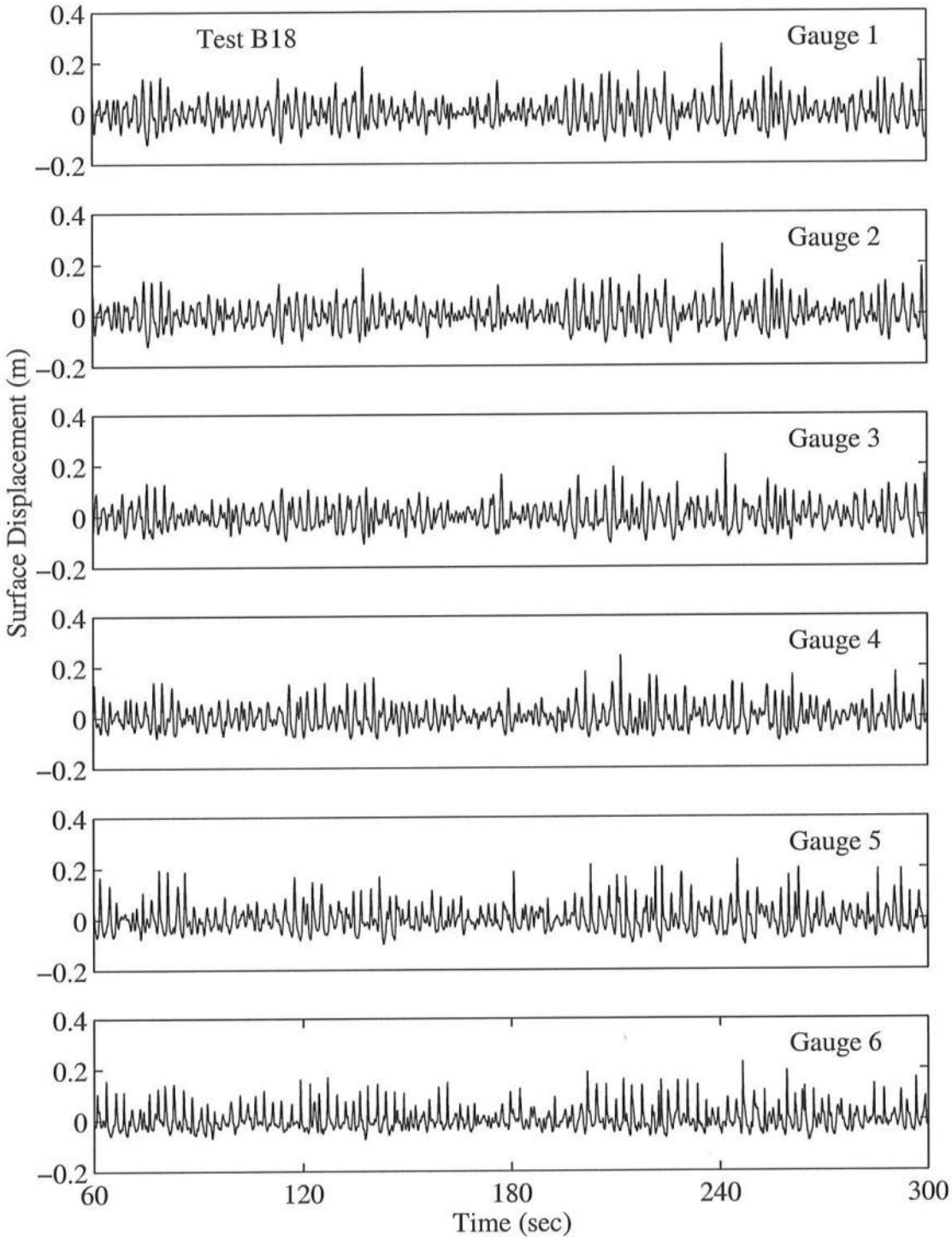

Figure A.33: Time Series for T_p = 2.4 s, d_t =18 cm, for Gauge 1 – Gauge 6.

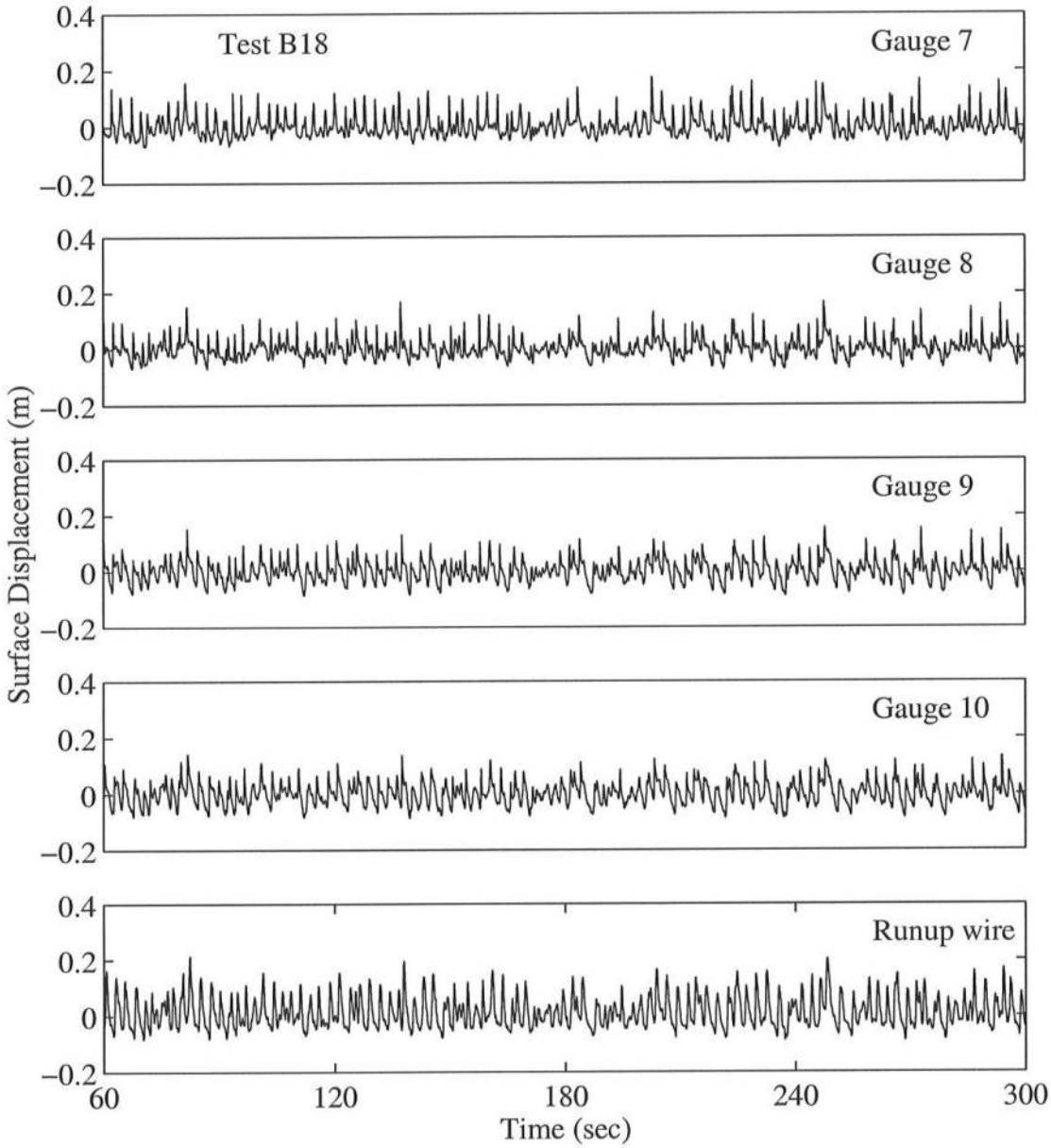

Figure A.34: Time Series for $T_p = 2.4$ s, $d_t = 18$ cm, for Gauge 7 – Runup Wire.

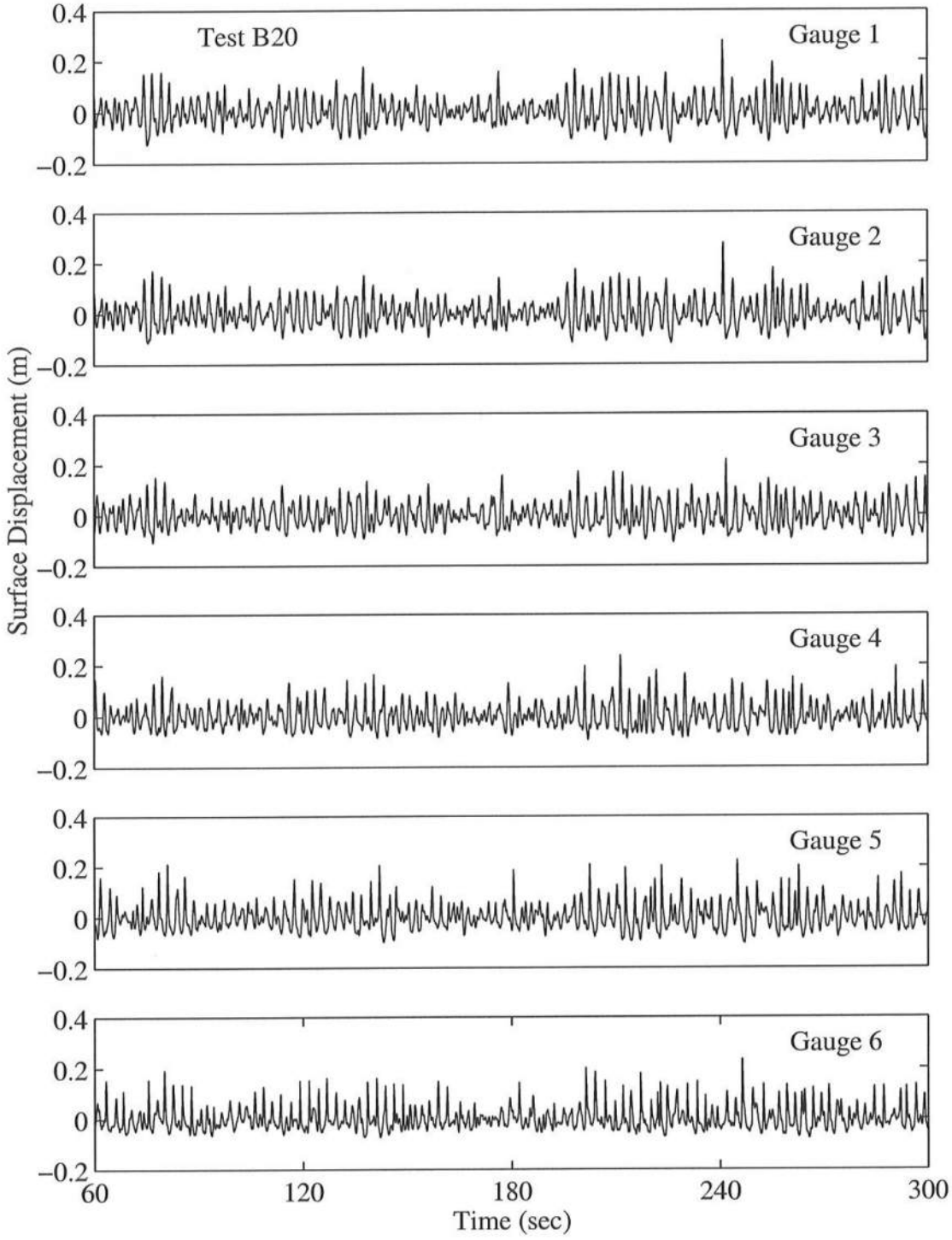

Figure A.35: Time Series for $T_p = 2.4$ s, $d_t = 20$ cm, for Gauge 1 – Gauge 6.

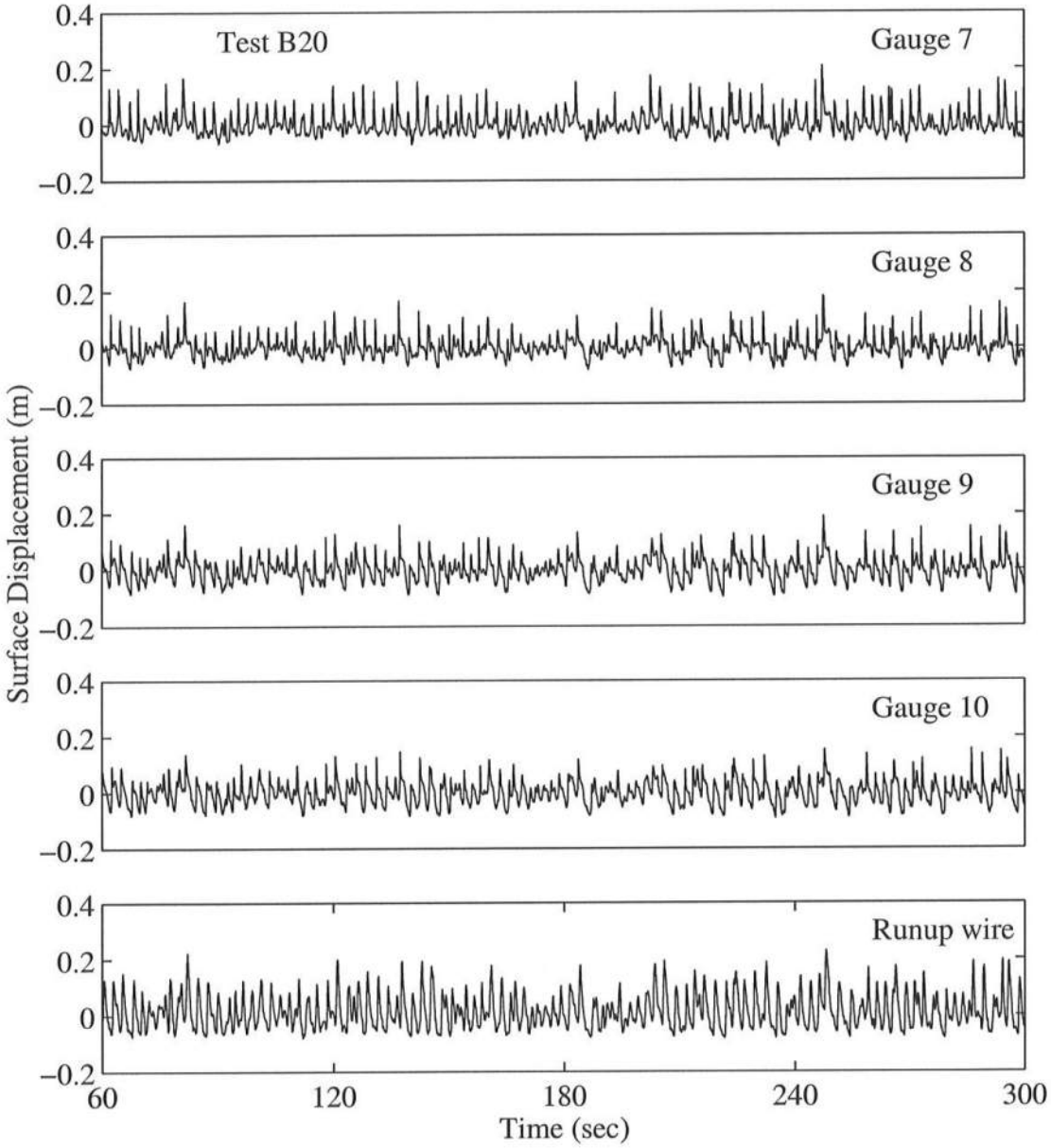

Figure A.36: Time Series for $T_p = 2.4$ s, $d_t = 20$ cm, for Gauge 7 – Runup Wire.

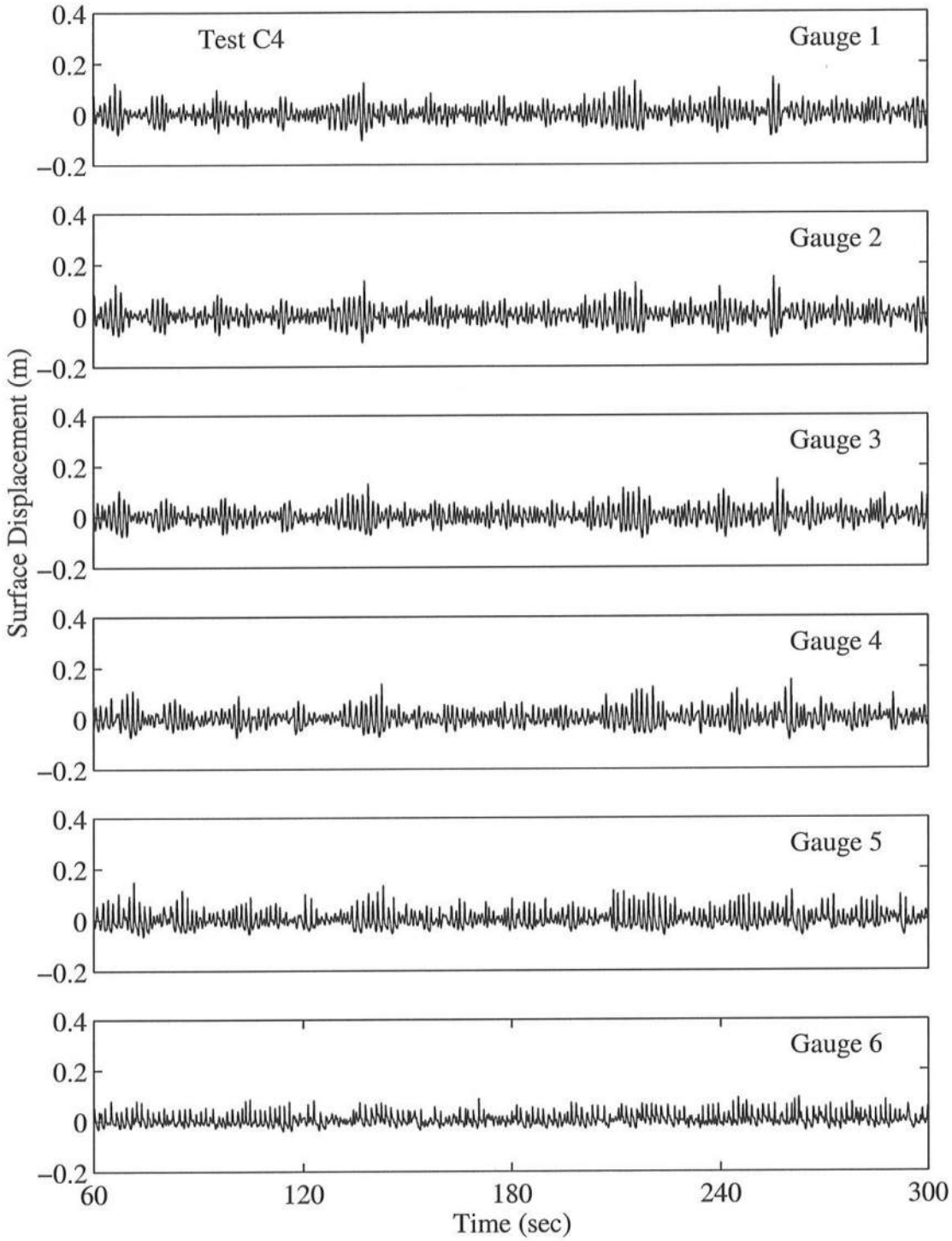

Figure A.37: Time Series for T_p = 1.5 s, d_t =4 cm, for Gauge 1 – Gauge 6.

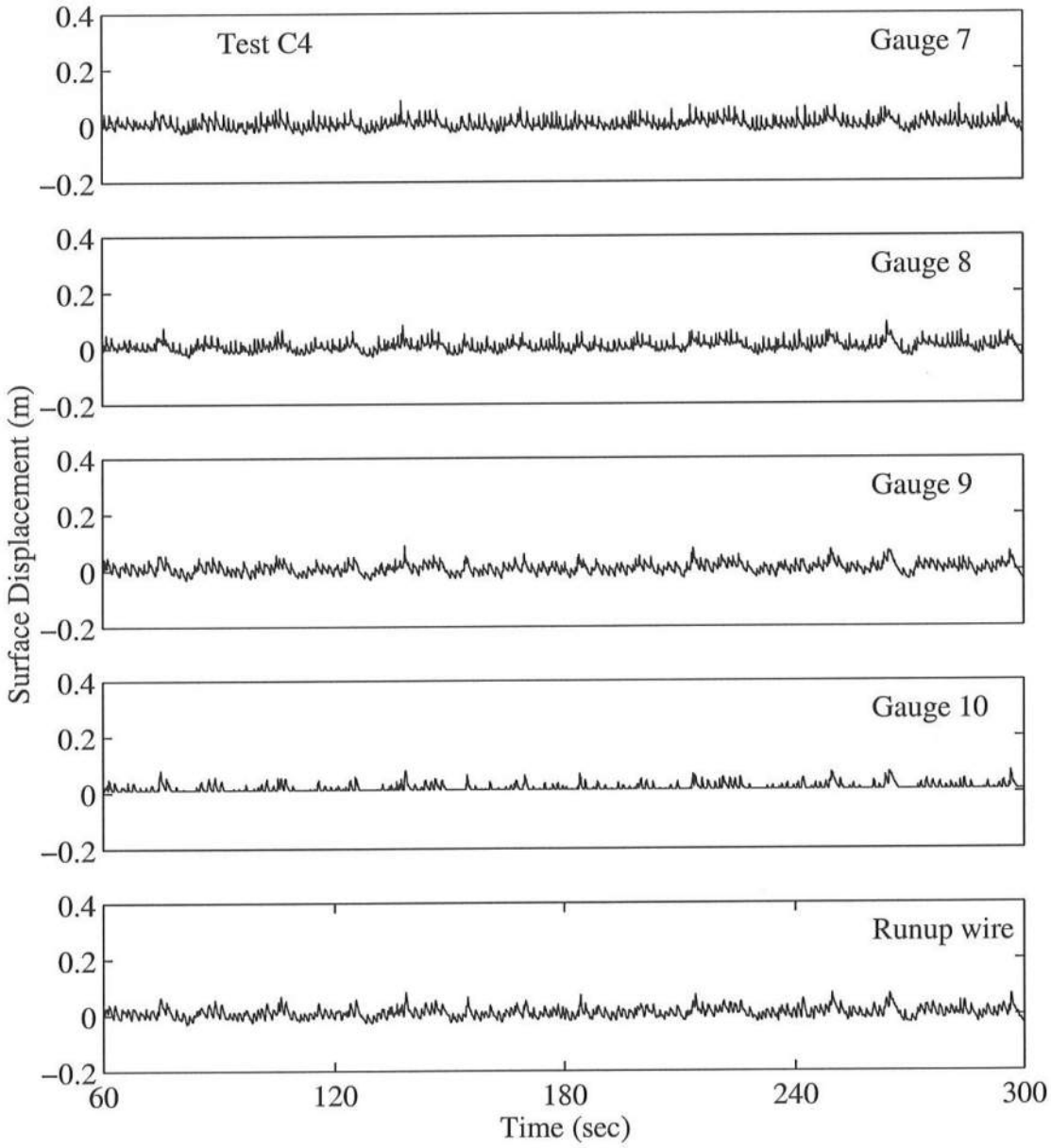

Figure A.38: Time Series for $T_p = 1.5$ s, $d_t = 4$ cm, for Gauge 7 – Runup Wire.

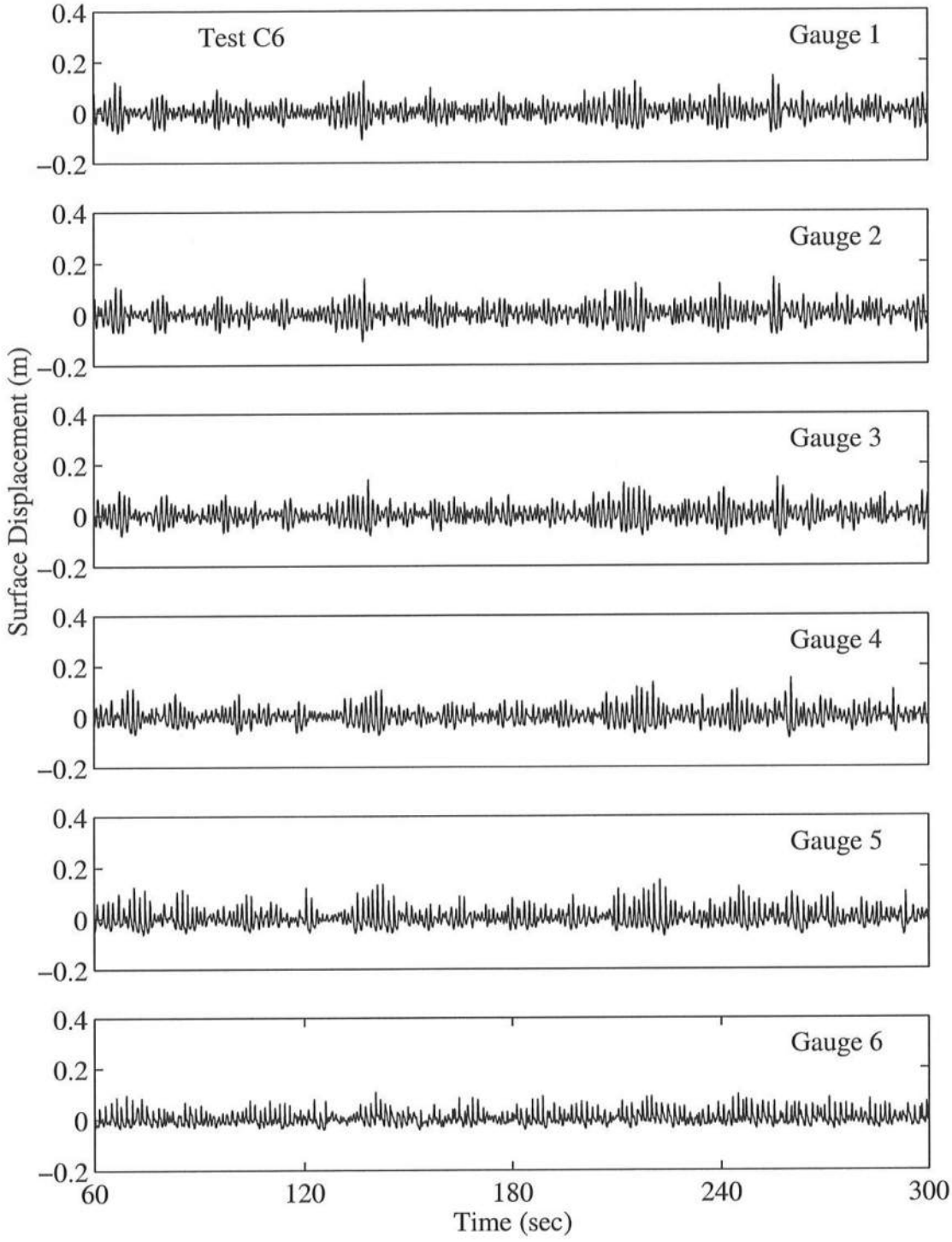

Figure A.39: Time Series for T_p = 1.5 s, d_t = 6 cm, for Gauge 1 – Gauge 6.

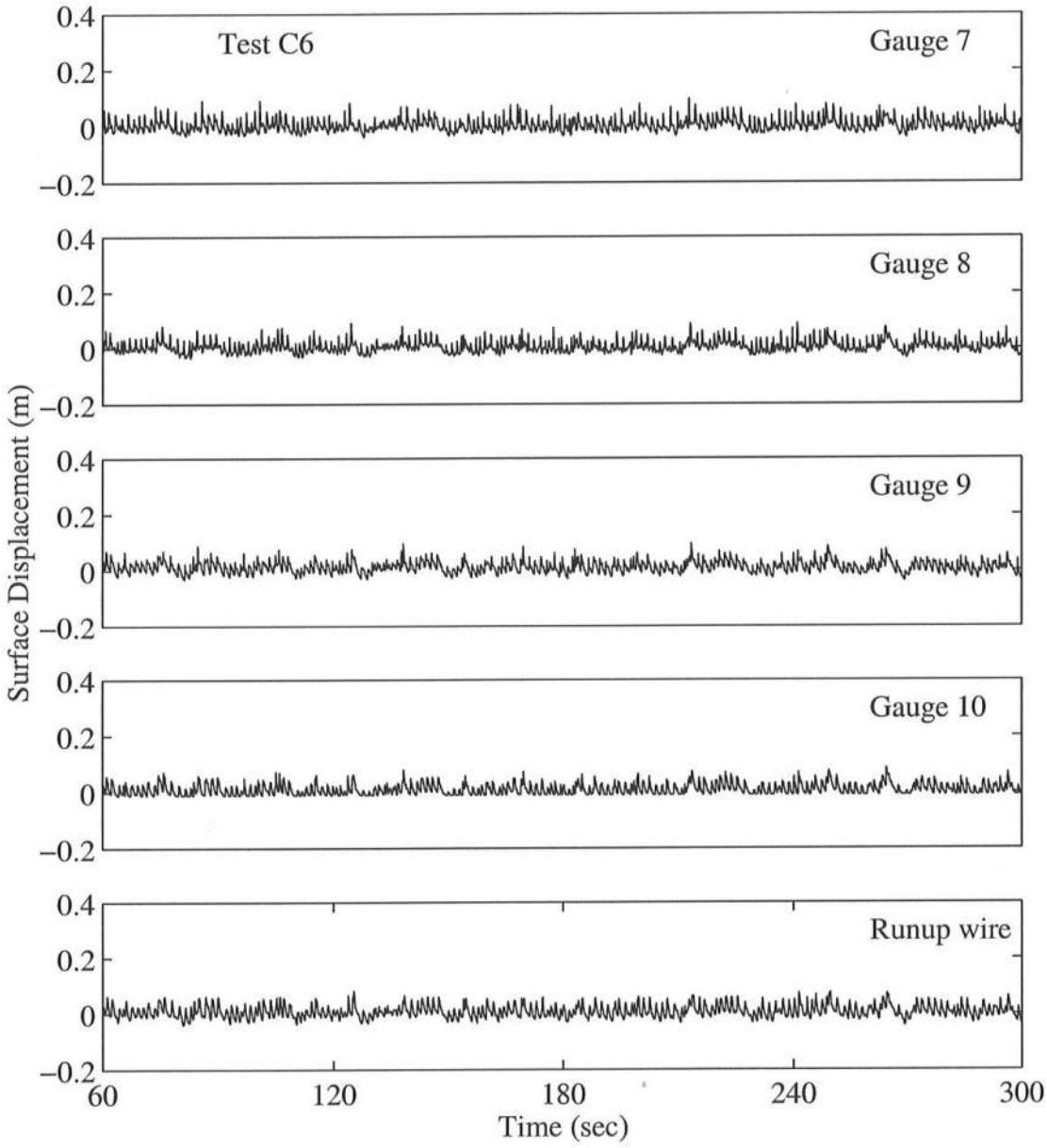

Figure A.40: Time Series for T_p = 1.5 s, d_t = 6 cm, for Gauge 7 – Runup Wire.

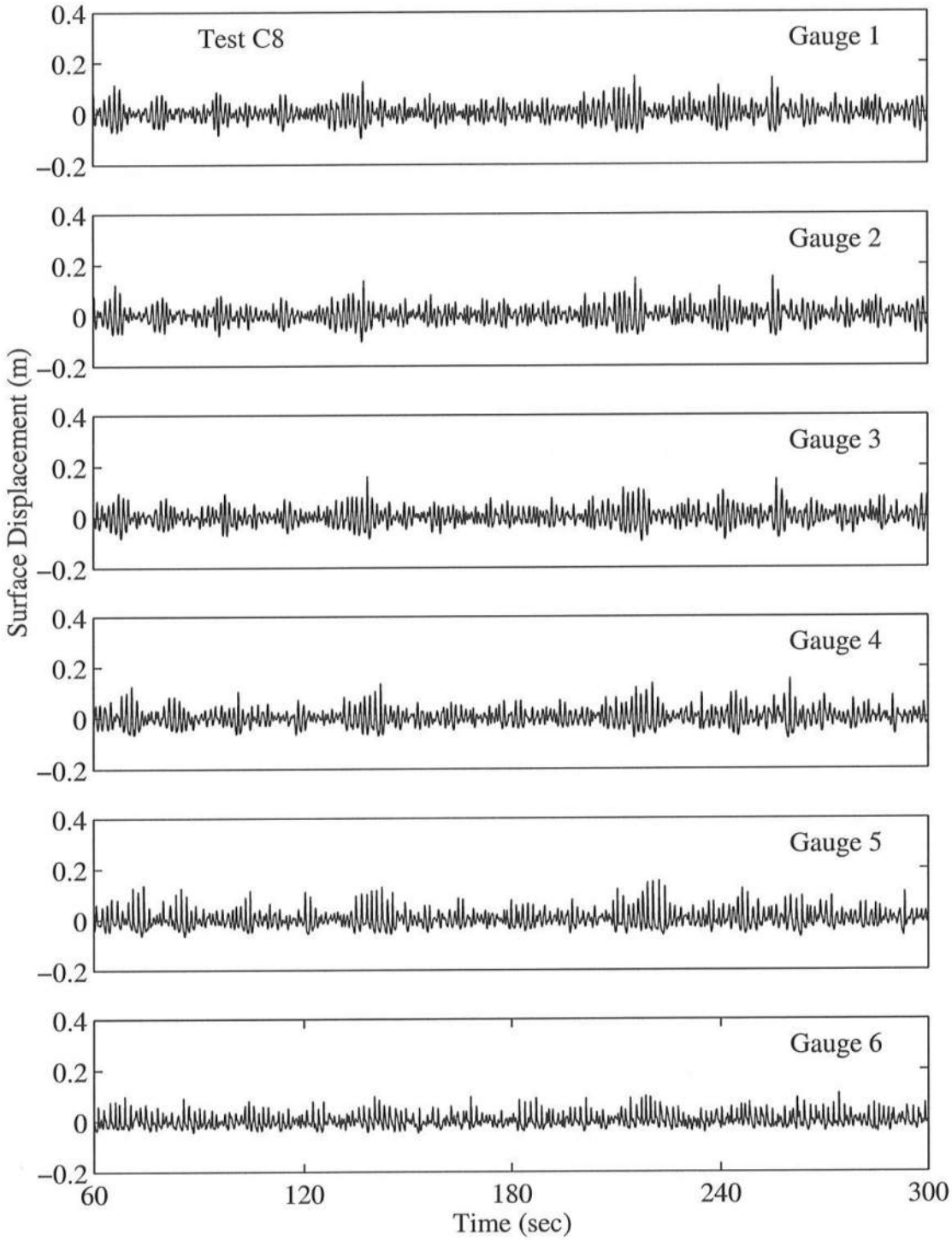

Figure A.41: Time Series for $T_p = 1.5$ s, $d_t = 8$ cm, for Gauge 1 – Gauge 6.

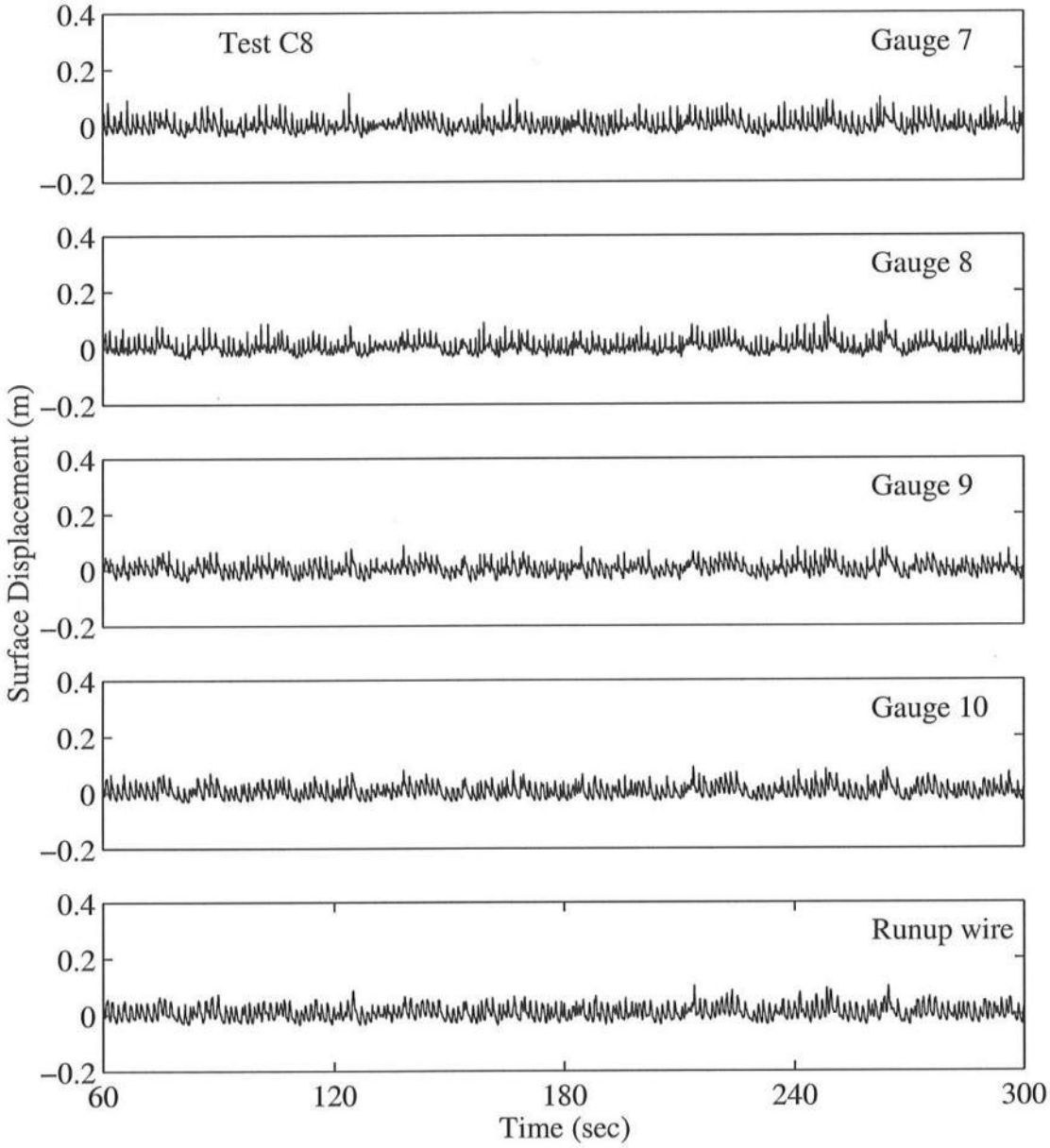

Figure A.42: Time Series for $T_p = 1.5$ s, $d_t = 8$ cm, for Gauge 7 – Runup Wire.

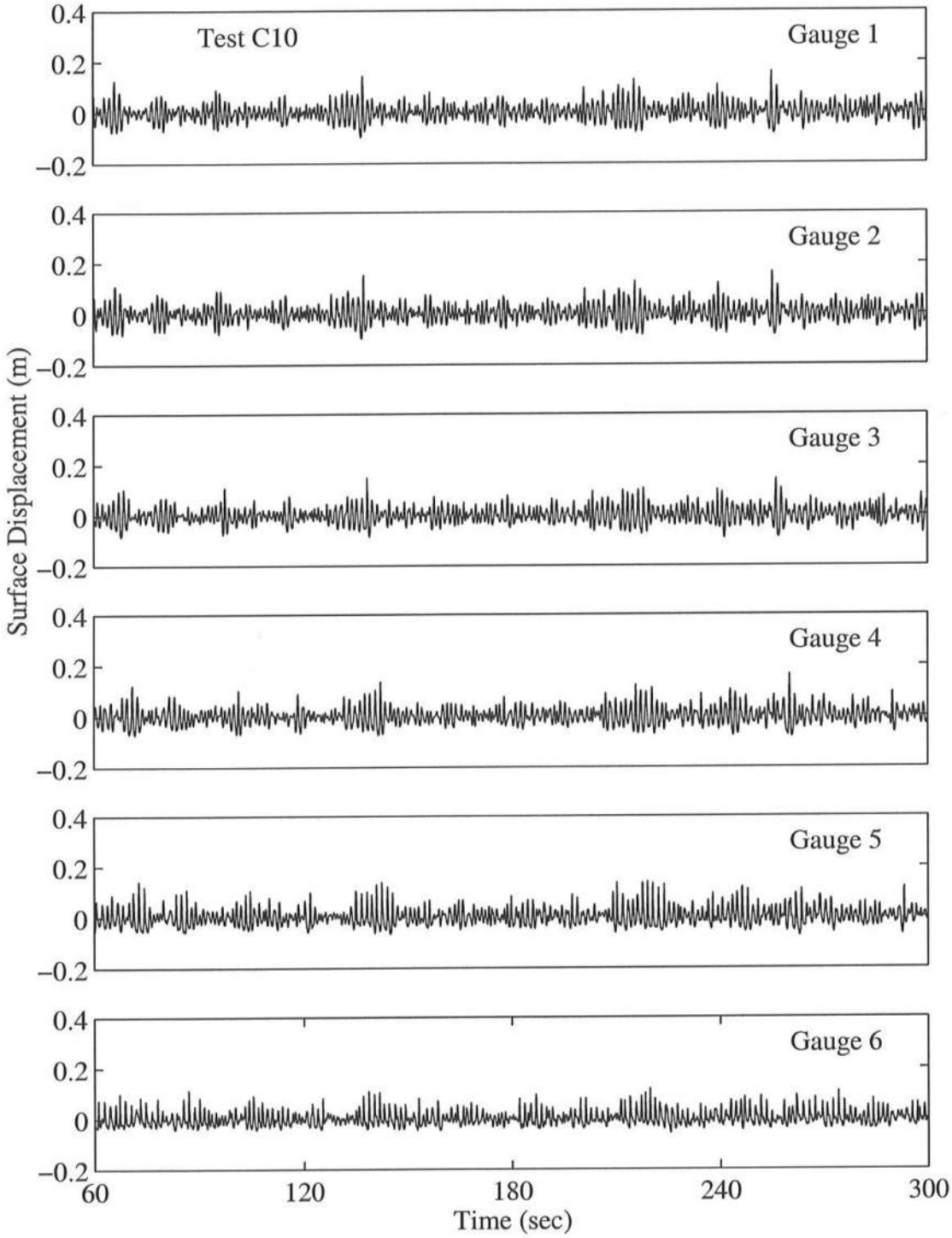

Figure A.43: Time Series for T_p = 1.5 s, d_t = 10 cm, for Gauge 1 – Gauge 6.

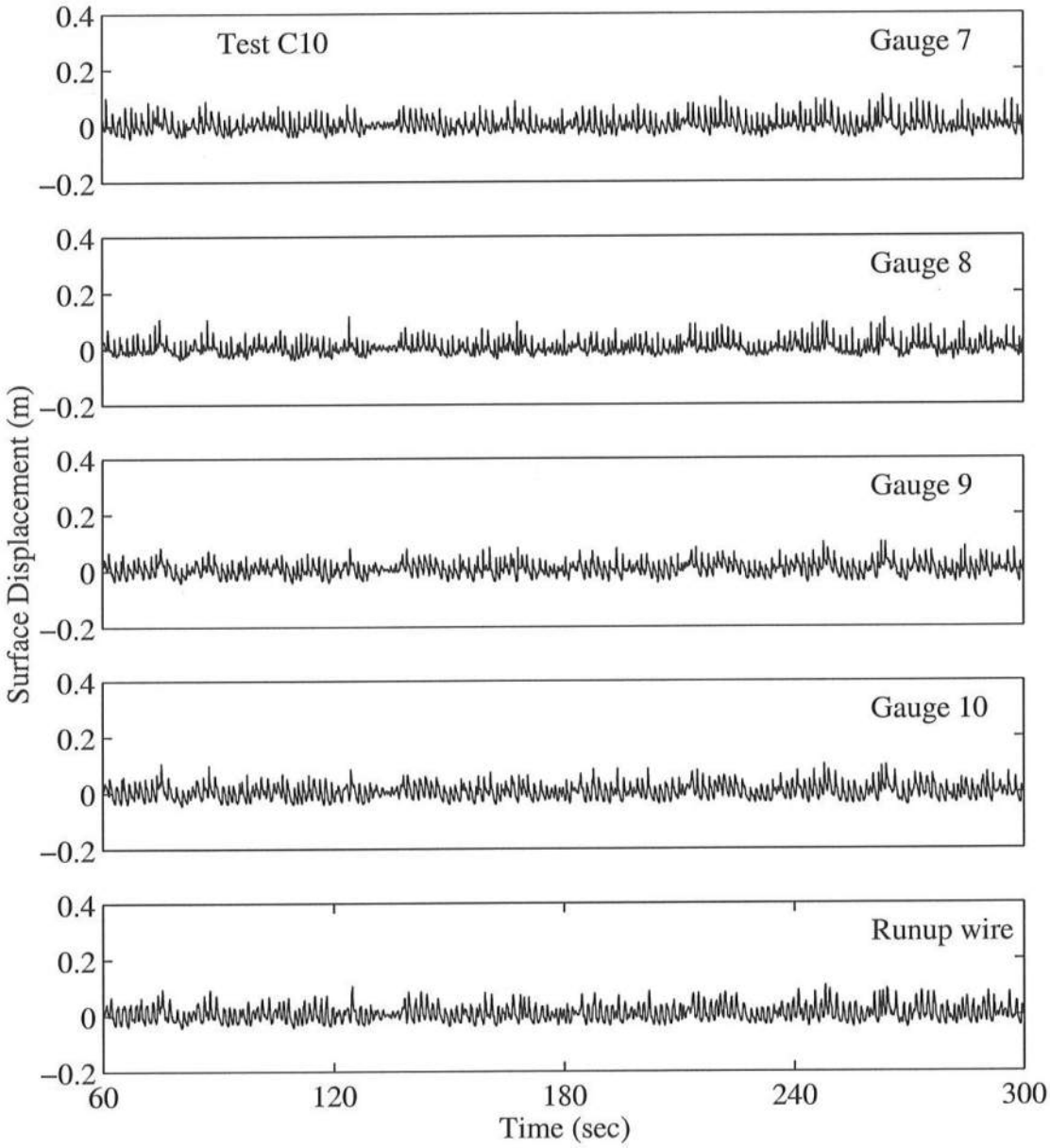

Figure A.44: Time Series for $T_p = 1.5$ s, $d_t = 10$ cm, for Gauge 7 – Runup Wire.

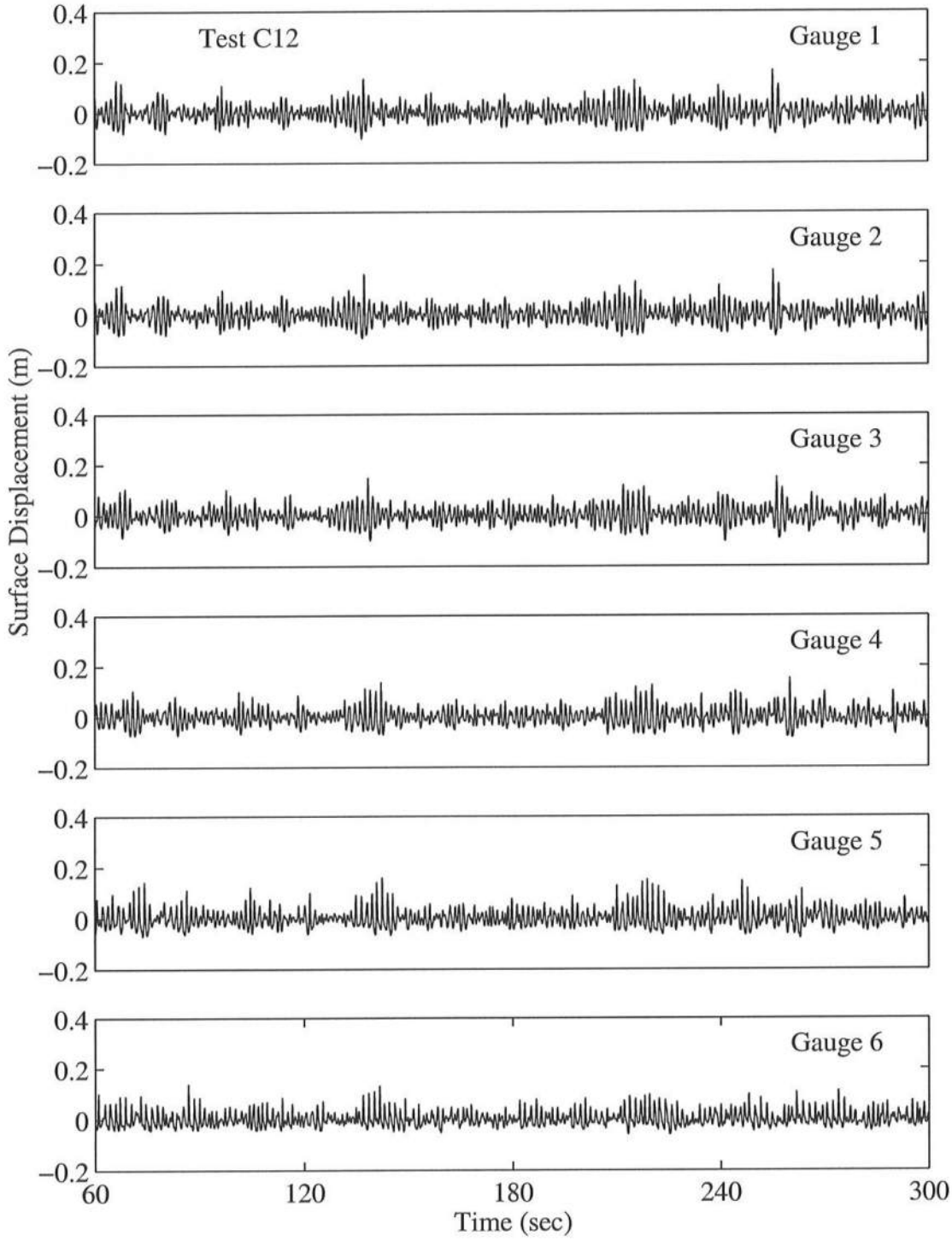

Figure A.45: Time Series for T_p = 1.5 s, d_t = 12 cm, for Gauge 1 – Gauge 6.

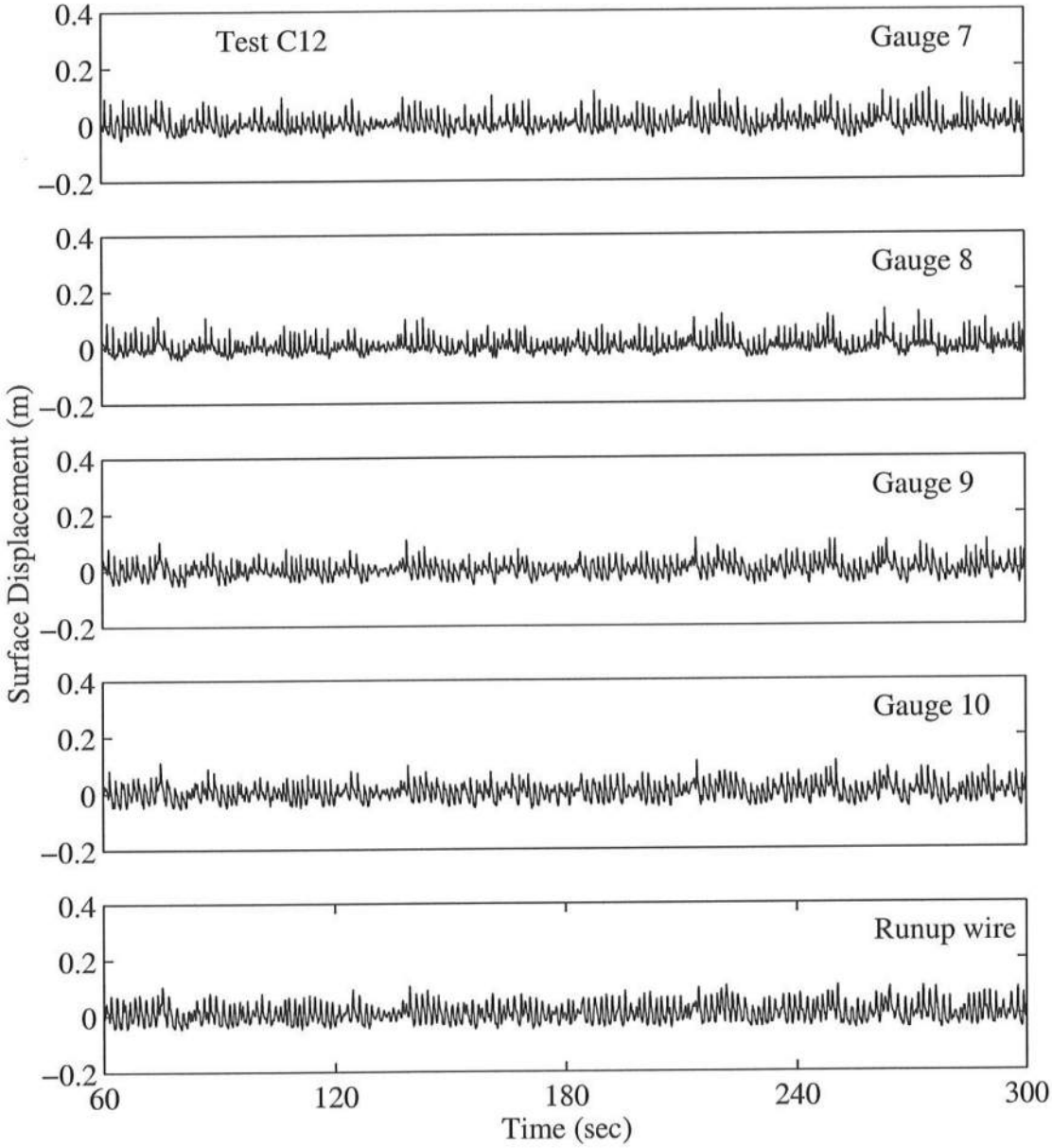

Figure A.46: Time Series for T_p = 1.5 s, d_t = 12 cm, for Gauge 7 – Runup Wire.

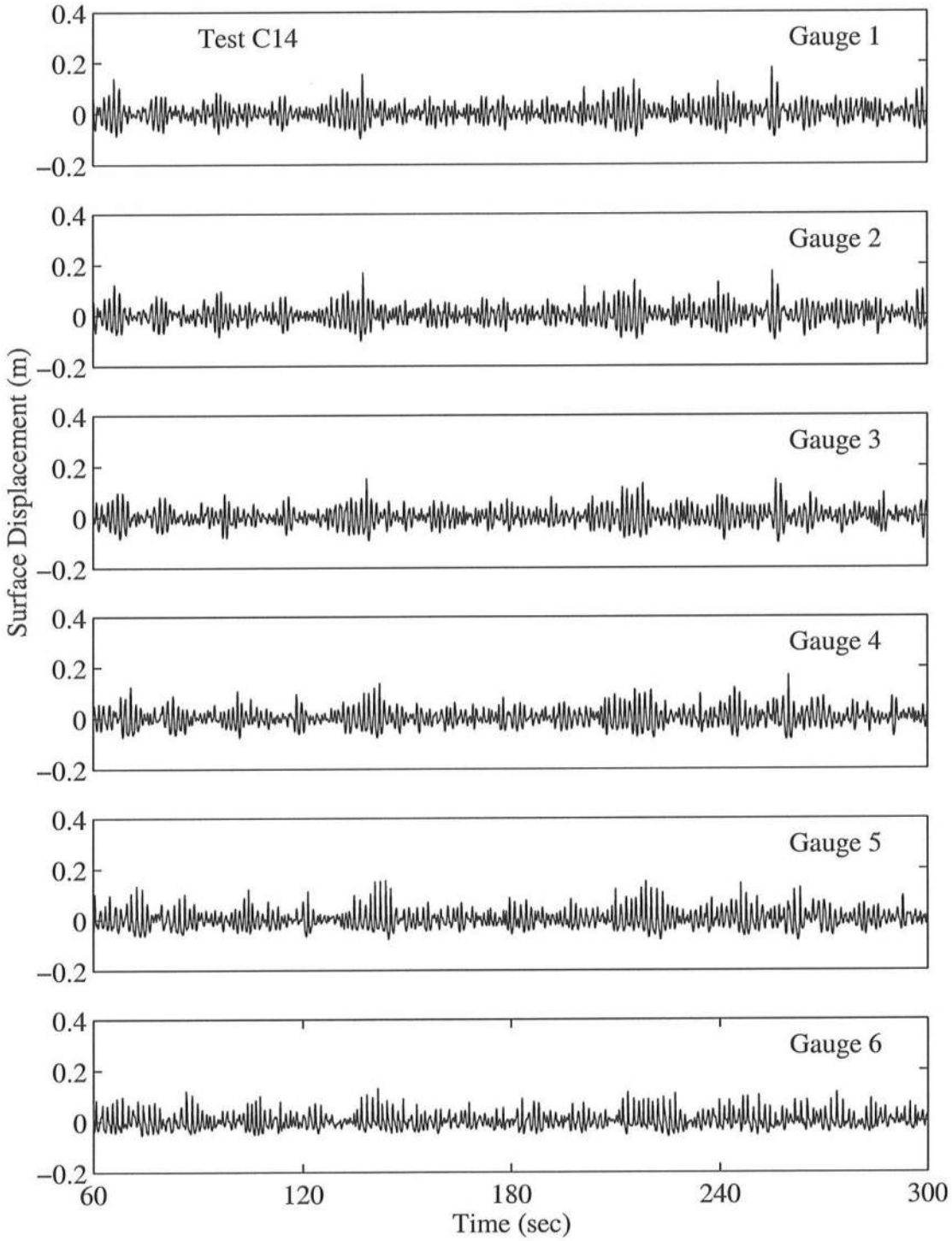

Figure A.47: Time Series for T_p = 1.5 s, d_t = 14 cm, for Gauge 1 – Gauge 6.

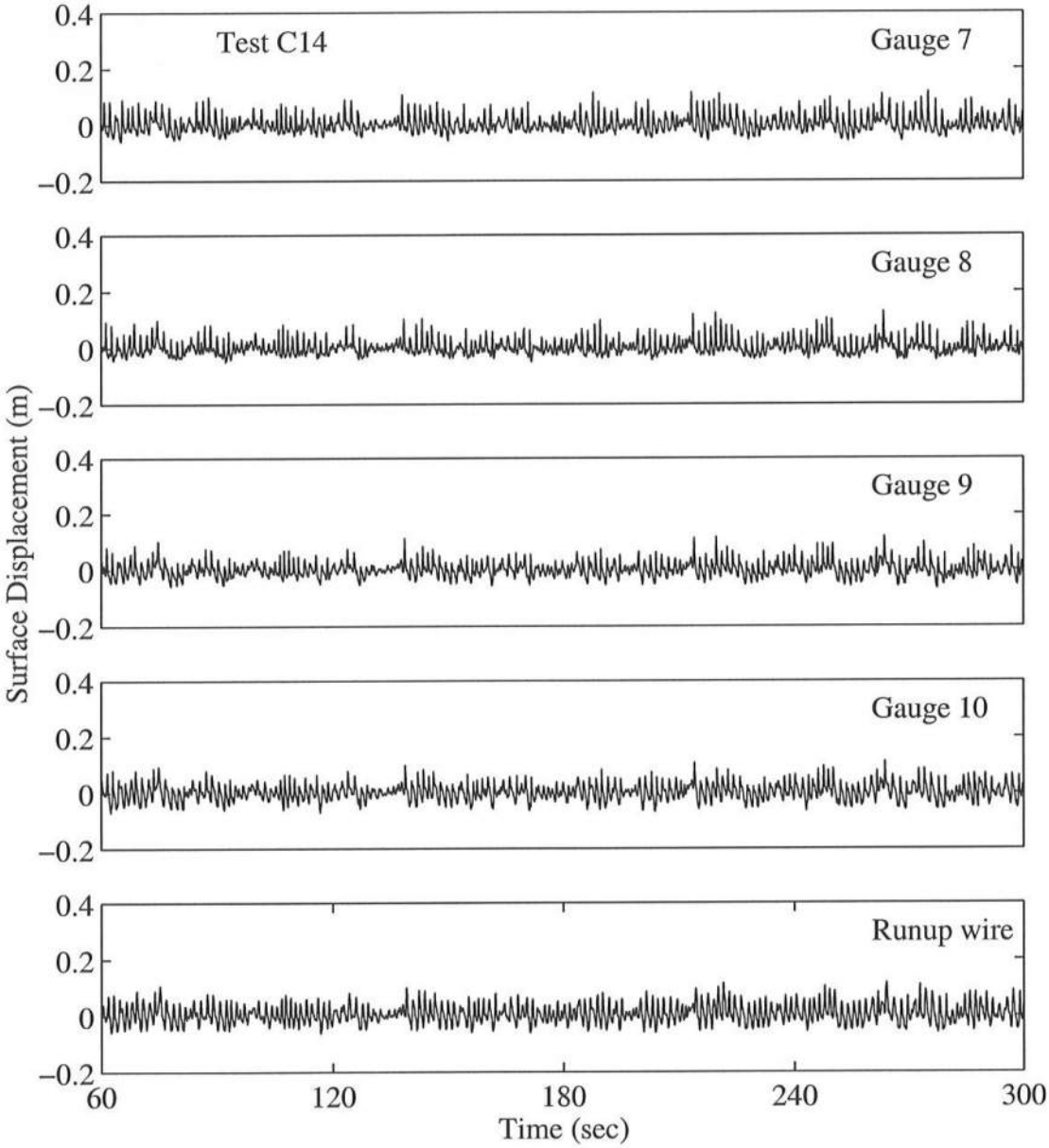

Figure A.48: Time Series for T_p = 1.5 s, d_t = 14 cm, for Gauge 7 – Runup Wire.

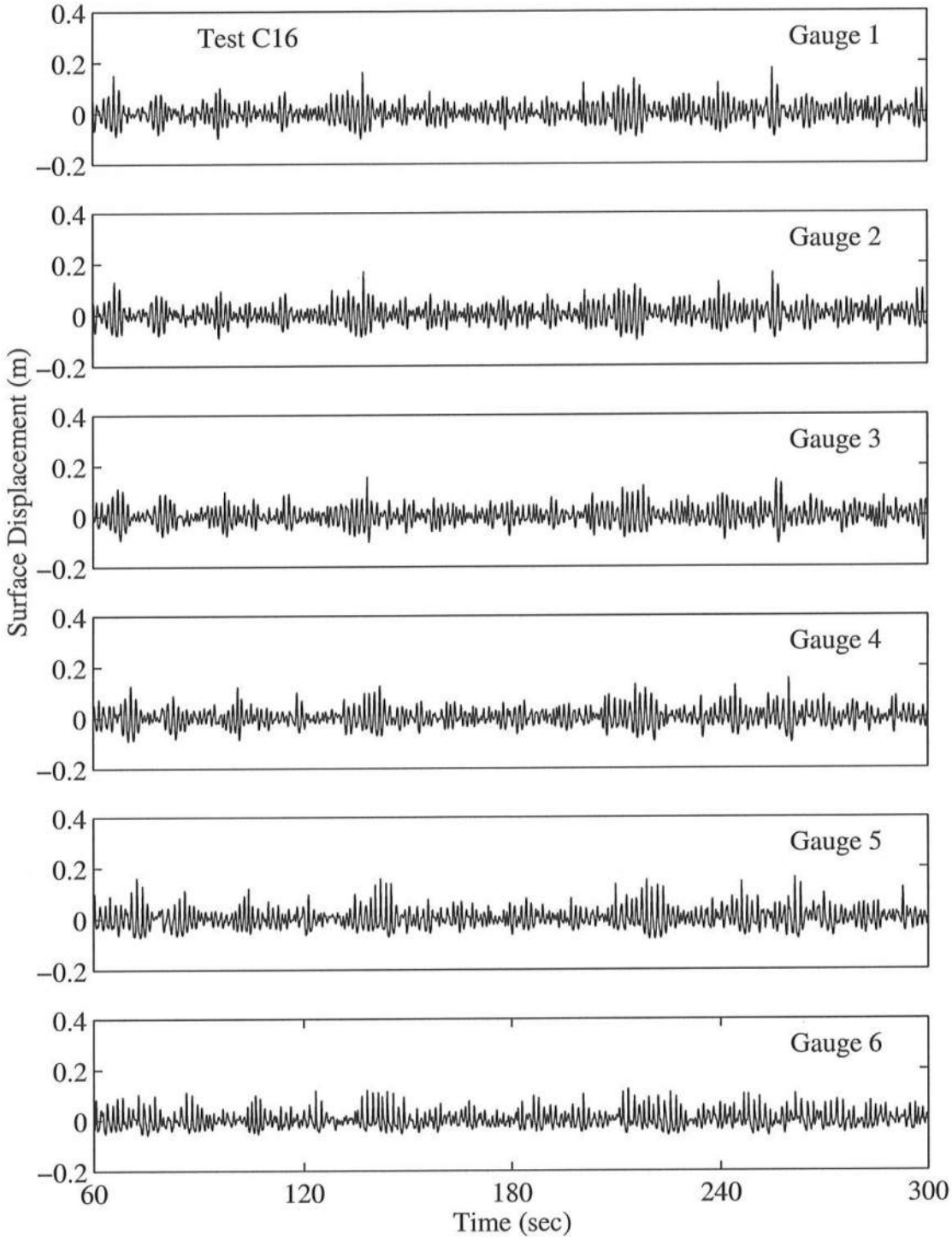

Figure A.49: Time Series for T_p = 1.5 s, d_t =16 cm, for Gauge 1 – Gauge 6.

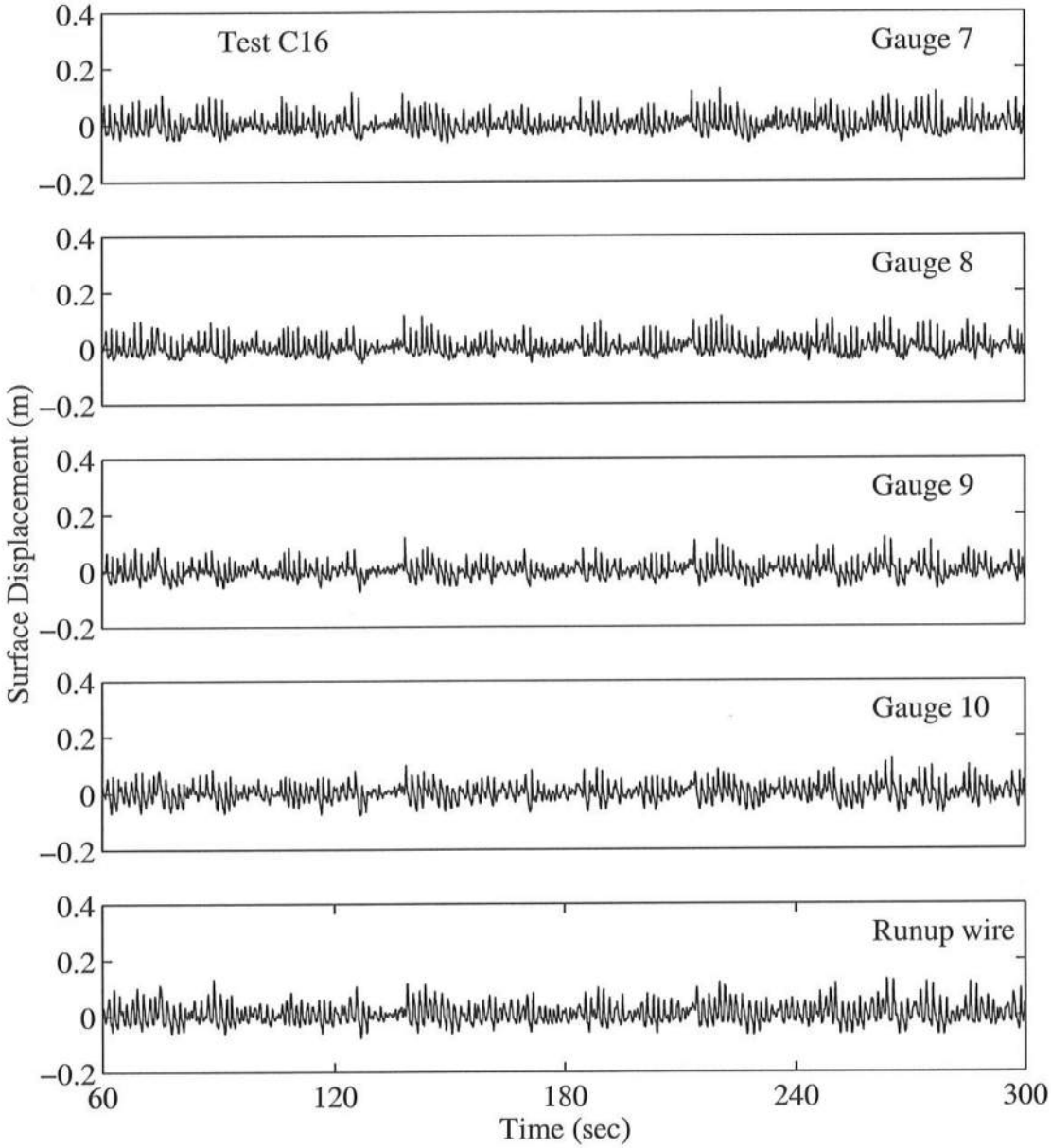

Figure A.50: Time Series for T_p = 1.5 s, d_t =16 cm, for Gauge 7 – Runup Wire.

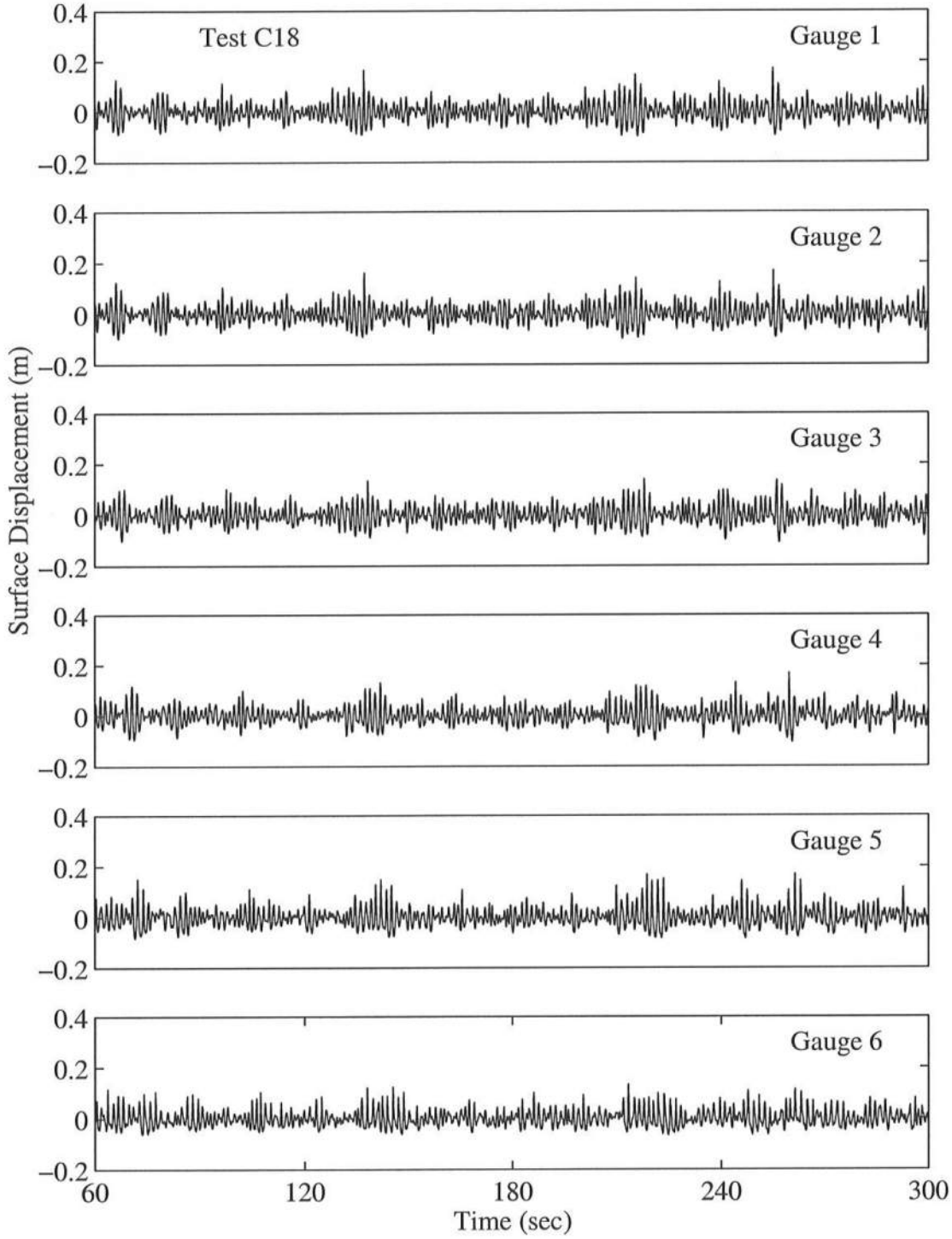

Figure A.51: Time Series for T_p = 1.5 s, d_t =18 cm, for Gauge 1 – Gauge 6.

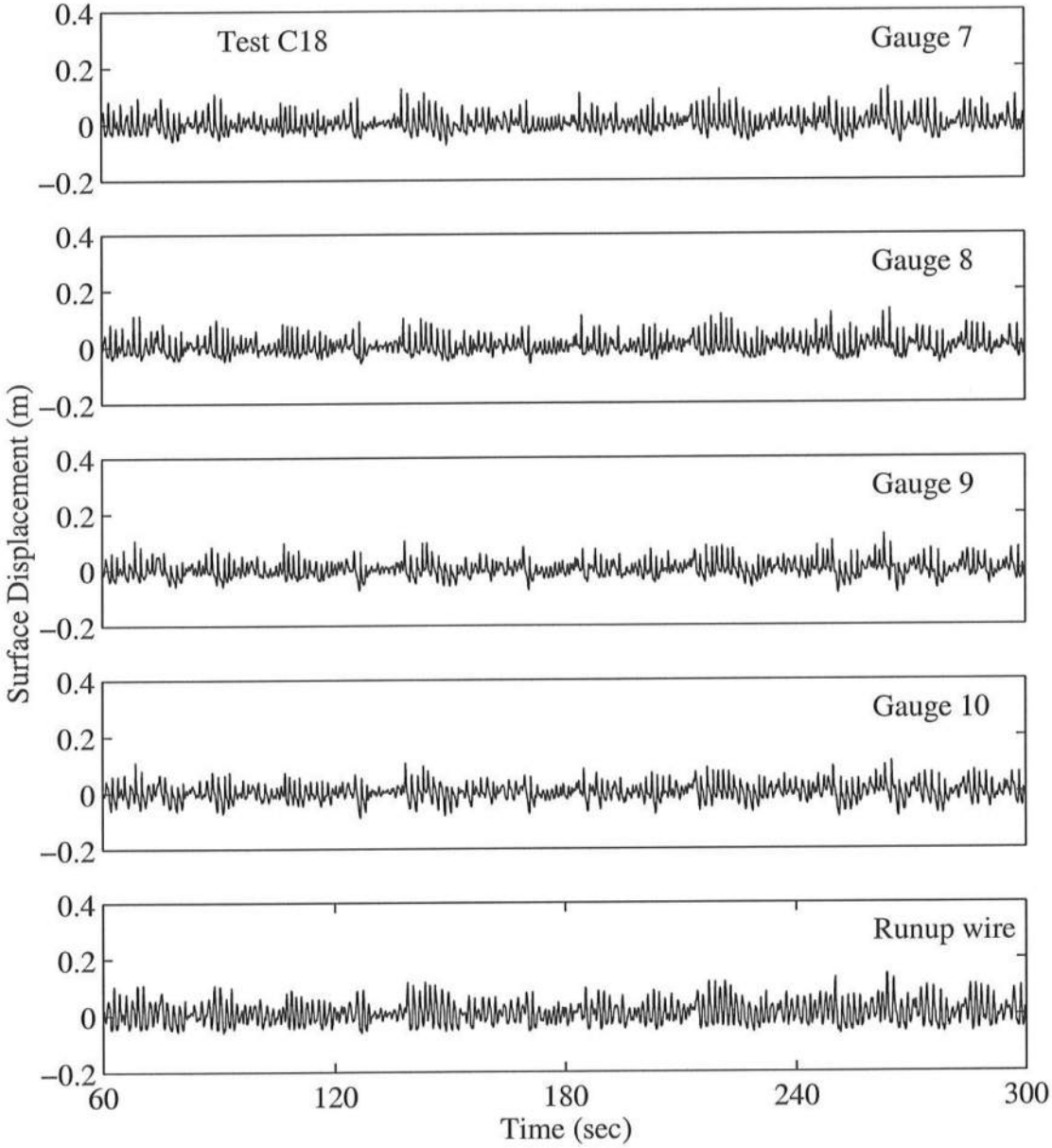

Figure A.52: Time Series for T_p = 1.5 s, d_t = 18 cm, for Gauge 7 – Runup Wire.

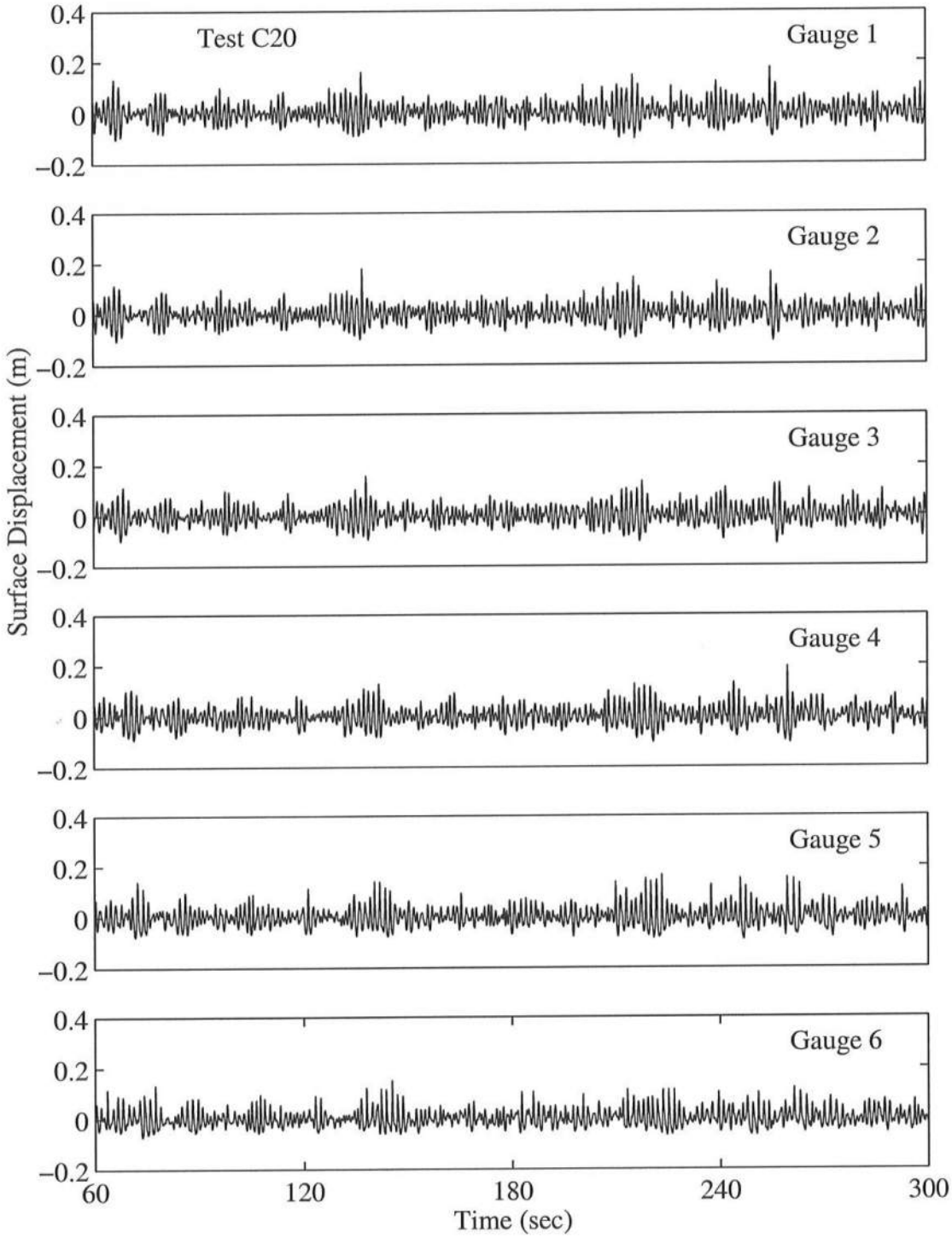

Figure A.53: Time Series for $T_p = 1.5$ s, $d_t = 20$ cm, for Gauge 1 – Gauge 6.

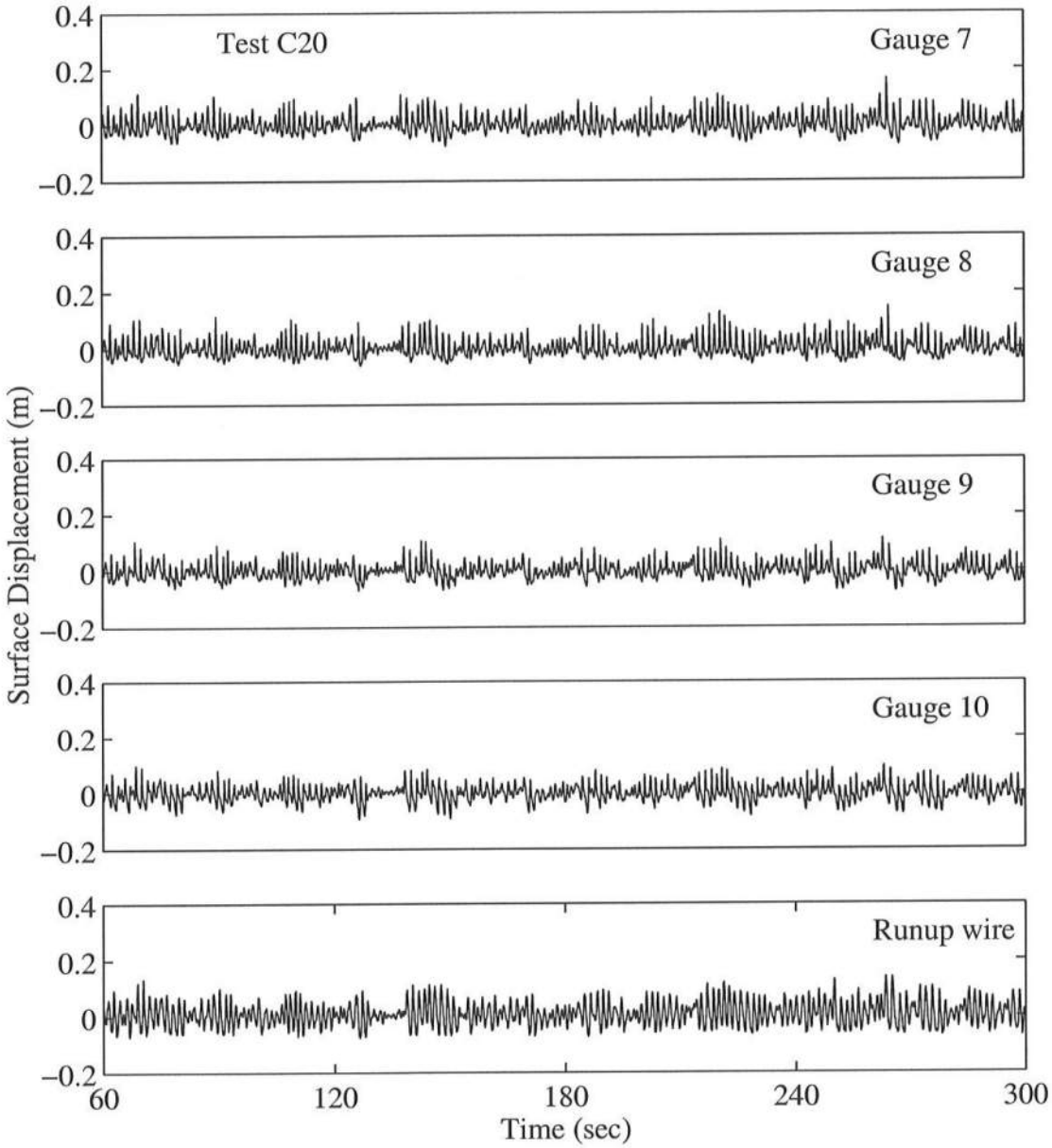

Figure A.54: Time Series for $T_p = 1.5$ s, $d_t = 20$ cm, for Gauge 7 – Runup Wire.

APPENDIX B

FREE SURFACE FREQUENCY SPECTRAL PLOTS

This appendix contains representative frequency spectra for all tests performed.

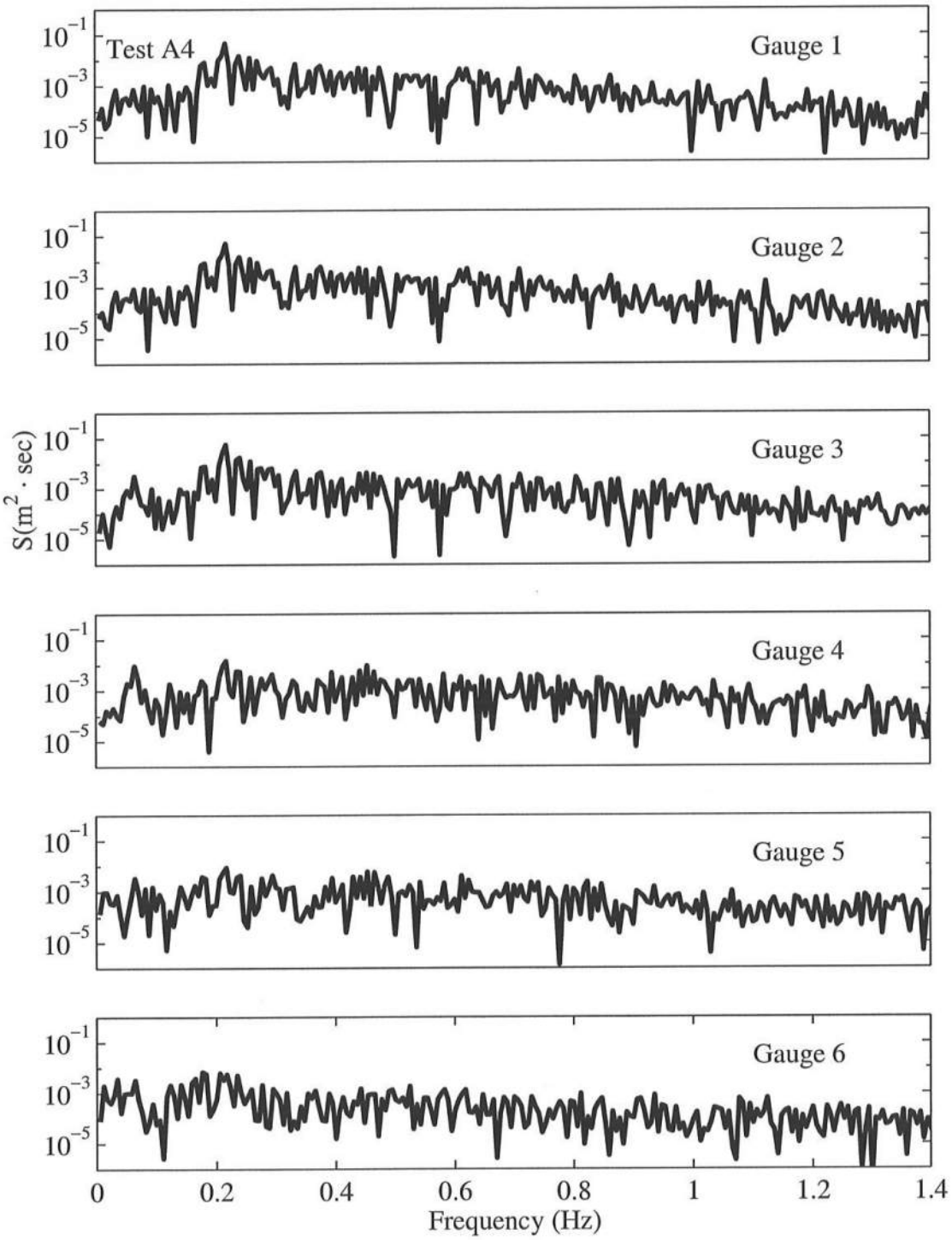

Figure B.1: Frequency Spectra for $T_p = 4.7$ s, $d_t = 4$ cm, for Gauge 1 – Gauge 6.

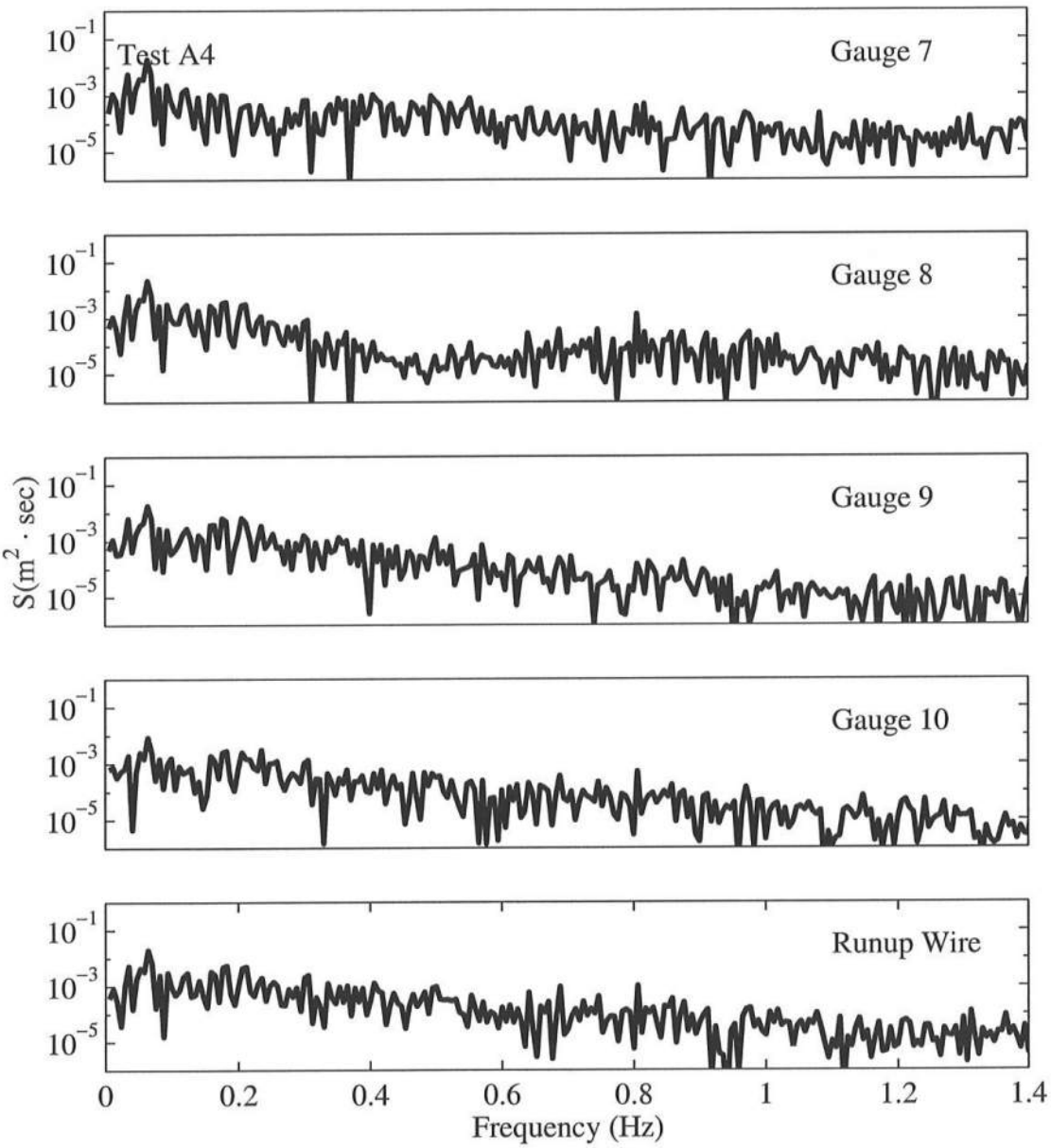

Figure B.2: Frequency Spectra for $T_p = 4.7$ s, $d_t = 4$ cm, for Gauge 7 – Runup Wire.

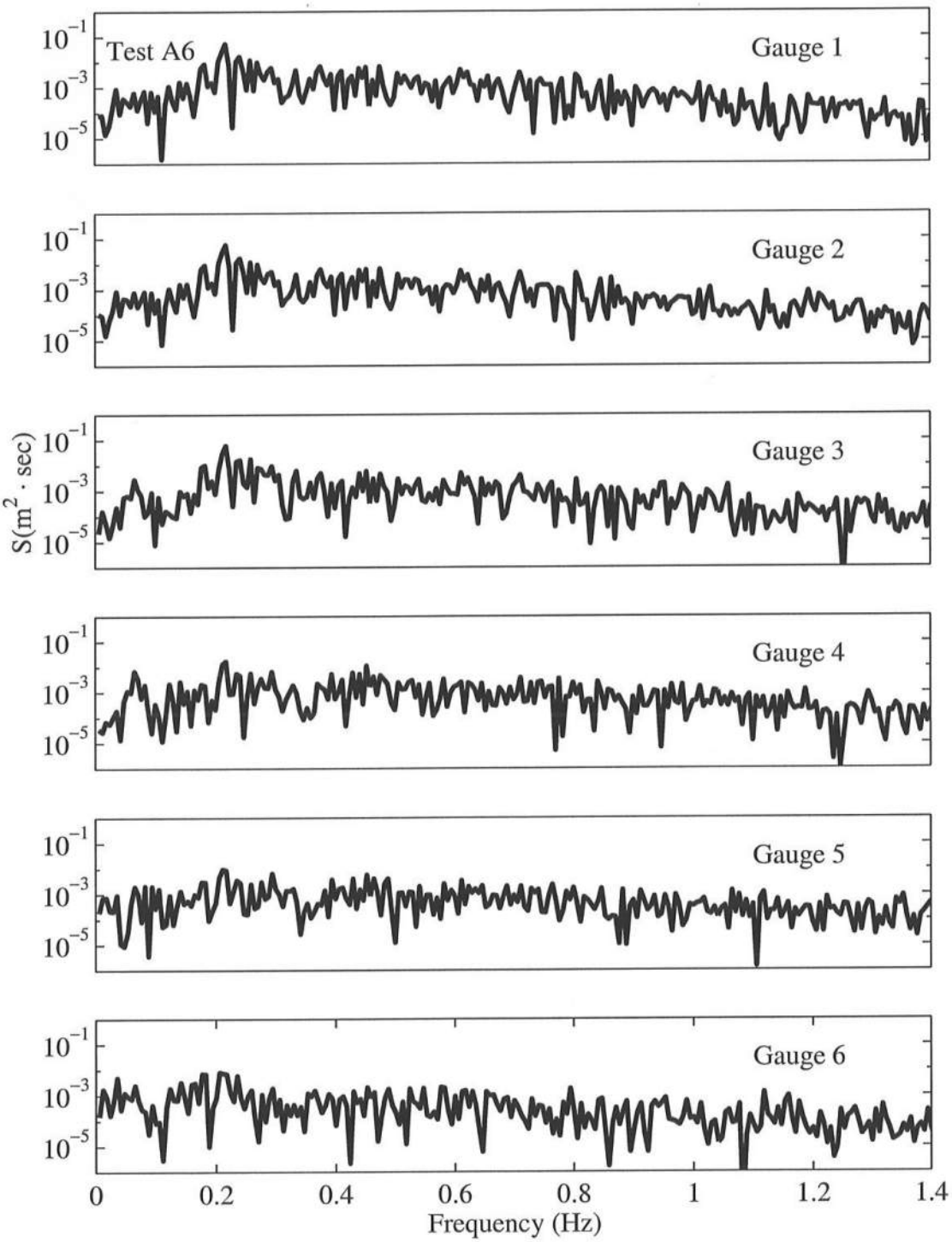

Figure B.3: Frequency Spectra for $T_p = 4.7$ s, $d_t = 6$ cm, for Gauge 1 – Gauge 6.

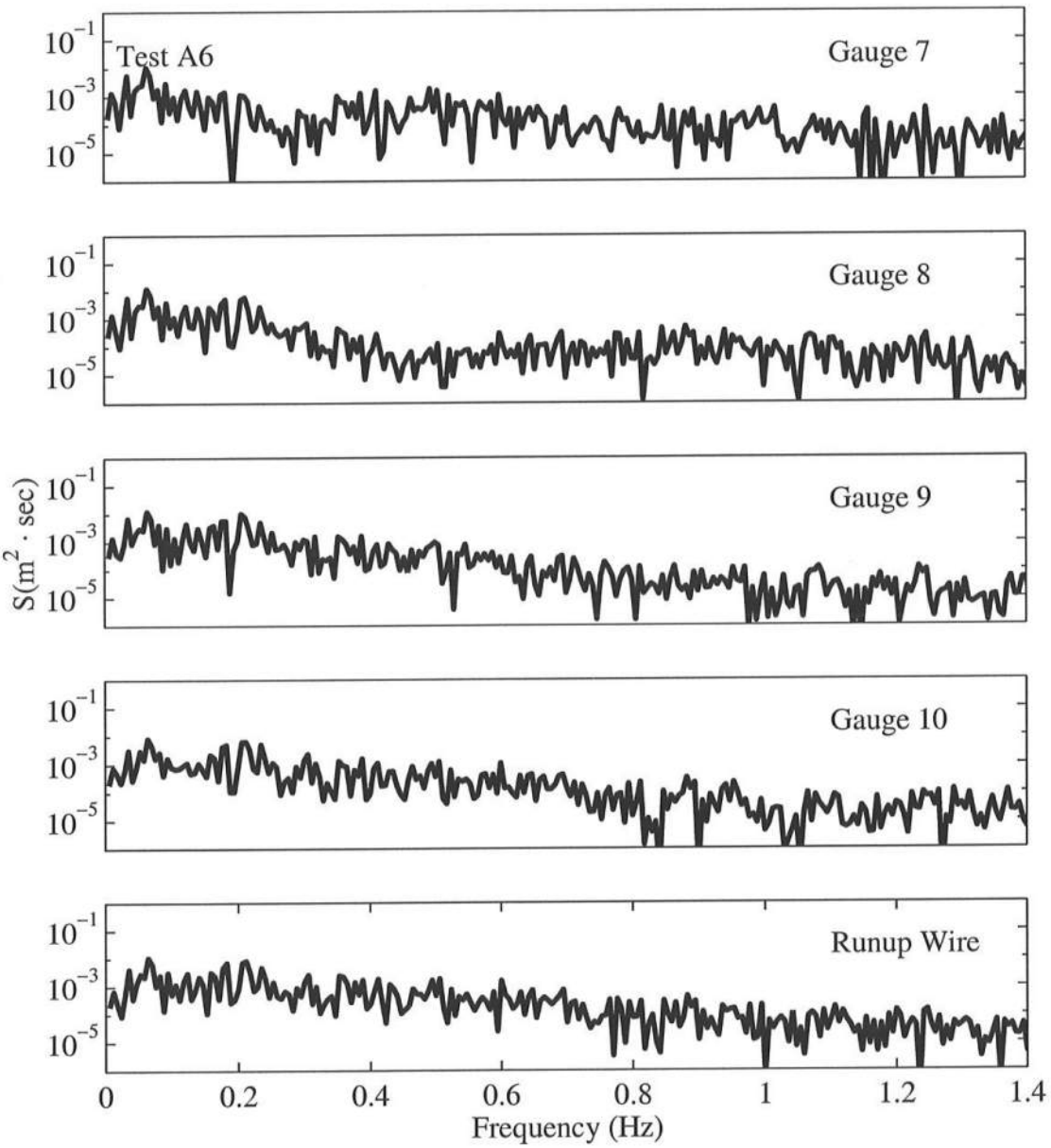

Figure B.4: Frequency Spectra for $T_p = 4.7$ s, $d_t = 6$ cm, for Gauge 7 – Runup Wire.

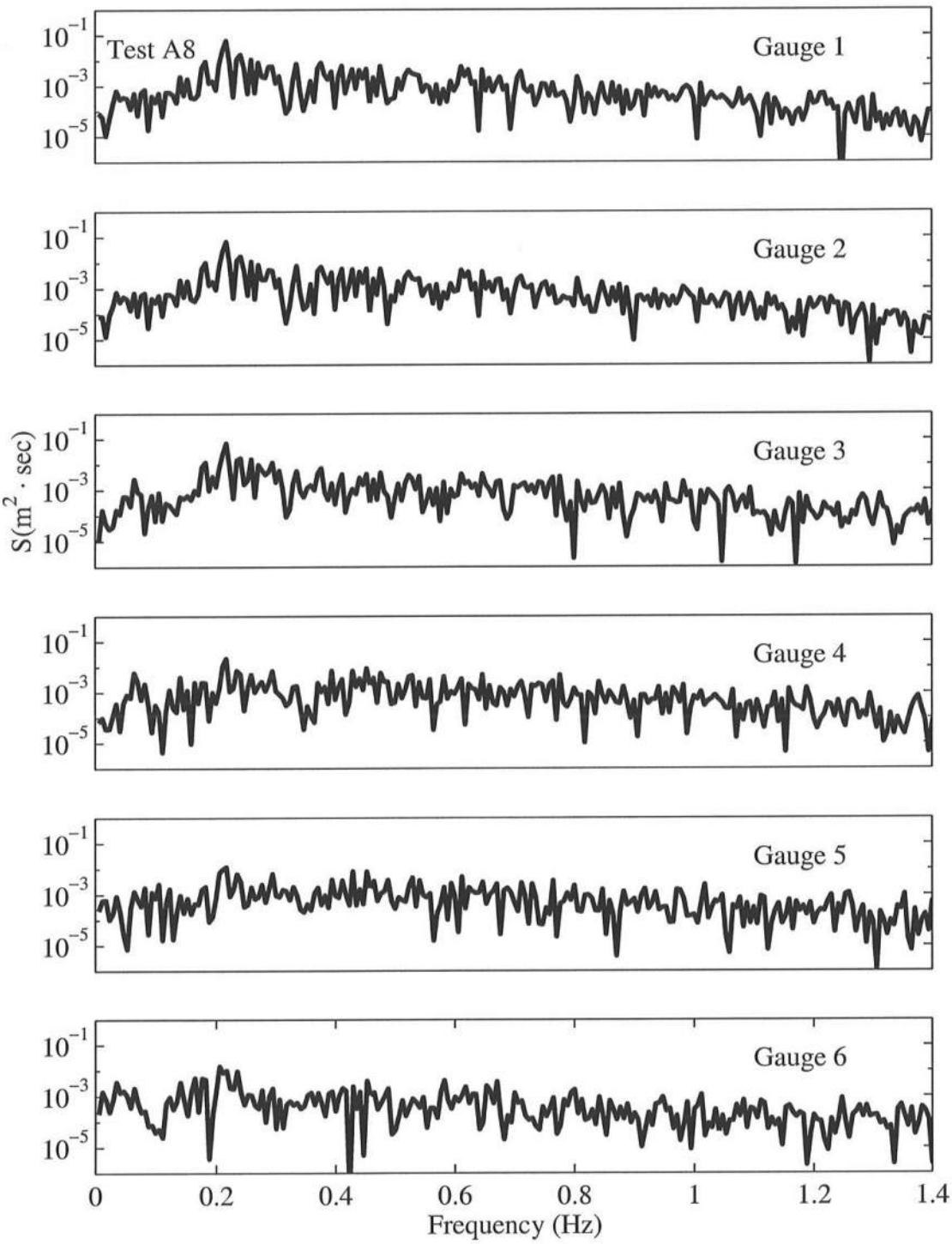

Figure B.5: Frequency Spectra for $T_p = 4.7$ s, $d_t = 8$ cm, for Gauge 1 – Gauge 6.

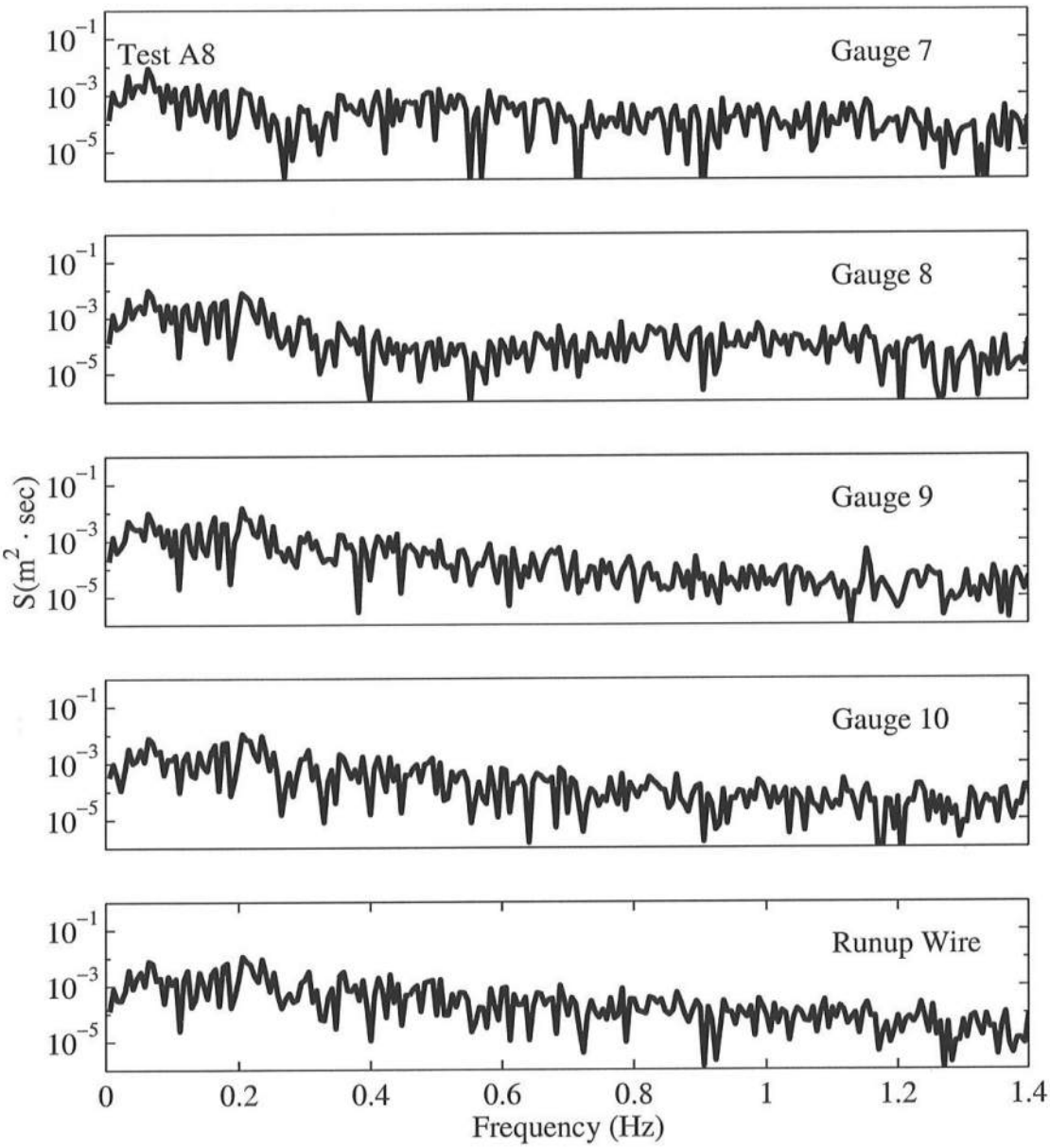

Figure B.6: Frequency Spectra for $T_p = 4.7$ s, $d_t = 8$ cm, for Gauge 7 – Runup Wire.

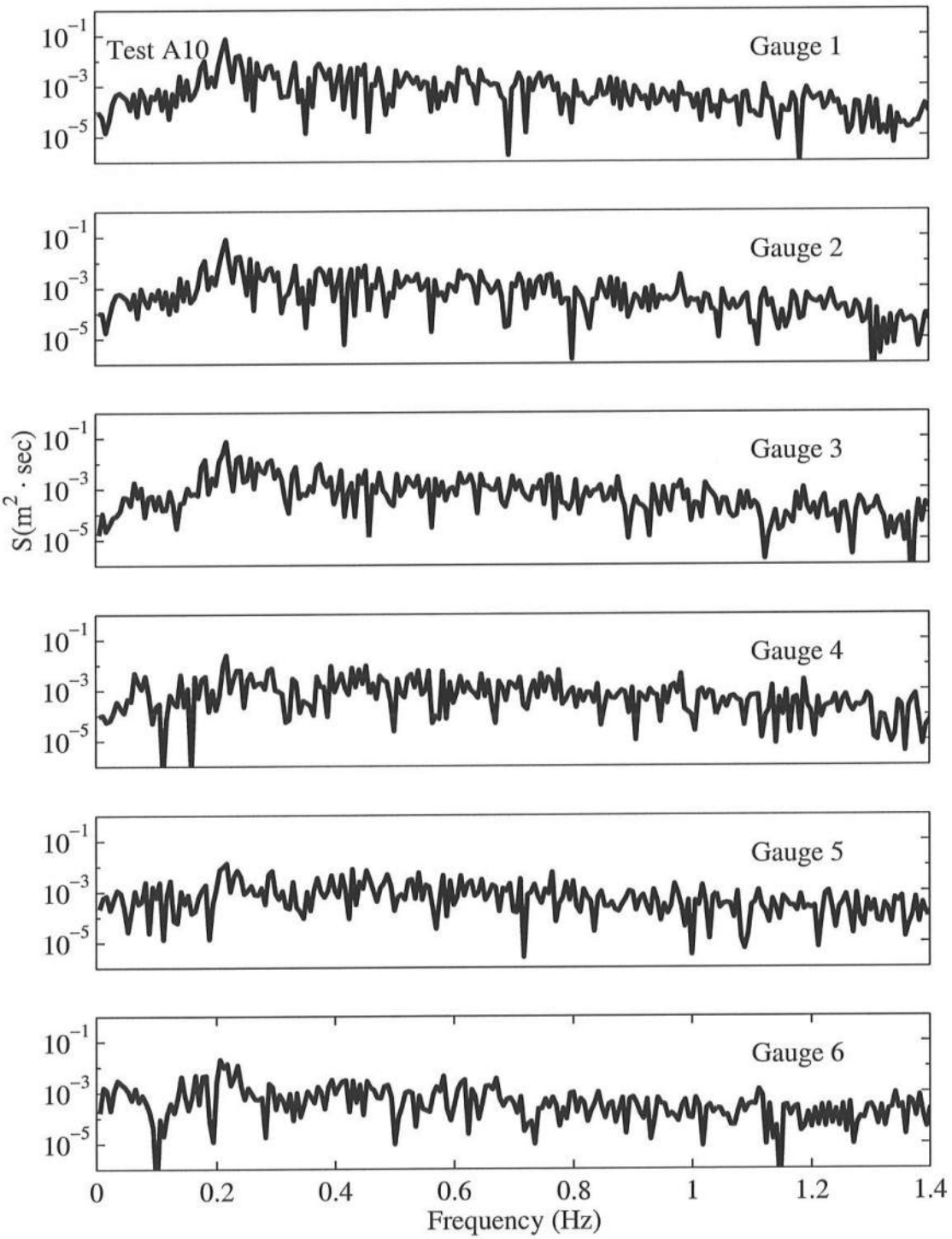

Figure B.7: Frequency Spectra for $T_p = 4.7$ s, $d_t = 10$ cm, for Gauge 1 – Gauge 6.

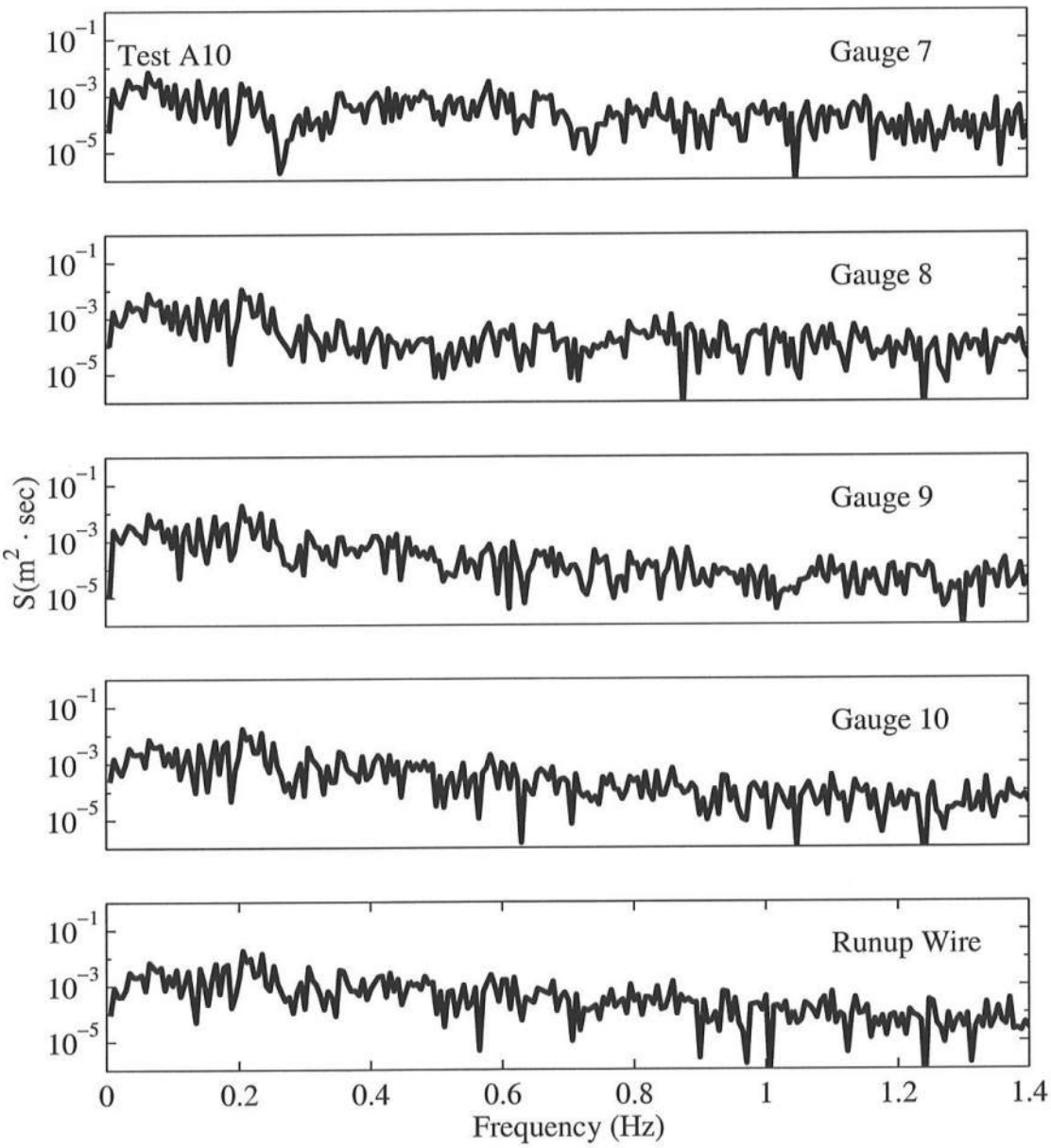

Figure B.8: Frequency Spectra for $T_p = 4.7$ s, $d_t = 10$ cm, for Gauge 7 – Runup Wire.

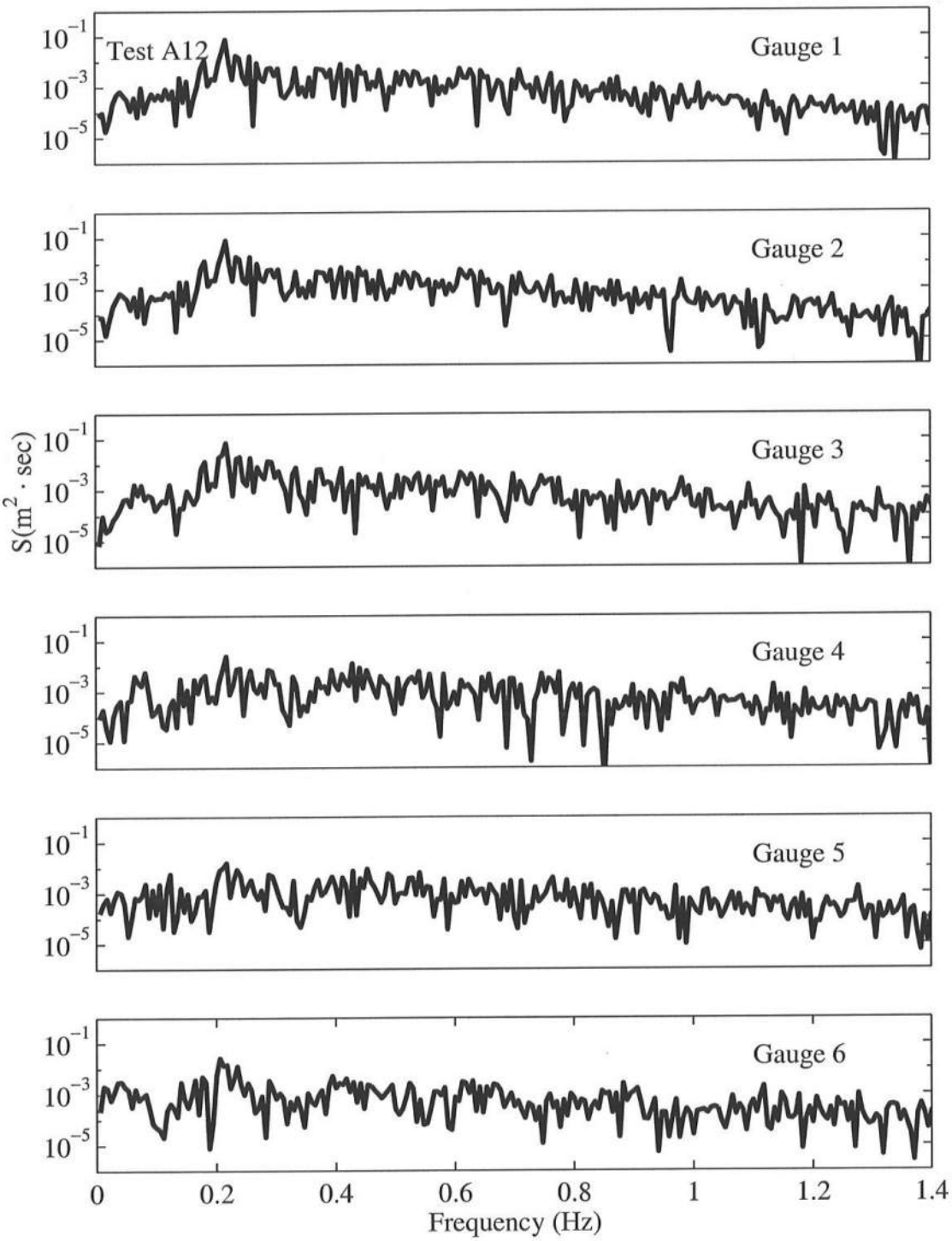

Figure B.9: Frequency Spectra for $T_p = 4.7$ s, $d_t = 12$ cm, for Gauge 1 – Gauge 6.

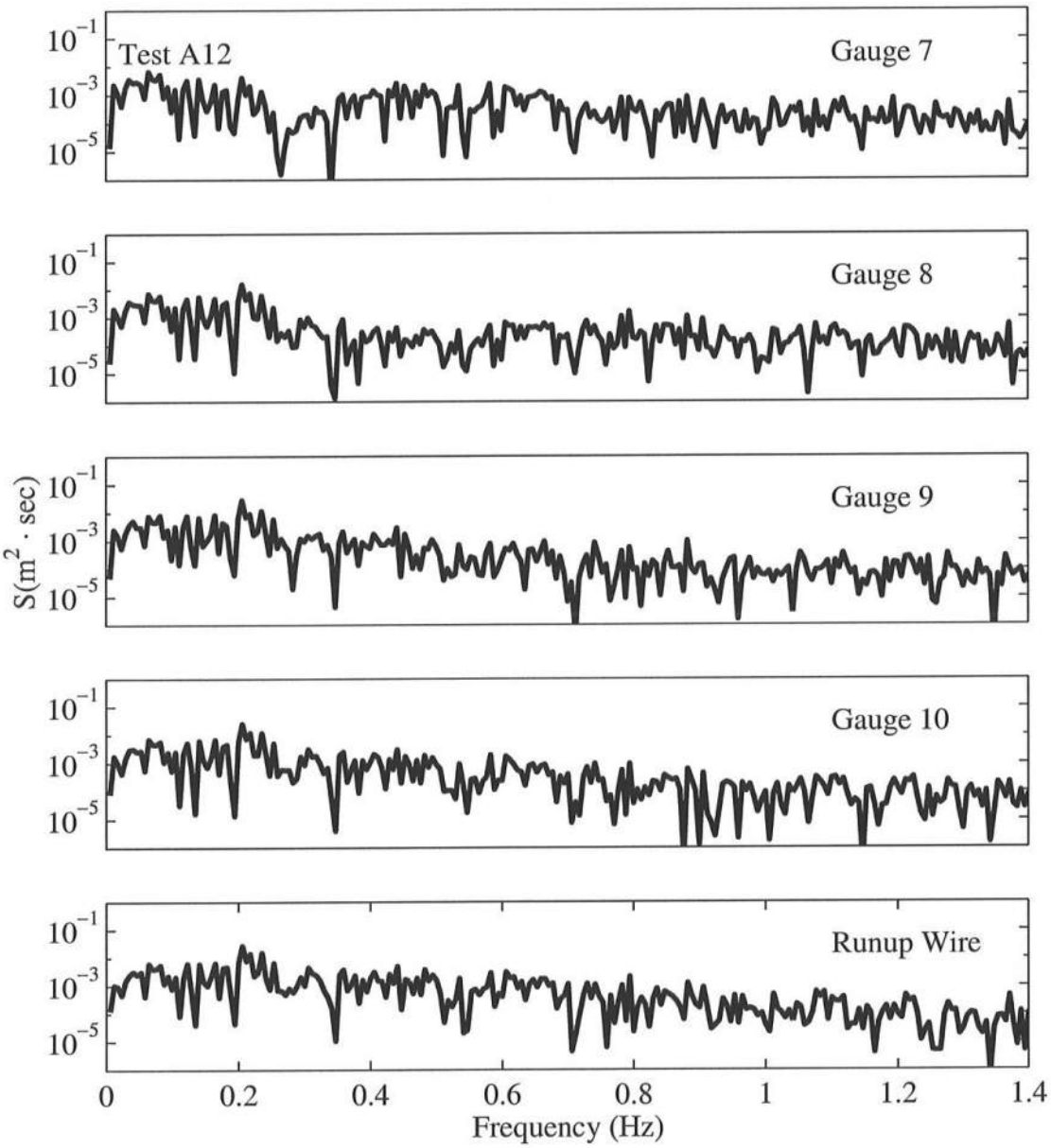

Figure B.10: Frequency Spectra for $T_p = 4.7$ s, $d_t = 12$ cm, for Gauge 7 – Runup Wire.

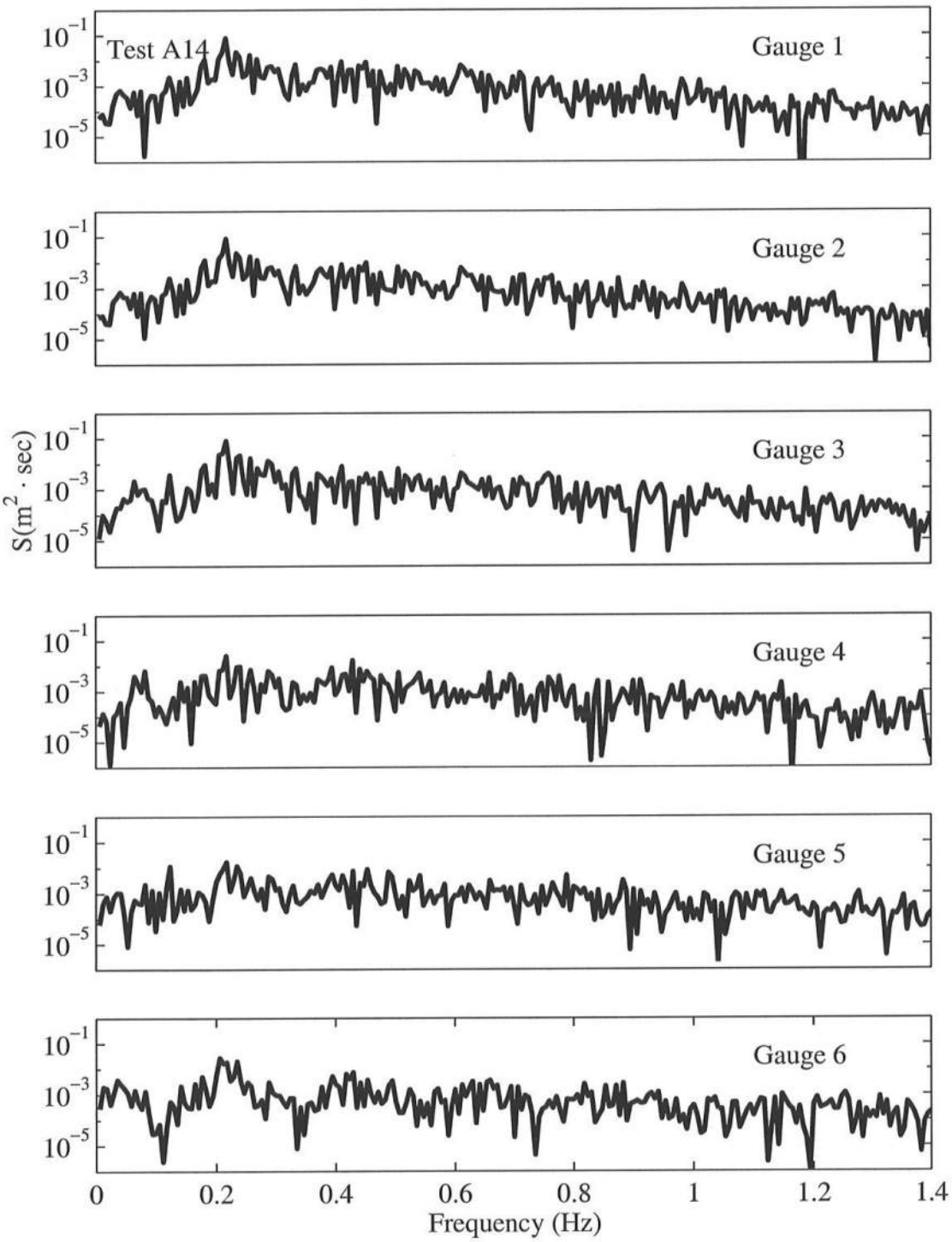

Figure B.11: Frequency Spectra for $T_p = 4.7$ s, $d_t = 14$ cm, for Gauge 1 – Gauge 6.

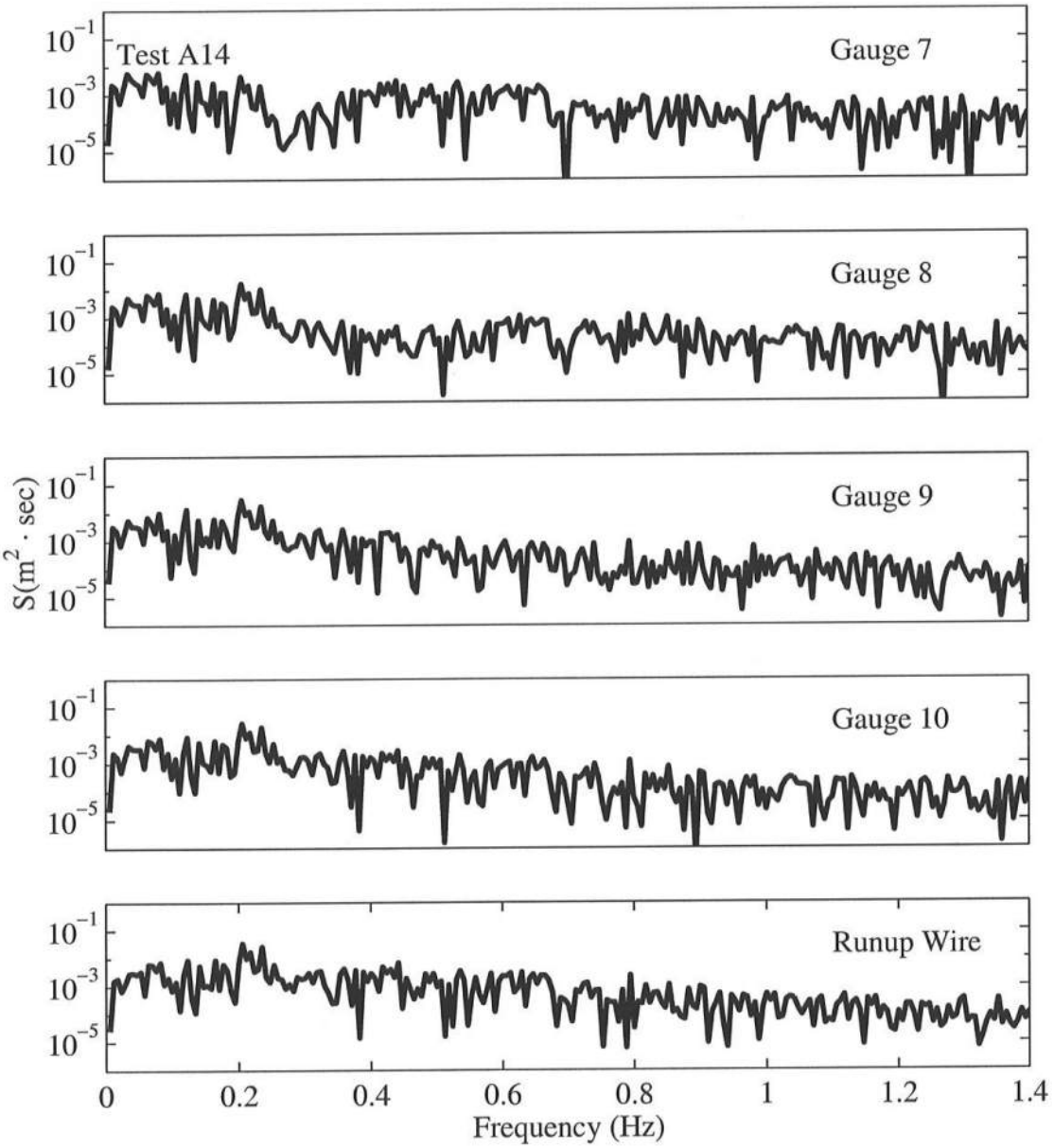

Figure B.12: Frequency Spectra for $T_p = 4.7$ s, $d_t = 14$ cm, for Gauge 7 – Runup Wire.

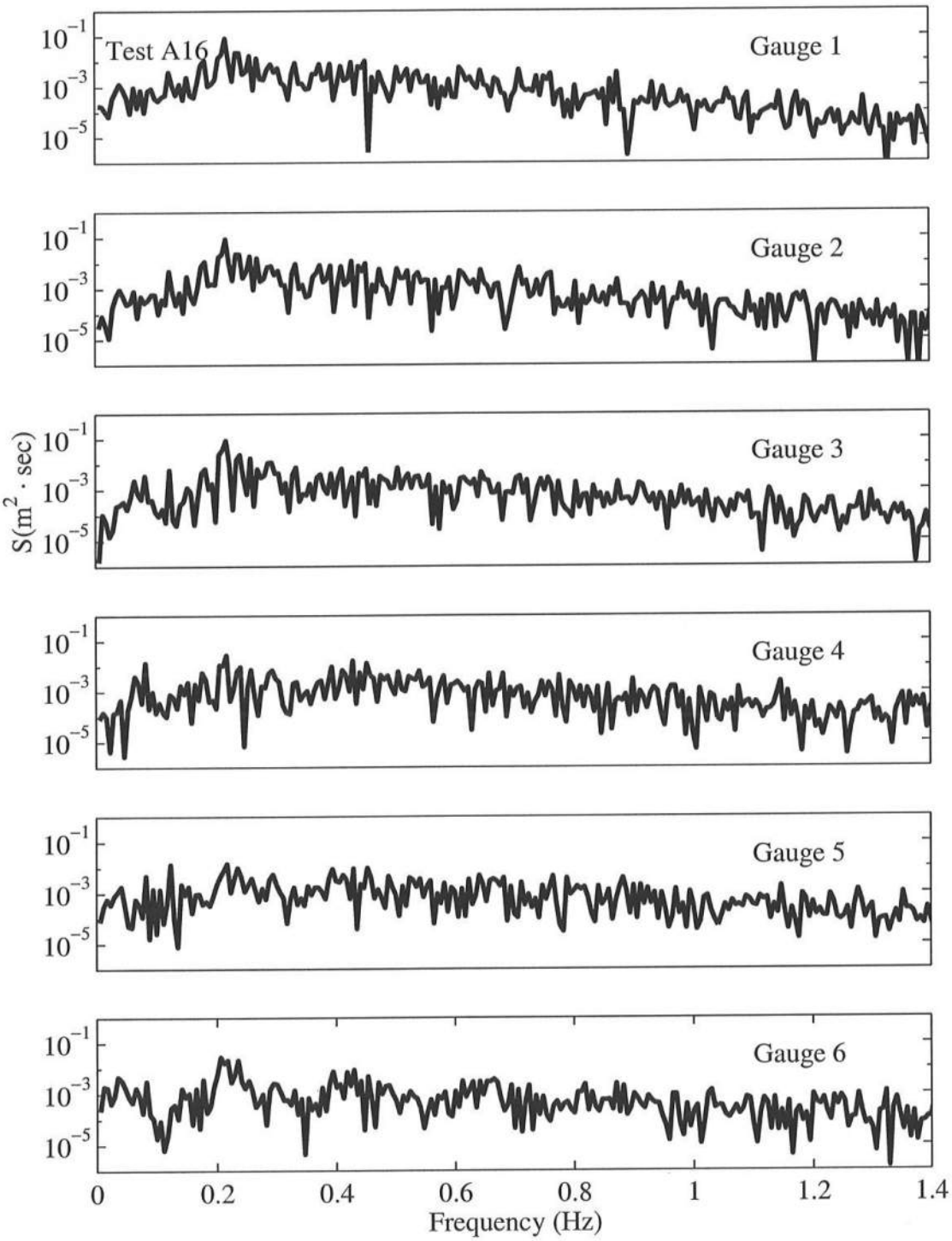

Figure B.13: Frequency Spectra for $T_p = 4.7$ s, d_t =16 cm, for Gauge 1 – Gauge 6.

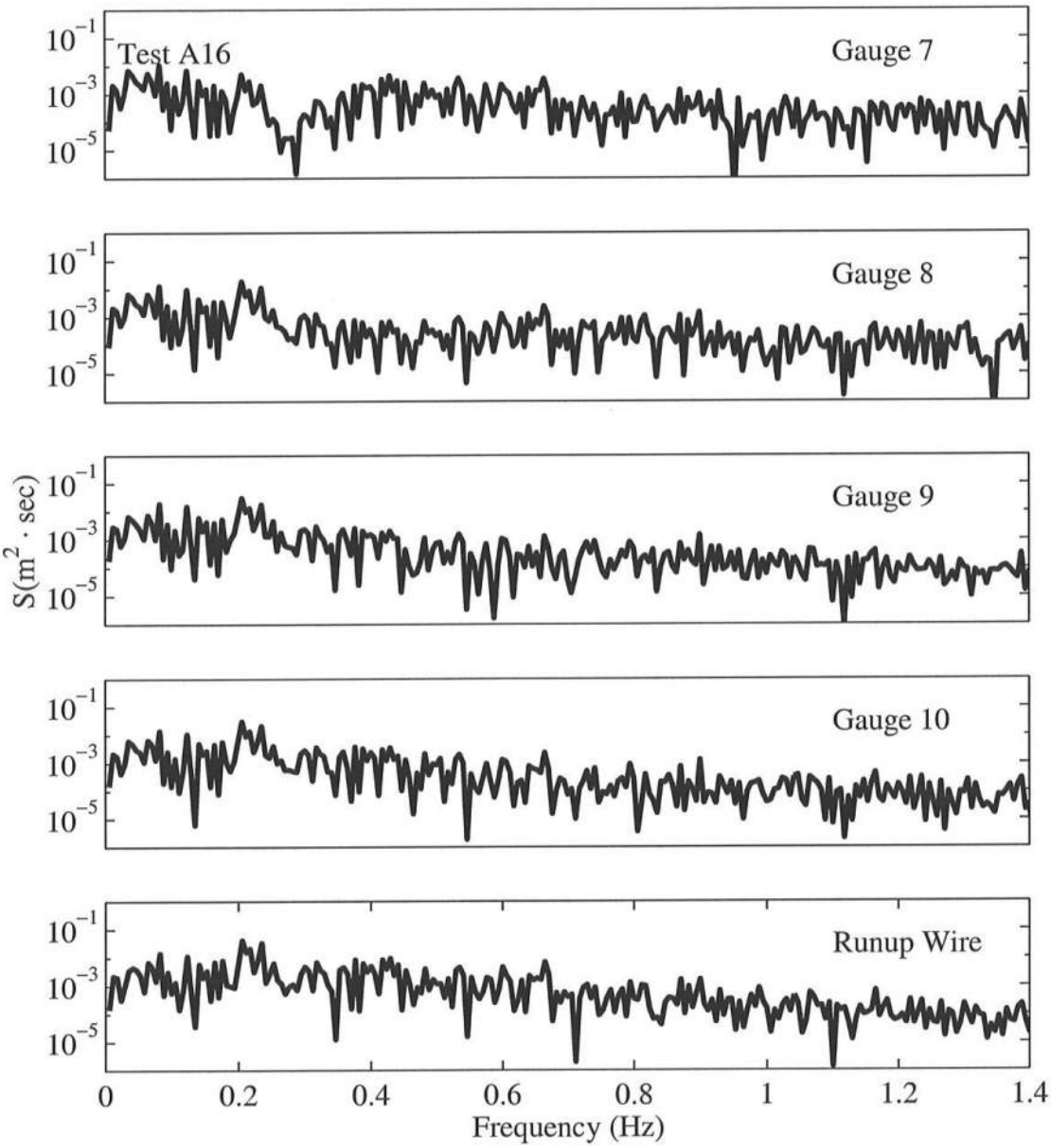

Figure B.14: Frequency Spectra for $T_p = 4.7$ s, $d_t = 16$ cm, for Gauge 7 – Runup Wire.

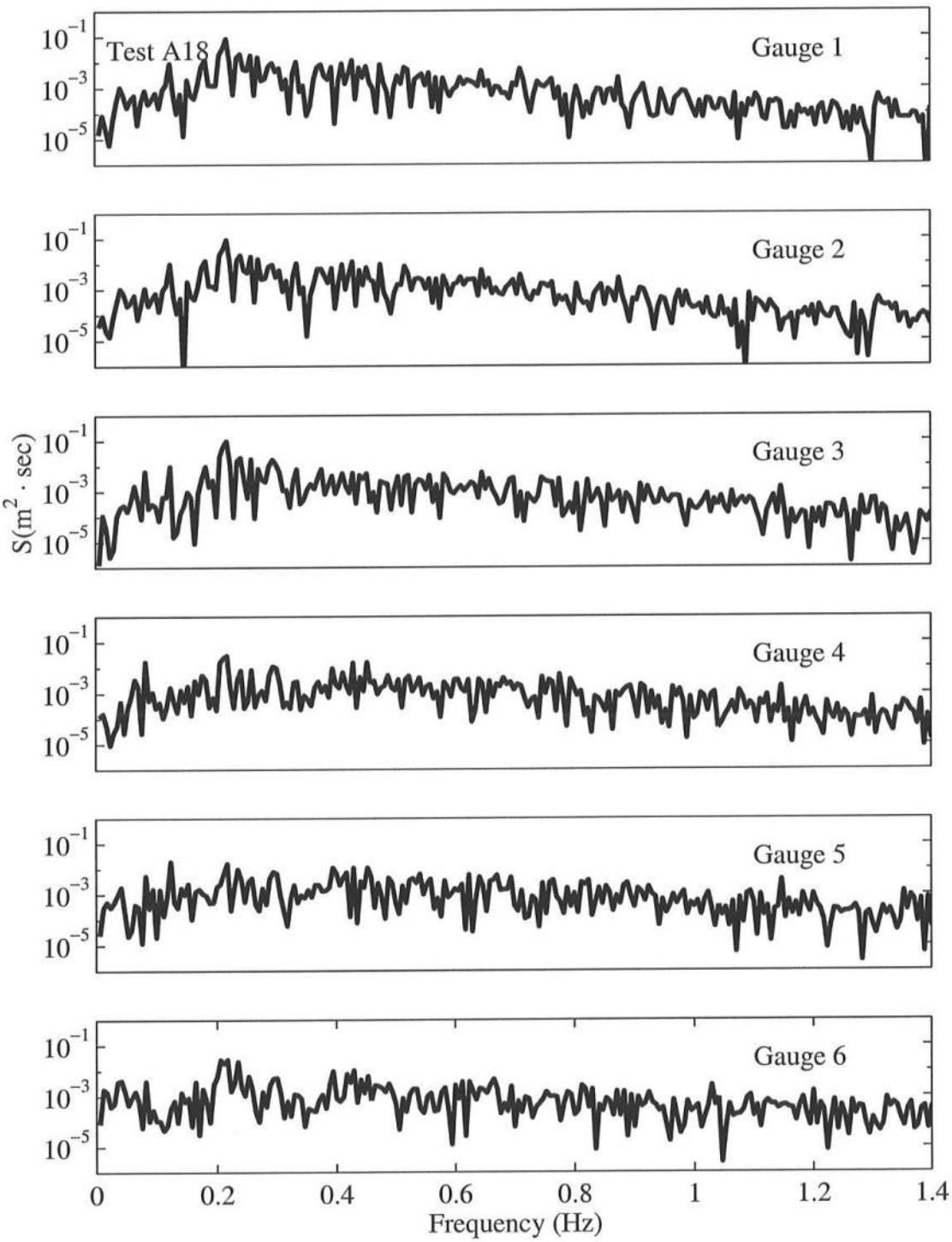

Figure B.15: Frequency Spectra for $T_p = 4.7$ s, $d_t = 18$ cm, for Gauge 1 – Gauge 6.

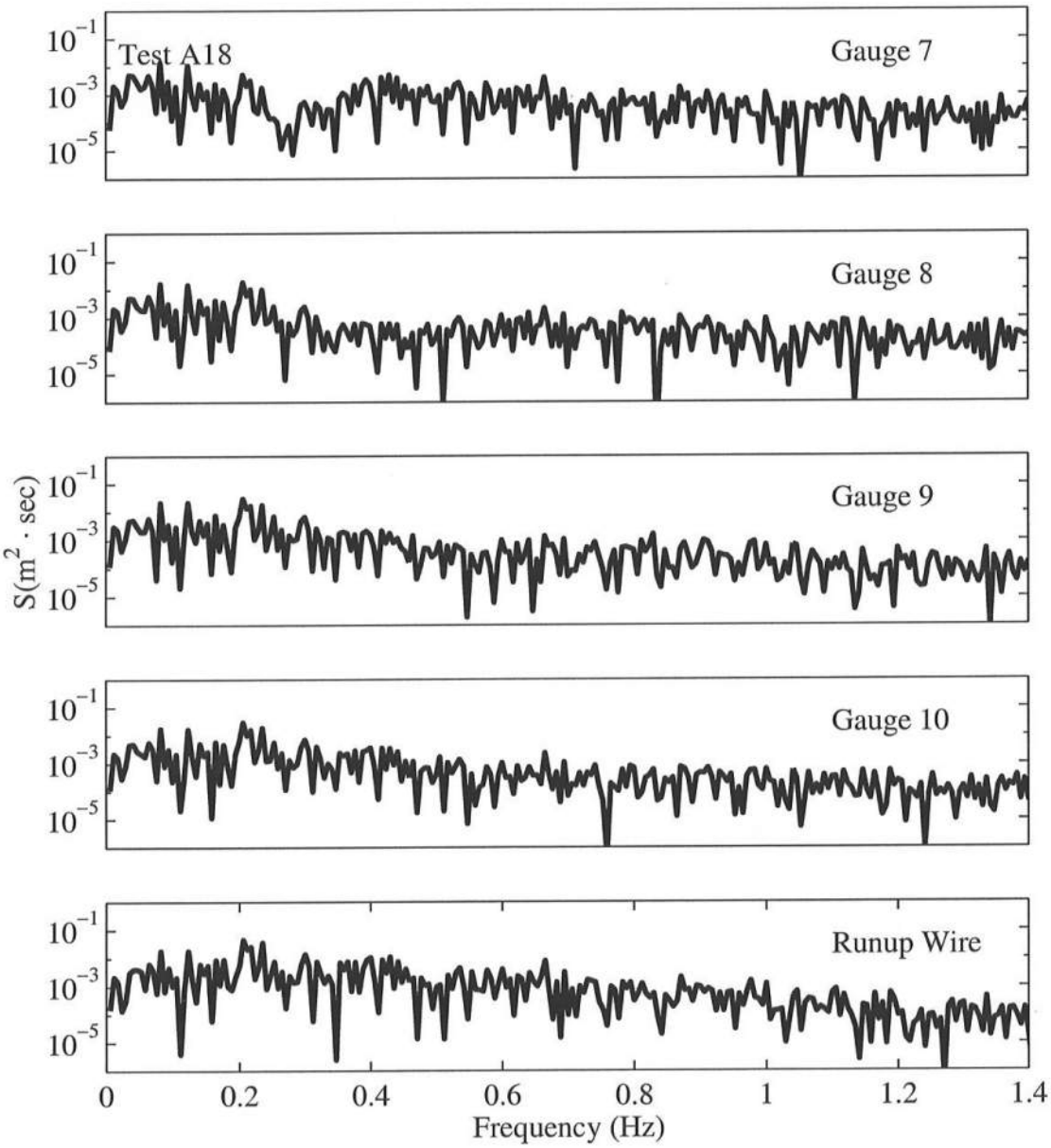

Figure B.16: Frequency Spectra for $T_p = 4.7$ s, $d_t = 18$ cm, for Gauge 7 – Runup Wire.

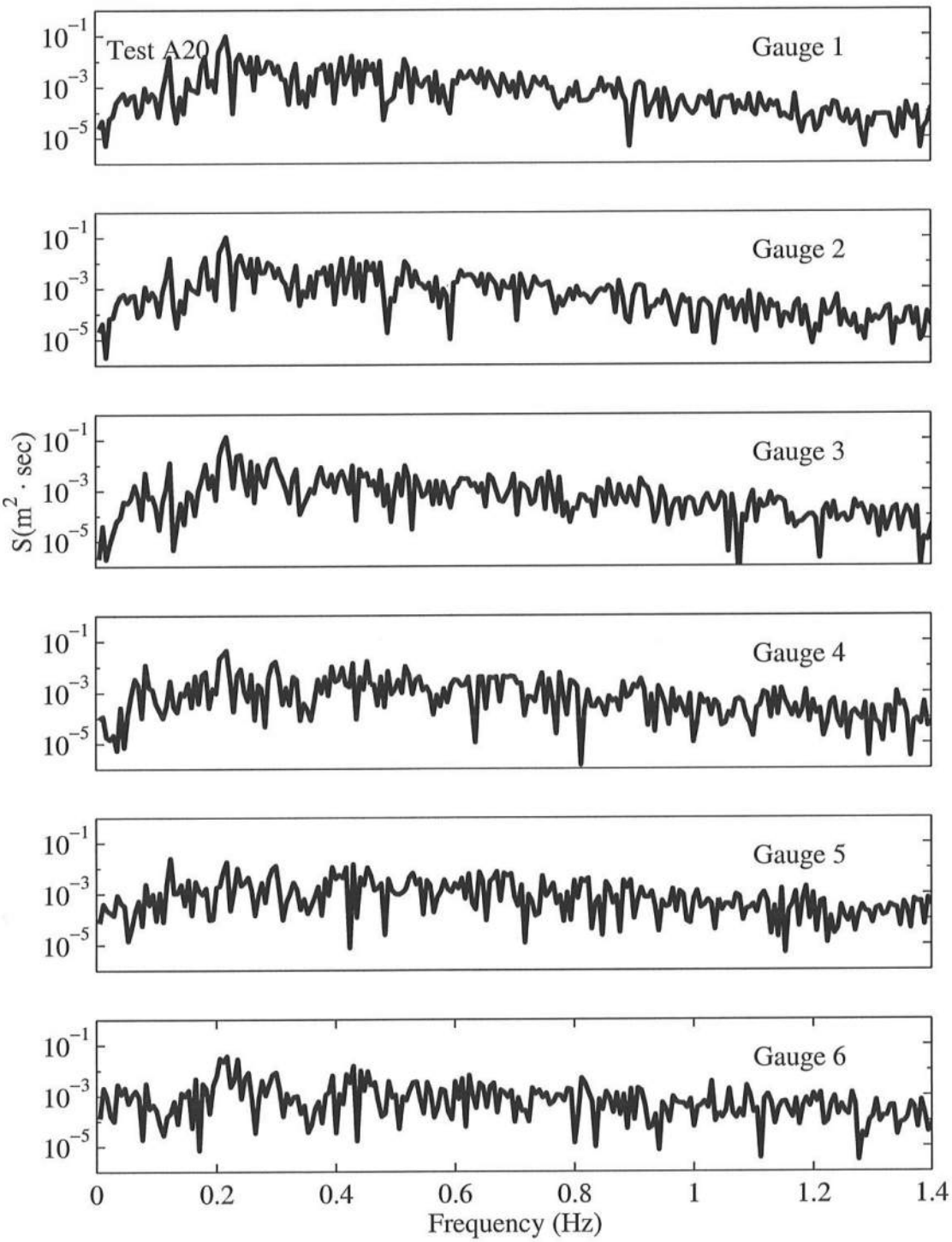

Figure B.17: Frequency Spectra for $T_p = 4.7$ s, $d_t = 20$ cm, for Gauge 1 – Gauge 6.

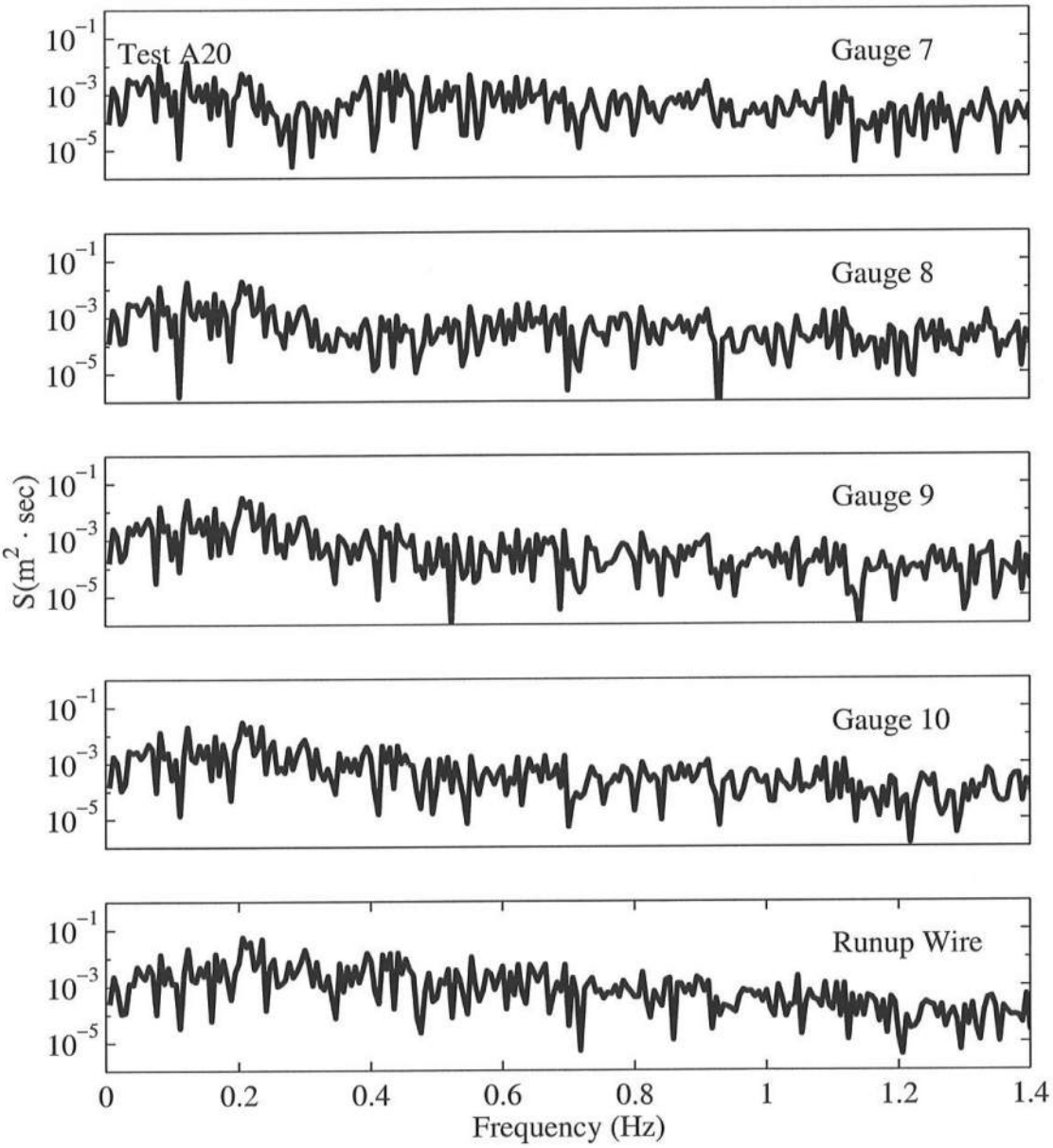

Figure B.18: Frequency Spectra for $T_p = 4.7$ s, $d_t = 20$ cm, for Gauge 7 – Runup Wire.

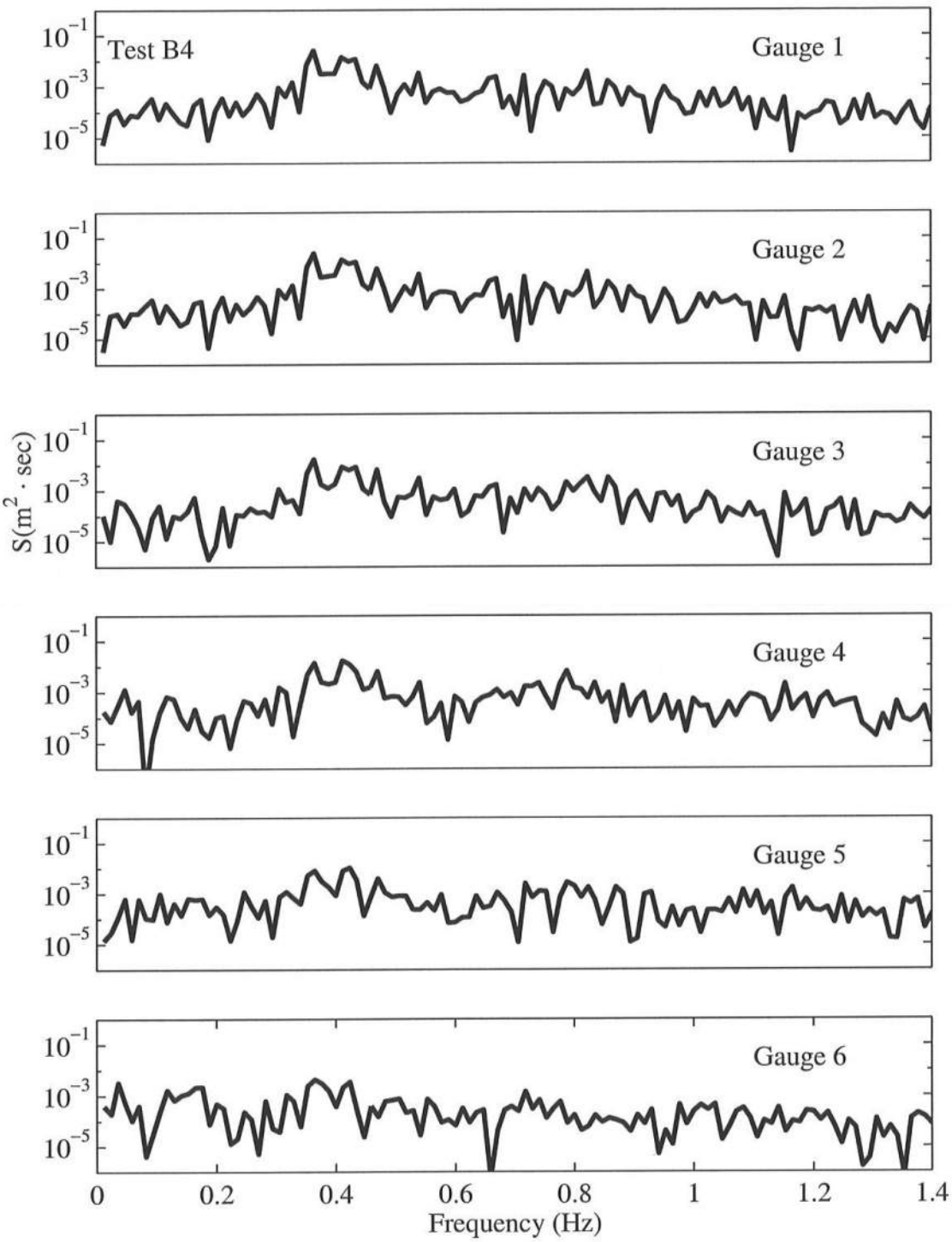

Figure B.19: Frequency Spectra for $T_p = 2.4$ s, $d_t = 4$ cm, for Gauge 1 – Gauge 6.

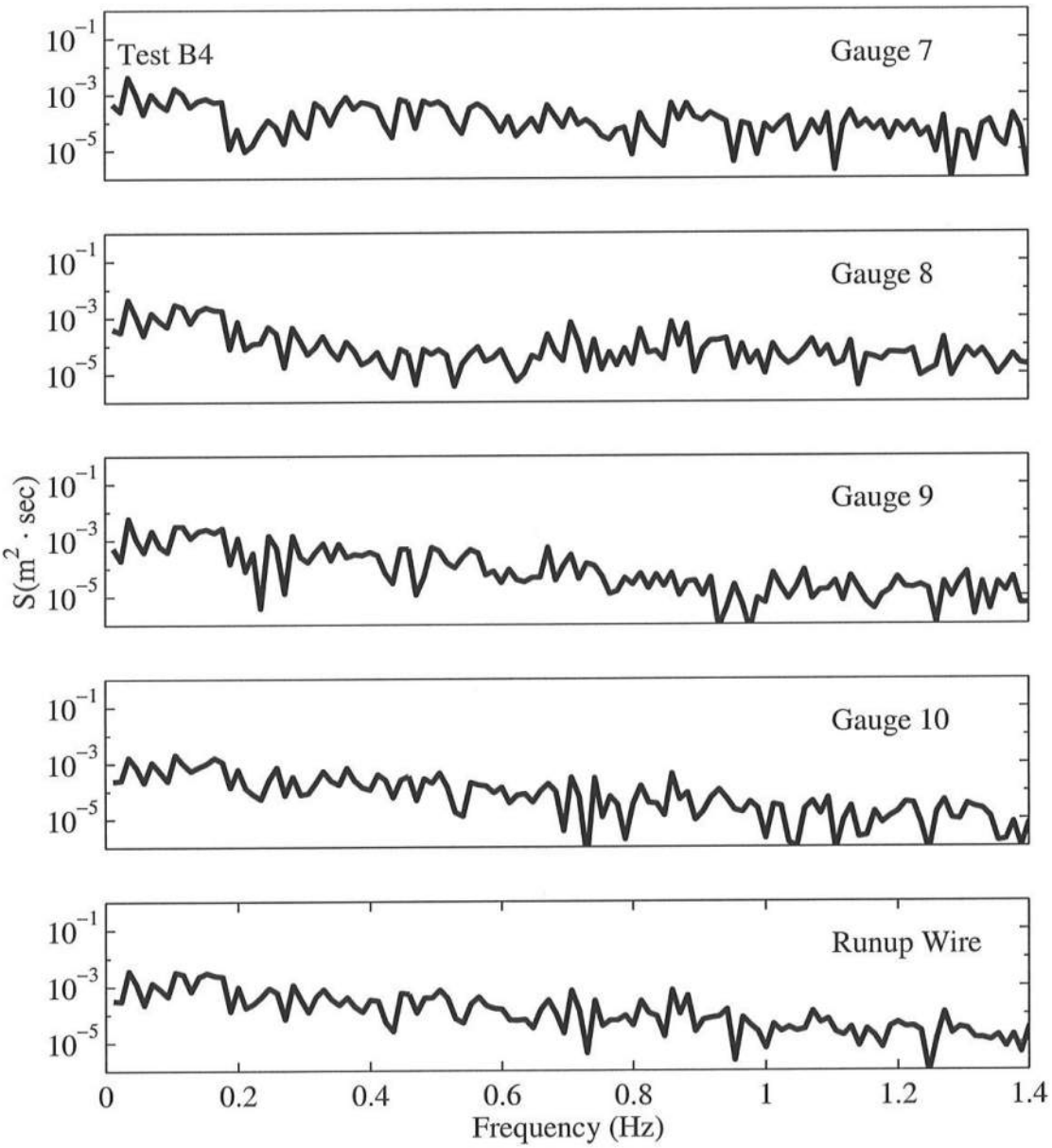

Figure B.20: Frequency Spectra for $T_p = 2.4$ s, $d_t = 4$ cm, for Gauge 7 – Runup Wire.

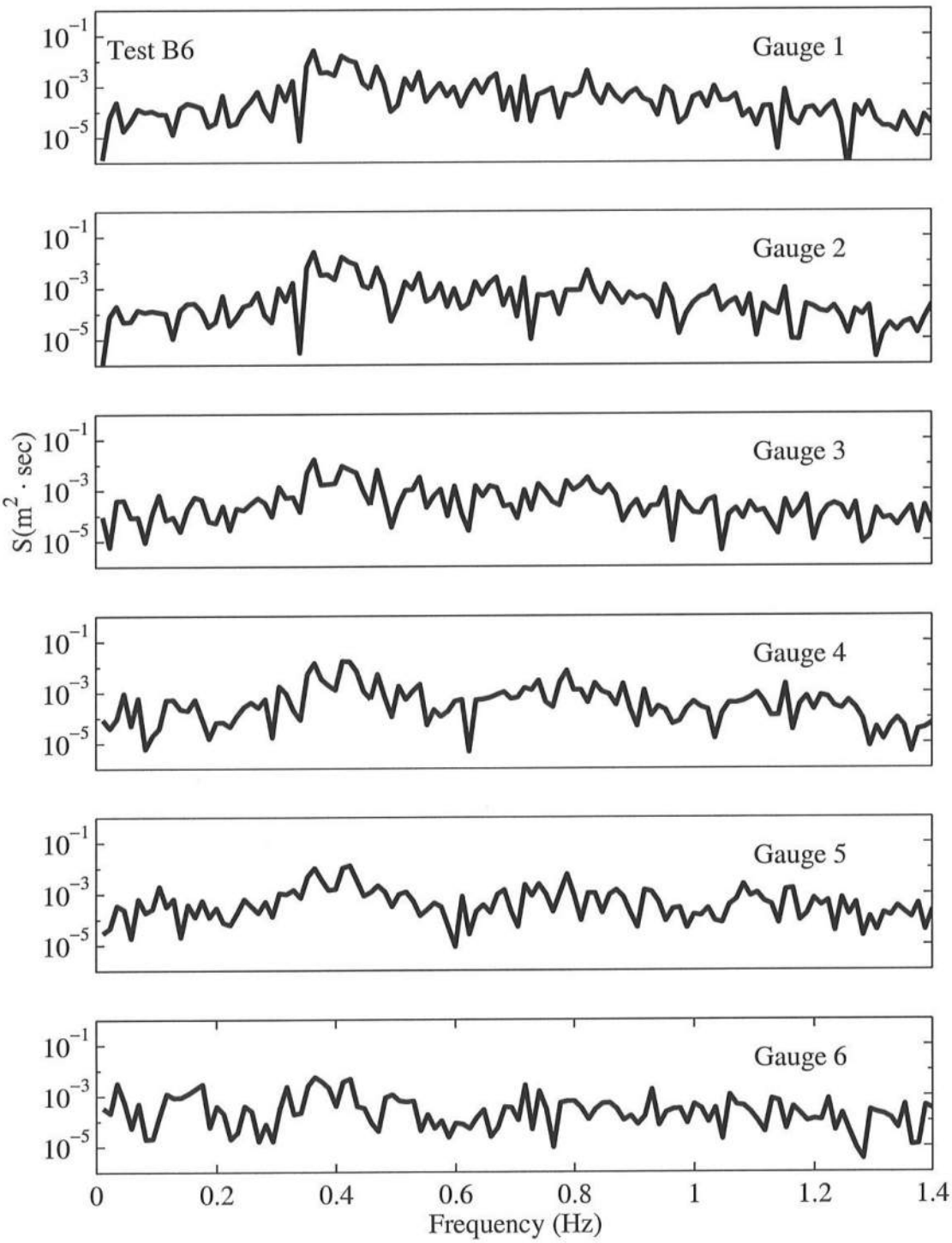

Figure B.21: Frequency Spectra for $T_p = 2.4$ s, $d_t = 6$ cm, for Gauge 1 – Gauge 6.

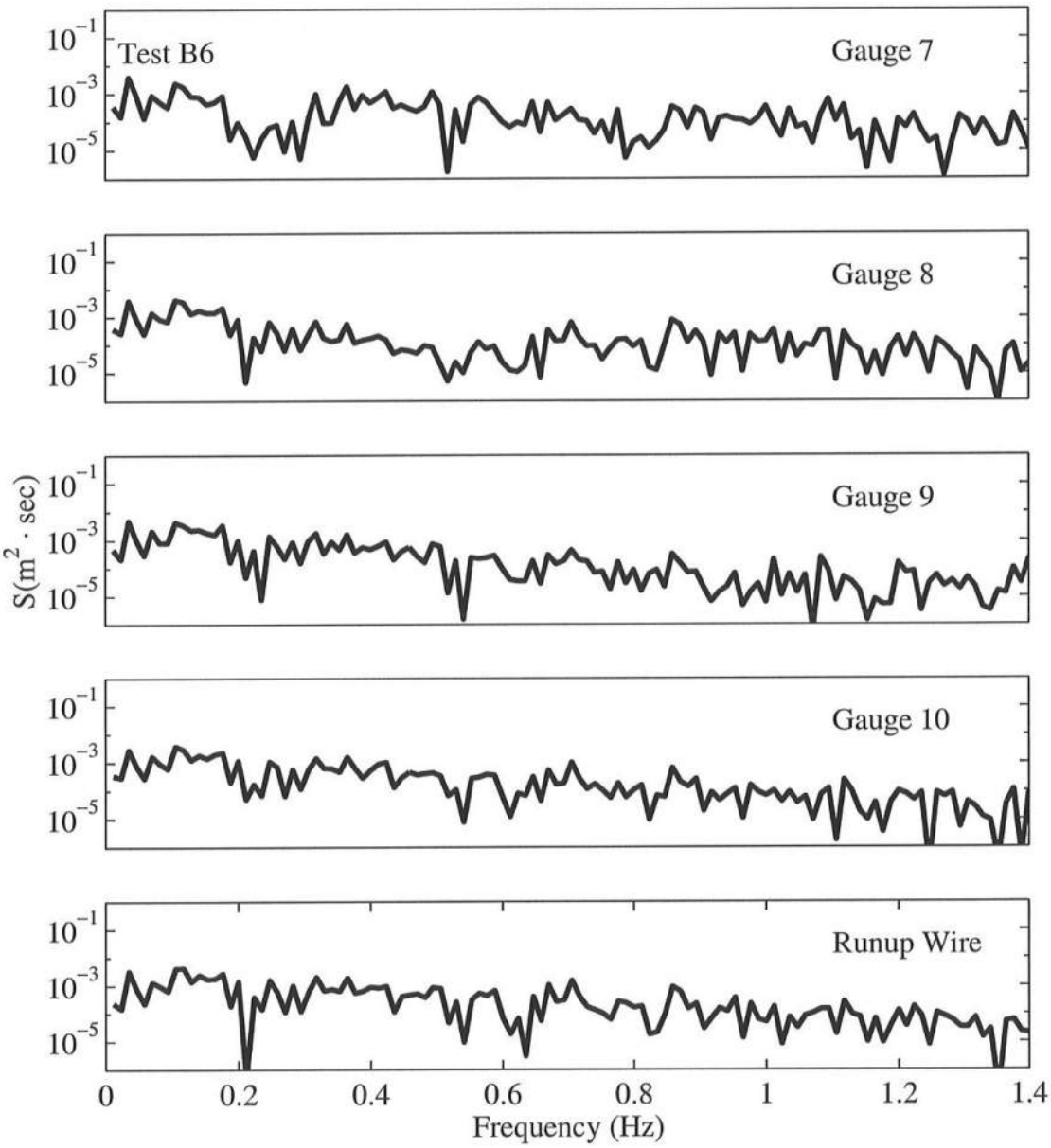

Figure B.22: Frequency Spectra for $T_p = 2.4$ s, $d_t = 6$ cm, for Gauge 7 – Runup Wire.

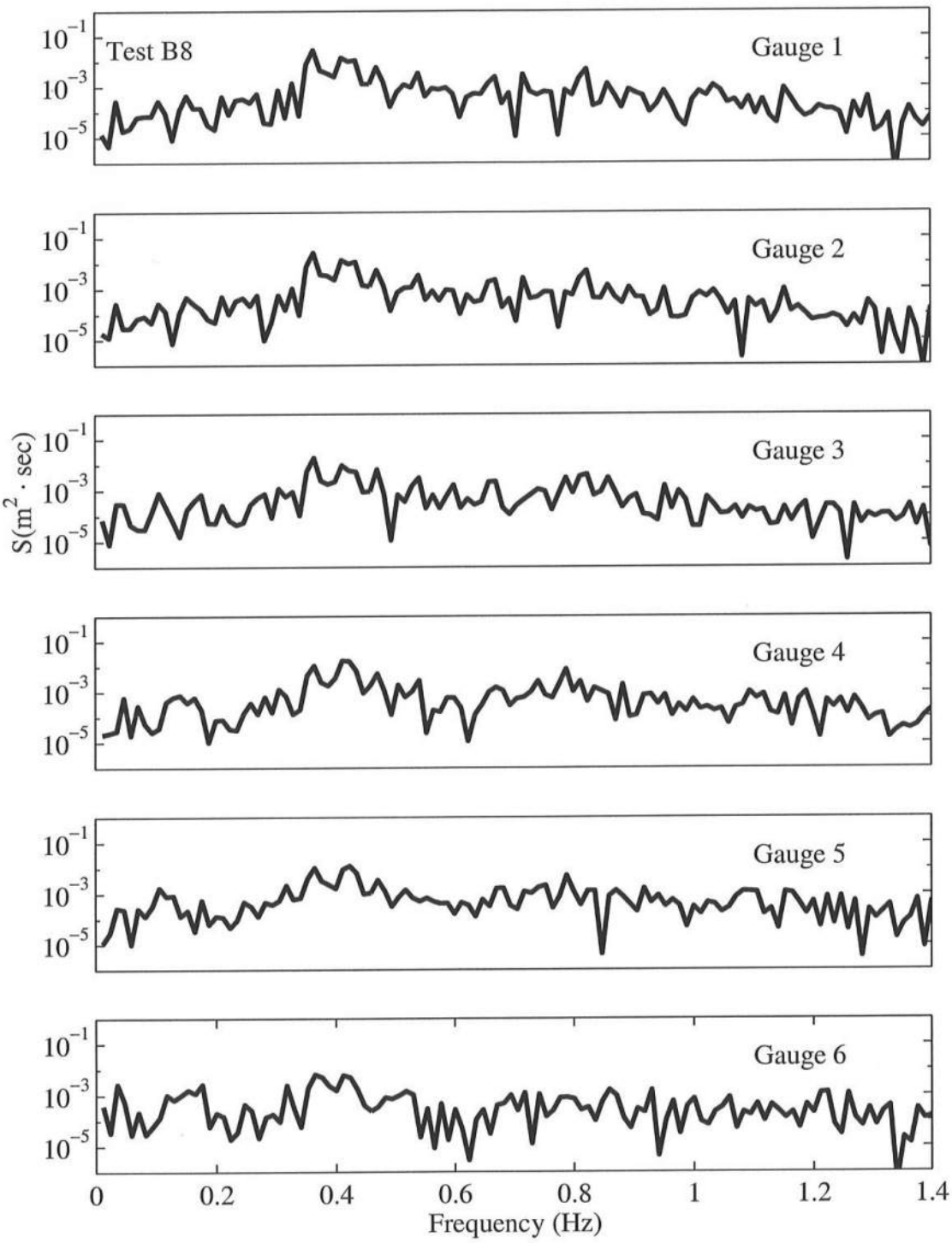

Figure B.23: Frequency Spectra for $T_p = 2.4$ s, $d_t = 8$ cm, for Gauge 1 – Gauge 6.

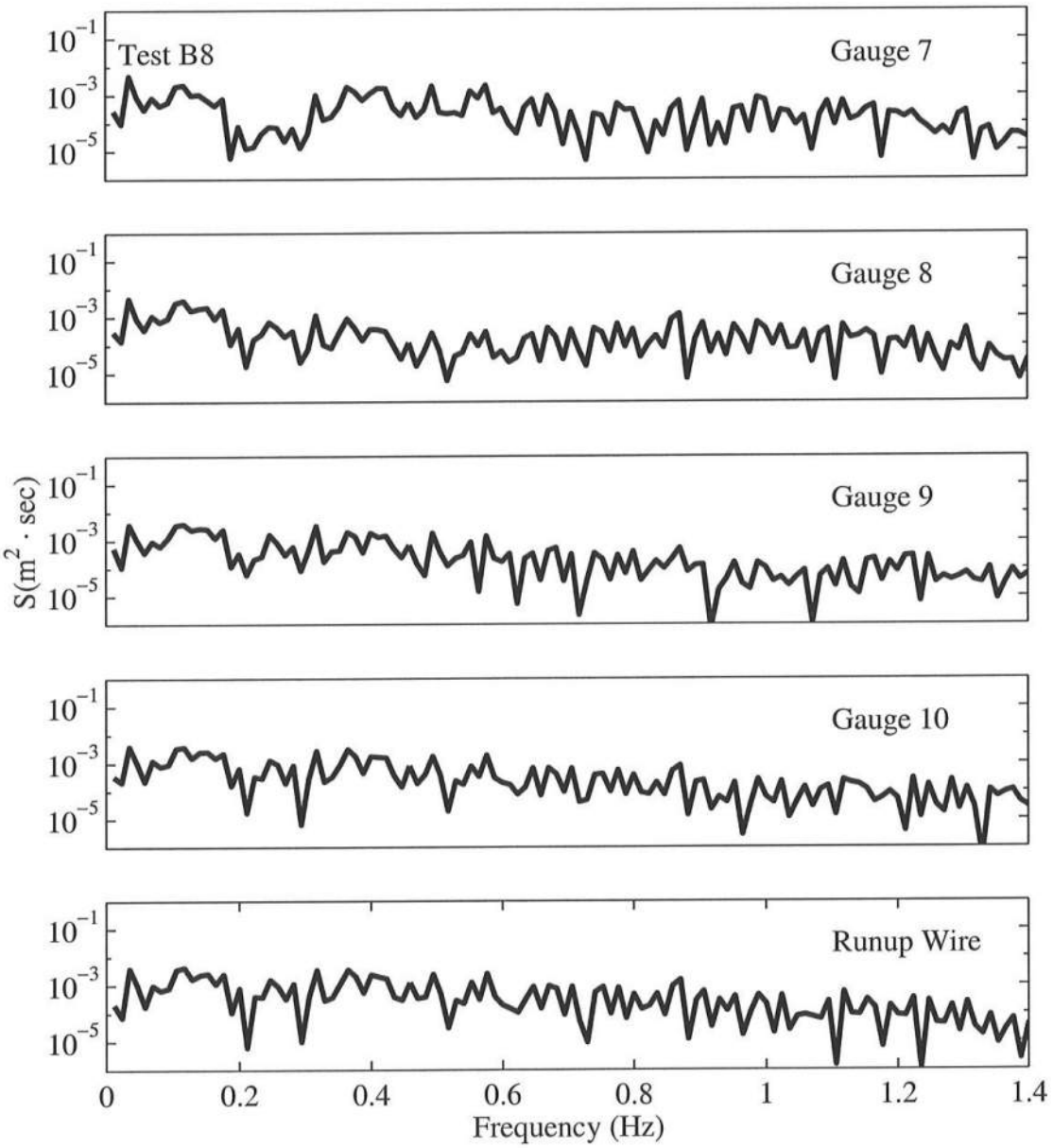

Figure B.24: Frequency Spectra for $T_p = 2.4$ s, $d_t = 8$ cm, for Gauge 7 – Runup Wire.

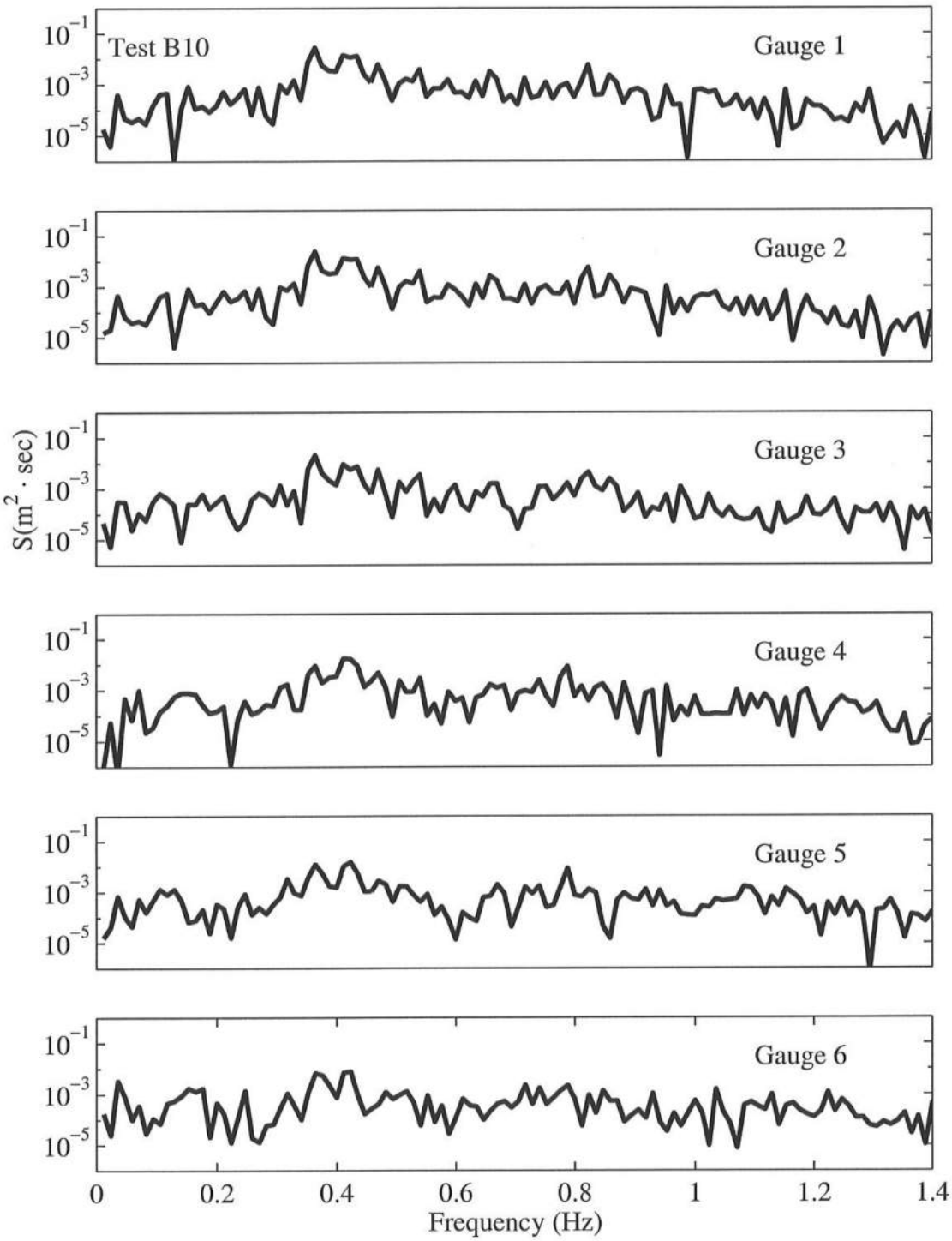

Figure B.25: Frequency Spectra for $T_p = 2.4$ s, $d_t = 10$ cm, for Gauge 1 – Gauge 6.

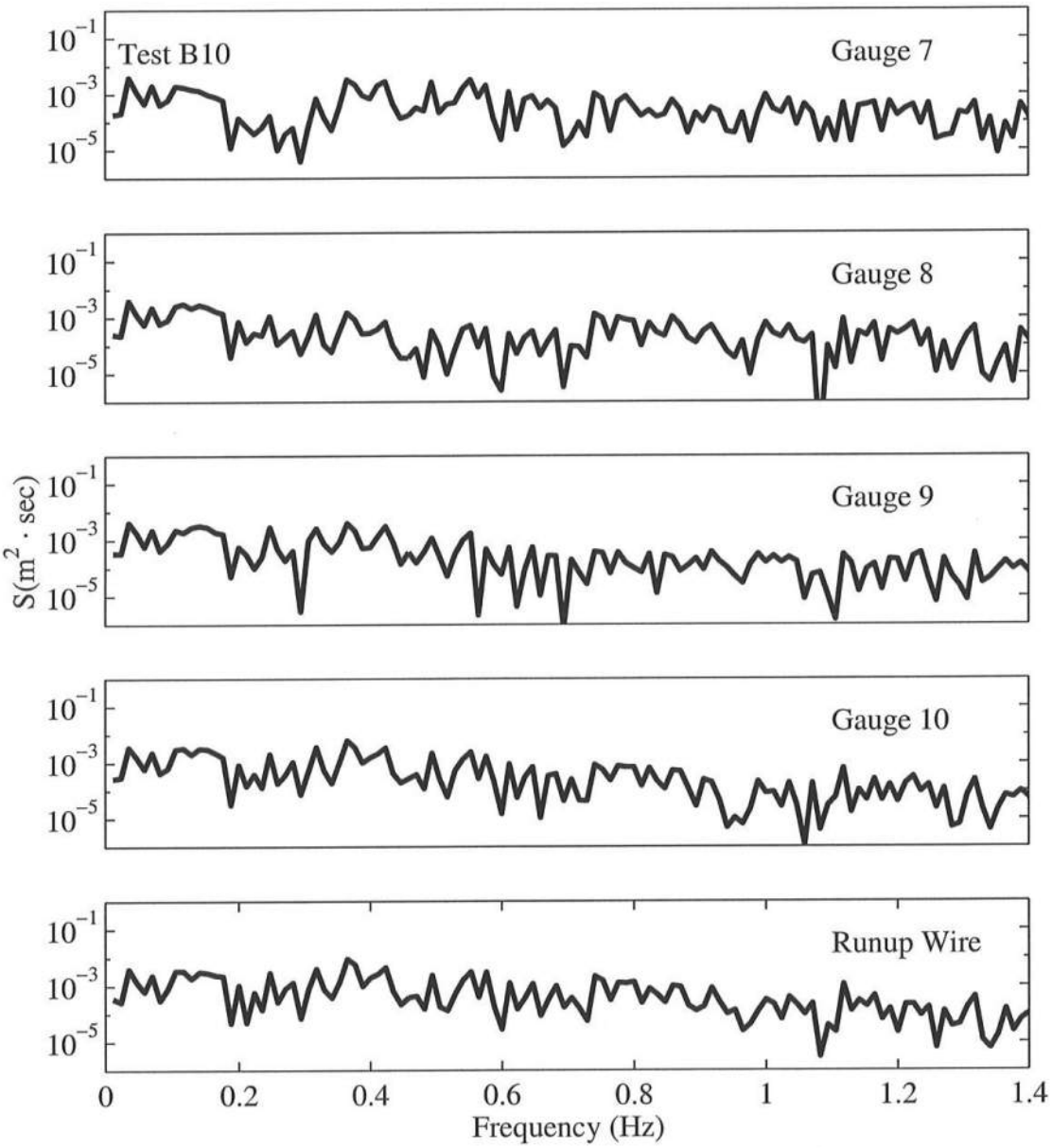

Figure B.26: Frequency Spectra for $T_p = 2.4$ s, $d_t = 10$ cm, for Gauge 7 – Runup Wire.

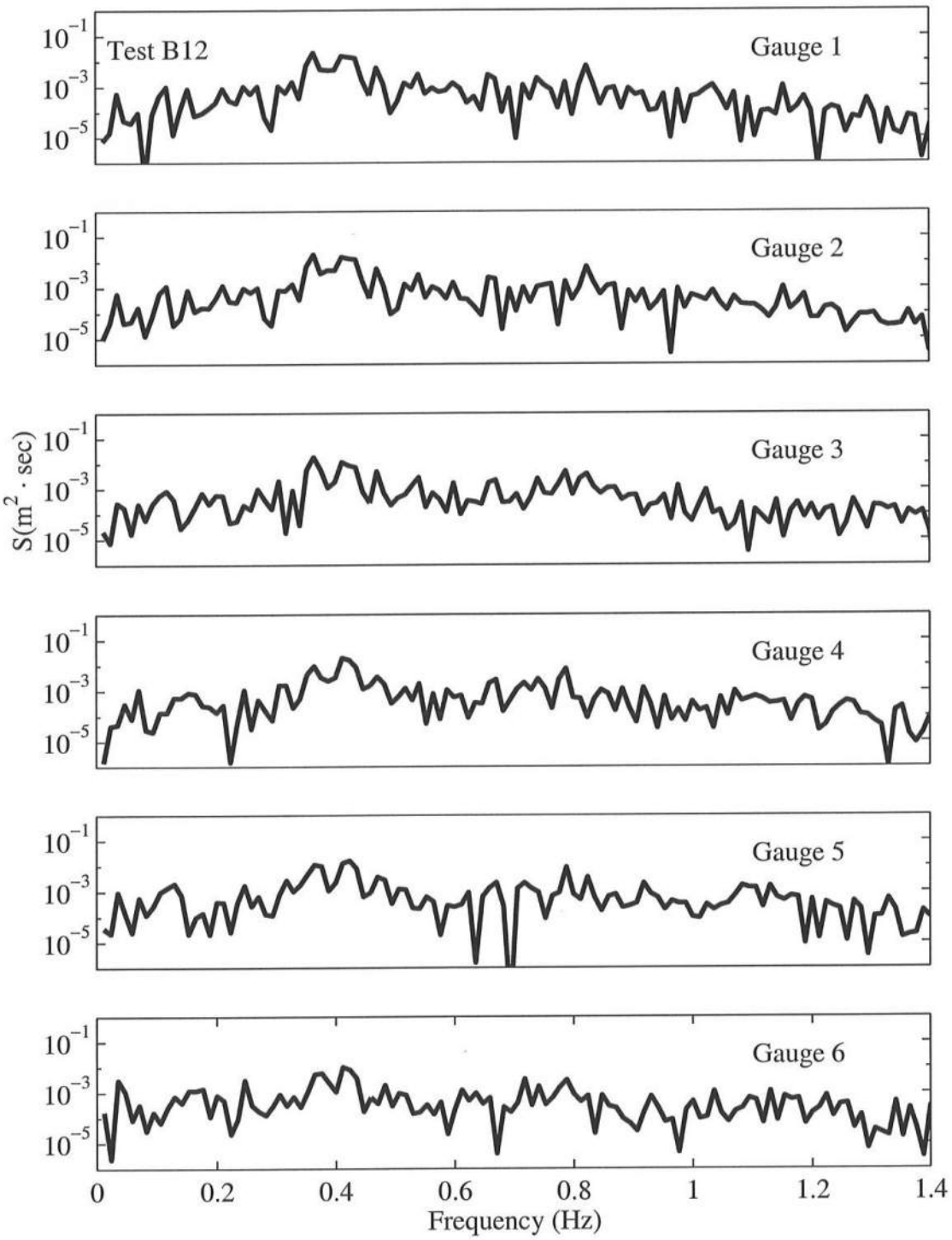

Figure B.27: Frequency Spectra for $T_p = 2.4$ s, $d_t = 12$ cm, for Gauge 1 – Gauge 6.

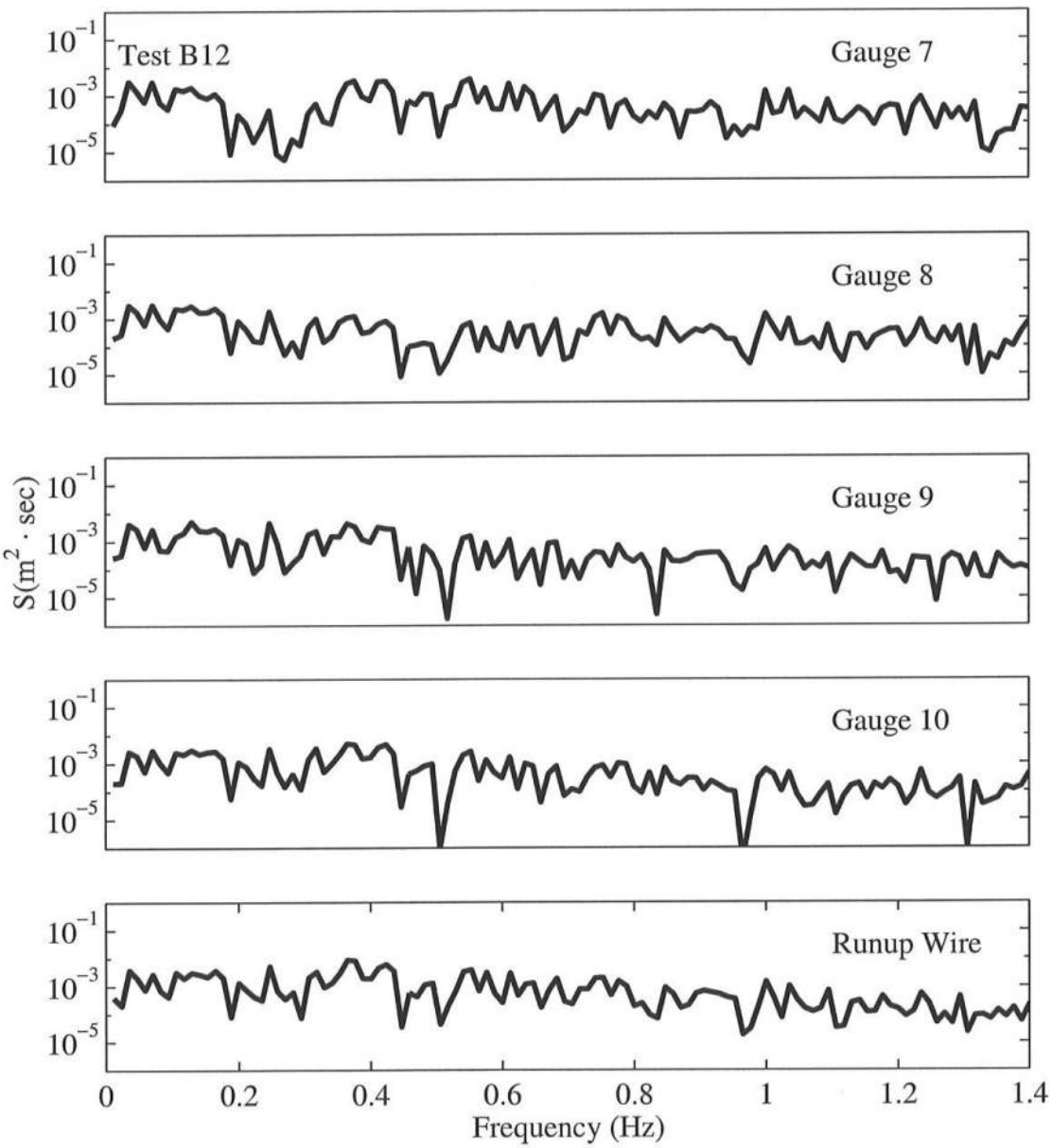

Figure B.28: Frequency Spectra for $T_p = 2.4$ s, $d_t = 12$ cm, for Gauge 7 – Runup Wire.

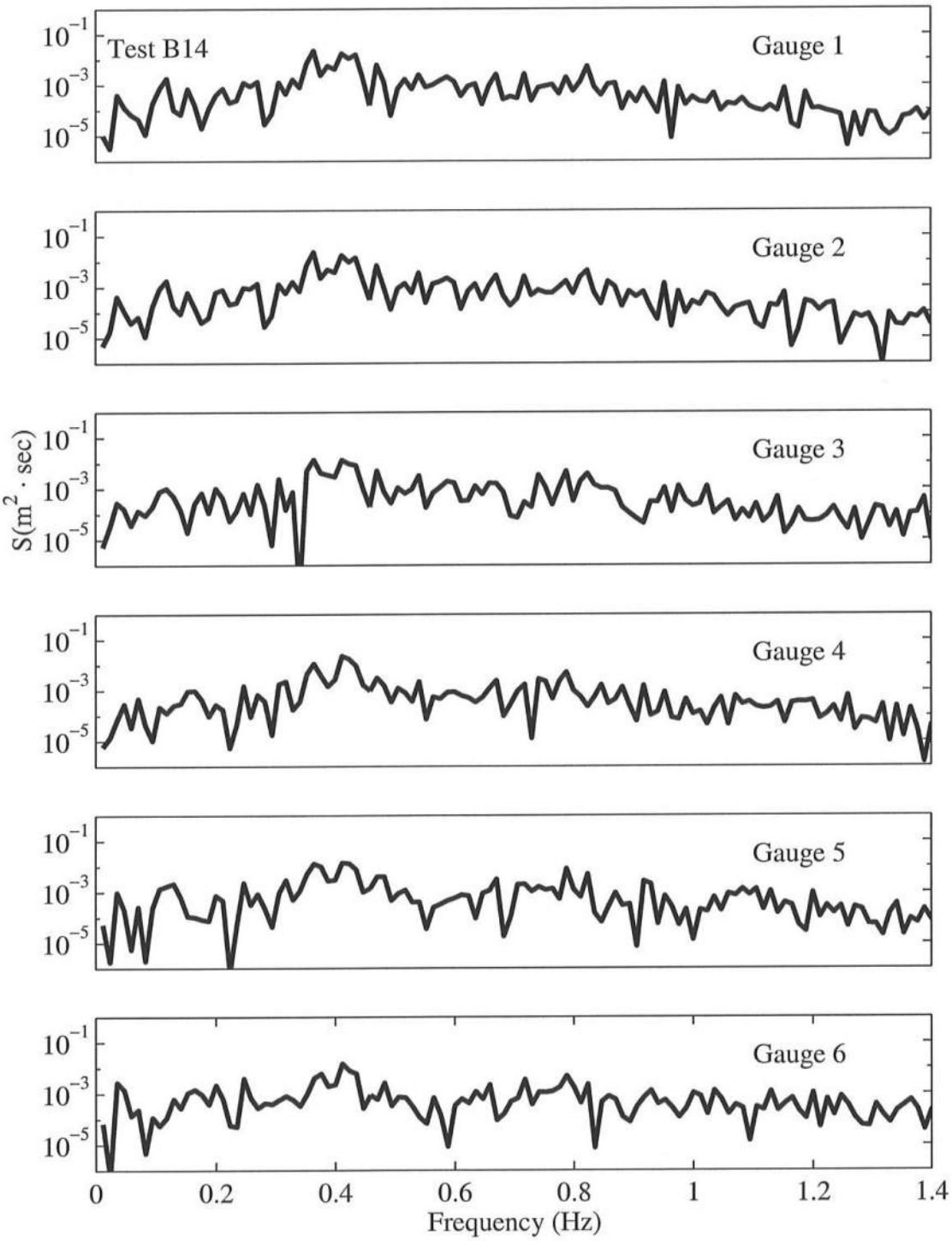

Figure B.29: Frequency Spectra for $T_p = 2.4$ s, $d_t = 14$ cm, for Gauge 1 – Gauge 6.

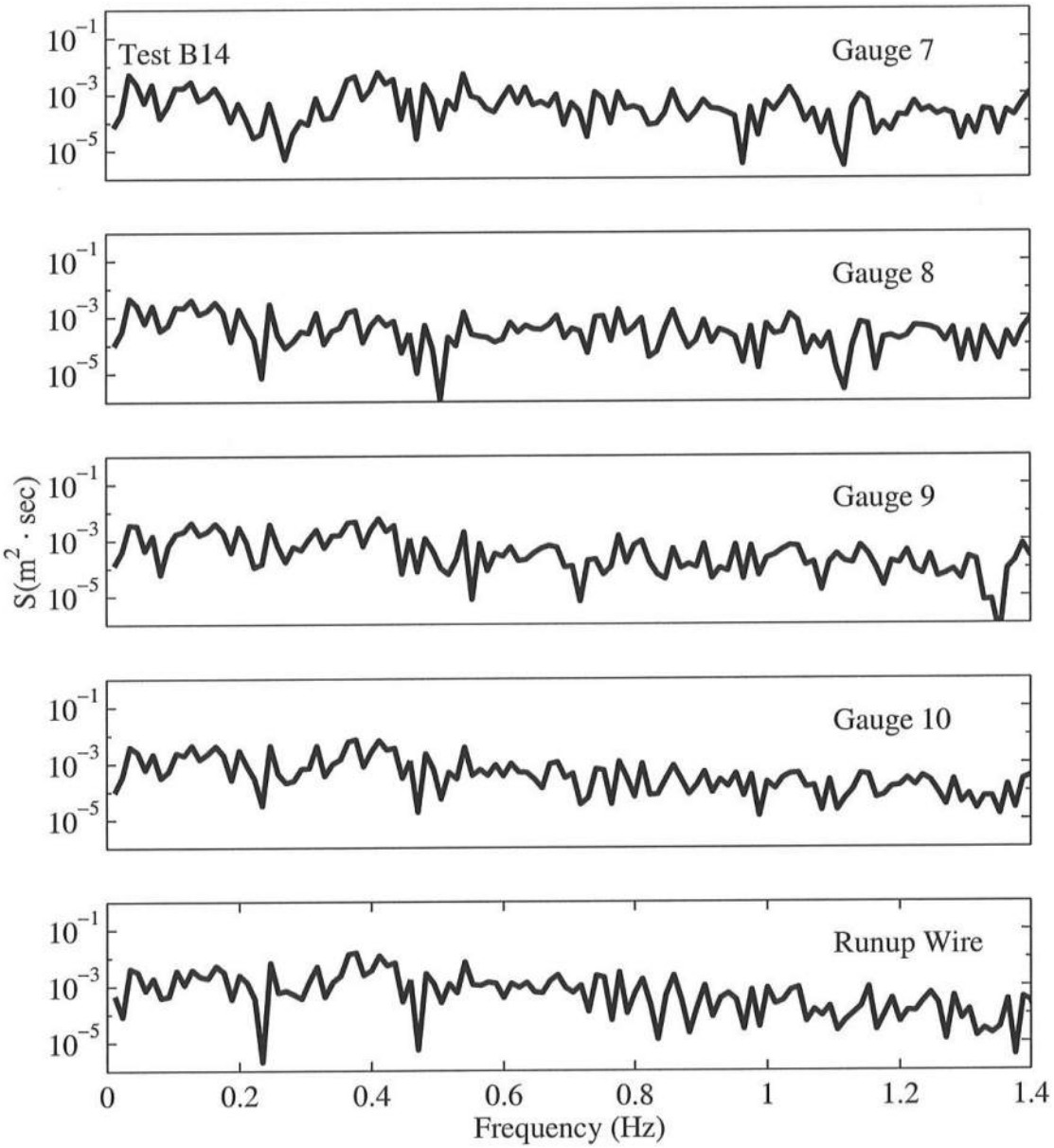

Figure B.30: Frequency Spectra for $T_p = 2.4$ s, $d_t = 14$ cm, for Gauge 7 – Runup Wire.

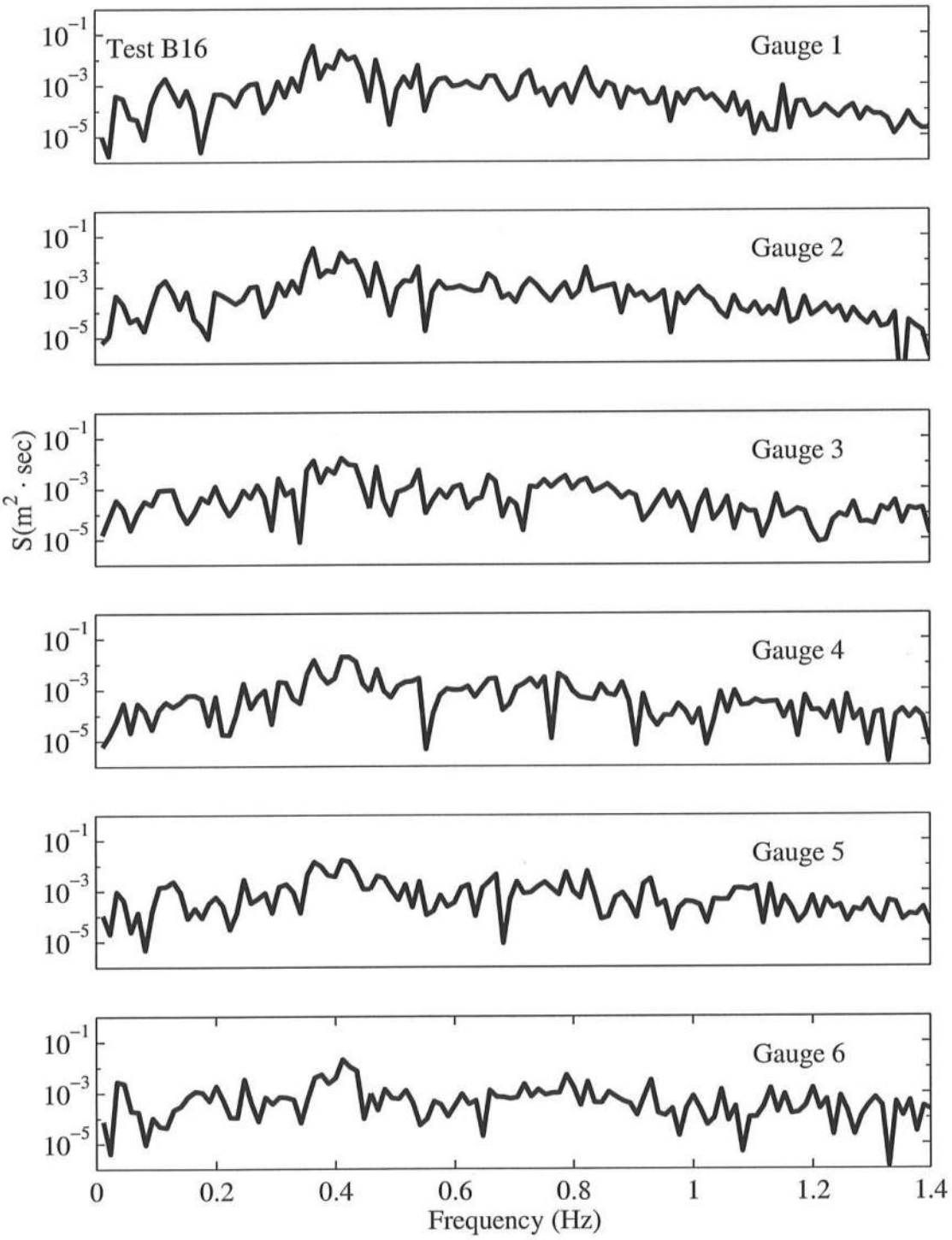

Figure B.31: Frequency Spectra for T_p = 2.4 s, d_t =16 cm, for Gauge 1 – Gauge 6.

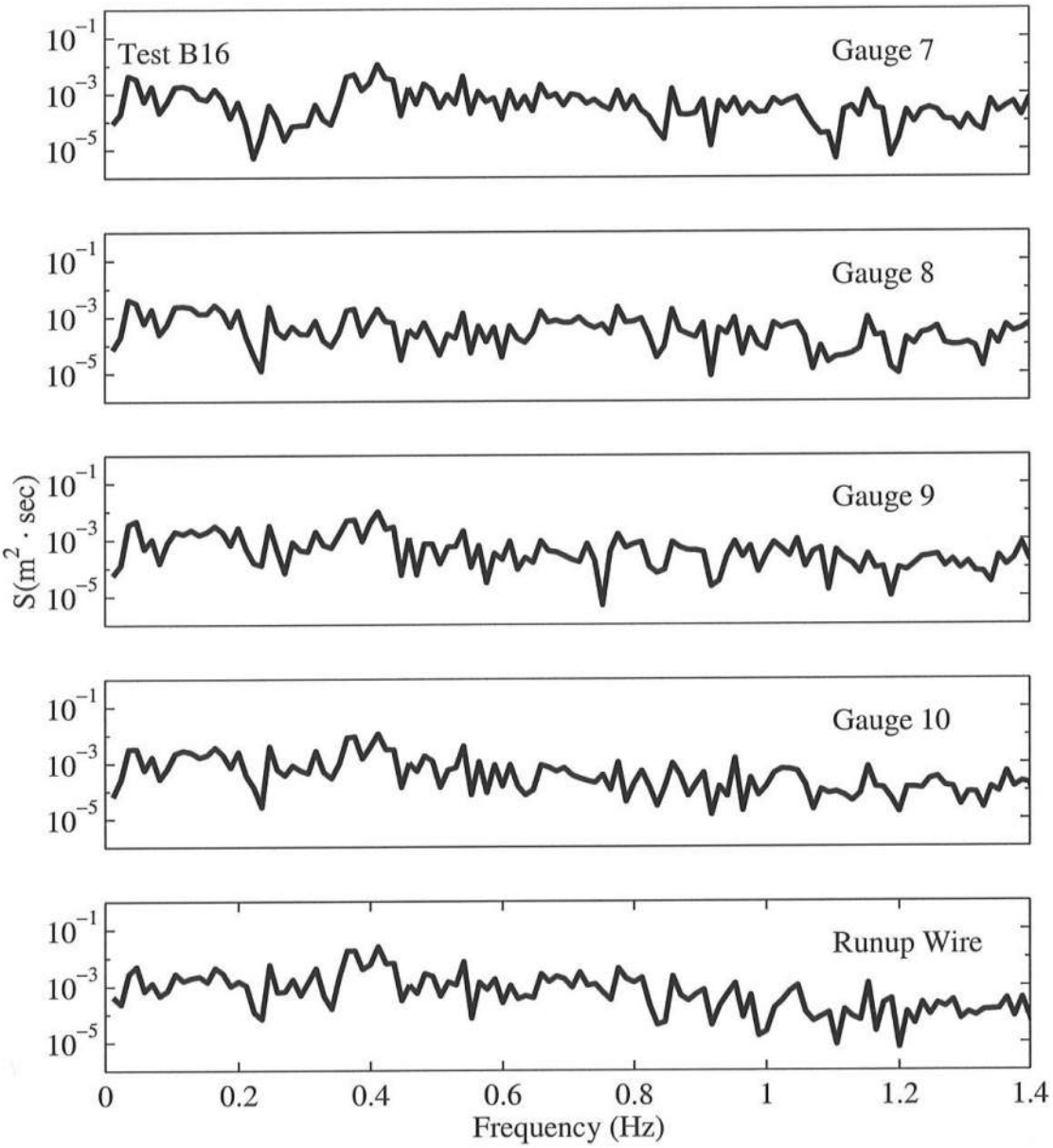

Figure B.32: Frequency Spectra for $T_p = 2.4$ s, $d_t = 16$ cm, for Gauge 7 – Runup Wire.

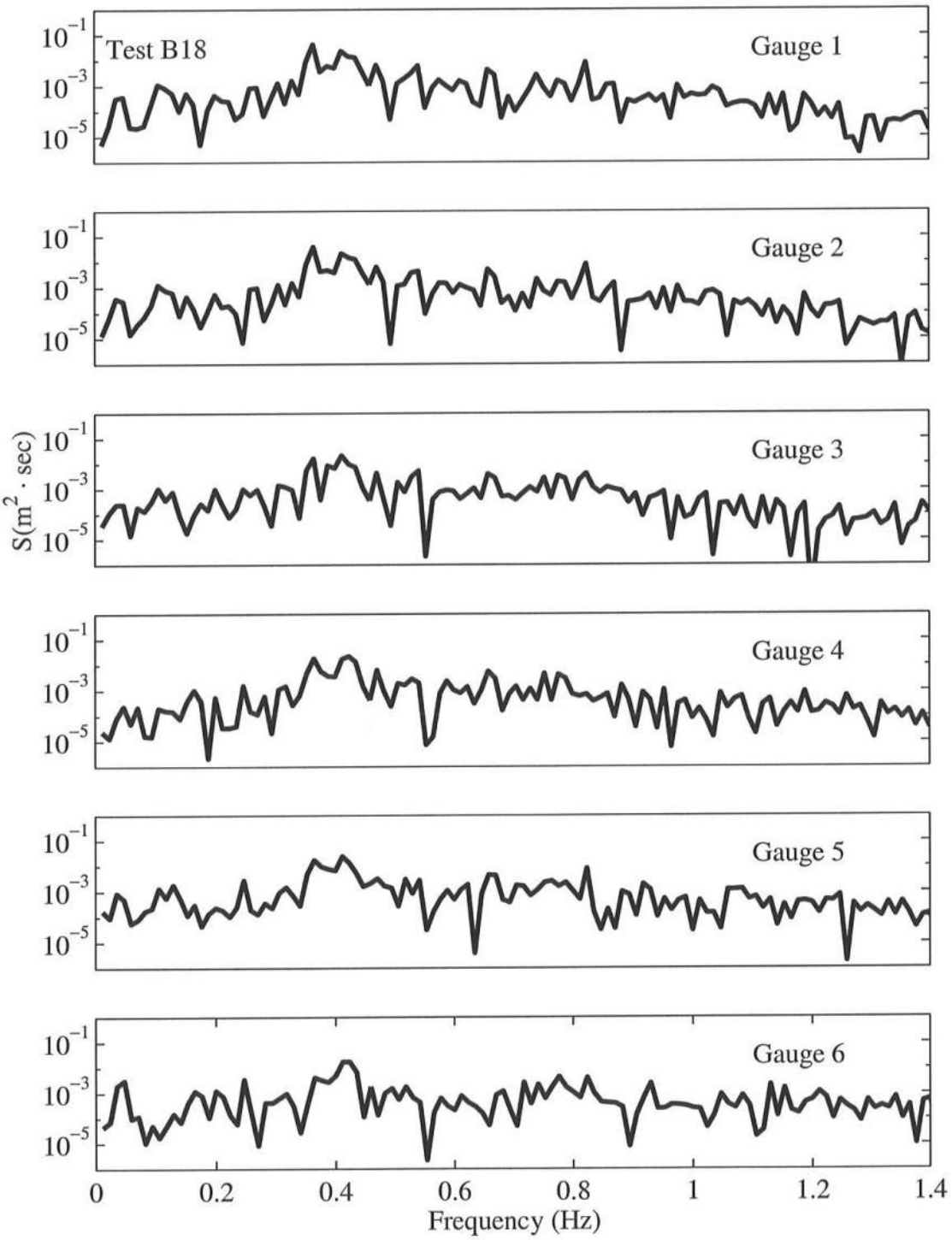

Figure B.33: Frequency Spectra for $T_p = 2.4$ s, $d_t = 18$ cm, for Gauge 1 – Gauge 6.

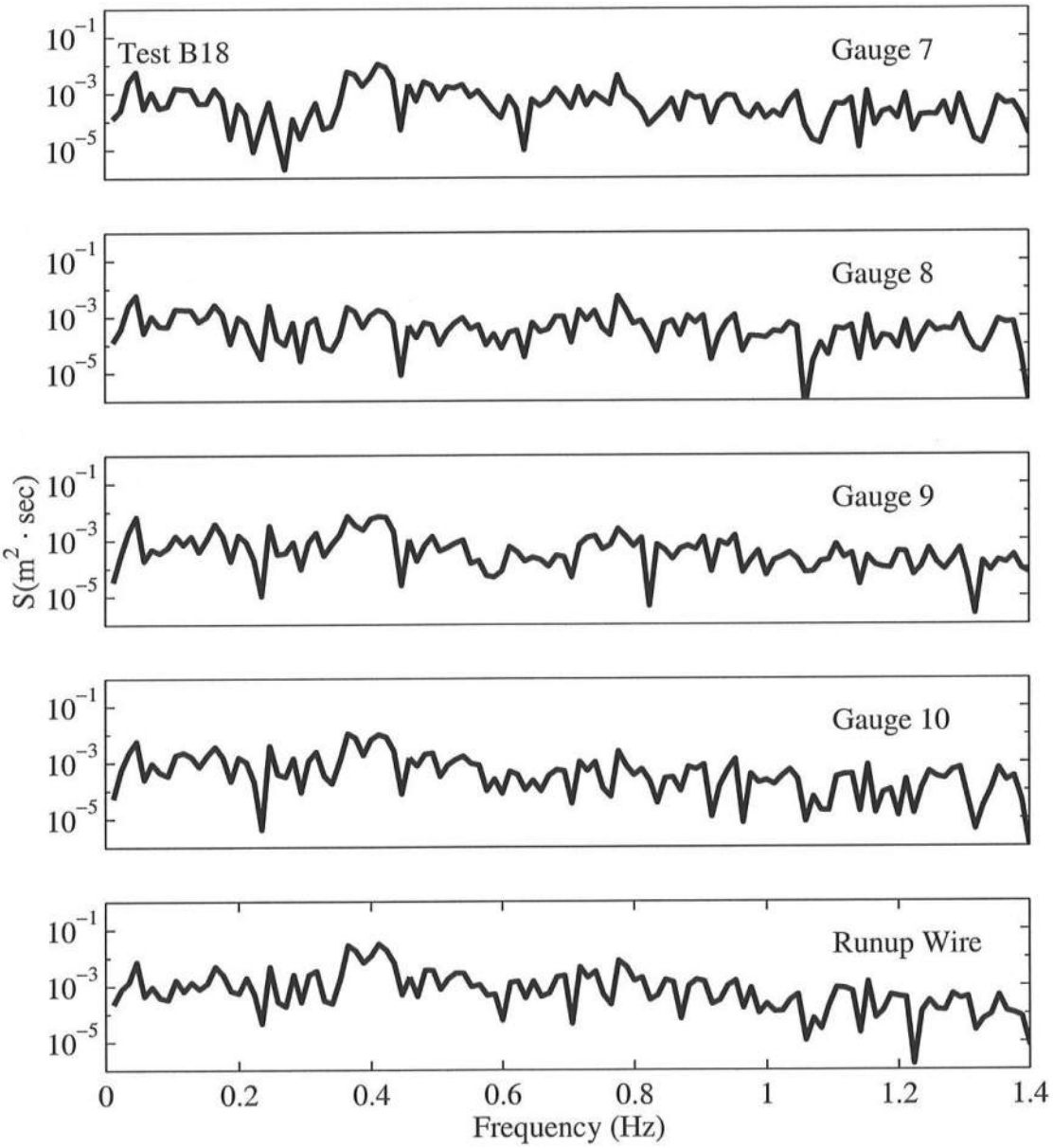

Figure B.34: Frequency Spectra for $T_p = 2.4$ s, $d_t = 18$ cm, for Gauge 7 – Runup Wire.

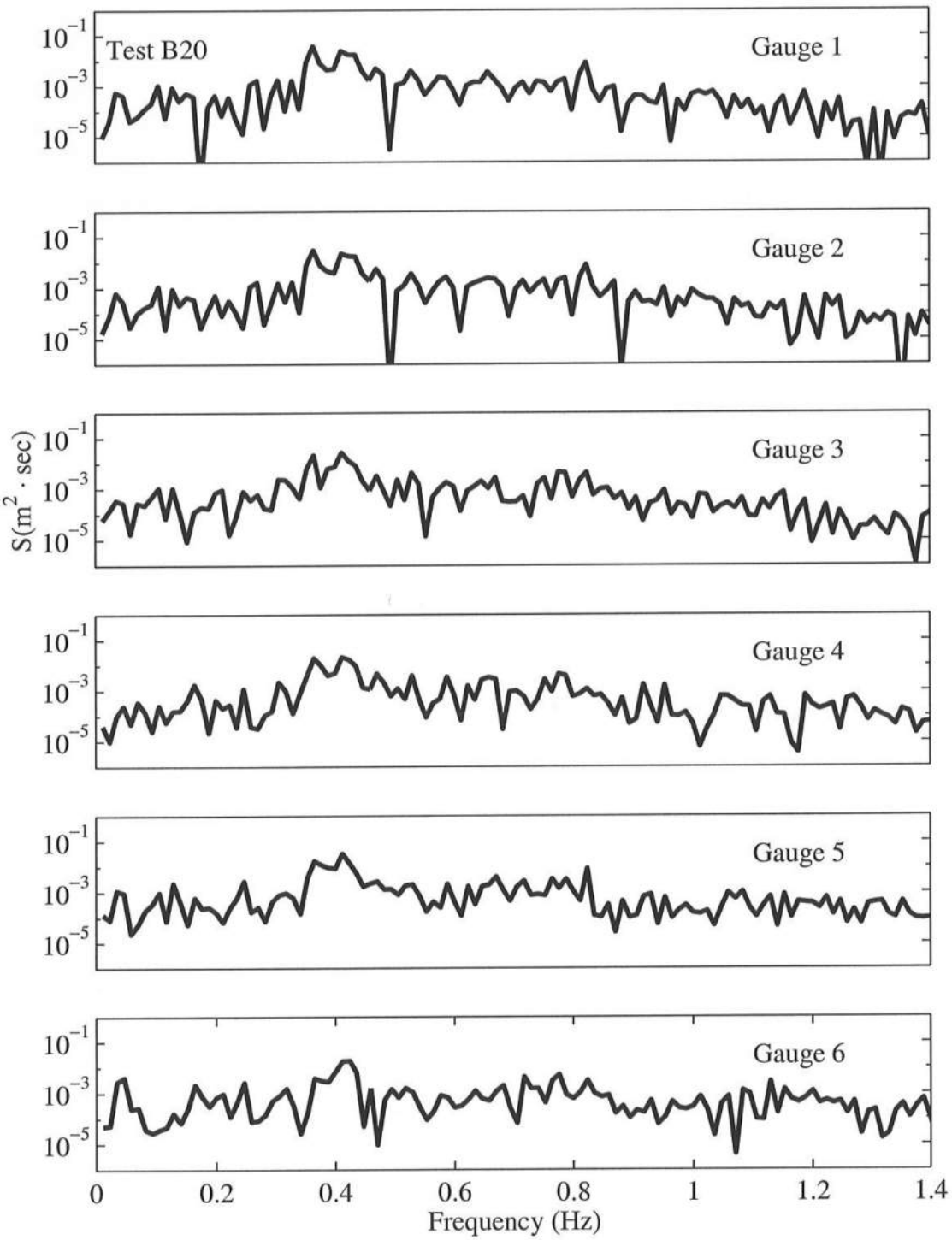

Figure B.35: Frequency Spectra for $T_p = 2.4$ s, $d_t = 20$ cm, for Gauge 1 – Gauge 6.

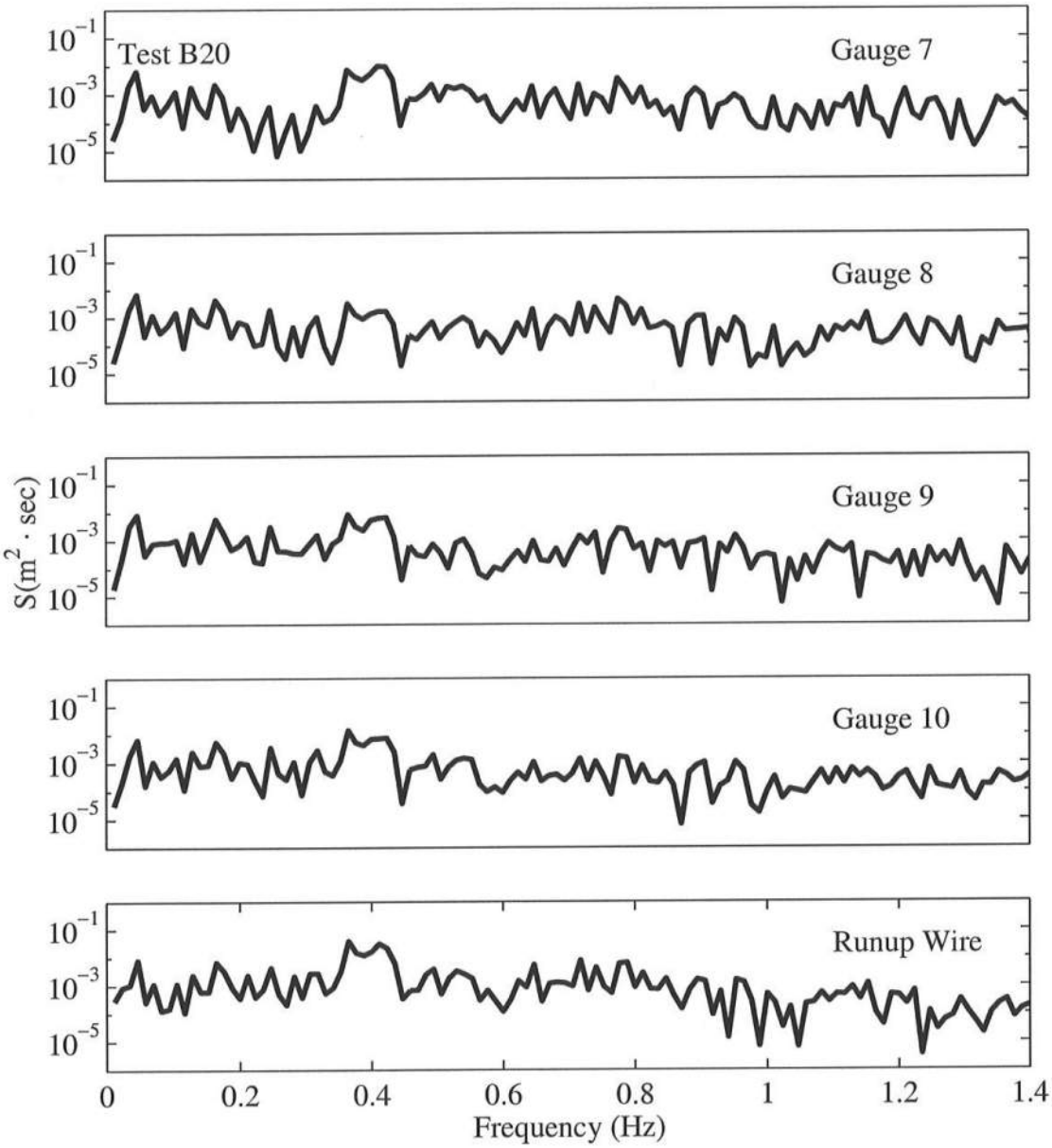

Figure B.36: Frequency Spectra for $T_p = 2.4$ s, $d_t = 20$ cm, for Gauge 7 – Runup Wire.

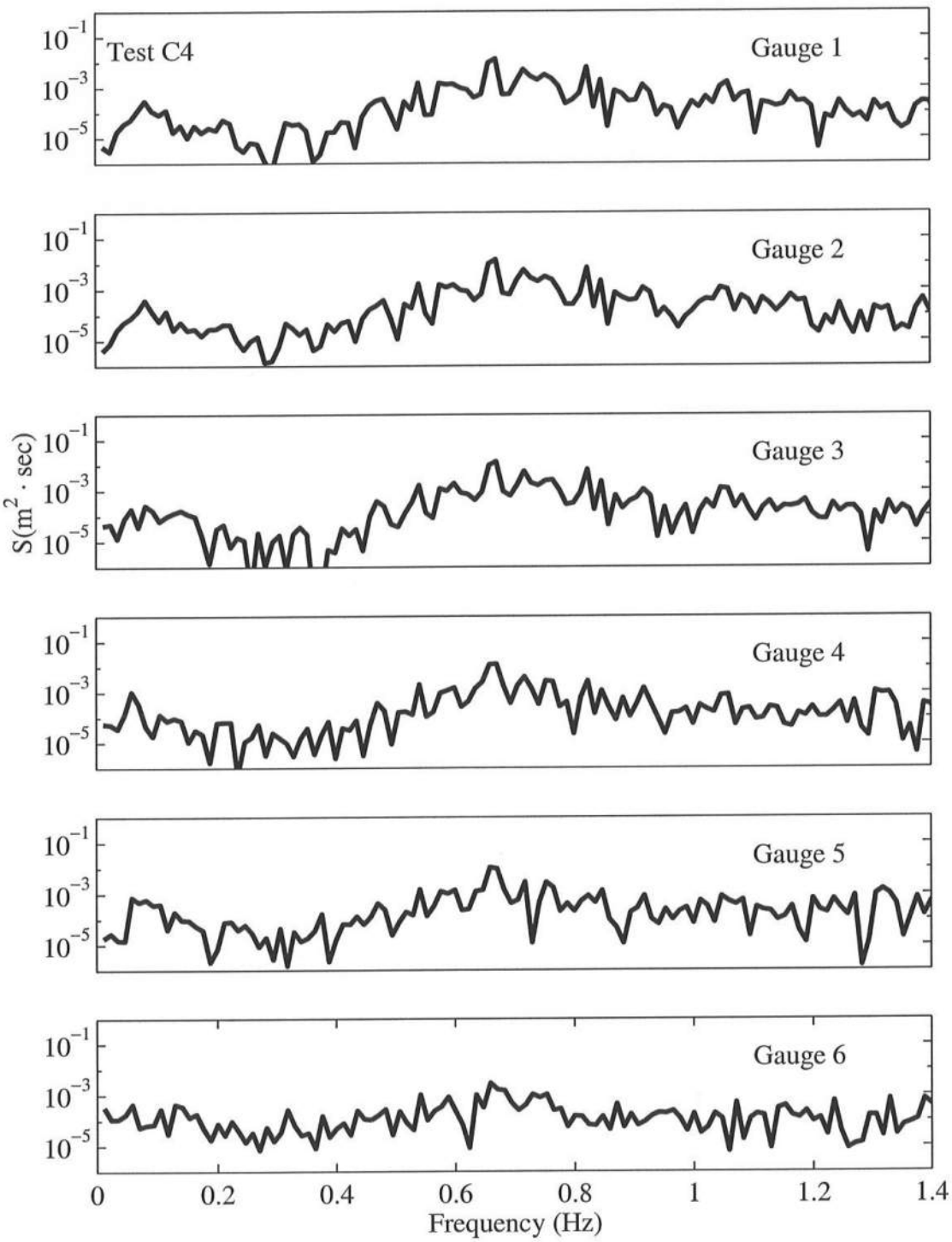

Figure B.37: Frequency Spectra for $T_p = 1.5$ s, $d_t = 4$ cm, for Gauge 1 – Gauge 6.

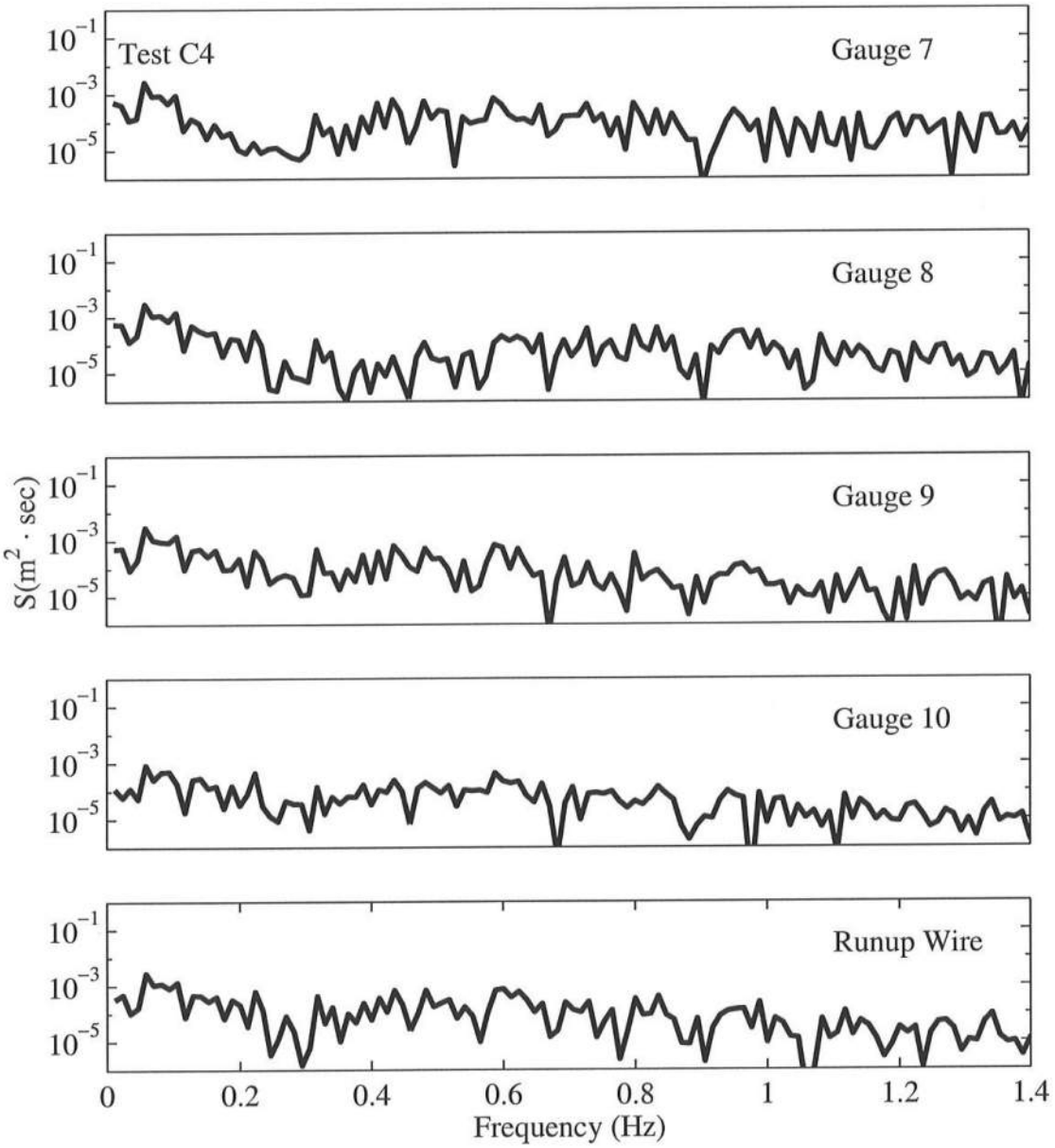

Figure B.38: Frequency Spectra for $T_p = 1.5$ s, $d_t = 4$ cm, for Gauge 7 – Runup Wire.

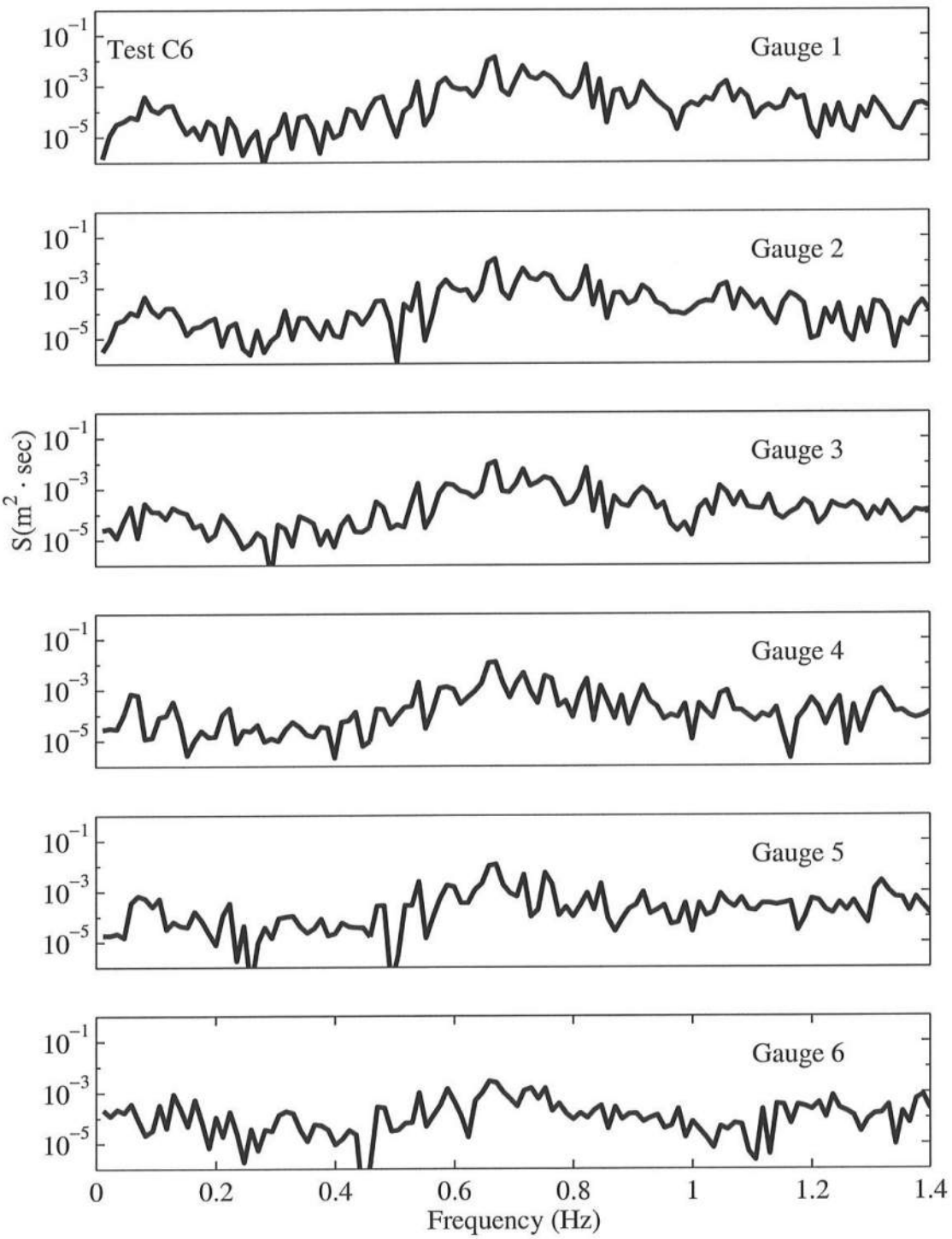

Figure B.39: Frequency Spectra for $T_p = 1.5$ s, $d_t = 6$ cm, for Gauge 1 – Gauge 6.

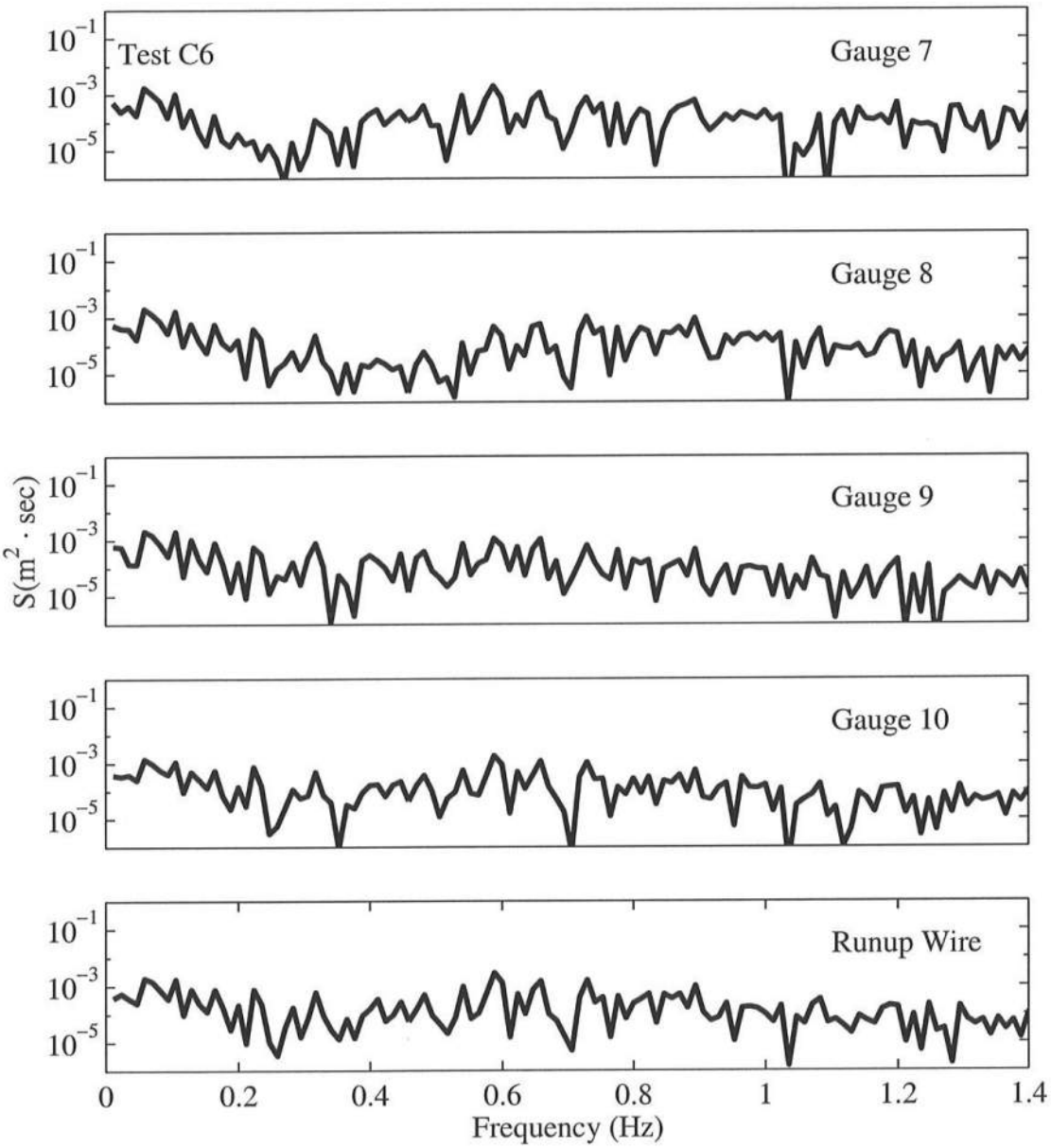

Figure B.40: Frequency Spectra for T_p = 1.5 s, d_t = 6 cm, for Gauge 7 – Runup Wire.

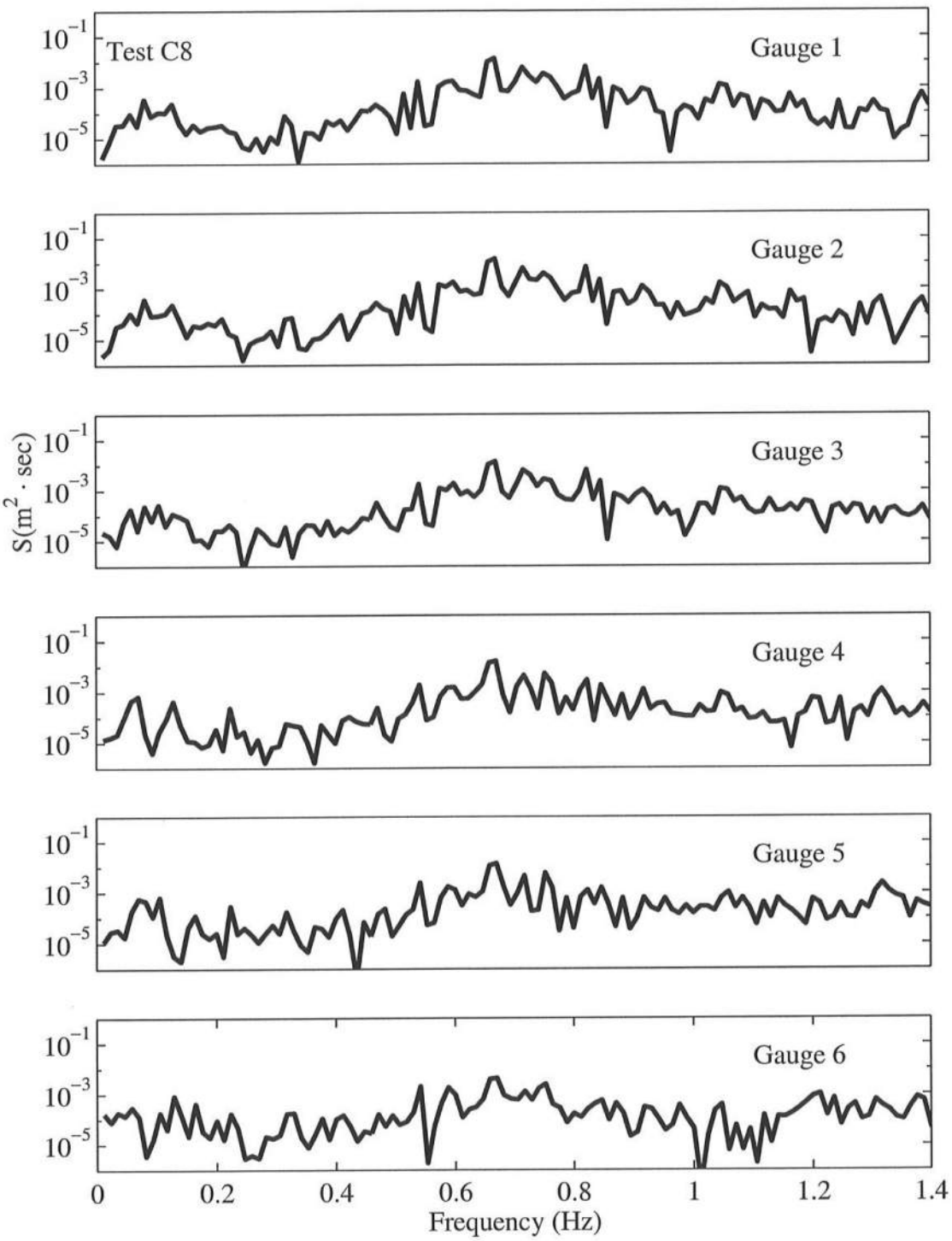

Figure B.41: Frequency Spectra for $T_p = 1.5$ s, $d_t = 8$ cm, for Gauge 1 – Gauge 6.

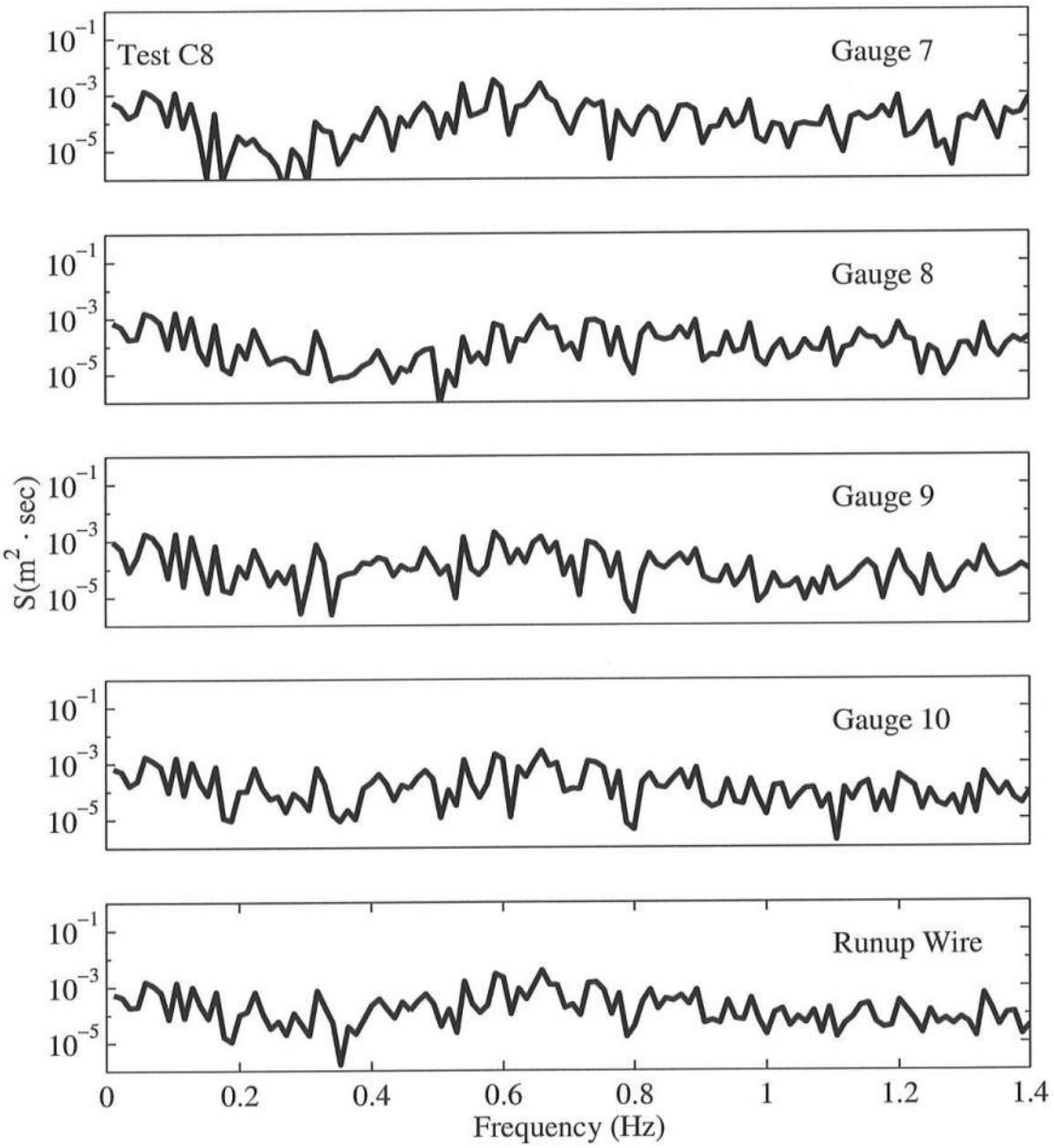

Figure B.42: Frequency Spectra for $T_p = 1.5$ s, $d_t = 8$ cm, for Gauge 7 – Runup Wire.

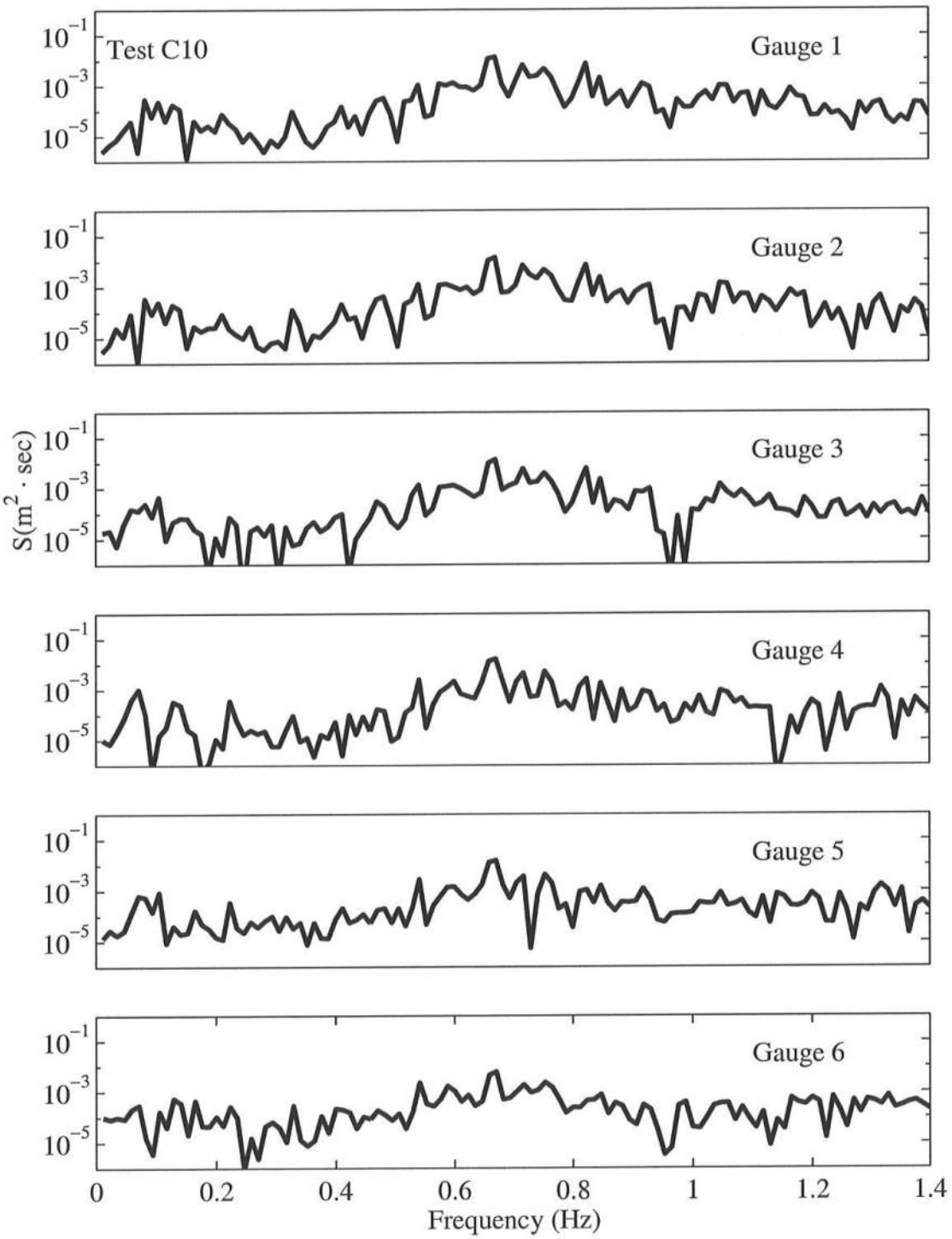

Figure B.43: Frequency Spectra for T_p = 1.5 s, d_t = 10 cm, for Gauge 1 – Gauge 6.

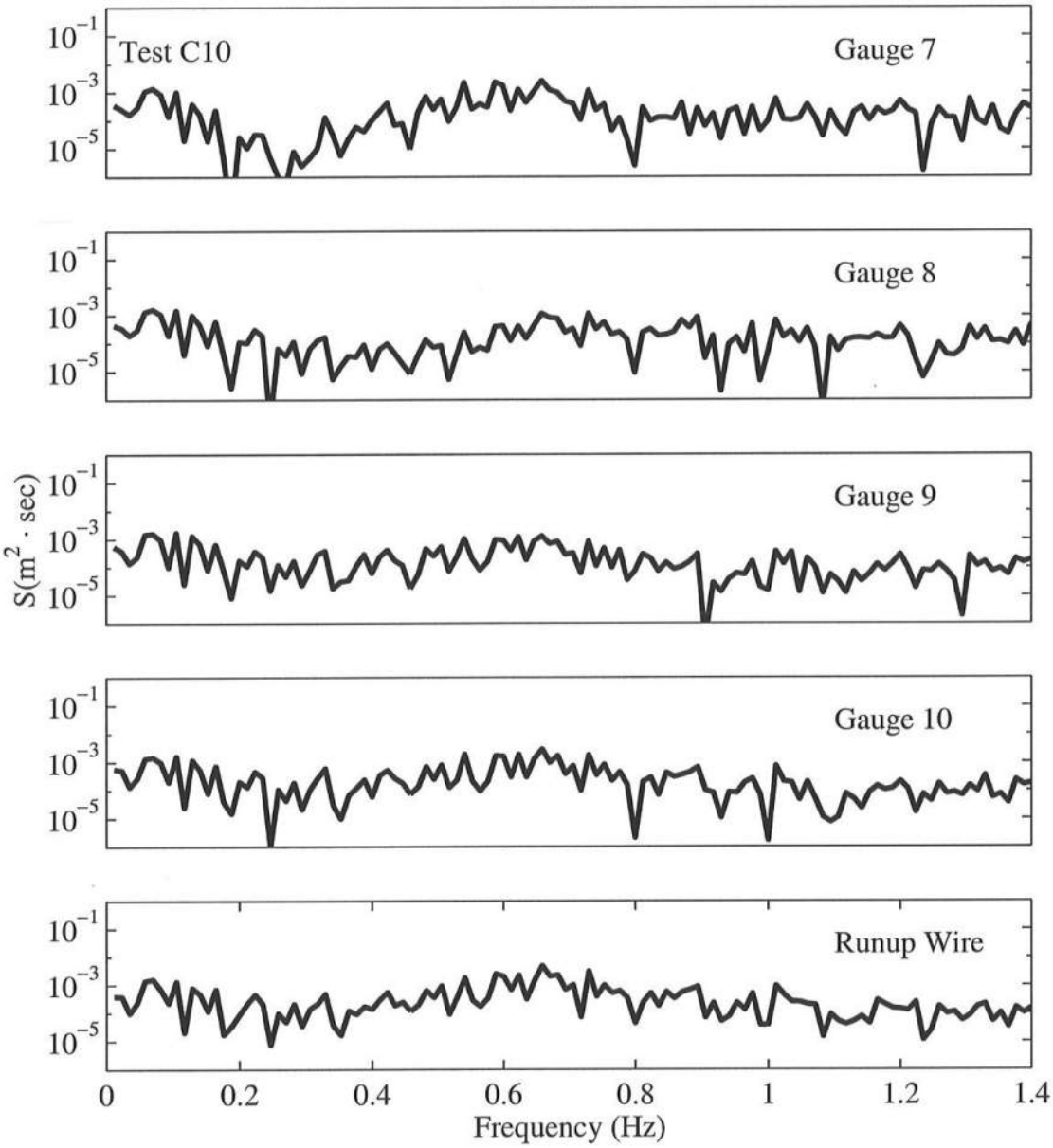

Figure B.44: Frequency Spectra for T_p = 1.5 s, d_t = 10 cm, for Gauge 7 – Runup Wire.

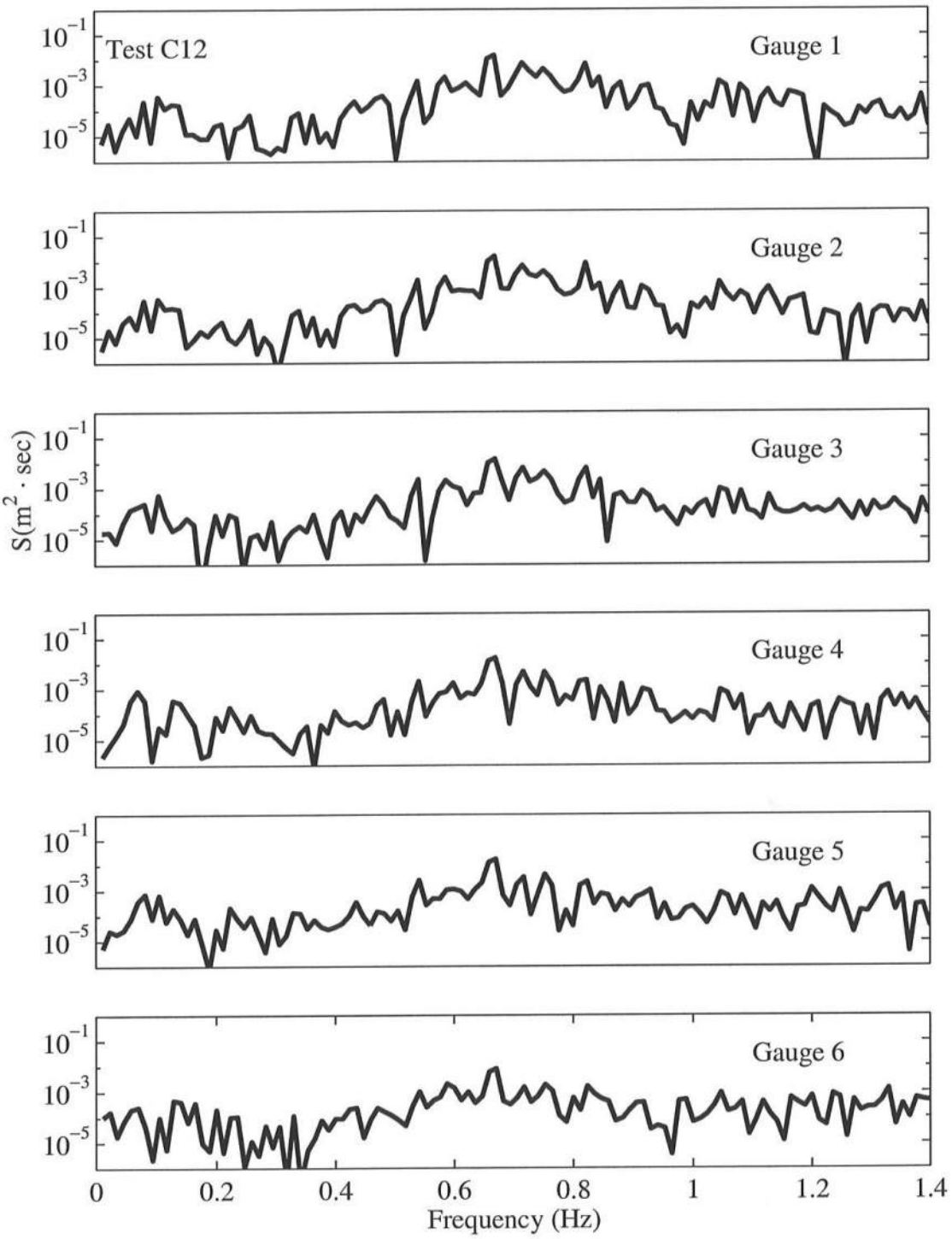

Figure B.45: Frequency Spectra for $T_p = 1.5$ s, $d_t = 12$ cm, for Gauge 1 – Gauge 6.

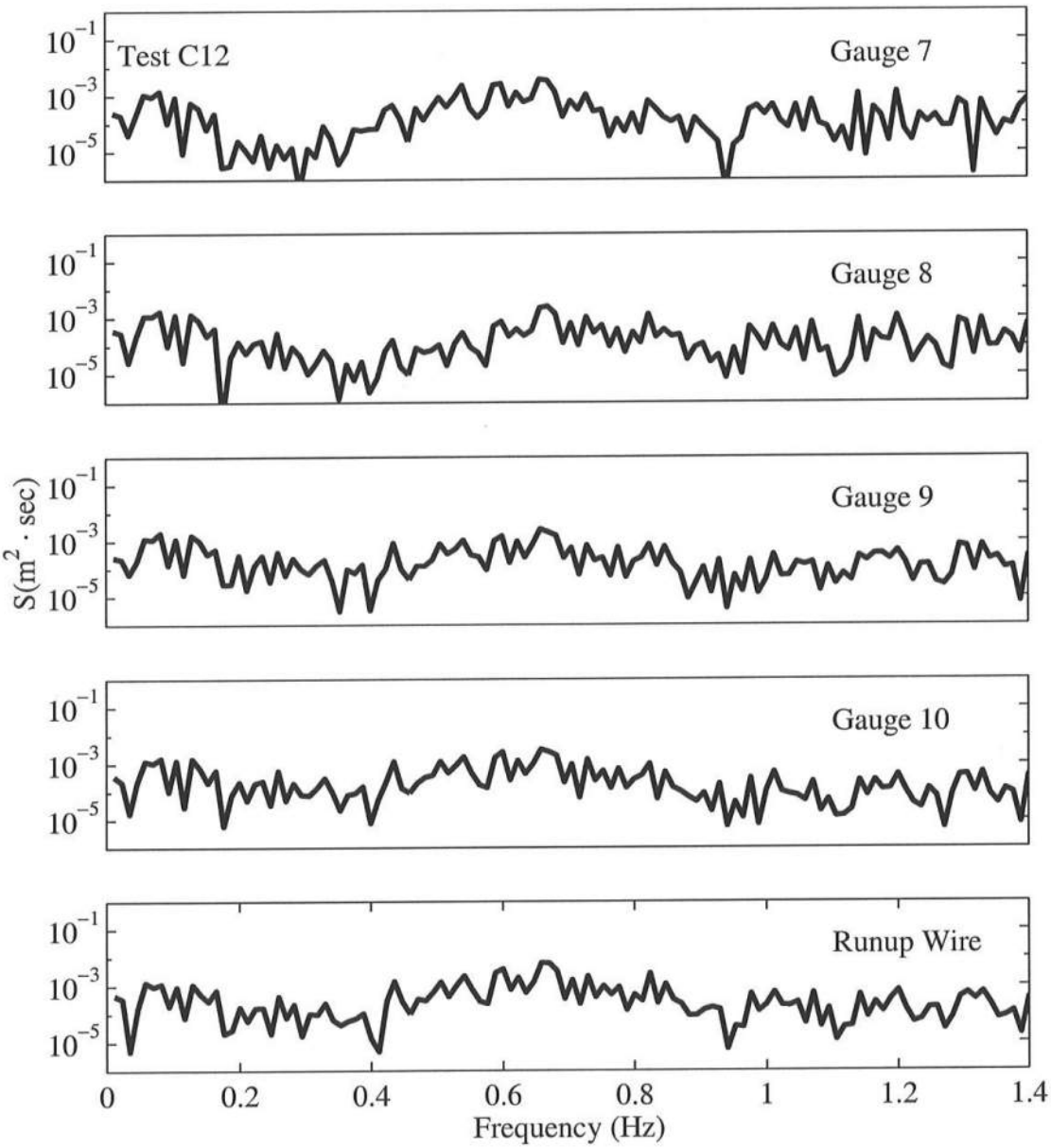

Figure B.46: Frequency Spectra for $T_p = 1.5$ s, $d_t = 12$ cm, for Gauge 7 – Runup Wire.

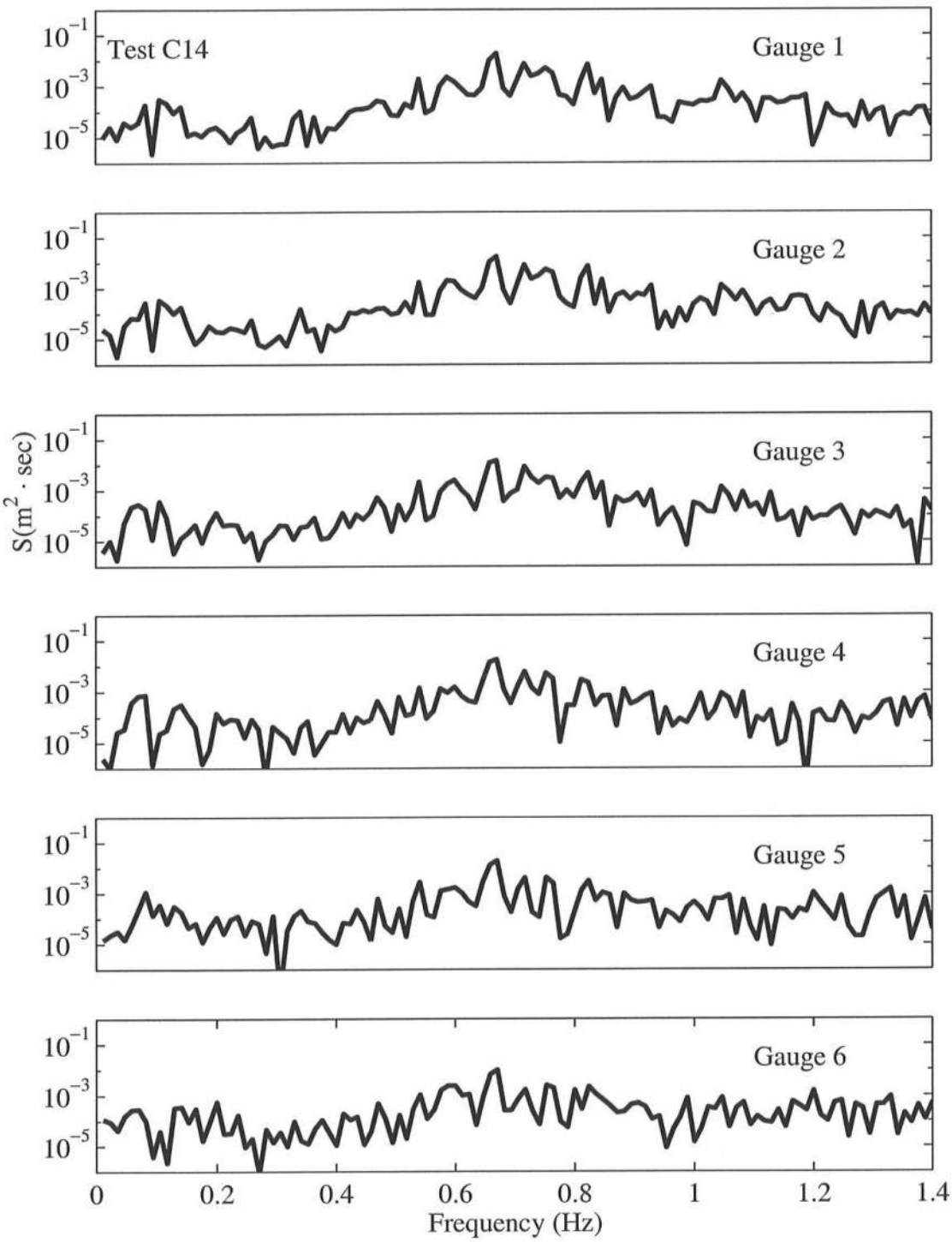

Figure B.47: Frequency Spectra for $T_p = 1.5$ s, $d_t = 14$ cm, for Gauge 1 – Gauge 6.

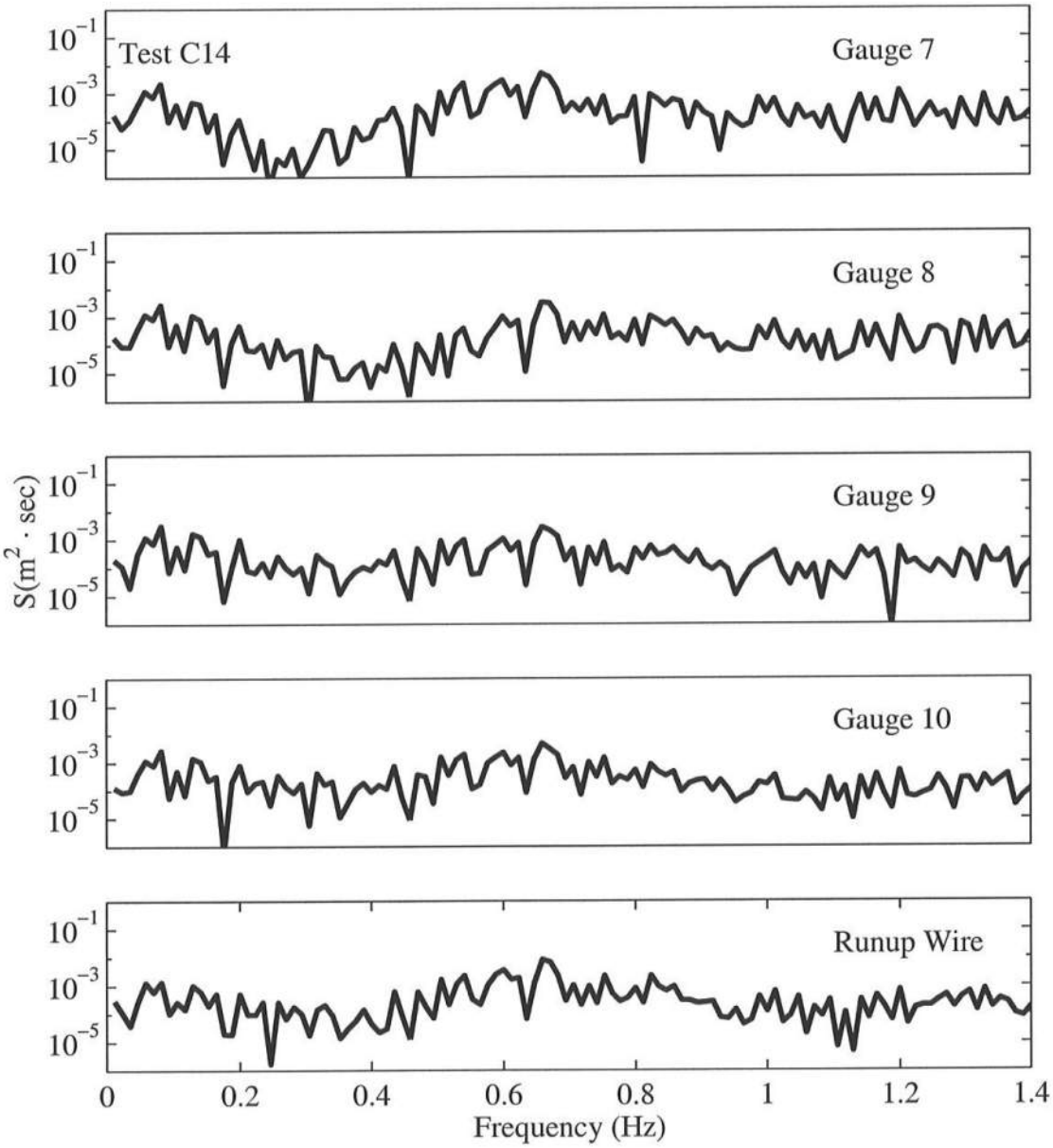

Figure B.48: Frequency Spectra for T_p = 1.5 s, d_t = 14 cm, for Gauge 7 – Runup Wire.

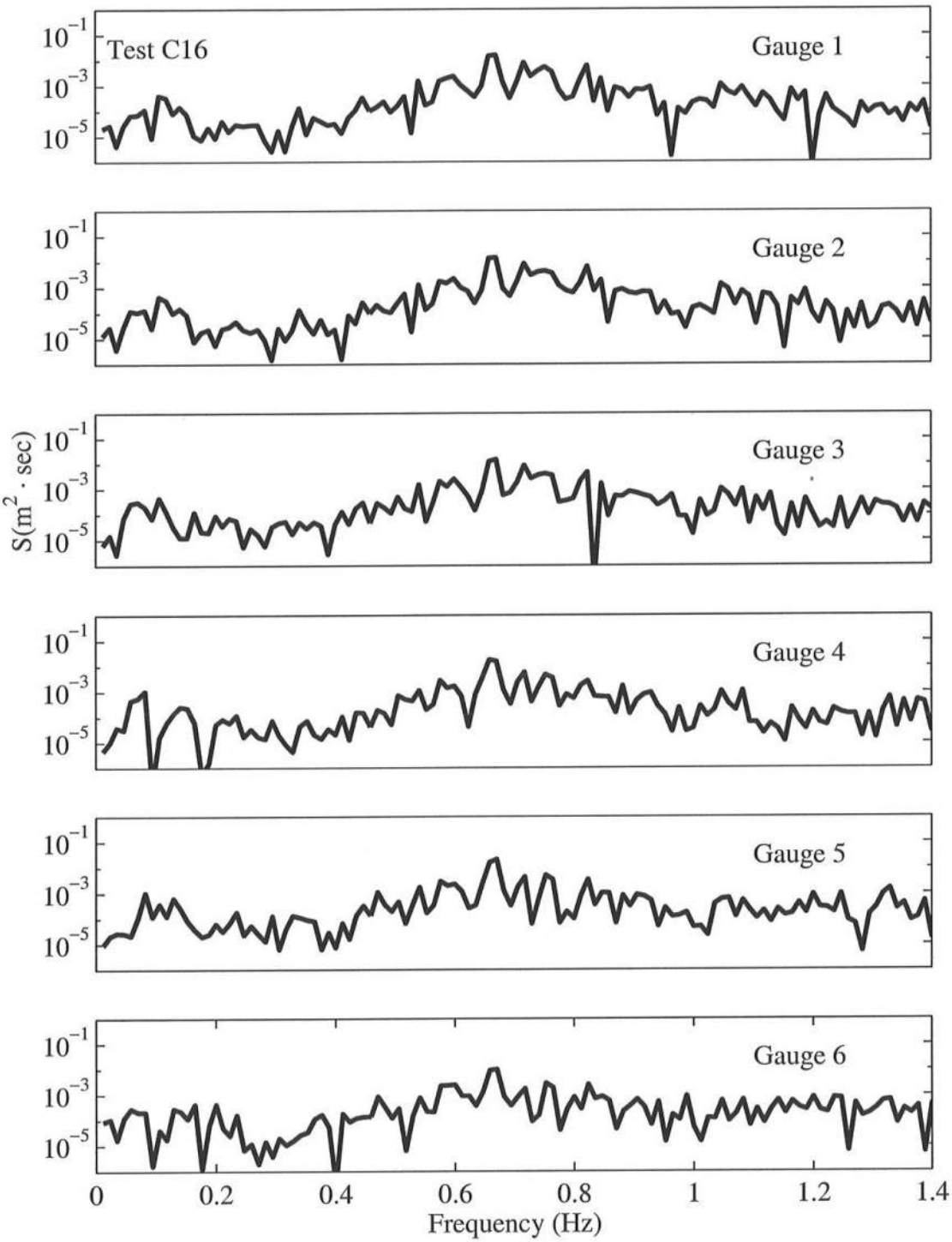

Figure B.49: Frequency Spectra for T_p = 1.5 s, d_t =16 cm, for Gauge 1 – Gauge 6.

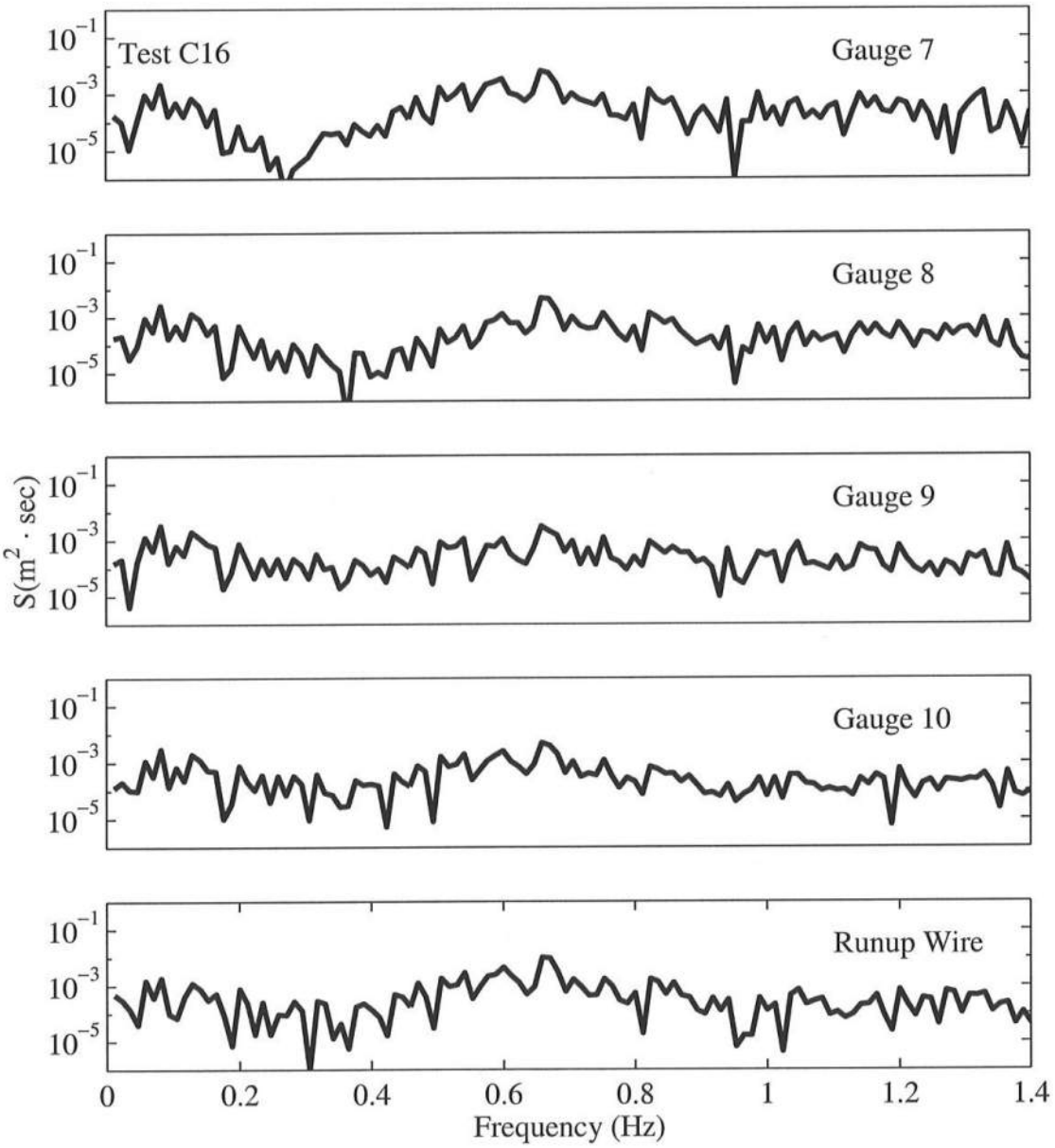

Figure B.50: Frequency Spectra for T_p = 1.5 s, d_t =16 cm, for Gauge 7 – Runup Wire.

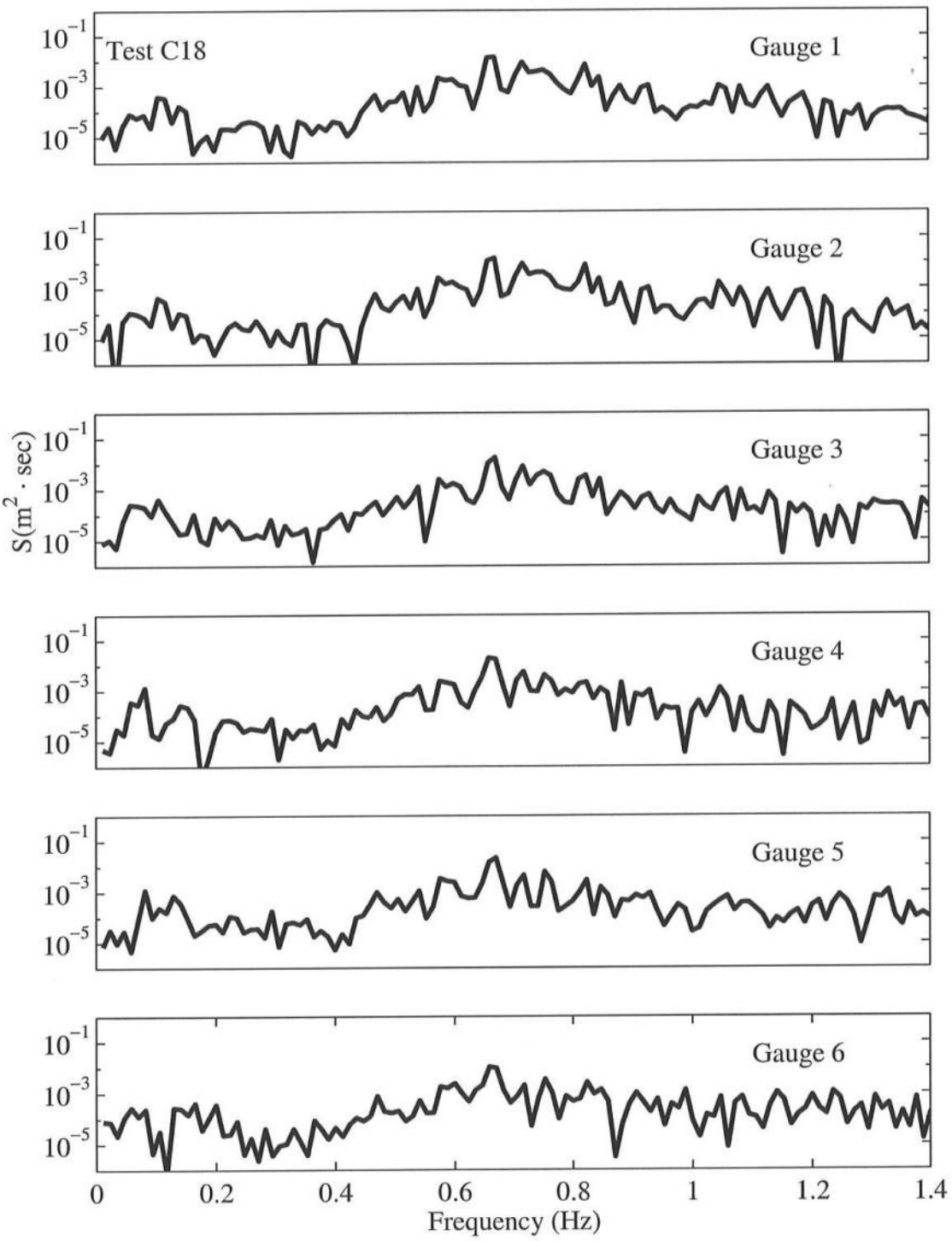

Figure B.51: Frequency Spectra for T_p = 1.5 s, d_t =18 cm, for Gauge 1 – Gauge 6.

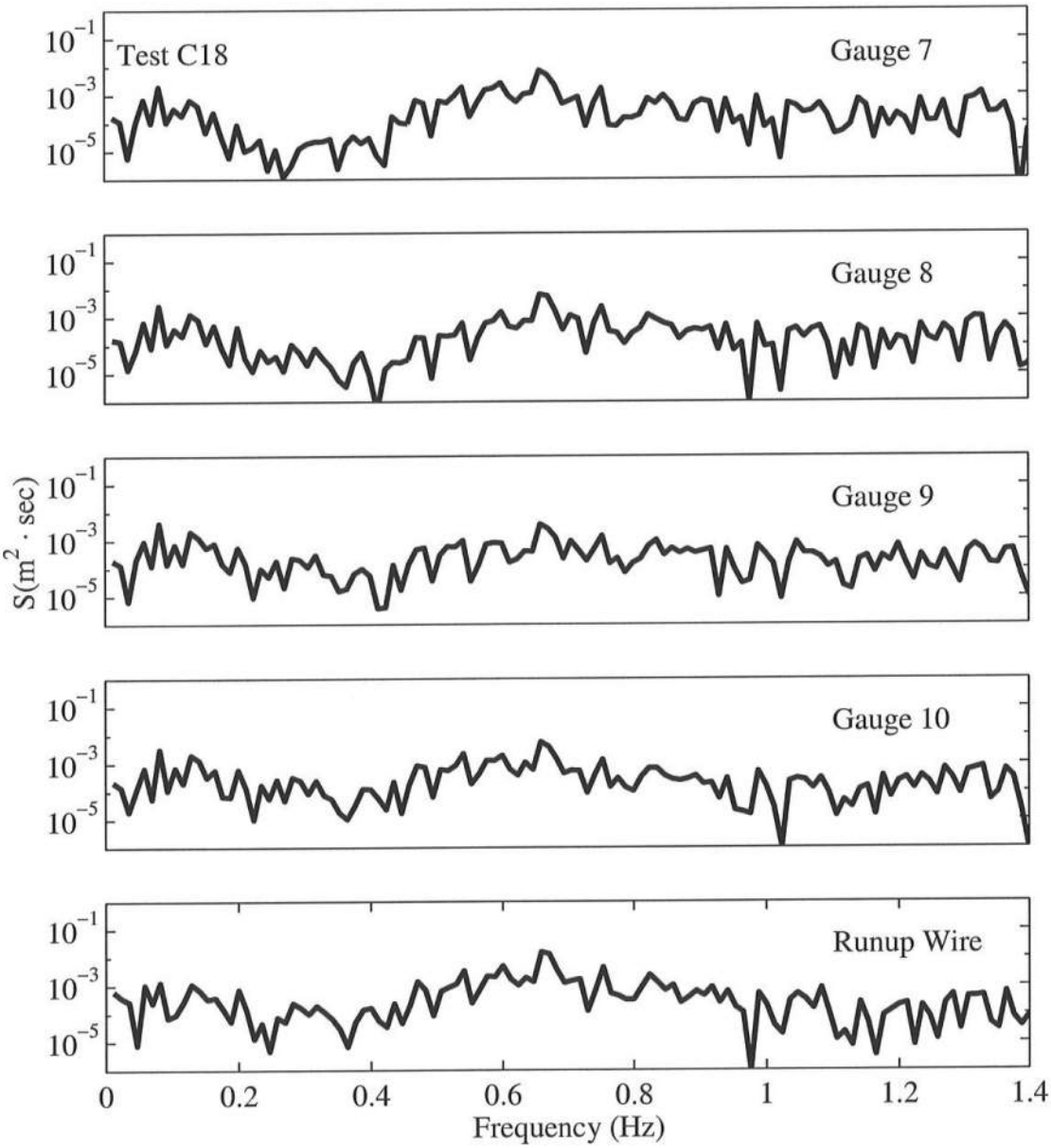

Figure B.52: Frequency Spectra for T_p = 1.5 s, d_t = 18 cm, for Gauge 7 – Runup Wire.

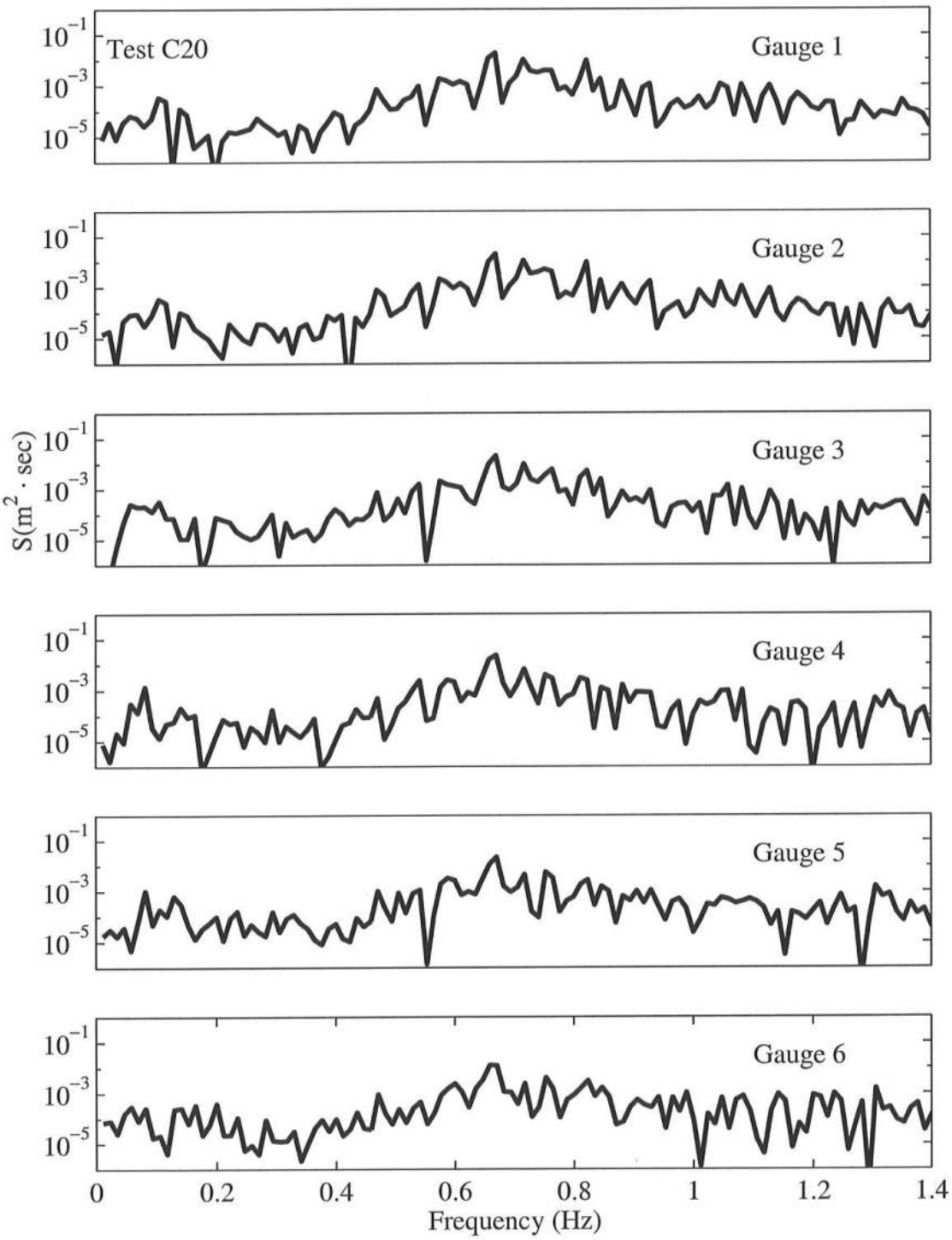

Figure B.53: Frequency Spectra for T_p = 1.5 s, d_t = 20 cm, for Gauge 1 – Gauge 6.

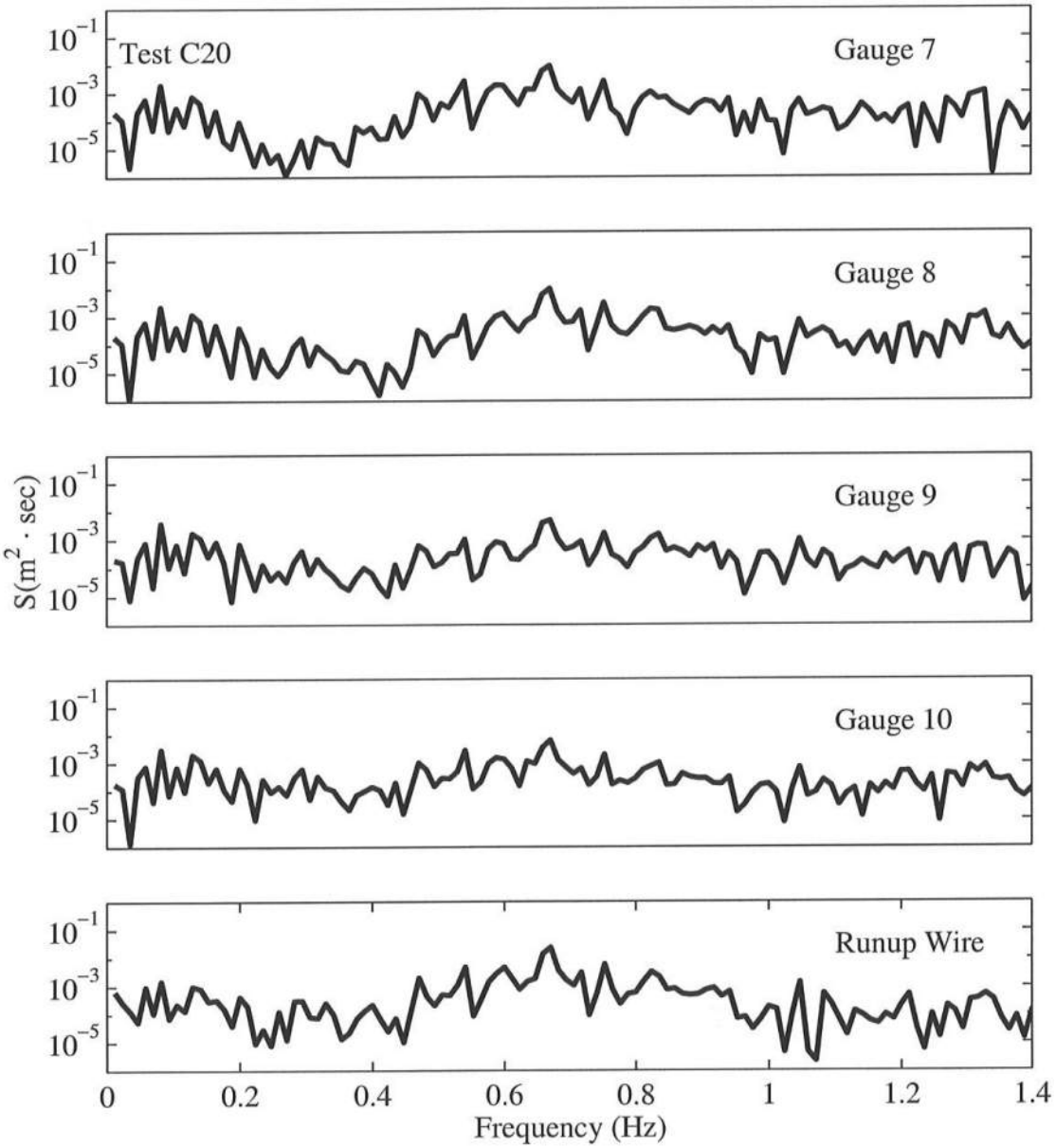

Figure B.54: Frequency Spectra for $T_p = 1.5$ s, $d_t = 20$ cm, for Gauge 7 – Runup Wire.

APPENDIX C

PROBABILITY DISTRIBUTIONS

This appendix contains comparison plots of the measured probability distribution and the exponential gamma distribution for all tests performed.

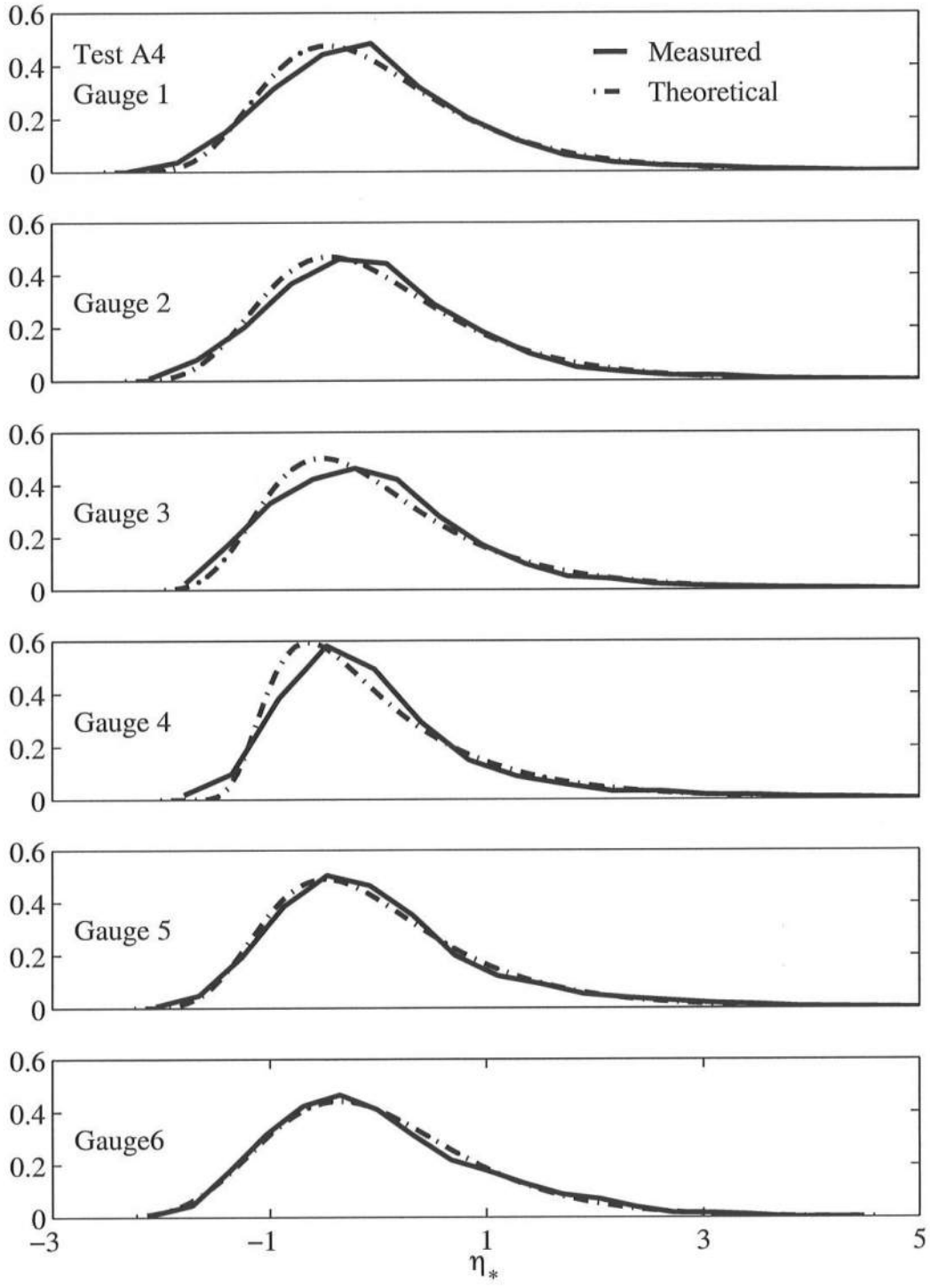

FigureC.1: Free Surface Comparison of Measured Probability Distributions to the Exponential Gamma Distribution for $T_p = 4.7$ s, $d_t = 4$ cm, Gauge 1 – 6.

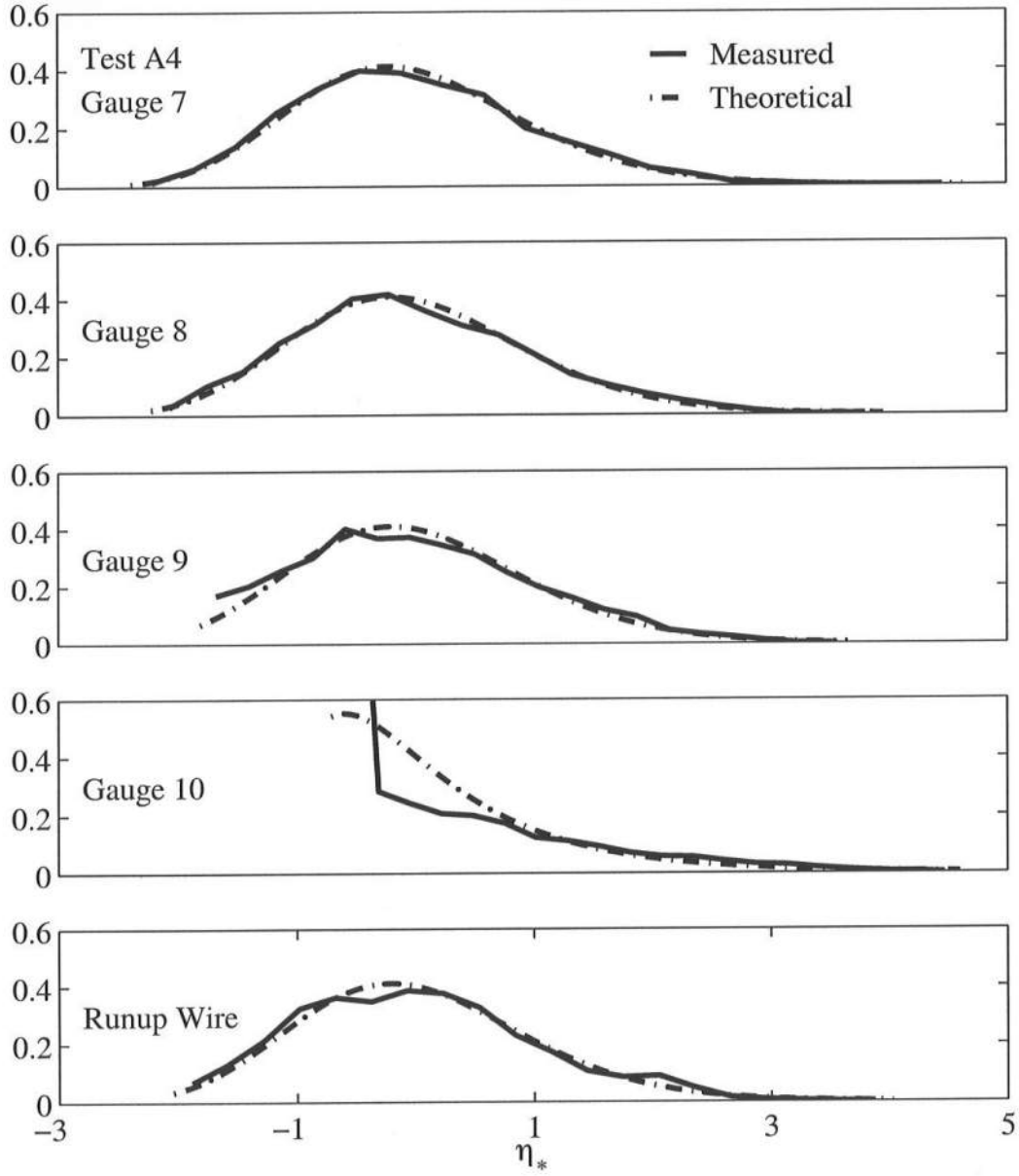

FigureC.2: Free Surface Comparison of Measured Probability Distributions to the Exponential Gamma Distribution for $T_p = 4.7$ s, d_t.= 4 cm, Gauge 7 – Runup Wire

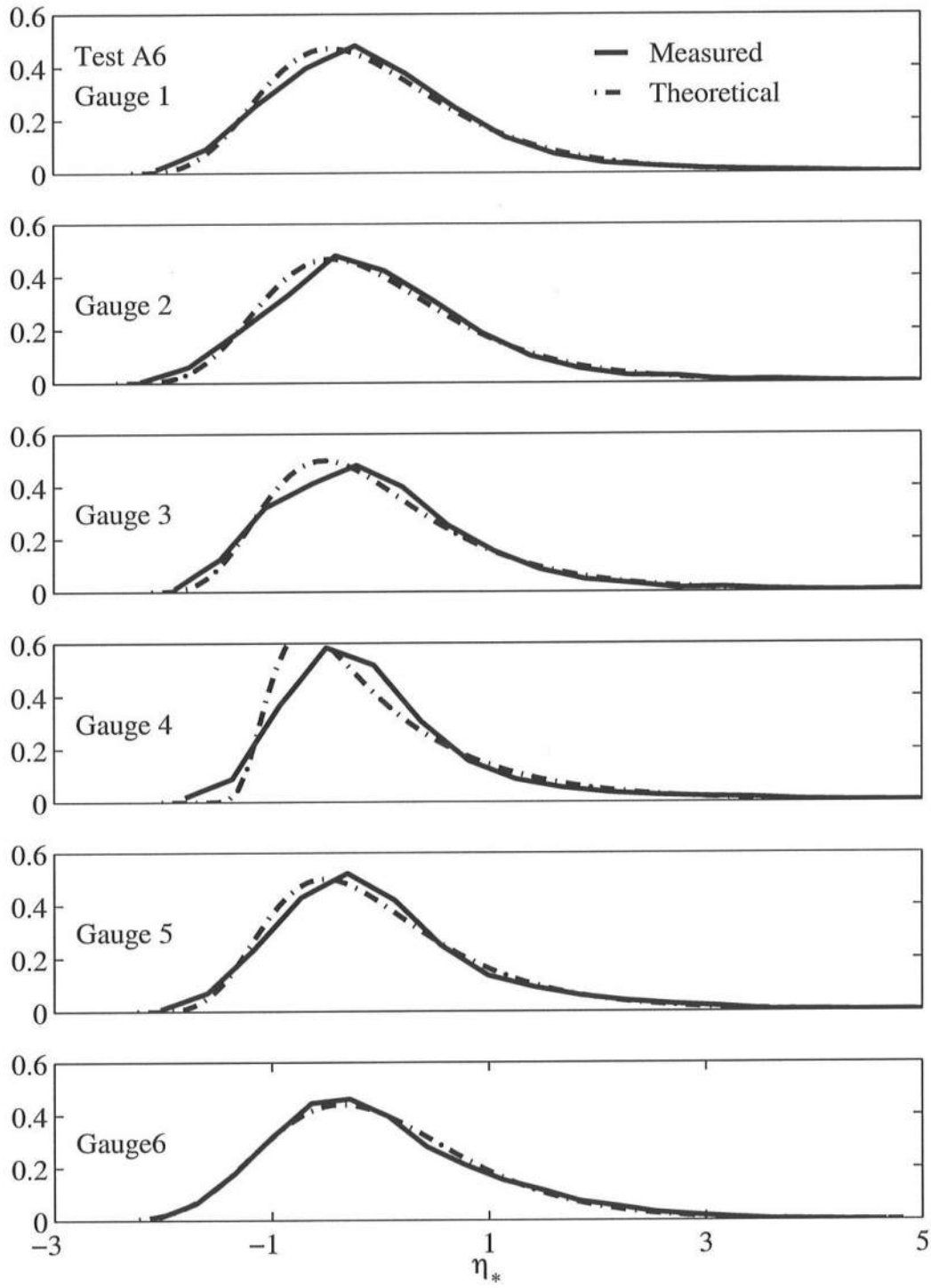

FigureC.3: Free Surface Comparison of Measured Probability Distributions to the Exponential Gamma Distribution for $T_p = 4.7$ s, d_t.= 6 cm, Gauge 1 – 6.

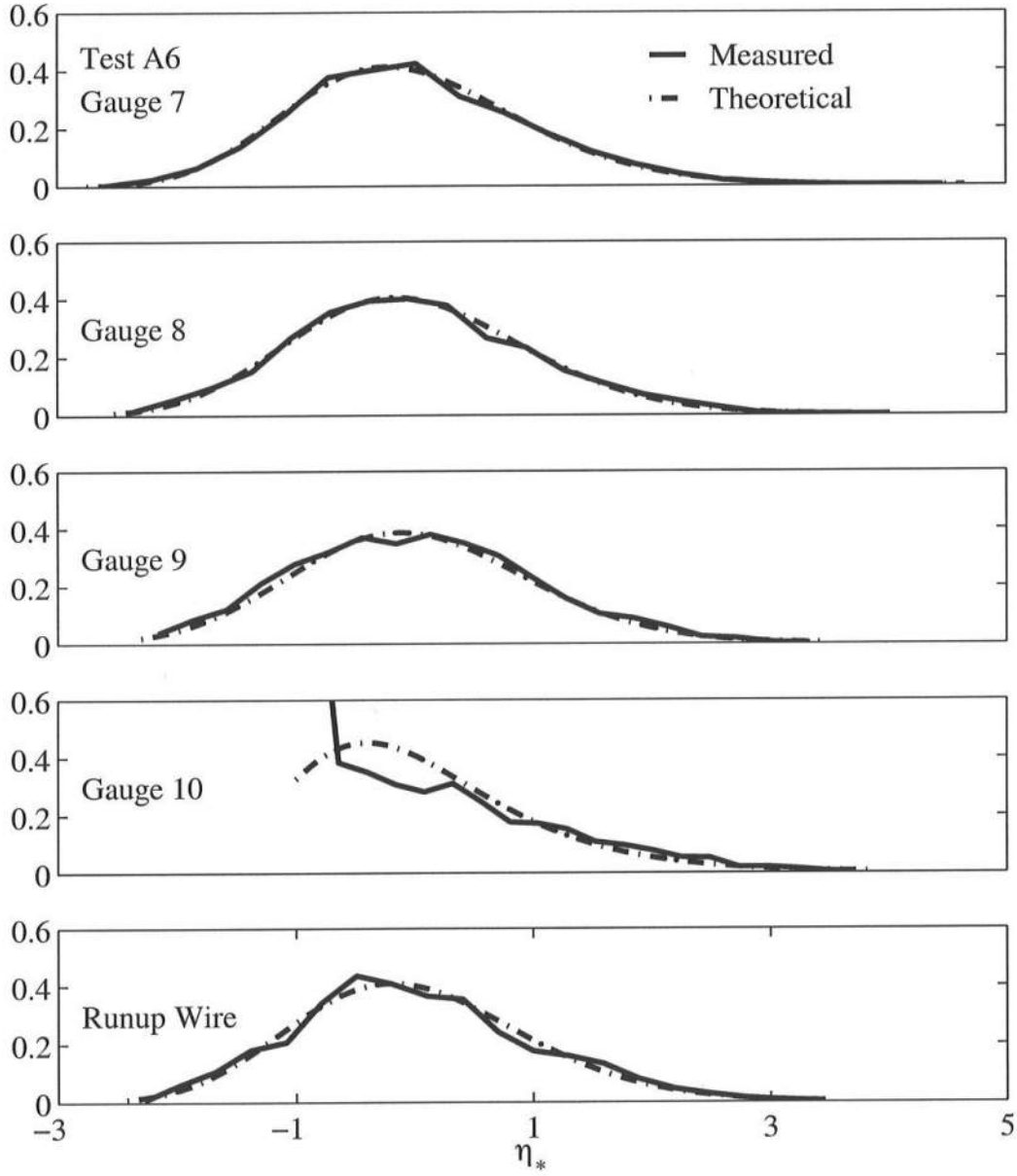

FigureC.4: Free Surface Comparison of Measured Probability Distributions to the Exponential Gamma Distribution for $T_p = 4.7$ s, d_t.= 6 cm, Gauge 7 – Runup Wire

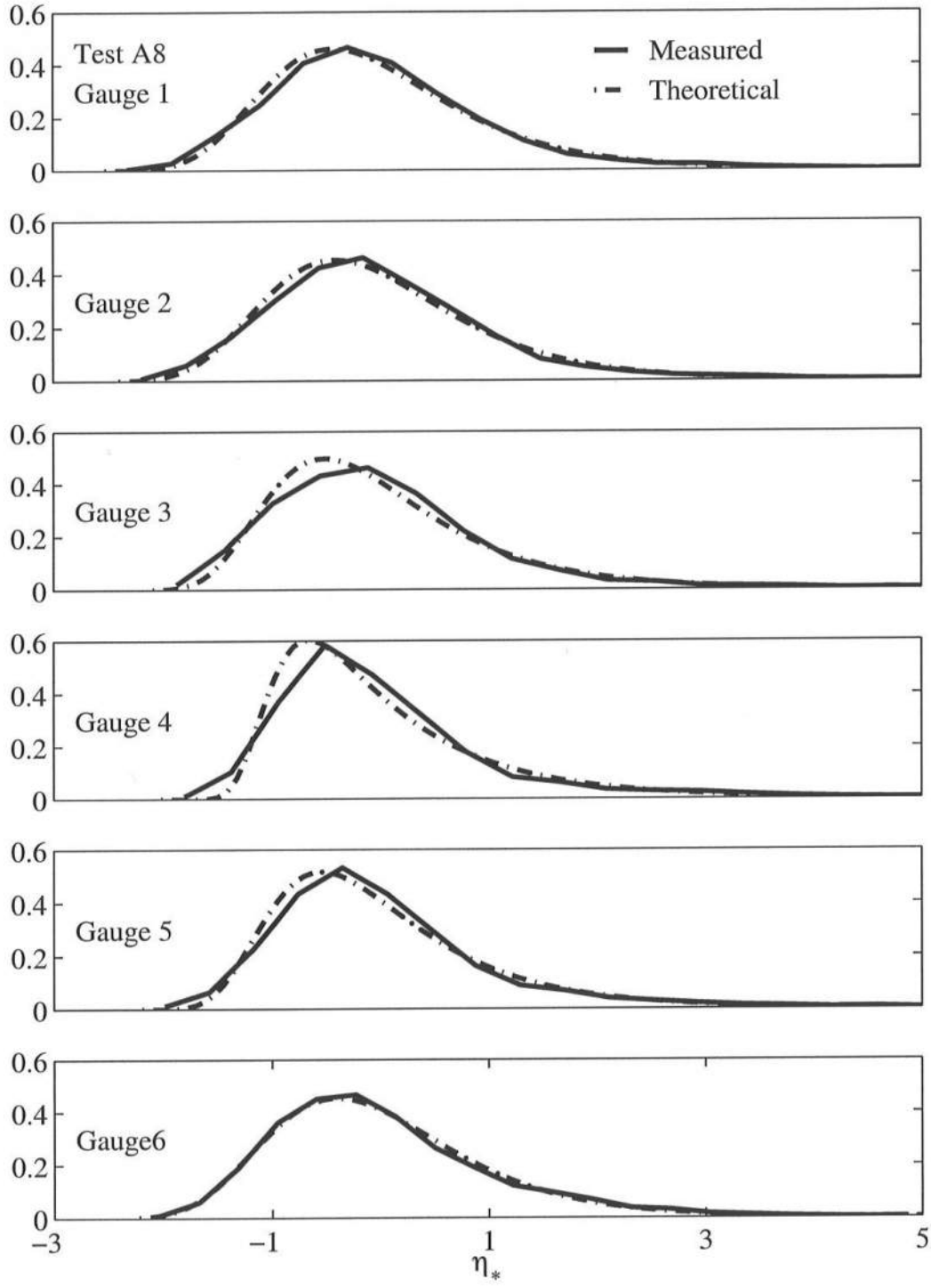

FigureC.5: Free Surface Comparison of Measured Probability Distributions to the Exponential Gamma Distribution for $T_p = 4.7$ s, d_t.= 8 cm, Gauge 1 – 6.

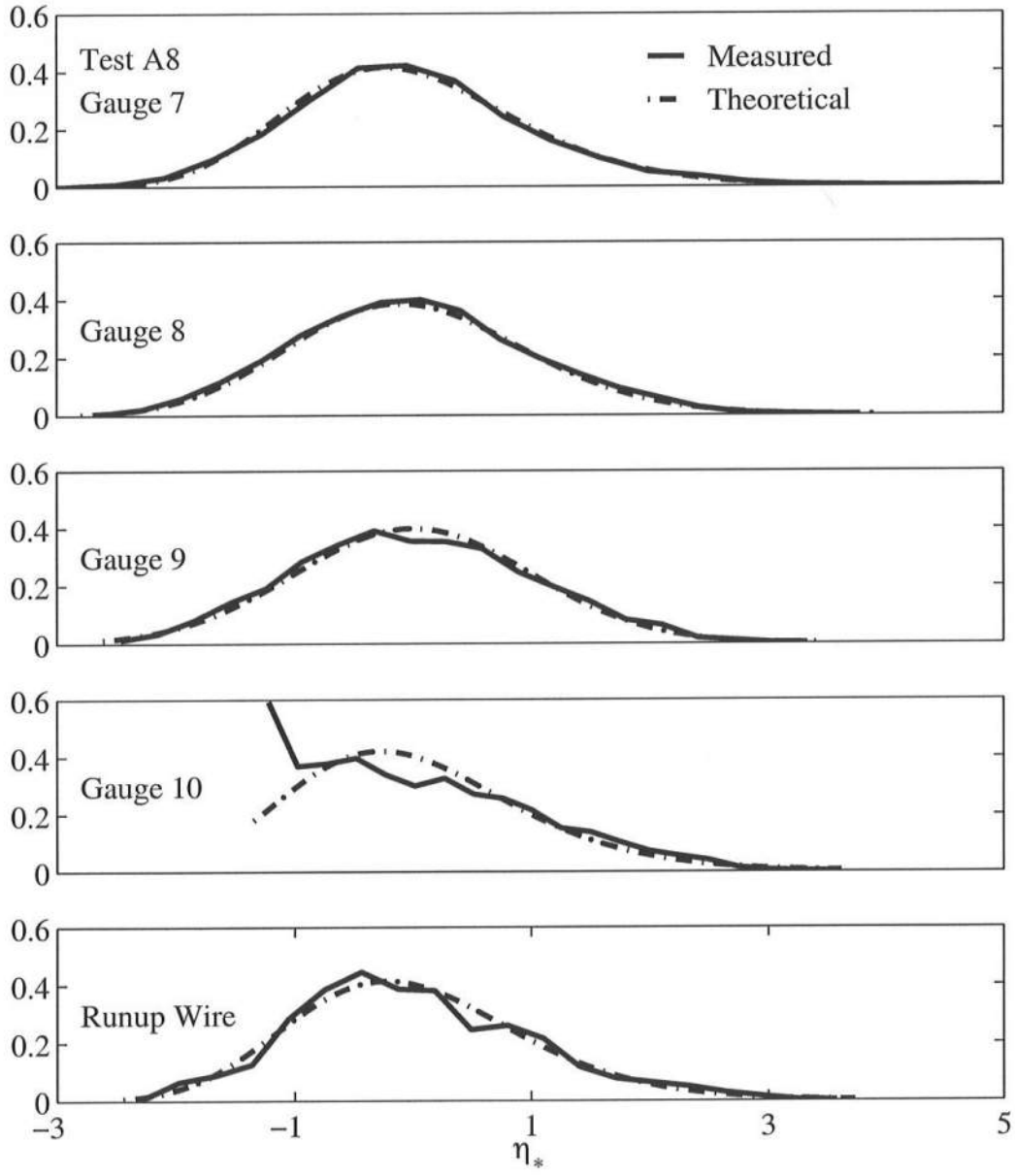

FigureC.6: Free Surface Comparison of Measured Probability Distributions to the Exponential Gamma Distribution for $T_p = 4.7$ s, d_t.= 8 cm, Gauge 7 – Runup Wire

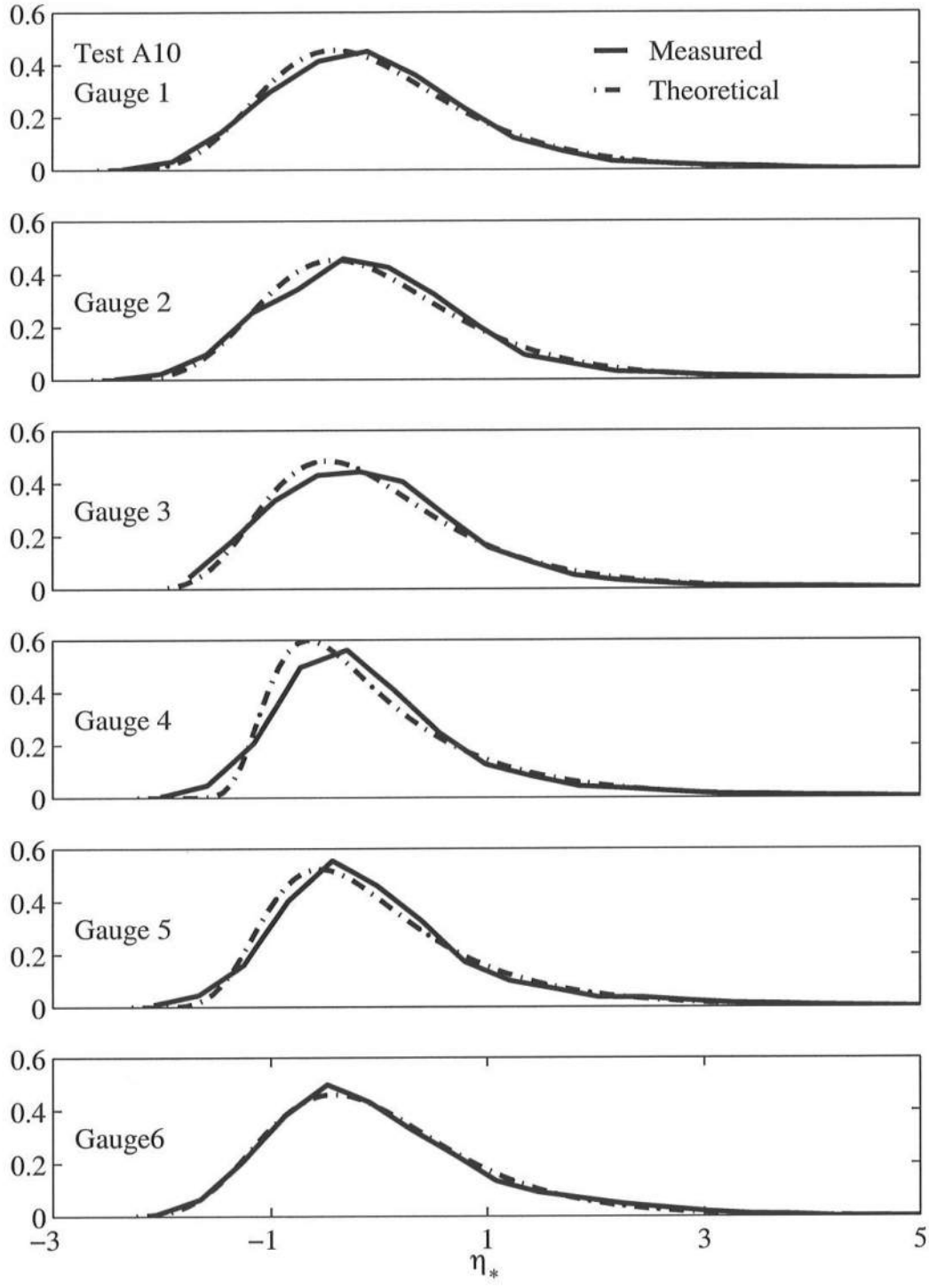

FigureC.7: Free Surface Comparison of Measured Probability Distributions to the Exponential Gamma Distribution for $T_p = 4.7$ s, d_t.= 10 cm, Gauge 1 – 6.

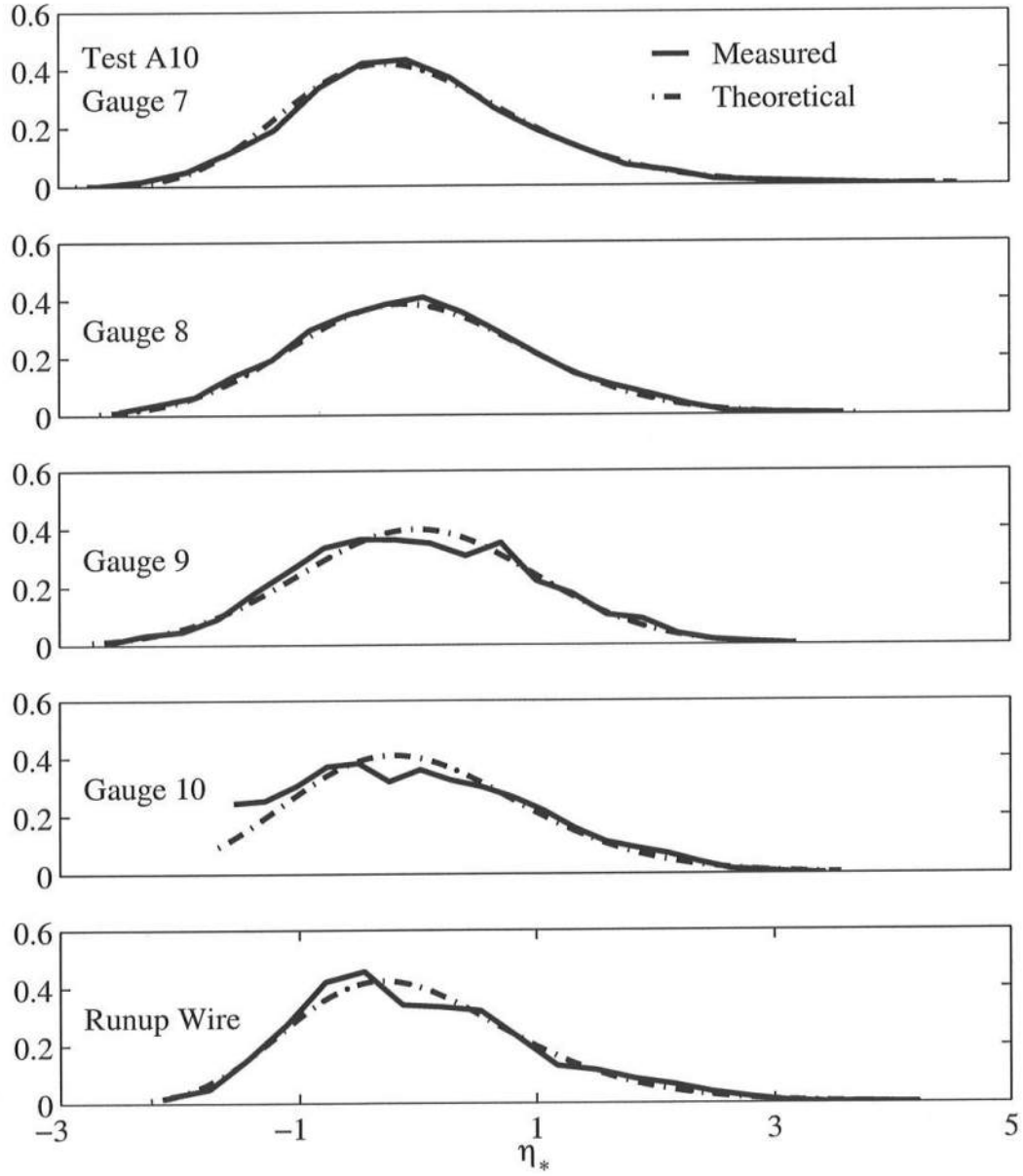

FigureC.8: Free Surface Comparison of Measured Probability Distributions to the Exponential Gamma Distribution for T_p = 4.7 s, d_t.= 10 cm, Gauge 7 – Runup Wire

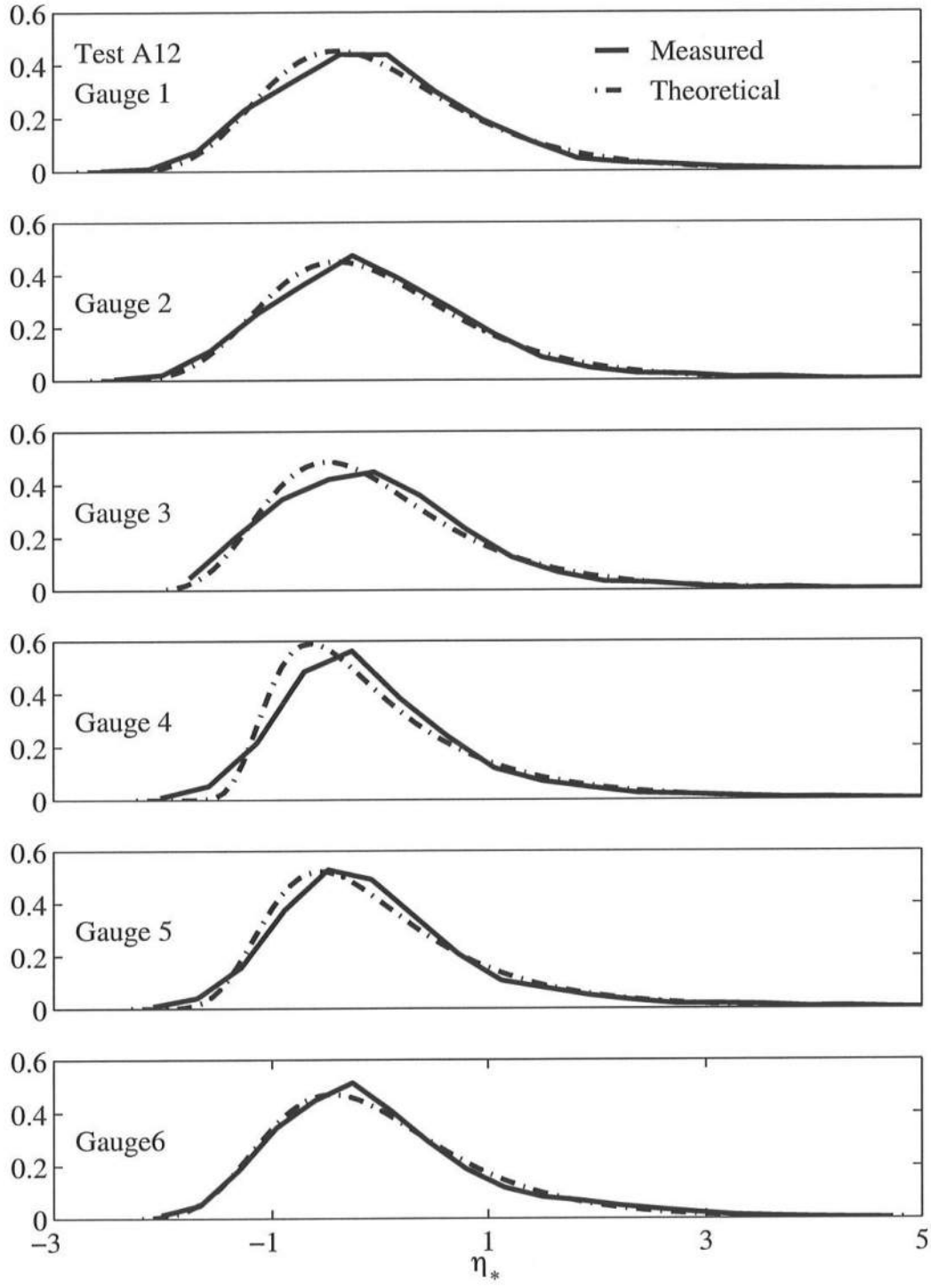

FigureC.9: Free Surface Comparison of Measured Probability Distributions to the Exponential Gamma Distribution for $T_p = 4.7$ s, d_t.= 12 cm, Gauge 1 – 6.

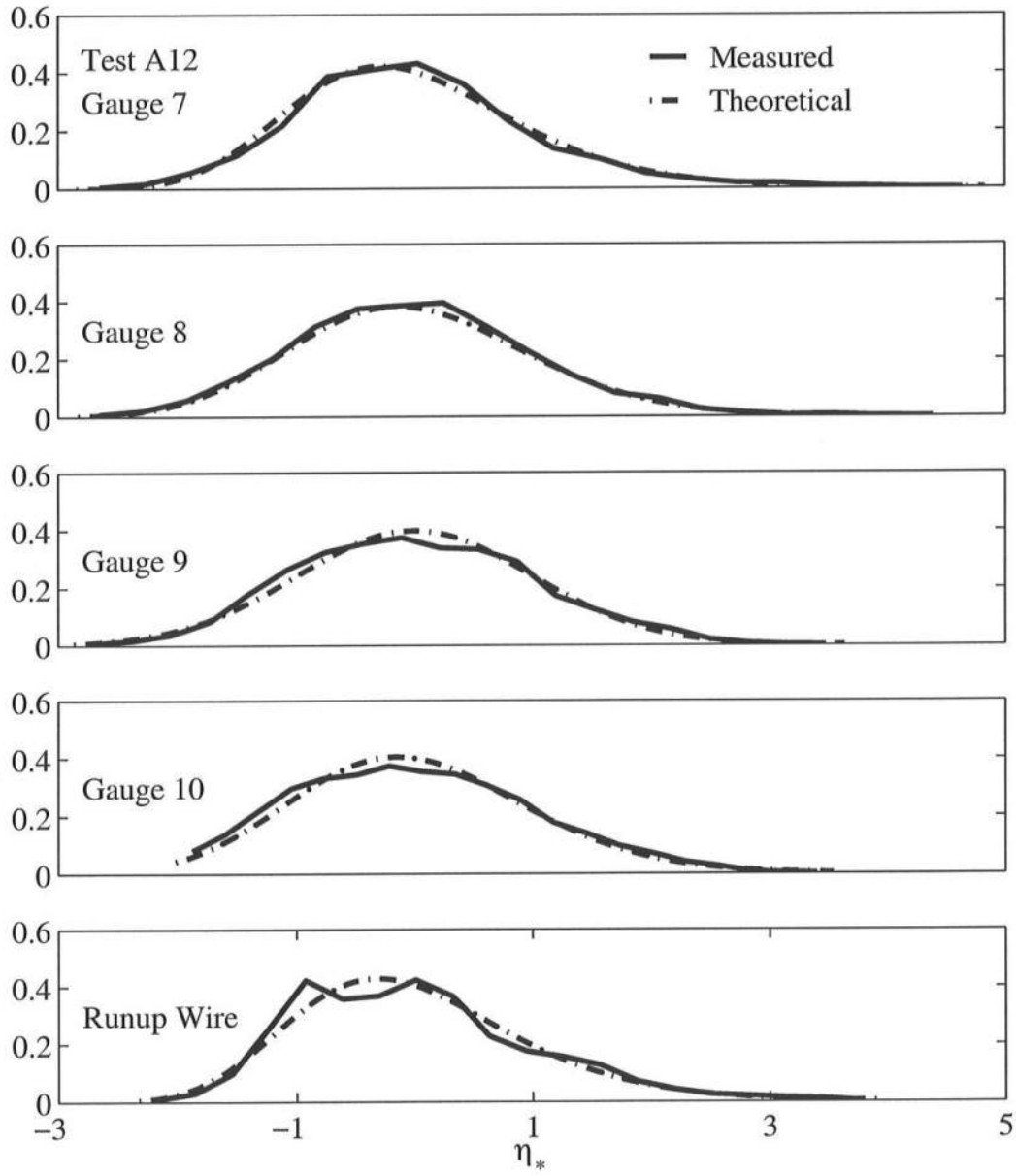

FigureC.10: Free Surface Comparison of Measured Probability Distributions to the Exponential Gamma Distribution for $T_p = 4.7$ s, $d_t = 12$ cm, Gauge 7 – Runup Wire

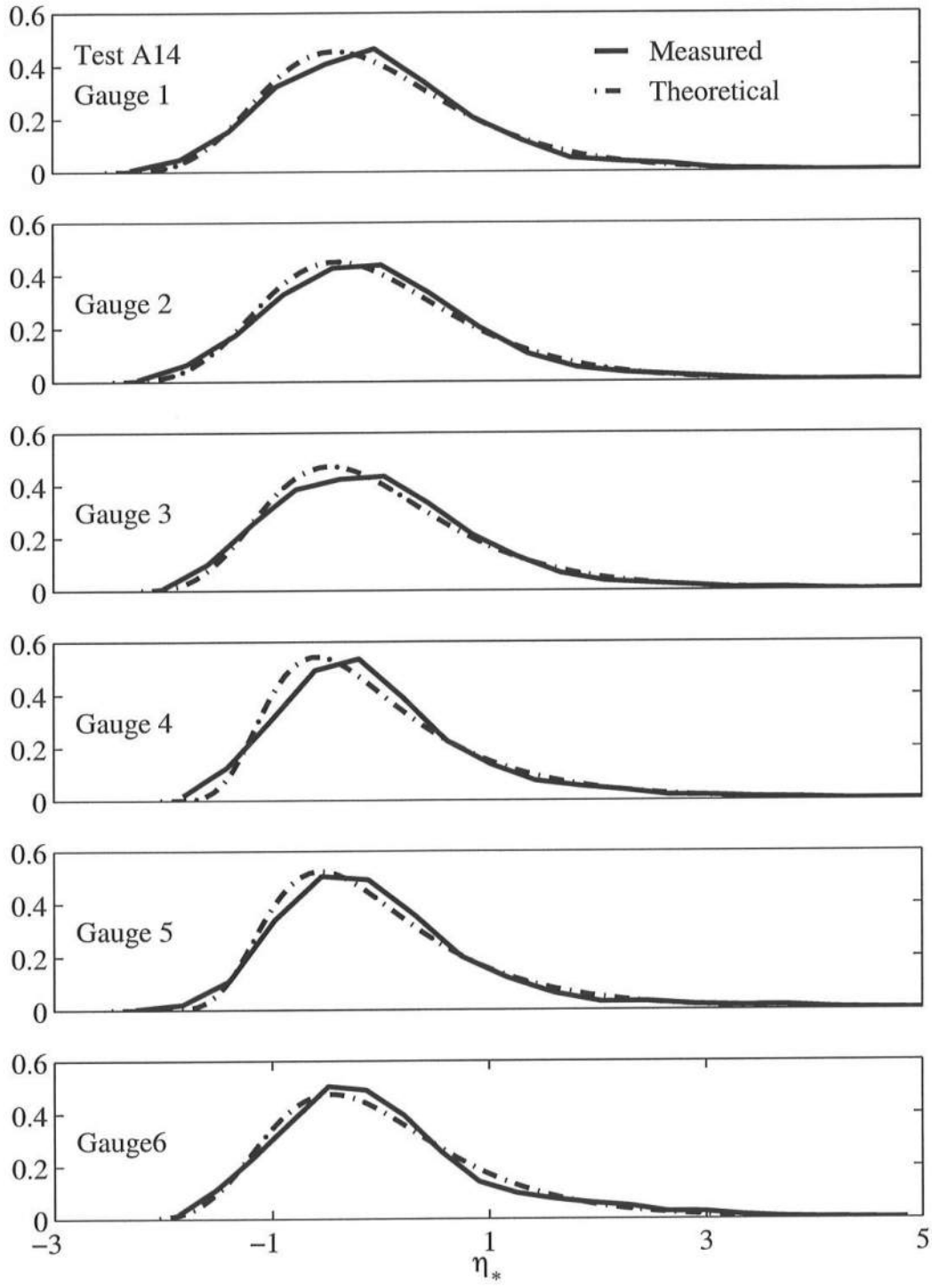

FigureC.11: Free Surface Comparison of Measured Probability Distributions to the Exponential Gamma Distribution for $T_p = 4.7$ s, d_t.= 14 cm, Gauge 1 – 6.

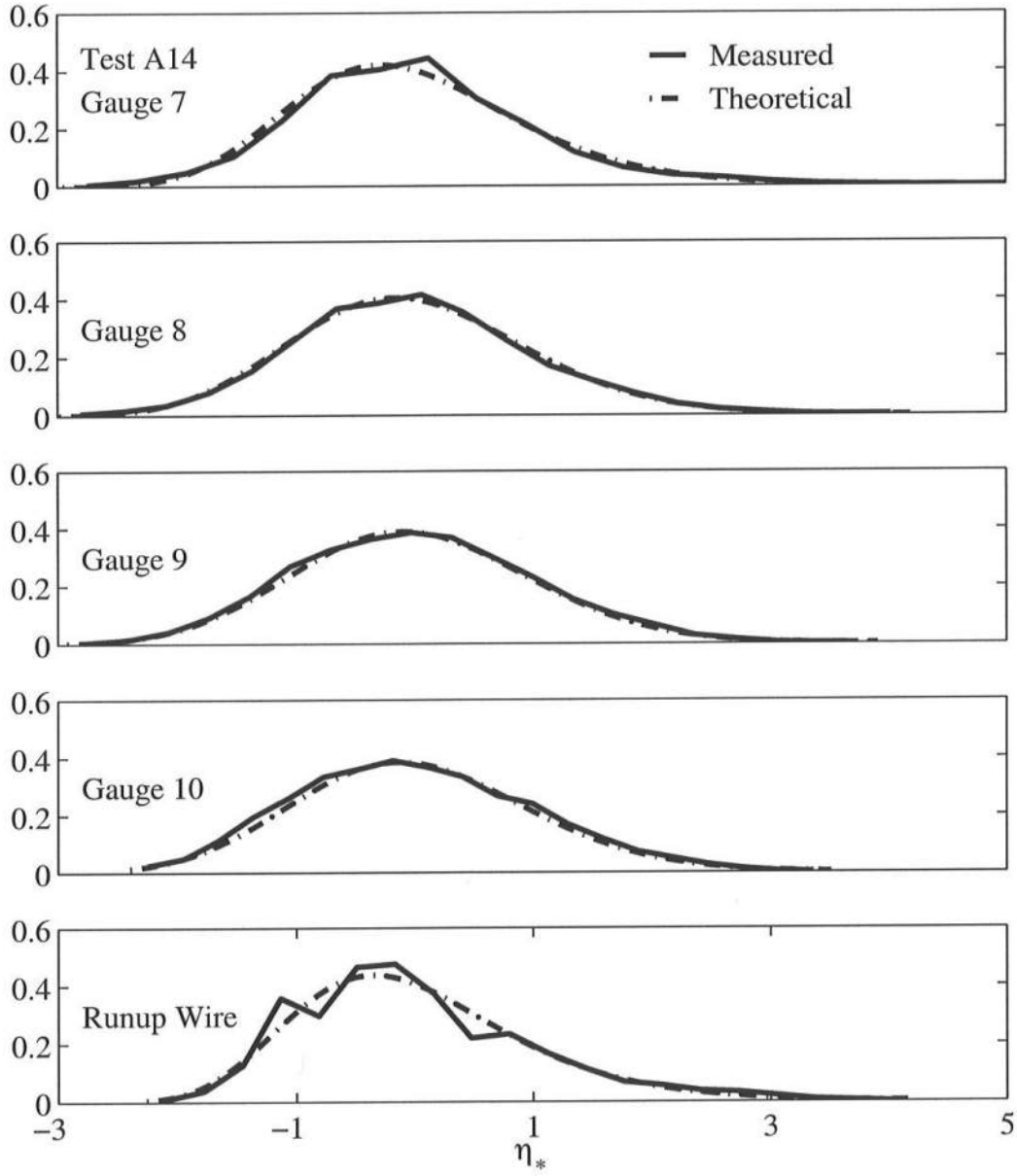

FigureC.12: Free Surface Comparison of Measured Probability Distributions to the Exponential Gamma Distribution for $T_p = 4.7$ s, d_t.= 14 cm, Gauge 7 – Runup Wire

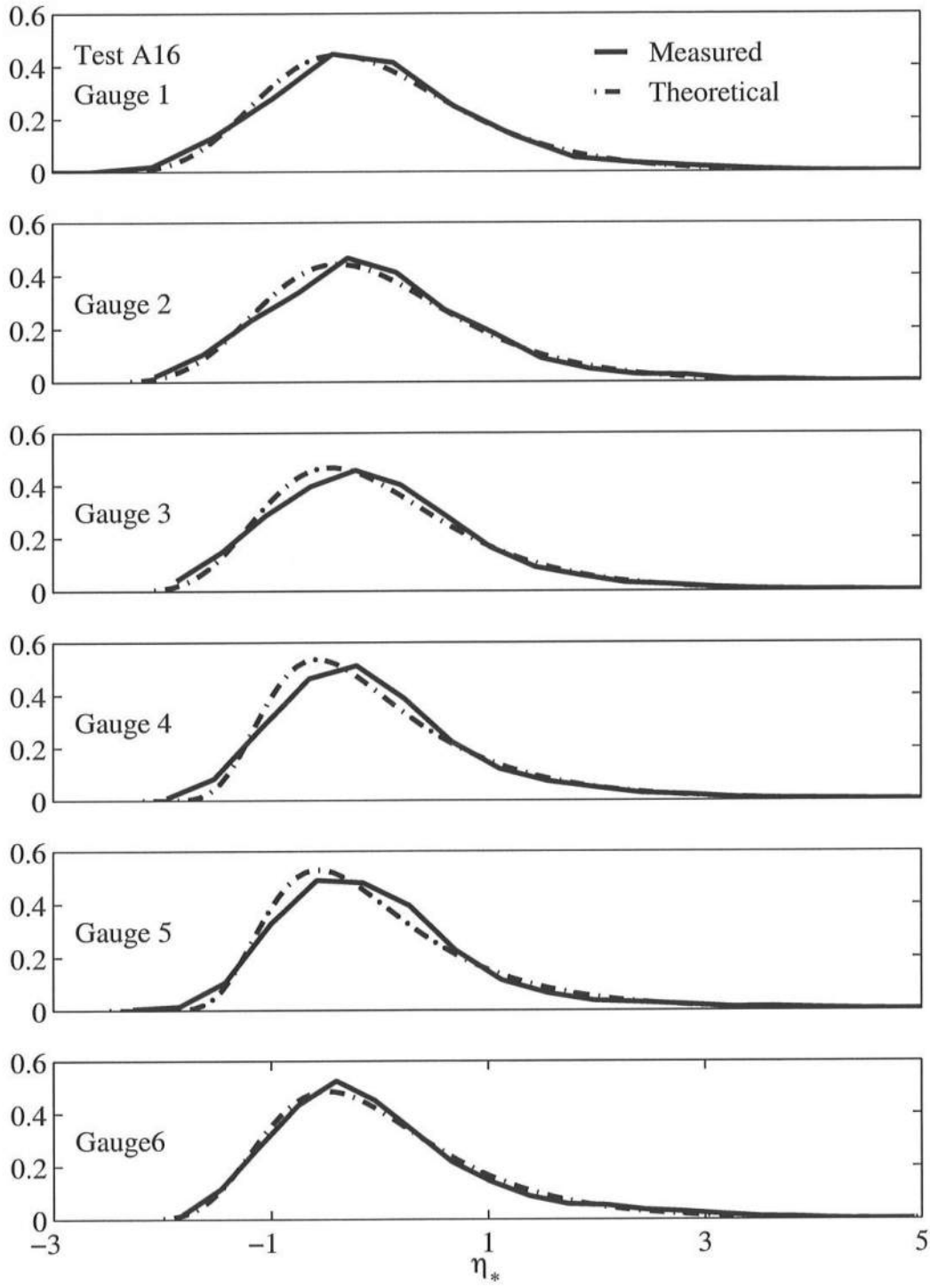

FigureC.13: Free Surface Comparison of Measured Probability Distributions to the Exponential Gamma Distribution for $T_p = 4.7$ s, d_t.= 16 cm, Gauge 1 –- 6.

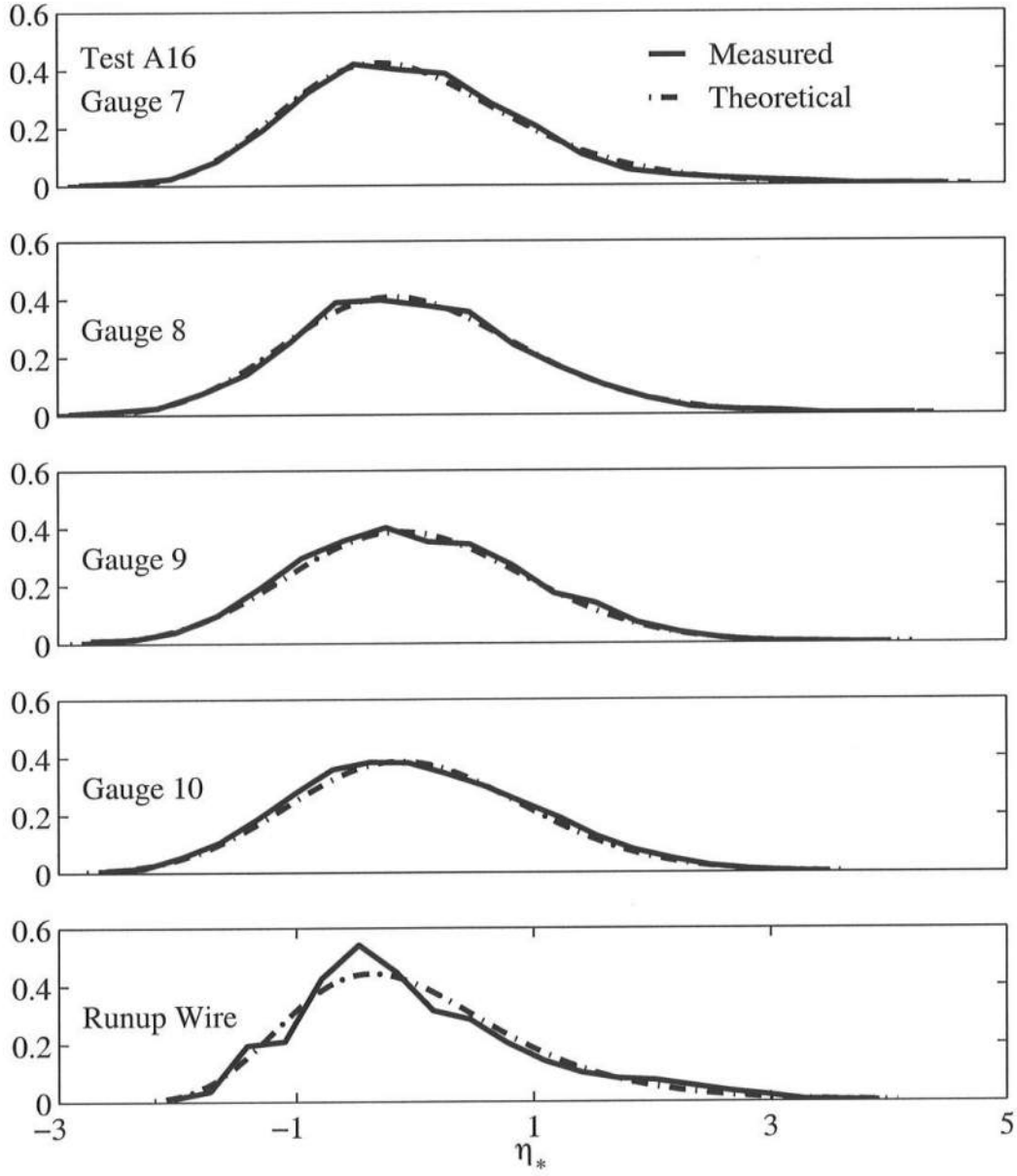

FigureC.14: Free Surface Comparison of Measured Probability Distributions to the Exponential Gamma Distribution for T_p = 4.7 s, d_t.= 16 cm, Gauge 7 – Runup Wire

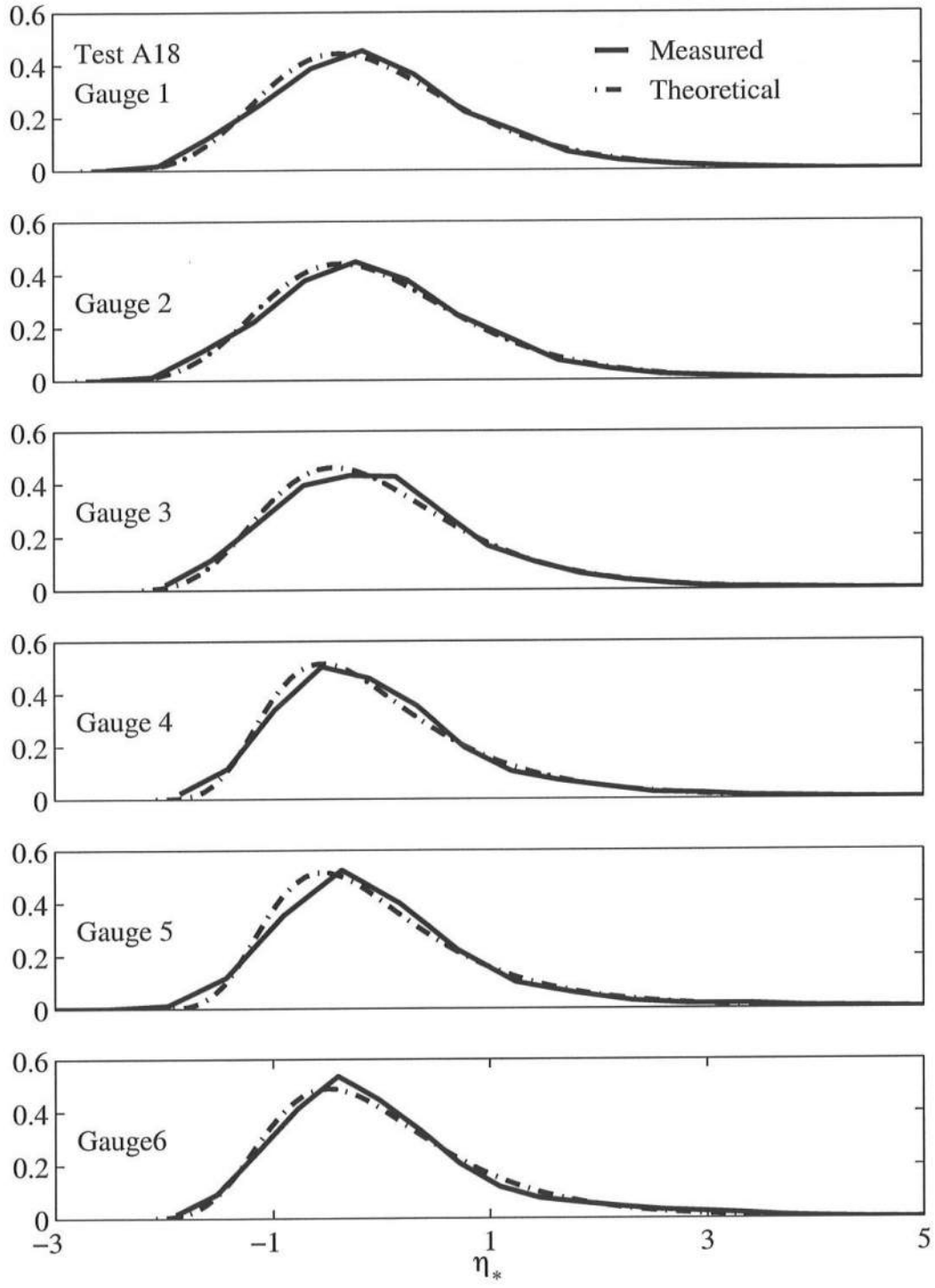

FigureC.15: Free Surface Comparison of Measured Probability Distributions to the Exponential Gamma Distribution for $T_p = 4.7$ s, d_t.= 18 cm, Gauge 1 – 6.

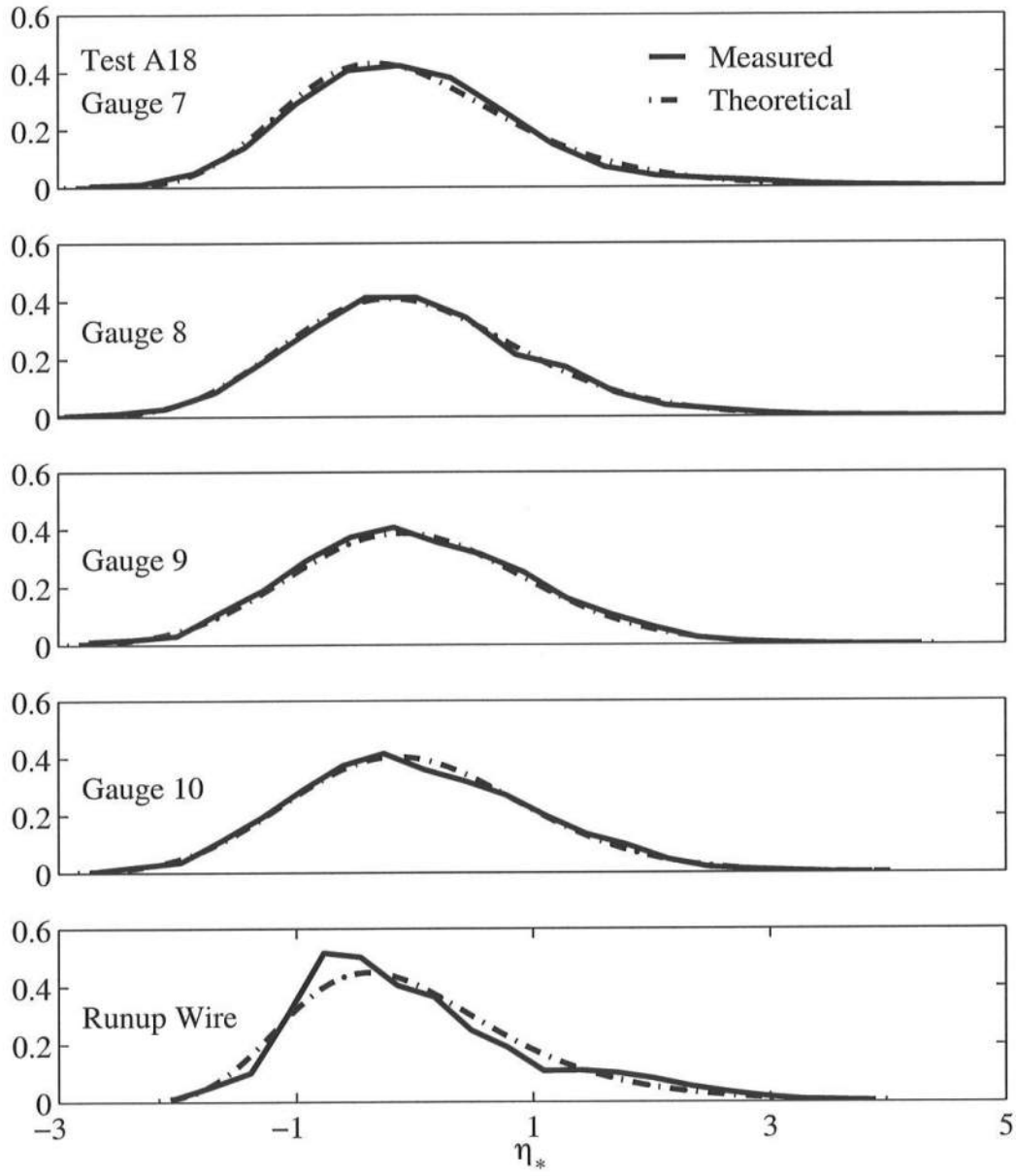

FigureC.16: Free Surface Comparison of Measured Probability Distributions to the Exponential Gamma Distribution for $T_p = 4.7$ s, d_t.= 18 cm, Gauge 7 – Runup Wire

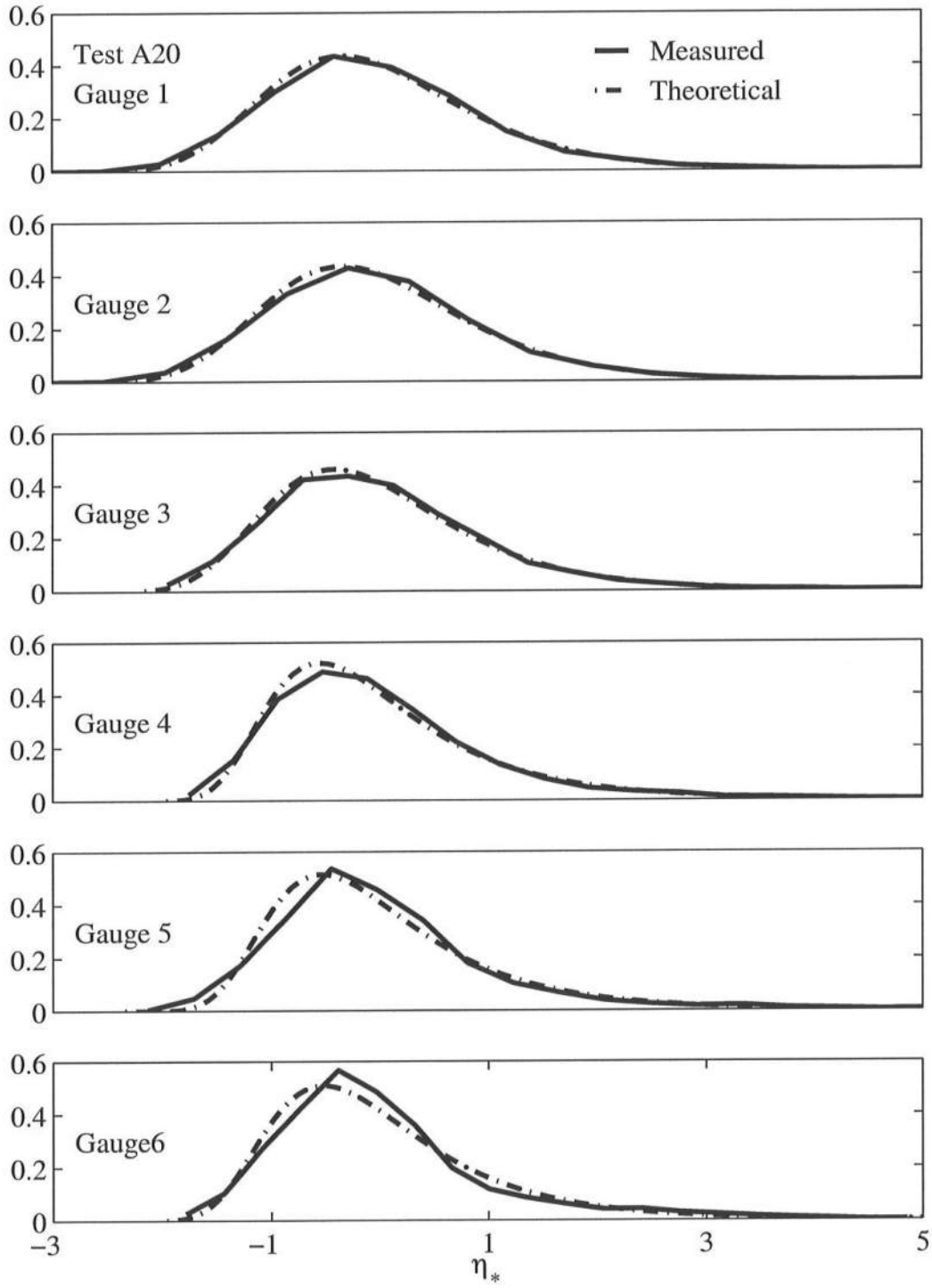

FigureC.17: Free Surface Comparison of Measured Probability Distributions to the Exponential Gamma Distribution for T_p =4.7 s, d_t.= 20 cm, Gauge 1 – 6.

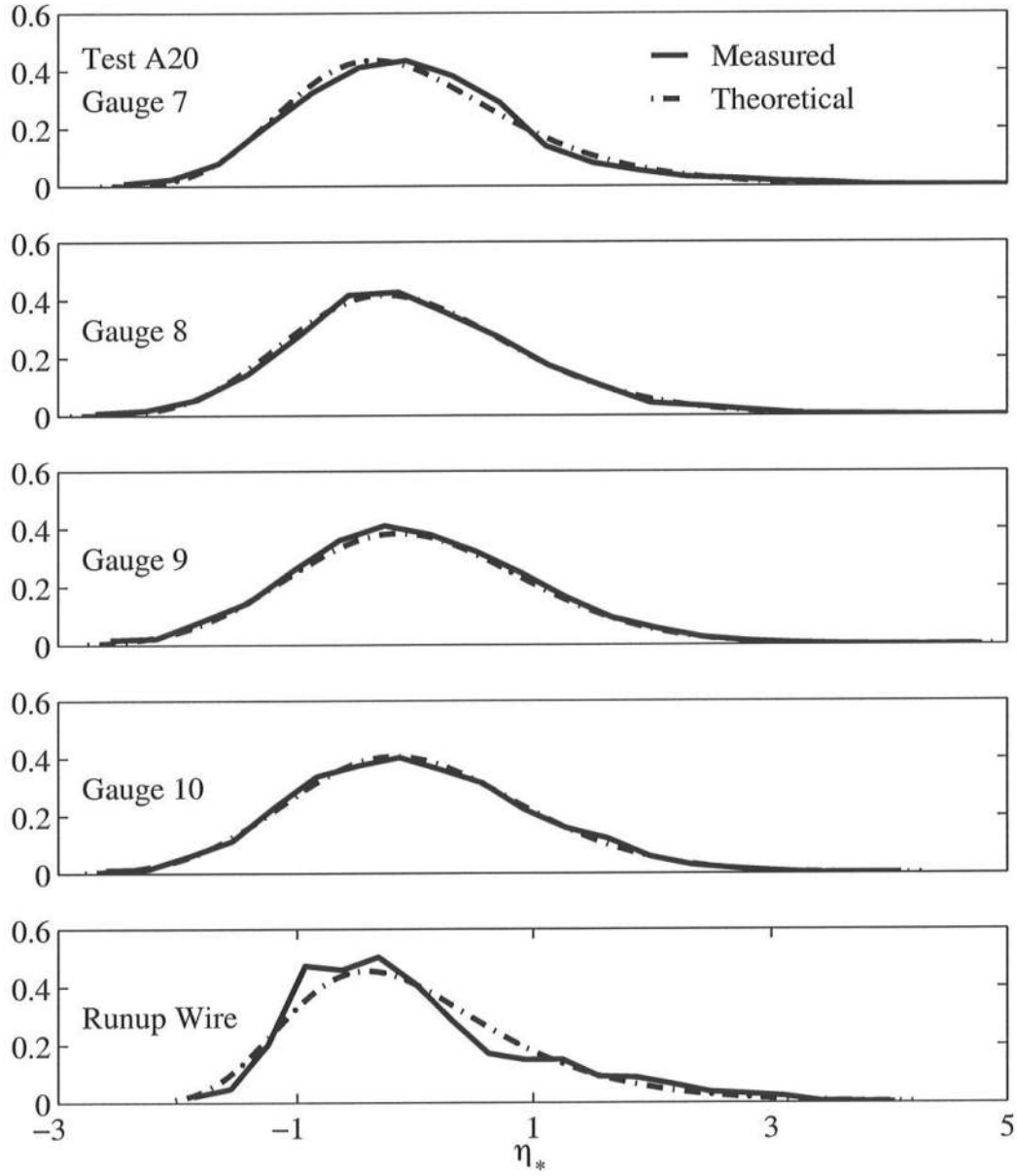

FigureC.18: Free Surface Comparison of Measured Probability Distributions to the Exponential Gamma Distribution for $T_p = 4.7$ s, d_t.= 20 cm, Gauge 7 – Runup Wire

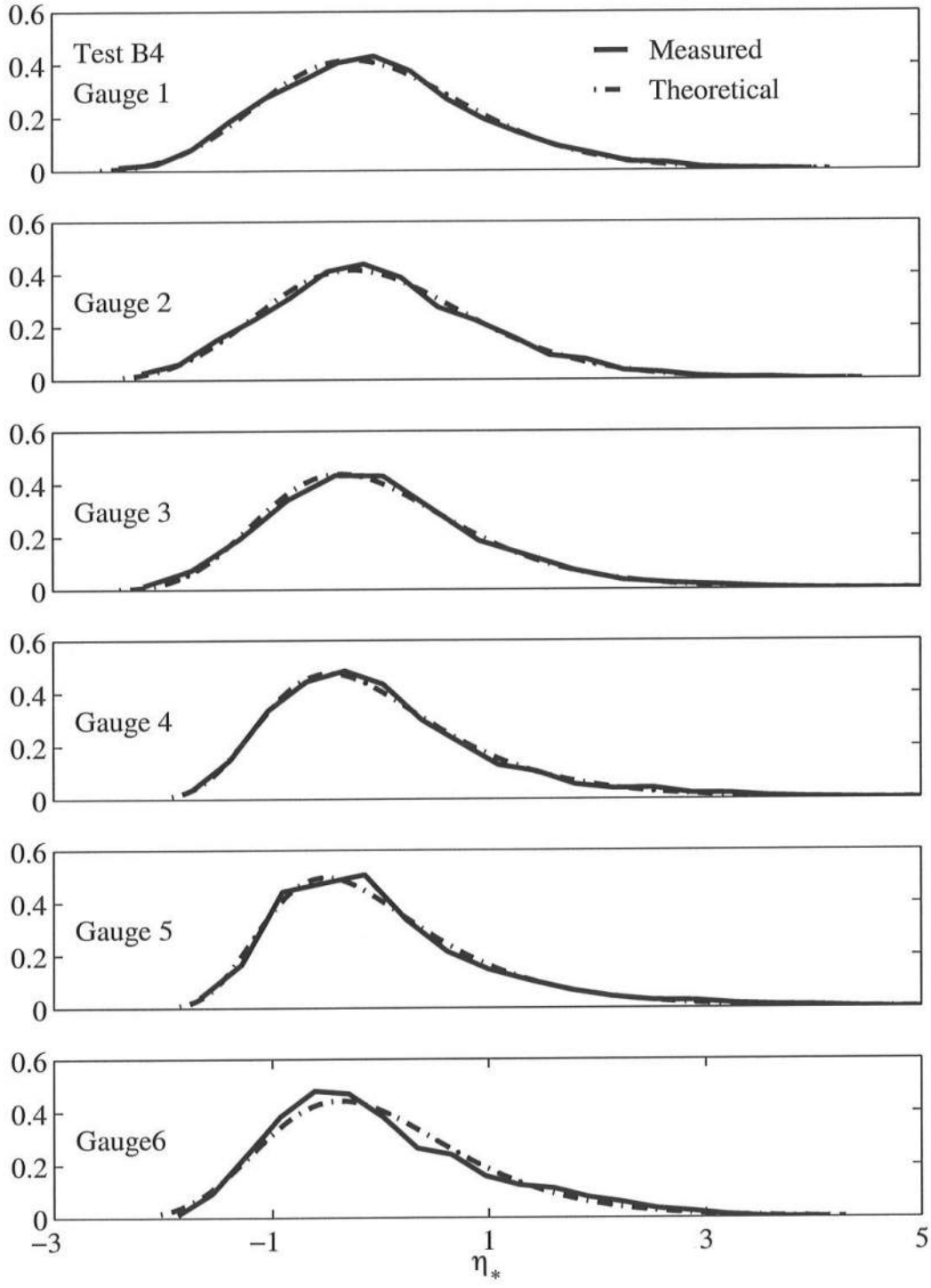

FigureC.19: Free Surface Comparison of Measured Probability Distributions to the Exponential Gamma Distribution for $T_p = 2.4$ s, $d_t = 4$ cm, Gauge 1 – 6.

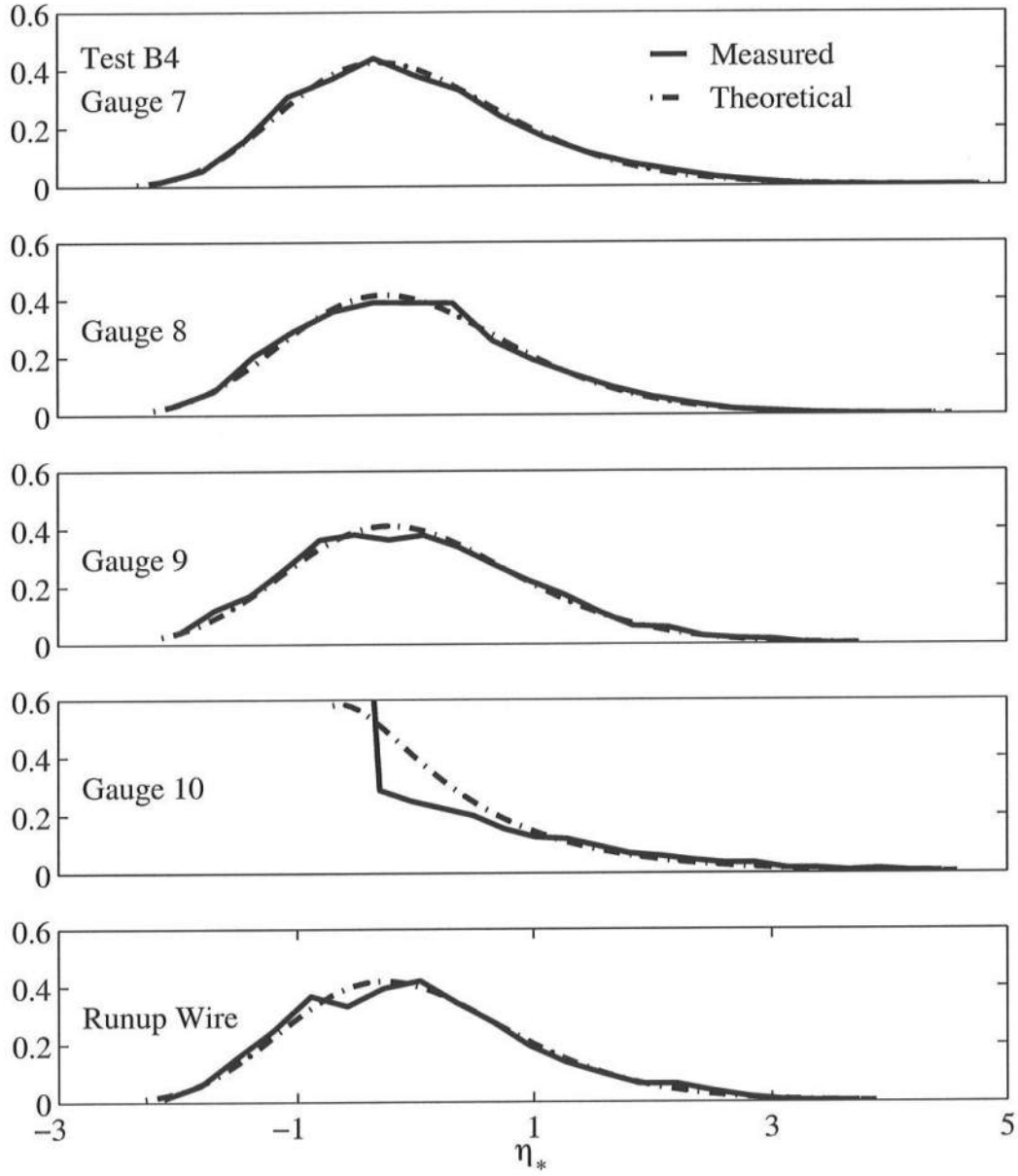

FigureC.20: Free Surface Comparison of Measured Probability Distributions to the Exponential Gamma Distribution for $T_p = 2.4$ s, $d_t = 4$ cm, Gauge 7 – Runup Wire

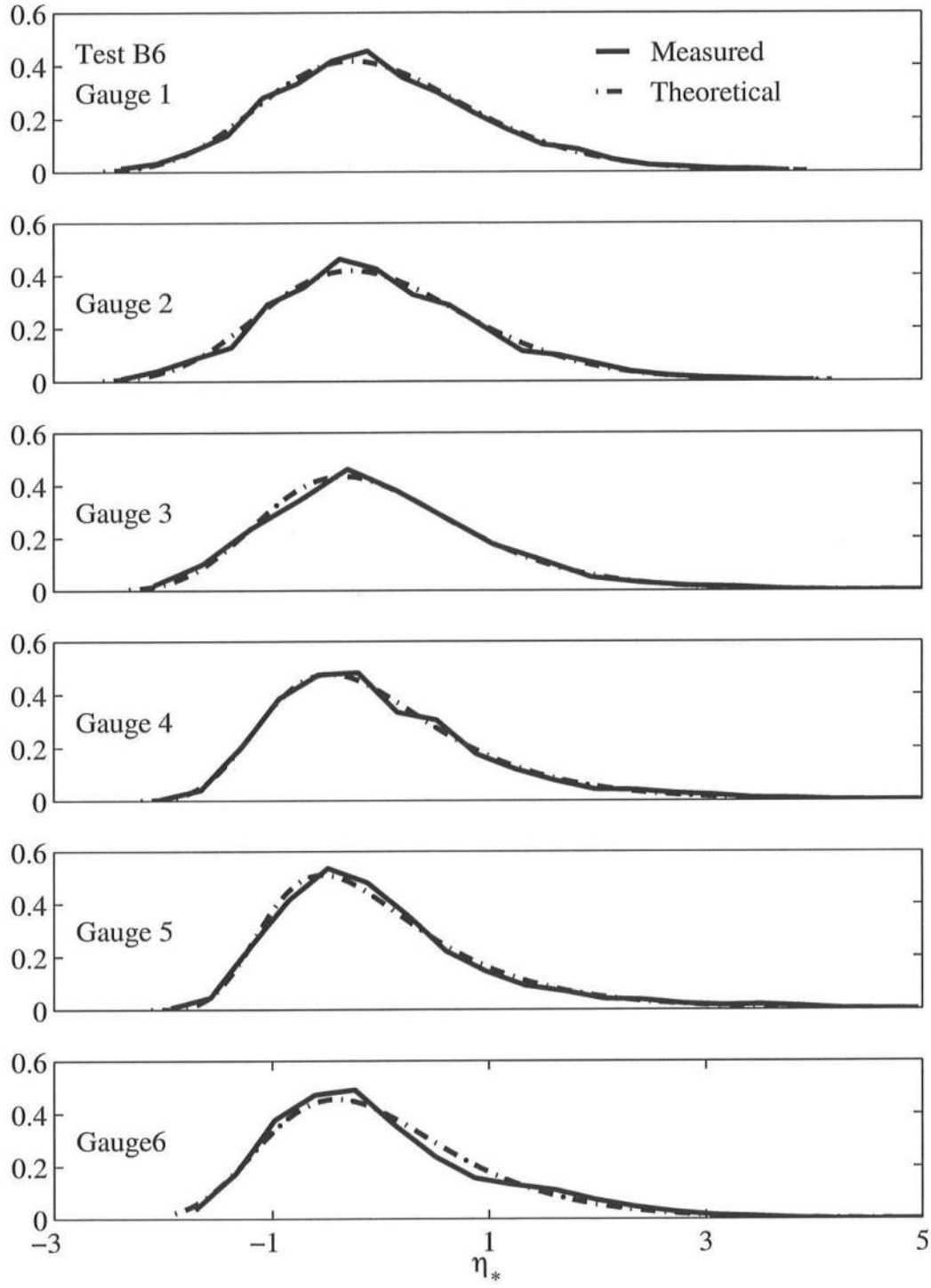

FigureC.21: Free Surface Comparison of Measured Probability Distributions to the Exponential Gamma Distribution for $T_p = 2.4$ s, d_t.= 6 cm, Gauge 1 – 6.

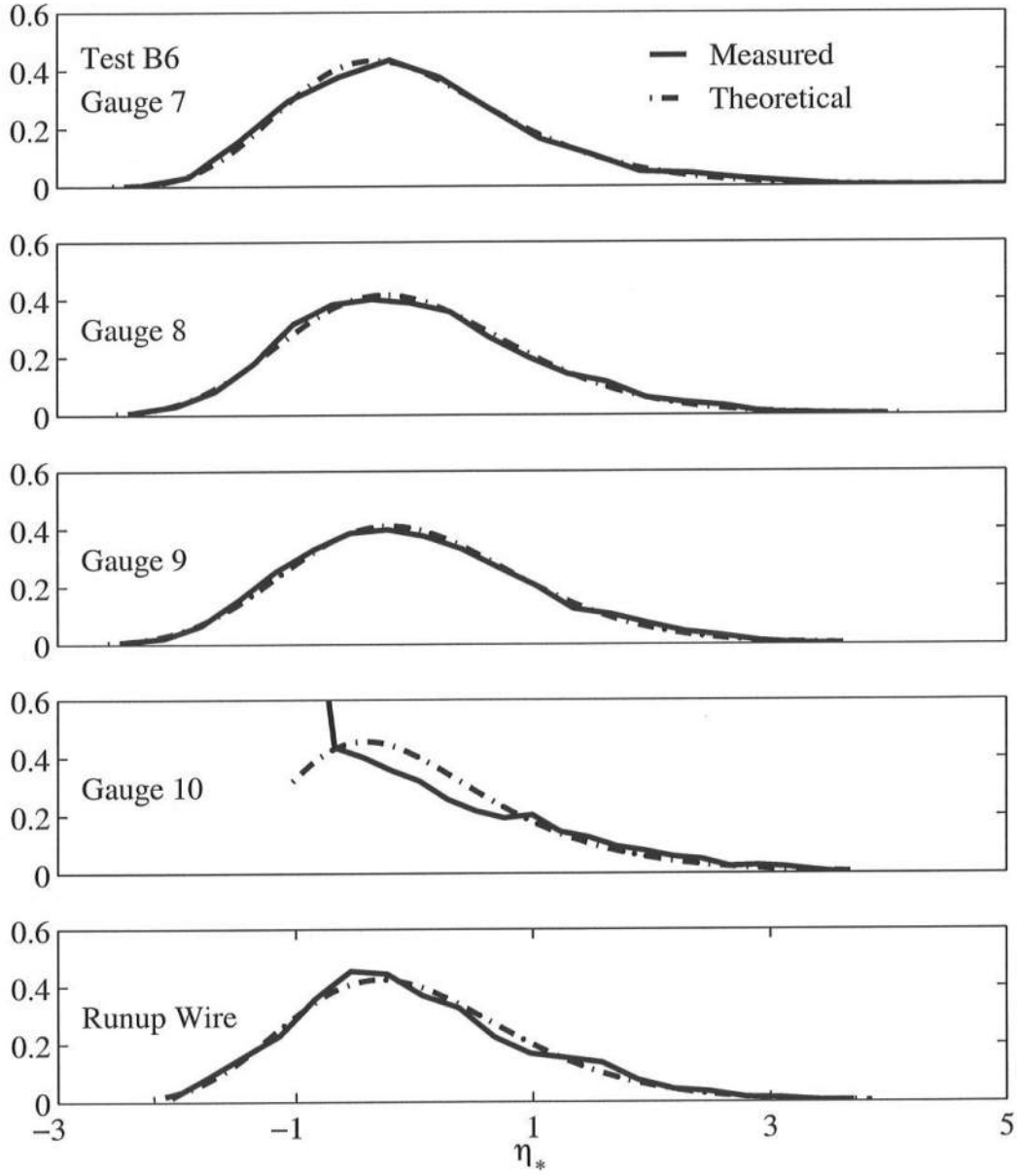

FigureC.22: Free Surface Comparison of Measured Probability Distributions to the Exponential Gamma Distribution for T_p = 2.4 s, d_t.= 6 cm, Gauge 7 – Runup Wire

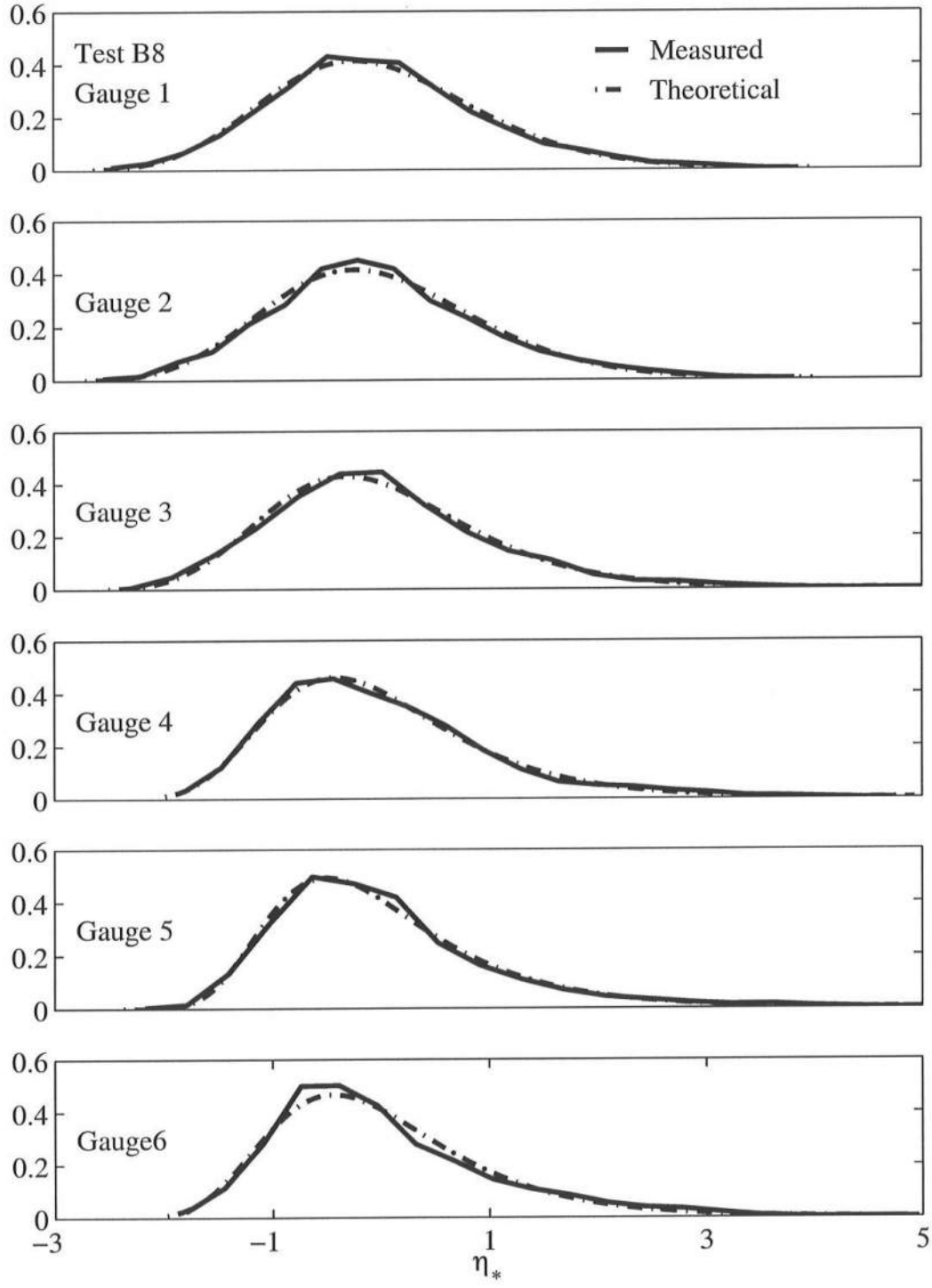

FigureC.23: Free Surface Comparison of Measured Probability Distributions to the Exponential Gamma Distribution for $T_p = 2.4$ s, $d_t = 8$ cm, Gauge 1 – 6.

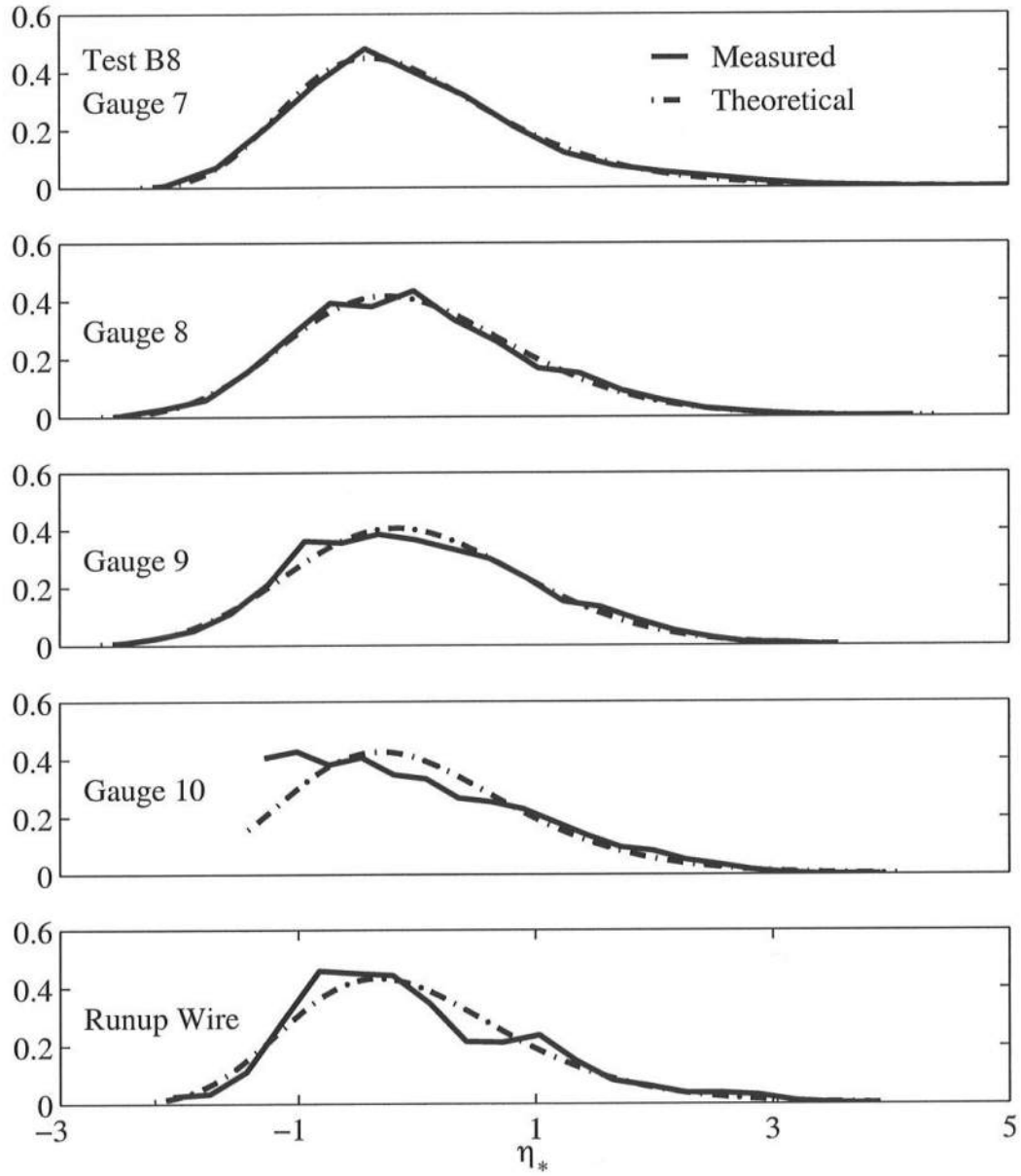

FigureC.24: Free Surface Comparison of Measured Probability Distributions to the Exponential Gamma Distribution for $T_p = 2.4$ s, d_t.= 8 cm, Gauge 7 – Runup Wire

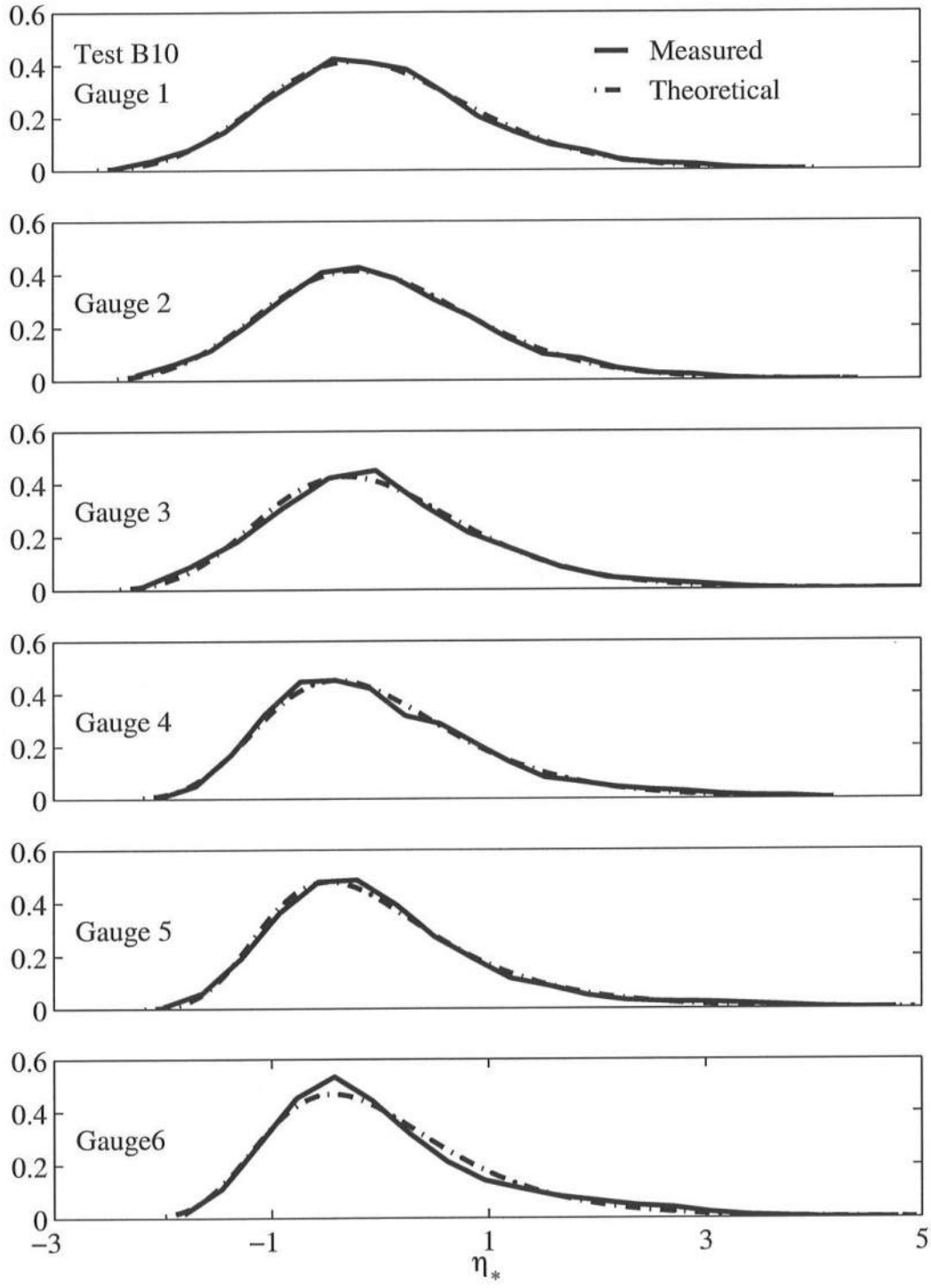

FigureC.25: Free Surface Comparison of Measured Probability Distributions to the Exponential Gamma Distribution for $T_p = 2.4$ s, d_t.= 10 cm, Gauge 1 – 6.

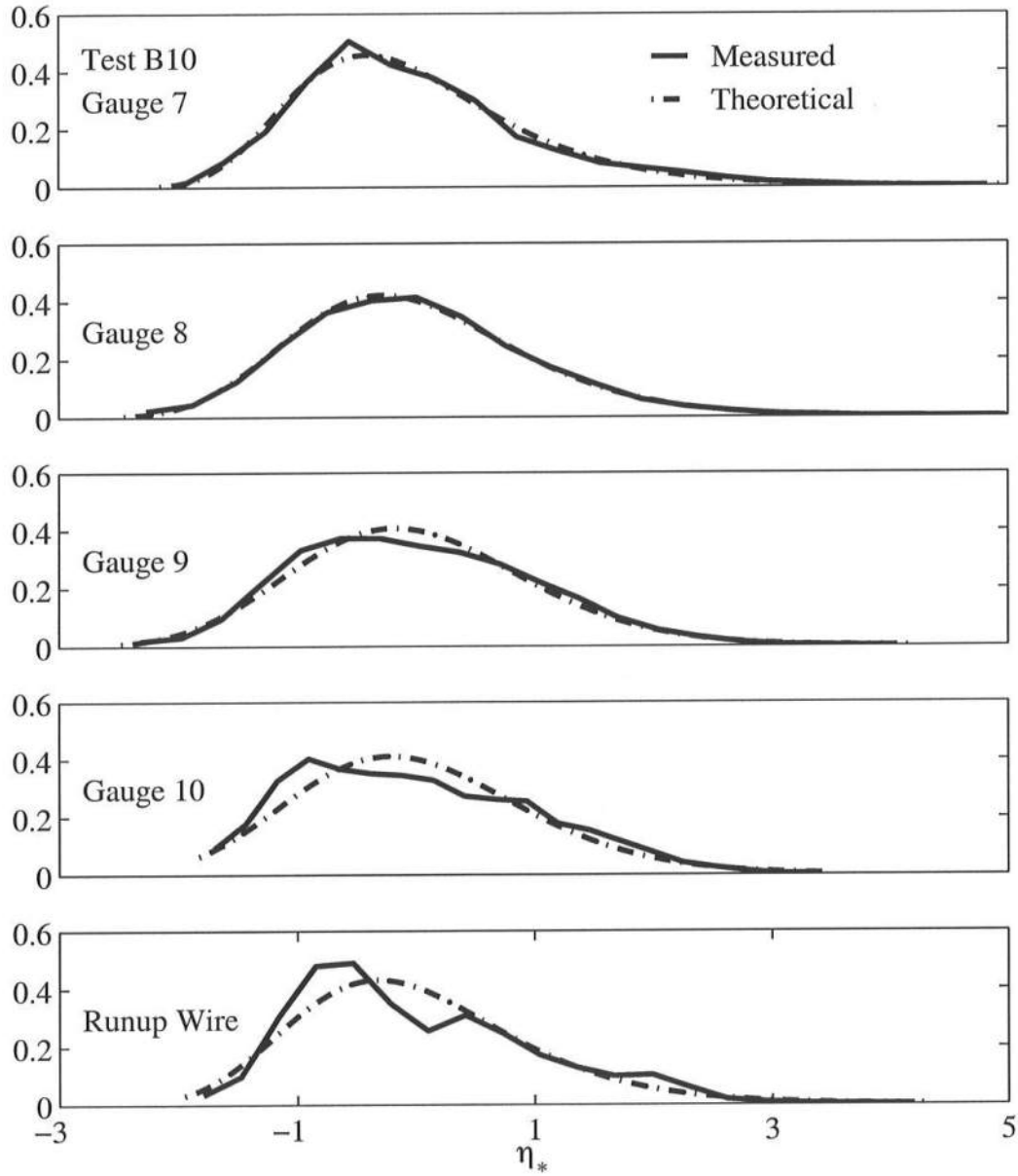

FigureC.26: Free Surface Comparison of Measured Probability Distributions to the Exponential Gamma Distribution for $T_p = 2.4$ s, $d_t = 10$ cm, Gauge 7 – Runup Wire

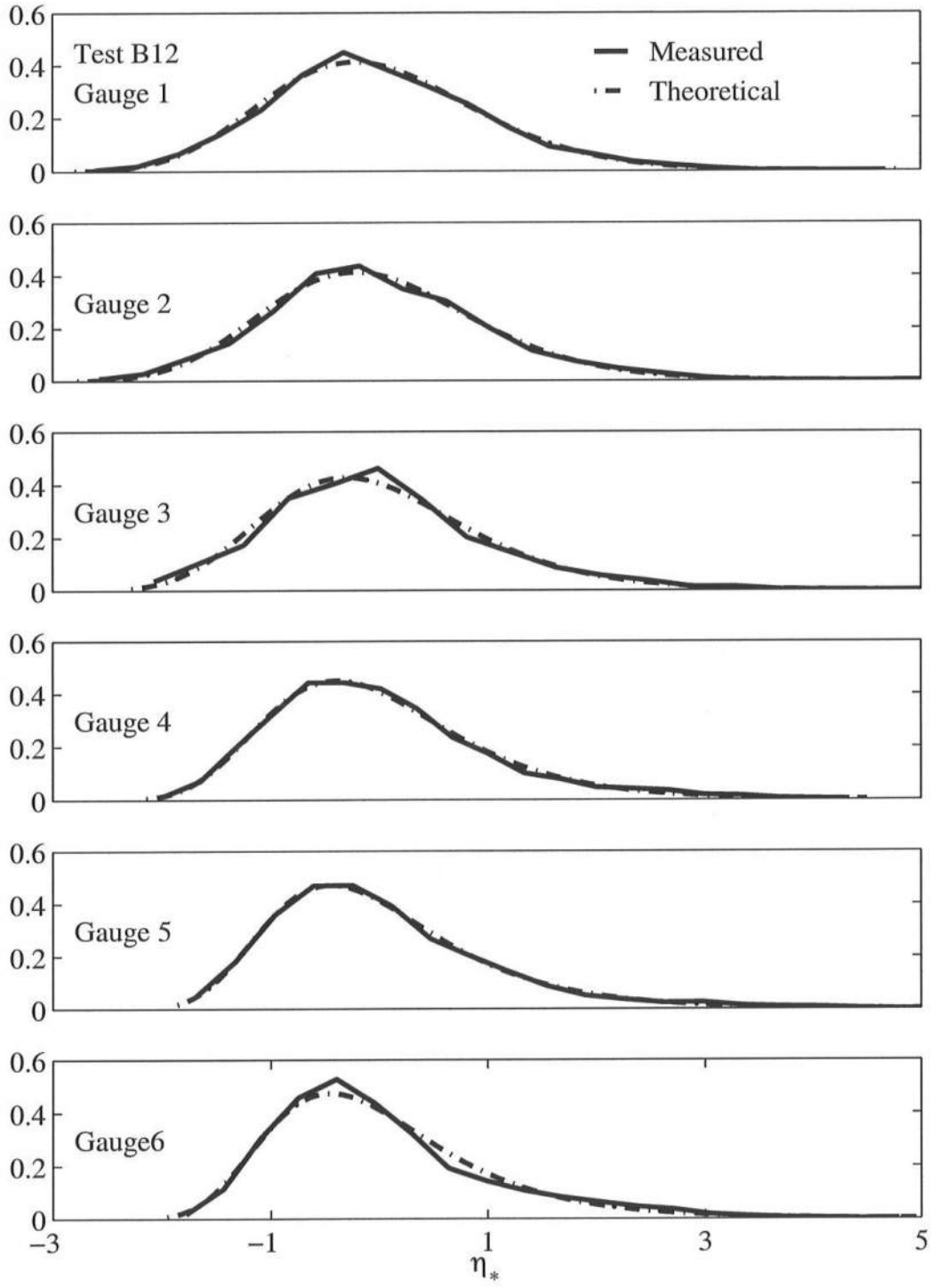

FigureC.27: Free Surface Comparison of Measured Probability Distributions to the Exponential Gamma Distribution for $T_p = 2.4$ s, $d_t = 12$ cm, Gauge 1 – 6.

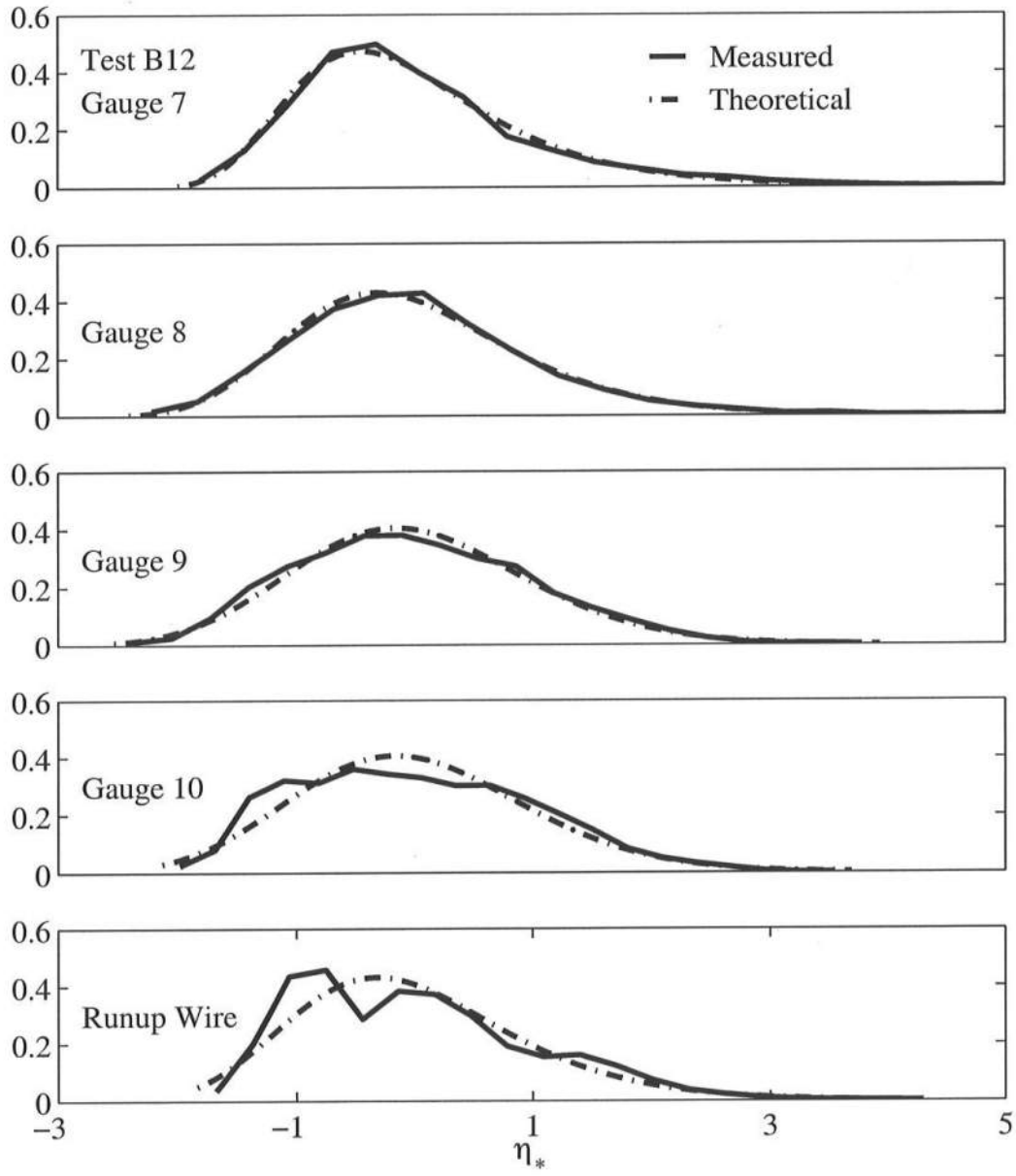

FigureC.28: Free Surface Comparison of Measured Probability Distributions to the Exponential Gamma Distribution for T_p = 2.4 s, d_t.= 12 cm, Gauge 7 – Runup Wire

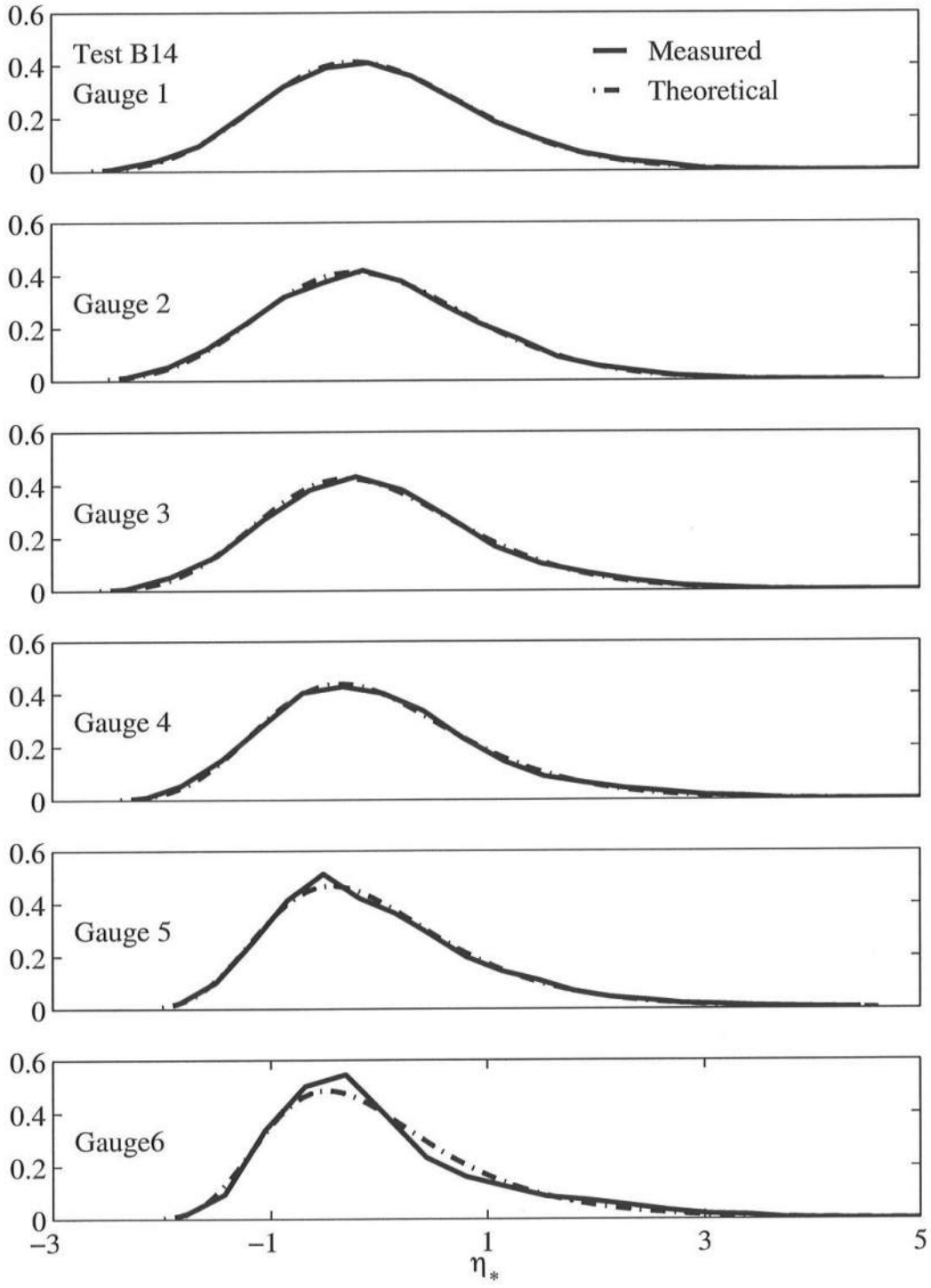

FigureC.29: Free Surface Comparison of Measured Probability Distributions to the Exponential Gamma Distribution for T_p = 2.4 s, d_t.= 14 cm, Gauge 1 – 6.

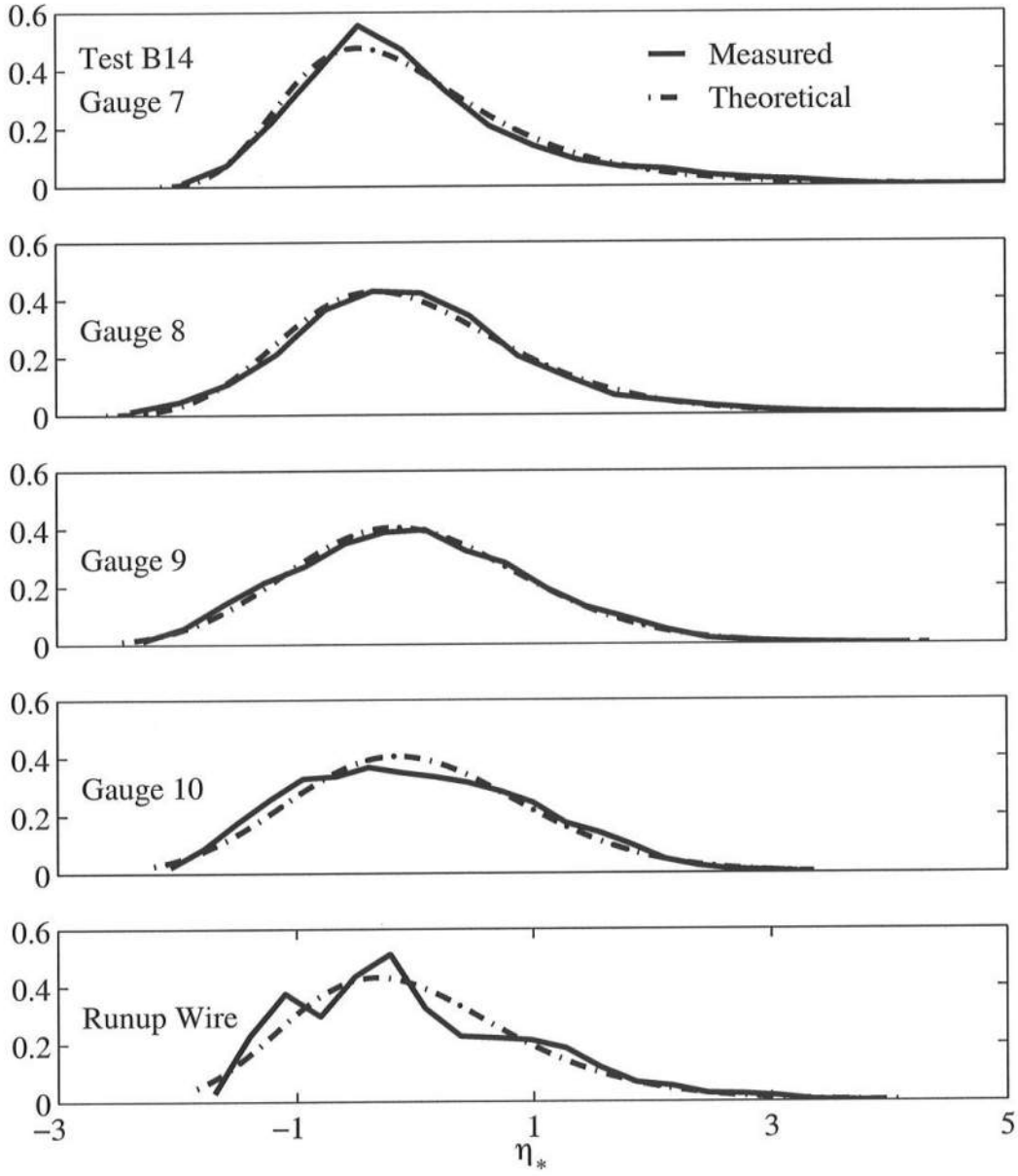

FigureC.30: Free Surface Comparison of Measured Probability Distributions to the Exponential Gamma Distribution for $T_p = 2.4$ s, d_t.= 14 cm, Gauge 7 – Runup Wire

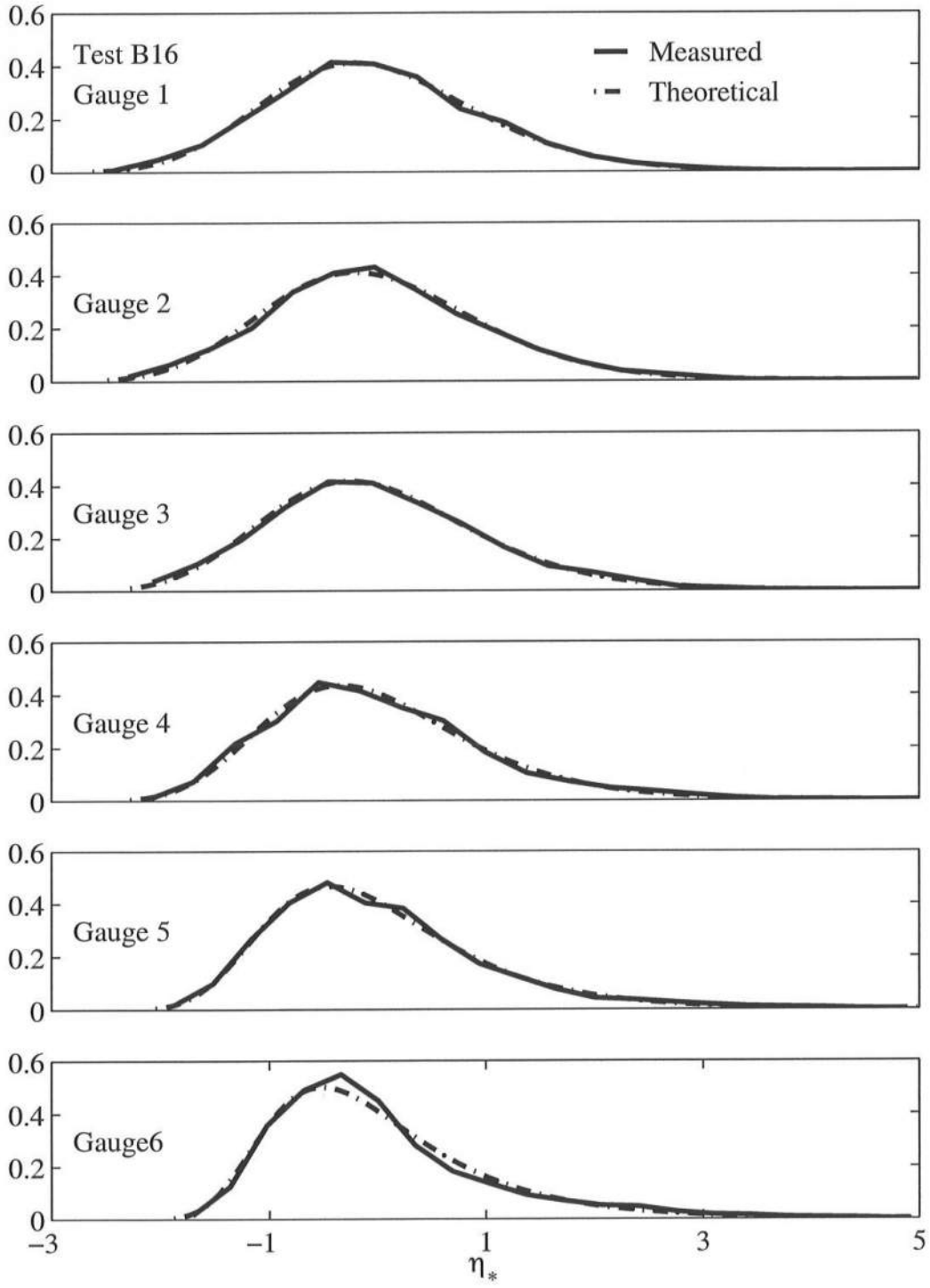

FigureC.31: Free Surface Comparison of Measured Probability Distributions to the Exponential Gamma Distribution for $T_p = 2.4$ s, d_t.= 16 cm, Gauge 1 – 6.

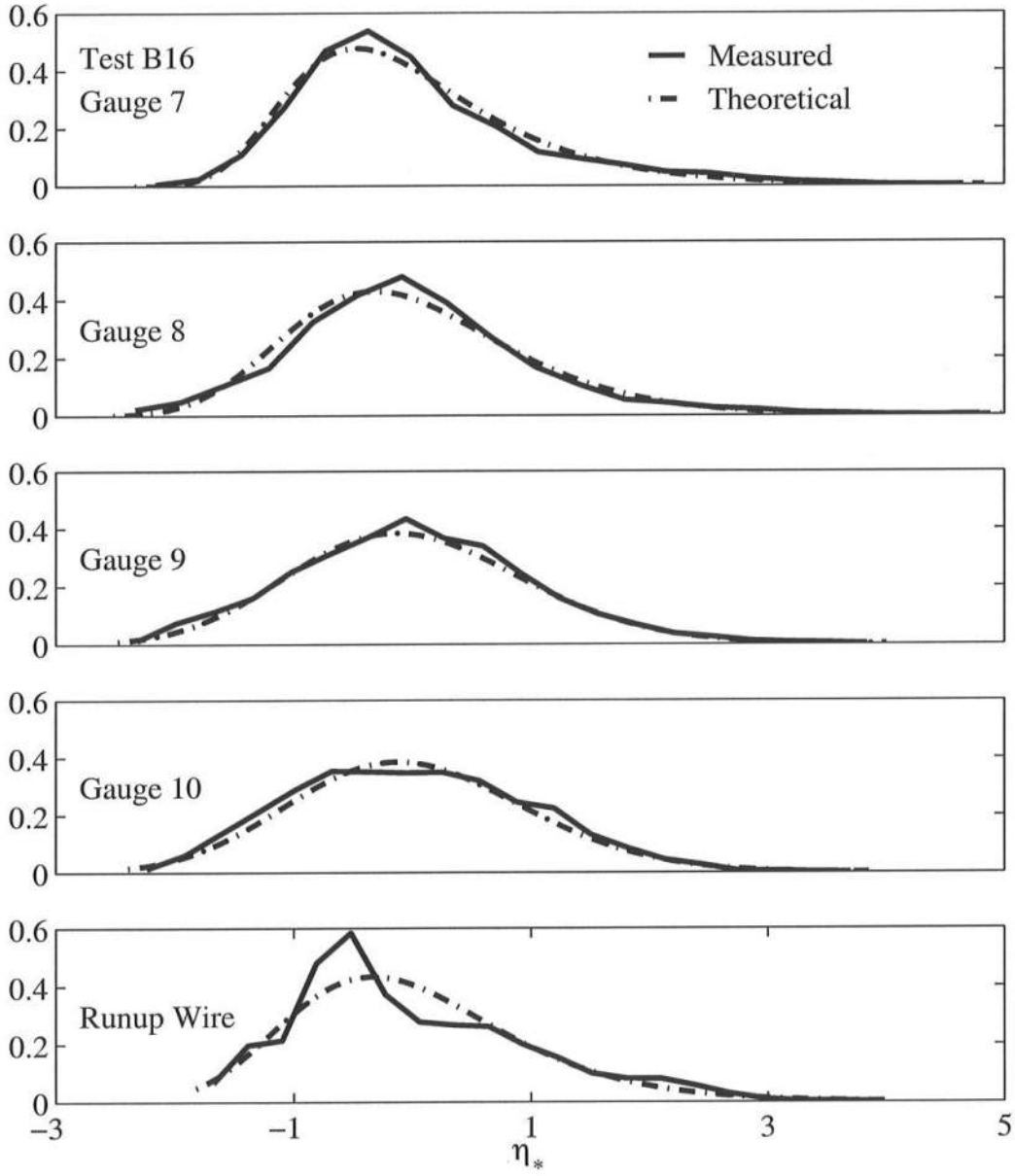

FigureC.32: Free Surface Comparison of Measured Probability Distributions to the Exponential Gamma Distribution for $T_p = 2.4$ s, d_t.= 16 cm, Gauge 7 – Runup Wire

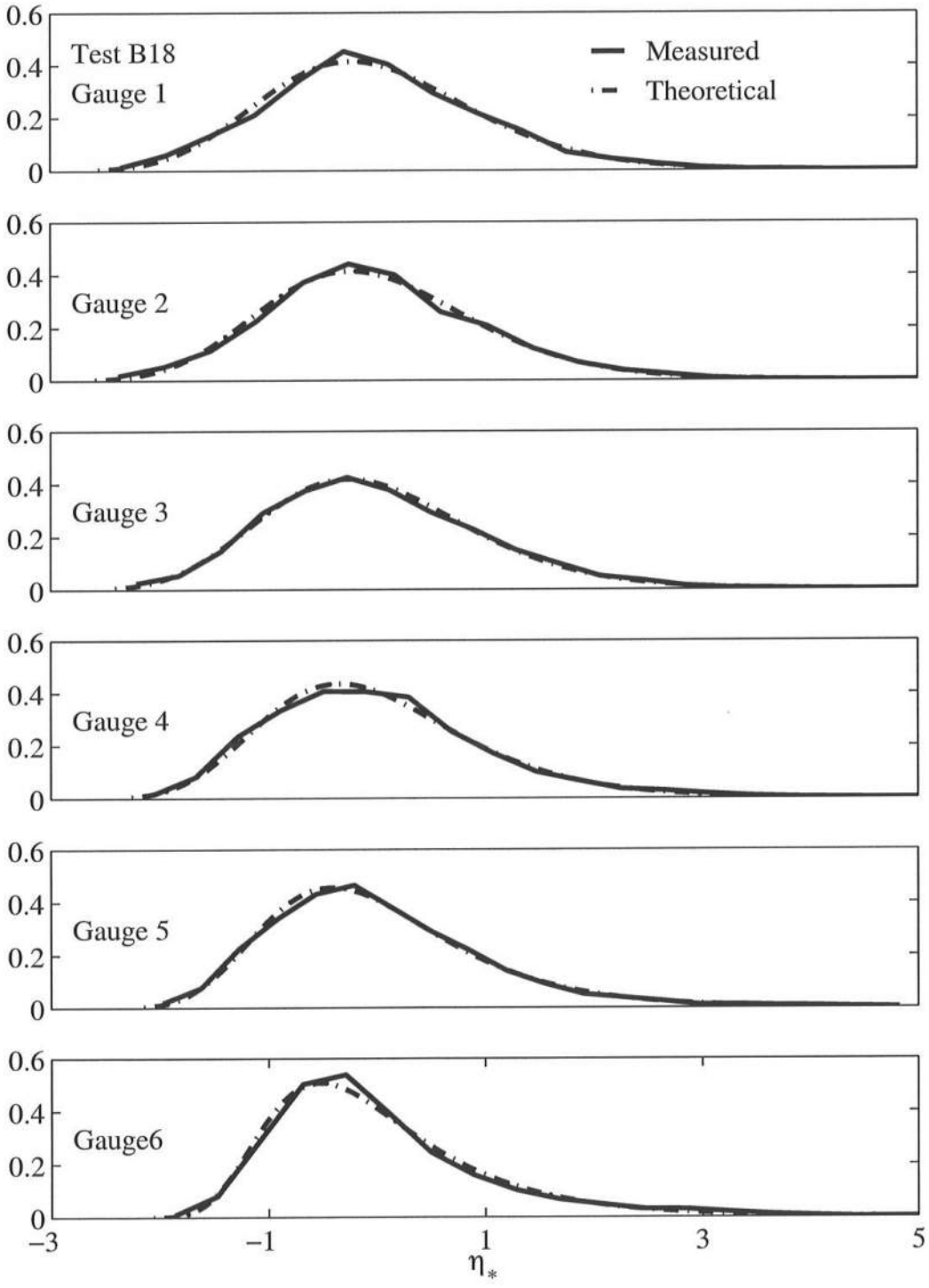

FigureC.33: Free Surface Comparison of Measured Probability Distributions to the Exponential Gamma Distribution for T_p = 2.4 s, d_t.= 18 cm, Gauge 1 – 6.

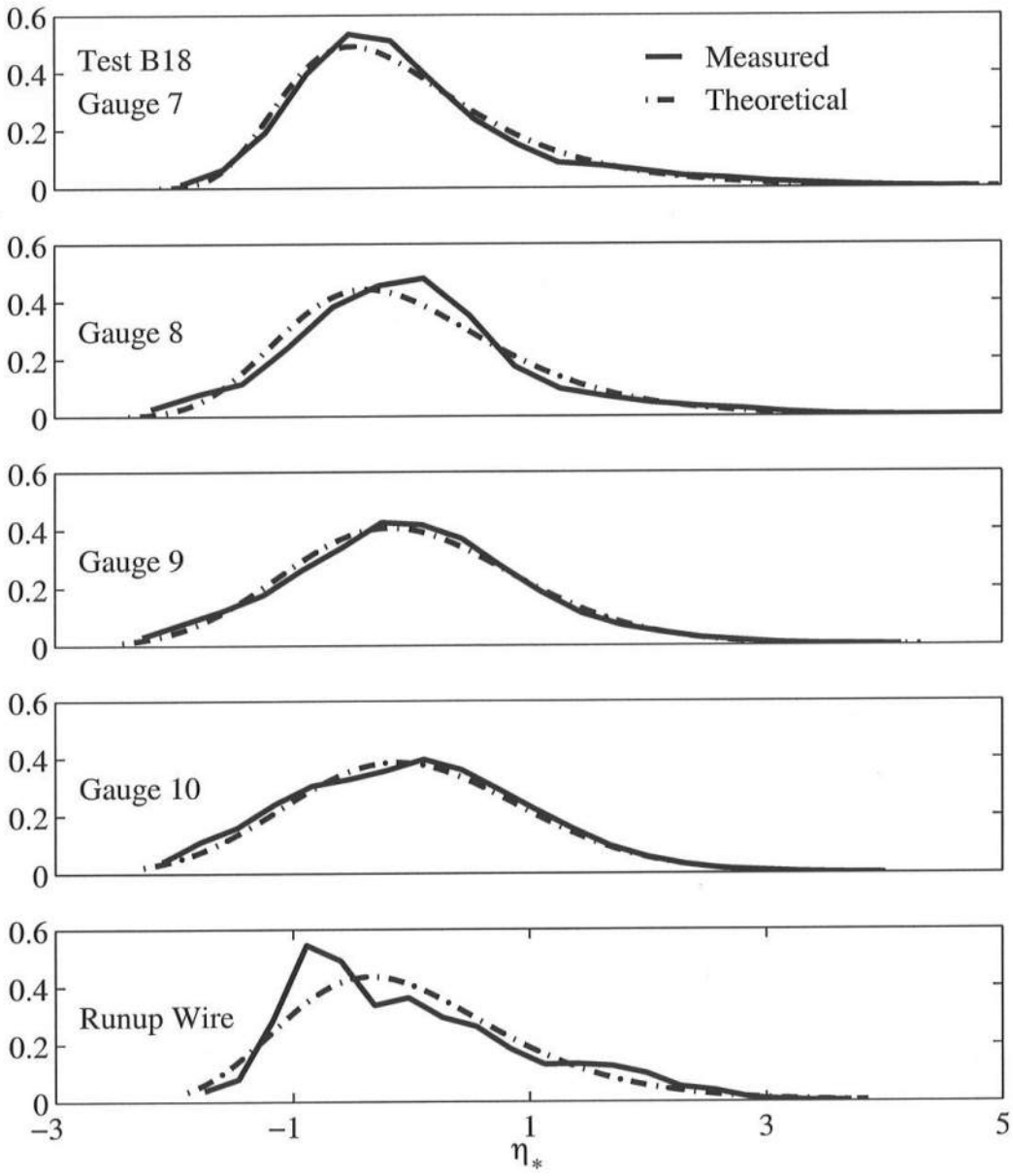

FigureC.34: Free Surface Comparison of Measured Probability Distributions to the Exponential Gamma Distribution for T_p = 2.4 s, d_t.= 18 cm, Gauge 7 – Runup Wire

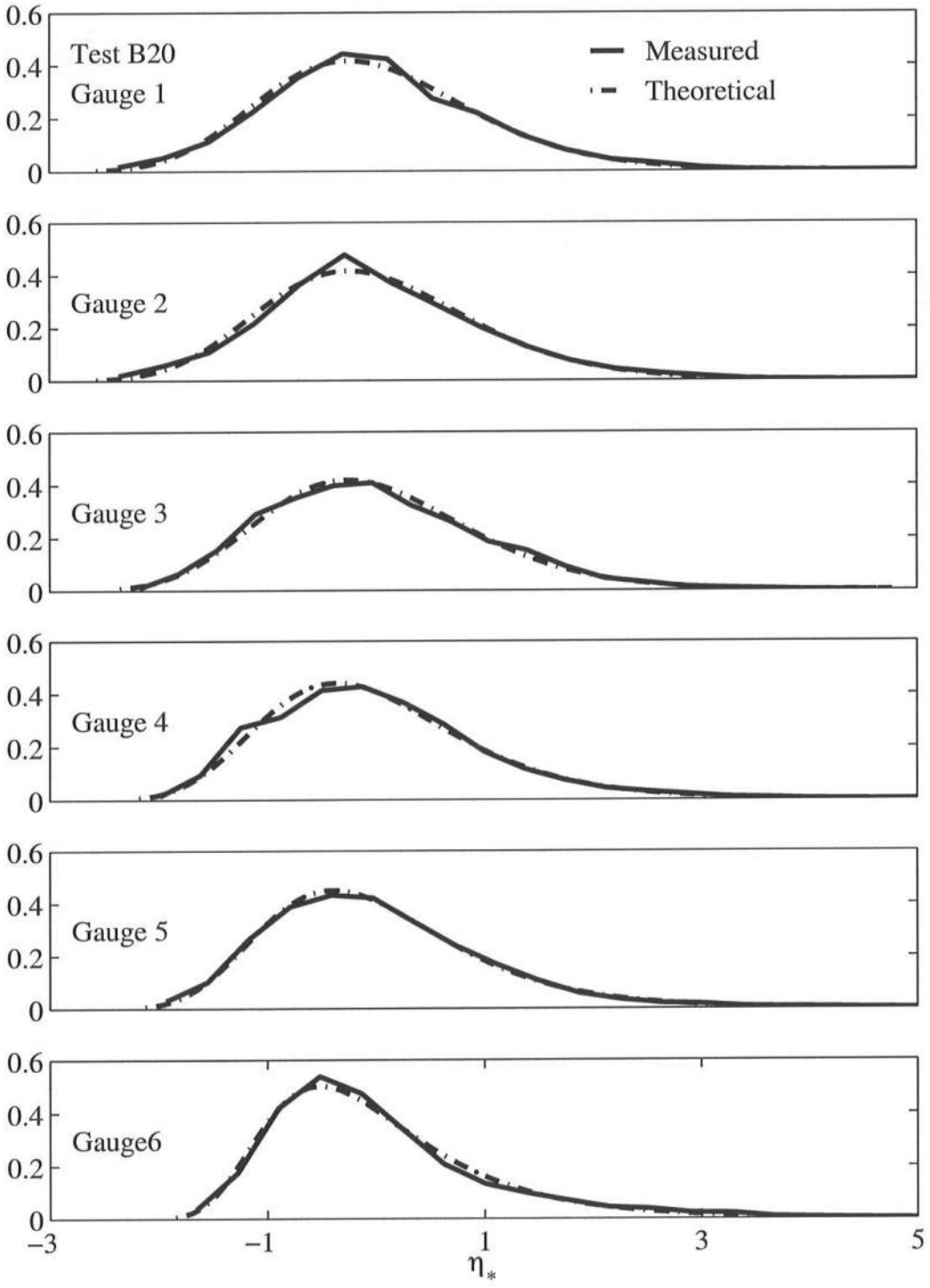

FigureC.35: Free Surface Comparison of Measured Probability Distributions to the Exponential Gamma Distribution for $T_p = 2.4$ s, $d_t = 20$ cm, Gauge 1 – 6.

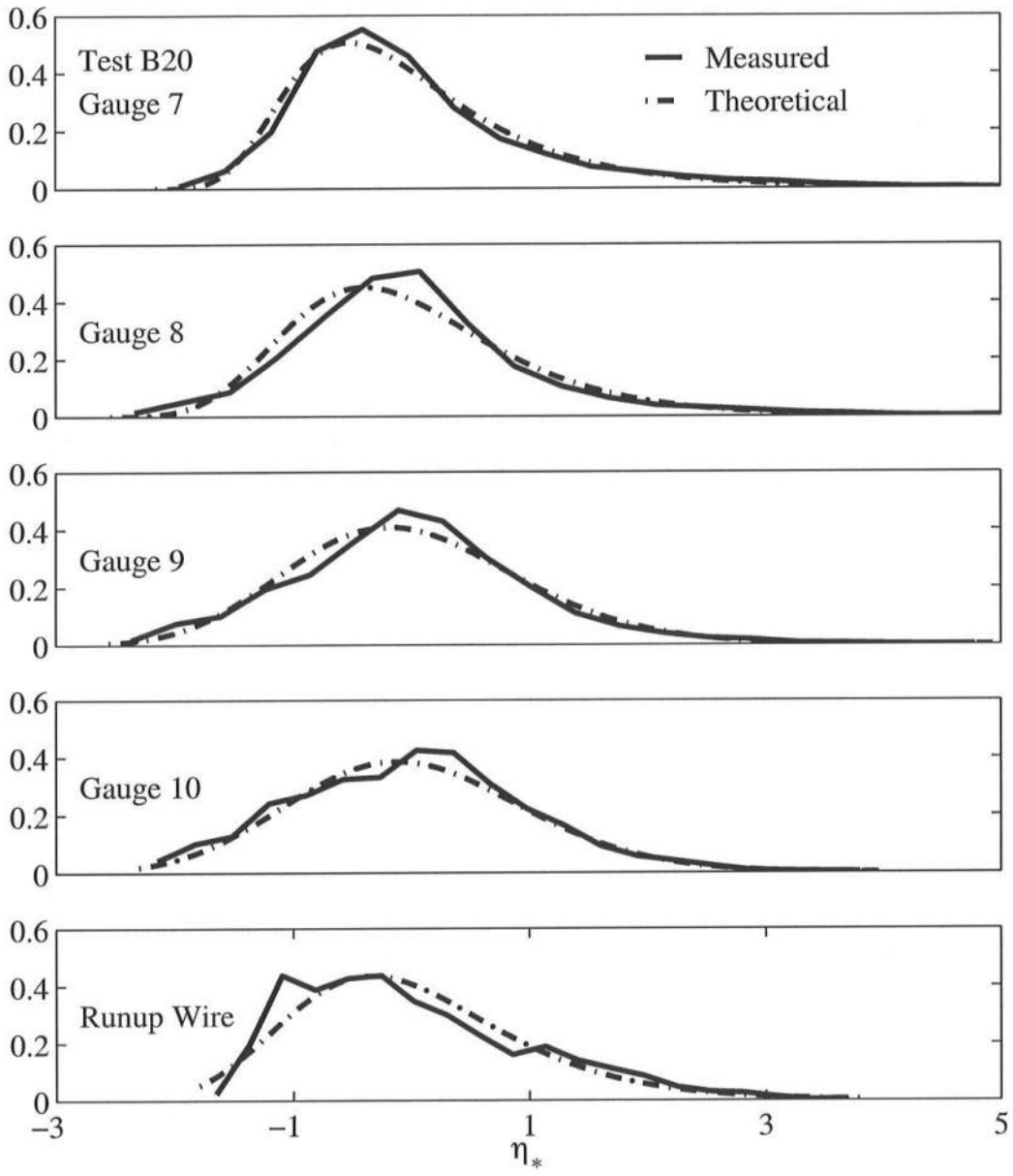

FigureC.36: Free Surface Comparison of Measured Probability Distributions to the Exponential Gamma Distribution for T_p = 2.4 s, d_t.= 20 cm, Gauge 7 – Runup Wire

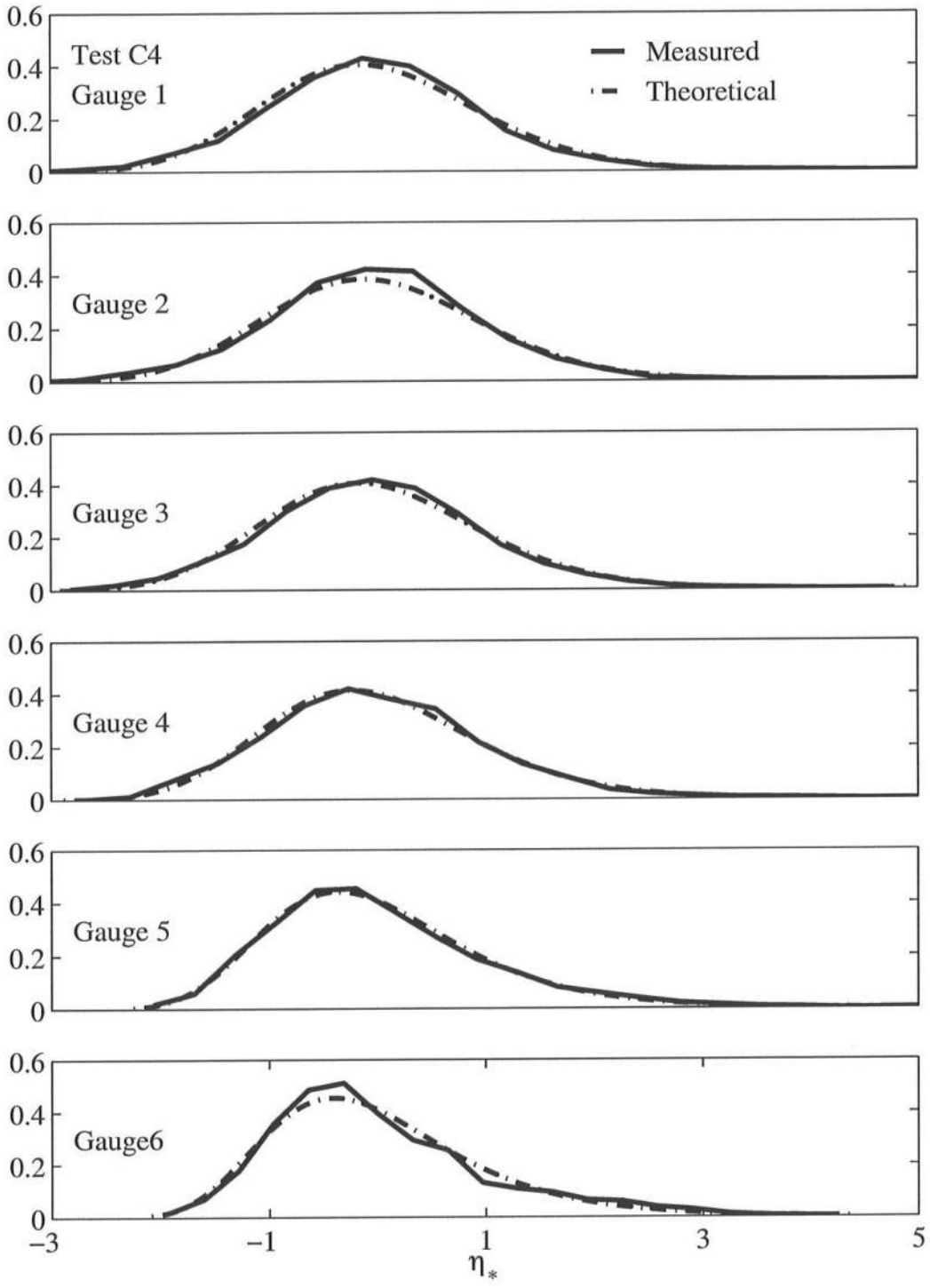

FigureC.37: Free Surface Comparison of Measured Probability Distributions to the Exponential Gamma Distribution for T_p = 1.5 s, d_t.= 4 cm, Gauge 1 – 6.

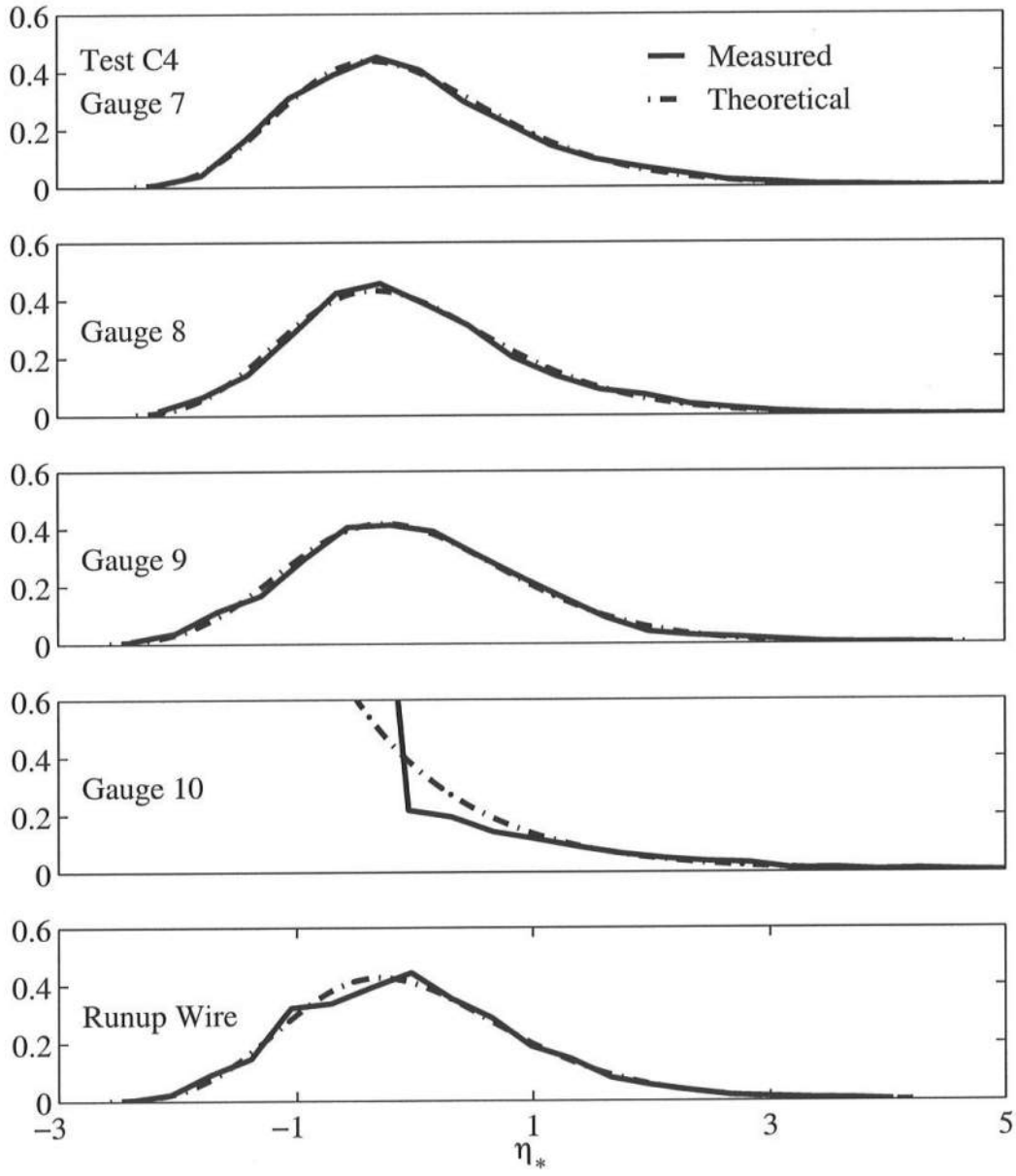

FigureC.38: Free Surface Comparison of Measured Probability Distributions to the Exponential Gamma Distribution for T_p = 1.5 s, d_t.= 4 cm, Gauge 7 – Runup Wire

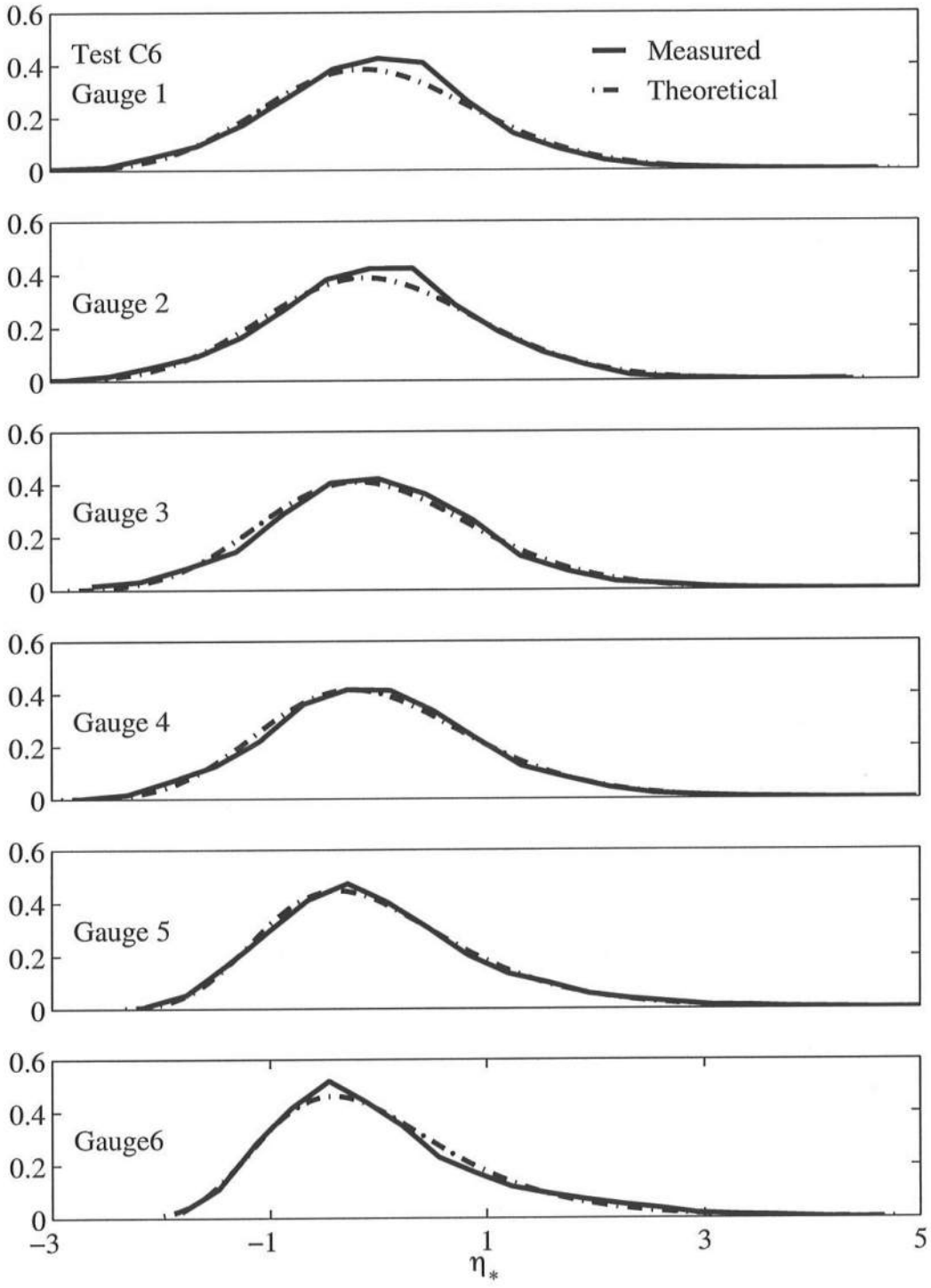

FigureC.39: Free Surface Comparison of Measured Probability Distributions to the Exponential Gamma Distribution for T_p = 1.5 s, d_t.= 6 cm, Gauge 1 – 6.

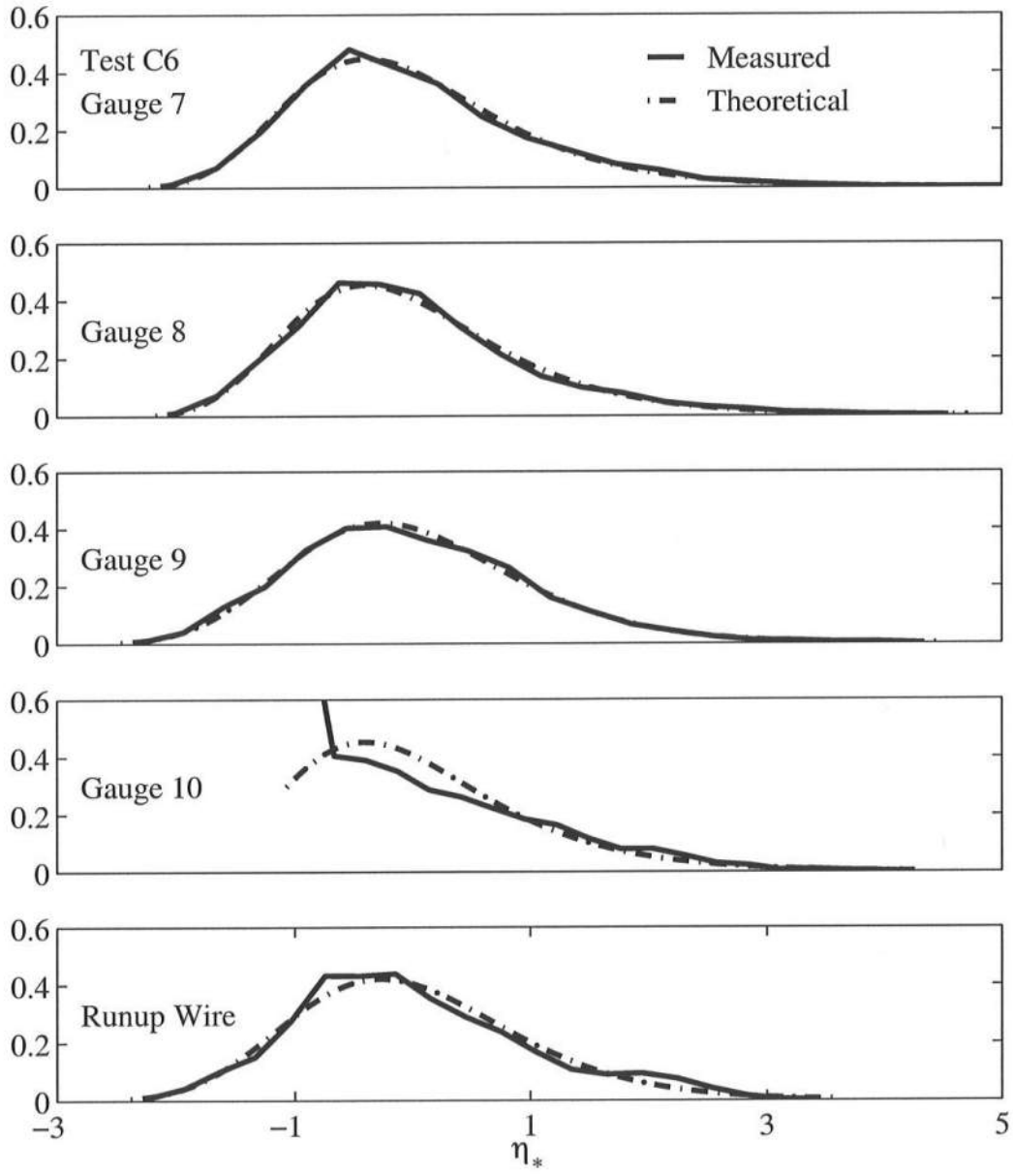

FigureC.40: Free Surface Comparison of Measured Probability Distributions to the Exponential Gamma Distribution for T_p = 1.5 s, d_t.= 6 cm, Gauge 7 – Runup Wire

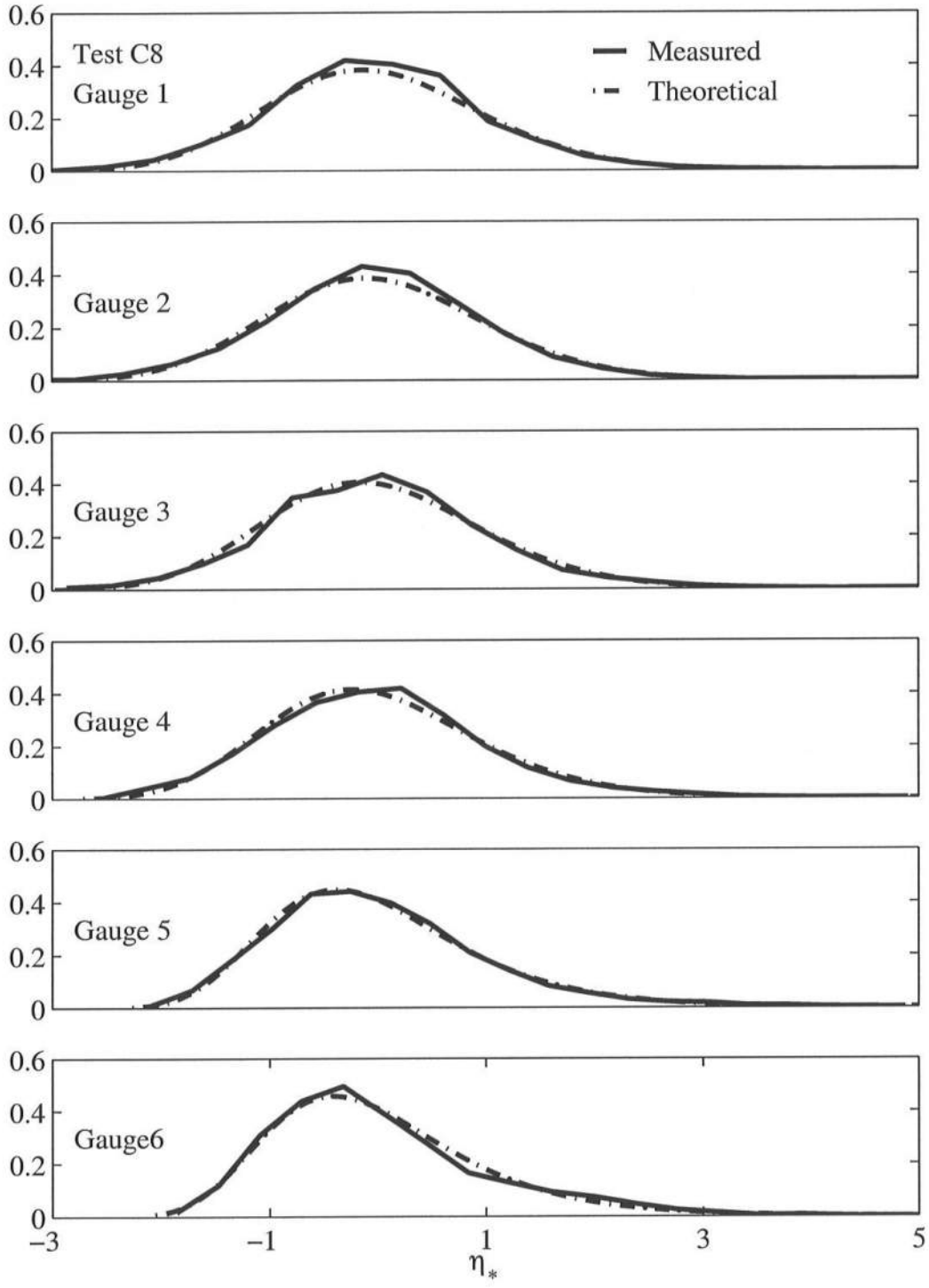

FigureC.41: Free Surface Comparison of Measured Probability Distributions to the Exponential Gamma Distribution for T_p = 1.5 s, d_t.= 8 cm, Gauge 1 – 6.

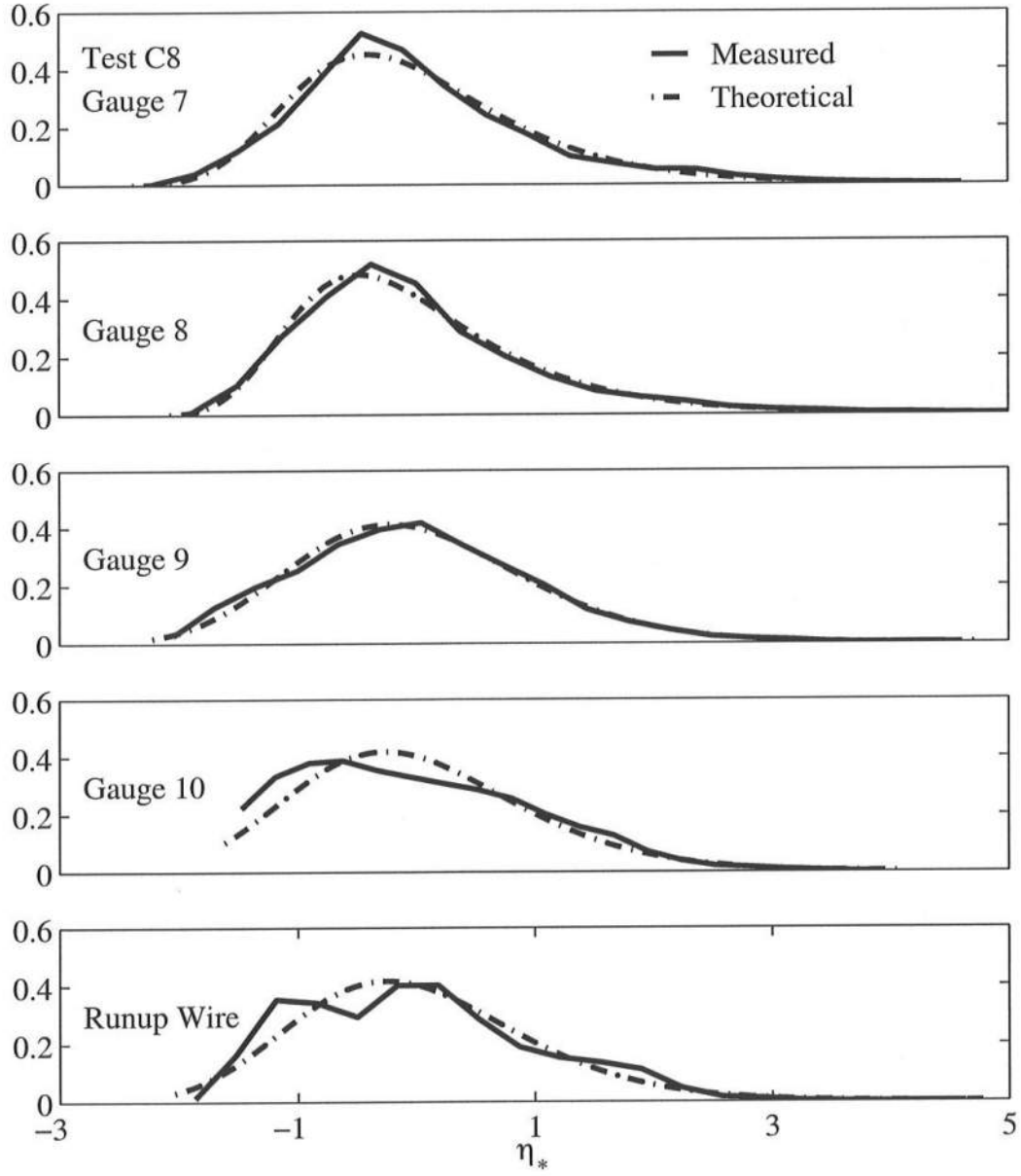

FigureC.42: Free Surface Comparison of Measured Probability Distributions to the Exponential Gamma Distribution for T_p = 1.5 s, d_t.= 8 cm, Gauge 7 – Runup Wire

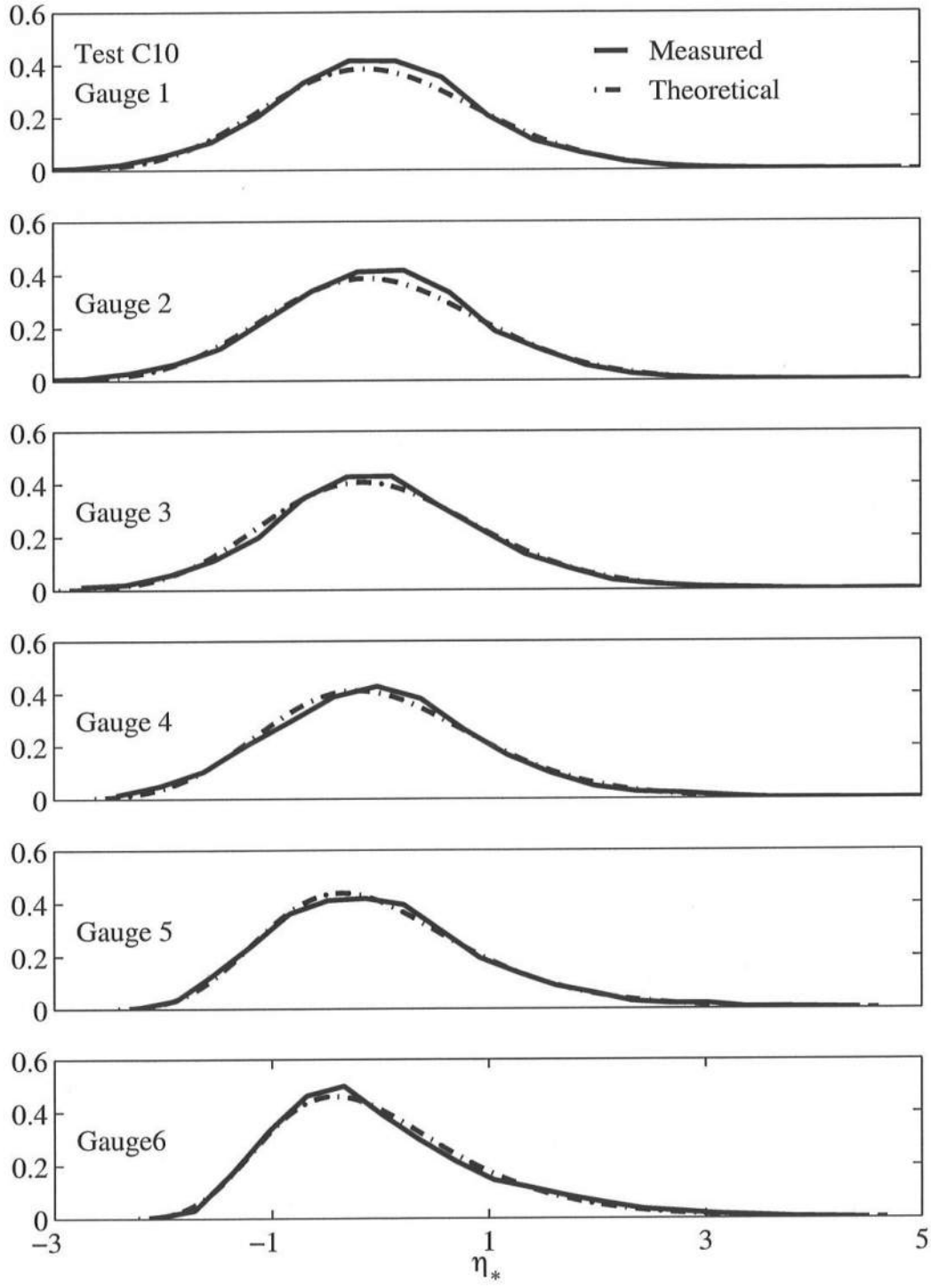

FigureC.43: Free Surface Comparison of Measured Probability Distributions to the Exponential Gamma Distribution for T_p = 1.5 s, d_t.= 10 cm, Gauge 1 – 6.

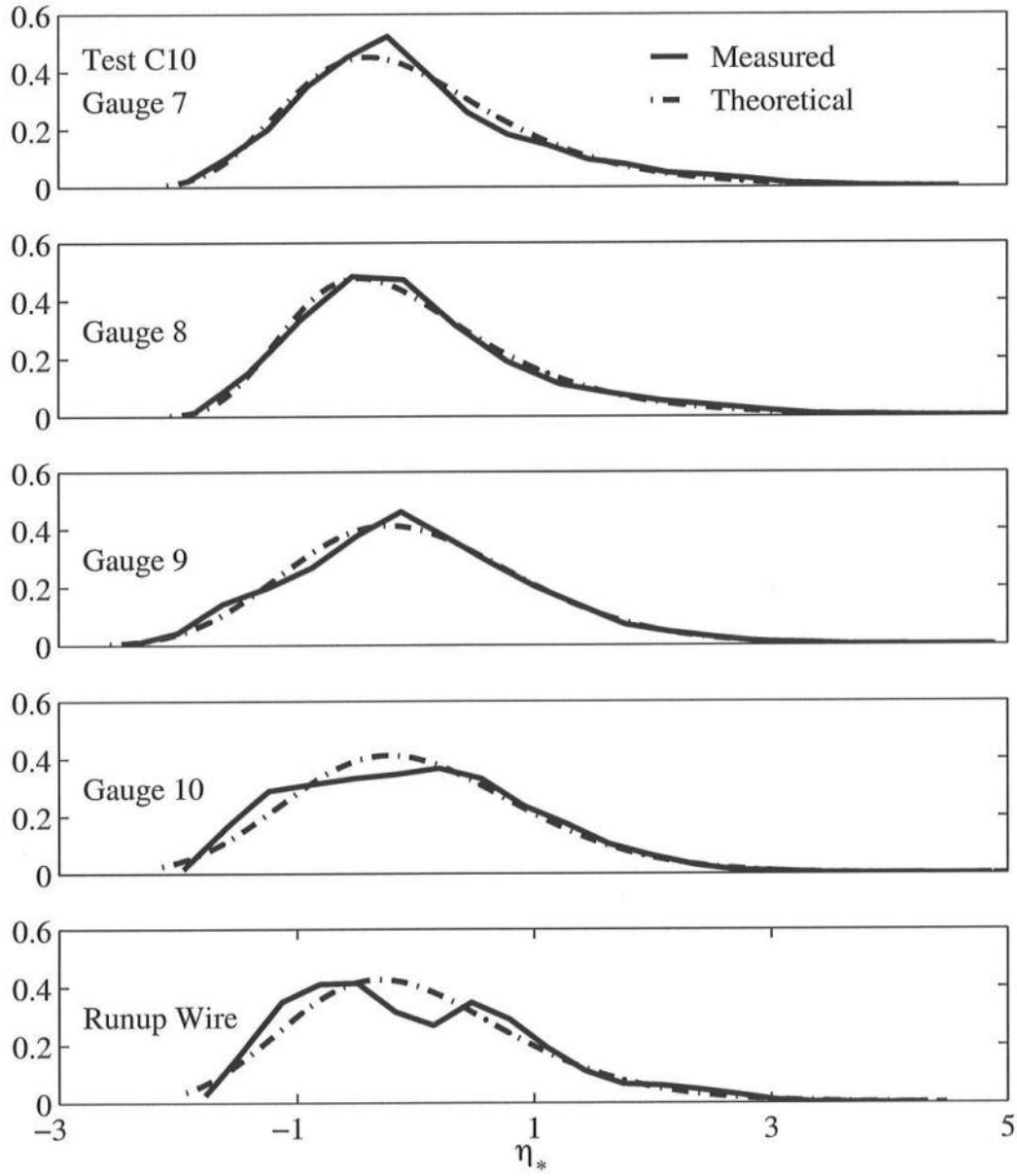

FigureC.44: Free Surface Comparison of Measured Probability Distributions to the Exponential Gamma Distribution for T_p = 1.5 s, d_t.= 10 cm, Gauge 7 – Runup Wire

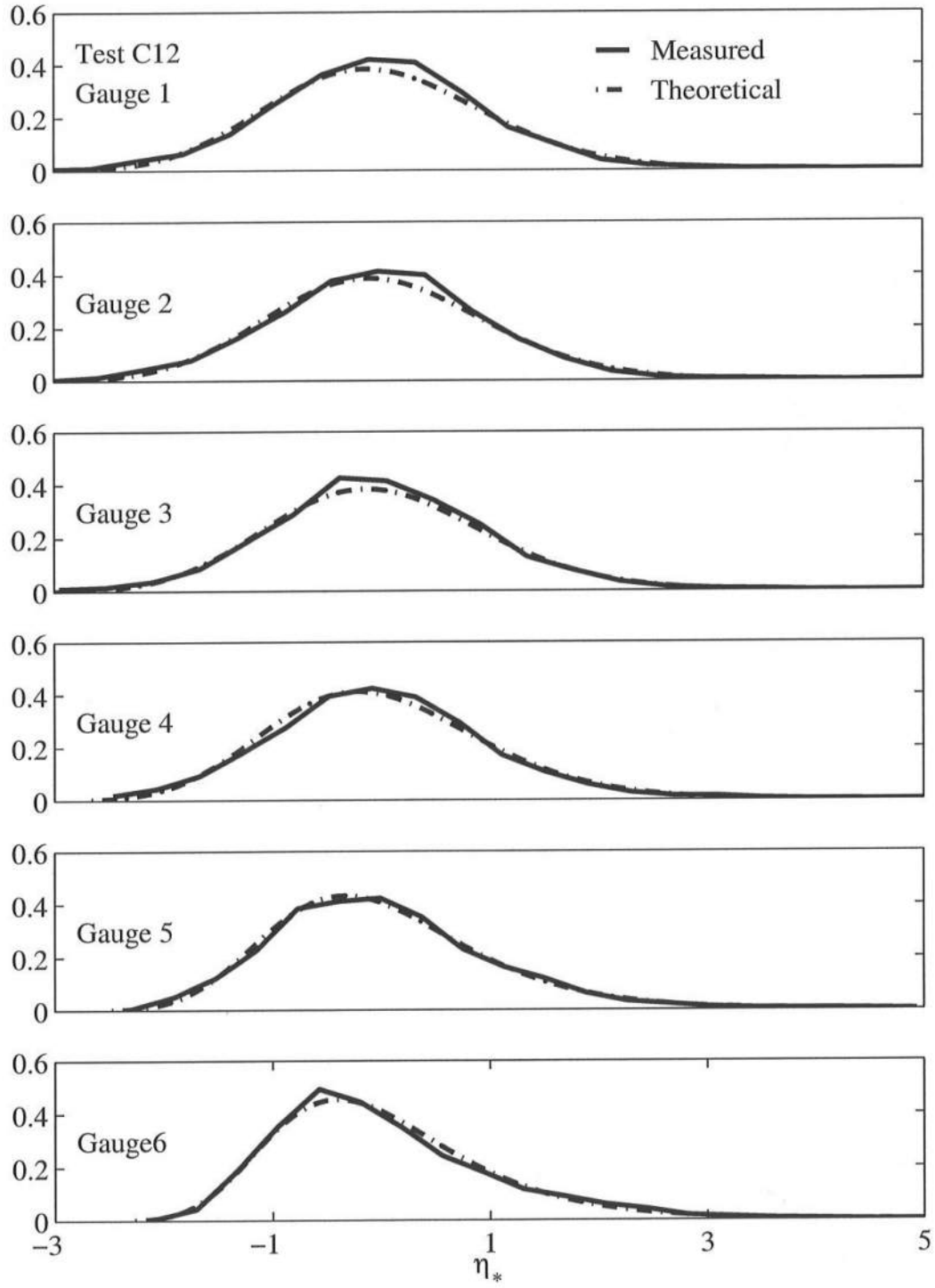

FigureC.45: Free Surface Comparison of Measured Probability Distributions to the Exponential Gamma Distribution for T_p = 1.5 s, d_t.= 12 cm, Gauge 1 – 6.

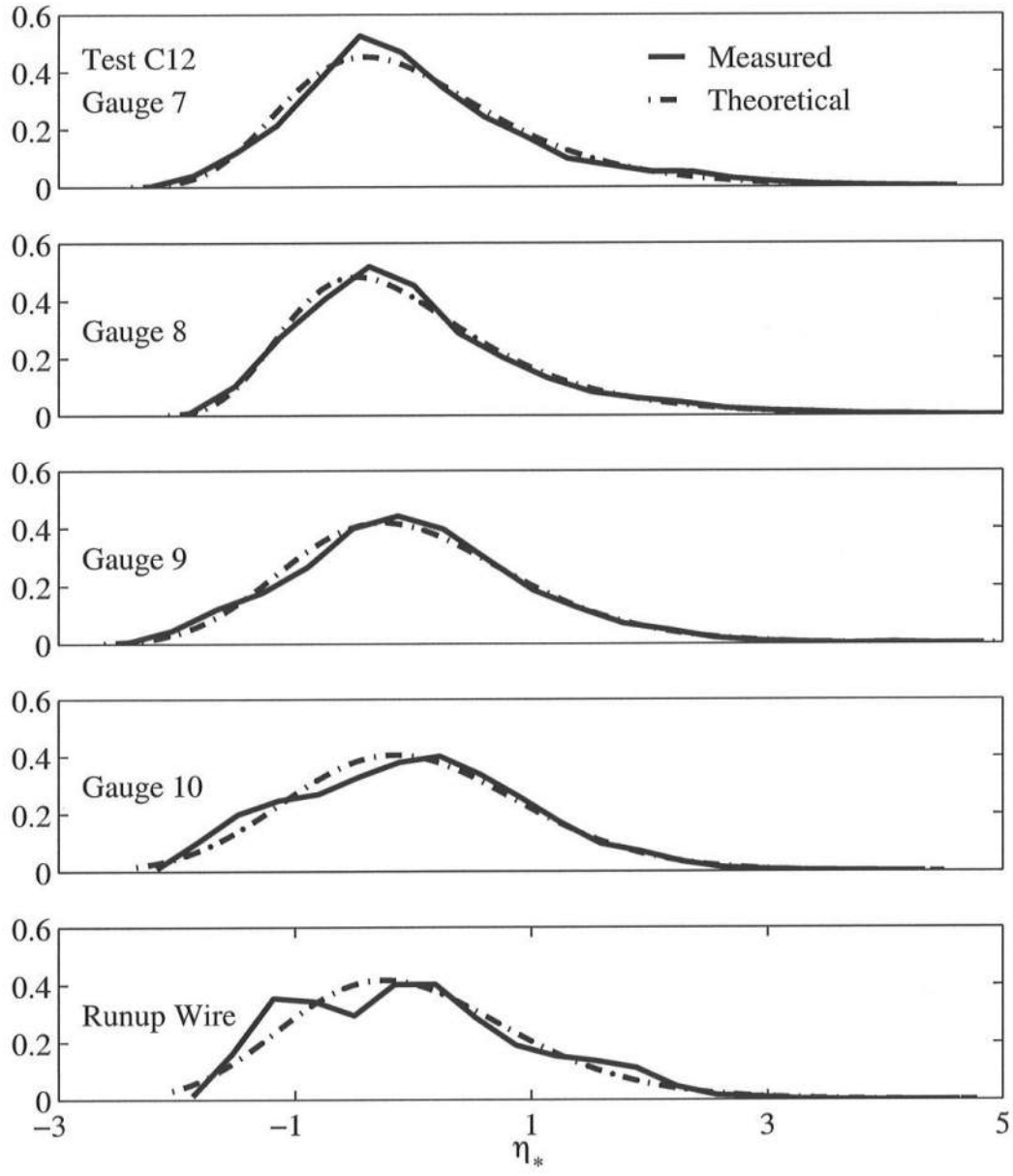

FigureC.46: Free Surface Comparison of Measured Probability Distributions to the Exponential Gamma Distribution for T_p = 1.5 s, d_t.= 12 cm, Gauge 7 – Runup Wire

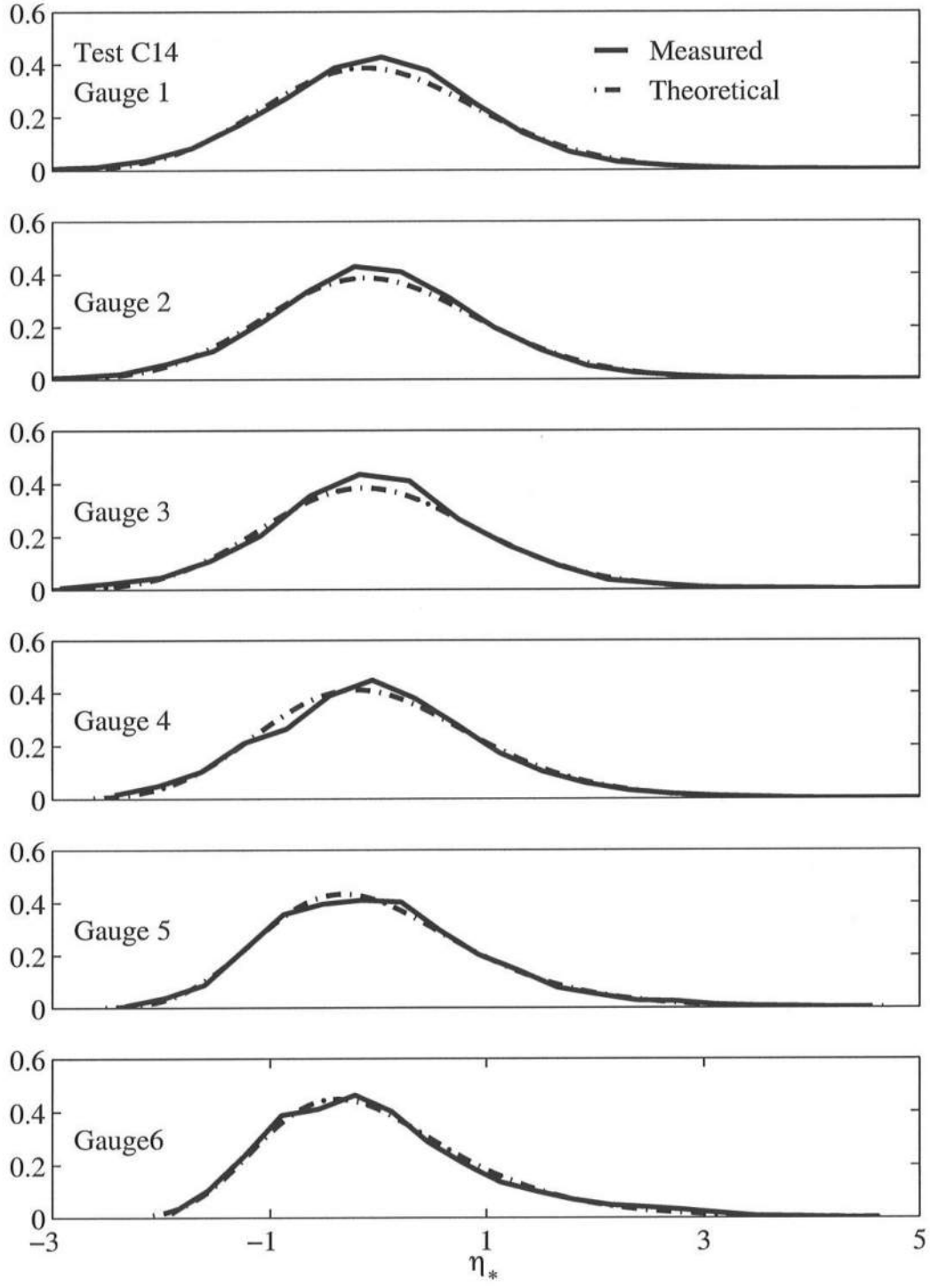

FigureC.47: Free Surface Comparison of Measured Probability Distributions to the Exponential Gamma Distribution for T_p = 1.5 s, d_t.= 14 cm, Gauge 1 – 6.

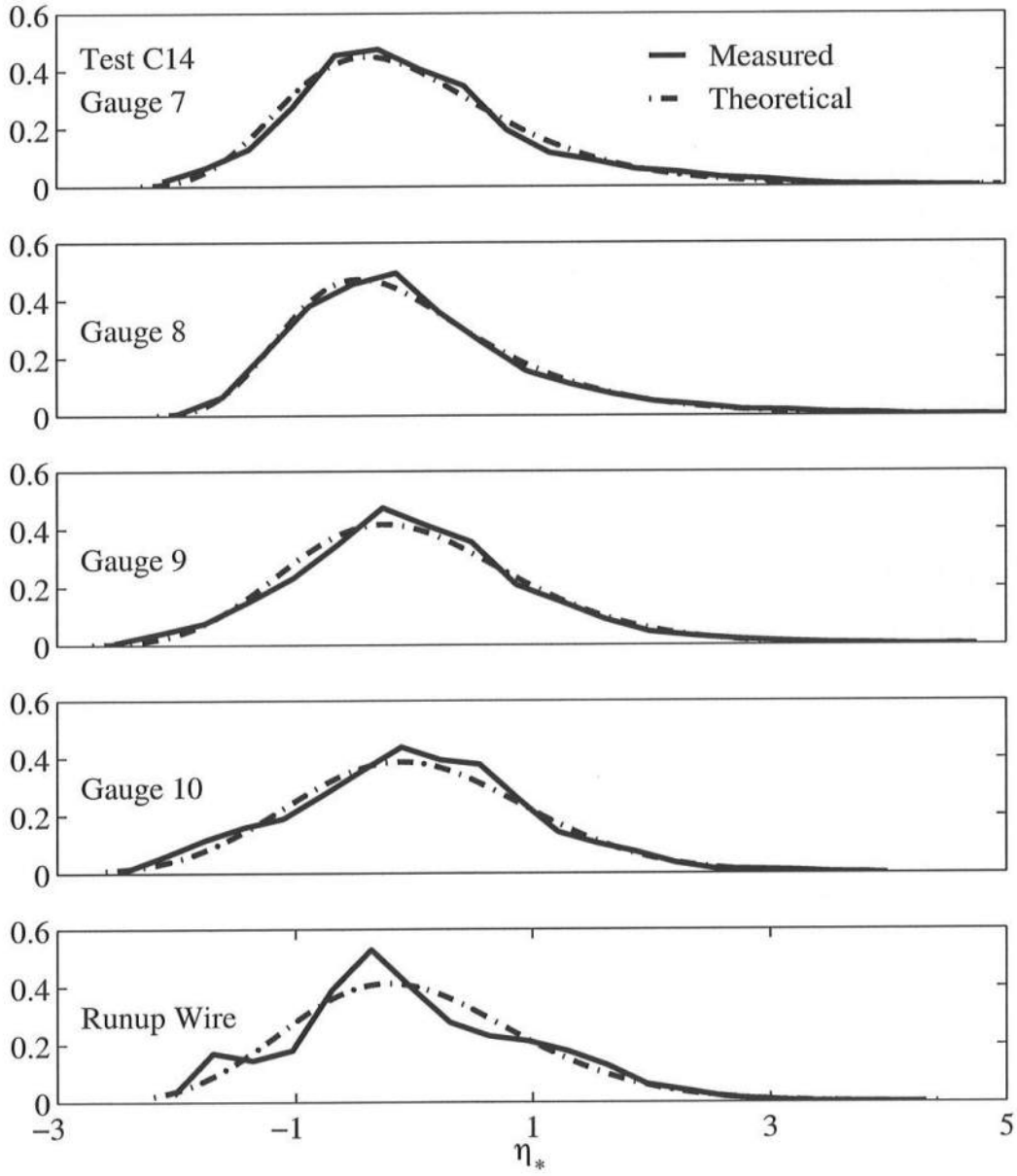

FigureC.48: Free Surface Comparison of Measured Probability Distributions to the Exponential Gamma Distribution for T_p = 1.5 s, d_t.= 14 cm, Gauge 7 – Runup Wire

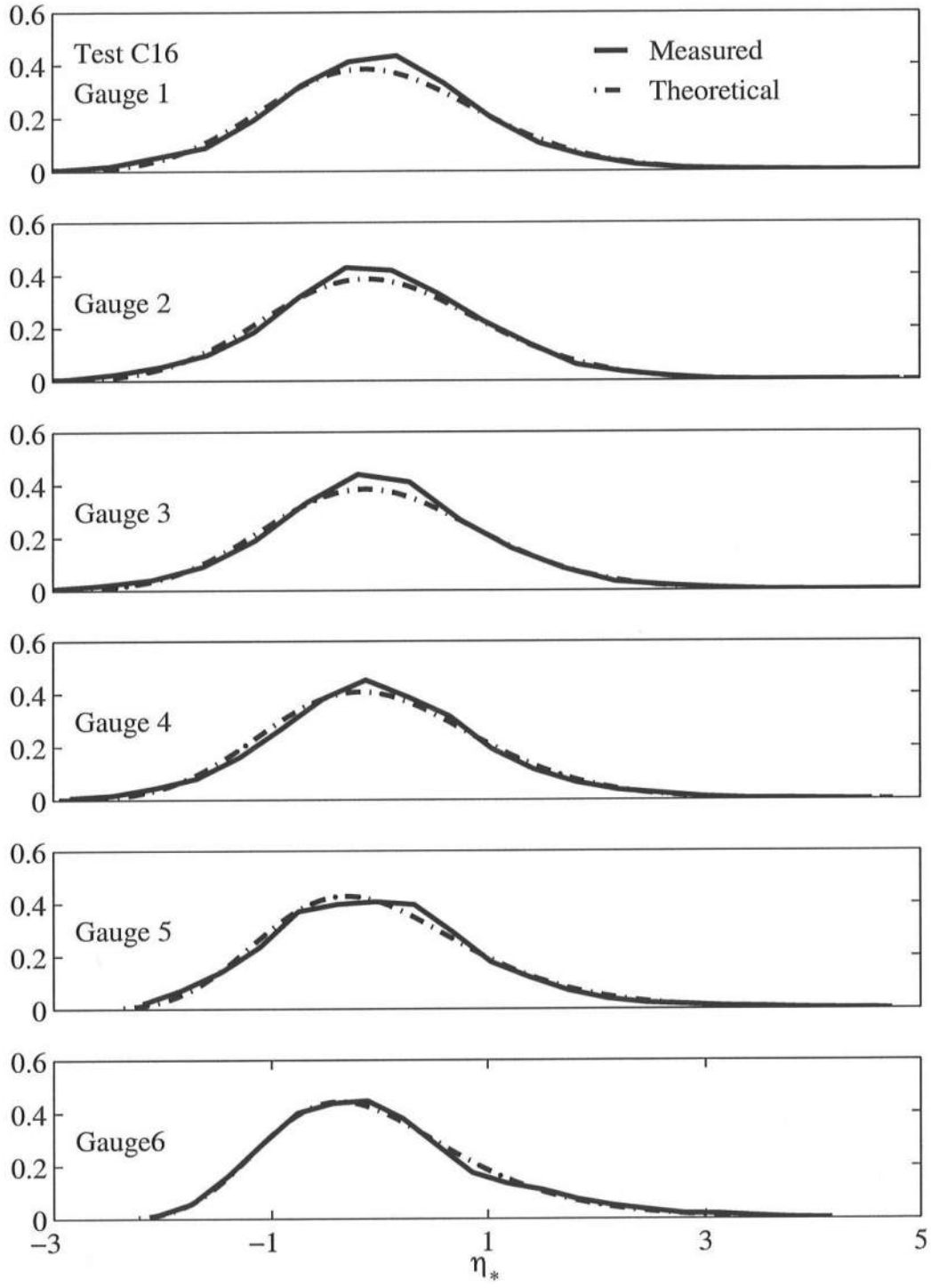

FigureC.49: Free Surface Comparison of Measured Probability Distributions to the Exponential Gamma Distribution for T_p = 1.5 s, d_t.= 16 cm, Gauge 1 – 6.

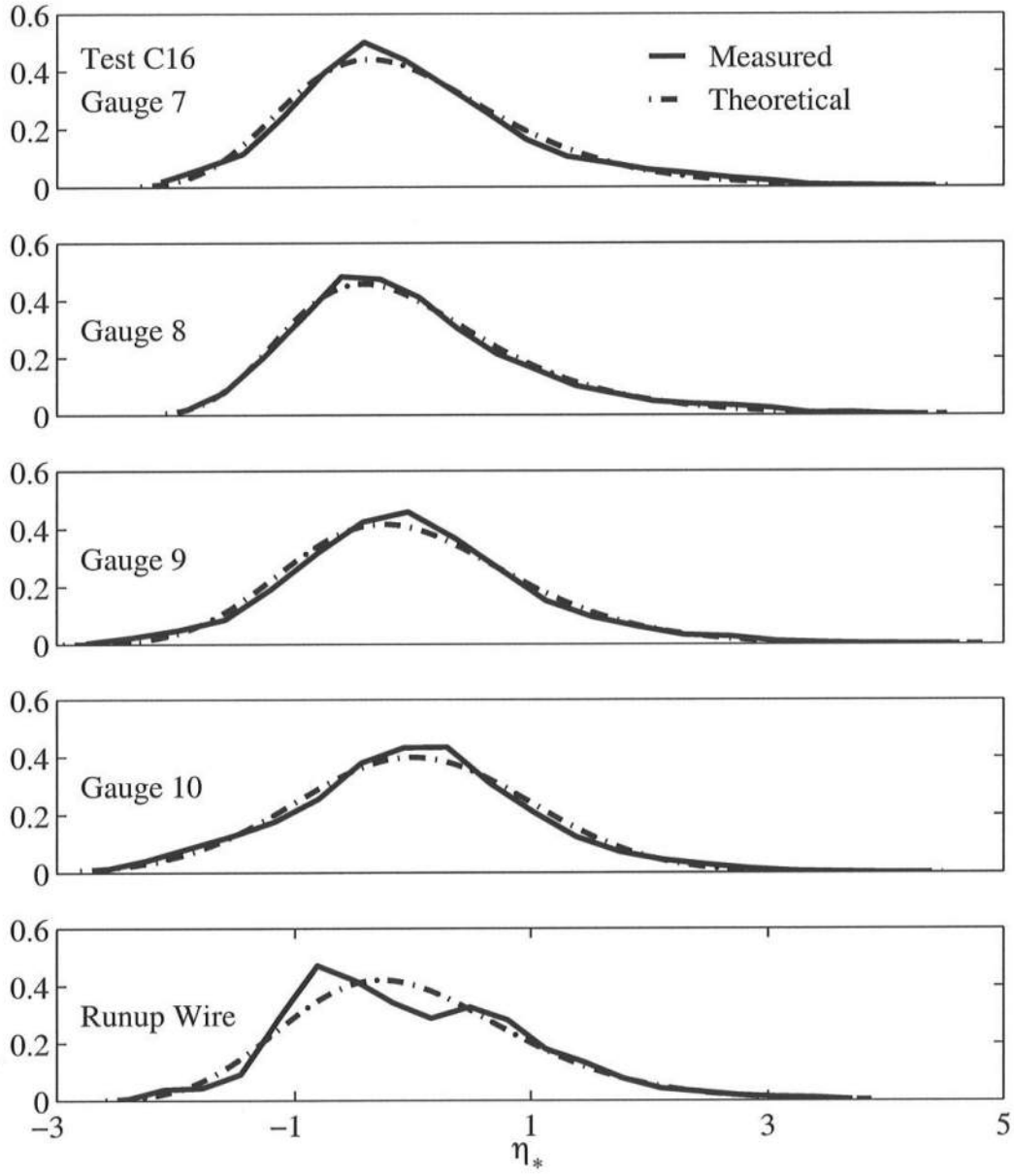

FigureC.50: Free Surface Comparison of Measured Probability Distributions to the Exponential Gamma Distribution for T_p = 1.5 s, d_t.= 16 cm, Gauge 7 – Runup Wire

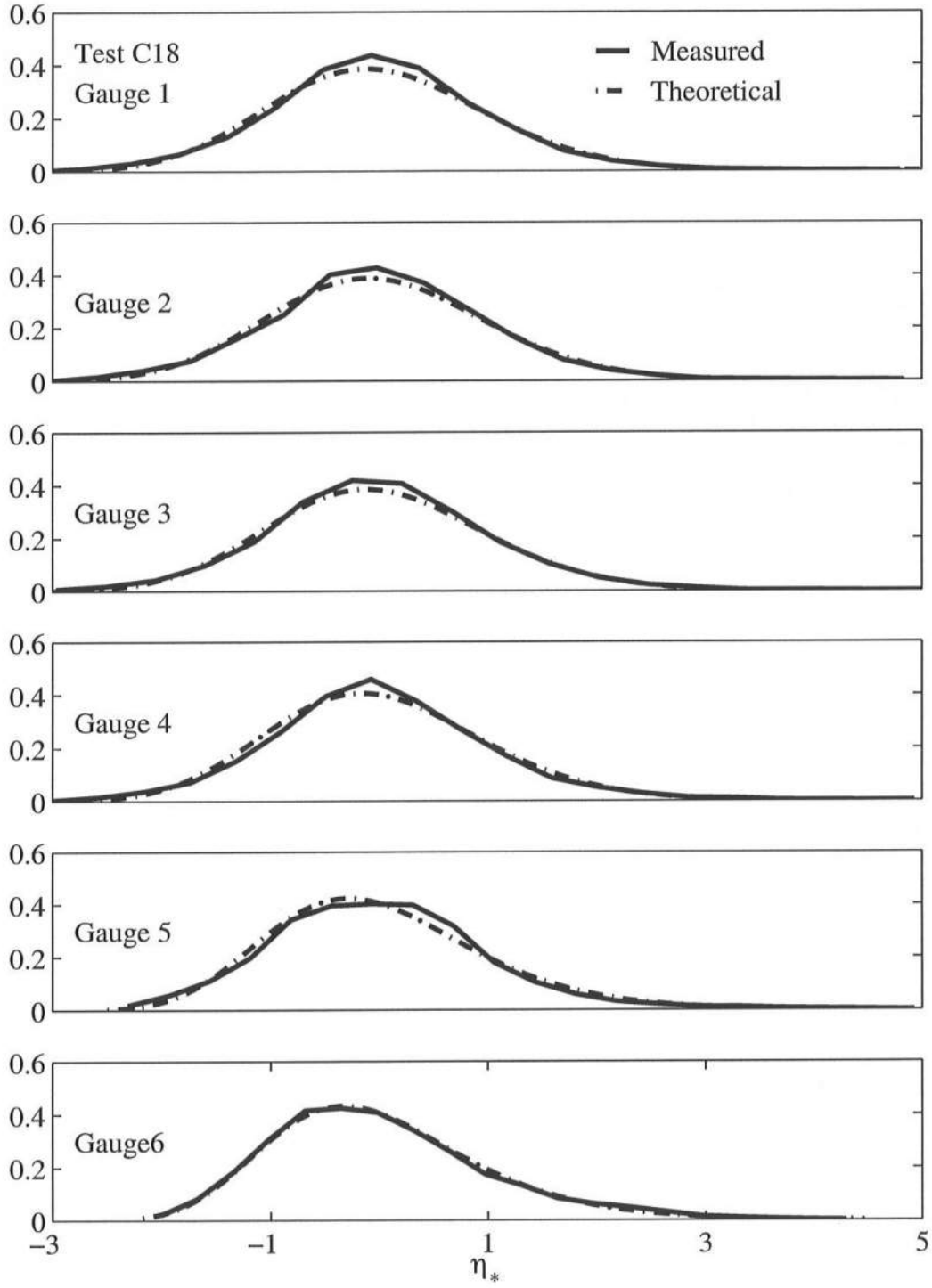

FigureC.51: Free Surface Comparison of Measured Probability Distributions to the Exponential Gamma Distribution for T_p = 1.5 s, d_t.= 18 cm, Gauge 1 –- 6.

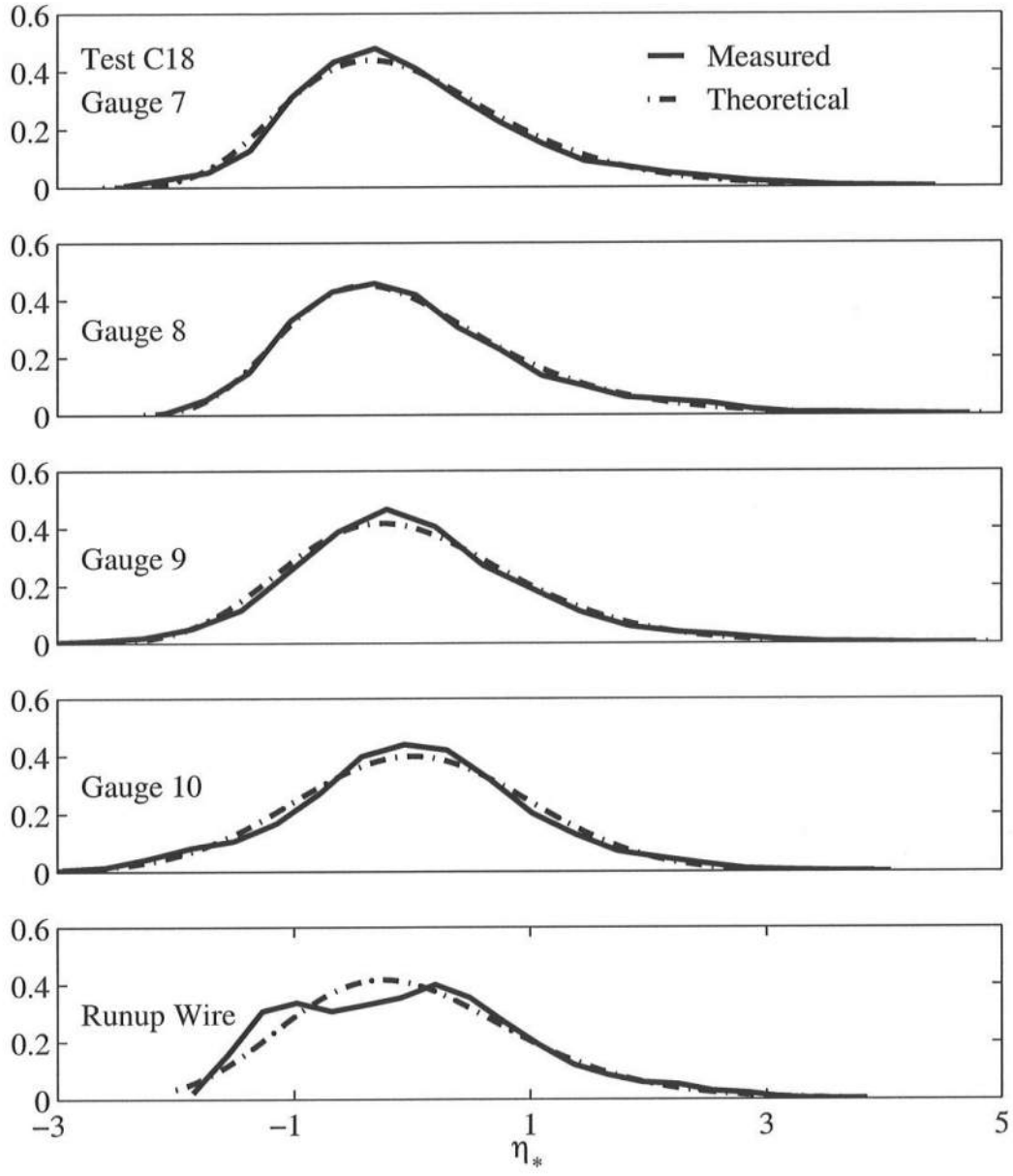

FigureC.52: Free Surface Comparison of Measured Probability Distributions to the Exponential Gamma Distribution for T_p = 1.5 s, d_t.= 18 cm, Gauge 7 – Runup Wire

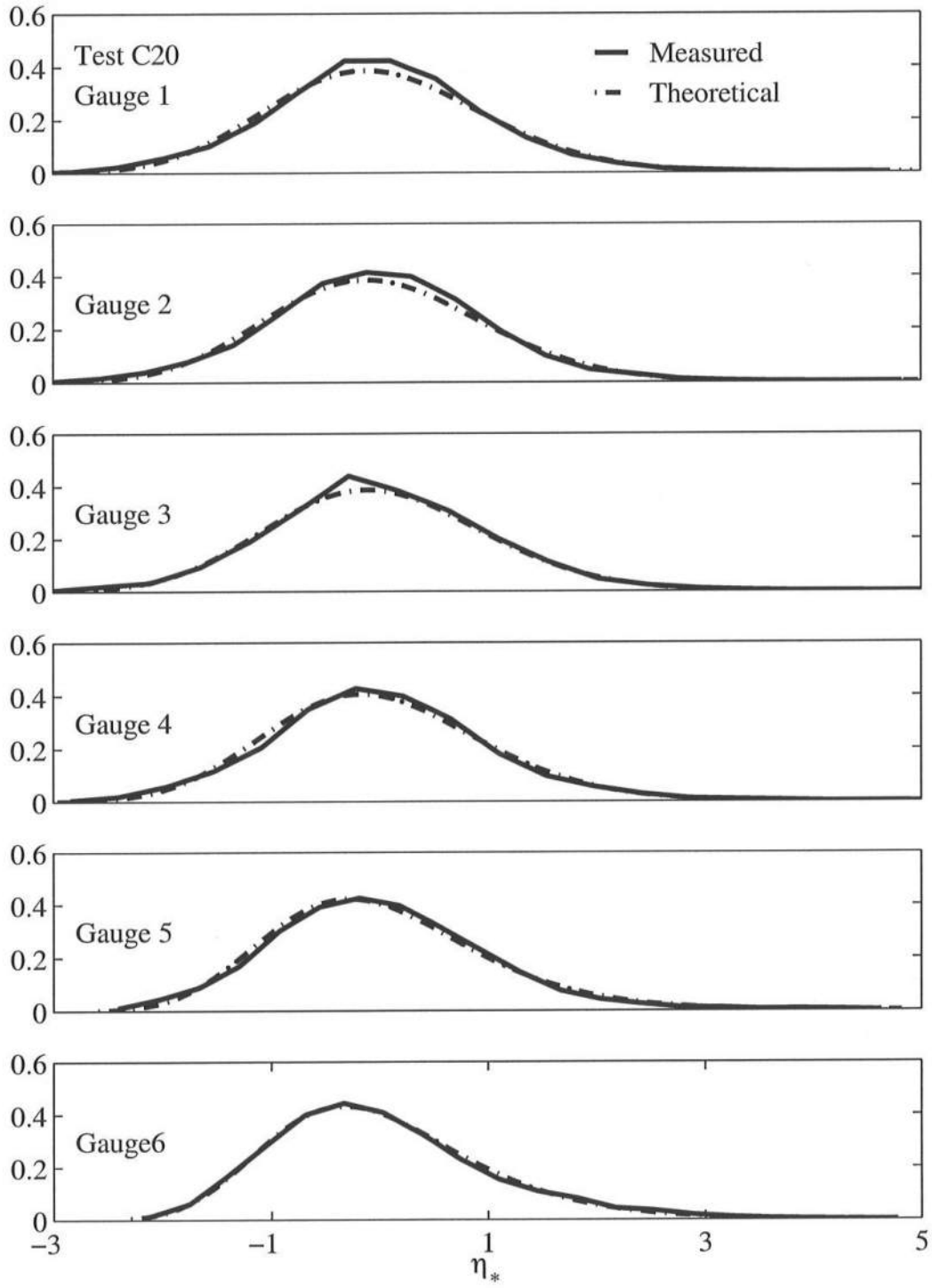

FigureC.53: Free Surface Comparison of Measured Probability Distributions to the Exponential Gamma Distribution for T_p = 1.5 s, d_t.= 20 cm, Gauge 1 – 6.

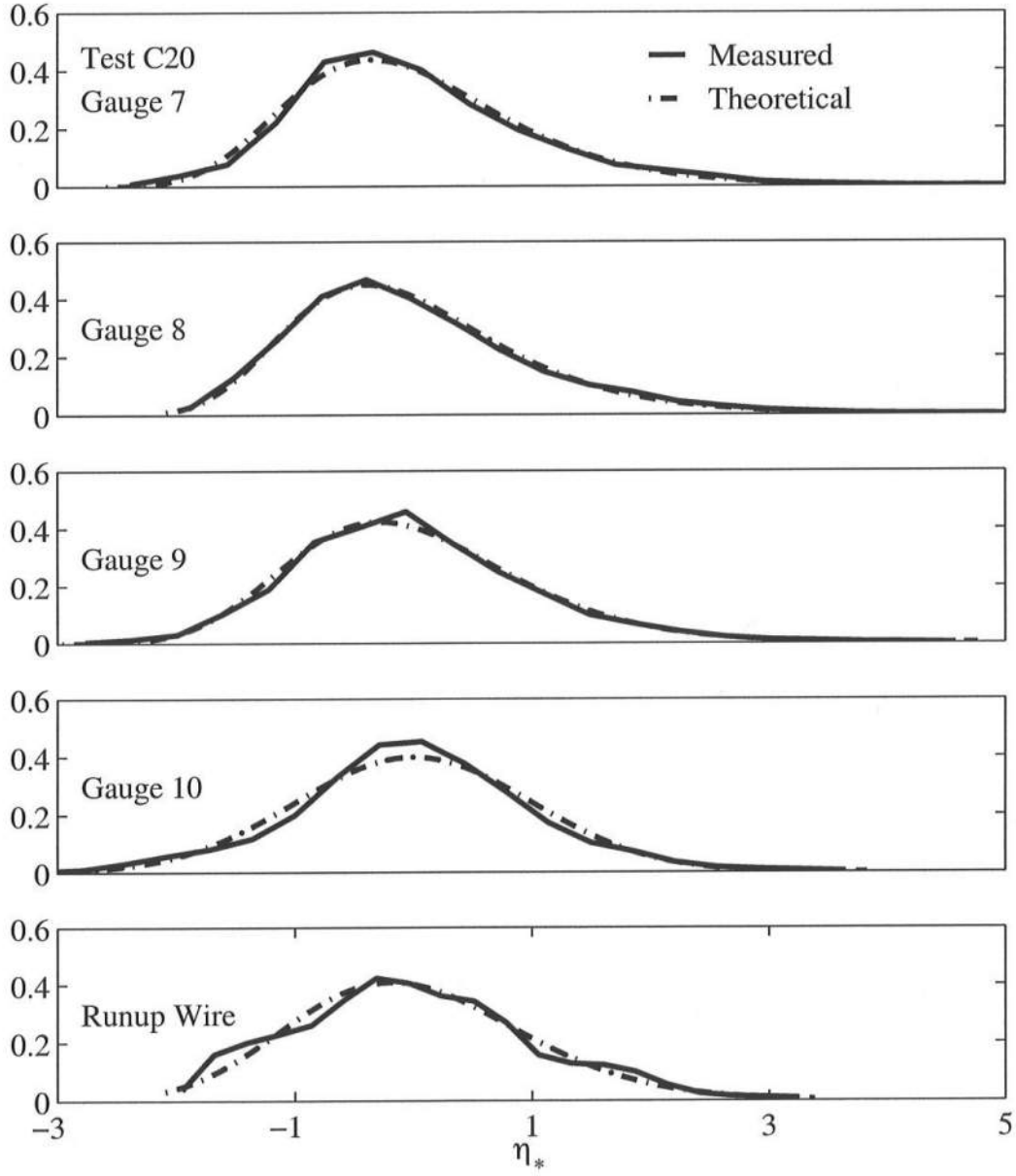

FigureC.54: Free Surface Comparison of Measured Probability Distributions to the Exponential Gamma Distribution for T_p = 1.5 s, d_t.= 20 cm, Gauge 7 – Runup Wire